Space Photovoltaic Research and Technology 1980

High Efficiency, Radiation Damage, and Blanket Technology

NASA

Space Photovoltaic Research and Technology 1980

High Efficiency, Radiation Damage, and Blanket Technology

NASA

FOREWORD

The silicon solar cell has been an essential element in the exploration of space. It can be said with certainty that our present state of knowledge of the universe and our solar system would be virtually non-existent without this device. Throughout the decades of space flight, the silicon solar cell has proven to be outstanding and reliable. Its outstanding performance has also meant that improvements in the device have been incremental rather than radical and that there has been no pressing urgency for new devices with better capability. However, over the past several years, an important shift in photovoltaic device development philosophy has taken place. An atmosphere of new optimism and realization of the potential for radical advance has burst forth in the space community. Thus, it is fitting that the experts working on the forefront of this new wave of exploration meet periodically to establish new goals and directions, to review progress and assess problems, and to exchange information for the benefit of all.

This meeting is the fourth in a series that began in 1974. These meetings, in contrast to other professional society-sponsored conferences, are intended to serve as forums in which the experts in photovoltaics can express their individual and collective judgements on suitable, attainable goals for space solar cells, the barriers remaining, the knowledge needed and the most viable approaches past the barriers to the goals. A strong emphasis is placed on the exchange and discussion of ideas and opinions against the background of technical presentations. The atmosphere is informal, yet structured and individual interaction is encouraged.

A steady evolution in meeting content has occurred since the first meeting was held in November 1974. In that meeting, the primary focus was on efficiency improvement in the silicon solar cell. Improvement of the radiation tolerance of the silicon cell was noted as a major need and potential thrust. In April 1977, at the second meeting, both silicon cell efficiency improvement and radiation damage reduction shared equally and discussions were initiated on the emerging, promising, gallium arsenide solar cell technology. The June 1979 meeting branched into yet another new area--30% conversion. In this meeting, silicon efficiency improvement, radiation tolerance and gallium arsenide cell technology shared equal emphasis. The major conclusions from that meeting were as follows:

Silicon High Efficiency Solar Cells

o Maximum practical efficiency is between 18 and 20%.

o Open-circuit voltage is a limiting barrier, 0.7 V
  a reasonable goal.

o Possible voltage limiting mechanisms list is expanding.

o High beginning-of-life and end-of-life efficiencies are not incompatible.

o Need for silicon with low carbon and oxygen content was stressed.

o Need for round-robin measurements was cited.

Silicon Solar Cell Radiation Damage

o Well-controlled, high purity silicon is needed.

o Defect-and impurity-free processing is desired.

o Basic research still needed on radiation-induced defect structures.

o Increased sensitivity for detecting impurities such as carbon, oxygen and copper is needed.

o Annealing of radiation damage has high potential.

Gallium Arsenide Solar Cell Performance and Radiation Damage

o Maximum efficiency is above 20%.

o Technology improvements and space qualification are needed.

o Cost reductions and high performance cells are possible with both LPE and MO-CVD techniques.

o Radiation tolerance of n-type versus p-type material not established.

o Models that predict cell behavior need further examination.

o Space radiation damage equivalence needs to be established.

30% Devices

o 30% is a reasonable goal.

o Sunlight concentration is desirable but not necessary.

o Tandem cells of III-V materials are the most promising approach.

o MOCVD process appears to be a good tradeoff between versatility, throughput and cost.

o Innovative concepts should be examined.

The 1980 workshop has also added a new area: High Performance Blanket Technology. This is in clear recognition of the parallel blanket developments required to capitalize upon the advances in cell technology presently being achieved. Five workshops were held:

Silicon High Efficiency Solar Cells

Chairman, Andrew Meulenberg, COMSAT Laboratories.

Silicon Solar Cell Radiation Damage

Chairman, Patrick Rahilly, Wright Patterson AFB.

GaAs Solar Cell Performance and Radiation Damage

Chairman, G. Sanjiv Kamath, Hughes Research Laboratories

30 Percent Devices

Chairman, James Hutchby, Research Triangle Institute

Blanket Technology

Chairman, John Scott-Monck, Jet Propulsion Laboratory

An oral report of each workshop was presented and discussed in a plenary session. Written summaries of workshop conclusions prepared by the workshop chairman are included in these proceedings.

The meeting was coordinated by Cosmo Baraona and his committee, Evelyn Anagnostou and George Mazaris. The stimulating comments aroused by the presentations and the resulting discussions made this meeting particularly successful, and the next meeting to be anticipated.

Henry Brandhorst, Chairman
NASA Lewis Research Center

CONTENTS

ix

NASA'S HIGH EFFICIENCY AND RADIATION DAMAGE SOLAR CELL PROGRAM

Lynwood P. Randolph
National Aeronautics and Space Administration
Washington, D. C.

ABSTRACT

The NASA High Efficiency and Radiation Damage (HERD) Solar Cell Program has the objective of improving the conversion efficiency and increasing the end of life efficiency of solar cells and arrays for space applications. The accomplishment of this objective rests upon developing and applying an improved understanding of the conversion of electromagnetic radiation to useful forms of energy. To this end a broad range of advanced concepts are being evaluated.

The research and technology under this program is conducted by four NASA Centers: Jet Propulsion Laboratory (JPL), Langley (LaRC), Lewis (LeRC), and Marshall (MSFC). The elements of NASA program are closely coordinated with similar activities under DOD and DOE sponsorship. This cooperative effort is focussed on a number of key milestones for both cells and arrays as shown in figure. Among these two major components the cell work stresses silicon, gallium arsenide, and multibandgap materials; the array technology includes both planar and concentrator tasks, annealable arrays and advanced systems. In addition related work includes updating the solar cell radiation handbook and maintaining a national testing capability.

The major thrusts of the JPL work are to develop pilot cell production capability for the thin (50mm) Si cell, develop advanced high performance GaAs cells, advance the state-of-the-art of efficient array structures, develop the technology for blankets with a specific power greater than 300 W/kg, develop the technology for concentrator arrays, and to conduct subsystem testing of cells. In addition another important activity is to monitor DOE technology for applicability to space cells.

The LaRC program is devoted at this time to GaAs cell activities. The thrusts include radiation damage and annealing studies, thin cell development using CVD and graphotaxy and developing the technology for high temperature operations.

The LeRC program's major thrust are to produce an 18%-AMO-efficient silicon solar cell, reduce the radiation damage suffered by silicon solar cells in space, develop high efficiency wrap-around contact and thin (50mm) silicon cells for space use, develop GaAs solar cells for concentrator applications, investigate the feasibility of 30% AMO solar energy conversion and develop reliable encapsulants for space blankets.

1

The MSFC activity is focussed on evaluation of advanced systems for high power applications. Current concepts under study are the spectrophoto-voltaics and thermophotovoltaics.

The NASA HERD Program encompasses a range of activities from fundamental science and engineering to applications of advanced technology. The need for future research and technology is evidenced by continuing challenges faced in this important endeavor.

HIGH EFFICIENCY AND RADIATION DAMAGE (HERD)
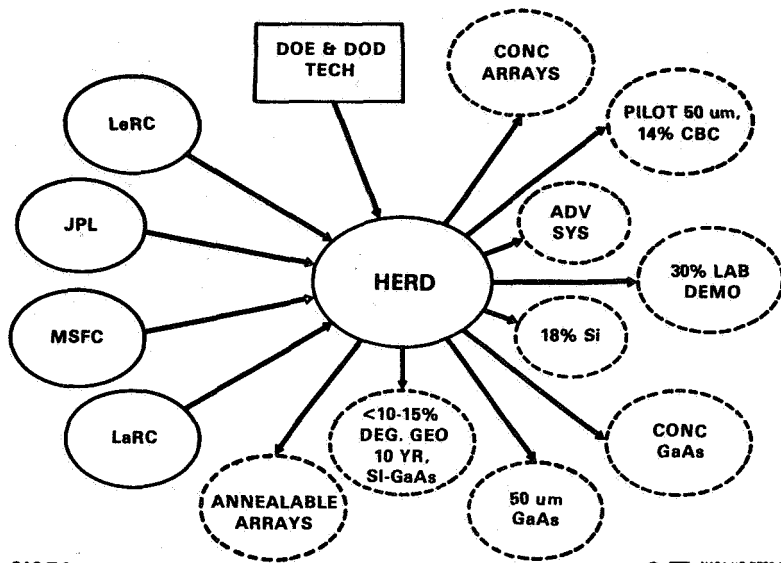
NASA

OAST NASA HQ RT80-4402 (1)
8-1-90

3

SOLAR POWER R&D FOR AIR FORCE SPACE REQUIREMENTS

Joseph F. Wise
AF Wright Aeronautical Laboratories
Wright-Patterson AFB, Ohio

INTRODUCTION

The requirements for improved solar power system technology for DOD satellites have been stated in several studies and conference papers (ref. 1). These summarize requirements up to 100KW by the year 2000 plus need to greatly reduce the power system weight and improve lifetime. Technology is required in several areas including solar cells, array blanket technology, energy storage and power system operation, regulation and control. As the missions become more critical to Defense, we must also address military aspects such as survivability, hardening and eventually, defense.

REQUIREMENTS

The mission areas requiring power system technology advances are shown in Figure 1. The traditional roles of communication, surveillance and navigation will continue and new roles are assigned in areas of weapons. The traditional missions, however, will require more power as follows. Communications will increase in volume as the military increase reliance on satellite systems. We will also need more power to counter jamming threats and also communicate with smaller ground units. Surveillance missions power requirements increase in order to detect aircraft, ground forces and naval units in both greater detail and to handle more traffic. Early candidates for these expanded capabilities are space based radar and deep space surveillance missions using infrared detection. Some of these missions also will operate in very high radiation levels in intermediate altitude orbits and will require hardening to a variety of weapon effects such as nuclear and laser. Figure 2 shows a projection of these requirements.

TECHNOLOGY PROGRAM

The Air Force solar power system technology developments can be divided into three areas: solar cell development, hardening technology, and power system development. I will briefly discuss these three areas:

As you are all aware, we have been working on three basic solar cell thrusts, silicon, gallium arsenide and multibandgap technology. The silicon work, summarized in Figure 3, is aimed at increasing the end of life efficiency as well as reducing weight, hardening to laser weapon effects, and reducing potential costs. Main thrusts at present are the veritical junction solar cell and the development of the cold crucible CZ techniques for growing high purity starting material at reduced costs. Both the Space Division and NASA Lewis are jointly supporting this technology program. The main objectives are high

5

efficiency, 17% BOL and maximum EOL power system, after $5x10^{16}/cm^2$ 1MEV electron equivalent dose to provide technology for the mid altitude orbit missions. The GaAs program, shown in Figure 4, which Lt Masloski will later discuss, addresses higher efficiency, demonstration of flight readiness and development of lower cost technical approaches using web technology and growth on lower cost substrates.

The multibandgap cell technology addresses demonstration of concept feasibility and is aiming for 22 to 25% efficiency with an AlGaAs/GaAs monolythic cell approach. Growth methods include both liquid phase epitaxy and chemical vapor deposition. Dr Rahilly will discuss this area in a later paper. We are also interested in the possibility of bandgap tailoring to optimize the single junction solar cell in hopes of reaching better than 20% efficiency. The area of solar power system hardening to laser radiation effects is briefly summarized in Figure 5. This area deals with two thrusts - (1) increase the temperature capability of all array components by use of welded interconnects, integral coverglass and high temperature adhesive, and (2) minimize energy absorption using reflection and filtering or avoidance. Most efforts in the past dealt with silicon cell technology but as the GaAs cell technology matures, we need to harden it also. Therefore, the advanced cell vulnerability and hardening, integral covers and high temperature contact areas address both GaAs and silicon. We are also re-evaluating concentration concepts as a means to increase system hardness. Most schemes to date involve a reduction in efficiency and increased weight to achieve hardness.

Power system technology is under development and planned by both the Air Force and NASA. To achieve the capability needed in the late 80's to 2000, the programs shown in Figure 6 are in being or planned. The early exploratory development program is basically to define the technology needed to achieve power system weight and life goals and the AD program scheduled for FY 81 is to develop the component technology needed for these advanced systems. Key developments needed are lightweight hardened blanket technology, using thin cells and substrates, high temperature technology in covers, adhesives and interconnections, etc. Much use can be made of some early NASA technology, especially the thin cell work. Newer satellites are planned over a wide spectrum of orbits including between 400NMI and 10,000NMI. These have been shown in the Lockheed programs to date to require withstanding $4.8 x 10^{16}cm^2$/electron equivalent and maximize EOL efficiency. At these dose levels, approaches such as annealing (GaAs and Si) should be investigated. Efforts along these lines will be done as part of our basic investigations studies with such individuals as Dr. Drevinski and Henry D'Angeles of RADC and in close cooperation with the various NASA centers. Power system work in areas of regulation, control, management, energy storage and waste heat utilization and rejection are also planned for development in this program. Component technology development is planned for the next 5 years with a flight type program after that.

SUMMARY

The next two decades will see an evolution in satellite usage to support more critical military missions which will require higher end of life efficiency, lower weight and volume, autonomous operation and hardening to a variety of potential threats. We have in being, programs to provide for this

improved technology. The goals of these technology programs from a system standpoint are shown in Figure 7. Many technology improvements are needed to achieve these goals and they are further complicated by hardening requirements. It is hoped that the results of the three day meeting will assist us in developing and demonstrating technology needed in the next two decades.

REFERENCES

1. E. Tom Mahefkey, Future Space Power - The DOD Perspective, CP# 809016, 15th IECEC, 18-22 August 1980.

Military Space System Functions

SPACE MISSION AREAS	SPACE SYSTEM FUNCTIONS — TIME PERIOD

PRINCIPAL
 	
• INTELLIGENCE COLLECTION & TREATY MONITORING
• STRATEGIC FORCE MANAGEMENT
• THEATER & NAVAL FORCE MANAGEMENT
• ACTIVE DEFENSE
  - OF FRIENDLY SPACE ASSETS
  - AGAINST SPACE-BASED THREAT
  - AGAINST TERRESTRIAL THREAT ?
SUPPORT
 	
• SPACE LOGISTICS
• SATELLITE CONTROL
• PASSIVE DEFENSE
	OBSERVATION — NOW
	
	COMMUNICATIONS
	  • INFO RELAY — NOW
	  • CMD/CONTROL
	
	NAVIGATION — NOW
	
	WEAPONRY — FUTURE?

• CURRENT SPACE SYSTEMS CAN BE REGARDED AS c^3i SYSTEMS

• SPACE WEAPONRY WILL FORCE NEW COMMITMENTS & PERCEPTIONS

FIGURE 1

Power Requirements
1980 - 2000
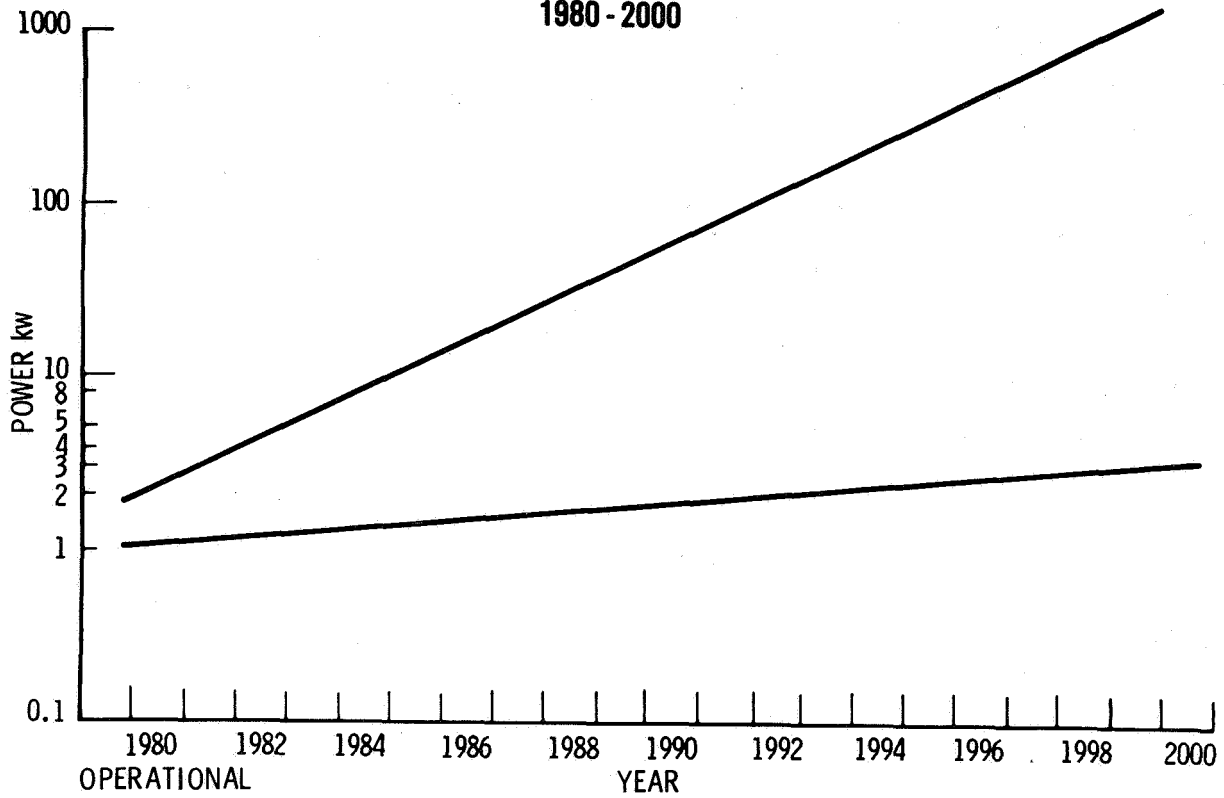
FIGURE 2

SILICON CELL PROGRAMS

WORK UNIT TITLE	FY 80	FY 81	FY 82	FY 83	FY 84	FY 85

SILICON CELL OPTIMIZATION

CZ HIGH PURITY SILICON

HESP-Si-PHASE 2

INTEGRAL COVER EFFORT

IN HOUSE EVALUATION/ ANALYSIS

FIGURE 3

8

III-V PROGRAMS

WORK UNIT TITLE	FY 80	FY 81	FY 82	FY 83	FY 84	FY 85
HESP-GaAs-PHASE 2	▭					
GaAs PANEL	▭▭▭▭▭					
GaAs SHEET DEVELOPMENT	▭▭▭					
LOW COST GaAs CELLS		▭▭▭▭▭▭▭				
MULTIBANDGAP (RI)	▭					
MULTIBANDGAP (RTI)	▭					
CASCADE CELL ADV. DEV.				▭▭▭▭▭		
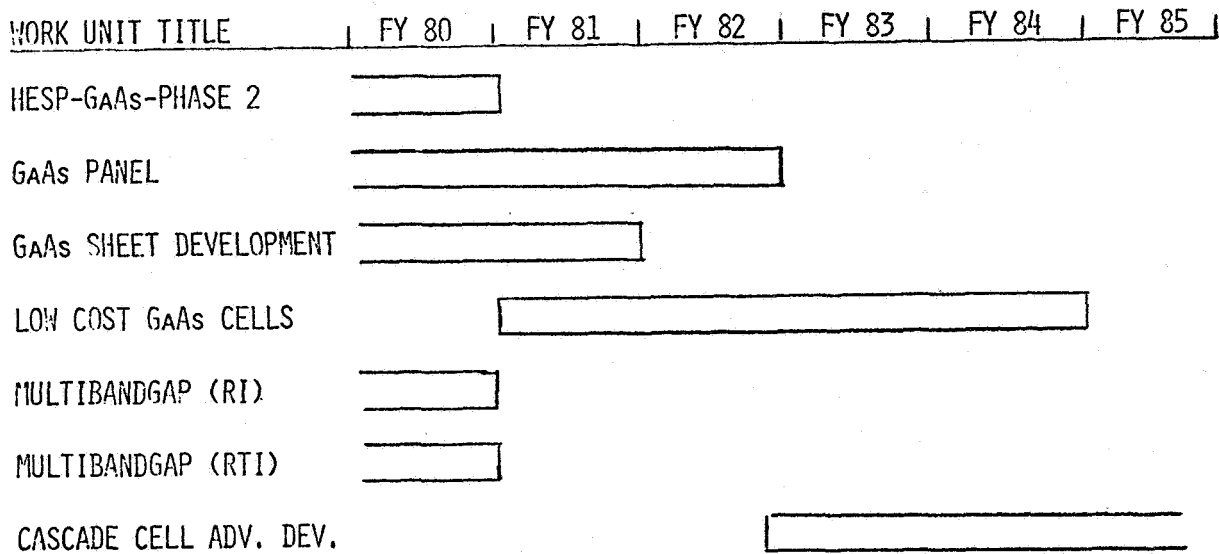
FIGURE 4

HARDENING PROGRAMS

WORK UNIT TITLE	FY 80	FY 81	FY 82	FY 83	FY 84	FY 85
ESB OPTIMIZATION	▭					
HIGH TEMP. ADHESIVES		▭▭▭▭				
VUL/HARDENING ADV. CELL	▭▭▭▭▭					
HIGH TEMP. CONTACT METALLIZATION		▭▭▭▭▭				
MULTI-THREAT HARDENING			▭▭▭▭▭			

FIGURE 5

9

WORK UNIT TITLE	FY 80	FY 81	FY 82	FY 83	FY 84	FY 85

HI VOLTAGE HARDEN.
 POWER SYS.

HI VOLTAGE HI POWER
 SYSTEM

EXPLORATORY CONCENTRATOR
 STUDY

CONCENTRATOR CELL/PANEL
 DEVEL.

ADV. DEV. CONCENTRATOR
 STUDY

SPACECRAFT POWER
 PROCESSING
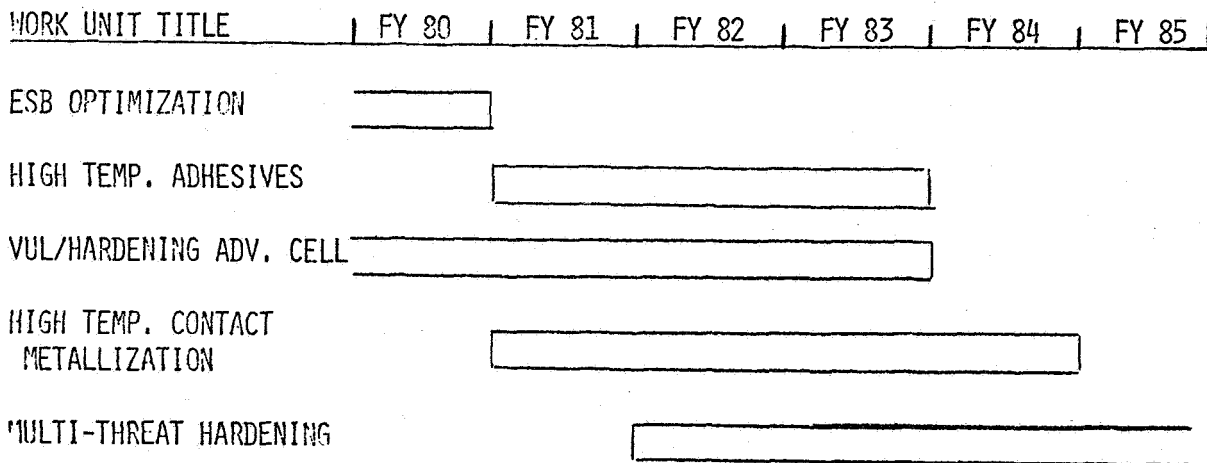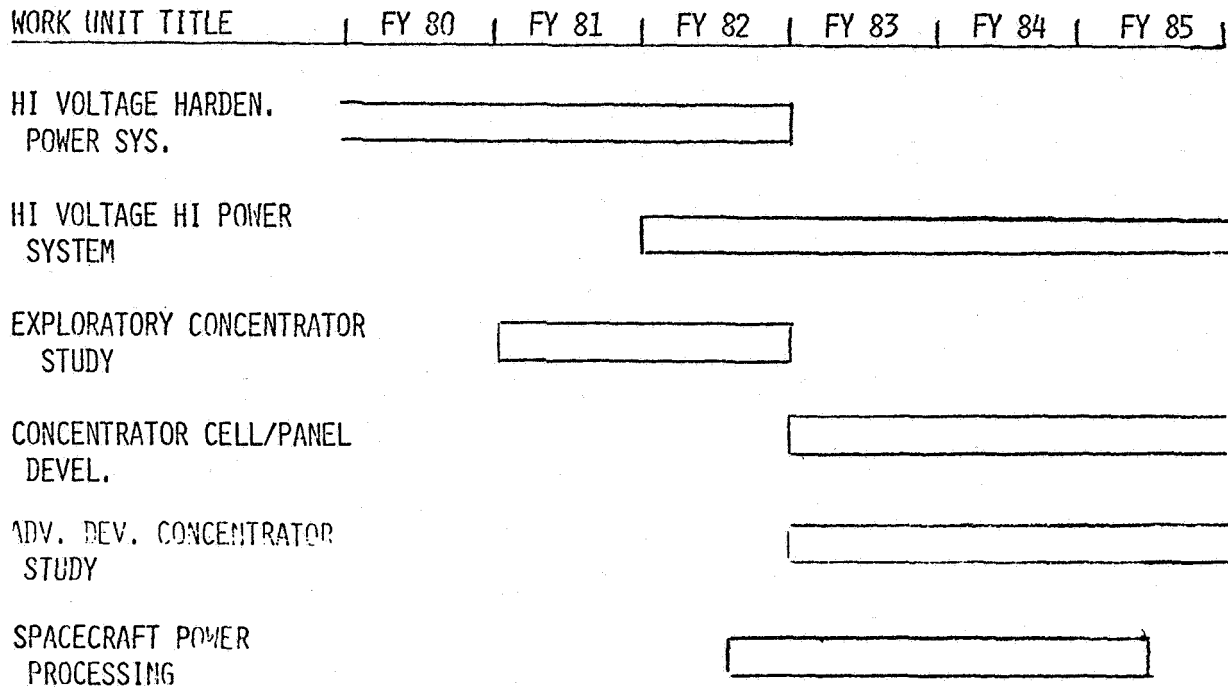
FIGURE 6

SOLAR POWER SYSTEMS

Ni-Cd   7 WHR/LB GEO
        4 WHR/LB LEO

HEDRB   50 WHR/lb GEO
        25 WHR/LB LEO

Ni-H$_2$ 15 WHR/LB GEO
          7 WHR/LB LEO

16% → 20% GaAs

10% → 14% SI

22% → 30 MBG

SPECIFIC POWER (W/LB)

SPECIFIC POWER (W/KG)

1970   1980   1990   2000

FIGURE 7

10
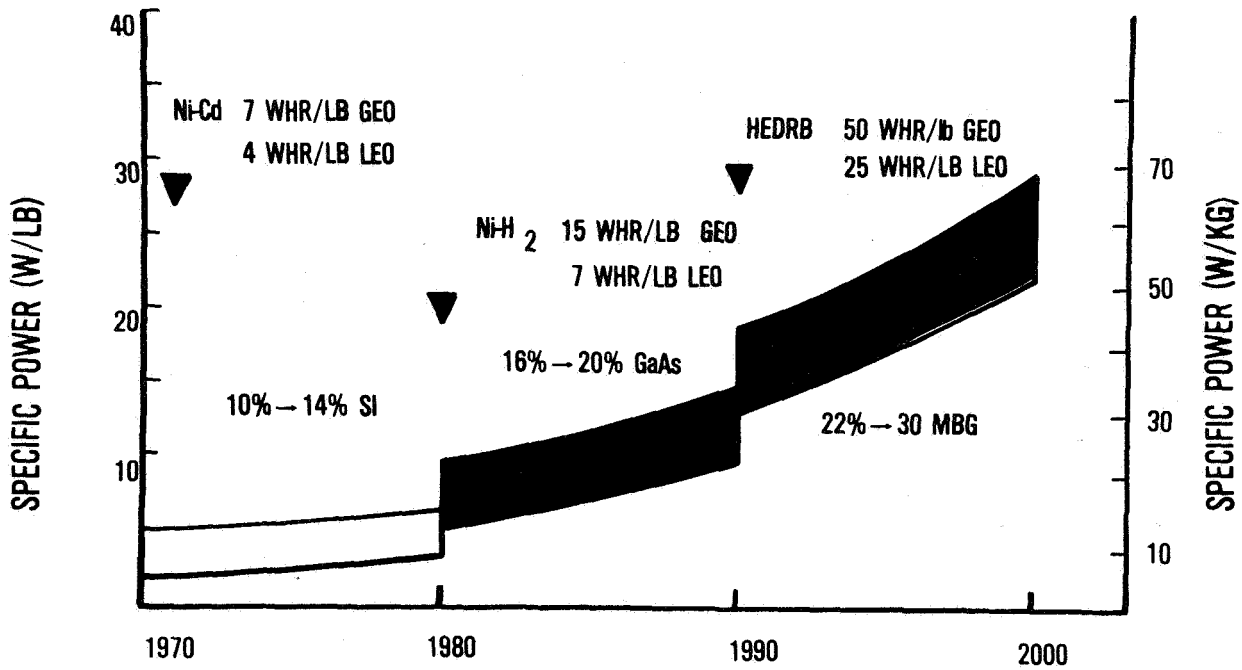
RECENT PROGRESS IN HIGH-OUTPUT-VOLTAGE SILICON SOLAR CELLS*

A. Meulenberg, R. A. Arndt, and J. F. Allison
COMSAT Laboratories
Clarksburg, Maryland

and

V. Weizer
NASA Lewis Research Center
Cleveland, Ohio

High-quality shallow-junction planar solar cells have been fabricated on 0.1 Ω-cm float zone refined silicon using Emulsitone N250 spin-on dopant, aluminum-alloyed back contacts, and "dot" contact front grids (ref. 1). Use of a process similar to the NASA-Lewis double-diffusion process (ref. 2) has reduced shunt leakage and junction recombination currents while adding 10 mV to the best open-circuit voltages obtained from the single-diffusion process.

The present status of a 0.1-Ω-cm covered solar cell (153-mA short-circuit, 654-mV open-circuit voltage, 77.5-mW maximum power, and 14.4-percent AM0 efficiency) is characterized in figure 1 before and after covering. The short-circuit current (ISC) is about 6 percent less than that observed in typical higher resistivity ($\geq$1-Ω-cm) violet cells (ref. 3) but the open-circuit voltage (VOC) is about 9 percent higher. During covering or subsequent handling, the cell fill factor was reduced in an unexplained manner (analysis indicates a lowered shunt resistance). If it had been maintained, the maximum power would have exceeded 79.5 mW.

The quantum-yield data are presented in figure 2 along with data from a deeper junction cell ($x_j \sim 1.6$ μm) from the same batch and a shallow junction ($x_j \sim 0.1$ μm) cell made by a different process. An important feature of this figure is the unusual shape of the set A curves. A conventional cell with a surface dead layer displays a much more abrupt drop in the short wavelength region rather than the more gentle the slopes observed in figure 2 below 700 nm. It would appear that the double-diffusion process alters the cell characteristics in a manner quite different than expected from a simple change in the diffused layer (see ref. 2 for a possible explanation). Set A had an overnight diffusion with N250 at 880°C followed by different etch times prior to an N250 diffusion at 820°C for 15 minutes; set B was diffused with N250 at 820°C for 15 minutes.

The advantages of a 2-step diffusion process are delineated by comparisons of the data from two sets of cells (table I). The data indicate several differences resulting from a prediffusion; most important are a 10-mV increase in VOC and an improved fill factor of set A. The improved VOC is explained by the lower bulk dark current (JD); the better fill factor (FF) is

due to the lower preexponential of the n = 2 term (JRC) and higher shunt resistance (RSH). The penalty is reduced ISC and blue response (IB), as seen in figure 2. The long wavelength response ($\lambda \gtrsim 1000$ nm) and the currents (I_γ) from γ-ray irradiation of the two sets are nearly equal and indicate diffusion lengths comparable to or greater than the cell thickness (200 μm). This point is supported by the values of ISC in set B, which are almost as high as those for 1- to 2-Ω-cm violet cells.

Efforts are continuing to better understand the mechanism responsible for increased voltage resulting from the double-diffusion process. Once this mechanism is understood, work can be directed toward further voltage gains and reduction of short-circuit current losses.

REFERENCES

1. Lindmayer, J.; and Allison, J. F.: Dotted Contact Fine Geometry Solar Cell. U.S. Patent 3,982,964, Sept. 28, 1976.

2. Godlewski, M. P.; Klucker, T. M.; Mazaris, G. A.; and Weizer, V. G.: Open-Circuit Voltage Improvements in Low Resistivity Solar Cells. 14th IEEE Photovoltaic Specialists Conference, Jan. 7-10, 1980, San Diego, CA, Proc., pp. 166-171.

3. Haynos, J.G.; Allison, J. F.; Arndt, R. A.; and Meulenberg, A.: The COMSAT Non-Reflective Silicon Solar Cell: A Second Generation Improved Cell, International Conf. on Photovoltaic Power Generation, Sept. 1974, Hamburg, Germany, Proc., pp. 487-500.

Table I. UNCOVERED CHARACTERISTICS OF A BATCH OF SINGLY DIFFUSED CELLS (SET B) AND A BATCH OF DOUBLY DIFFUSED CELLS (SET A)

Cell No.	Process	ISC (mA)	VOC (mV)	IB (mA)	F.F.	I_γ [a]	JD (pA)	JRC (nA)	RSH (Ω)
				Set A					
1	N250	130.4	647	29.6	0.82	6.9	0.32	20	365
2	1.6 μm	123.7	642	27.9	0.80	6.8	0.37	32	111
3	N250	133.9	640	33.3	0.80	6.6	0.44	32	1 K
4	~0.9 μm	136.7	646	33.5	0.80	6.7	0.35	31	540
5	N250	142.8	644	37.3	0.80	6.5	0.40	36	1 K
6	~0.3 μm	143.1	646	37.2	0.80	6.6	0.35	43	1 K
7	N250	142.8	648	37.5	080	6.5	0.31	50	1 K
8	~0.15 μm	142.6	650	37.3	0.80	6.2[c]	0.3	39	1 K
				Set B					
1	N250	149.3	629	41	0.73	6.8	0.54	111	46
2	N250	150.8	630	40.8	0.71	7.2	0.54	110	37
3	0.1 μm	150.1	637	40.8	0.77	6.8	0.46	88	134
4		149.2	634	41	0.73	6.4	0.47	97	49

[a] An I_γ of 7.0 corresponds to a diffusion length of $\geqq 180$ μm.
[b] Variable etch depth.
[c] Measured with coverslide.
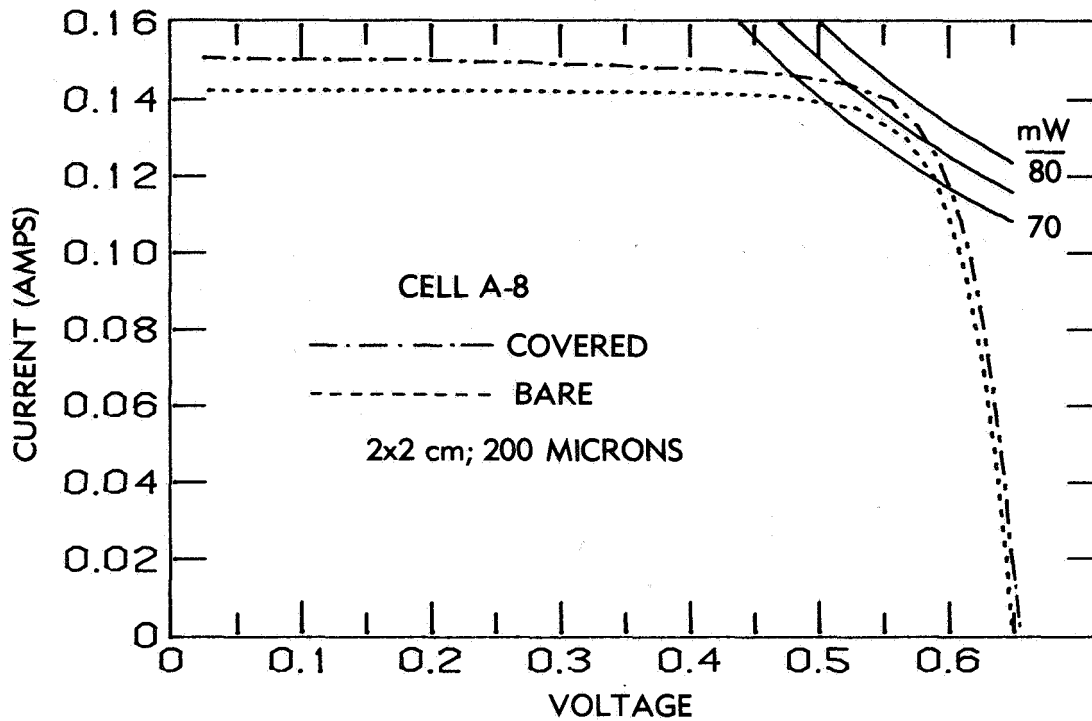
Figure 1. IV Curves for Cell Set A-8 Bare (Dots) and Covered
(Broken) Under Simulated AMO Conditions
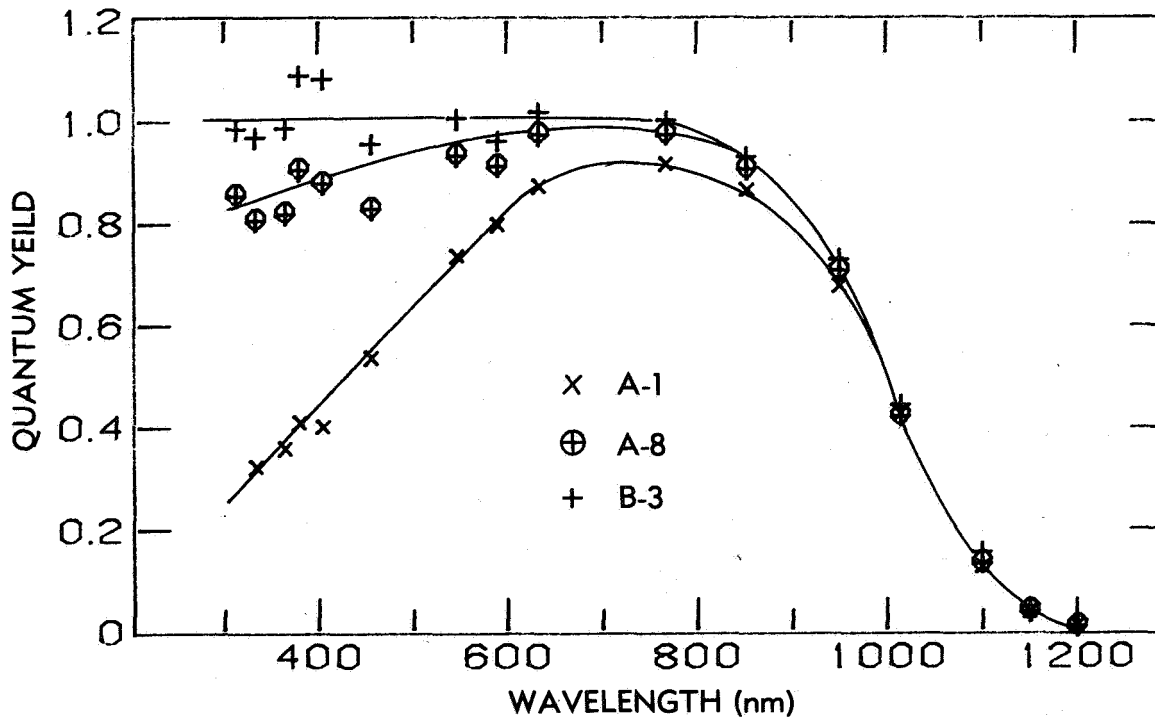
Figure 2. Quantum Yield Results for Cell A-8 (x $_j$ ≅ 0.15 µm) along
with Shallow (B-3) and Deep (A-1) Junction Cells

14

A COMPARISON BETWEEN PULSED AND CW LASER ANNEALING
FOR SOLAR CELL APPLICATIONS

G. E. Jellison, Jr., R. T. Young, and R. F. Wood
Oak Ridge National Laboratory*
Oak Ridge, Tennessee

and

A. Gat
Coherent Laser, Inc.
Palo Alto, California

ABSTRACT

It has been shown previously that pulsed laser annealing is an excellent technique for emitter fabrication in solar cells. Here it is shown that using shallow ^{75}As implantation (5 keV), plus the addition of a back-surface field and a gettering step, solar cell efficiencies of 16.6% have been obtained. Our initial attempts at fabrication of solar cells from CW laser-annealed material resulted in cells of inferior quality compared to cells fabricated using pulsed laser annealing techniques; this was because the CW laser annealing introduced recombination centers well into the base region of the cells.

INTRODUCTION

Over the last few years, it has been shown that pulsed laser annealing is an excellent technique for solar cell processing (refs. 1 and 2). Pulsed laser annealing is superior to conventional thermal annealing for 1) removal of lattice damage after ion implantation, 2) restoration of electrical activity, and 3) the preservation of the minority carrier diffusion length in the base region. It is widely believed that pulsed laser annealing involves the melting of the front damaged layer, followed by epitaxial regrowth from the perfect single crystal substrate. The resultant dopant profiles are usually considerably broadened from the preannealed condition; this broadening is readily explained by the melting model (see ref. 3). In addition to laser annealing of ion-implanted material, two other laser-assisted junction formation techniques have been employed: 1) laser-induced diffusion of deposited dopant films, and 2) laser-induced recrystallization of doped amorphous films (see ref. 1).

Continuous wave (CW) laser annealing has also been useful for the anneal-
ing of ion-implanted emitter regions (ref. 4). However, CW laser annealing
apparently takes place via a solid-phase recrystallization process, which does
not change the initial dopant profile appreciably (ref. 5). This allows one to
obtain extremely shallow junctions (< 200 nm), but results in a Gaussian emit-
ter profile, which is less than optimum for solar cell applications, and also
introduces several deep-lying defect states which can act as recombination cen-
ters (ref. 6).

This paper presents the latest results of our studies of the use of laser
processing in solar cell fabrication. In particular, we will present a process
developed at Oak Ridge National Laboratory for the fabrication of a 16.6% sili-
con solar cell using pulsed laser processing. Also, we will present results
comparing pulsed laser annealing with CW laser annealing in solar cell fabrica-
tion.

HIGH EFFICIENCY SOLAR CELLS FROM PULSED LASER PROCESSING

Table 1 outlines the process that we have used for the fabrication of high
efficiency silicon solar cells using pulsed laser processing on 10 Ω-cm sub-
strates. The first step is ion-implantation using 5 keV As (n-on-p cells) or 5
keV B (p-on-n cells). This step results in a Gaussian impurity distribution
profile with peaks < 20 nm deep; however, the front surface is either highly
damaged (for the case of B) or amorphous (for the case of As), and the impuri-
ties are not fully electrically active. The laser annealing (step 3) is per-
formed in air with a Q-switched ruby laser (λ = 694 nm, pulse width 15 ns)
and with the substrate heated to 400°C. This results in nearly perfect recrys-
tallization of the emitter region. The back side gettering (step 4) is per-
formed to enhance the base minority carrier diffusion length. A high energy
laser pulse (2.2-2.5 J/cm^2) is passed through a rough ground glass diffuser
plate to homogenize the beam before it impinges on the sample. This pulse
results in random but evenly distributed surface damage and introduces a high
density of dislocations. The sample is then heated in an oxygen atmosphere at
1000°C for 1 h; this gettering step improves the minority carrier diffusion
length from 100 μm to 400 μm in the best cases. The back-surface field (step
6) is then fabricated by the deposition of 10 nm of B or Sb followed by laser
irradiation with a 1.8 J/cm^2 pulse. Fabrication of the finished cell is then
completed by steps 7-10.

Our progress in the fabrication of solar cells using laser annealing tech-
niques is outlined in Table 2. With just As implantation followed by laser
annealing, cells with efficiencies up to 15.1% have been obtained (all solar
cell parameters quoted were measured using a calibrated AM1 solar cell simula-
tor). The total cell area is $\sim$ 2 cm^2); if a back-surface field is added by
laser-induced diffusion, cells with efficiencies up to 16.1% can be obtained.
The addition of the gettering step (steps 4 and 5) results in efficiencies of
16.6% and an open circuit voltage of 605 mV.

It should be noted that we use a single-layer Ta$_2$O$_5$ antireflection coating
and no special solar cell geometries are employed. In spite of this, we

16

achieve very high cell efficiencies. For these reasons, we believe that laser techniques will prove to be extremely useful for the manufacture of high-efficiency solar cells.

COMPARISON OF PULSED AND CW LASER PROCESSING TECHNIQUES

Solar cells were fabricated from p-type substrates (10 Ω-cm), ion-implanted with As at 100 keV, and CW laser annealed using an argon-ion laser. The laser power was 11 watts, with a spot size of 100 μm, a scan rate of 25 cm/sec and a 50 μm lateral step after each scan. A back-surface field was fabricated by depositing B (10 nm) on the back of the cell and pulse laser annealing with a 1.8 J/cm^2 pulse (step 6 of Table 1). In addition to this procedure, some of the CW laser-annealed cells were subjected to a 700°C furnace anneal for 1 h. For comparison purposes, similar solar cells were fabricated using pulsed laser annealing techniques but with no gettering step (steps 1-3, 6-10 of Table 1). Three different implantation doses at 5 keV and one dose at 25 keV As implants were used. As mentioned above, CW laser annealing is a solid-phase epitaxial process that results in negligable dopant redistribution (refs. 4 and 5). Therefore, in order to get similar junction depths ($\sim$ 200 nm), a higher energy As implant had to be employed for the CW laser-annealed samples than for the pulsed laser-annealed samples. The resulting solar cell parameters are shown in Table 3. The results quoted for cells fabricated using pulsed laser annealing techniques were averaged over 2 to 4 cells, while the results quoted for the CW laser-annealed cells are for the best cells. Clearly, the pulsed laser-annealed cells perform better than the CW laser-annealed cells: both V_{oc} and J_{sc} are less in the CW laser-annealed samples, compared with the pulsed laser-annealed samples, though a 700°C furnace anneal for 1 h increases both V_{oc} and J_{sc} somewhat. Note also that V_{oc} is decreased in the pulse laser-annealed cells if the As acceleration voltage is increased from 5 keV to 25 keV, though J_{sc} remains constant.

A further comparison can be made by examining the spectral response (or quantum efficiency) data (shown in Fig. 1) for cells with no AR coating. As can be seen, the CW laser-annealed cells have a lower quantum efficiency than the pulsed laser-annealed cells at all wavelengths. A 700°C furnace anneal increases the quantum efficiency somewhat at all wavelengths, but this increase does not compare to the increase achieved using pulsed laser annealing. The poor blue response of the CW laser-annealed cells indicates very poor collection efficiency in the emitter region, while the poor red response is attributed to a low value of the minority carrier diffusion length in the base. Note that the CW laser-annealed cells were fabricated on different substrates than the pulsed laser-annealed samples, and the minority carrier diffusion length should not be expected to be the same.

Figure 2 a), b), and c) show the spectral response data for each individual cell, along with a calculated spectral efficiency. The calculated curve was obtained using a simple abrupt junction solar cell model with 9 parameters (H = cell thickness; W = depletion width, Xj = junction depth; Se, Sb = surface recombination velocity of the emitter and the base regions; Le, Lb = minority carrier diffusion length of the emitter and the base region; De, Db = the

diffusion coefficient of the emitter and the base regions.) Many of the parameters (H, W, Xj, De, Db) are known for each individual cell and were not varied, the absorption coefficient and reflectivity were taken from known data, and the back-surface field was modeled by setting Sb small (= 10^2 cm/sec), thus leaving 3 parameters to be determined (see Table 4) by minimizing the difference between the calculated and experimental points. The results of the modeling (shown in Fig. 2 and Table 4) indicate that: 1) It is necessary to eliminate the contribution of the emitter region of the CW laser-annealed cells in order to fit the blue response of these cells. 2) The minority carrier diffusion length required to fit the response of the CW laser-annealed cells was 100 µm (without furnace anneal) and 130 µm (with furnace anneal). 3) It was impossible to fit the data for the CW laser-annealed sample without post furnace anneal in the region from 0.5 to 0.85 µm using this simple model; this is possibly due to a layer of defects lying just below the depletion region (see the data described below) apparently produced by the CW laser annealing process.

Specific defects in CW laser-annealed material can be identified from DLTS (Deep Level Transient Spectroscopy) data. For the DLTS measurements, samples were prepared from the original solar cells by etching mesa diodes. One sample was fabricated by pulsed laser annealing a sample which had previously been CW laser annealed. Sample DLTS spectra are shown in Fig. 3 for the CW laser-annealed samples. No DLTS signal was observable from samples which had only been pulsed laser-annealed, and only a weak signal was observable in the CW laser-annealed sample after a 700°C furnace anneal. There are 3 traps observable: 2 (or more) electron (or minority carrier) traps, and 1 hole (or majority carrier trap).

The trap E-2 was observable only in the CW laser-annealed sample which had not also been pulsed laser annealed: Clearly the laser pulse annealed it out. Also, it has a broad spectrum, which indicates that it is in reality several traps. No further characterization of this trap was attempted.

The DLTS data for the traps E-1 and H-1 are presented in Table 5. Trap E-1 is a minority carrier trap close to the conduction band. It has a large minority carrier capture cross section, but once filled, a small majority carrier (or recombination) capture cross section. The pulsed laser annealing does not remove all of the E-1 traps, since the melt front produced by the ruby laser penetrates to a depth of less than 1 µm (ref. 3). By comparison, at a bias of -8V, the depletion regions of all our diodes extend to 4 µm beyond the junctions (the depletion region is the region of detectability in DLTS). Therefore, one would expect a maximum of ∿ 25% of the traps to be annealed out with the laser pulse, if the traps are evenly distributed throughout the depletion region. This is just what is observed. A trap with approximately this energy has been seen previously in CW laser-annealed samples (ref. 6), and in samples irradiated with electrons (ref. 7); it has been tentatively assigned to the familiar oxygen-vacancy complex, or A-center.

Trap H-1 is a majority carrier (or hole) trap, which lies closer to the conduction band than the valence band. It also is not removed by the pulsed laser-annealing process, but is removed by the furnace anneal. It has a majority carrier thermal capture cross section of 4 x 10^{-18} cm^2. To our knowledge, this trap has not been observed previously.

CW laser annealing has been shown to be useful for many semiconductor device fabrication applicatons; however, the data presented here shows that our best pulsed laser-annealed solar cells are better than solar cells we fabricated using the CW laser-annealing process. It was found that the CW laser-annealing process introduced a large number of recombination centers well into the bulk of the material, and that the emitter of CW laser-annealed solar cells was a very inefficient collector of minority carriers. However, it must be pointed out that this is our first attempt at fabricating solar cells from CW laser-annealed material and several improvements can be envisioned. For an ion implantation energy of 100 keV, the peak of the As profile is at 70 nm; therefore, the region from the surface to 70 nm will be ineffective for minority carrier collection, since the minority carriers will tend to be forced to the surface rather than to the junction. Therefore, one obvious improvement would be to implant through a thin SiO_2 layer to bring the concentration peak to the surface. Also, since CW laser annealing does not result in significant dopant redistribution, the emitter could be molded to any desired profile using this technique. At present, we are trying these and other ideas to optimize the CW laser-annealing process for solar cell applications.

REFERENCES

1. Young, R.T., Wood, R.F., Narayan, J., White, C.W., and Christie, W.H., "Pulsed Laser Techniques for Solar Cell Processing," IEEE Trans. on Electron Devices ED-27, No. 4, pp. 807-815, 1980.

2. White, C.W., Narayan, J. and Young, R.T., "Laser Annealing of Ion-Implanted Semiconductors," Science 204, pp. 461-468, 1979.

3. Wang, J.C., Wood, R.F., and Pronko, P.P., "Theoretical Analysis of Thermal and Mass Transport in Ion-implanted Laser-Annealed Semiconductors," Appl. Phys. Lett. 33, pp. 455-458, 1978.

4. Gat, A., Gibbons, J.F., Magee, T.J., Perg, J., Deline, V.R., Williams P., and Evans, C.A., Jr., "Physical and Electrical Properties of Laser Annealed Ion Implanted Silicon," Appl. Phys. Lett. 32, pp. 276-278 1978.

5. Auston, D.H., Golovchenko, J.A., Smith, P.R., and Surko, C.M., "CW Argon Laser Annealing of Ion-Implanted Silicon," Appl. Phys. Lett. 33, pp. 539-541, 1978.

6. Johnson, N.M., Gold, R.B. and Gibbons, J.F., "Electronic Defect Levels in Self-Implanted CW Laser-Annealed Silicon," Appl. Phys. Lett. 34, pp. 704-706, 1979.

7. Kimerling, L.C., "Defect States in Electron-Bombarded Silicon: Capacitance Transient Analyses," Radiation Effects in Semiconductors 1976 (Inst. Phys. Conf. Ser. 31, Bristol, 1977), pp. 221-230.

8. Watkins, G. and Corbett, J.W., "Defects in Irradiated Silicon. I. Electron Spin Resonance of the Si-A Center," Phys. Rev. 121, pp. 1001-1014, 1961.

Table I.- PROCESS STEPS FOR HIGH-EFFICIENCY SOLAR CELLS USING LASER ANNEALING

1. Ion implantation (5 keV B or As)

2. "Quick" clean

    1. $H_2O_2 + H_2SO_4$
    2. $HNO_3 + H_2SO_4$
    3. $H_2O + HF$

3. Laser anneal ($E_d = 1.2$ J/cm^2 with ruby Q-switched laser, substrate at 400°C)

4. Back side gettering

    A. Laser pulse (2.2 - 2.5 J/cm^2 through rough ground glass)
    B. "Quick" clean (see 2)
    C. Heat at 1000°C for 1 h in oxygen atmosphere

5. Polish the back

6. Back-surface field

    A. Deposit 100 A (B, p-type; Sb, n-type)
    B. Laser anneal at 1.8 J/cm^2

7. Mask front and back to etch the edge

8. RCA clean

    1. 5-1-1 of H_2O - 30% H_2O_2 - 27% NH_4OH (80°C for 15 min)
    2. 6-1-1 of H_2O - 30% H_2O_2 - 37% HCl (80°C for 15 min)
    3. $H_2O + HF$

9. Put on contacts (Ti/Pd/Ag) sinter 500°C/2 min

10. AR coating Ta_2O_5 at 500°C substrate

TABLE II. — RESULTING SOLAR CELL PARAMETERS FOR STEPS IN TABLE I

Method of fabrication	V_{oc} (mV)	J_{sc} (mA/cm^2)	FF	(%)
o As implantation, laser annealing for emitter region				
No BSF	565	35.2	0.76	15.1
No gettering (steps 1-3, 7-10)				
o As implantation, laser annealing for emitter region				
BSF by laser-induced diffusion	595	34.6	0.78	16.1
No gettering (steps 1-3, 6-10)				
o As implantation, laser annealing for emitter region				
BSF by laser-induced diffusion	605	35.1	0.78	16.6
Minority carrier diffusion length enhancement by laser gettering (100 μm → 400 μm)				

TABLE III.- A COMPARISON OF SOLAR CELL PARAMETERS FOR CW LASER ANNEALING AND PULSED LASER ANNEALING

Laser annealing technique	As Implant energy (keV)	Dose ($\times 10^{15}/cm^2$)	Substrate Temp. °C	FF (%)	V_{oc} (mV)	J_{sc} (mA/cm^2)	η (%)
Pulse	5	1	400	79	585	34.1	15.8
Pulse	5	2	400	78	587	34.2	15.7
Pulse	5	4	400	78	595	34.6	16.1
Pulse	25	2	400	77	550	34.7	14.7
CW	100	3	500	78	510	26.5	10.5
CW[1]	100	3	500	78	532	27.5	11.4

[1]These samples were subjected to a 700°C furnace anneal for 1 h.

TABLE IV.- THE PARAMETERS USED FOR THE CALCULATED QUANTUM
EFFICIENCIES SHOWN IN FIG. 2

	a)	b)	c)
Junction depth (μm)	.18	.18	.18
Cell thickness (μm)	280	280	350
Depl. region thickness (μm)	.91	.91	.88
Emitter diff. length (μm)	.01	.01	1.01
Base diff. length (μm)	100	130	500
Emitter diff. const. (cm^2/sec)	1.4	1.4	1.7
Base diff. const. (cm^2/sec)	34.2	34.2	34.1
Emitter recomb. vel (cm/sec)	10^7	10^7	2×10^5
Base recomb. vel (cm/sec)	10^2	10^2	10^2
Emitter dopant conc.(/cm^3)	1.5×10^{21}	1.5×10^{21}	1×10^{20}
Base dopant conc. (/cm^3)	1.4×10^{15}	1.4×10^{15}	1.5×10^{15}

TABLE V.- TRAP CHARACTERIZATION OF TRAPS FOUND IN n-on-p
CW LASER-ANNEALED DIODES

QUANTITY	E-1	H-1
1. Trap type	Minority	Majority
2. Activation energy (E,eV)	0.174 ± 0.001	$0.674 + 0.012$
3. Majority capture cross section (cm^2)	1.3×10^{-20} at 77 K	4.1×10^{-18}
4. Minority capture cross section (cm^2)	$> 3 \times 10^{-15}$ at 77 K	-
5. Concentrations ($\times 10^{13}$/cm^3)		
1. CW Laser Annealed	0.4 ± 0.1	1.7 ± 0.1
2. CW Laser Annealed + Pulse Laser Annealed	0.3 ± 0.1	1.7 ± 0.1
3. CW Laser Annealed + 700°C Furnace Anneal	< 0.02	0.05 ± 0.05

6. Both defect profiles were independent of distance from the junction for the region measured (1 to 4 m).
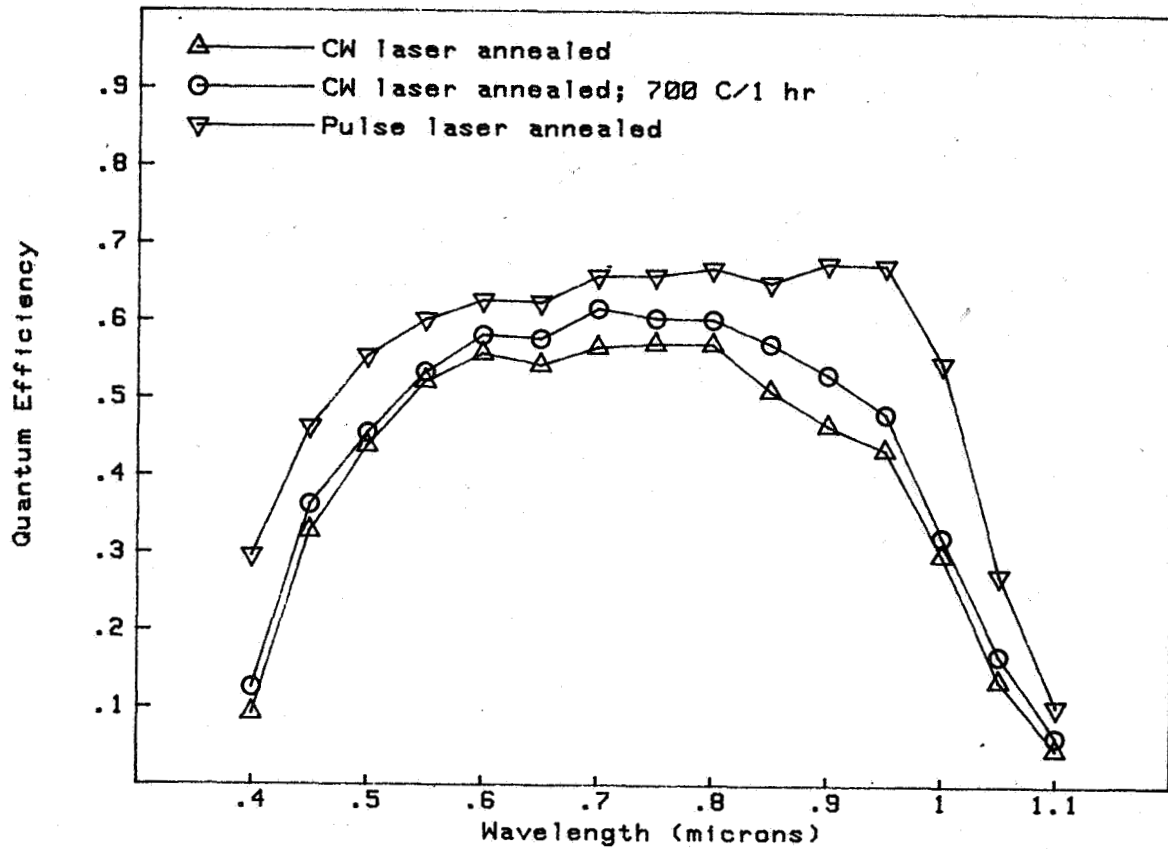
Fig. 1. Quantum efficiency measurements for solar cells without AR coatings fabricated using a) CW laser annealing, b) CW laser annealing plus 700°C furnace annneal for 1 h, and c) pulsed laser annealing.
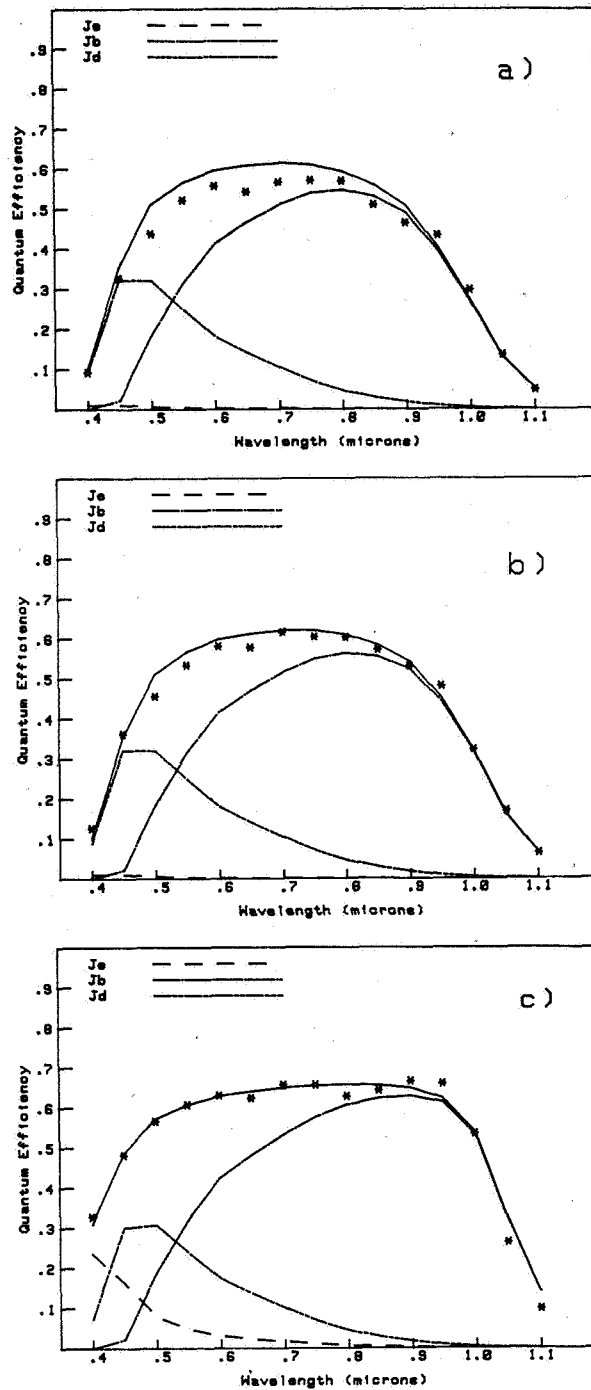
Fig. 2.   Quantum efficiency measurements plus calculated quantum efficiencies
showing total quantum efficiency (solid line), and the contributions
from the emitter (Je, dashed line), the base (Jb, dashed-dotted
line) and the depletion region (Jd, dashed double-dotted line). The
cells are the same as those of Fig. 1, where a) is CW laser
annealed, b) is CW laser annealed plus 700°C furnace anneal, and c)
is pulsed laser annealed.

27
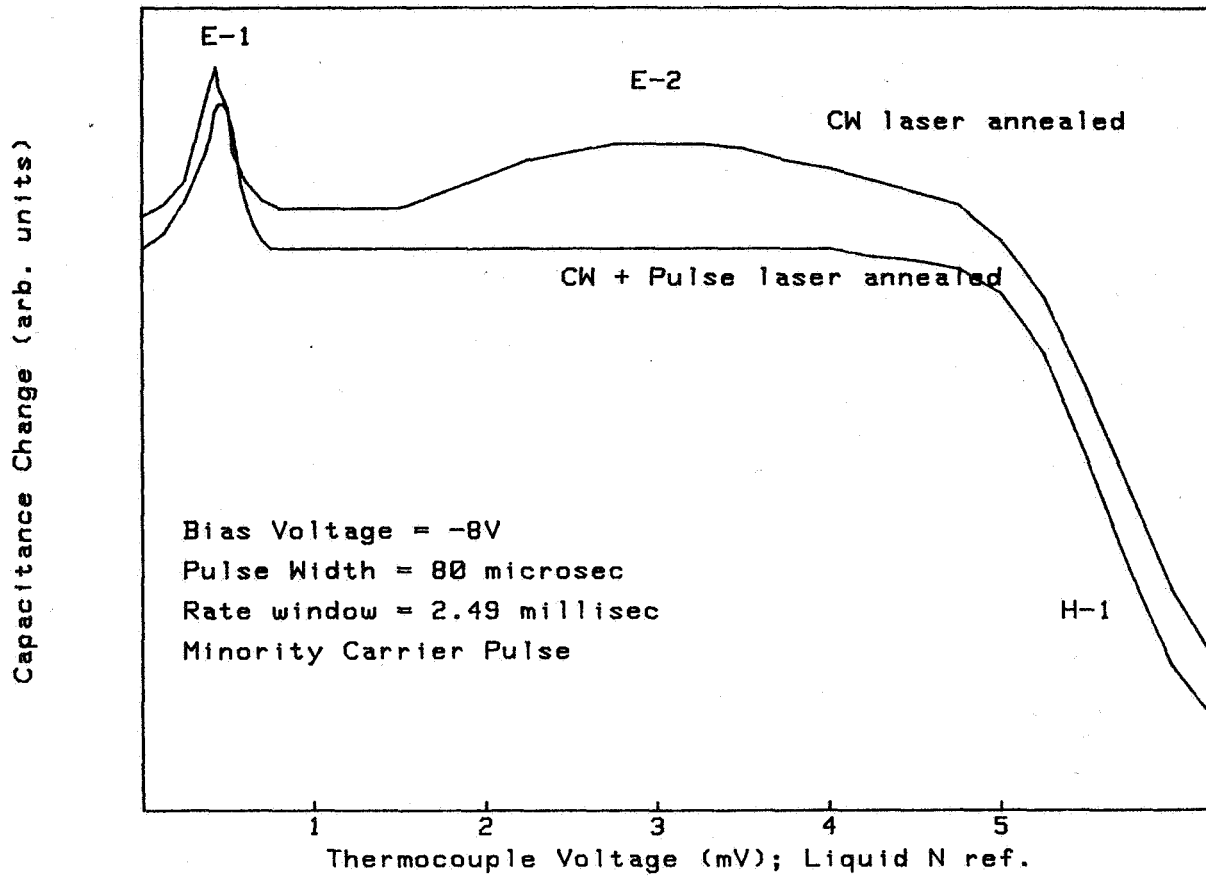
Fig. 3.   DLTS spectra for diodes fabricated from 1) CW laser annealing and
2) CW laser annealing plus pulsed laser annealing.

THE EFFECT OF MINORITY CARRIER MOBILITY VARIATIONS ON THE
PERFORMANCE OF HIGH VOLTAGE SILICON SOLAR CELLS

V. G. Weizer and M. P. Godlewski
NASA Lewis Research Center
Cleveland, Ohio

INTRODUCTION

The Lewis Research Center has been engaged in an effort to understand and optimize a multistep diffusion (MSD) processing schedule which has enabled the attainment of high open circuit voltages in 0.1 ohm-centimeter silicon solar cells. The schedule, described elsewhere (ref. 1), consists of a deep primary diffusion, followed by an acid etch of the emitter surface, which is then followed by a shallow secondary diffusion. In the course of our work we have been able to correlate the voltage increases we have observed with the time of primary diffusion. We found that as the primary diffusion time is increased, the voltage rises monotonically (ref. 1).

The working hypothesis we have devised to explain this correlation is based on localized changes in the base minority carrier mobility. The mobility changes are thought to be caused by stress fields emanating from the emitter, which is itself in a state of high diffusion-induced stress. The existence of highly stressed regions in the cell base near the junction can be inferred from the presence of diffusion-induced dislocations in these regions (refs. 2 and 3). Specifically, it is suggested that the stress fields from the highly doped emitter extend beyond the junction into the base and there cause a localized piezoresistive decrease in the minority carrier mobility. It is further suggested that the width of this region of low mobility increases as the time of primary diffusion increases. The observed voltage increases, therefore, are due to the increasing width of a region of low mobility.

The purpose of this paper is twofold. We first will describe some surprising results obtained while trying to model this variable-mobility structure. Second, we will show how the variable-mobility structure was used to explain some unexpected experimental data obtained from high-voltage MSD cells.

MODELING THE VARIABLE MOBILITY STRUCTURE

Figure 1 shows the calculated variation in the open-circuit voltage with the width of the low-mobility region for the cell described in the figure. As can be seen the voltage rises as the width of the low mobility region

increases. Voltage variations such as these should be expected when changes are made in the mobility since the mobility occupies a prominent position in the expression for the device saturation current.

On the other hand, one would not expected the short-circuit current or the spectral response to be affected by mobility changes. It is known, for example, that for a homogeneous base cell, the current and the spectral response are completely independent of the value of the base minority carrier mobility as long as the rear surface recombination velocity differs from the diffusion velocity by a couple of orders of magnitude. We were surprised, therefore, when we derived the current equations for the case of a cell with an abrupt mobility variation in the base. We found, in contrast to the homogeneous base case, that the current expressions contained the ratio of the mobilities employed in the two base regions. Thus, while the current and the spectral response are independent of the actual values of the mobility, they are functions of the change in mobility from one base region to the other.

Figure 2, for example, shows the variation of the 0.9-micrometer spectral response as a function of the width of the low-mobility region for the cell described in figure 1. The plot is independent of the absolute values of the mobility, depending only on their ratio, which in this case is an arbitrarily chosen 10:1. A parametric study has shown that the current variations increase as the ratio increases for a given region width. Also, as the ratio is increased, the current minimum occurs at lower region widths. Lower diffusion lengths also cause a decrease in the region width for minimum current. As expected, the blue response is not affected by these base mobility changes. The total current shows essentially the same behavior as the red response. It should be noted that the red response (and the total current) are extremely sensitive to mobility variations that occur within a few micrometers of the junction, a region that would be most highly affected by fabrication procedures such as diffusion.

In Summary, it has been found that (1) both the short-circuit current and the spectral response are functions of the mobility ratio, (2) the magnitude of the current and spectral response variations depend on the degree and location of the mobility change, and (3) the short-circuit current and the spectral response are extremely sensitive to mobility changes occurring within a few micrometers of the junction.

COMPARISON WITH EXPERIMENT

The present Lewis MSD high-voltage cell is a deep-junction device. Final junction depths of 3 to 4 micrometers are typical. Inherent in such a device is a low blue response and thus a less-than-desired short-circuit current. In an effort to increase the blue response, the junction depth in each of several completed cells was reduced by chemically etching the emitter surface between the grid fingers. The expected improvements are illustrated in figure 3 where the calculated spectral response and short-circuit current are plotted for several values of the junction depth

for a cell with a homogeneous base. As the junction depth is decreased, we would expect a rise in the blue response, no change in the red response, and a rise in the total current.

The measured variations in current and spectral response at various stages in the etching procedure are shown in figure 4. Here, the blue response increases with junction depth reduction as expected, but the red response and the short-circuit current exhibit severe and unexpected decreases. It appears that we have significantly altered the electrical characteristics of the base without touching it directly. While we cannot explain this behavior with a homogeneous base models, we can get some insight into what is happening by invoking the variable base mobility concept.

If, as we have proposed above, long diffusions cause stress fields to be propagated into the base from the highly doped and highly stressed emitter, it then follows that, when we remove highly stressed emitter surface regions, we also allow stress relief to occur in the base; that is, we allow the width of low-mobility region to shrink. If we calculate, then, the variation of the spectral response as the width of the low-mobility region decreases as a result of the surface etching, we obtain the set of curves shown in figure 5. In this figure, an arbitrary mobility ratio of 100:1 was used, and the junction depth (and hence the blue response) was held constant at about 3 micrometers for simplicity. The results are quite similar to what was observed experimentally.

It thus appears that we can explain, qualitatively at least, the unexpected drop in red response with emitter etching by using a model that relates the highly stressed regions in the emitter with regions of lowered minority carrier mobility in the base.

CONCLUSIONS

The results of this study can be summarized as follows:

1. While the short-circuit current and the spectral response are independent of mobility in an homogeneous base cell, they are functions of the change in mobility in an inhomogeneous base cell.

2. Short-circuit current and spectral response variations depend on the degree and location of the change in mobility.

3. The short-circuit current and the spectral response are extremely sensitive to changes in mobility that occur in a narrow (<5 μm) region adjacent to the junction.

4. Unexpected spectral response changes due to emitter etching in MSD cells can be explained using a mobility variation model.

REFERENCES

1. Godleweki, M. P.; et al.: Open-Circuit Voltage Improvements in Low
   Resistivity Solar Cells. Conference Record, Fourteenth Photovoltaic
   Specialists Conference. IEEE, 1980, pp. 166-169.

2. Schwuttke, G. H.; Queissar, H. J.: X-Ray Observations of Diffusion-
   Induced Dislocations in Silicon. J. Appl. Phys., vol. 33, no. 4, Apr.
   1962, pp. 1540-1542.

3. Lawrence, J. E.: Diffusion-Induced Stress and Lattice Disorders in
   Silicon. J. Electrochem. Soc., vol. 113, no. 8, Aug. 1966, pp. 819-824.

EFFECT OF MOBILITY VARIATION ON OPEN CIRCUIT VOLTAGE
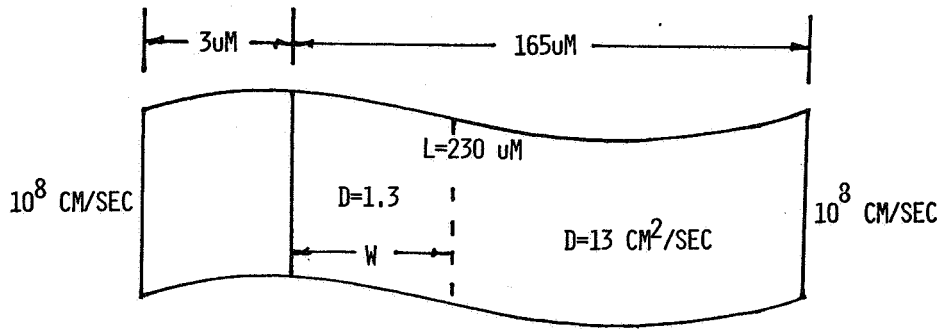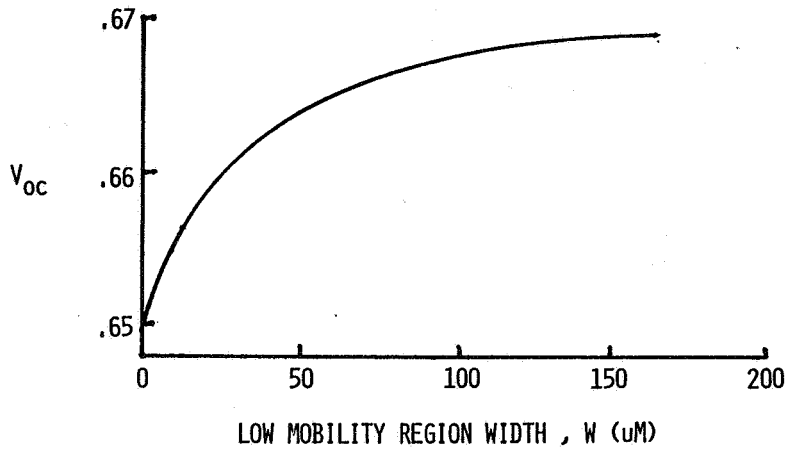
FIGURE 1

EFFECT OF MOBILITY VARIATION ON RED RESPONSE
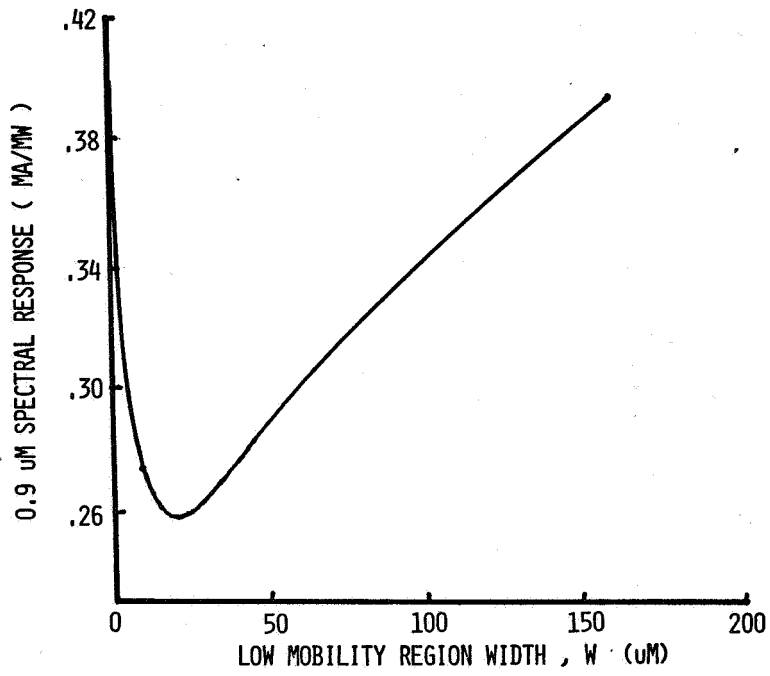
FIGURE 2

UNIFORM BASE CELL : EFFECT OF JUNCTION DEPTH VARIATIONS
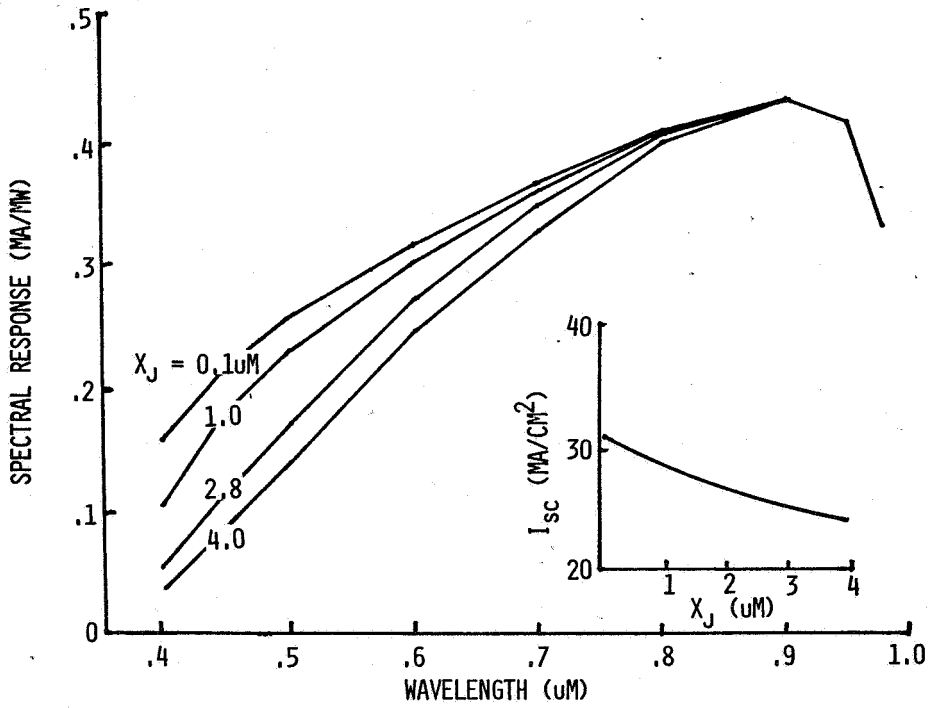
FIGURE 3

EMITTER THINNING EXPERIMENT
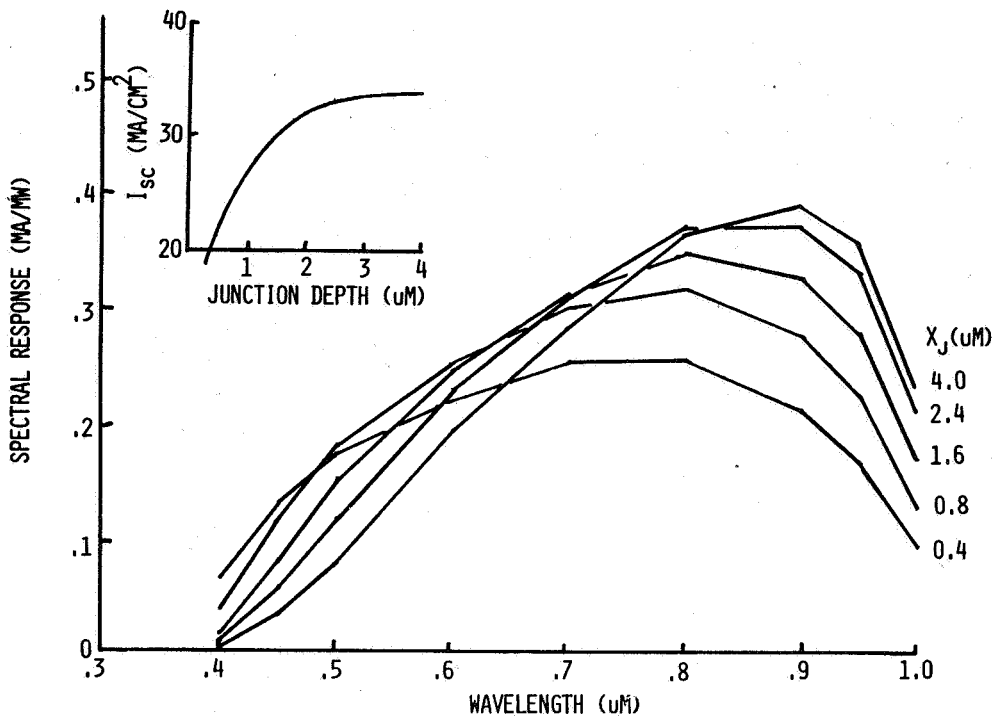
FIGURE 4

CALCULATED VARIATION OF SPECTRAL RESPONSE WITH LOW MOBILITY REGION WIDTH
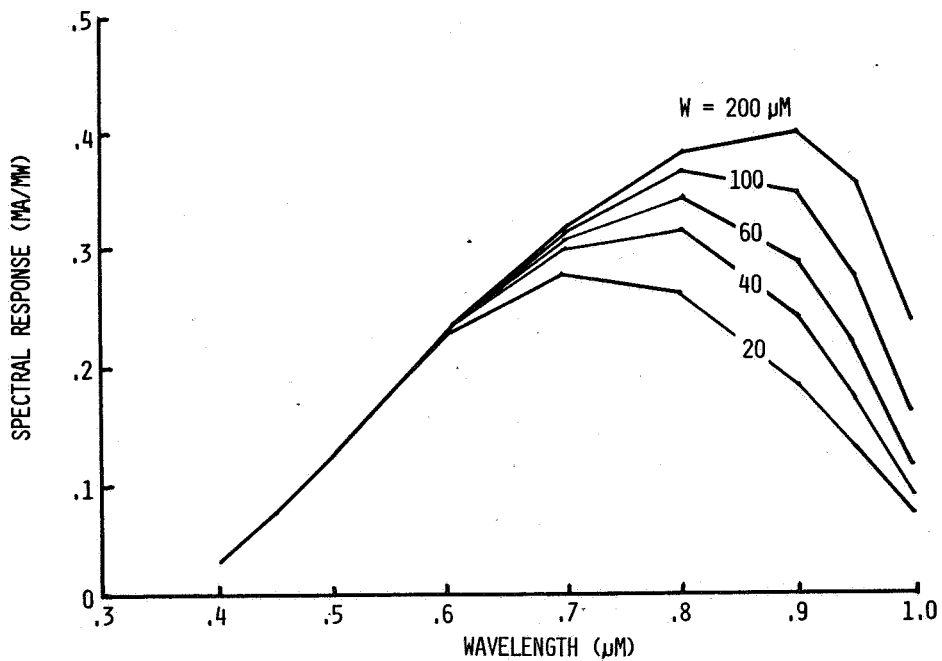
FIGURE 5
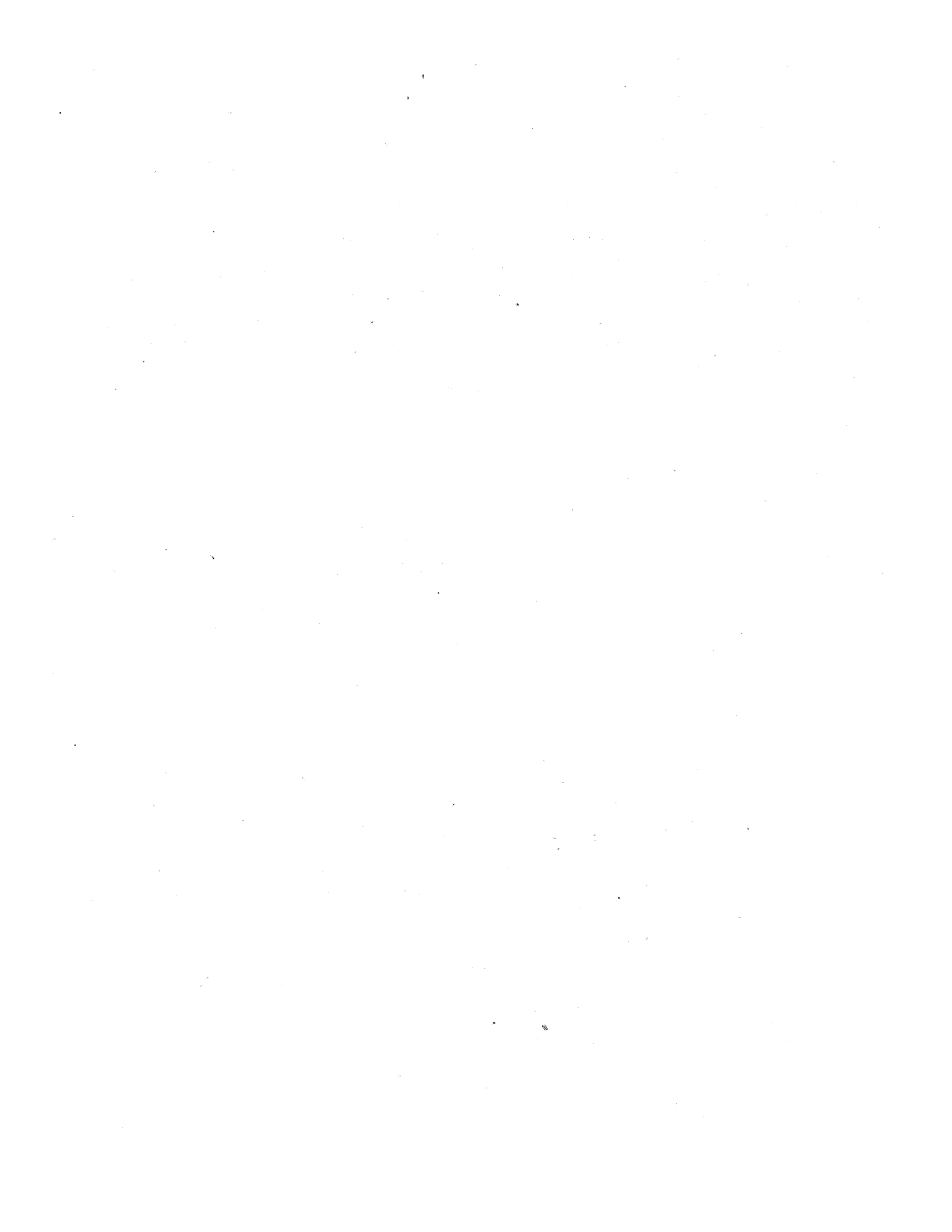
COMPUTER MODELING OF HIGH-EFFICIENCY SOLAR CELLS*

R. J. Schwartz and M. S. Lundstrom
Purdue University
Lafayette, Indiana

ABSTRACT

Transport equations which describe the flow of holes and electrons in the heavily doped regions of a solar cell are presented in a form that is suitable for device modeling. Two experimentally determinable parameters, the effective bandgap shrinkage and the effective asymmetry factor are required to completely model the cell in these regions. Nevertheless, a knowledge of only the effective bandgap shrinkage is sufficient to model the terminal characteristics of the cell. The results of computer simulations of the effects of heavy doping are presented. The insensitivity of the terminal characteristics to the choice of effective asymmetry factor is shown along with the sensitivity of the electric field and quasi-electric fields to this parameter. The dependence of the terminal characteristics on the effective bandgap shrinkage is also presented.

INTRODUCTION

The need for accurate modeling of the physical phenomenon which control the behavior of solar cells has long been recognized as being necessary to the development of high-efficiency solar cells. This paper is concerned with the accurate modeling of heavy doping effects and the proper technique for incorporating experimentally determined heavy doping parameters into a numerical solar cell model.

Since both the emitter and the high-low junction regions of a high-efficiency solar cell are heavily doped, the performance of these regions is controlled by the various heavy doping effects which occur. Among the considerations for correct modeling of these regions are: 1) the regions are degenerate and, therefore, require the use of Fermi-Dirac statistics, 2) the density-of-states function is expected to have a change of shape due to band tailing or the formation of an impurity band, 3) the original energy states are expected to be shifted in energy due to free carrier-ionized impurity interactions, and correlation effects. Recent papers have presented theoretical calculations of the magnitude of these various phenomenon, references 1 to 3. The problem, however, is that the present state-of-the

theory is not sufficiently developed. For example, the shape of the density-of-states functions is unknown, and without this information one is unable to compute the parameters which appear in the formulation of the transport equations in the presence of heavy doping effects.

NOTATION

γ	effective asymmetry factor
E_G	bandgap
ΔE_G	bandgap shrinkage
Δ_G	effective bandgap shrinkage
D_p, D_n	hole (electron) diffusion coefficient
$\vec{J}_p, \vec{J}_n$	hole (electron) current density
k	Boltzmann's constant
n_{io}	intrinsic carrier concentration in a semiconductor with an unperturbed band structure
n_{ie}	effective intrinsic carrier concentration
p, n	hole (electron) carrier concentration
q	magnitude of the electronic charge
T	absolute temperature (Kelvin)
V	electrostatic potential
μ_p, μ_n	hole (electron) mobility
X	electron affinity
$\nabla^{\eta_v}, \nabla^{\eta_c}$	The gradient operator with η_v (η_c) held constant

Equilibrium values of the parameters listed above are denoted by a superscript o.

TRANSPORT EQUATIONS

If the existence of a mobility edge separating localized from delocalized states is postulated, transport equations for materials with a position-dependent band structure can be written. These equations in the form given by Marshak and van Vliet (refs. 4, 5) are:

$$J_p = -pq\mu_p \left[\nabla(V + \frac{\chi + E_G}{q} - \frac{\Gamma_p}{q}) \right] - qD_p \nabla_p \tag{1}$$

$$J_n = -nq\mu_n \left[\nabla(V + \frac{\chi}{q} + \frac{\Gamma_n}{q}) \right] + qD_n \nabla_n \tag{2}$$

where

$$D_p = \frac{kT}{q} \frac{p}{\frac{\partial n}{\partial \eta_c}} \mu_p \tag{3}$$

and

$$D_n = \frac{kT}{q} \frac{p}{\frac{\partial n}{\partial \eta_c}} \mu_n \tag{4}$$

are the Einstein relations, and

$$\nabla \Gamma_p = \frac{kT}{\frac{\partial p}{\partial \eta_v}} \nabla^{\eta_c} n \tag{5}$$

$$\nabla \Gamma_n = \frac{kT}{\frac{\partial n}{\partial \eta_c}} \nabla^{\eta_c} n \tag{6}$$

are the density-of-states effects.

Without a knowledge of the shape of the density-of-state function and the location of the band edges these equations cannot be utilized for device modeling. Others have formulated transport equations under more restrictive assumptions, such as the rigid band approximation (ref. 6) or under conditions for which Boltzmann statistics apply, (ref. 7). While these formulations allow one to perform numerical calculations, they are restricted to cases which are known to be violated in the emitter and the back surface field region of high efficiency solar cells.

A recent reformulation of the transport equation by Lundstrom, Schwartz and Gray (refs. 8, 9) provides a means of avoiding these complications while retaining a precise model of the effects of heavy doping on the transport equations, and consequently upon the behavior of a solar cell (refs. 8, 9). They have shown that equations 1 and 2 can be rewritten as

$$J_p = -pq\mu_p \left[\nabla(V - (1-\gamma)\frac{\Delta_G}{q}) \right] - kT\mu_p \nabla_p, \tag{7}$$

and

$$J_n = -nq\mu_n \left[\nabla(V + \frac{\gamma\Delta_G}{q}) \right] + kT\mu_n \nabla_n, \tag{8}$$

where

$$\Delta_G = (\Delta E_G + \Theta_n + \Theta_p) \tag{9}$$

is the effective bandgap shrinkage and

$$\gamma = \frac{\Delta\chi + \Theta_n}{\Delta_G} \tag{10}$$

is the effective asymmetry factor.

The parameters, Θ_n and Θ_p, which contain the information on the position dependence of the density-of-states and the influence of Fermi-Dirac statistics are defined by,

$$\nabla\Theta_p = \nabla\Gamma_p - kT \left[\frac{qD_p - kT\mu_p}{p\mu_p} \right] \tag{11}$$

and

$$\nabla\Theta_n = \nabla\Gamma_n - \left[\frac{qD_n - kT\mu_n}{n\mu_n} \right] \tag{12}$$

The significance of recasting the Marshak and van Vliet equations in the form shown by equations (7) and (8) is that the parameters which appear in equations (7) and (8), namely Δ_G and γ, are experimentally determinable. These experimentally determinable parameters contain the information on the band structure and the influence of Fermi-Dirac statistics necessary to model heavily doped semiconductor devices. In addition, the simple, Boltzmann-like form of these equations facilitates their use in device modeling.

The effective gap shrinkage, Δ_G, is the parameter inferred from typical, electrical measurements of heavy doping effects (refs. 10 to 12). Although this parameter is frequently referred to as the bandgap shrinkage, equation 9 shows that Δ_G also accounts for the modified density-of-states and the influence of Fermi-Dirac statistics. The effective gap shrinkage can be related to the effective intrinsic carrier concentration as (refs 8, 9).

$$n_{ie}^2 = n_{io}^2 e^{\Delta G^o/kT} , \qquad (13)$$

where n_{io} is the intrinsic carrier concentration for a material with unperturbed band structure.

The parameter γ, which we refer to as the effective asymmetry factor, accounts for the asymmetry in the shift of the band edges as well as the modified density-of-states and the influence of Fermi-Dirac statistics. Like Δ_G, γ can be determined from electrical measurements, but unlike Δ_G, no measurements of γ have been reported.

Equations (7) and (8) can be used by the semiconductor device modeler to account for the complicated effects associated with heavy impurity doping. Unfortunately, information on Δ_G is quite limited, and no information on γ exists. Fortunately, the terminal characteristics of the device are insensitive to γ when the heavily doped regions are in low injection, quasi-neutral, and the dopants fully ionized, (refs. 8, 9). While it is true that the terminal characteristics of the device are unaffected by the choice of γ, it is not true for some of the internal parameters of the cell. For example, the built-in potential, electric field and quasi-electric fields are strongly affected by γ.

The remainder of this paper is devoted to showing the results of computer simulations of solar cells to illustrate the use of the heavy doping model described above. The sensitivity of solar cell performance to the two heavy doping parameters, γ and Δ_G is considered.

SENSITIVITY OF SOLAR CELL PERFORMANCE TO γ

A set of computer simulations was performed in order to test the sensitivity of the device model to the choice of the effective asymmetry factor.[*] For these simulations, a p^+nn^+ solar cell, described by the parameters listed in Table I, was chosen. The doping profile of the p-n junction in

---

[*]The numerical model used for these simulations is described in reference 9.

this device is shown in figure 1. Complete ionization of the impurities was assumed in all simulations. Two different choices for γ were considered. In Case I, we set $\gamma = 0.5$, and in Case II we put all of the effective band edge shift into the majoirty carrier band (i.e. $\gamma = 0$ for p-type, $\gamma = 1$ for n-type). Comparison of the computed, one sun IV curves, shown in Table II, shows that the terminal characteristics of the cell are relatively unaffected by the choice for γ. Similar agreement was observed when the spectral responses for the two cases were compared.

The comparisons of the computed I-V curves for the two cases confirms the prediction (refs. 9, 10) that the terminal characteristics of typical heavily doped semiconductor devices are not sensitive to the choice for γ. Figure 2, however, which compares the open-circuit electric fields within the p-n junction region for the two cases, shows that the electric field is quite sensitive to the choice of γ. The quasi-electric fields for holes and electrons are shown in figure 3. The two choices of γ are seen to result in very different quasi-electric fields, nevertheless, the effective fields which act on the carriers are not affected by γ. The effective fields are the sums of the electric and quasi-electric fields for each carrier. Figures 2 and 3 show that the effective fields for holes and electrons are nearly identical for the two cases.

The open-circuit carrier concentrations within the p-n junction region are plotted in figure 4. As expected, (refs. 8, 9) the carrier concentrations are not sensitive to the choice of γ. Since both the effective fields and carrier concentrations are independent of γ, the current densities are also expected to be unaffected by γ. Figure 5 shows that the expected result is observed.

SENSITIVITY OF SOLAR CELL PERFORMANCE TO Δ_G

The solar cell simulations showed that the terminal IV characteristics of typical silicon solar cells are, as expected (refs. 9, 10) not sensitive to the choice of γ. The performance of silicon solar cells, however, is quite sensitive to the effective bandgap shrinkage, Δ_G. In order to study the effect of Δ_G, we compared the simulated performance of the p^+nn^+ solar cell with the simulated performance of an identical cell in which bandgap narrowing was suppressed (i.e., $\Delta_G = 0$). For these comparisons we chose $\gamma = 0.5$ (all the results to be discussed, however, are independent of the choice of γ).

The computed current versus voltage curves for the p^+nn^+ cell with and without bandgap narrowing are compared in figure 6 which shows the well-known (refs. 13, 14) reduction in open-circuit voltage, V_{OC}, caused by bandgap narrowing. The cause for the reduction in open-circuit voltage can be ascertained by examining figure 7, a plot of the open-circuit energy band diagram for the p-n junction region of the cell. This energy band diagram was computed by employing the rigid band approximation and is for illustrative purposes only. A reduction of the potential barrier for electrons injected into the heavily doped p-type region is shown by figure 7. This reduction of

the potential barrier is caused by Δ_G and it is not affected by γ. The reduced potential barrier results in increased injection of minority carriers into the heavily doped regions which increases the recombination currents associated with these portions of the device and, therefore, reduces the open-circuit voltage.

The computed characteristics of the p^+nn^+ cell, with and without bandgap narrowing, are summarized in Table III. Because this cell was designed (ref. 15) to minimize the deliterious effects associated with heavy impurity doping, the open-circuit voltage of the cell is not severely degraded by bandgap narrowing. In addition, since the short-circuit current of the cell is not significantly affected by bandgap narrowing, the fill factor of the cell is actually improved by bandgap narrowing. This effect, clearly shown by figure 6, minimizes the degradation of cell efficiency caused by bandgap narrowing.

SUMMARY AND CONCLUSIONS

A set of transport equations for use in analyzing heavily doped semiconductor devices has been considered in this paper. The equations were first presented, and the interpretation of the two parameters, Δ_G and γ, used to describe the effects associated with heavy impurity doping was discussed. The influence that these two parameters have on solar cell performance was then illustrated by the results of computer simulation.

The most important conclusion reached in this paper is that heavily doped semiconductor devices can be modeled in terms of two experimentally determinable parameters. The effects associated with heavy impurity doping (i.e., band edge shifts, changes in the density-of-states and the influence of degenerate statistics) can be modeled accurately by using the two parameters in simple, Boltzmann-like transport equations. To model heavily doped semiconductor devices, there is no need to introduce additional, unproven assumptions as is done in the frequently used rigid band approximation. In addition, we have demonstrated that the terminal I-V characteristics of typical, high-efficiency, single-crystal, silicon solar cells are not sensitive to the effective asymmetry factor, γ.

REFERENCES

1. Abram, R. A.; Rees, G. J.; and Wilson, B. L. H.: "Heavily Doped Semiconductors and Devices," Advances in Physics, Vol. 27, pp. 799-892, 1978.

2. Lanyon, H. P. D.; and Tuft, R. A.: "Bandgap Narrowing in Heavily Doped Silicon," IEEE Trans. Electron Devices, Vol. ED-26, pp. 1014-1018, 1979.

3. Mahan, G. D.: "Energy Gap in Si and Ge: Impurity Dependence," J. Appl. Phys., Vol. 51, pp. 2634-2646, 1980.

4. Marshak, A. H.; and van Vliet, K. M.: "Electrical Current in Solids with Position-Dependent Band Structure," Solid-State Electron., Vol. 21, pp. 417-427, 1978.

5. Marshak, A. H.; van Vliet, K. M.: "Carrier Densities and Emitter Efficiency in Degenerate Materials with Position-Dependent Band Structure," Solid-State Electron., Vol. 21, pp. 429-434, 1978.

6. Marshak, A. H.; Shibib, M. A.; Fossum, J. G.; and Lindholm, F. A.: "Rigid Band Analysis of Heavily Doped Semiconductor Devices," IEEE Trans. Electron Devices, submitted for publication.

7. Mock, M. S.: "Transport Equations in Heavily Doped Silicon, and the Current Gain of Bipolar Transistors," Solid-State Electron., Vol. 16, pp. 1251-1259, 1973.

8. Lundstrom, M. S.; Schwartz, R. J.; and Gray, J. L.: "Transport Equations for the Analysis of Heavily Doped Semiconductor Devices," to be published in Solid-State Electron.

9. Lundstrom, M. S.; and Schwartz, R. J.: "Annual Report on Interdigitated Back-Contact Solar Cells, Purdue Univ., School of EE, Tech. Rep., TR-EE 80-14, Jan. 1980.

10. Slotboom, J. W.; and de Graaff, H. C.: "Measurements of Bandgap Narrowing in Si Bipolar Transistors," Solid-State Electron., Vol. 19, pp. 857-862, 1976.

11. van Merbergen, J.; Nijs, J.; Mertens, R.; and van Overstraeten, R.: "Measurement of Bandgap Narrowing and Diffusion Length in Heavily Doped Silicon," in Rec. 13th IEEE Photovoltaic Specialists Conf., 1978.

12. Tang, D. D.: "Heavy Doping Effects in p-n-p Bipolar Transistors," IEEE Trans. Electron Dev., Vol. ED-27, pp. 563-570, 1980.

13. Iles, P. A.; and Soclof, S. I.: "Effect of Impurity Doping Concentration on Solar Cell Output," Conf. Rec., 11th IEEE Photovoltaic Spec. Conf., pp. 19-24, 1975.

14. Godlewski, M. P.; Brandhorst, Jr., H. W.; and Barona, C. R.: "Effects of High Doping Levels on Silicon Solar Cell Performance," Conf. Rec., 11th IEEE Photovoltaic Spec. Conf., pp 32-35, 1975.

15. Fossum, J. G.; Nasby, R. D.; and Burgess, E. L.: "Development of High-Efficiency P^+NN^+ Back-Surface-Field Silicon Solar Cells," Conf. Rec., 13th IEEE Photovoltaic Spec. Conf., pp. 124-129, 1978.

TABLE I   PARAMETERS USED TO MODEL THE p^+nn^+ CELL.

Temperature	27°C
Device thickness	300µm
Base doping density	$5 \times 10^{14} cm^{-3}$
PN junction depth	0.35µm
High-Low junction depth	1.0µm
P^+ surface concentration	$1.5 \times 10^{20} cm^{-3}$
N^+ surface concentration	$3.0 \times 10^{20} cm^{-3}$
Doping profiles	complementary error function
SRH lifetime parameter, τ_{po}	400µsec
SRH lifetime parameter, τ_{no}	400µsec
Auger coefficient, A_p	$9.9 \times 10^{-32} cm^6 sec^{-1}$
Auger coefficient, A_n	$2.8 \times 10^{-31} cm^6 sec^{-1}$
Front surface recombination velocity	5000 cm/sec
Back contact	ohmic
Solar spectrum	AM1
Optical reflection losses	0
Bandgap narrowing model (Δ_G)	Slotboom and DeGraaf
Effective asymmetry (γ):	
CASE I	$\gamma = 0.5$
CASE II	$\gamma = 0$ for p-type
	$\gamma = 1$ for n-type

TABLE II. COMPARISON OF 1 SUN I-V CURVES FOR TWO EFFECTIVE
ASYMMETRY FACTOR MODELS.

Voltage	Current Density (MA/Cm^2)		Deviation
	Case I	Case II	
0	37.4273	37.4245	7.5×10^{-5}
0.1	37.4259	37.4232	7.2×10^{-5}
0.2	37.4243	37.4216	7.2×10^{-5}
0.3	37.4219	37.4192	7.2×10^{-5}
0.4	37.3932	37.919	3.5×10^{-5}
0.5	36.3423	36.3910	-1.3×10^{-3}
0.6	14.0828	14.9401	-6.1×10^{-2}
0.62	6.1596	4.5492	2.6×10^{-1}

$V_{OC \ Case \ I}$ = 0.61512 volts

$V_{OC \ Case \ II}$ = 0.61632 volts

TABLE III. COMPARISON OF p^+nn^+ CELL PERFORMANCE WITH AND WITHOUT
BANDGAP NARROWING.

	With BGN	Without BGN
Short-Circuit Current	37.43 mA/cm^2	37.59 mA/cm^2
Collection Efficiency	0.98	0.99
Open-Circuit Voltage	0.615 Volts	0.676 Volts
Fill Factor	0.80	0.76
Efficiency	0.192	0.201
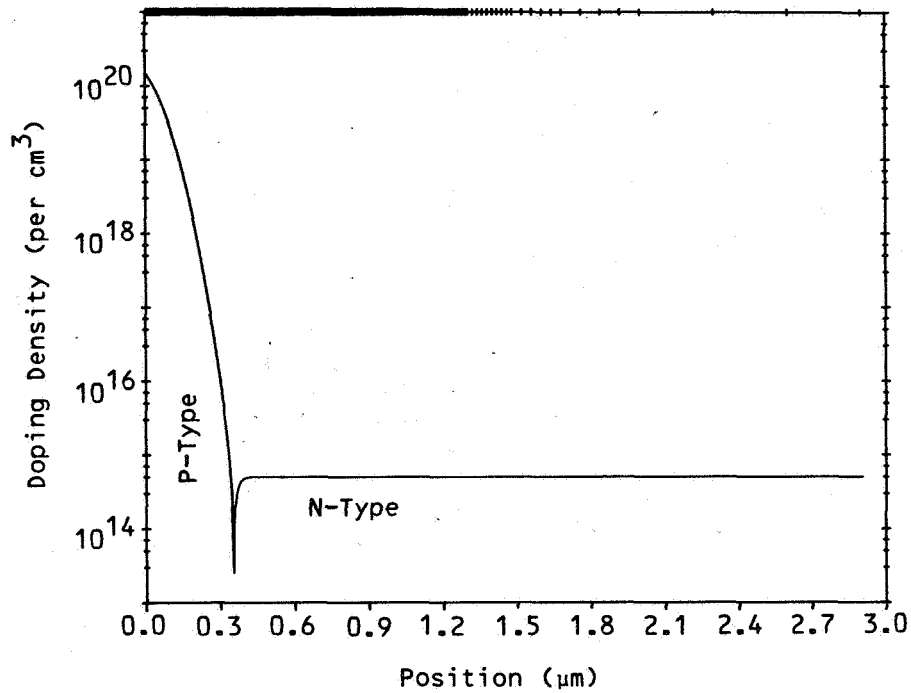
Figure 1. Doping profile for the p-n junction
region of the p+nn+ solar cell.
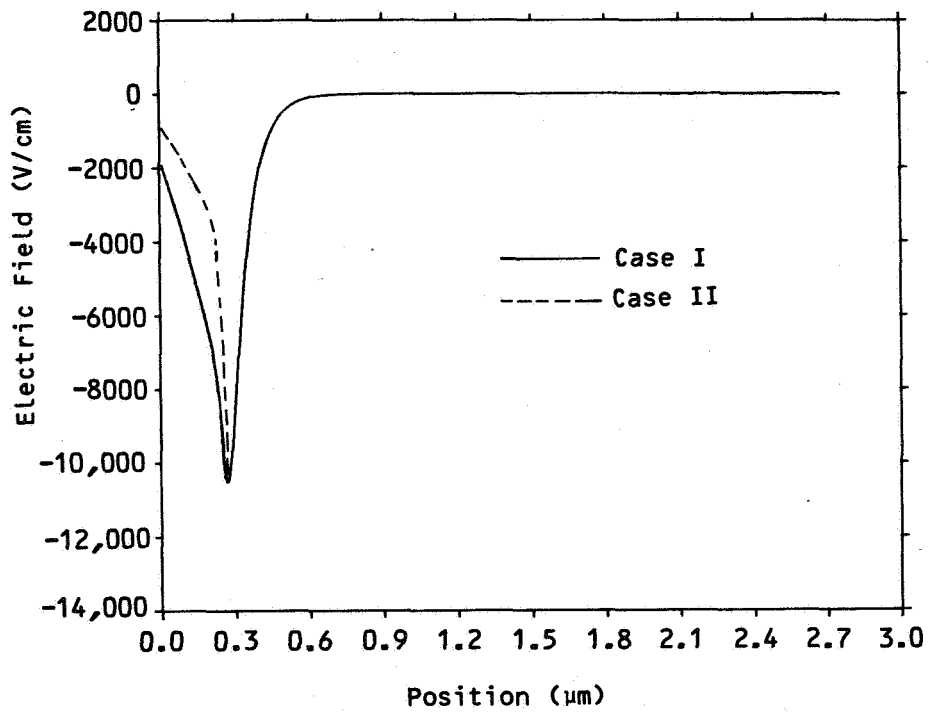
Figure 2. Open-circuit electric field within
the p-n junction region of the
p+nn+ cell.
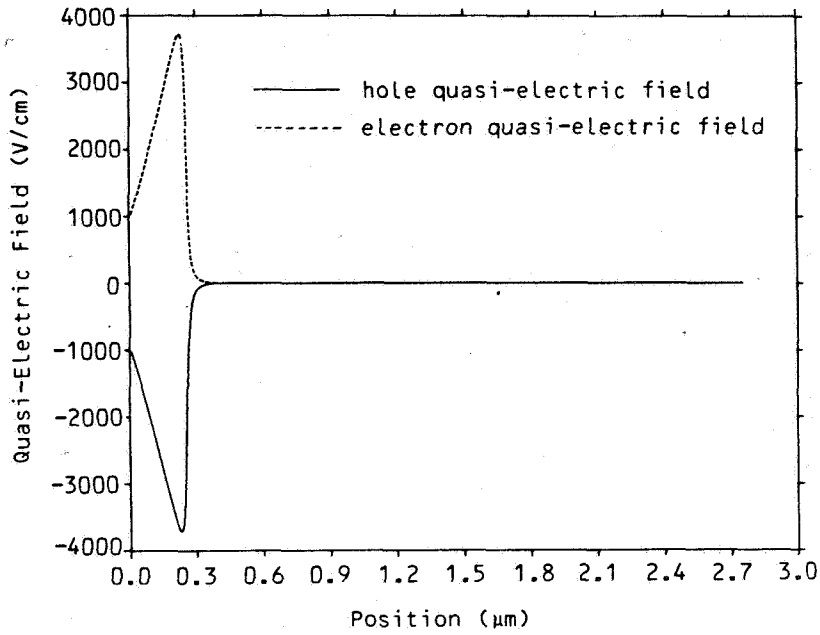
Figure 3a. Quasi-electric fields in the p-n
junction region of the p^+nn^+ cell
(Case I).
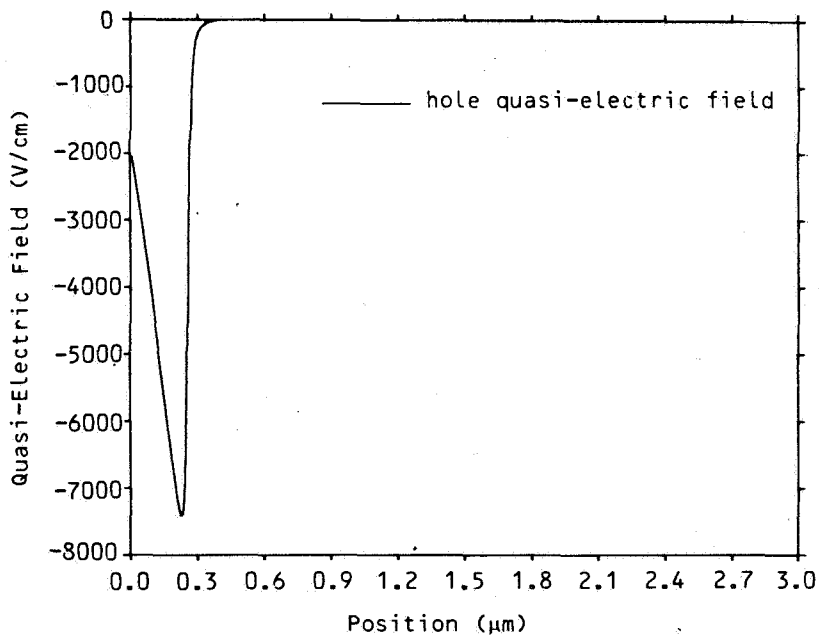
Figure 3b. Quasi-electric field within the
p-n junction region of the p^+nn^+
cell (Case II). The electron
quasi-electric field is zero
for this case.
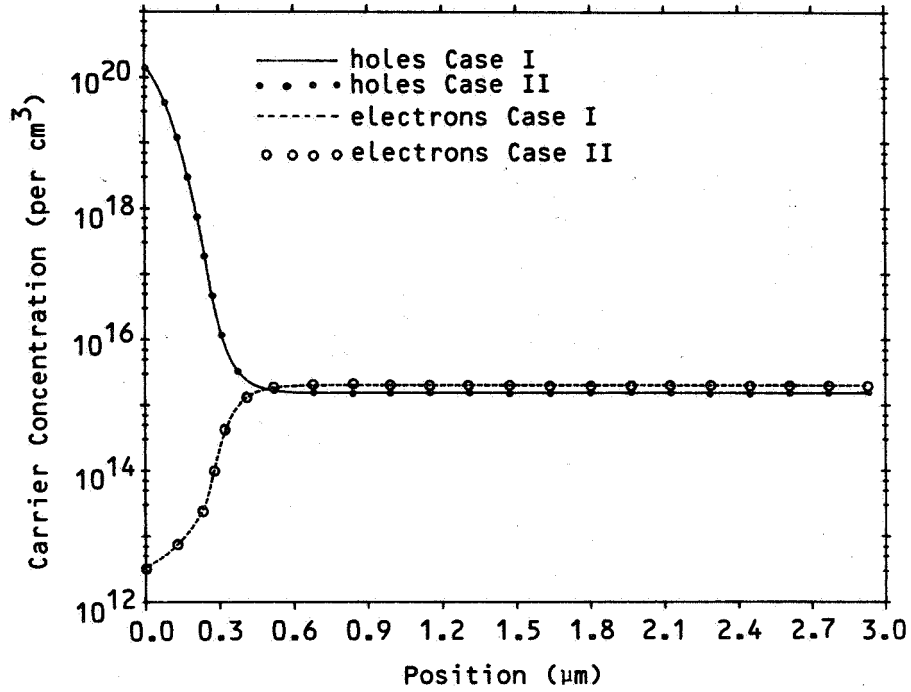
Figure 4. Open-circuit carrier concentrations within the p-n junction region of the p^+nn^+ cell.
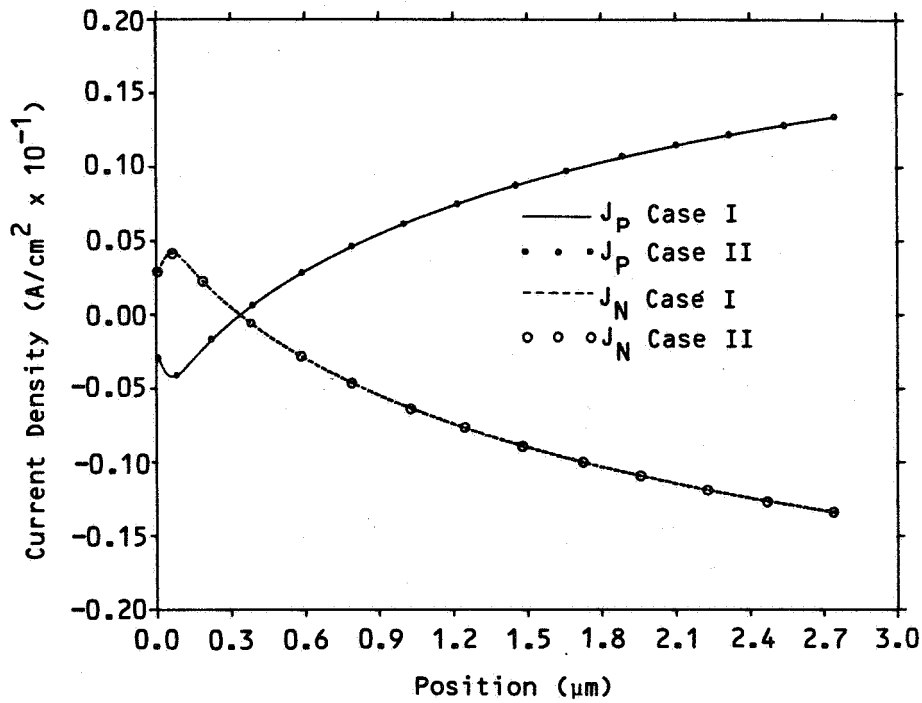
Figure 5. Open-circuit current densities in the p-n junction region of the p^+nn^+ cell.
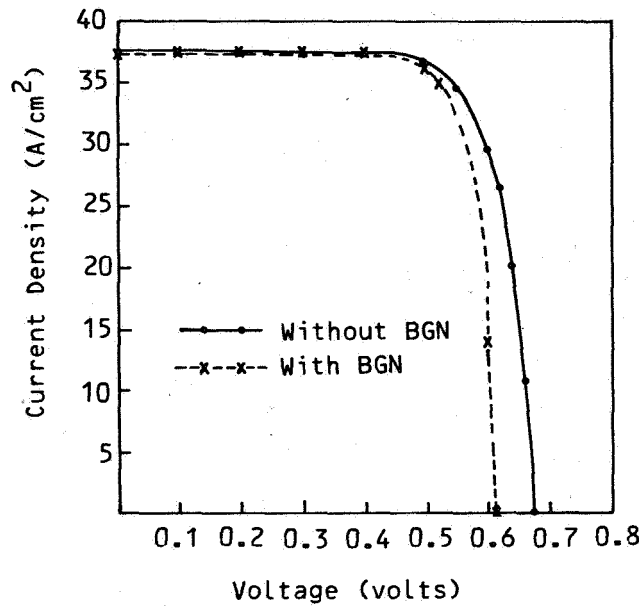
Figure 6. Current-voltage characteristics
for a p+nn+ solar cell with and
without bandgap narrowing.
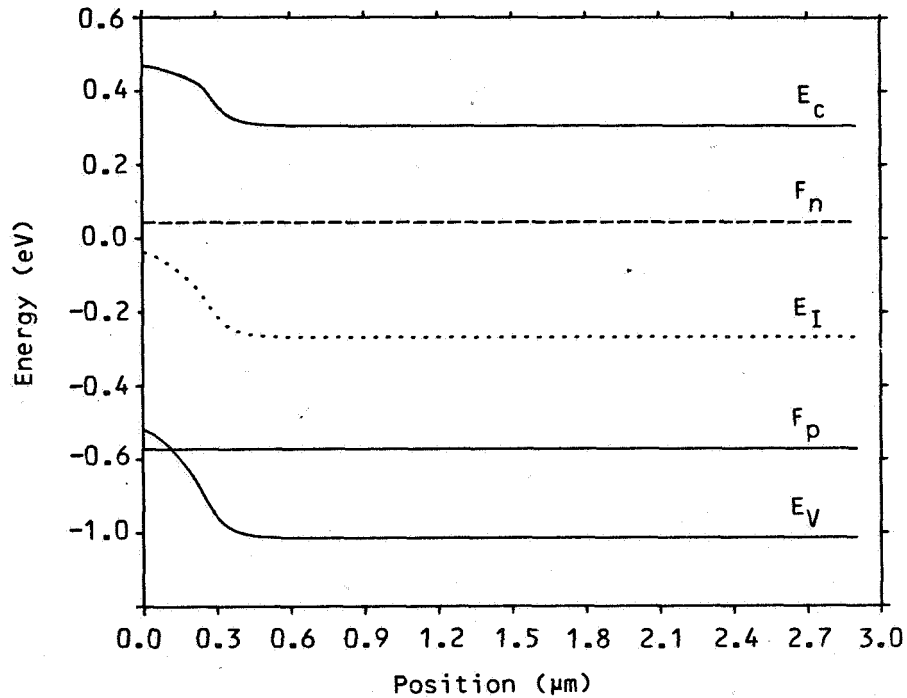
Figure 7. Open-circuit energy band diagram
for the p+nn+ cell with bandgap
narrowing.

THEORETICAL RESULTS ON THE DOUBLE-COLLECTING
TANDAM JUNCTION SOLAR CELL

Chandra Goradia and John Vaughn
The Cleveland State University

and

Cosmo R. Baraona
NASA Lewis Research Center
Cleveland, Ohio

SUMMARY

Results of computer calculations using a one-dimensional model of the Silicon Tandem Junction Solar Cell (TJC) with both front and back current collection are presented. Using realistically achievable geometrical and material parameters, our model predicts that with base widths of 50μm and 100μm and base resistivities between 1 ohm-cm and 20 ohm-cm, beginning-of-life (BOL) efficiencies of 14% to 17% and end-of-life (EOL) efficiencies of 12% to 14%, after about seven years in synchronous orbit, can be obtained.

INTRODUCTION

Both theoretical (ref. 1,2) and experimental (ref. 3) results show that the back-only collection Tandem Junction silicon solar cell (TJC) suffers a significant degradation in efficiency after exposure to 1 MeV electron fluences greater than 10^{14} electrons/cm^2. The reduction of the short-wavelength (<0.6μm) spectral response to negligible values at high fluences of 1 MeV electrons indicated that the one primary cause of the radiation-induced degradation was the reduction of the base diffusion length and hence of the minority carrier collection efficiency by the back-only collector contacts.

It was reasoned then that with current collection from both the front and back n$^+$ regions, as shown in figure 1, the radiation degradation could be significantly reduced while still retaining the advantages offered by coplanar back contacts. In the double-collecting TJC structure of figure 1, the front metal grid fingers may be wrapped around one edge of the cell and connected to the bus bar of the metal fingers contacting the back n$^+$ stripes. The structure could then be regarded as either a TJC with additional collection from the front or as a conventional wraparound contact solar cell with additional collection from the interdigitated back n$^+$ stripes. However, since the primary current collection would be expected to be from the front, one would expect the structure to behave more like a conventional front-collecting solar cell with respect to radiation degradation. It would clearly be of interest to see if, in theory, this double-collecting TJC structure offers a higher BOL efficiency and higher radiation tolerance than either the front-only collecting wraparound

contact solar cell or the back-only collecting tandem junction solar cell. To this end, we derived a one-dimensional model of the double-collecting TJC.

THEORETICAL MODEL

The model of the double-collecting TJC was derived by considering this device as a composite of eight solar cells in parallel, corresponding to the front surface being illuminated or dark (under metal grid fingers), the surface recombination velocity at the front surface being low or high (allowing for dotted front metal contacts), and the back surface being n^+ collector or not. The Ebers-Moll type currents were calculated for each of the eight cells under appropriate boundary conditions and added to give the overall illuminated current-voltage characteristic of the device. The model also accounts for separate series resistance components in the emitter, base and collector current paths as shown in figure 2, and allows the calculation of all performance parameters as functions of the geometrical and material parameters, and 1 MeV electron fluence.

Computer calculations were made using this model for various base resistivities, base widths, base diffusion lengths, surface recombination velocities and 1 MeV electron fluences. The results of these calculations are presented in this paper. All calculated results are for a 2 cm x 2 cm double-collecting TJC with 18 grid fingers on the front face, 36 n^+ and p^+ interdigitated stripes in the back and the total back n^+ and p^+ areas of 3.4 cm^2 and 0.4 cm^2 respectively. The nominal values of all other parameters used in the calculations are given in table 1.

In the radiation damage calculations, two sets of damage coefficients were used. These were the lowest and the highest ranges (curves) from the plots of 1 MeV electron damage coefficient versus p-type silicon resistivity as given by Srour et. al. (ref 4.) and they fit the following equations:

$$\text{Lowest Curve:} \quad K = 1.034 \times 10^{-10}/(\rho_B)^{0.6254} \tag{1}$$

$$\text{Highest Curve:} \quad K = 3.296 \times 10^{-10}/(\rho_B)^{0.6164} \tag{2}$$

where K is the 1 MeV electron damage coefficient and ρ_B is the resistivity in ohm-cms of the p-type silicon base material. The above damage coefficient dependences on base resistivity are based on experimentally determined values and should be valid for base resistivities between 1 ohm-cm and about 50 – 100 ohm-cm. These allowed the calculation of the minimum and the maximum amounts of radiation degradation that can be expected for the double-collecting TJC solar cell for various combinations of geometrical and material parameters. The calculated results are given in the following section.

CALCULATED RESULTS AND DISCUSSION

Figure 3 shows the effect of base width and base diffusion length on the BOL AMO efficiency for a 1 ohm-cm base resistivity solar cell. As would be expected, for a given base width, longer diffusion lengths yield greater AMO efficiencies and, for a fixed diffusion length, the smaller its value, the shorter the base width at which the peak efficiency occurs. Note that since BOL diffusion lengths greater than 300μm are now becoming possible for fully processed 1 ohm-cm base material solar cells, BOL AMO efficiency approaching 17% and higher should be possible for the double-collecting TJC.

Figure 4 shows the effect of varying the surface recombination velocity at the uncontacted front and back surfaces on the performance parameters, namely, the short-circuit current I_{sc}, the open-circuit voltage V_{oc}, the fill factor FF and the conversion efficiency η. The results are for a 1 ohm-cm 100μm thick cell with a BOL diffusion length of 300μm. It is seen that the conversion efficiency is essentially constant for surface recombination velocities less than about 10^3cm/s. Thus, it is essential to maintain the surface recombination velocity at less than 10^3cm/s. We do not presently have a physical explanation for the very slight improvement in the fill factor for surface recombination velocities greater than 10^6cm/s.

Figures 5 and 6 show the conversion efficiency η versus 1 MeV electron fluence for 50μm and 100μm wide cells respectively, for base resistivities of 1,6 and 20 ohm-cm. The solid curves in each figure correspond to the lowest range of damage coefficients while the dashed curves correspond to the highest range of damage coefficients. Note that, as expected, the theoretical radiation damage behavior of the double-collecting TJC is indeed similar to that of the conventional front-collecting solar cell and much better than that of the back-only collecting TJC (ref 1,2,3). If we define end-of-life (EOL) as an exposure to a fluence of 3 x 10^{14} 1 MeV electrons/cm^2 or the equivalent of roughly seven years in geosynchronous orbit, then it is seen from figures 5 and 6 that while the best EOL efficiency is obtained for a 50μm thick 1 ohm-cm cell, the least amount of percentage degradation in efficiency occurs for the 50μm thick 20 ohm-cm cell. This fact is shown even more clearly in figure 7 which plots the percentage degradation in efficiency versus the base resistivity for 50μm and 100μm thick solar cells. It is then seen that even with the highest damage coefficient, a percentage degradation in efficiency of 15% can be achieved in a 50μm thick, 10 ohm-cm cell whose BOL efficiency would be about 14.5%. On the other hand, if the processing-induced increase of damage coefficient can be almost eliminated so that the lowest damage coefficient curves in figure 7 apply, then a percentage degradation of 15% can be achieved with a 50μm thick, 1 ohm-cm cell with a BOL efficiency of about 16.5%.

Figure 8 plots both the BOL and the EOL efficiencies versus base resistivity for 50μm, 100μm and 200μm thick cells. This figure can serve as a design guide in the choice of base width and base resistivity to obtain specified values of BOL or EOL efficiencies.

CONCLUDING REMARKS

The theoretical radiation tolerance of the double-collecting TJC is significantly superior to that of the back-only collecting TJC. Since we have presently not made theoretical calculations on the radiation damage in conventional front-collecting solar cells with identical geometrical and material parameters, no quantitative comparison can as yet be made to the radiation tolerance of these cells.

Using realistically achievable values of geometrical and material parameters, our model of the double-collecting TJC predicts that in addition if the 1 MeV electron damage coefficient in a finished solar cell can be kept as low as in bulk material of the same resistivity, then a 1 ohm-cm, 50µm thick double-collecting TJC will degrade by only 15% from a BOL η of 16.5% to an EOL η of 14.1%.

In theory, the double-collecting TJC offers high BOL efficiency, high radiation tolerance, and the convenience of coplanar back contacts. In practice, the greater complexity of fabrication of the double-collecting TJC compared to conventional 50µm thick cells with standard or wraparound contacts may be an important consideration in its acceptance as a space solar cell.

REFERENCES

1. Goradia, C.; Vaughn, J.; and Baraona, C.: Theoretical Results On The Tandem Junction Solar Cell Based On Its Ebers-Moll Transistor Model. Conf. Rec. Fourteenth IEEE Photovoltaic Specialists Conference, San Diego, CA, Jan. 1980, pp. 172-177.

2. Goradia, C.: A One-Dimensional Theory of High Base Resistivity Tandem Junction Solar Cells In Low Injection. IEEE Trans. Elec. Dev. Vol. ED-27, No. 4, Apr. 1980, pp. 777-785.

3. Anspaugh, B.E.; Miyahira, T.F.; and Scott-Monck, J.A.: Electron Irradiation of Tandem Junction Solar Cells. Proc. of Third High Efficiency and Radiation Damage Solar Cell Meeting, Cleveland, OH, June 1979, NASA CR-2097, pp. 131-136.

4. Srour, J.R.; Othmer, S.; Chiu, K.Y.; and Curtis, O.L. Jr.: Damage Coefficients in Low Resistivity Silicon. NASA CR-134768, NRTC 75-23R, 1975, p. 48.

TABLE I
Parameter Values Used in Calculations

Temperature	=	300K
Spectrum	=	AMO
Front Refl. Coeff. $R_F(\lambda)$	=	Measured values for AR-coated non-reflective surface
Illuminated Area	=	4 cm^2
Number of n^+ and p^+ Back Stripes	=	36 each
n^+ Back Collector Area	=	3.4 cm^2 (85% coverage)
p^+ Back Stripe Area	=	0.4 cm^2 (10% coverage)
p Gap Area in Back	=	0.2 cm^2 (5% coverage)
Front Grid Finger Number & Area	=	18, 0.2 cm^2 (5% coverage)
Surface Recombination Velocity at uncontacted front and back surfaces	=	10^3 cm/s
Surface Recombination Velocity at Metal Contacts	=	10^9 cm/s
n^+ Emitter and Collector Dopings	=	$2.5 \times 10^{19} \text{ cm}^{-3}$
n^+ Emitter and Collector Depths	=	$0.3 \mu\text{m}$
BOL Diffusion Length in n^+ Emitter and Collector	=	$2 \mu\text{m}$
Base Width	=	$100 \mu\text{m}$, variable
BOL Base Diffusion Length	=	$300 \mu\text{m}$, variable
Base Resistivity	=	1 ohm-cm, variable
Base Series Resistance	=	0.022 ohm
Emitter and Collector Series Resistances	=	Functions of Base Width and Base Resistivity
n^+ Emitter and Collector Damage Coefficients	=	2.0×10^{-8} per electron
Base Damage Coefficient	=	Function of Base Resistivity
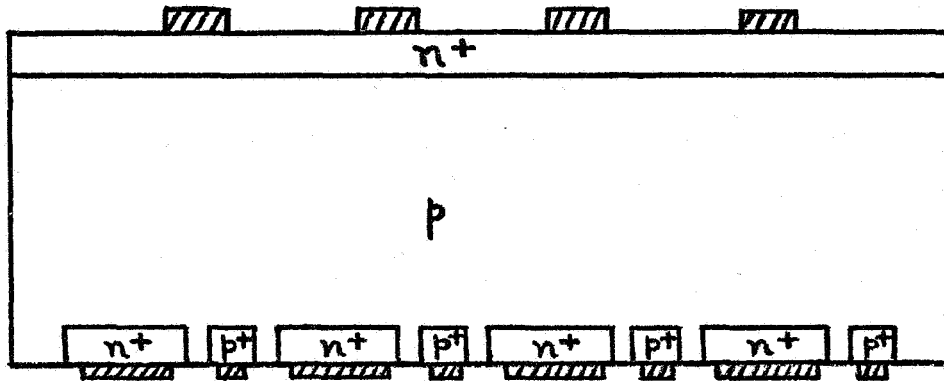
Figure 1. Schematic Diagram of a Double
Collecting Tandem Junction Solar Cell.
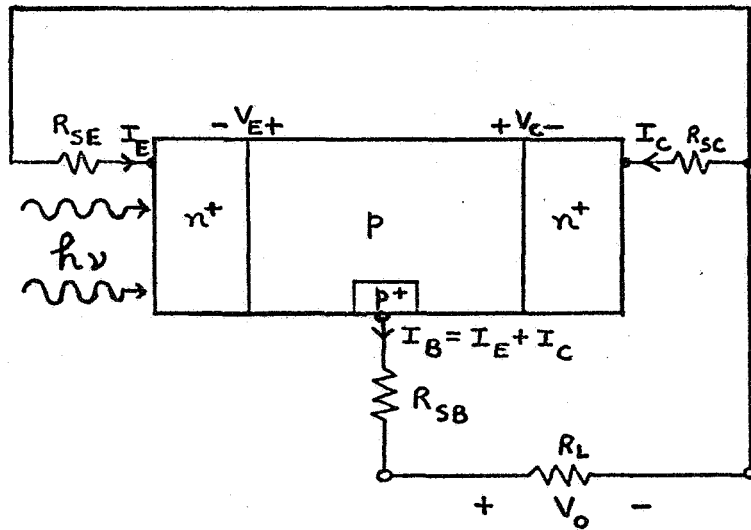
Figure 2. Schematic Representation of Double
Collecting TJC With Emitter, Base and Collector
Components of Series Resistance.
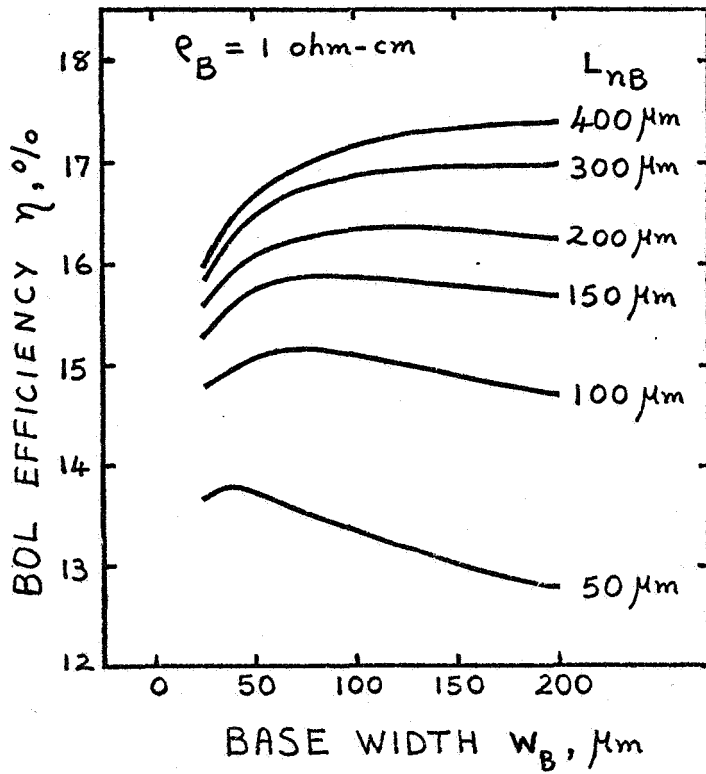
Figure 3. Effect of Base Width and Base Diffusion Length on BOL Efficiency.
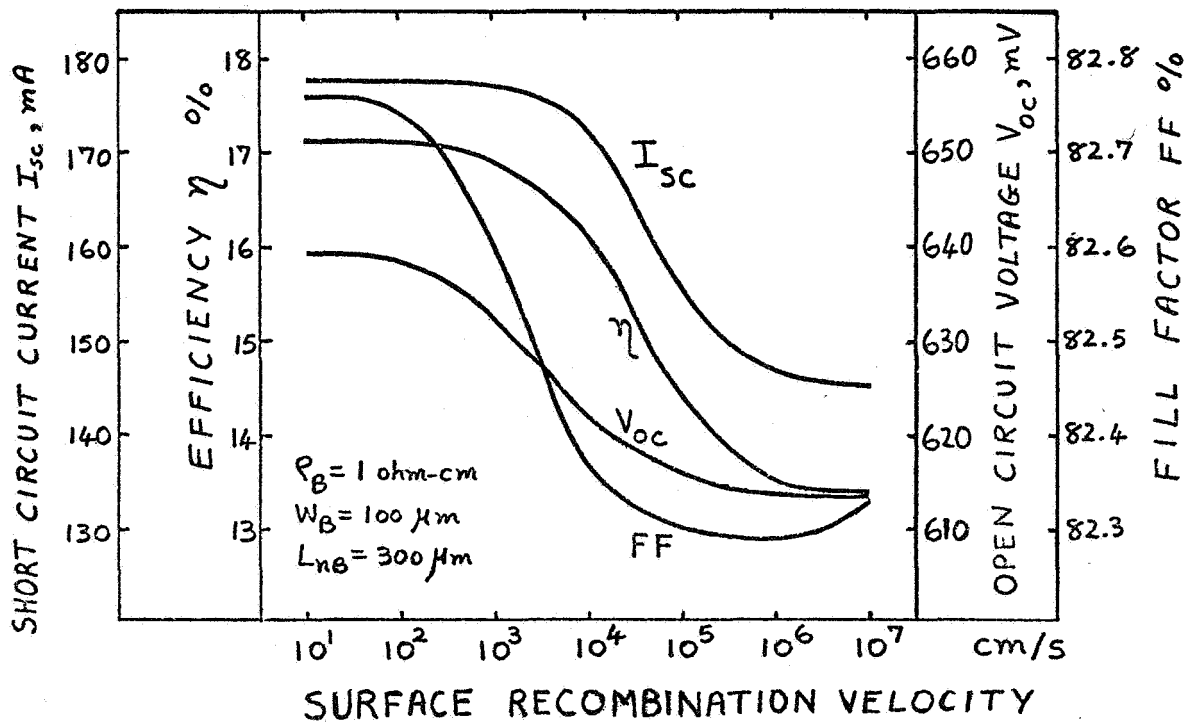
Figure 4. Effect of Surface Recombination Velocity on Performance Parameters.
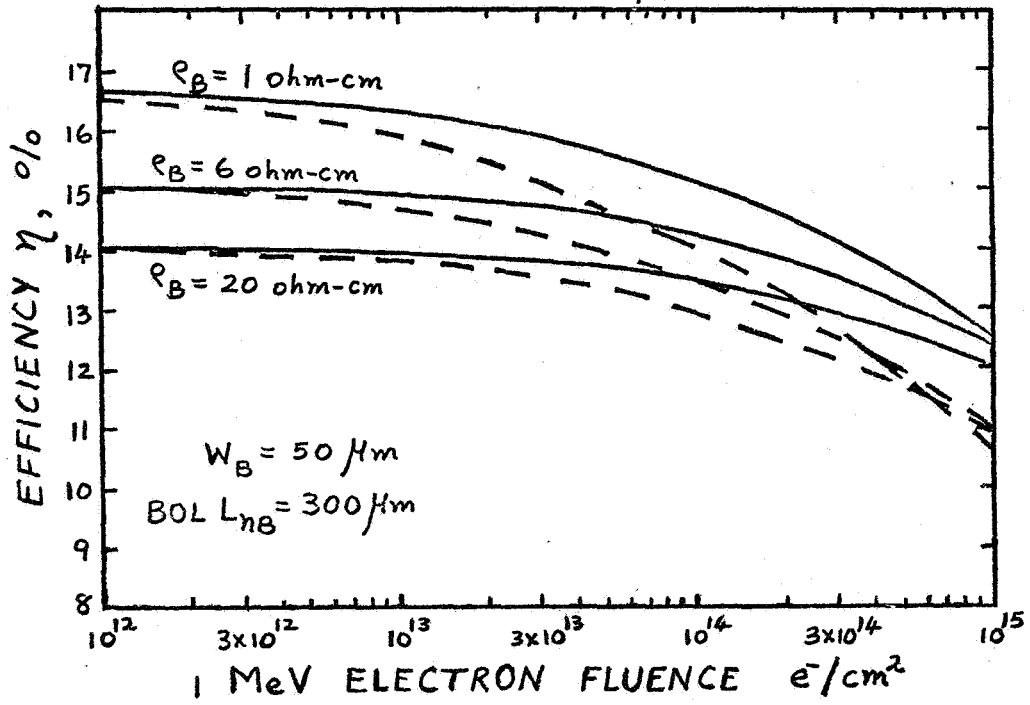
Figure 5. Efficiency versus 1 MeV Electron
Fluence for 50μm Thick Cell.
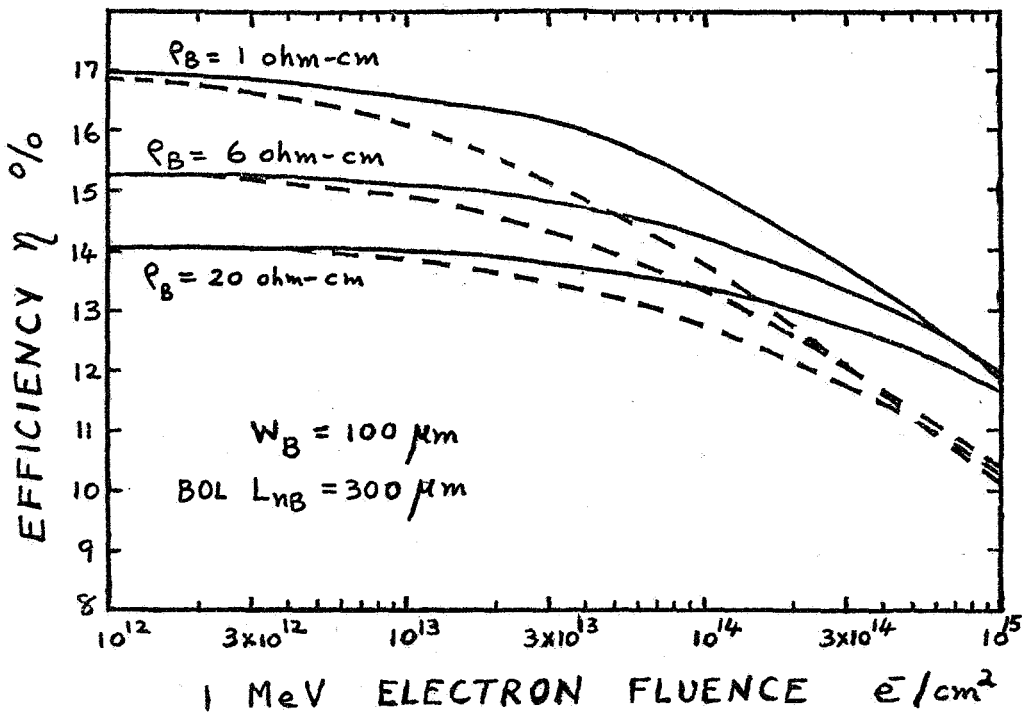
Figure 6. Efficiency versus 1 MeV Electron
Fluence for 100μm Thick Cell.
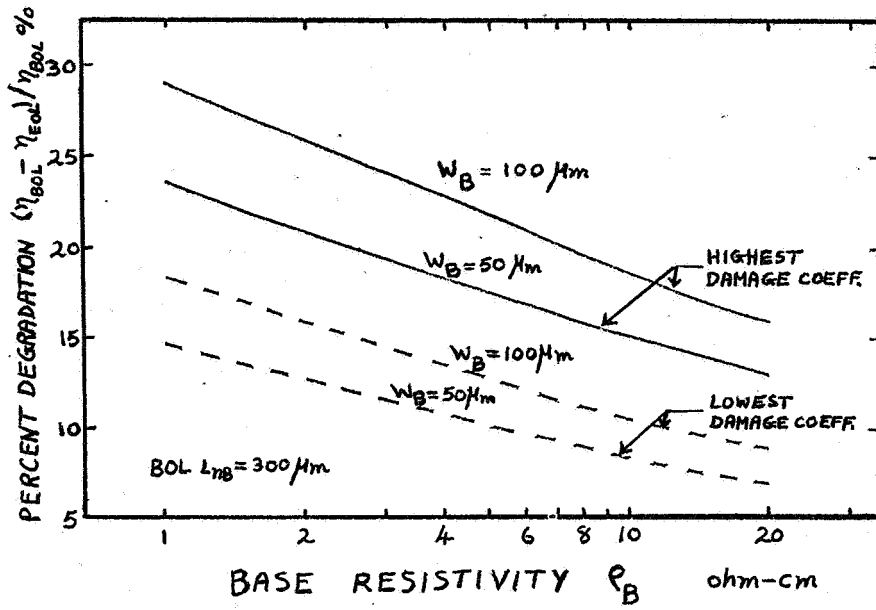
Figure 7. Percent Degradation in Efficiency versus Base Resistivity.
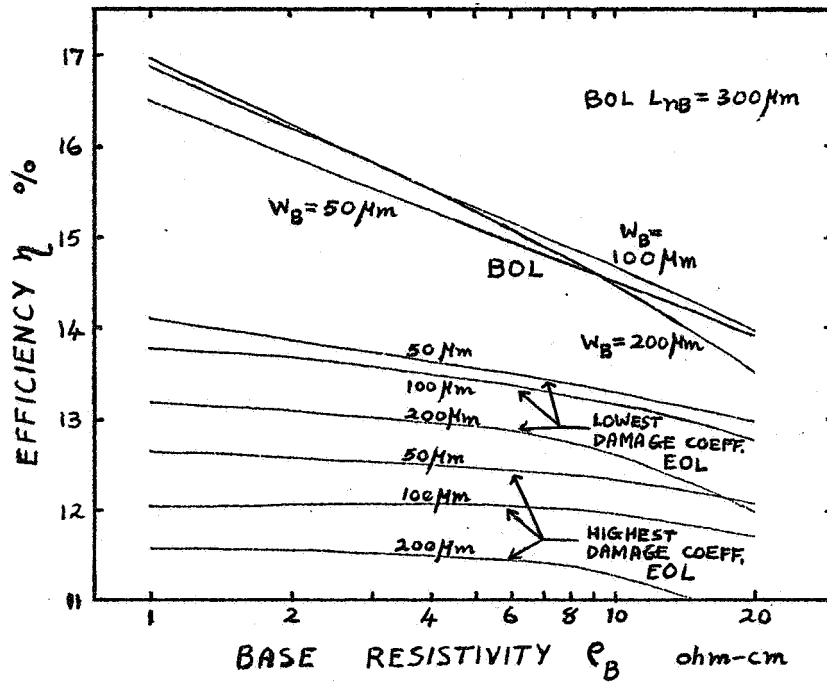
Figure 8. BOL and EOL Efficiencies versus Base Resistivity.

MEASUREMENT OF MINORITY-CARRIER DRIFT MOBILITY IN SOLAR CELLS
USING A MODULATED ELECTRON BEAM*

Siegfried Othmer and M. A. Hopkins
Northrop Research and Technology Center
Palos Verdes Peninsula, California

The hypothesis has been advanced that processing effects on minority-carrier drift mobility may explain variations in open-circuit voltage among space-quality silicon solar cells subjected to different processing protocols.[1] Also, some evidence exists that integrated circuit process flows may result in degradation of drift mobility.[2] It is therefore of interest to determine the mobility or, equivalently, the diffusivity in solar cells, without subjecting them to additional processing steps.

A determination of diffusivity on solar cells is here reported which utilizes a one-dimensional treatment of diffusion under sinusoidal excitation. Cells used were the same as those employed in Ref. 1. An intensity-modulated beam of a scanning electron microscope (SEM) was used as a source of excitation. The beam was injected into the rear of the cell, and the modulated component of the induced terminal current was recovered phase-sensitively. A Faraday cup to measure the modulated component of beam current was mounted next to the sample, and connected to the same electronics, as shown in Figure 1. A step-up transformer and preamplifier were mounted on the sample holder. Beam currents on the order of 400 pA were used in order to minimize effects of high injection. The beam voltage was 34 kV, and the cell bias was kept at 0 V.

The amplitude of the junction terminal current as a function of modulation frequency is presented in Figure 2 for two types of specimens. The ratio of the sample current to measured beam current is shown. Initially, little response was detected as the beam was injected into the back surface. Good results were obtained after a groove was cut into the back surface using a diamond saw. This served to cut through a back surface layer characterized by high recombination velocity. Curves shown are for model calculations to be discussed below. Measurements of phase delay of sample current with respect to Faraday cup current are given in Figure 3 for the same two cells.

Results were analyzed using a one-dimensional treatment of diffusion under sinusoidal excitation, following McKelvey.[3] Low injection conditions were assumed. The continuity equation to be satisfied for excess density $\Delta n(x,t)$ is

$$D \frac{\partial^2 \Delta n}{\partial x^2} - \frac{\Delta n}{\tau} = \frac{\partial(\Delta n)}{\partial t} \quad ,$$

---

where D is the diffusivity and τ the minority-carrier lifetime. The solution for sinusoidal excitation is

$$\Delta n(x,t) = \Delta n(x) \cos(\omega t) = \Delta n(0) e^{-\beta x/L} \cos(\omega t - \gamma x/L)$$

for diffusion in the positive x-direction and excitation source at the origin. L is the diffusion length. Here β and γ are given by

$$\beta = \left[\frac{1}{2} \left(1 + \sqrt{1 + \omega^2 \tau^2} \right) \right]^{1/2}$$

and

$$\gamma = \left[\frac{1}{2} \left(-1 + \sqrt{1 + \omega^2 \tau^2} \right) \right]^{1/2}$$

In the present case, the solar cell junction samples the excess density at some distance $x = R$ from the point of injection. A best fit to the observed amplitude dependence is obtained by varying the diffusion length and the lifetime. (In this manner, an approximate value of diffusivity can be obtained by use of the equation $L^2 = D\tau$.) The best fits are shown in Figure 2, along with fits for other values of L to indicate the sensitivity of the fit to choice of L. Using the best value for L, a fit of the phase dependence (Fig. 3) is obtained by choice of lifetime or, equivalently, diffusivity. An additional fit to the data, obtained using a different value of diffusion length (discussed below), is also shown.

The best value of diffusivity for specimen 672-5 appears to be 17 cm^2/sec, and for 664-1, 14 cm^2/sec. Equivalent mobilities may be determined using the Einstein relationship, $eD = \mu kT$. The calculated mobilities are 660 and 540 cm^2/V-sec, respectively. The base resistivity in these cells is 0.1 ohm-cm,[1] and published values of drift mobility for this resistivity are in the range of 400-440 cm^2/V-sec.[4,5] The present experimental values exceed the reported ones, contrary to expectations on the basis of processing effects. The quality of the theoretical fits suggest that application of a one-dimensional model is legitimate. The magnitude of scatter in the data indicates that diffusivities are obtained to within about 15% precision. Possible sources of systematic error include effects of high injection, and our assumption that excitation occurs at the surface, rather than at finite depth. Effective depth of excitation could be as large as 3 μm for the 25 keV beam used, amounting to $\leq 6\%$ of the effective cell thickness (measured from the bottom of the cut). Effects of high injection were tested for by measurement of phase delay for different degrees of beam defocus. No observable effect on the phase was noted. (By contrast, the amplitude showed a slight ($<10\%$) decrease upon defocussing.)

The cells measured here had been subjected to an unconventional processing sequence.[1] A long emitter diffusion was followed by etch-back and a

secondary emitter diffusion. An increase in open-circuit voltage under illumination conditions yielding identical short-circuit currents (25 mA/cm^2) was observed for long primary diffusion times. A decrease in diffusivity was postulated to explain this result. This supposition was supported by cell measurements which showed that the diffusion lengths in the samples were nearly identical, but that lifetimes differed. Judging from the amplitude dependence shown in Figure 2, it appears that neither the diffusion lengths nor the lifetimes in the two samples are identical. We are reluctant to draw quantitative conclusions from the amplitude data, since the assumption of one-dimensional transport is much more questionable in that case than in the case of the phase measurements. Moreover, effects of rear surface recombination have not been taken into account. Finally, the diffusion lengths measured under ac conditions may be governed by trapping rather than recombination, and would be smaller than those determined under dc conditions. Fortunately, assumptions of diffusion length have only minor influence on the determination of drift mobility on the basis of the phase data. If we assume, for example, that the diffusion lengths are ~250 μm, as determined from cell measurements,[1] the diffusivities calculated are found to be 18 and 15 cm^2/sec for the samples 672-5 and 664-1, respectively, vs. 17 and 14 determined above. It should be noted that the diffusion length which yielded the best fit to the amplitude data of sample 664-1, about 35 μm, also yielded the best fit to the phase data. It was anticipated that sample 664-1, which was subjected to a 4-hour primary diffusion, should exhibit a higher diffusivity than the specimen 672-5, which was subjected to a 41-hour primary diffusion. This has not been confirmed in the present measurements.

REFERENCES

1. M.P. Godlewski, T.M. Klucher, G.A. Mazaris, and V.G. Weizer, Conference Record, 14th IEEE Photovoltaic Specialists Conference, 1980, p. 166.

2. S. Othmer, Scanning Electron Microscopy, 1978, Vol. I, SEM, Inc., p. 727.

3. John P. McKelvey, Solid State and Semiconductor Physics, Harper & Row, New York, 1966, p. 439.

4. S.M. Sze and J.C. Irvin, Solid State Electronics 11, 599 (1968).

5. K.B. Wolfstirn, J. Phys. Chem. Solids 16, 279 (1960).
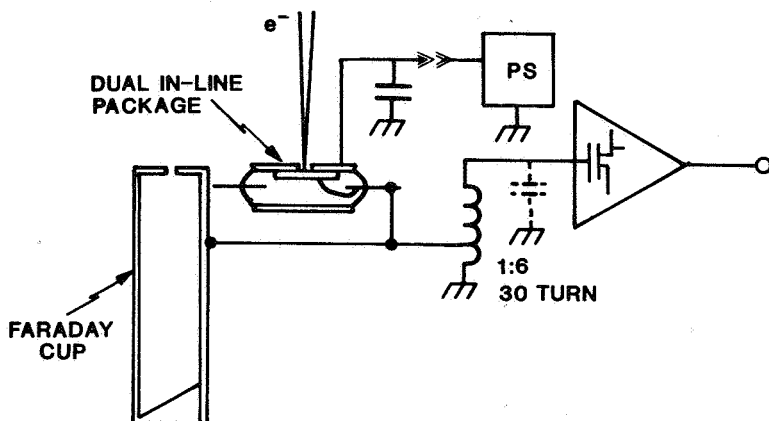
Figure 1. Experimental arrangement for the measurement of cell response in amplitude and phase under conditions of rear-surface injection using a modulated beam.

80118
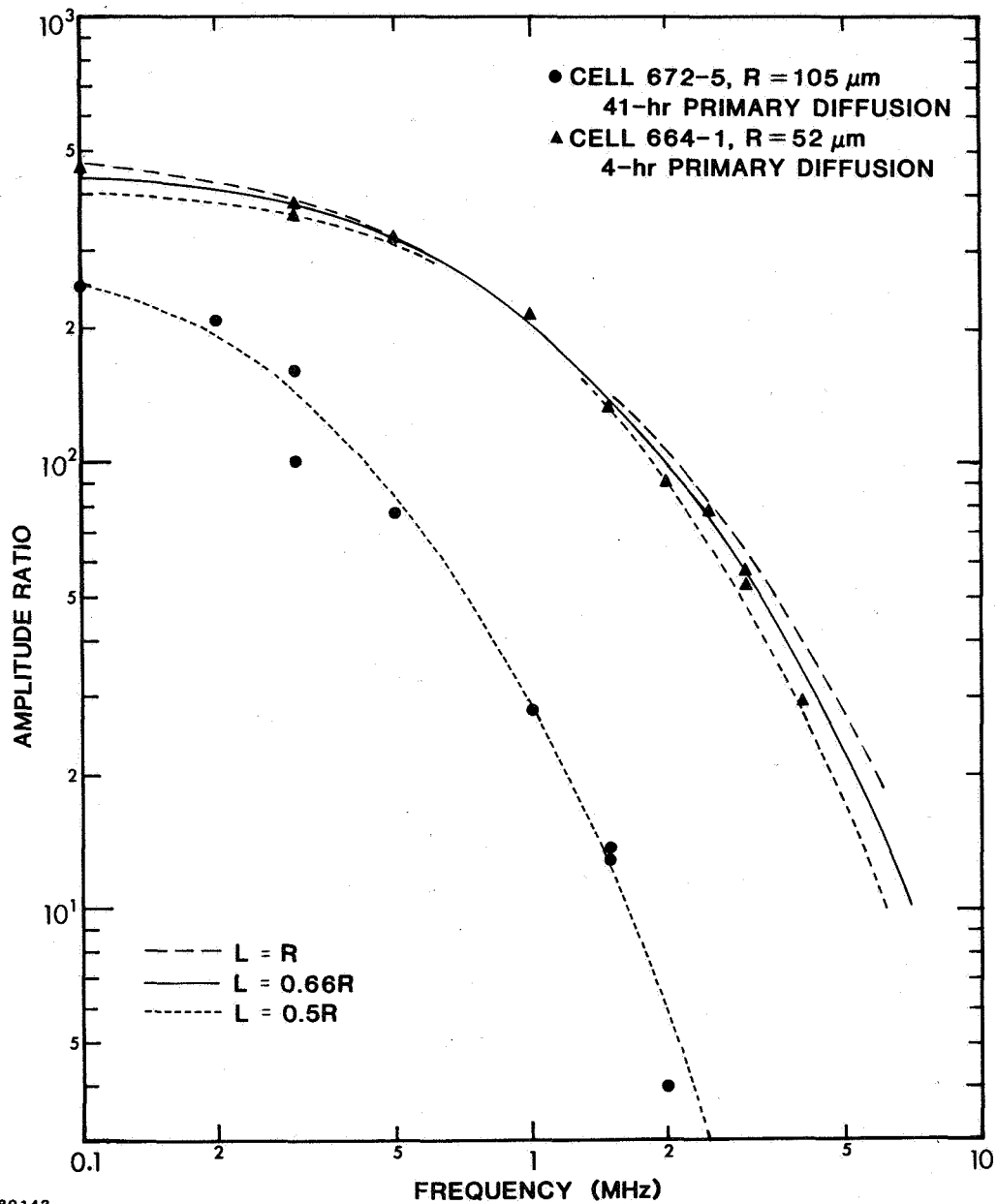
63

Figure 2. Amplitude ratio of solar cell current to beam current as a function of frequency for two solar cells. Theoretical fits are shown for different assumptions of bulk diffusion length. R is the distance of the point of injection from the junction.
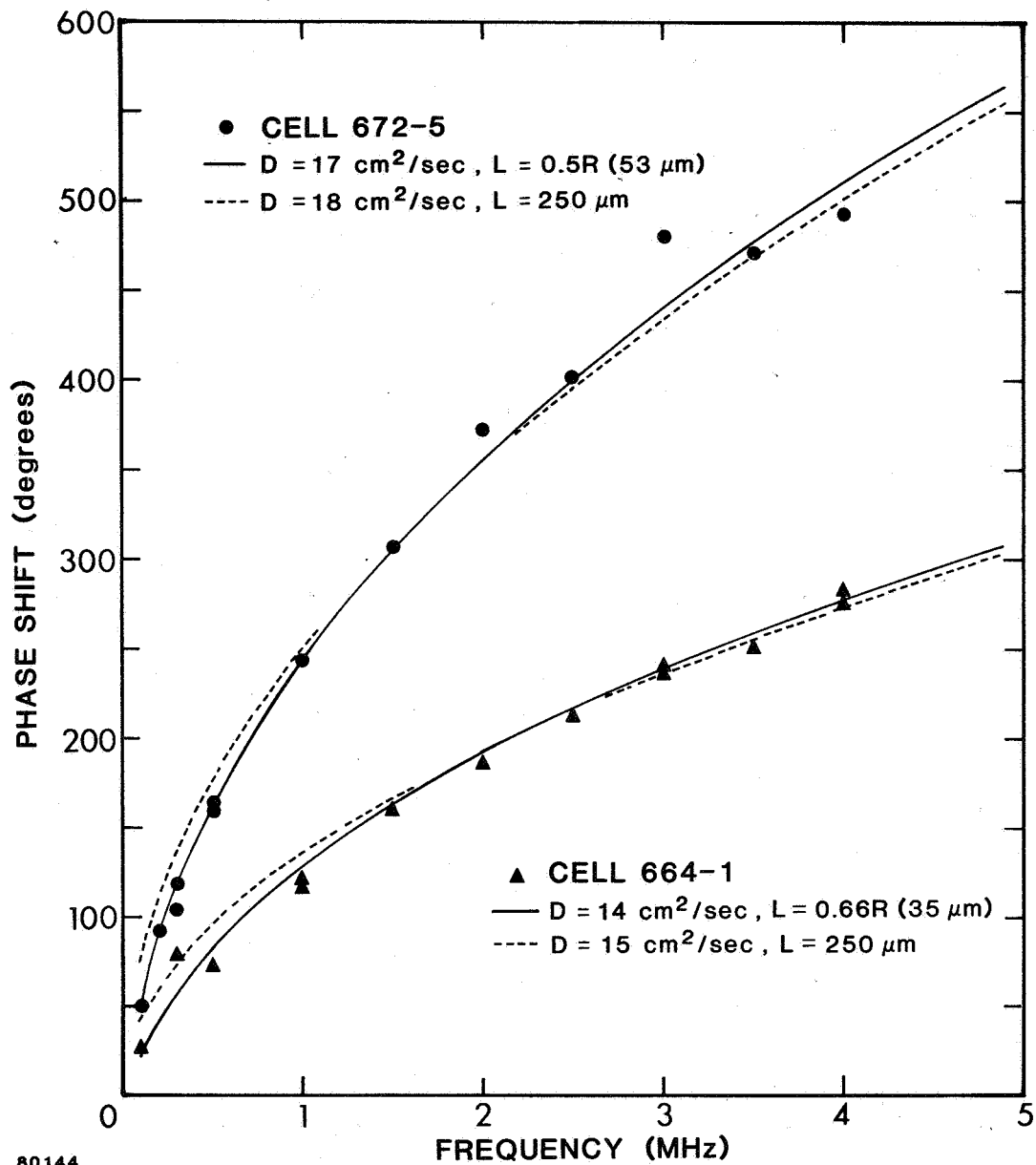
Figure 3. Phase shift of solar cell current with respect to beam current for the two cells treated in Figure 2. Shown is the theoretical fit for the best choice of diffusivity under assumption of diffusion lengths determined from Figure 2, as well as the fit under assumption of 250 μm diffusion length.

SHORT-CIRCUIT CURRENT IMPROVEMENT IN THIN CELLS
WITH A GRIDDED BACK CONTACT*

Michael Giuliano and John Wohlgemuth
Solarex Corporation
Rockville, Maryland

The use of a gridded back contact was undertaken recently on thin silicon solar cells (50 μm) with the objective of decreasing the weight of the cells still further for space application. An unexpected increase in short-circuit current of almost 10 percent was experienced for 2 cm x 2 cm cells. Figure 1 is a photograph which shows the contact grid pattern on both the front and back of the cell as viewed in a mirror. Control cells with the standard continuous contact metallization were fabricated at the same time as the gridded back cells with all processes identical up to the formation of the back contact. The gridded back contact pattern was delineated by evaporation of Ti-Pd over a photo-resist mask applied to the back of the wafer; the Ti-Pd film on the controls was applied in the standard fashion in a continuous layer over the back of the cell. Ti-Pd contacts were similarly applied to the front of the wafer, and the grid pattern on both sides of the cell was electroplated with 8-10 μm of silver. A p^+p back surface field (BSF) had been previously formed by alloying a screen-printed film of aluminum and chemically cleaning off the excess aluminum and other film residues.

Figure 2 compares the I-V plots for the 2 x 2 cells, showing the increase in short-circuit current which resulted for the gridded back contact cells in this experiment. The reasons for the increase in I_{sc} are presently under investigation. Among the possible mechanisms are:

o   Optical reflection off the silicon/air interface of the gridded back which increases the light path through the silicon for thin cells.

o   Improved bulk minority carrier lifetime because the gridded back results in stress release on the solar cell as compared to a continuous back metal contact.

o   Improved back surface recombination velocity with the removal of the metal/silicon interface.

In an attempt to evaluate some of these possibilities, we compared IV characteristics for the gridded back thin cells with illumination from the front and back. These are illustrated in Figure 3 on cells which had no AR coat. There is an appreciable response with back illumination which suggests that back surface and bulk recombination are not excessive in this cell. The investigation is continuing and the results will be reported in a later publication.
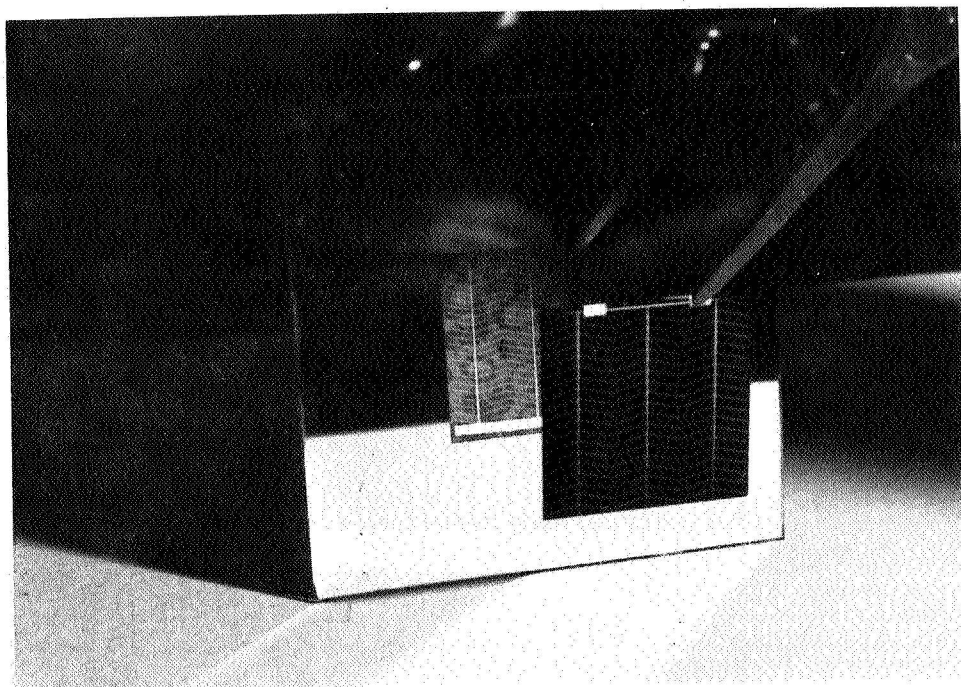
Figure 1.   Contact Grid Pattern on Front and Back of Thin Cell.

Figure 3.   IV Curves comparing Front (solid lines) vs Back (dashed lines) Illumination of Gridded-Back Contact Thin Cells. No AR Coat.

69

Figure 2.
IV Curves for Gridded vs
Continuous Back Contacts on a
Sampling of 3 Cells Each From the
Same Batch of Processed 2cmx2cm
Thin Cells

70
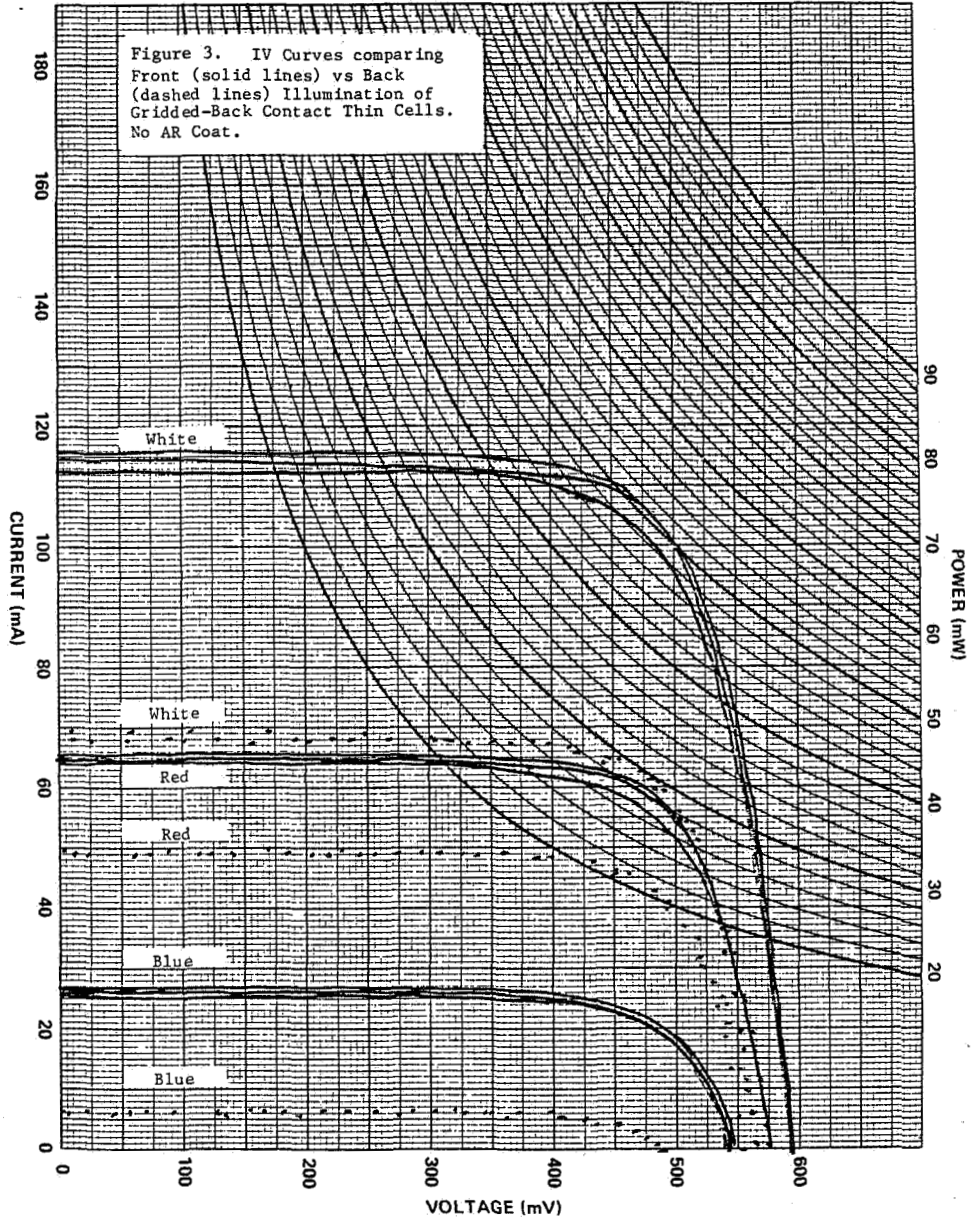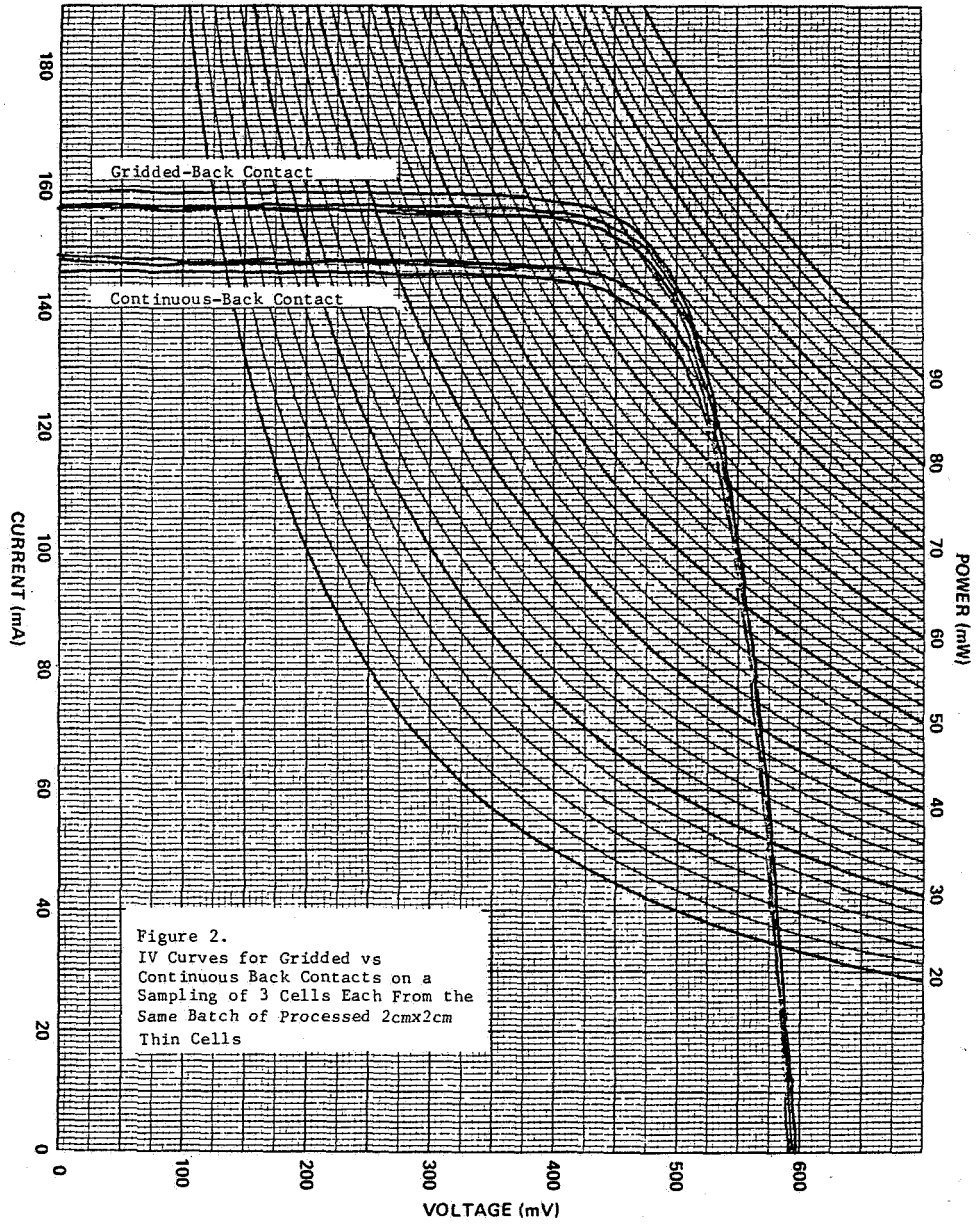
SILICON RESEARCH AND TECHNOLOGY WORKSHOP REPORT

A. Meulenberg, Jr.
COMSAT Laboratories
Clarksburg, Maryland

The Silicon Research and Technology Workshop discussed materials, structures, processing, modeling and measurements of high efficiency silicon solar cells. In the materials area, highlights included: 1) the possibility of improving cell voltages by reducing minority carrier mobilities in critical regions of the solar cell; 2) the need for and possibility of lowering the surface recombination velocity for improvement of open circuit voltage in shallow junction cells; 3) the present need for improved lifetime in high resistivity cells; and 4) the potential for new materials such as polycrystalline or dendritic web material to perform well at end-of-life in a radiation environment.

In the area of structures, distinction was made between those for terrestrial use and those that would survive radiation environments. It was felt that tandem junction, induced junction and M-I-S cells have promise in the terrestrial area but have shown limitations under irradiation. Use of thin cells, "dot" contacts, thin, heavily doped, surface layers, and back surface fields have shown their importance under the proper conditions; improvements are still expected from these areas. The use of back surface reflectors, transparent back cells, and IR transparent arrays are all deemed necessary for low temperature operation in space.

Processing was covered to some extent in the discussions of structures and materials but new areas such as epitaxial growth and laser or electron-beam annealing (and diffusion) were proposed as having certain advantages over more conventional techniques. More work on these techniques should help overcome problems which have limited their full utilization. The means of reducing the surface recombination velocity and of improving the influence of P^+ back layers on heavily doped silicon were highlighted as critical problems at the present time. Solar cell modeling appears to be adequate for guidance of research at the present time. However, as fabrication limits are pushed, the uncertainties in structure and nature of thin, heavily doped, silicon layers and the associated surfaces may require new data and probably new models. The study of these limiting structures will require some new measurement techniques and some methods were discussed for a more sensitive determination of surface recombination velocity on appropriate test structures rather than on finished cells. If mobility control is envisioned, measurement techniques compatible with studying gradients throughout the material may be necessary.

In general, the discussion pointed out present results as material and processing limited. Theoretical structures have been proposed to overcome these problems, but even if practice cannot meet theory, there was optimism about the knowledge obtained in pursuit of the goals providing new avenues to follow. The possibility of a quantum jump in cell efficiency must not be discounted so that the reality of an 18 percent silicon solar cell might be practical and not just a one-shot laboratory accident.

THE GaAs SOLAR CELL RESEARCH AND DEVELOPMENT
PROGRAMS OF THE AIR FORCE

Kenneth T. Masloski
AF Wright Aeronautical Laboratories
Wright-Patterson AFB, Ohio

INTRODUCTION

GaAs has received much interest for space application photovoltaics due to its inherent advantages over silicon. Higher efficiencies, superior radiation hardness, and a greater temperature resistance are the major advantages of GaAs over Si. Present and future Air Force programs will look for ways of maximizing these advantages while minimizing disadvantages such as higher costs and weights. Currently, four programs in GaAs photovoltaics are underway and each program will be discussed in terms of its objective, approach and present status.

HIGH EFFICIENCY SOLAR PANEL (HESP) PHASE II GaAs

The HESP Phase II GaAs program is being performed by Hughes Aircraft Company (ref. 1). The program began in September 1977 and will conclude by October 1980. The objective of the program is the development of space qualified solar cells having a beginning-of-life (BOL) efficiency of 16%, at 25°C, under air mass zero (AMO) illumination. After 7 years in the synchronous orbit radiation environment, which is approximated by 3×10^{14} 1MEV electrons/cm^2 for laboratory simulation, these cells shall have an end-of-life (EOL) efficiency of 14%, at 25°C, under AMO illumination. Hardening the contacts and interconnects against laser and nuclear weapon effects and the development of weldable contacting and interconnecting techniques will also be considered. Also the fabrication methods developed from this program must be documented to provide a potential mass production capability.

The approach chosen was to use GaAs substrates grown through the Horizontal Bridgeman Growth Method. The cell is then fabricated using the liquid phase epitaxy (LEP) method (ref. 2).

The first step in this process, the Horizontal Bridgeman Growth of GaAs substrates, is being performed by a subcontractor, Crystal Specialties. This method is diagramed in figure 1. Gallium is placed in a quartz boat container, that is contained inside a three zone furnace. Support liners of boron nitride are placed on the sides and under the boat to provide support at high temperatures. A small amount of tellurium dopant is placed in the growth ampoule in front of the boat and a stoichiometric amount of arsenic is placed on the other end of the growth ampoule. The ampoule is evacuated and sealed. The gallium is heated to 1247°C, while the arsenic is heated to 600°C. The arsenic sublimes and reacts with the gallium forming a GaAs melt. The melt is slowly cooled to form a single crystal, n+ doped GaAs substrate. Ingots of 2x2 inch size have been produced using this method. The ingots are sawed, lapped and polished into

wafers of 8 and 12 mil thickness. The thin wafers had a high rate of failure (62% rejects) compared to the thicker wafers (25% rejects), due mostly to handling problems. The acceptable wafers are shipped to Hughes for cell processing.

The wafers are processed into cells by infinite solution liquid phase epitaxy (LPE). As shown in figure 2, a molten solution of GaAs and dopants of Al, Be, or Sn is maintained at the growth temperature (750°C). While the wafers are lowered into the solution, the growth temperature is reduced a few degrees to initiate growth. Each growth run takes about one hour. The wafer holder has been modified to hold (8) 2x2 inch wafers therefore producing (64) 2x2cm cells in each batch.

The finished cell is shown in figure 3. The substrate is the 12 mil tellurium n+ doped wafer. The first layer grown by LPE is the Sn doped n-type buffer layer of 10 micron thickness. The next layer is the Be doped p-type window layer of the AlGaAs of .5 micron thickness. The junction is formed by diffusion of Be through the window layer into the buffer layer. The depth of this junction is critical to the radiation hardness of the cell. The cells developed by this program have .3 micron junction depths.

The upper p contact of AuZn is applied by sputtering through a 24 finger mechanical mask. The AuZn layer is an alloy of 85% Au and 15% Zn by weight and is about 2000Å in thickness. About 5 microns of silver is applied and the contact is sintered at 480°C.

The lower n contact of AuGeNi is applied by thermal evaporation. This alloy is 85% Au, 12% Ge and 1.5% Ni by weight and is also about 2000Å in thickness. A 5 micron silver overlay is applied.

A 750Å thickness anti-reflection (AR) coating of Ta_2O_5 is applied. A 12 mil thick fused silica coverglass with a second AR coating of MgF_2 is applied using Dow Corning DC 93-500 adhesive. The finished cell is 30 mils thick with a weight of 1.1 grams.

The program is near completion and the final report will be out in a few months. Based on results from the qualification testing most of the program objectives have been met. Specifically the goals for BOL and EOL efficiency have been met and were exceeded. The tests have demonstrated the superior radiation hardness and higher temperature capability of the GaAs cells compared to state-of-the-art silicon cells. The fabrication process has been documented and based on the success of this program is capable of a pilot line production if the need should arise.

The biggest disappointment of this program was a very high rate of failure of the welded back tabs. Thirty-three (33) percent of the back tabs failed the .55lb pull test, while only 8% of the front tabs failed. Each cell has 6 front contact tabs and 6 back contact tabs used to interconnect the cells. One broken tab does not prevent an electrical interconnection, in fact, the connection between cells can be carried by a single tab. Based on a 33% failure rate, the mathematical probability of all 6 rear tabs being broken at .55lbs pull strength is only 1 in a 1000. However, of the 24 cells tested, there were 2 which had all 6 rear tabs fail. This indicates that an abornally

high rate of failures are occurring on certain cells. Furthermore most of the failures are occurring in a series of tabs located next to each other. This would indicate that contamination due to handling may be causing the welding problem. Further work will be required in this area and this will be scheduled into the GaAs panel program.

GaAs SOLAR CELL PANEL

The GaAs Solar Cell Panel program is being performed by Hughes Aircraft Company. The program began in October 1979 and will conclude by April 1983. The original objective of the program was to design and build a space qualified GaAs solar panel of at least 1.2 square meters with a five year EOL power density of $125w/m^2$ at 27VDC. The plan was to build this panel to the requirements of the GPS Phase II spacecraft, however, that has been cancelled. The new objective is to design and build 3 panels and possibly fly as an experiment on another spacecraft. The new design parameters are dependent on the spacecraft and therefore have not yet been determined. These panels will utilize cell technology developed from the HESP Phase II program. At the present time Hughes is in the process of making cells for the program.

RIBBON GROWTH OF SINGLE CRYSTAL GaAs FOR SOLAR CELL APPLICATION

The GaAs ribbon growth program is being performed by Westinghouse Electric Corp (ref. 2). The work began in July 1978 and will conclude by July 1981. The objective of the program is to produce very thin layers of single crystal GaAs substrate material thru the dendritic web process. The success of this program will lead to a reduction in cost and weight of GaAs cells. The dendritic web techniques has been very successful for the growth of both Si and Ge crystals and it is hoped that this process can be useful in growth of GaAs crystals.

The general process of dendritic web growth is shown in figure 4. A dendrite seed having twin plane structure is lowered into molten GaAs at such a temperature that the seed neither melts nor nucleates growth. By slowly cooling the melt, a "button" shaped growth begins to form over the top of the seed. As the button is slowly pulled upward, two dendrites form columns that extend into the melt. Between these two dendritic columns a very thin film of liquid forms. This film freezes rapidly into a smooth single crystal surface producing excellent substrate material. This process was first used on GaAs by Westinghouse in 1964 under an AF contract. However, thermal control problems led to As vaporization and as a result, the quality of the web was poor. To correct these problems, a liquid encapsulation technique was developed using B_2O_3 which acts essentially like a cover over the liquid GaAs. The B_2O_3 encapsulation method has been thus far proven effective in trapping the vaporizing As. In addition, a computer heat flow analysis has been developed for this method and the computer indicates favorable results for dendritic web growth. Further developments will include growing larger width webs and the growth of n doped webs.

At present several 12 inch long, one centimeter wide ribbons have been grown using this technique. The thickness has varied considerably between the dendrites. Also, the ribbons contained multiple dendrites rather than one on

each edge. It is suspected that this is a result of a larger than expected thermal gradient in the pull direction. In the remaining months of the program it is hoped that these problems can be resolved through finer control of the ribbon growth parameters.

THIN FILM GaAs SOLAR CELL RESEARCH

The Thin Film GaAs Solar Cell Research program is being performed by Howard University. It is a 6 month program which began in June 1980. The objective is to fabricate a Schottky barrier gallium-silicon oxide MIS solar cell with a BOL AMO efficiency of at least 12% at 25°C. EOL efficiency should not be degraded by more than 30% when irradiated at a fluence of 1×10^{16} electrons/cm^2 at 1MEV.

The Schottky barrier solar cells are majority carrier devices whose life-times are 5 orders of magnitude more radiation resistant than minority carrier devices. The major obstacle in the development of these cells has been finding a stable oxide. This program will fabricate Shottky barrier cells by using a spin-on gallium-silica oxide on GaAs.

At this time Howard University is in the process of optimizing both growth parameters and oxide thickness. Also some "spin-on" oxide layers were deposit-ed onto the layers of GaAs that were grown by LPE. The thickness of these layers is presently unknown. In the next few months the Air Force expects some completed cells for delivery.

LOW COST GaAs SOLAR CELL DEVELOPMENT

The Low Cost GaAs Solar Cell Development Program is expected to begin in the near future. It is scheduled to be a 3 year program leading to a high efficiency, radiation hardened GaAs solar cell with a greater than 50% cost reduction at device level. This will be achieved by building the cell on a dendritic ribbon substrate. The approach to this program will be highly depen-dent on the GaAs Ribbon Growth Program mentioned earlier.

CONCLUSIONS

The five GaAs solar cell programs discussed are indicative of AF efforts to achieve the ultimate solar cell for space use. High efficency, low cost and weight cells that are hardened to both natural and man-made hazards is the goal of the AF solar cell program. GaAs shows much potential towards meeting those goals. Future developments will likely include thinner substrates thus reduc-ing cost and weight; reducing the junction depth which may lead to an increased particle irradiation hardness; utilizing the higher temperature capability of GaAs to increase laser hardness; and increasing efficiency to over 20%. Successful completion of these objectives will undoubtedly lead to the opera-tional use of GaAs in future AF space missions.

REFERENCES

1. High Efficiency Solar Panel, Phase II, Gallium Arsenide Interim Report by Hughes Aircraft Co., AFAPL-TR-79-2058.

2. Ribbon Growth of Single Crystal GaAs for Solar Cell Application by Westinghouse Electric Corp., AFAPL-TR-79-2094.
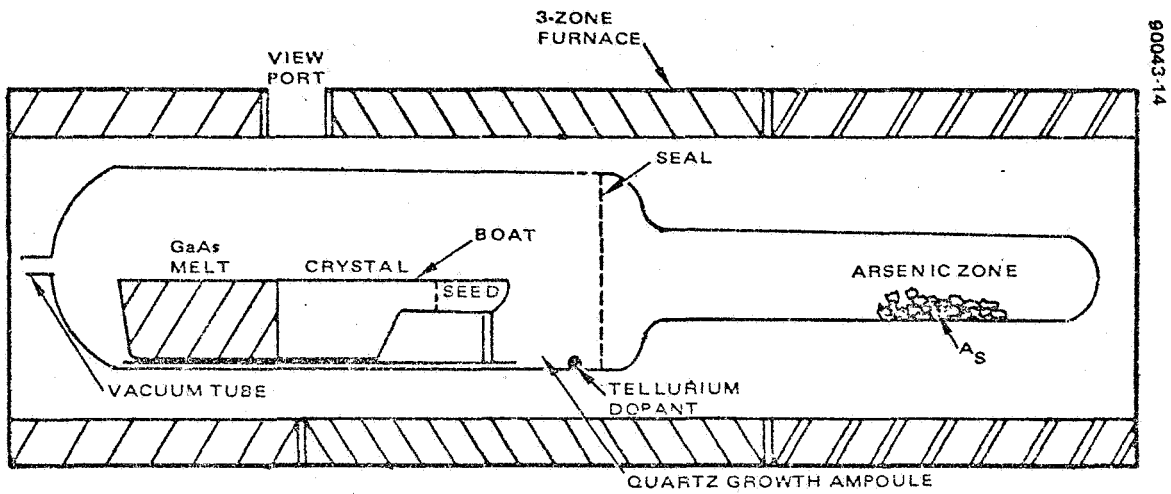
Figure 1   Horizontal Bridgman Growth.
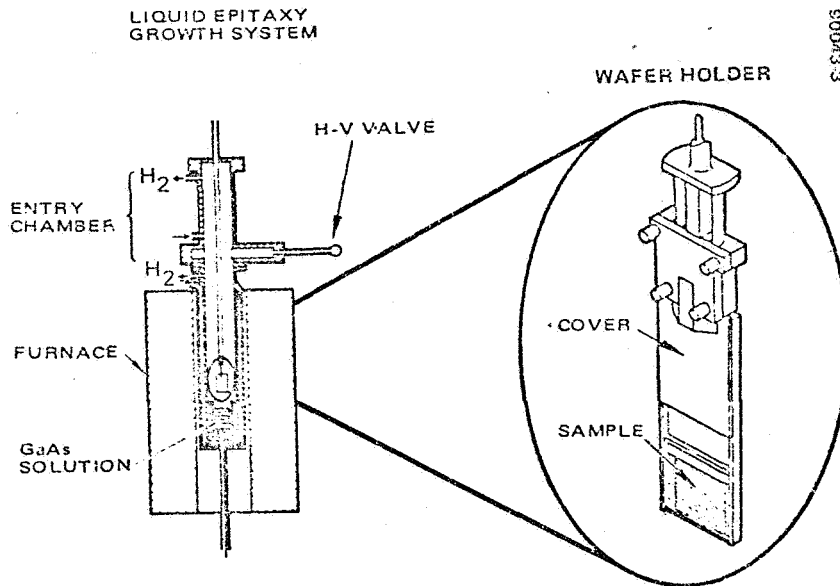
Figure 2. LPE fabrication of GaAs solar cells.

AR COATING

p CONTACT

LIGHT

p $Al_x Ga_{1-x}$ As   D   (AlGa)As

p GaAs X_j

n GaAs   t   GaAs

n^+ GaAs

p-n JUNCTION   n CONTACT

$p = 10^{18} CM^{-3}$ (Be)
$n = 10^{17} CM^{-3}$ (Sn)
$n^+ = 10^{18} CM^{-3}$ (Te)
$D \leqslant 0.5 \mu M$
$X_j \leqslant 0.5 \mu M$
$t \geqslant 10 \mu M$
NUMBER OF FINGERS = 24
p Contact: Au-Zn-Ag
n Contact: Au-Ge-Ni-Ag
AR COATING: $Ta_2 O_5$
p $Al_x Ga_{1-x}$ As
x = 0.9
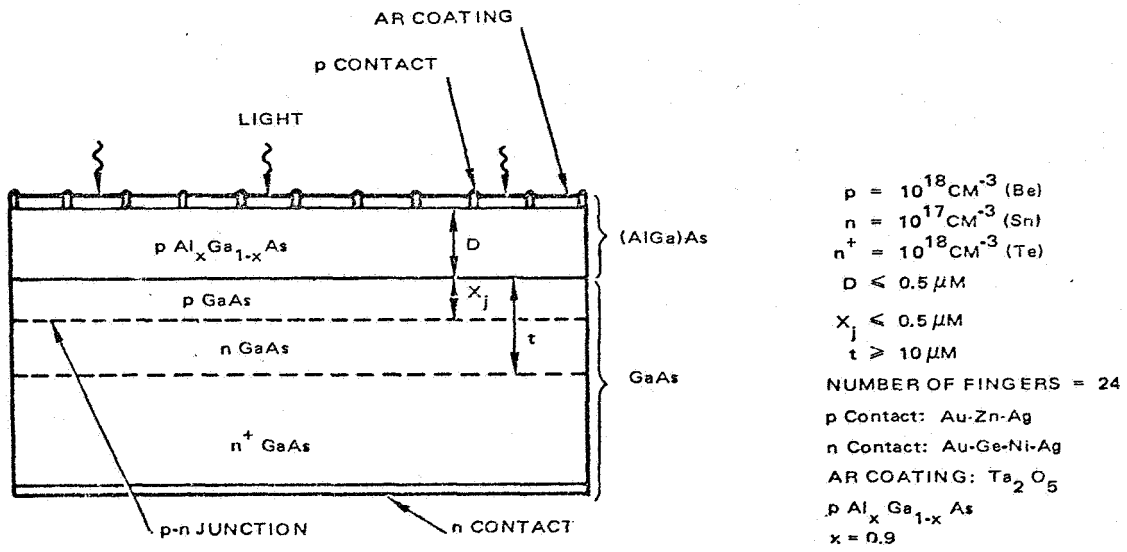
Figure 3   GaAs solar cell baseline design.

Dwg.6256A82

Dendrite Seed

Button

Bounding Dendrites

Web

Twin Planes

Liquid GaAs

Dendrite H-Arm Region

Dendrite Tip and Transition Region
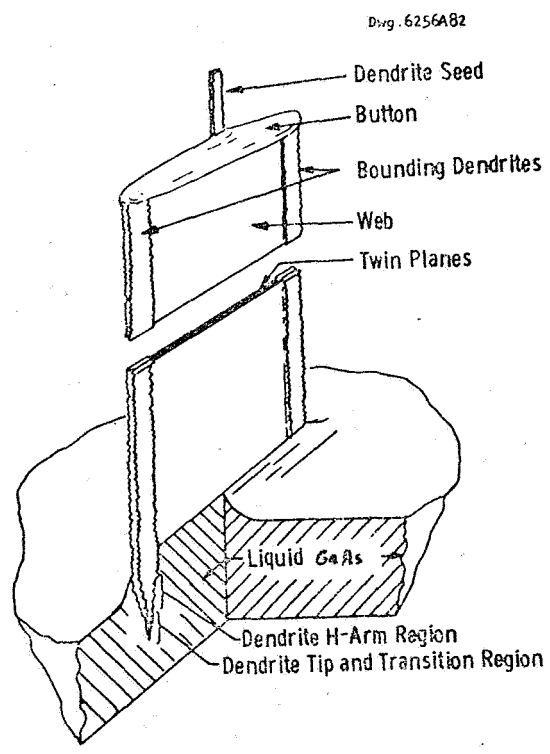
Fig. 4 —Schematic section of web growth

78

THE CLEFT PROCESS, A TECHNIQUE FOR PRODUCING EPITAXIAL
FILMS ON REUSABLE SUBSTRATES*

John C. C. Fan, C. O. Bozler, and R. W. McClelland
Massachusetts Institute of Technology
Lexington, Massachusetts

Using a new peeled film technique which we have named the CLEFT process
we have grown single-crystal GaAs films by vapor-phase epitaxy on reusable
GaAs substrates. A growth mask with narrow, widely-spaced stripe openings is
first deposited on a single-crystal GaAs substrate with (110) orientation.
The mask material is chosen to have low adhesion to GaAs. Epitaxial growth
initiated within the openings is followed by lateral growth over the mask,
which produces a continuous single-crystal GaAs film. The film is bonded to a
secondary substrate and then mechanically cleaved from the GaAs substrate,
leaving the surface of the latter in condition for repeating the procedure.
In an initial demonstration of the CLEFT process, a solar cell with conversion
efficiency of 15% at AM1 has been fabricated from a GaAs film only 8 μm thick
mounted on a glass plate 300 μm thick. Because it can greatly reduce the
quantity of bulk single-crystal material now being used in the fabrication of
solar cells, the CLEFT process should permit a drastic reduction in cell cost
without a significant reduction in efficiency. The CLEFT process should also
be applicable to other semiconductors such as Si and InP.

HIGH EFFICIENCY EPITAXIAL GaAs/GaAs AND GaAs/Ge
SOLAR CELL TECHNOLOGY USING OM-CVD*

K. L. Wang, Y. C. M. Yeh, R. J. Stirn, and S. Swerdling
Jet Propulsion Laboratory
Pasadena, California

EXTENDED ABSTRACT

INTRODUCTION

The objective of this research program is to develop a technology for fabricating high-efficiency, thin-film GaAs solar cells on substrates appropriate for space and/or terrestrial applications. The approach adopted utilizes organometallic chemical vapor deposition (OM-CVD) to form a GaAs layer epitaxially on a suitably prepared Ge epi-interlayer deposited on a substrate, especially a light weight silicon substrate which can lead to a 300 Watt-per-kilogram array technology for space. The proposed cell structure is shown in Figure 1. The intermediate goals of the program are to investigate GaAs epilayer growth on single-crystal GaAs and Ge wafer substrates and to develop related cell-fabrication technology.

EXPERIMENTAL

GaAs layers were grown on (100) single-crystal GaAs substrates in a horizontal CVD reactor at 700 - 725°C with a growth rate of 0.2 micrometer/min. By alternately adding dimethylzinc and hydrogen sulfide to the gas stream as p and n- type dopants, a shallow n^+/p homojunction GaAs structure was produced. The active p-layer about 2 micrometers thick was doped to $1-2 \times 10^{17}$ cm^{-3}, whereas the n^+ layer about 500-1000Å thick was doped to 4×10^{18} cm^{-3} for low sheet resistance. Electroplated gold was used for grid and back surface contact coating and the anti-reflection coating was made by anodization. A similar configuration and process was used for GaAs cells fabricated on single-crystal Ge substrates.

RESULTS AND DISCUSSION

High quality GaAs epi-layers have been obtained by using OM-CVD. Undoped GaAs films on Cr-doped substrates showed a Hall mobility as high as 8000 cm^2/v-sec and an electron concentration of 3×10^{14} cm^{-3} at room temperature. The electron or hole concentration in the n-type or p-type GaAs epi-layers, respectively, was found to have a linear relationship to the dopant concentration in the gas stream. Although the maximum electron concentration in GaAs doped with hydrogen sulfide can reach 5.8×10^{18} cm^{-3}, the mobility of electrons decreases when the concentration exceeds 4×10^{18} cm^{-3}, so that the sheet resistance of the top n^+ layer would deleteriously increase instead of decreasing. The best energy conversion efficiency of 19.7% measured under simulated AM1 conditions (ELH lamp) was achieved with an n^+/p GaAs solar cell made on a single-crystal GaAs substrate with 1-cm^2 area, as shown in Figure 2. The values of open-circuit voltage (V_{oc}), short-circuit current density (J_{sc}) and fill-factor (FF) for this cell were about 0.988 volt, 25.6 mA/cm^2 and 0.78, respectively.

The GaAs epi-layers grown at 700°C or above on single-crystal Ge substrates were found to be heavily doped by the substrate, with $N_d \simeq 10^{18}$ cm^{-3} for undoped GaAs as determined by Hall measurements. To reduce this autodoping to an acceptable level (less than 10^{17} cm^{-3}) the growth temperature had to be lowered to 650°C or less. However, the surface morphology (as shown in Fig. 3 and Fig. 4) of GaAs grown on Ge was also found to be strongly influenced by the growth temperature, deteriorating as the temperature was lowered. In order to achieve good surface morphology and yet to avoid high autodoping, a method using sequential GaAs growths at two temperatures was developed. This involved using a higher temperature ($\sim$700°C) for initial nucleation continuous coverage and good morphology and a lower one ($\sim$650°C) for continued growth. By using this method, GaAs solar cells with an n^+/p shallow homojunction structure were made. The best cell exhibited an AM1 efficiency of 18.4% (Fig. 5), with other cells having efficiencies just a little less. The values of V_{oc}, J_{sc} and FF for this best solar cell are 1.0 V, 24 mA/cm^2 and 0.79, respectively.

Recently, thin epitaxial layers of GaAs, bright and shiny, were successfully grown by OM-CVD onto Ge epi-interlayers which were grown onto (100) Si substrates. X-ray diffraction measurements showed that the Ge interlayer and the GaAs top layer were completely single-crystal, having the same (100) orientation as the Si substrate. This is the first report of successful growth of this structure. After cleaving the substrate, SEM photographs of the cleaved surfaces clearly showed the uniform layered structure. Growth optimization, characterization measurements of the thin films, as well as solar cell fabrication and performance measurements will be done, the procedures and results for which will be reported at a later date.
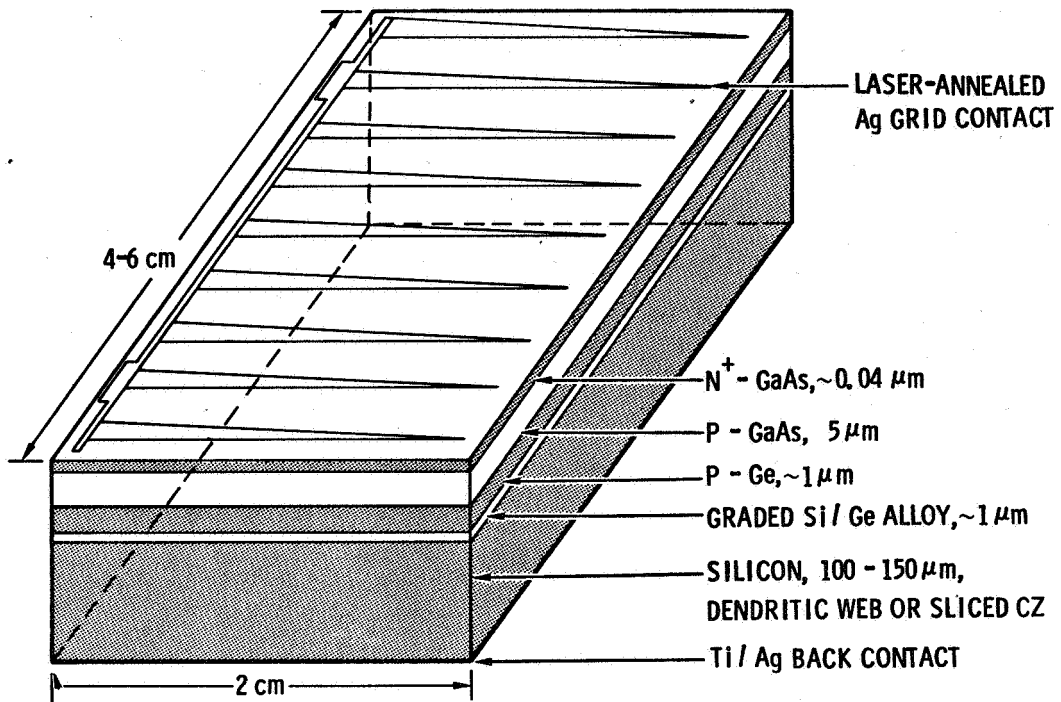
Figure 1. Light weight GaAs solar cell structure.
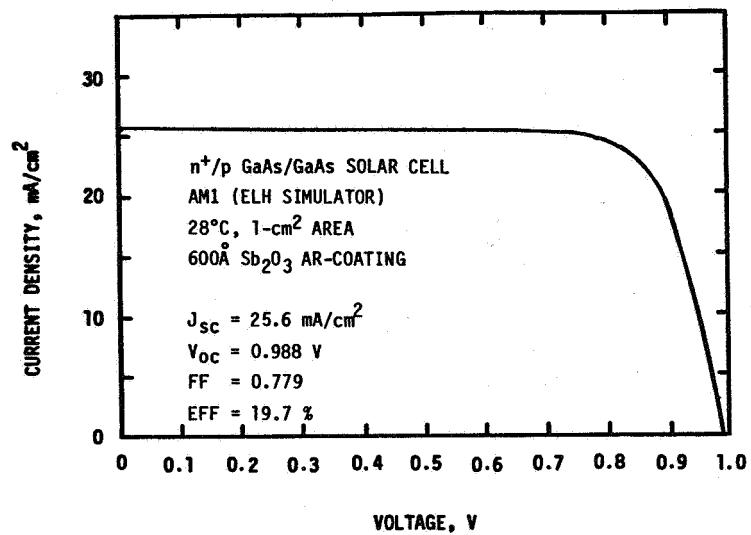
Figure 2. Light I-V characteristics of an n[+]/p GaAs/GaAs solar cell.
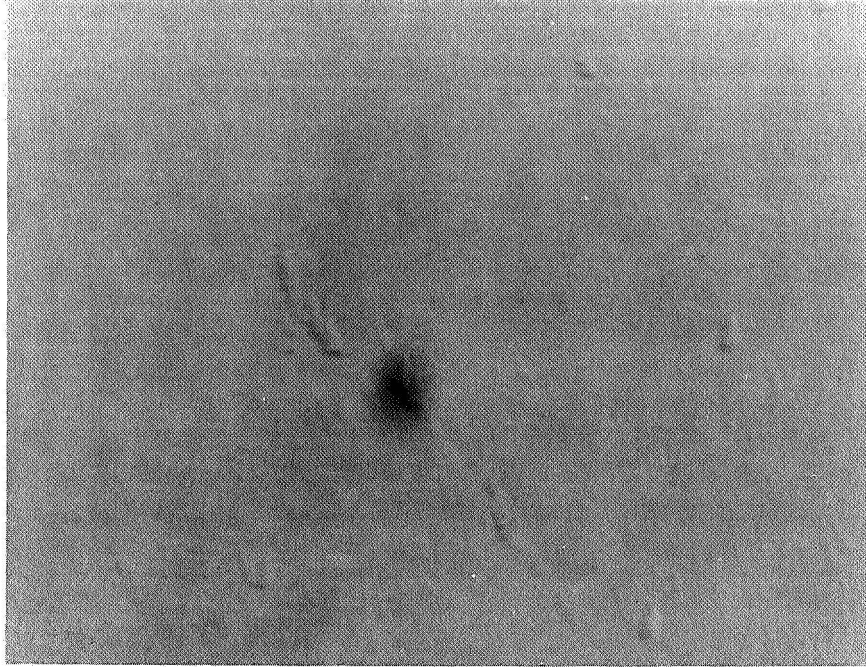
Figure 3. Photomicrograph (250X) showing surface morphology of
GaAs epi-layer grown at 700°C on Ge substrate.
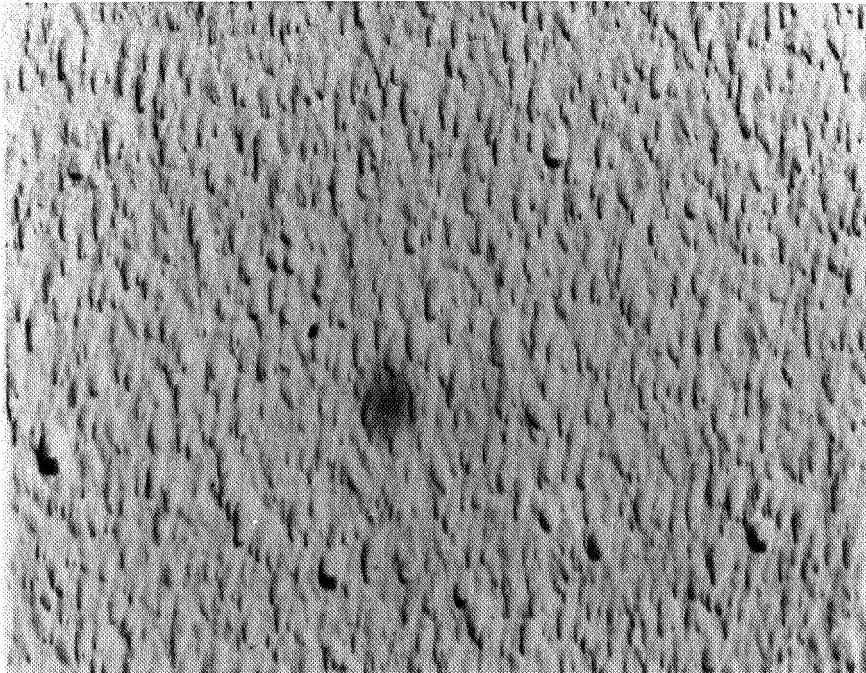
Figure 4. Photomicrograph (250X) showing surface morphology of
GaAs epi-layer grown at 650°C on Ge substrate.
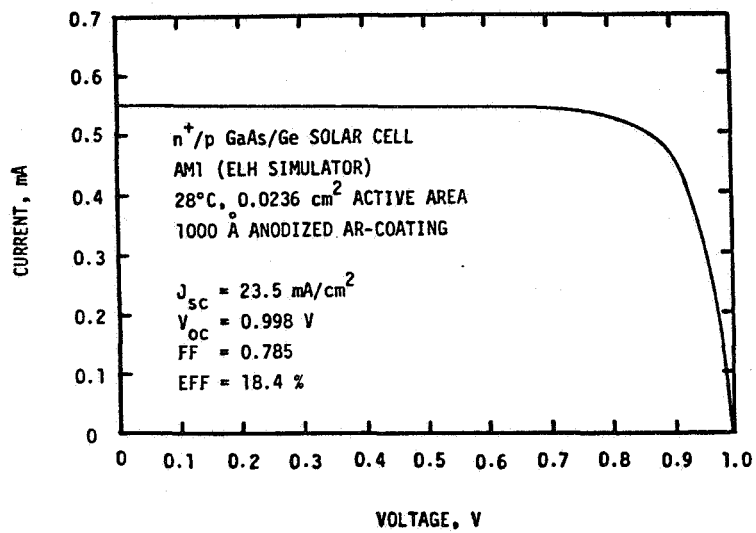
Figure 5. Light I-V characteristics of an n^+/p GaAs/Ge solar cell.

The figure contains the following annotations:

n^+/p GaAs/Ge SOLAR CELL
AM1 (ELH SIMULATOR)
28°C, 0.0236 cm^2 ACTIVE AREA
1000 Å ANODIZED AR-COATING

J_{sc} = 23.5 mA/cm^2
V_{oc} = 0.998 V
FF = 0.785
EFF = 18.4 %

Axis labels: CURRENT, mA (vertical), VOLTAGE, V (horizontal)

STUDY OF PROCESS TECHNOLOGY FOR GaAlAs/GaAs HETEROFACE SOLAR CELLS

Edmund J. Conway, Gilbert H. Walker, and Charles E. Byvik
NASA Langley Research Center
Hampton, Virginia

and

David W. Almgren
Arthur D. Little, Inc.

SUMMARY

Process technology for producing 10,000 single-crystal GaAlAs/GaAs solar cells per year was studied. The only technique that is presently developed to the point that 10,000 cells could be produced in one year is the infinite melt liquid phase epitaxy process. The lowest cost per cell is achieved with the advanced metal organic chemical vapor deposition process. Molecular beam epitaxy is limited by the slow growth rate. The lowest cost for an 18-percent efficient cell at air mass zero is approximately $70 per watt.

INTRODUCTION

This study of process technology assumes a requirement for 10,000 2 cm x 2 cm single-crystal pGaAlAs/pGaAs/n-GaAs heteroface solar cells per year. For the purpose of this study, the processes evaluated for fabricating these solar cells are liquid phase epitaxy (LPE), chemical vapor deposition (CVD), and molecular beam epitaxy (MBE). Each of these processes utilizes an n-GaAs single crystal substrate approximately 250 μm thick on which the epitaxial layers are grown. Two LPE processes are considered: the infinite melt process and the finite melt process. In the infinite melt process, two separate reusable melts are maintained. One 5-kg melt of Ga, As, and the n dopant is used to grow an n-GaAs buffer layer on the substrate wafer. A second 3-kg melt of Ga, As, Al, and the p-dopant is used to grow the p-GaAlAs window layer. During the growth of the p-GaAlAs, the p dopant diffuses into the buffer layer, forming the p-GaAs. In the finite melt LPE process, the smaller melts are not reused. One finite melt LPE technique, however, does not require the growth of the n-GaAs buffer layer. This method uses an etch back epitaxy process. The CVD process considered utilizes organometallic compounds of Ga, Al, and AsH_3 for the gallium, aluminum, and arsenic sources. These compounds react on the surface of the heated substrate to form the GaAs and the GaAlAs. In the MBE process, molecular beams of Ga, As, and Al are directed from effusion cells onto a heated GaAs substrate in an ultrahigh vacuum such that the GaAs and GaAlAs are formed. The MBE technique is characterized by slow growth rates

(typically 1 µm per hour); however, the uniformity and composition of the layers are very precisely controllable. Growth rates for the CVD process are approximately 0.25 µm/min, and for the LPE process approximately 0.5 µm/min.

Substrates

Common to all these processes is the need for 250-µm thick single-crystal GaAs substrates. Considering saw kerf losses, polishing losses, and cleavage losses, annual production of 10,000 2 cm x 2 cm cells would require 15.1 kg of Ga and 16.2 kg of As, and results in a purchase price of $5.00 for each of the polished substrates.

Major Costs

Table 1 shows the major direct costs per cell for growth of the epitaxial layer for 10,000 2 cm x 2 cm solar cells per year using the various processes. The costs per cell shown in this table do not include the $5.00 cost for each polished 2 cm x 2 cm substrates which is common to all processes. For the purpose of this study, percent yield is defined as the percent of the input material that is incorporated in the epitaxial layer. The lowest costs per cell are for the infinite melt LPE (IM-LPE) process and for the metal organic CVD (MO-CVD) process. Assuming an 18-percent cell at AMO, the cost for the IM-LPE process is $71 per watt including the substrate cost, and the cost for the OM-CVD process is $70 per watt including the substrate cost. From table 1, notice that the major items affecting the cost per cell for the epitaxial layer are the time to fabricate, the labor costs, and the capital equipment costs; however, the materials costs become important in some cases when the percent yield is lower than 100 percent. In no cases, however, are the energy costs a significant percentage of the cost per cell. Each of these items will now be discussed separately.

Fabrication Time

Table 2 shows the fabrication times for the various processes using one growth chamber of current design. From this table it can be seen that only the IM-LPE process can produce 10,000 cells per year using one growth chamber of current design. Table 2 shows that even if higher quality substrates were available such that no GaAs buffer layers were needed, a single MBE system could not produce the 10,000 cells in one year. The current MO-CVD systems in use are limited to growing one cell per cycle. The time to grow 10,000 cells is therefore 31 months. In order to grow the 10,000 cells in one year by this process, three systems would be required. A commercially available four-loop MO-CVD system can grow approximately 11 cells per cycle; therefore, this advanced system could produced the required cells in approximately three months. Scale-up of the MO-CVD process to produce 36 cells per cycle appears feasible. Thus, less than

one month would be required to grow 10,000 cells using the most advanced system. Scale-up of the MBE process using a third-generation MBE system to produce about seven cells per run appears feasible; however, in order to use only two systems to produce 10,000 cells per year, the buffer layer must be eliminated.

Materials

Table 3 shows the material requirements for the 10,000 cells. The percent yield for the IM-LPE process is shown only at 100 percent since the use of all of the material removed from the confined melts is incorporated in the epitaxial layer. The MBE process is shown at a maximum percent yield of 50 percent since geometrical considerations would limit the percent yield to 50 percent. Additional experimental effort is needed to quantify the percent yield for the MO-CVD process and for the LM-LPE process; however, collection and recycling of the OM-CVD exhaust gases and the LM-LPE melts may be possible.

Labor Costs

Table 4 shows the labor costs for producing the required 10,000 cells. The three-month fabrication time for the MO-CVD process assumes the four-loop system. The 31-month fabrication time for the MBE process assumes a third-generation MBE system.

Capital Equipment

Table 5 shows the amoritized costs for the capital equipment. Note that the cost per cell is $0.42 for the IM-LPE process; however, the amortized cost per cell for advanced MO-CVD process is also low at $0.50 per cell.

CONCLUSIONS

Referring again to table 1, this study has shown that for producing 10,000 4-cm^2 GaAℓAs-GaAs heteroface solar cells per year, the lowest cost per cell is for the four-loop MO-CVD system with a 100-percent yield. The cost of cells produced by the MBE process is the highest for all processes studied; however, MBE is a useful tool for studying and optimizing solar cells. For both the MO-CVD process and the IM-LPE process, the substrate cost dominates the cost of the epitaxial layer. For both processes, the substrate cost is greater than 70 percent of the cell cost. Including the substrate cost, the lowest cost identified for GaAℓAs/GaAs heteroface solar cells is $70 per watt assuming 18 percent AMO efficiency.

● EXCLUDING OVERHEAD AND PROFIT

PROCESS	YIELD[1] (%)	TIME TO FABRICATE (MONTHS)	MATERIAL COSTS	UNBURDENED LABOR COSTS	CAPITAL EQUIPMENT COSTS	ENERGY COSTS	COST PER CELL[2]
LPE – INFINITE MELT	100	4	$ .006	$ 1.54	$ .42	$ .016	$ 1.98
– FINITE MELT	100	63	$ .006	$14.11	$ 2.67	$ .015	$ 16.80
	10	63	$ .06	$14.11	$ 2.67	$ .015	$ 16.86
	1	63	$ .62	$14.11	$ 2.67	$ .015	$ 17.42
MO-CVD	100	31	$ .23	$ 6.94	$ 5.17	$ .002	$ 12.34
	10	31	$ 2.29	$ 6.94	$ 5.17	$ .002	$ 14.40
	1	31	$22.94	$ 6.94	$ 5.17	$ .002	$ 35.05
	100	3	$ .23	$ 1.15	$ .50	$ .002	$ 1.88
	10	3	$ 2.29	$ 1.15	$ .50	$ .002	$ 3.94
	1	3	$22.94	$ 1.15	$ .50	$ .002	$ 24.59
MBE	50	344	$ .03	$77.06	$33.37	$3.95	$114.41
	5	344	$ .30	$77.06	$33.37	$3.95	$114.68
	50	31	$ .03	$ 6.94	$17.24	$ .36	$ 24.57
	5	31	$ .30	$ 6.94	$17.24	$ .36	$ 24.84

1. YIELD IS DEFINED AS THE RATIO OF THE MATERIAL IN THE EPITAXIALLY GROWN LAYERS TO THE MATERIAL INPUTTED TO THE PROCESS.
2. DOES NOT INCLUDE A $1.24/cm^2 PURCHASE PRICE FOR POLISHED SUBSTRATES.

Table 1: Summary of major direct costs per cell for growth of the epitaxial layers of 10,000 2-cm x 2-cm (AlGa)As/GaAs solar cells.

90

PROCESS	CYCLE TIME (HOURS)	NO. OF CELLS (2cm × 2cm)	TIME PER CELL (HOURS)	TIME FOR[1] 10,000 CELLS (MONTHS)
LPE – INFINITE MELT	2	32[2]	.06	4
– FINITE MELT	1	1	1.0	63
MO-CVD	0.5	1	0.5	31
	0.5	11	0.5	3
MBE – 11µm GROWTH	11	2	5.5	344
– 1µm GROWTH	1	2	0.5	31

1. BASED ON 160 HOURS OF OPERATION PER MONTH.
2. BASED ON A SYSTEM THAT HAS BEEN DEVELOPED TO SATISFY (LIMITED) PRODUCTION REQUIREMENTS.

Table 2: Summary of fabrication times for different epitaxial growth procedures using one growth chamber of current design.

● 250μm n-GaAs SUBSTRATE
● 10μm n-GaAs BUFFER LAYER
● 0.5μm p-GaAs LAYER
● 0.5μm p-(AlGa)As WINDOW LAYER

PROCESS	YIELD (%)	GALLIUM OR GALLIUM CONTAINING COMPOUND (g)	ARSENIC OR ARSENIC CONTAINING COMPOUND (g)
SUBSTRATE PREPARATION	17	15,084	16,210
LPE – INFINITE MELT	100	108	121
– LIMITED MELT	100	108	121
	10	1,080	1,212
	1	10,800	12,120
CVD – Ga(CH$_3$)$_3$	100	178	126
–AsH$_3$	10	1,779	1,261
	1	17,790	12,611
MBE – As/Ga = 10	50	216	2,424
	5	2,160	24,240

Table 3: Summary of material requirements to fabricate 10,000 2-cm x 2-cm GaAs solar cells assuming no recovery of lost material.

● ONE OR TWO FULL TIME OPERATING PERSONS AT $10.00 PER HOUR

● ONE PART TIME (20%) SUPERVISOR AT $20.00 PER HOUR

PROCESS	TOTAL TIME[1] (MONTHS)	NO. OF OPERATORS	TOTAL LABOR COST	LABOR COST PER CELL
LPE - INFINITE MELT	4	2	$ 15,360	$ 1.54
- FINITE MELT	63	1	$141,120	$14.11
MO-CVD	31	1	$ 69,440	$ 6.94
	3	2	$ 11,520	$ 1.15
MBE	344	1	$770,560	$77.06
	31	1	$ 69,440	$ 6.94

1. ASSUMING A SINGLE 8 HOUR SHIFT PER DAY.

Table 4: Summary of unburdened labor costs to grow epitaxial layers for 10,000 (AlGa)As/GaAs solar cells with a single growth chamber.

93

● ASSUMING A FIVE YEAR DEBT AT 12% INTEREST

PROCESS	TOTAL CAPITAL EQUIPMENT COSTS	FABRICATION TIME (MONTHS)	TOTAL AMORTIZATION COST ALLOCATED TO SOLAR CELLS	AMORTIZATION COST PER CELL
LPE - INFINITE MELT	$ 47,424[1]	4	$ 4,219.68	$ .42
- FINITE MELT	$ 20,000	63	$ 26,693.40	$ 2.67
MO-CVD	$ 75,000	31	$ 51,718.23	$ 5.17
		3	$ 5,004.99	$ .50
MBE	$250,000	344	$333,666.60	$33.37
		31	$172,394.47	$17.24

[1] INCLUDES $7,424.00 FOR 8,000 GRAMS OF MELT HELD IN INVENTORY IN TWO GROWTH CHAMBERS

Table 5: Summary of capital equipment amortization cost for different solar cell fabrication processes assuming a minimum number of growth chambers.

HIGH EFFICIENCY COMPOUND SEMICONDUCTOR
CONCENTRATOR PHOTOVOLTAICS

Peter Borden, Paul Gregory, Ram Saxena,
Richard Owen, and Ozzie Moore
Varian Associates, Inc.
Palo Alto, California

SUMMARY

Work on compound semiconductor concentrator photovoltaics at Varian is
reviewed. Special emphasis is given to projects that have achieved significant
results in the last six months. These include the high yield pilot production
of packaged AlGaAs/GaAs concentrator solar cells, using organometallic VPE for
materials growth, the demonstration of a concentrator module using 12 of these
cells which achieved 16.4% conversion efficiency at 50°C coolant inlet tempera-
ture, and the demonstration of a spectral splitting converter module that
achieved in excess of 20% conversion efficiency. This converter employed ten
silicon and ten AlGaAs cells with a dichroic filter functioning as the beam
splitter. Finally, a monolithic array of AlGaAs/GaAs solar cells will be
described.

INTRODUCTION

Varian has a number of ongoing programs related to the development and
demonstration of high efficiency compound semiconductor concentrator photo-
voltaic devices at both the cell and module level. The purpose of this paper
is to review some significant developments that have occurred during the last
six months. These include the following:

- Organometallic vapor phase epitaxy (OM-VPE) has been successfully applied
  to the pilot production of AlGaAs/GaAs solar cells. This epitaxial
  growth technique has the advantages of exceptional control, uniformity,
  provides good surface morphology, and naturally lends itself to high
  throughput. As a consequence, production yields of packaged cells,
  measured at 50°C and 400 AM2 suns, are 87% greater than 18% efficiency,
  67% greater than 20%, and about 45% greater than 22%, with the best cell
  to date running at 23.2% efficiency.

- A module of 12 AlGaAs/GaAs cell illuminated by 12 curved-groove fresnel
  lenses providing 400 suns has been built and tested. This module achieved
  a conversion efficiency of 16.4% with AM2 insolation. The coolant tempera-
  ture was 50°C, and pumping losses have been subtracted from the output
  power.

- A spectral splitting module has also been built and tested. This achieved
  20.34% at 839 W/m^2, with a 37°C coolant inlet temperature. Here, curved-
  groove fresnel lenses illuminated dichroic filters, which split the beam

into a high energy component transmitted to AlGaAs cells with bandgaps of 1.65 eV and a low energy component reflected to silicon cells. The module had a total of 20 cells, ten of each type. In the test, they were wired together for a single output.

A high voltage AlGaAs/GaAs solar cell is being developed. This consists of an array of solar cells monolithically integrated onto a single substrate. Because of on-chip series interconnection, high voltage-low current terminal characteristics are obtained. The fabrication, rather than the bandgap, determines the operating voltage, so that the cell can be optimized for a number of applications.

In the following sections, each of these topics will be discussed individually.

OM-VPE AlGaAs/GaAs SOLAR CELLS

Varian is currently engaged in the pilot production of AlGaAs/GaAs solar cells. These devices are designed for use in point focus concentrator systems operating at 400 AM2 suns, with coolant temperatures up to about 150°C. Through this program, we have gained considerable experience in the fabrication, packaging and testing of AlGaAs/GaAs solar cells, and have demonstrated that they can be produced with high yield.

A principal reason for seeing good yields has been a switch from liquid phase epitaxy (LPE) to organometallic vapor phase epitaxy (OM-VPE). The OM-VPE cell structure is described in another paper [1]. From a processing standpoint, OM produces wafers with a minimum number of morphological defects. This translates into higher yields, especially during photolithography. Results of an extensive life test program have shown that degradation under stress is correlated to surface defects, so that the OM-VPE cells show a longer life than LPE devices. Significantly, since OM-VPE is a vapor phase process, it can be scaled up for high throughputs.

Figure 1 shows the grid structure appropriate for a concentrator cell. The chief design feature is a nearly constant grid line spacing to reduce emitter series resistance. The lines are spaced 60 microns; the diameter is .49 inches. The contact metal scheme is a Au-Mg-Au sandwich followed by a TiW barrier and a layer of gold. The back contact is similar, except that Sn replaces the Mg to provide contact to the n-type substrate.

A packaged cell is shown in Fig. 2. The alumina baseplate has a moly-manganese pattern to which the cell die is vacuum soldered with a silver-tin solder. The leadframe is bonded to the top of the cell with lead-indium paste. Copper tabs brazed to the baseplate carry out the current.

Packaged cells are tested at one sun in a xenon-source solar simulator, and at concentration in a computer-controlled xenon source flash tester. The latter unit consists of a photographic strobe mounted above the cell. A computer triggers the flash, then captures the peak voltage and current on peak detectors. By varying an active load, the computer plots the cell IV curve and finds the cell short circuit current, open circuit voltage, fill

factor and efficiency. By varying the power and strobe-cell spacing, a concentration range from a few suns to several thousand suns can be obtained. The flash spectrum does not exactly match the sun's; we have found, however, that measured efficiencies at room temperature in the flash tester compare within the error of the system to tests with an AM2 spectrum and the cell at 50°C.

Typical pilot production yield data on packaged cells measured at 400 AM2 suns by flash testing shown in Fig. 3. For comparison, the yield on a batch of LPE cells appears. The difference in performance can be attributed to the better doping and thickness control, and better morphology obtained with OM-VPE.

A life test program is currently in progress [2]. It began before the OM-VPE cell was well developed, and has focused largely on unpackaged LPE cells. These devices use magnesium as a p-type dopant in the emitter, and have proven stable at one sun in a variety of tests. These include storage at 400°C in a N_2 ambient and thermal cycling between room temperature at 425°C, also in nitrogen. The short circuit currents of the test cells are plotted in Figs. 4 and 5 for these two tests. Note that in the thermal storage experiment, significant degradation sets in after about 600 hours and failure of the entire batch occurs only after 3000 hours. The primary failure mode appears to be delamination of the silicon nitride AR coating. Other storage tests at 425°C in nitrogen and 250 and 350°C in air are presently underway to better identify failure mechanisms and to estimate the time to failure at normal operating temperatures.

12-CELL CONCENTRATOR MODULE

As part of a program sponsored by DOE and Sandia [3], Varian has built and tested a module consisting of 12 AlGaAs/GaAs cells illuminated at 400 suns with 12 curved-groove fresnel lenses. Figure 6 shows a breakdown of the module. From top to bottom, it consists of a parquet of 12 lenses. A heat shield, made of aluminum, protects plastic components from damage during off-track operation. The cells are connected in a four in parallel-three in series arrangement, and fit in the base of a housing made of foamed lexan. An integral cooling manifold uses a jet impingement technique to cool the backs of the cells. The completed module is shown in Fig. 7, mounted on a tracker for testing.

Module performance as a function of insolation at 28 and 50°C is shown in Fig. 8. Coolant pumping losses have been subtracted from these data. The AM2 performance of 16.4% at 50°C considerably exceeds the best reported performance of about 12% for modules using silicon cells and operating at about the same coolant inlet temperature and insolation level.

10-UNIT SPECTRAL SPLITTER MODULE

Under sponsorship of Sandia [4], a spectral splitter module has been designed and built. The module is shown schematically in Fig. 9. One of the units is shown in Fig. 10. The entire module consists of 10 units supported with an I beam. Each unit has a f4.2 hexagonal curved groove fresnel lens

focusing light onto a dichroic filter. This filter ideally has a cutoff of 1.65 eV, reflecting light below this energy to a silicon cell and transmitting light above this energy to a 20% AlGaAs cell with a bandgap of 1.65 eV. The effective concentration (that is, the ratio of lens area to spot size on the AlGaAs cell with the filter removed) is 477 suns. The system is actively cooled; all 20 cells are mounted in plastic jet-impingement coolers, using water as a cooling fluid.

Both types of cell have been made and packaged at Varian. A grid mask, similar to that shown in Fig. 1 but with a 1/3-inch diameter, is used. The package is the same as that shown in Fig. 2. The silicon cell has a .07-micron deep diffused p-type emitter; a deep emitter is acceptable since low emitter resistance is more important than blue response in this application. The substrate is 111 n-type FZ silicon, with a diffused back surface field. Such cells, packaged, have been tested at 15-16% full spectrum 400-sun AM2 efficiency.

The AlGaAs cells are grown by LPE and otherwise processed in a manner identical to the AlGaAs/GaAs solar cell. The bandgaps vary from 1.58 to 1.68 eV as a consequence of the extreme sensitivity of aluminum incorporation into the solid to aluminum concentration in the LPE melt. These cells, as well as the silicon cells, have cover glasses to protect from environmental degradation and allow cleaning.

The completed module appears in Fig. 11. This is wired for a single output by connecting all silicon cells in one series string and forming two series strings with five AlGaAs cells in each. Since the operating voltage of the AlGaAs cells is nearly twice that of the silicon, these three strings are then connected in parallel.

Testing is presently underway. The best results to date, 20.34% efficiency with 839 W/m2 insolation and a cooling water temperature of 37°C, appears in Fig. 12. It should be noted that the filters in the present system have a cutoff of 1.55 eV, due to design compromises made between the manufacturer and Varian. Also, losses in the fresnel lens are 15-20%. Taking these into account, the performance of this module matches or exceeds the results reported by Varian in 1978 for a single converter [5].

A comparison of the spectral splitting and GaAs concentrator modules gives a measure of the advantages and drawbacks of going to a spectral splitting approach, given the present state-of-the-art. The obvious advantage is a 25% increase in conversion efficiency (about 16% compared to about 20%). The drawbacks are the cost of the filter, which must necessarily consist of multiple dielectric layers to achieve a sharp enough cutoff, and the increased complexity of the optical system which makes alignment and optimization of performance more difficult. A longer focal length system with the spectral splitter increases the cost of materials. We have noted no problems with reliability of the cells, filters, or lenses; the module has remained on the laboratory roof in the weather for about four months to date. The optics, however, have required realignment from time to time.

HIGH VOLTAGE CELLS

In work sponsored by SERI [6], we are developing monolithic series-connected arrays of AlGaAs/GaAs solar cells, or "High Voltage Cells". The device structure, shown in Fig. 13, consists of a number of subcells grown on an insulating GaAs substrate, isolated with etched grooves, and interconnected with metal lines. Because the device has a high voltage-low current output (by virtue of its series connection), grid line widths can be reduced -- indeed, with n-on-p structures, with higher emitter mobilities, grid lines may not be needed. This compensates for obscuration introduced by the interconnects, so that these devices can have efficiencies comparable to planar solar cells. An advantage of working with GaAs is the short absorption length, allowing the use of shallow structures that are simple to fabricate by standard monolithic processes.

Use of these devices should considerably facilitate array design, since the cell terminal voltage can now be decided by the designer rather than the material bandgap. An obvious application is in spectral splitters, where the oft-imposed constraint of matching the short circuit currents of the high and low bandgap cells could be removed. Another application is in the design of high voltage photovoltaic systems which use long strings of cells. Because the performance of the entire string is affected by the degradation of even one cell, it is desirable to use as many strings as possible, each covering as little a fraction of the total array area as possible. Use of high voltage solar cells obviously allows minimization of the array area occupied by each series string.

A four-cell device has been fabricated and tested; Fig. 14 shows the IV characteristic at about 1 AM2 sun and, for comparison, the IV characteristic of a single-junction AlGaAs/GaAs solar cell. The details of the performance of this device are described elsewhere [7]; note that the open circuit voltage is about four times that of the single-junction device. Work in the lab is proceeding toward the demonstration of an optimized 10-subcell device.

CONCLUSION

Since initial demonstration of a high-efficiency AlGaAs/GaAs solar cell, the thrust of the Varian program has been to produce a reliable, high-efficiency packaged device that is not a laboratory experiment, but a device that can be readily used in photovoltaic systems and can be cheaply produced in large quantities. The development of OM-VPE epitaxial growth and the ceramic base-plate package configuration, and the demonstration of high yield in pilot production have been significant accomplishments in this direction.

At the module level, recent results with a GaAs module and a spectral splitter module have demonstrated the state-of-the-art efficiency advantage of GaAs over other technologies, and the advantages accrued by pursuing a spectral splitting approach. The latter is of relevance to work on cascade cells, since it represents, in some ways, an "ideal" approach, because effects due to individual components of the system can be isolated and the cells can be carefully chosen and matched.

REFERENCES

1. R. R. Saxena, C. B. Cooper III, M. J. Ludowise, P. G. Borden and P. E. Gregory, "OM-VPE Grown Materials for High Efficiency Solar Cells," paper to appear in this volume.

2. Varian Associates reports on contract SAND 13-5674.

3. Varian Associates reports on contract SAND 42-7248.

4. Varian Associates reports on contract SAND 13-0308.

5. Varian Associates reports on contract SAND 13-6953 and 13-6953A.

6. Varian Associates reports on contract SERI XS-0-9010-10.

7. Peter G. Borden, "A Monolithic AlGaAs/GaAs Solar Cell Array," Appl. Phys. Lett. 35(7), 553 (1979).
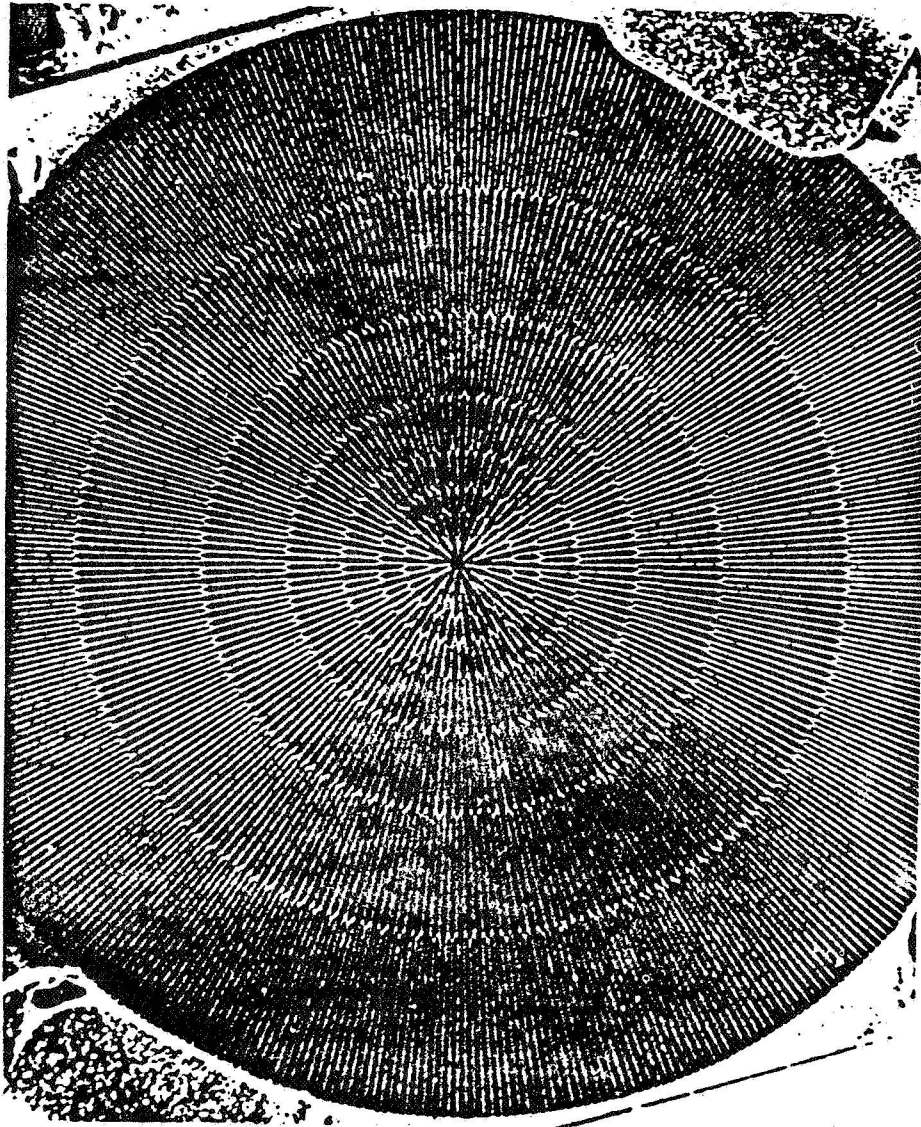
Fig. 1 Grid structure for AlGaAs/GaAs concentrator
solar cell.
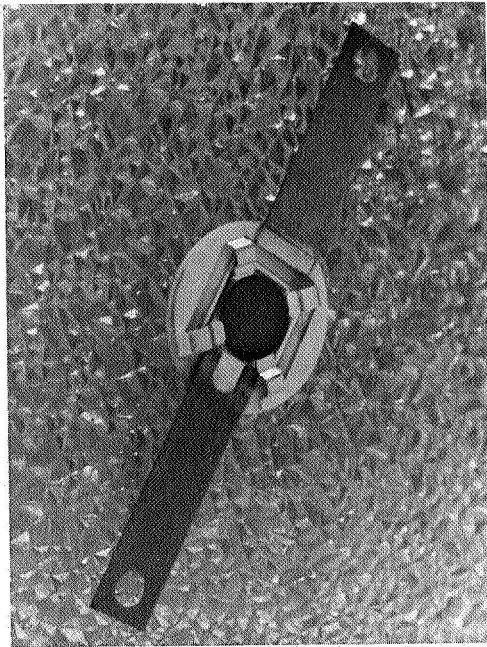
Fig. 2 A packaged AlGaAs/GaAs concen-
trator solar cell. Active area is
.49" in diameter.

LPE - OM VPE Comparison

LPE   15 cells
19.1 ± 0.85 %

Number

Efficiency %

OM-VPE 18 cells
21.2 ± 1.5 %

Number

Efficiency %
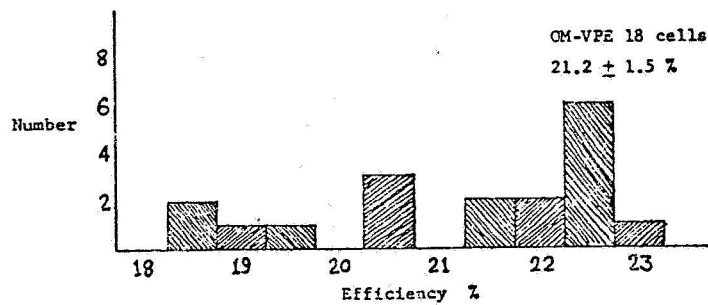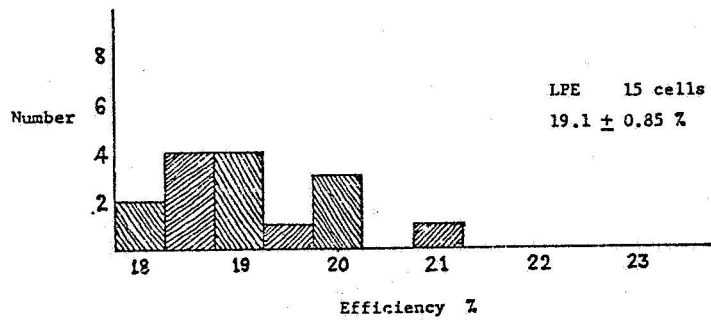
Fig. 3   Pilot production yields at 400 AM2 suns/50°C for
packaged OM-VPE and LPE solar cells, fabricated by
the same process.
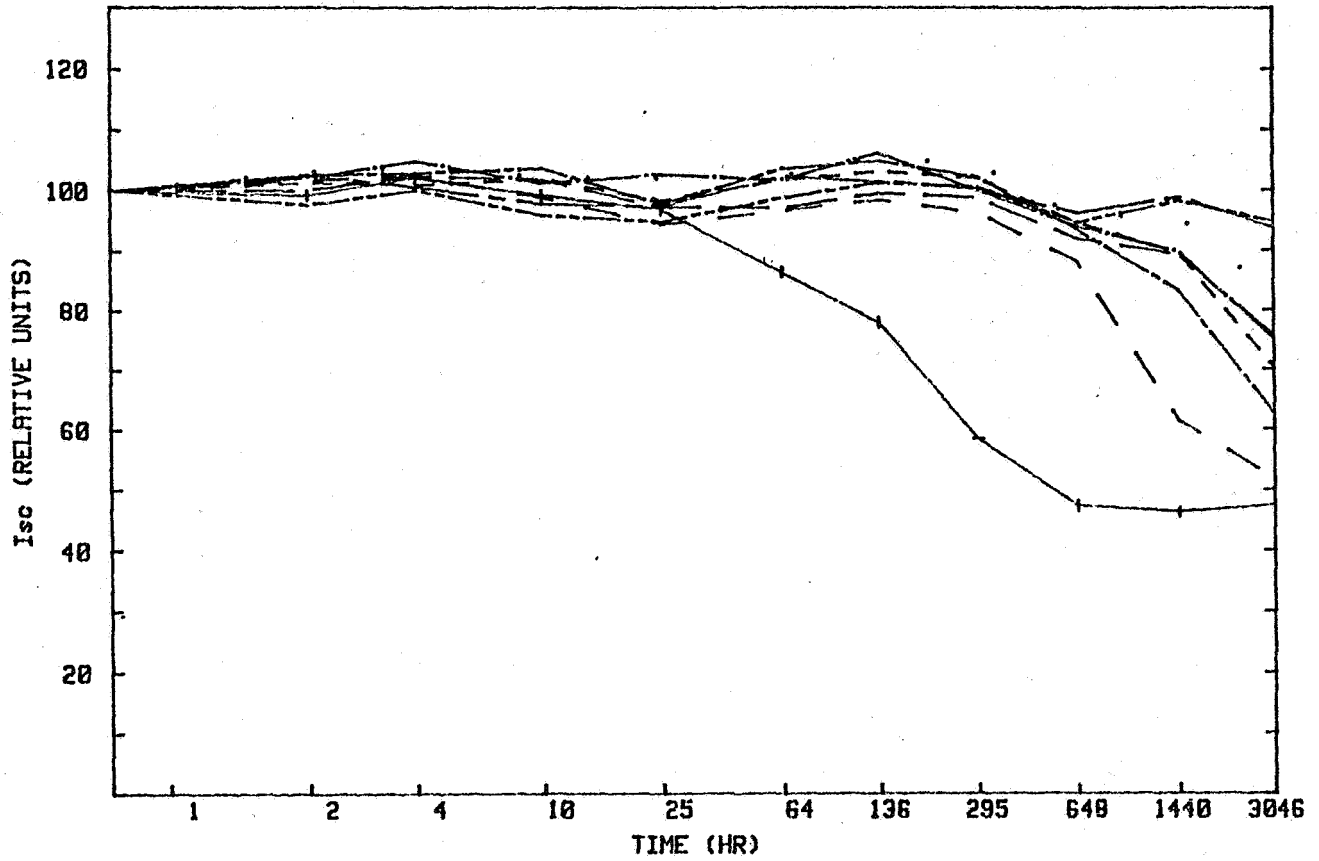
Fig. 4   Normalized AM1 short circuit currents for 9 unpackaged cells
         stored at 400°C in nitrogen plotted as a function of time.
         The cells were unpackaged and tested at AM1 conditions.
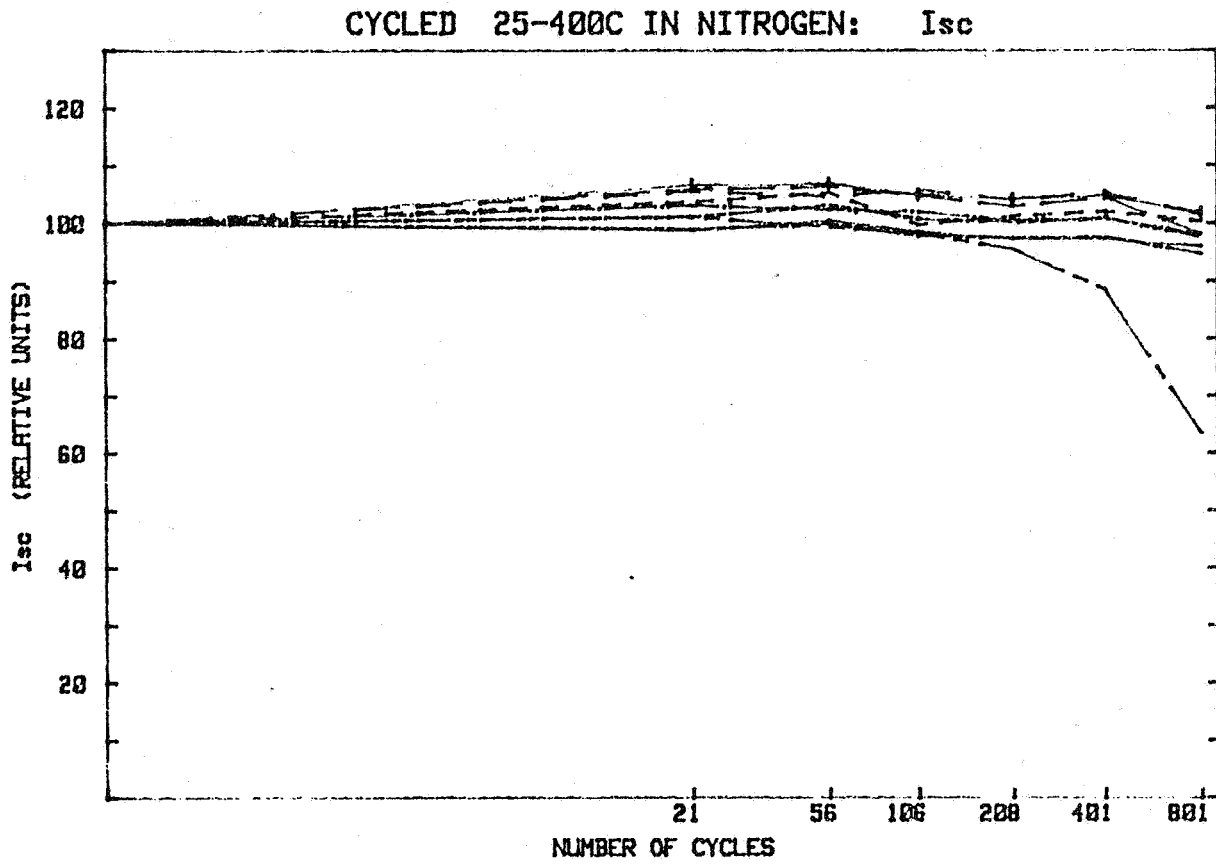
Fig. 5   Normalized short circuit currents for 9 unpackaged cells thermally cycled between room temperature and 400°C at 30 minutes per cycle.

LENS PANEL

THERMAL SHIELD

ELECTRICAL CONNECTION

HOUSING

COOLANT MANIFOLD
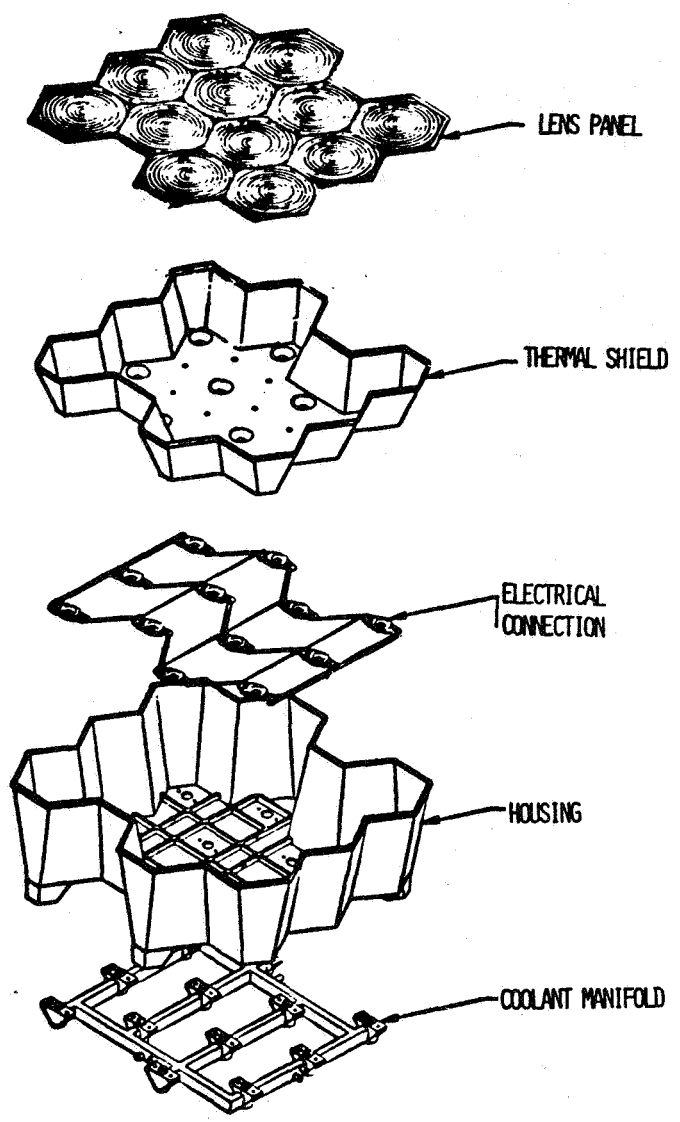
SOLAR MODULE

Fig. 6   A breakdown of 12-cell solar module.
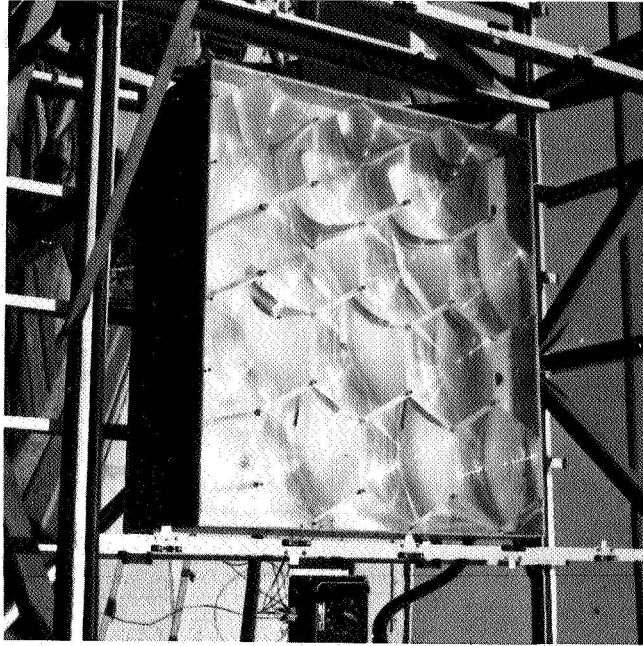
Fig. 7   The prototype module mounted on a
            solar tracker.
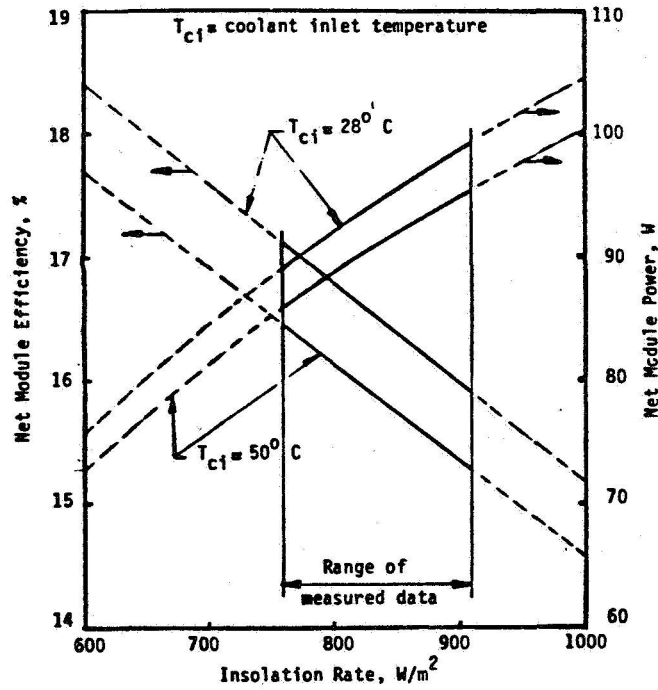
FIGURE 8- MEASURED MODULE PERFORMANCE

FRESNEL LENS

"I" BEAM SUPPORT

"I" BEAM FOR ATTACHING
TO TRACKING DEVICE

CELL COOLER
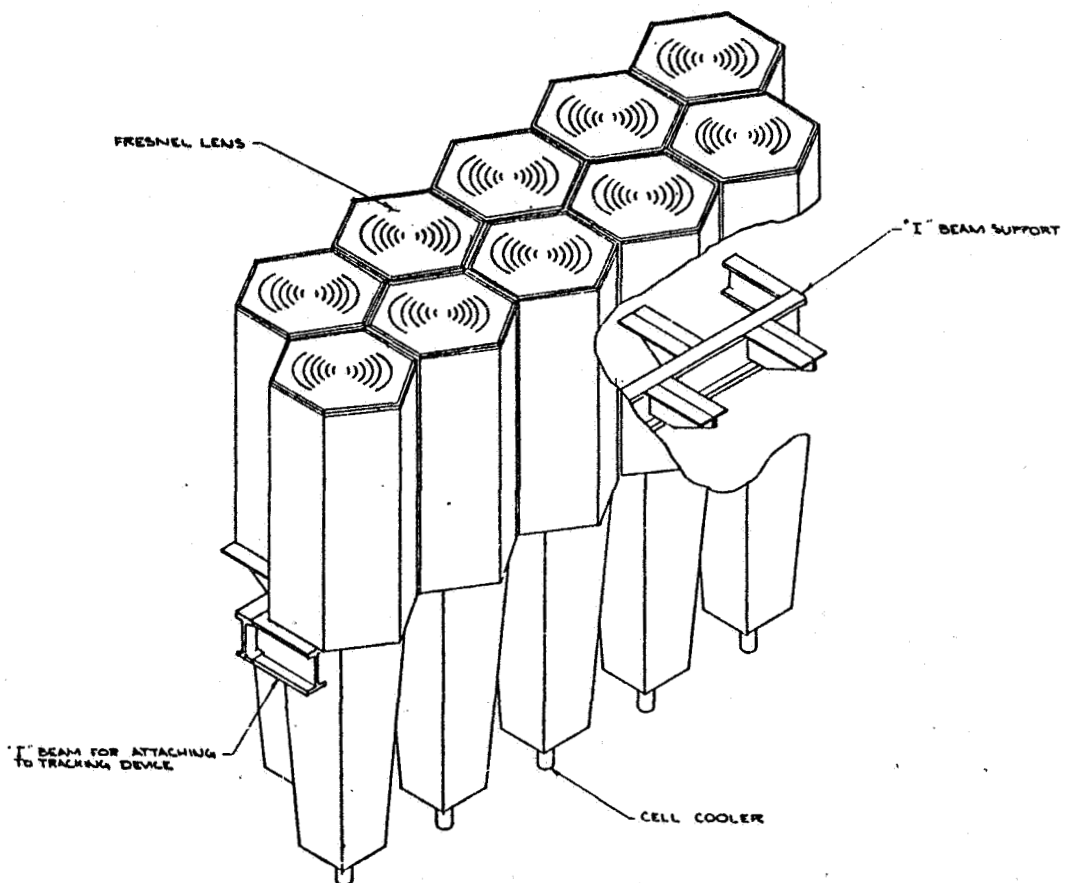
Fig. 9   A drawing of the spectral splitter module.
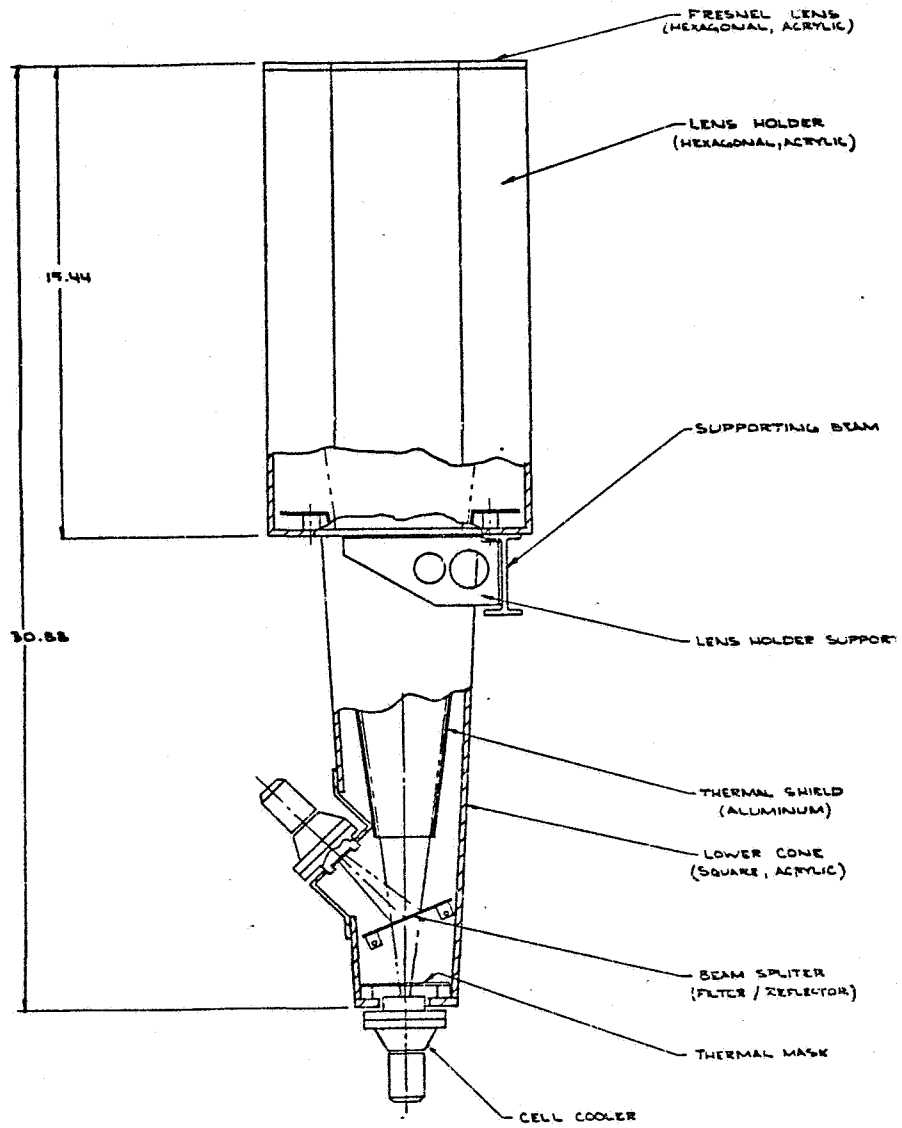
Fig. 10 Cutaway drawing of one unit of spectral splitter module.
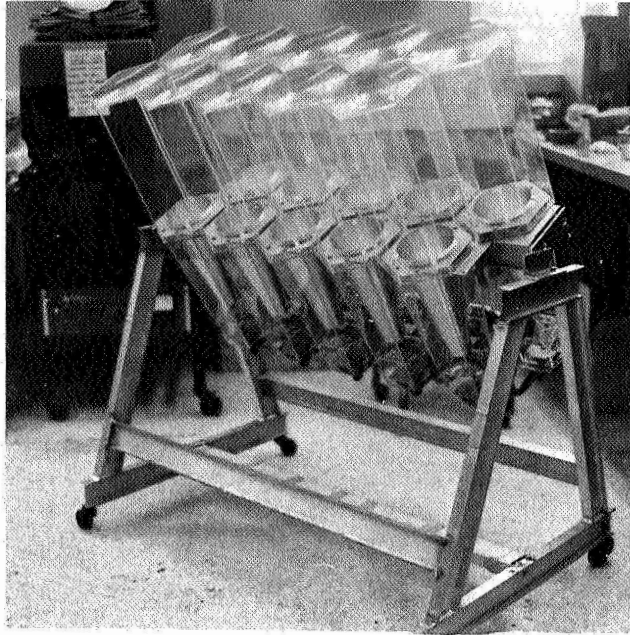
Fig. 11   A photograph of the completed
           spectral splitter module.
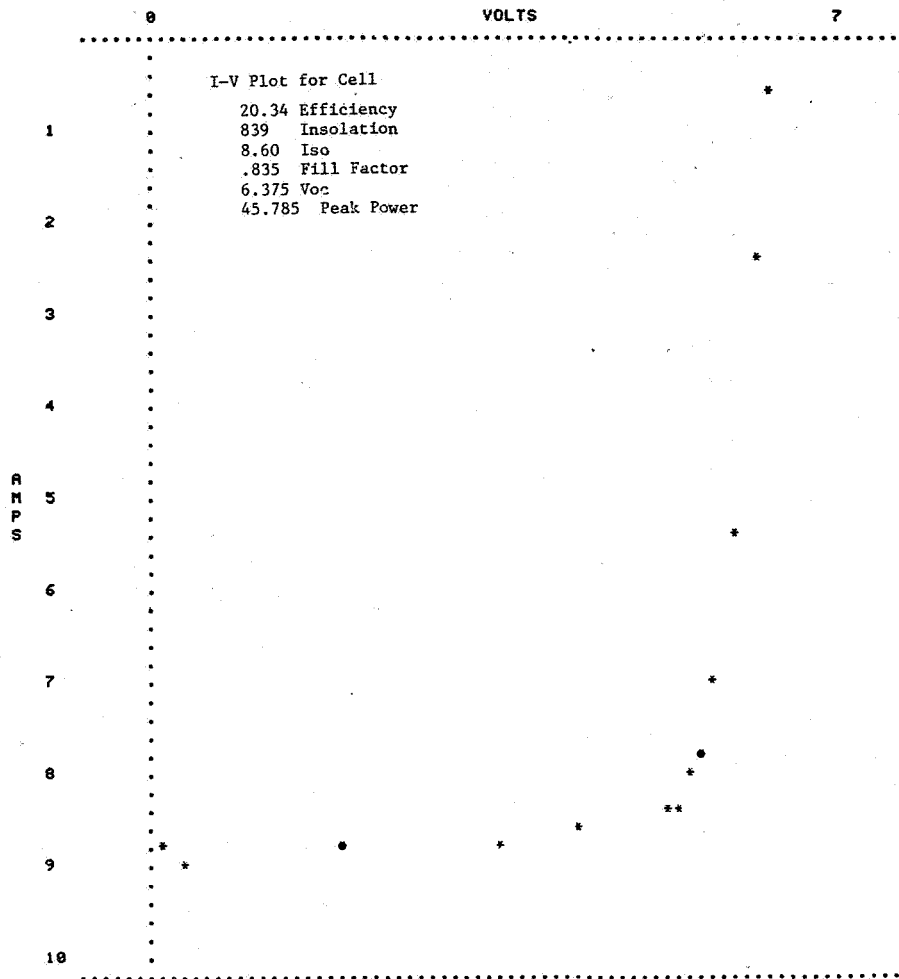
Fig. 12   A measured IV curve from the spectral splitter module.
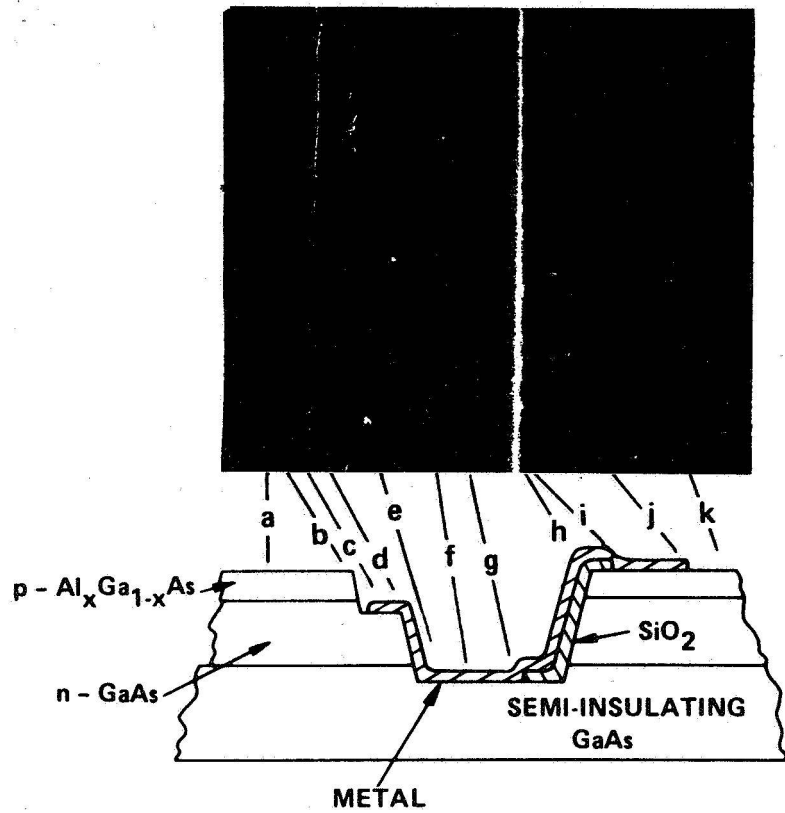
Fig. 13   High voltage cell device structure.
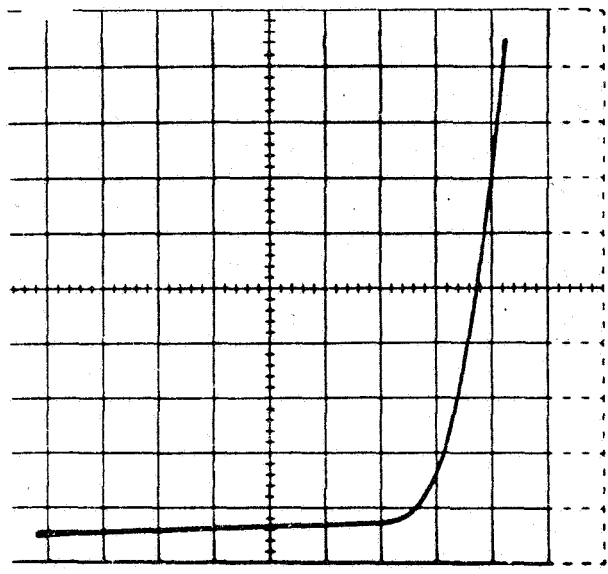
VERTICAL

200 μA

PER DIV.

HORIZ.   (a

1 V

PER DIV.
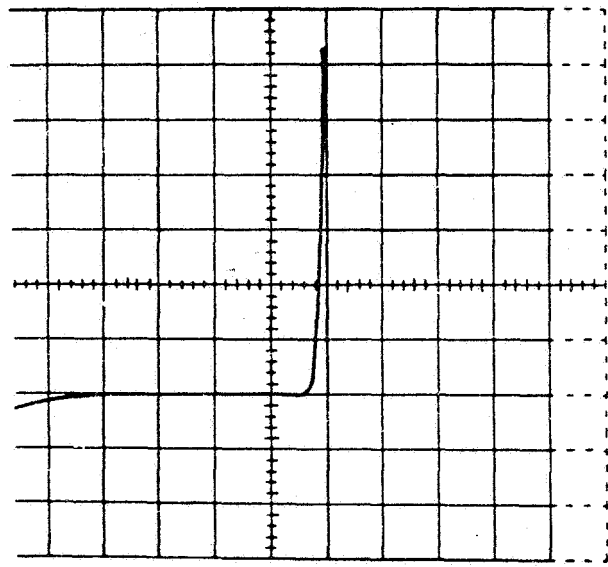
VERTICAL

5 mA

PER DIV.

HORIZ.   (b

1 V

PER DIV.

Fig. 14   IV characteristic of a 4-subcell high-voltage solar cell at
about 1 AM2 sun and, for comparison, the IV characteristic
from a single-junction AlGaAs/GaAs solar cell.

STATUS OF ROCKWELL-ERC HIGH EFFICIENCY SOLAR CELL PROGRAMS

S. W. Zehr, J. A. Cape, D. L. Miller, and H. T. Yang
Rockwell International Electronics Research Center
Thousand Oaks, California

INTRODUCTION

Rockwell International's Electronics Research Center is engaged in a long term effort to develop practical high efficiency photovoltaic devices for both terrestrial and space applications.

The effort includes programs aimed at developing large area, high efficiency GaAs heteroface cells for low concentration ($\leq$10 SUNs) space applications and high concentration (100-1000 SUNs) terrestrial applications as well as other programs aimed at developing high efficiency ($>$25%) multicolor devices for use in similar applications. An additional program is aimed at achieving improved power-to-weight ratio by parting thin film solar cells from their growth substrates prior to their incorporation into an array assembly. There is potential for multiple reuse of the substrates which could lead to reduced costs for such devices.

Highlights of these programs and their interrelated contributions toward the goals of reducing specific weight, volume and cost of photovoltaic space power systems are discussed below. Overall goals are summarized and current programs and their funding sources are listed in Fig. 1.

MULTICOLOR SOLAR CELL PROGRAMS

Two approaches toward achieving high efficiency by means of multicolor, multiple bandgap devices are being pursued. The goal of the Air Force (APL) sponsored program is to demonstrate a device with 1 SUN AMO efficiency of $\sim$25%. The approach has been to first survey a number of candidate materials combinations, growth techniques and converter designs and then choose the most promising combinations of these for final development to meet the performance goal. The materials combinations considered have been limited to closely lattice-match combinations of III-V compounds and/or Ge. The growth techniques examined have included LPE, conventional CVD, MO-CVD, and MBE. The candidate converter designs have all been variations on the theme of series connected subcells of appropriate high and low bandgap materials joined by an optically transparent tunnel junction ohmic contact.

Our current baseline configuration for such a device is shown schematically in Fig. 2. A significant feature of this design is the semi-transparent nature of the high bandgap $Al_x Ga_{1-x} As$ subcell which allows an appropriate fraction of high energy photons to pass through to the underlying GaAs subcell. This is done to optimize the opposite trends of current matching and

good AlGaAs subcell performance with variation of Al content. An additional feature of the design is the use of ultra thin tunnel junction structures of GaAs. By maintaining the n^+ and p^+ layer thickness $\leqslant 200\text{\AA}$, the optical absorption losses in the tunnel junction are in the range of 1-2%. The use of GaAs rather than higher bandgap AlGaAs facilitates growth of low resistance structures.

Devices of this type have been fabricated having $V_{oc} \sim 2.1$ volts and conversion efficiencies $\sim 2\%$. A typical plot spectral response as a function of electrical bias is shown in Fig. 3. The complicated interaction of the I-V characteristics of the two subcells and intervening tunnel junction is apparent in the plot.

The goal of the SERI sponsored program is primarily to demonstrate high efficiencies from multicolor devices at high concentrations under terrestrial illumination. However, success with this program could be directly applied to producing enhanced performance space cells.

The approach here is to attempt to fabricate two cell, non-lattice matched, monolithic stacked devices incorporating optimum pairs of individually grown subcells having bandgaps in the range of 1.6-1.7 eV and 0.95-1.1 eV. The high bandgap subcells are being grown by MO-CVD to produce layers of AlGaAs of appropriate thickness, composition and doping to give optimum performance heteroface homojunction structures. The low bandgap subcells are being similarly fabricated from AlGaAsSb compositions by LPE.

These subcells are then to be joined to form the final monolithic converter by an appropriate laser bonding technique. The bonding is also intended to produce the needed transparent intercell ohmic contact (IOC) and ultimately provide in-situ formation of an AlGaAsSb window layer, lattice-matched and epitaxial to the low bandgap cell. The overall device structure before and after the laser bonding operation is shown in Fig. 4.

The current status of the combined multibandgap effort is summarized in Fig. 5. Major future challenges remain in developing AlGaAs subcells with improved performance and developing improved intercell ohmic contacts using tunnel junctions and laser bonded structures. Because of the criticality of maintaining good current match between the individual subcells, it is anticipated that multibandgap devices may be more affected by radiation damage than are conventional single junction cells. It remains to be seen whether this will occur in practice.

PEELED FILM GaAs SOLAR CELLS

The objective of this program is to determine the technical merit and cost feasibility of basic process steps involved in the fabrication of GaAs peeled film solar cells. Several approaches to cell growth, bonding the cell to a low cost carrier, separating the cell from the reusable substrate, and processing methods are being investigated.

A photograph of a 0.5 x 0.5 cm peeled film GaAs heteroface solar cell supported by (wrapped around) a porous alumina rod appears in Fig. 6. The important processing steps needed to produce peeled film cells are shown schematically in Fig. 7. The current status of our peeled film effort is summarized in Fig. 8. It still remains to show that acceptable efficiencies can be realized with these cells. It also remains to be determined what the best configuration is for supporting the cell structure during ultimate use.

GaAs EFFICIENCY IMPROVEMENT STUDY

The goal of this program is the achievement of high yields of high efficiency GaAs heteroface cells. To this end, the project is focused on identifying the efficiency limiting factors in cell materials and cell processing, and improving materials growth and cell fabrication methods so as to mitigate these factors. Specifically, the program plan calls for (1) developing an in-house capability for directly synthesizing up to 3" diameter GaAs boules by the liquid encapsulant method, (2) establishing 2" and 3" diameter MO-CVD (metal organic chemical vapor deposition) epitaxy as the method of solar cell layer growth, (3) studying the defects in the GaAs substrate and epigrown layers and correlating materials quality with the cell efficiency, and (4) as materials evidence for the results of this program, delivering a minimum number (150) 1 cm. diameter concentrator cells meeting specified performance characteristics to the sponsor.

Figure 9 shows the configuration of the current structure of our high efficiency MO-CVD grown GaAs heteroface solar cells. Figure 10 shows typical performance data for this type of cell. Such structures have been repeatedly grown on areas of up to ~2 in^2 with all 0.5 x 0.5 cm cell AMO efficiencies lying in the 18±1.5% range. Efforts are currently under way to scale up the MO-CVD reactor to accept 3" diameter substrates. 1.7 x 1.7 cm and 5 x 5 cm masks are being designed for fabrication of large area cells. Experiments are under way to explore potential advantages of lower temperature epitaxial growth. There is accumulating evidence that growth at ~650°C significantly reduces the detrimental effects of recombination centers which can rapidly diffuse from the substrate into the growing layers during higher temperature (~750°C) growth.

GOALS

- HIGH POWER/WEIGHT RATIO
- LARGE AREA DEVICES (5 CM x 5 CM)

CURRENT PROGRAMS

- STACKED MULTIBANDGAP SOLAR CELLS (APL)
- ADVANCED CONCENTRATOR CELLS (SERI)
- GaAs PEELED FILM SOLAR CELLS (SERI)
- GaAs EFFICIENCY IMPROVEMENT (SANDIA)
- BULK CRYSTAL GROWTH (NASA)
- ADVANCED SPACE CELL CONCEPTS (IR&D)

Fig. 1.

- MOCVD-GROWN ALGaAs AND GaAs SUBCELLS
- MBE-GROWN GaAs TUNNEL JUNCTION IOC
- TWO LAYER AR COATING

FRONT CONTACT
600Å SiO_2
800Å Ta_2O_5 } AR COAT
500Å p^+ $Al_{.85}Ga_{.35}As$:Zn
0.7μm p $Al_{.35}Ga_{.65}As$:Zn } 1.85 eV SUBCELL
0.4μm n $Al_{.35}Ga_{.65}As$:Se
200Å n^+ GaAs:Sn
200Å p^+ GaAs:Be } TUNNEL JUNCTION
1.0μm p GaAs:Zn
} 1.42 eV SUBCELL
~5.0 μm n GaAs:Se

n GaAs:Si Substrate
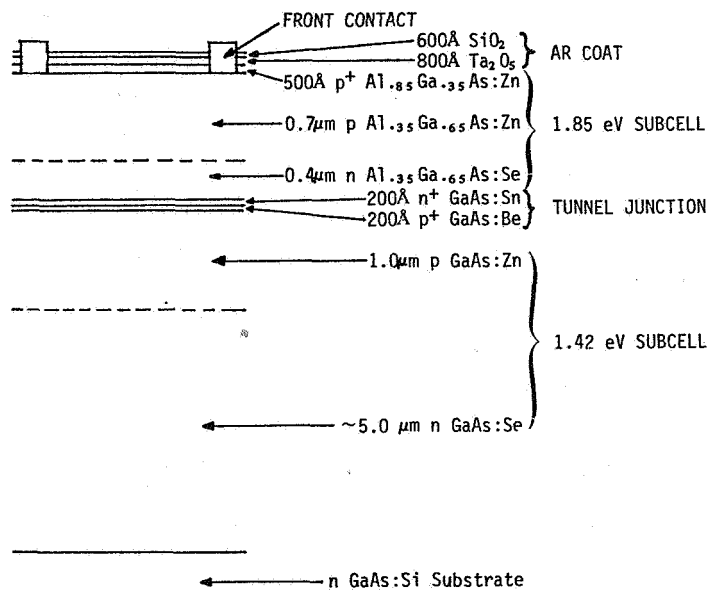
Fig. 2. Current baseline configuration of 2-cell SMBSC.

STACKED CELL SPECTRAL RESPONSE
AS FUNCTION OF ELECTRICAL BIAS

Nd GLASS LASER

1.06 μm

←—GaAs SUBSTRATE—→

←—AlGaAs WINDOW—→

←—p AlGaAs LAYER—→

←—n AlGaAs LAYER—→

←—Al

Sb   AlSb→

←—Al

←—p AlGaSb LAYER—→

←—n AlGaSb LAYER—→

←—GaSb SUBSTRATE—→

DEFECT
TUNNEL
JUNCTION

REGROWTH
INTERFACE
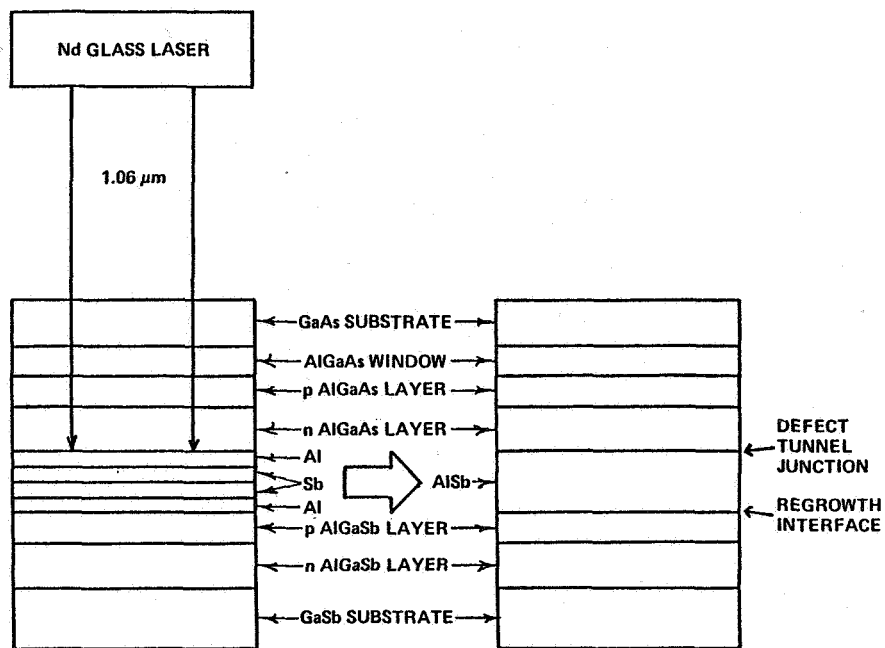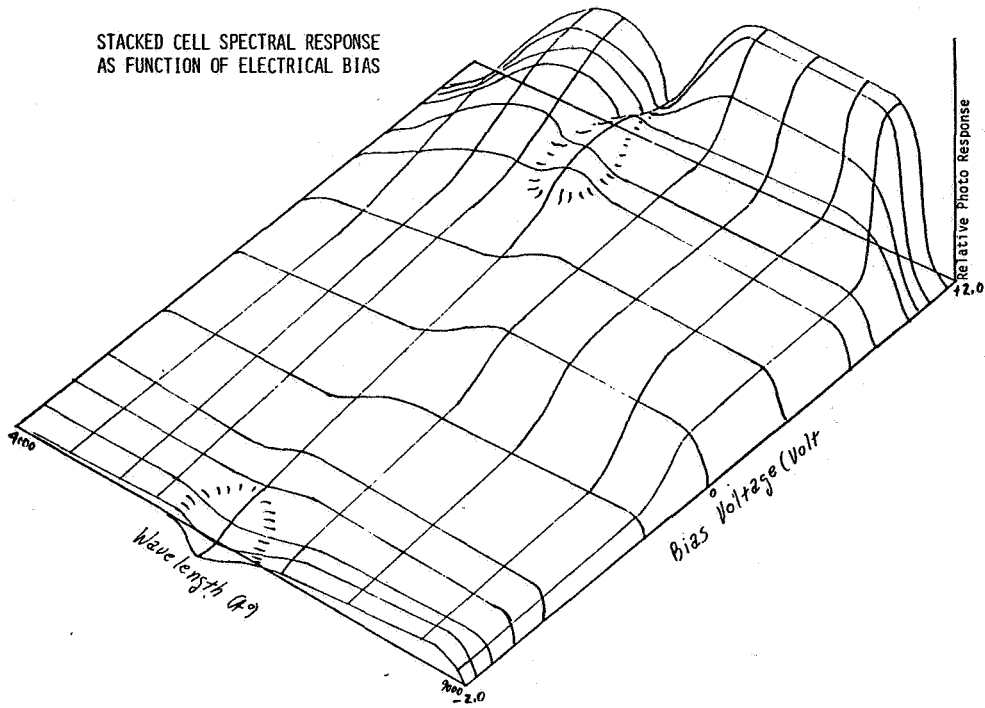
Fig. 4. Laser bonding.

117

AlGaAs SUBCELLS

- GOOD SPECTRAL RESPONSE ACHIEVED IN MO-CVD $Al_{.3}Ga_{.7}As$ SUBCELL
- HIGH SERIES RESISTANCE REMAINS A PROBLEM (FRONT CONTACT GRID)

INTERCELL OHMIC CONTACTS

- RELIABLE LOW RESISTANCE TUNNEL JUNCTIONS ACHIEVED WITH MBE
- LASER BONDING OF DISSIMILAR SEMICONDUCTORS DEMONSTRATED
- P DOPANT OTHER THAN Zn NEEDED FOR MO-CVD TUNNEL JUNCTIONS

COMPLETE CONVERTERS

- DIFFICULTIES IN ACHIEVING MATCHED HIGH CURRENT DENSITIES
- DEMONSTRATED EFFICIENCY ~2% vs. POTENTIAL EFFICIENCY ~24%
- LEVERAGED RADIATION DAMAGE IS A POTENTIAL CONCERN

Fig. 5. Current status of multibandgap solar cells.

Fig. 6.

118

① GaAs SUBSTRATE ‖ 750 μm

② 2-4 μm SOLAR CELL / 2-4 μm PARTING LAYER / EPILAYER GROWTH

③ CARRIER / CARRIER BONDING

④ (SUBSTRATE RE-USE) / PARTING

⑤ CELL PROCESSING
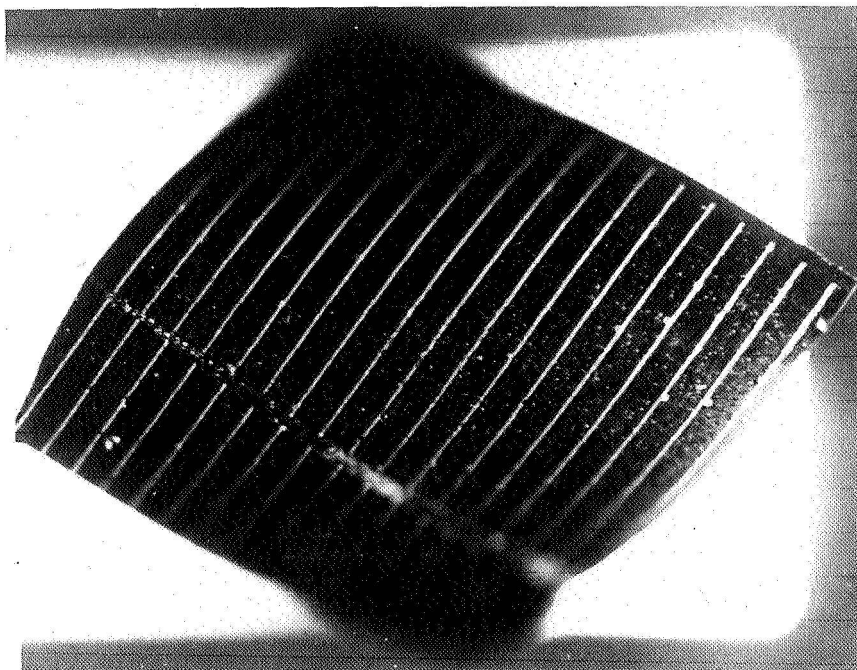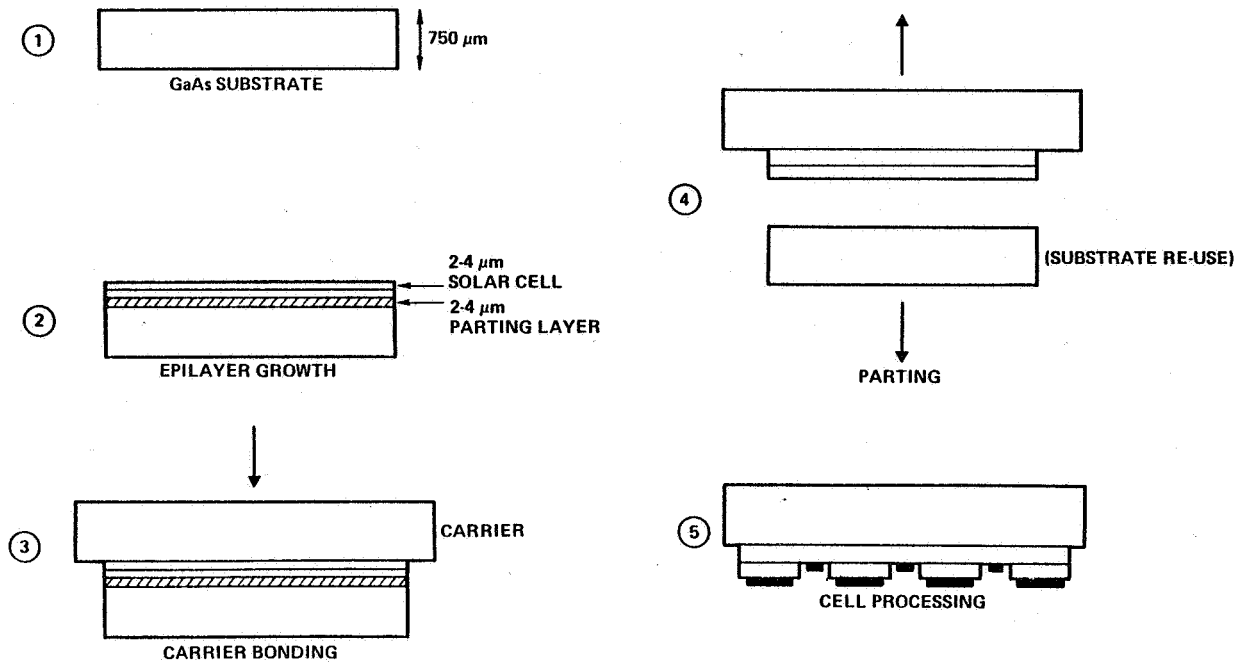
Fig. 7. Schematic of a GaAs peeled film solar cell fabrication process.

- FEASIBILITY OF PRODUCING A PEELED FILM GaAs SOLAR CELL DEMONSTRATED

- GLASS BONDING OF PEELED FILM STRUCTURES UNDER DEVELOPMENT

- REUSABILITY OF GaAs SUBSTRATE CONFIRMED

- PERFORMANCE OF PEELED FILM DEVICE NOT MEASURED

Fig. 8. Current status of peeled film solar cells.

CONTACT: Zn/Ag-Mn (7% coverage)

AR COAT: ~800Å SiO_2 on ~500Å Ta_2O_5

WINDOW LAYER: 600Å $Al_{.85}Ga_{.15}As$ (Zn 5E18)

p JUNCTION LAYER: 0.5 μm GaAs (Zn 1E18)

n JUNCTION & BUFFER LAYER: 6-7 μm GaAs (Se 5E17)

SUBSTRATE: (100) GaAs (Si ~1E18)

CONTACT: Au-Ge/Pt/Au
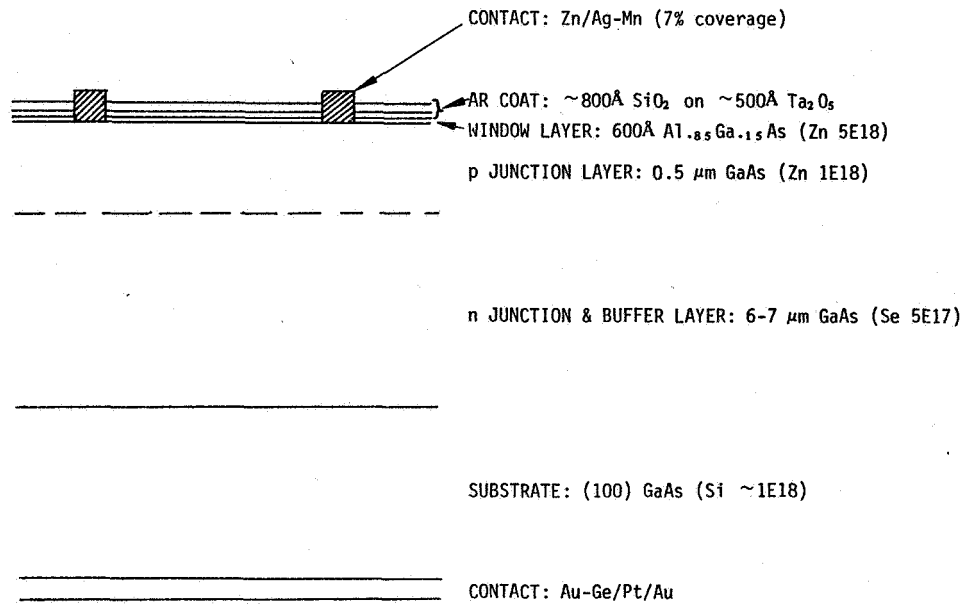
Fig. 9. Schematic structure of high efficiency GaAs solar cell grown by MO-CVD.

V_{oc} = 0.953
I_{sc} = 6.71175E-3
F.F. = 0.812
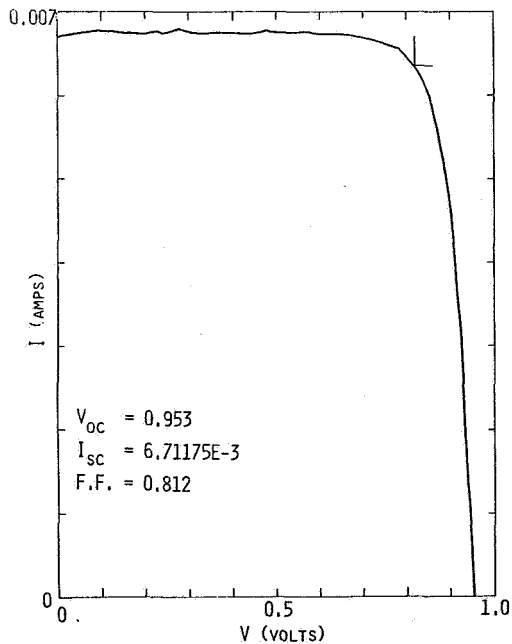
MO-CVD GaAs HETEROFACE CELL
0.5 CM x 0.5 CM MESA
2" DIAMETER WAFER

V_{oc} = 0.953
J_{sc} (1 SUN, AMO) = 33.5 mA/cm^2
F.F. = 0.812
η (1 SUN, AMO) = 19.2%

Fig. 10. GaAs efficiency improvement studies.

120

GaAs WORKSHOP REPORT

G. S. Kamath
Hughes Research Laboratories

The following report was the result of the workshop on GaAs solar cells held at NASA Lewis October 17, 1980, at the end of the Fourth High Efficiency and Radiation Damage Solar Cell Meeting. The members of the workshop were

Peter Borden	Varian
Dennis Flood	NASA Lewis
Sanyiv Kamath	Hughes Research Labs (Chairman)
John Lear	Martin Marietta
Ken Masloski	AFAPL
K. L. Wang	JPL
Gil Walker	NASA Langly

It was a productive workshop with active participation from all the members, and the following is a brief summary of the major conclusions reached about the status and future directions of work on GaAs solar cells.

The group felt very strongly that the advantages offered by the GaAs cells have been demonstrated in laboratory experiments and that it was time to fly the cells. The important next steps are to convey the information to the wider technical community, especially to the project offices that control the space satellite programs in the Air Force, Navy, NASA, and ESA. The group felt that a pilot line production of the cells to make the cells available to the missions in the near future could best be based on the present LPE technology and that this should be done as expeditiously as possible.

The findings of the workshop were divided into six main categories.

    I. GaAs: Advantages and Disadvantages
   II. The Substrate Problem
  III. Cell Fabrication
  IV. Future Trends
   V. Cost
 VI. Conclusions

I. GaAs: Advantages and Disadvantages

Advantages

1. 20 Percent higher η than silicon (BOL).
2. High temperature capability.[1]
3. High resistance to radiation damage vis-a-vis silicon. (We note that the 4-1/2 year old GaAs cell with deep junction flying in the NTS II package compares with the best silicon cell on the NTS II.)

---

[1]Note that by improving the solder and the glue for cover glass, GaAs solar cells can be made suitable for operation at $500°$ C or higher.

4. The possibility of continuous annealing of GaAs cells looks very exciting and real.

Items 2, 3 and 4 above combine to produce EOL η close to beginning of life, increasing the advantage over silicon for all space missions. Special advantage for missions such as near sun or high radiation environment are specially noteworthy.

5. Thin film capability because of the short ($<5 \mu$m) absorption length for solar radiation and the short minority carrier diffusion length ($\sim 10 \mu$m). John Fan (Lincoln Labs) has demonstrated that a "peeled film" with less than 10 μm thickness is capable of yielding 18 percent AMO efficiency. This compares with the 15 percent AMO, 50-μm cell in Si.

Disadvantages

1. Weight: The thinner cells eliminate this problem. However, the technology for thin cells still needs to be perfected. If the project office realizes the eventual advantages, the cost of development can be demonstrated to be fully justified by the reduction of system cost. The reduction in cover glass weight and packaging may be an additional possible advantage for GaAs.
2. Cost of material: GaAs now costs about $3/cm^2 more than does silicon. However, since the solar cell is an area (and therefore volume) intensive device, the increase in volume of cell demand will bring down the cost of material (see LED cost history, for example). In the long term we feel the GaAs cells will only cost $<$1/cm^2 extra for practical space cells. This is not an important consideration for any practical space system during the next 10 years or more. Furthermore, the cell cost may be more than offset by gain in efficiency (especially EOL) that the GaAs cells offer.
3. Mechanical reliability, especially in flight testing, needs to be established. This would be true for any new technology. Continuous annealing, which seems possible to minimize radiation damage, may lead to the elimination of the cover glass and thus reduce cell package weight even further.

II. The Substrate Problem

The committee considered the substrate problem. The present solution of growing a buffer layer to permit the use of the commercial GaAs available is admittedly costly. However, since the development of new techniques, such as solution regrowth (IBM), efficient epitaxial batch processing techniques (LPE, MOCVD) are reducing the additional fabrication cost. We feel strongly that radical improvements in the quality of substrates should not be financed by solar cell development, especially in view of the severe shortage of research funds in this area.

Additionally, the committee felt that other device requirements, especially in the microwave area, should be used as the prime driver for

substrate development in GaAs. This is especially true since the present thinking is that substrates such as Si can possibly be used as substrates for the GaAs solar cell. When we consider further that new technology, such as the Varian cells developed for DOE and the Lincoln Lab thin film cells (John Fan) made by the peeled film technology, are all aimed at elminating the extensive use of substrates altogether, we have to question the wisdom of using our limited research funds to finance GaAs bulk growth development. This argument gains further weight when we consider that the capability for diagnostics in GaAs to determine the degree of improvement is itself extremely limited.

The argument for improvement in silicon technology is more convincing since silicon needs to be at least 2 mils thick, and the development rides piggyback on the considerable existing technology. We discussed the Westinghouse ribbon growth in GaAs. While this is an attractive alternative, the cheap cell argument is so much stronger for the terrestrial applications; we felt they should be induced to at least share as the prime driver in this new development.

III. Cell Fabrication

The major conclusions were

1. LPE cells exist and should be flown as rapidly as possible to increase acceptance of the cell.
2. OMCVD is an attractive technique among all CVD techniques and should be considered the heat alternative to LPE. Long term advantages for both GaAs as well as for multijunction cells is an important consideration.
3. Ion implantation, laser annealing, and other processing tools should be used only when their development is sufficiently extensive on the basis of other needs.
4. MBE needs development that cannot be financed by solar cells alone. Piggyback effort may be justified if funds warrant it.
5. The n-on-p vs p-on-n question needs to be answered for the cell structure to see if there is any clear advantage for either. The topics to be considered are efficiency and radiation damage. The high temperature contacts may make homojunction cells impossible due to the shallow n layer. Questions: Is the n-on-p cell going to suffer in the blue response? Can you effectively contact it with suitable metals without the anodic oxide as a protection?

IV. Future Trends

Efficiency improvement

- Goal: 20 Percent AMO feasibility in 1981.
- Increase reproducible cell efficiency on pilot line to 18 percent AMO by 1982.

- Develop packaging (contacts, glass cover adhesive) to permit cell use at 400° C.
- With some typical missions in mind, develop panels that will deliver EOL efficiency close to BOL. Can a concentrator system be used to increased advantage for GaAs?
- Persuade JPL to include in the next handbook on radiation damage an expanded chapter on GaAs.
- Evaluate MOCVD.
- Evaluate thin cell capability for GaAs (2 mils and less); Peeled film, graphoepitaxy to be considered. The possibility of thin cells is not in question since the photocathodes developed by Varian have demonstrated the feasibility of using 10-µm material. Lincoln Lab's peeled film cell also proves the point very effectively. In the short run, is the polishing technique used by Varian effectiveµ It should at least be tried. Again, the terrestrial program on solar cells could be a partner in the development of a thin film cell.
- Ribbon growth. Evaluate economics of development (discussed previously in the substrates section).

V. Cost

The cost of the cell should be carefully evaluated with the cost of technology development, cell qualifications, and the cell production volumes in mind. The choice of specific missions as targets will greatly facilitate this exercise. Progressive cost reduction with increasing volume is possible on this approach. The various project officers could greatly facilitate the development by close coordination of the varying needs. NASA, DOD, and ESA are suggested as the prime agencies that could help identify realistic needs for the missions in 1983 and beyond.

VI. Conclusions

GaAs technology has arrived and has significant contributions to space power during the next decade. We have the prime responsibility as the technical community to make the relevant information available to the various mission project offices. Identify special areas such as near Sun missions, high radiation belts, orbit raising missions, concentrator cells, etc., where the special advantages offered by GaAs give it a definite edge to offset higher present cost. We feel that this procedure will result in the systematic development of the GaAs cell at a minimum of total cost with substantial benefit to the total space power program in the 1980s.

RESULTS OF THE AIR FORCE HIGH EFFICIENCY CASCADED
MULTIPLE BANDGAP SOLAR CELL PROGRAMS

W. P. Rahilly
AF Wright Aeronautical Laboratories
Wright-Patterson AFB, Ohio

SUMMARY

The III-V semiconductor materials system that was selected for continued cascade cell development in Phase II by both contractors was the AlGaAs cell-on-GaAs cell structure (ref. 1). The progress made by the contractors since October 1979 has been considerable. However, the tunnel junction used as transparent ohmic contact between the top cell and the bottom cell continues to be the central difficulty in achieving the program objective of 25% AMO efficiency at 25°C. During the tunnel junction and top cell developments within the last year, it became apparent that the AlGaAs cell has potential for independent development as a single junction converter and is a logical extension of the present GaAs heteroface technology.

INTRODUCTION

Air Force space missions will require power systems in the two to ten kilowatt range during the 1980's with expansion to two hundred kilowatts by the year 2000. Super-imposed on these power systems will be requirements for survival to various hostile environments as well as the normal space environment. Cascade cell development is critical to both near term and far term earth orbit missions. The main parameters that will drive the cascade cell development are watts/kilogram and cost/watt, both at mission end-of-life. Factors that strongly influence these parameters are cell conversion efficiency, cell weight (along with array blanket weight) and high cell yield in mass production. Air Force sponsorship of research development in these areas will receive very high priority.

This paper presents results of the cascade cell developments supported by the Air Force and discusses approaches to achieve high power-to-weight and low cost-to-power ratios.

AIR FORCE CASCADE CELL DEVELOPMENT - PRESENT STATUS

The objective of the Air Force cascaded cell research and development is to fabricate and demonstrate solar cells with greater than 25% AMO conversion efficiency at one-sun and at 25°C. Based on results of research conducted in Phase I, it became clear that a near term payoff could be made if the AlGaAs cell-on-GaAs cell structure was pursued in Phase II. This system is not the optimum one but certainly has potential for reaching the stated objective with

reduced difficulties in fabrication. The most significant advantages for this material selection are (a) lattice matching between AlGaAs and GaAs is essentially ideal, (b) the use of a single AR coating, such as Ta_2O_5, is expected to be consistent with high conversion efficiency, (c) the contact metallization system for the top cell (and window) is fairly well developed and (d) the technology used to fabricate this structure can be extended to a three cell stack for further efficiency gains. This latter advantage, however, would require considerable trickery or cleverness since there are a limited number of lattice matched systems available (Ge or a GaAs on Ge or Si cell). However, a development of the understanding and the use of "super lattices" can relieve lattice matching problems and thus provide for a wide range of materials for a botton cell of a three cell stack.

Both liquid phase epitaxy (LEP) and chemical vapor deposition by breakdown of metal-organic compounds (MO-CVD) are being investigated. The LPE efforts are being accomplished at Research Triangle Institute and the MO-CVD work is ongoing at Rockwell International.

RESEARCH TRIANGLE INSTITUTE

The difficulties encountered in the development of the four original semiconductor materials systems (GaInP on GaInAs, AlGaAs on GaInAs, AlGaAsSb on GaInAs and AlGaAsSb on GaAsSb) led to the decision to explore a special case of the second system wherein no indium is in the bottom cell. RTI has successfully demonstrated complete cascade structure with conversion efficiencies of greater than 15% AMO without an AR coating. Problems do remain with device area uniformity and control of the P dopant (Be) in the tunnel junction. RTI is now modelling the structure to determine the optimum aluminum composition in relation to the AMO spectrum, AR coating(s) and minority carrier diffusion lengths that are considered realistic based on available data. The modelling data will be used to guide the cell development to achieve the program objective (ref. 2). Since details of the AlGaAs on GaAs system development by RTI are presented elsewhere in this conference, the reader is referred to that paper (ref. 3).

ROCKWELL INTERNATIONAL (RI)

The four systems pursued by RI in Phase I were based on the AlGaAs/GaAs system with emphasis on MO-CVD material growth. These systems are discussed in some detail in reference (1). Many problems were encountered with these systems in Phase I and it was decided to pursue the AlGaAs cell on GaAs structure using MO-CVD with some effort directed at molecular beam epitaxy (MBE). The most serious problem encountered (and still remains) is control of the P dopant in the very highly doped tunnel junction during subsequent AlGaAs top cell growth. Since there is no available Be-organic compound suitable for CVD growth, RI chose to grow tunnel junction using MBE grown layers comprised of GaAs N+:Sn on GaAs P+Be (see Figure 1). If the GaAs tunnel layers can be made very thin, absorption of photons usable in the bottom cell will be negligible. Another advantage is that the transfer of the structure from the MBE apparatus to the MO-CVD system does not present severe oxygen related problems as would

be encountered if the tunnel were grown with AlGaAs in the MBE reactor. The bottom GaAs cell has posed no problems; in fact, the MO-CVD grown GaAs bottom cell has been measured by RI to be nominally 20% efficient AMO.

The current status of the RI effort can be summarized as follows: The AlGaAs top cell suffers severe losses from interface states for MO-CVD growths, however, the MO-CVD method has considerable promise in low temperature, low pressure growths and if a Be-organic can be synthesized (attempts will be made by RI), then complete cascade cell growth in one reactor system is feasible. The tunnel junctions (GaAs material) have been demonstrated to be reliably grown and grown very thin ($\approx 200\overset{\circ}{A}$). Growth of quality AlGaAs top cell material on the MBE tunnel remains to be accomplished. The GaAs MO-CVD cells are viewed as no development problem. As for a completed stacked structure, the optimum configuration (at least for GaAs MBE tunnels) has been defined and voltage addition has been consistent and repetitively demonstrated. However, because mismatches of generated current in the top and bottom cells, reasonably efficient cascade structures have yet to be demonstrated.

SPIN-OFF TECHNOLOGY

As a result of the AlGaAs top cell development, it was recognized that a single junction in the AlGaAs material can be superior to the present GaAs heteroface structure. The advantages of this approach are: (a) it is possible to select the proper Al composition in order to achieve better bandgap matching to the AMO spectrum, (b) if minority carrier lifetimes can be adequately controlled, then a diode factor of near unity at the maximum power point is feasible, (c) placement of the AlGaAs-GaAs heteroface will be moved far away from the P/N junction resulting in improved voltage performance over that expected with increased bandgap but nearness to interface recombination, (d) simplified AR coatings are possible, (e) well developed electrical contacting can be employed, and (f) the cell concept can be pursued with relative ease using existing AlGaAs LPE and MO-CVD growth technologies. The Air Force is planning development of this cell type as a logical extension of the GaAs heteroface cell. With proper support, this sturcture could be introduced into manufacturing technology development and brought into inventory in the very near term (three to four years).

CONCLUDING REMARKS

RTI has been fairly successful with the LPE growth AlGaAs on GaAs structure. However, the device area has been limited by the LPE reactor design and large area LPE growth of cascade cells remain to be demonstrated. RI has encountered difficulty in fabricating a complete cascade structure of reasonable conversion efficiency (at least as good as silicon cells). But in the long term, MO-CVD growth of the complete structure by employing low temperature and low pressure or with a Be-organic (to resolve the P dopant problem) is very attractive from the points of view of mass production and large area. The Air Force is planning to continue emphasis on the AlGaAs on GaAs structure for use in the late 1980's. Both LPE and MO-CVD will be considered as likely mass production candidates until one approach shows clear superiority over the other

in terms of yield and cost. Plans for three cell stacks have been defined for the 1980's and independent development of the three cell system will be pursued.

The AlGaAs homojunction cell will be pursued for the near term with the intention of using it by the mid 1980's. Also, independent research to develop the so called galicon substrate will be conducted. Reasonable results have already been achieved under joint Air Force and NASA sponsorship at the Jet Propulsion Laboratory (JPL) (ref. 4).

REFERENCES

1. Rahilly, W. P., "A Review of Air Force High Efficiency Cascaded Multiple Bandgap Solar Cell Research and Development", NASA Conference Publication 2097, June 1979.

2. LaMorte, M. F., Abbott, D. H., "A Study of the Two-Junction AlGaAs-GaAs Cascade Solar Cell", this conference.

3. Bedair, S. M., "Fabrication of an AlGaAs-GaAs Cascade Cell by LPE", this conference.

4. Private Communication, S. Zwerdling (Jet Propulsion Laboratory) and Author.

FRONT CONTACT

600Å SiO$_2$ } AR COAT
800Å Ta$_2$O$_5$ }

500Å p$^+$ Al$_{.85}$Ga$_{.35}$As:Zn

0.7μm p Al$_{.35}$Ga$_{.65}$As:Zn } 1.85 eV SUBCELL

0.4μm n Al$_{.35}$Ga$_{.65}$As:Se

200Å n$^+$ GaAs:Sn } TUNNEL JUNCTION
200Å p$^+$ GaAs:Be }

1.0μm p GaAs:Zn

1.42 eV SUBCELL

~5.0 μm n GaAs:Se

n GaAs:Si Substrate
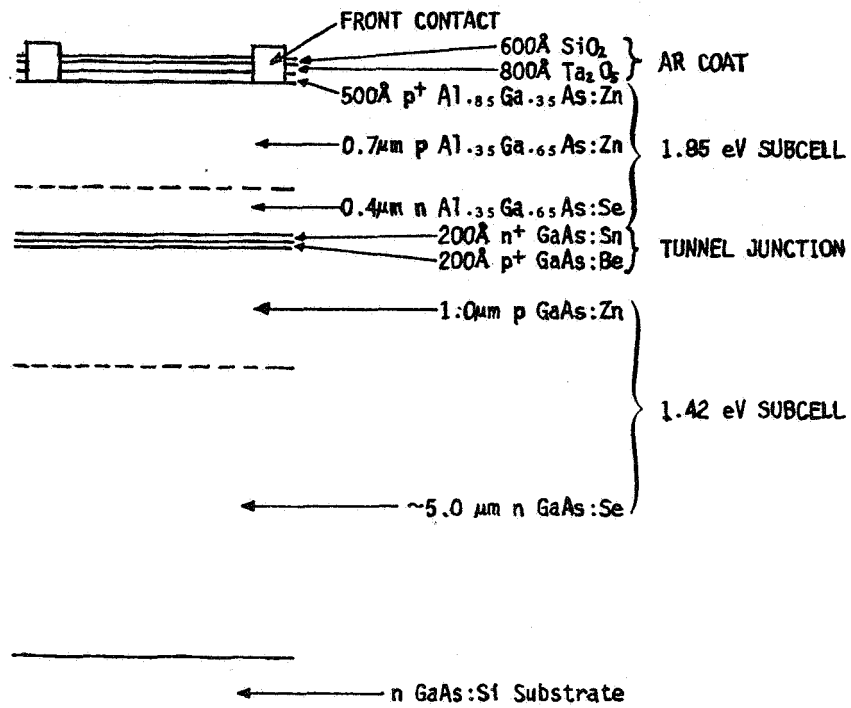
- MOCVD-GROWN AlGaAs AND GaAs SUBCELLS
- MBE-GROWN GaAs TUNNEL JUNCTION
- TWO LAYER AR COATING

FIGURE 1 ROCKWELL'S BASELINE CONFIGURATION OF THE TWO-CELL CASCADE STACK.

129

INCORPORATION OF SUPERLATTICE CRYSTAL LAYERS
IN MULTIJUNCTION SOLAR CELLS

A. E. Blackslee and K. W. Mitchell
Solar Energy Research Institute
Golden, Colorado

SUMMARY

This paper proposes the application of superlattice growth techniques in the fabrication of high efficiency multijunction solar cells in order to improve their crystalline perfection and hence enhance their output. Previous research has shown that superlattice layers are effective in decreasing the density of dislocations in lattice mismatched heterostructures at least four orders of magnitude. Hence it is proposed to utilize this feature of super-lattices to alleviate the problems due to misfit dislocations generated in the regions between two or more photovoltaic collecting junctions.

A further advantage is that the possibility is presented for using silicon as a low cost substrate as well as for the low band gap junction. In the test case proposed here, a silicon low gap cell will be connected to a $GaAs_{.7}P_{.3}$ high gap cell through a connecting region containing a GaAs/GaP superlattice.

INTRODUCTION

This paper proposes the application of superlattice[*] growth techniques for the fabrication of low cost substrates for high efficiency solar cells. Recent research has demonstrated the feasibility of achieving high photovoltaic conversion efficiencies (potentially above 35%) using multiple junctions in

----

[*] A superlattice, as the term has come to be used in solid state electronics, is a thin (~1μm) semiconductor structure comprised of many ultrathin layers (~100 Å each) of two different semiconductors alternating with one another. A schematic diagram of a superlattice composed of two hypothetical semiconductors A and B is shown in Fig. 1. This structure exhibits properties which tend to be intermediate between those of the two constituent materials but may be somewhat different from either one. It offers the possibility of creating semiconductors with made-to-order properties such as the band gap or optical absorption coefficient. It was first proposed by Esaki and Tsu (1) in 1970 as a quantum mechanical curiosity which might some day give rise to devices with extremely high frequency response. Several other device proposals based on the superlattice concept have followed. Although most superlattice growth to date has been done by the MBE process, the technical feasibility of growing superlattices by a CVD process was demonstrated in 1969 by Blakeslee (2) and improved recently, using MO-CVD, by Dupuis and Dapkus (3).

optimum band gap materials (4,5). In addition, multijunction converters are excellent candidates for hybrid photovoltaic/thermal systems. A hybrid converter of this type could have an electrical conversion efficiency of 25% while providing a thermal energy output in the range of 150°C to 250°C (6).

The GaAs substrate, which is used in structures currently being developed, is a drawback to widespread implementation of these high efficiency converters due to its high cost and extensive consumption of gallium resources. In addition, dislocations due to lattice mismatch between the various compositional layers involved in these structures degrade the quality of the electrically active regions of the cells. If a low cost substrate such as silicon could be substituted for the GaAs, a major breakthrough would result not only for III-V based solar cells, but for III-V device technology in general. The application of superlattice growth techniques, which have already shown great promise in coupling non-lattice matched layers, is proposed for utilizing low cost substrates in high efficiency solar cell structures. The proposed approach would alleviate the problem of device degradation due to dislocation propagation into the active regions of the cell. Furthermore, it would demonstrate the possibility of using silicon as both the low cost substrate and the low band gap cell of a two-junction high efficiency photovoltaic converter.

THE CONCEPT

Presently, only the III-V materials technology has been advanced sufficiently to address the materials requirements for growth of monolithic cascade cells, but the GaAs substrates which have been used thus far for the development of cascade devices are very expensive. Silicon substrates are a factor of twenty or so less expensive than GaAs, but, unfortunately, silicon does not have the proper lattice constant to be lattice-matched to the other candidate cells.

We propose to use superlattice structures in the fabrication of high efficiency tandem solar cells, not for the active photoelectric conversion layers but rather as a means of alleviating one of the most difficult problems facing the construction of monolithic tandem cells, namely that of lattice mismatch. The mismatch occurs because the two cells of the tandem, a high band gap cell and a low band gap cell, will in general be created out of two semiconductor materials having different lattice parameters. Figure 2 indicates the lattice constant values and band gaps of a number of candidate semiconductors for multijunction converters. The crosshatched regions represent the optimal range of band gaps for the top and bottom junctions of two-junction cascade cells. Presently only Ge and GaAs are considered as viable substrates for the cascade cells. Unfortunately, the band gap of Ge is too low to be optimal for the low band gap junction. Although Si has the proper band gap for the low band gap cell, it does not have the proper lattice constant to match the high band gap cell. Typically, a transitional, i.e., compositionally-graded, layer or series of layers is grown between the two cell regions in order to reduce the density of dislocations that inevitably arise to

relieve the misfit stress. At best these grading techniques, be they continuous or by steps, are only partially successful, and a large number of dislocations remains. They propagate through the active solar cell layers and cause recombination losses and, when present in extreme densities, can severly disrupt the crystal growth process. This is a very serious problem and one that is not generally sufficiently appreciated. It has been a major problem in achieving the necessary device quality layers in the present cascade cell structures.

However, a way around this problem does exist. Matthews and Blakeslee (7) have demonstrated that growth of a superlattice layer after the graded layer serves to confine all the dislocation lines in planes normal to the growth direction so that they do not propagate into the active solar cell region. They were able to reduce the dislocation density in a $GaAs/GaAs_{0.5}P_{0.5}$ super-lattice from 10^8 per cm^2 to almost zero. The details as to why and how this dislocation elimination can be effected are quite subtle; they are fully set out in the basic patent for the process granted to Blakeslee and Matthews (8).

A method has been suggested for constructing solar cells on silicon substrates (9). It consists of connecting the Si substrate with a deposited Ge layer through a graded alloy layer of $Ge_{1-x}Si_x$, followed by growth of GaAs on the Ge, to which it is lattice-matched. A better approach is to use the silicon as both the substrate and the low band gap junction. This reduces the complexity of the cascade structure substantially, with the benefit of better yields in a production line. The grading layer and superlattice layer in this case would couple the high band gap junction to the junction formed in the silicon.

IMPLEMENTATION OF THE CONCEPT

There are several tandem cell concepts which could benefit from the incorporation of a superlattice to alleviate the lattice mismatch problem. One in particular seems especially attractive as a test vehicle because it not only offers a good chance of relatively rapid reduction to practice with the least difficulty, but, if successful, could have a large impact on the problem of cost and availability of substrates for high efficiency solar cells.

The project selected is to link, by using a superlattice, a Si wafer, which serves as both substrate and low band gap cell, and a GaAs-based high band gap cell. The structure will be grown by the method of metal-organic chemical vapor deposition (MOCVD) which was shown to be useful for growth of high efficiency GaAs/GaAlAs solar cell structures by Dupuis et al. (10) in 1977. It has also been used to make double heterostructure lasers (11), FETs (12) and superlattice-like structures known as Bragg reflectors (3). Its principal advantage over other techniques such as liquid phase epitaxy is the ability to grow very thin (tens of angstroms), uniform layers of controllable composition.

It is necessary to go from Si with a band gap of 1.11 eV and a lattice constant of 5.43 Å to some ternary alloy of GaAs with a band gap ideally around 1.8 eV while undergoing as small a change in lattice parameter as possible. In view of the latter requirement, the GaP system is the best choice for forming a ternary with GaAs, since the lattice parameter difference between Si and GaP is only 0.37% and acceptable heteroepitaxy of GaP on Si by MOCVD has already been demonstrated (13). Thus, the major steps of the process would be the following:

(1) Start with a Si substrate and make a p-n junction by diffusion or by homoepitaxy.

(2) Grow a thin layer of GaP on the Si from a vapor containing $Ga(CH_3)_3$ and PH_3.

(3) Grow the graded layer by decreasing the PH_3 content of the reactant vapor and replacing it with AsH_3. Continue this process until the top of the graded layer has approximately the composition $GaAs_{.7}P_{.3}$, with a band-gap of 1.80 eV. This grading should be accomplished within 10μm or less.

(4) Remove the threading dislocations by inserting a thin asymmetric GaAs/GaP superlattice region containing 10 or so oscillations. In order to lattice match the superlattice to the underlayer with composition $GaAs_{.7}P_{.3}$, the thickness of the respective constituent layers GaAs and GaP should be in the ratio of 7 to 3.

(5) Grow a 2-3μm layer of essentially dislocation-free $GaAs_{.7}P_{.3}$ atop the superlattice and fabricate a junction therein by epitaxy or diffusion.

In carrying out the above procedure, two of the operations are particularly critical. One is the need for very precise control of the composition of the graded layer and of the top cell layer. This can be effected mainly by careful control of the input flow of reactant gases but might eventually incorporate in situ optical measurement of the solid composition. The other critical point is the ability to switch back and forth rapidly and reproducibly from GaAs to GaP in creating the superlattice. Both of these points can be accommodated within the scope of present technology by making modifications to present MOCVD systems. Other points requiring careful consideration are meticulous substrate surface treatment in order to assure good initial epitaxy of GaP on Si and careful experimentation to determine the absolute minimum thickness for each layer, since it is very important to eliminate as much of the expensive Ga-containing material as possible.

REFERENCES

1. L. Esaki and R. Tsu, IBM J. Res. Develop., $\underline{14}$ 61 (1970).

2. A.E. Blakeslee, J. Electrochem. Soc., $\underline{118}$ 1459 (1971).

3. R.D. Dupuis and P.D. Dapkus, Appl. Phys. Lett., $\underline{33}$ 68 (1978).

4. R.L. Moon, L.W. James, et al., Proc. 13th IEEE Photovoltaic Specialists Conf. (1978), pp. 859-867.

5. S.M. Bedair, M.F. Lamorte, J.R. Hauser, K.W. Mitchell, Proc. International Electron Device Meeting, Washington, D.C., December 1978, pp 250-253.

6. K.W. Mitchell, Proc. International Electron Device Meeting, Washington, D.C., December 1978, pp. 254-257.

7. J.W. Matthews and A.E. Blakeslee, J. Crystal Growth 27, $\underline{118}$ (1974); J. Crystal Growth $\underline{32}$, 265 (1976).

8. A.E. Blakeslee and J.W. Matthews, U.S. Patent 4,088,515, May 9, 1978.

9. Y.C.M. Yeh, K.L. Wang, B.K. Shin and R.J. Stirn, Proc. 14th IEEE Photovoltaic Specialists Conf. (1980), pp. 1338-42.

10. R.D. Dupuis, P.D. Dapkus, R.D. Yingling and L.A. Moudy, Appl. Phys. Lett;, $\underline{31}$ 201 (1977).

11. R.D. Dupuis and P.D. Dapkus, Appl. Phys. Lett., $\underline{31}$ 839 (1977).

12. J. Hallais, J.P. Andre, P. Baudet and D. Baccon-Gibod, Gallium Arsenide and Related Compounds 1978, (Inst. Phys. Conf. Ser. No. 45) p. 361.

13. H.B. Pogge, B.M. Kemlage and R.W. Broadie, J. Cryst. Growth, $\underline{37}$ (1977).

Superlattice Structure

Bandgap and Lattice Constant Values for the III-V Semiconductors
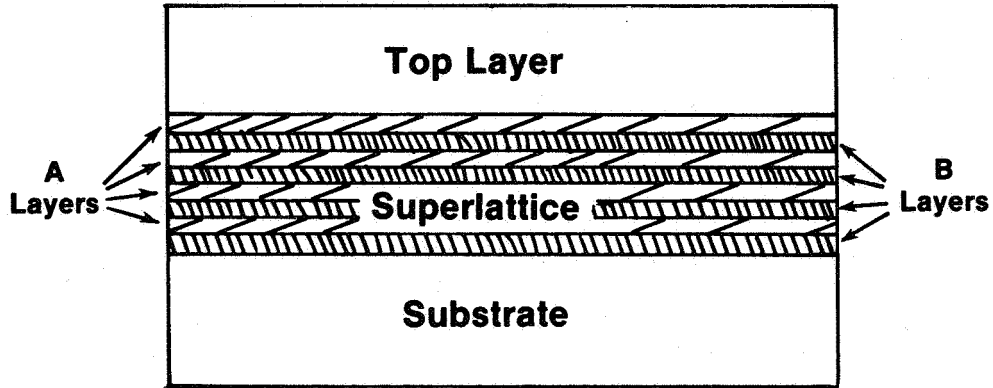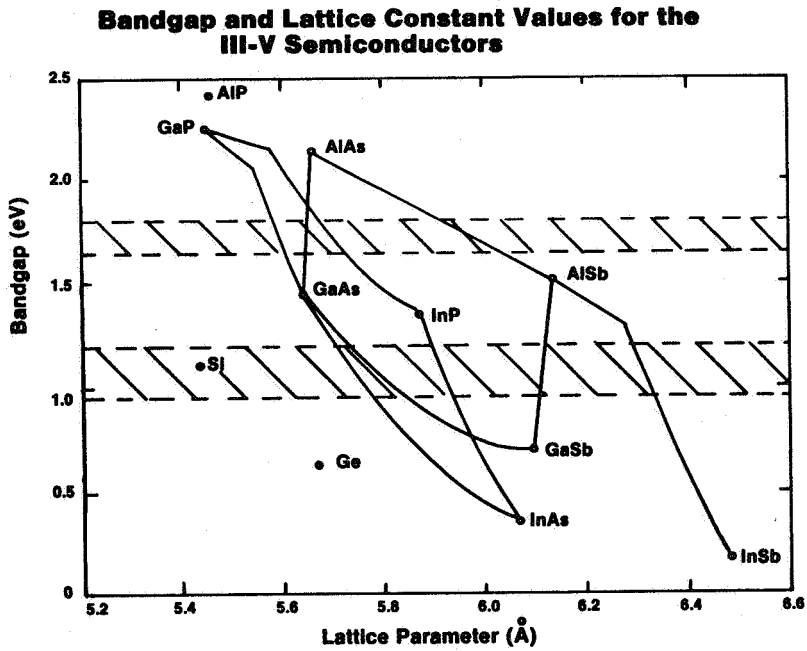
AlGaAs–GaAs CASCADE SOLAR CELL*

M. F. Lamorte and D. H. Abbott
Research Triangle Institute
Research Triangle Park, North Carolina

ABSTRACT

Computer modeling studies are reported for a monolithic, two-junction, cascade solar cell using the AlGaAs–GaAs materials combination. An optimum design is obtained through a serial optimization procedure by which conversion efficiency is maximized for operation at 300 K, AM 0, and unity solar concentration. Under these conditions the upper limit on efficiency is shown to be in excess of 29%, provided surface recombination velocity does not exceed 10^4 cm sec^{-1}.

INTRODUCTION

Computer modeling shows that conversion efficiency exceeding 30% may be realized from a two-junction cascade solar cell at 300 K and AM 0 [ref. 1-5]. These investigations show that the bandgap of the wide (top) and narrow (bottom) bandgap cells more strongly influence the efficiency than other design parameters. While steady progress has been made in the development of the technology required to obtain high efficiency, the technological problems encountered in this endeavor has generally limited the efficiency to 15% or less [ref. 6,7]. The major problem is the difficulty of fabricating a structure with an optimum bandgap combination because of lattice mismatch [ref. 4]. Related problems spring from the adverse effects arising from short diffusion length, control of layer thickness, space charge recombination current, p-n junction leakage current, and fabrication of a large area, low voltage drop tunnel junction.

The optimum bandgap combinations range from 1.62 eV/0.95 eV [ref. 1-4] to 1.84 eV/1.23 eV [ref. 5] where the efficiency is maximized at 300 K at AM 0 and 475 K at AM 1, respectively, using the AlGaAs–GaInAs materials combination. While the lattice mismatch is reduced with increasing bandgap values in this material system, cascade cells have not been fabricated with high efficiency using these bandgap combinations because of poor crystalline quality due to large lattice mismatch. However, one encouraging factor is that the upper limit efficiency for the 1.84 eV/1.23 eV [ref. 5] set at AM 1 is approximately 30% which is only slightly lower than the 31.5% obtained for the optimum combination 1.62 eV/0.95 eV [ref. 1-4] at 300 K and AM 0. If further compromise is made with respect to efficiency, a range of bandgap values may exist which are higher than the 1.84 eV/1.23 eV combination that give 25% or higher efficiency values for optimized designs [ref. 4]. The attractiveness of these considera-

tions is that further increases in bandgap continues to decrease the lattice mismatch, where at the extreme the AlGaAs-GaAs materials combination shows a very small lattice mismatch over its entire compositional range [ref. 4]. Although the electronic and optical properties of AlGaAs have not been studied as extensively as for GaAs, there is a sufficient body of experimental data to suggest that the properties of AlGaAs are favorable for the fabrication of cascade cells [ref. 8,9].

The major obstacle to the fabrication of high efficiency cells using the AlGaAs materials system is that its bandgap span does not encompass the optimum bandgap combinations which give efficiency values of 30% or greater [ref. 4]. Initial studies indicated that a non-optimized design may give cascade efficiency values less than 15% [ref. 4]. The efficiency which may be attainable for an optimized design has not been studied. Other problems such as the fabrication of a low voltage drop tunnel junction and low resistance ohmic contact to AlGaAs appear to be solved or nearing solution [ref. 10,11]. On balance, the seriousness with which this materials combination is to be considered in cascade cell fabrication depends heavily on the device design requirements and the corresponding upper limit on efficiency. In this paper computer modeling results are reported with presentation of an optimum design and its corresponding maximum efficiency for operation at 300 K, AM 0, and unity solar concentration.

The computer modeling program is applied to the bandstructure shown in figure 1 [ref. 1-5]. Top and bottom cells are joined electrically through a tunnel junction, and with the window layer form a monolithic structure. The cascade photovoltage is the sum of the top and bottom photovoltages which are of the same polarity. In this connection, it is essential that the tunnel junction should not absorb photons [ref. 1-5]. Should this occur, the photon flux available to the bottom cell is reduced and the resultant photovoltage generated in the tunnel junction subtracts from the sum of the top and bottom cell photovoltages. Also, this may produce a mismatch in the currents at the maximum power-point of the individual V-I curves of top and bottom cells. All of these effects serve to reduce cascade efficiency.

The bottom cell is assigned the value 1.44 eV, corresponding to the GaAs bandgap, because it is the minimum value which is obtainable from the AlGaAs-GaAs materials combination. Therefore, the optimum bandgaps of the top cell and window layer are required to be obtained from the optimization procedure [ref. 1-5]. Typically, setting the tunnel junction bandgap equal to the top cell bandgap produces an optimum design, while minimizing the technological difficulties. Also, the window layer thickness typically used is 0.1 µm, with $2 \times 10^{18} cm^{-3}$ acceptor concentration, and a linear bandgap grading to establish a 3000 V cm^{-1} built-in potential [ref. 1-5].

In the present fabrication process involving liquid phase epitaxy, the acceptor concentration in the p-type regions of top and bottom cells is $10^{18} cm^{-3}$ and cannot easily be changed [ref. 12]. Therefore, optimized acceptor concentrations are not determined for these regions. The tunnel junction donor concentration is set at $10^{19} cm^{-3}$, acceptor concentration at $10^{20} cm^{-3}$, and 0.1 µm thickness for the n- and p-regions. Optimized donor and acceptor concentrations and layer thicknesses are determined for all other regions.

138

The analytical method developed for cascade solar cells has been described elsewhere and is not discussed in detail in this paper [ref. 1,2,4]. By formulating the solution of the continuity equations in the framework of a boundary value problem, the cascade cell V-I relationship may be obtained, in principle, in closed form. However, in the simplest of cases solving for the current requires the solution of 14 simultaneous equations, for which the inversion is performed using a digital computer and the closed form equation is never explicitly obtained.

The other assumptions used in the analysis are that the thermal diffusion contribution to dark current is large compared to space-charge recombination and excess tunnel current components; the minority-carrier recombination rate is linearly proportional to excess carrier concentration [ref. 9,13]; recombination at heterojunction interfaces are negligible; efficiency is not corrected for grid contact shadowing or for power loss from joule heating arising in the structure's series resistance; and reflectivity at the window surface is 5%.

Device performance characteristics and parameters used in the study, for the most part, are those which have become standard in the photovoltaic literature. However, in cascade solar cells a number of additional parameters are needed to more completely characterize the device. They are usually defined in the discussion. In our studies the normalized collection efficiency is used exclusively, and is defined as the ratio of carriers collected by the p-n junction to the carriers generated through photon absorption in the region under consideration.

In the optimization study reported here, the invariant operating conditions imposed in all calculations are AM 0, unity solar concentration, and 10^6 cm$\cdot$s^{-1} surface recombination velocity.

COMPUTER MODELING RESULTS

In this section the computer modeling results are presented and discussed. Investigation is devoted to the determination of an optimized cascade cell design. Analysis of the device performance characteristics of this optimized structure, shows that the surface recombination loss may be the major loss factor in the AlGaAs-GaAs cascade cell.

Various optimization procedures may be used. The more desirable procedure is to allow all parameters to simultaneously vary over a specific range of values, which results in the determination of the optimum value for each parameter. Computer costs are usually prohibitive and this method is almost never used. The other extreme is a serial optimization that is used in this study. Computer costs in this case are typically low, but it usually requires greater skill in establishing the range of values for each of the parameters to avoid obtaining false optimum values [ref. 1,2,4]. In the serialization procedure used here the optimum value of one parameter is obtained by allowing only that parameter to vary over a judiciously selected range and determining the value for which the efficiency is a maximum. The values of the other parameters are held constant at values which are determined, by other considerations, to be in

139

the neighborhood of their optimum values. The optimum value of the one parameter so determined is then imposed on the structure. A second parameter is then allowed to vary and its optimum value determined and also imposed on the structure. This procedure is repeated for each parameter in a selected sequence. After having determined the optimum value for each parameter, the procedure is repeated a second time for each parameter in the same sequence. Typically, the same optimum values are obtained, while in some cases there are corrections for one or more of the parameter values. If the corrections are significant, the procedure is repeated for each of the parameters until the same optimum values are obtained. In the serial optimization used here, the optimum values of the parameters of the top cell are determined first, and then those of the bottom cell. Thus, in this sequence the performance characteristics of the top cell are unaffected when the bottom cell parameters are permitted to vary. However, when the bottom cell parameters are permitted to vary the current mismatch between top and bottom cells is affected.

Serial Optimization Results

The computer modeling results presented below are those obtained for the second serialization. The optimum values obtained from the second serialization are not significantly different from those obtained from the first set of optimum values, therefore, a third serialization procedure is not necessary.

Figures 2(a) to 2(d) show the effects when the top cell bandgap is allowed to vary in the range 1.88 eV to 1.98 eV, while all other parameters are held constant as given in figure 1. Maximum efficiency is 27.6% which occurs at 1.94 eV in figure 1(a). This is considerably lower than the 31.5% value obtained in the more favorable cascade cell using AlGaAs-GaInAs where the optimum top cell bandgap is 1.62 eV.

A figure-of-merit which is useful in describing cascade cell operation is the excess current of the top cell defined by

$$\Delta J_{exT} = J_{mp} - J_{mpT} \tag{1}$$

and for the bottom cell by

$$\Delta J_{exB} = J_{mp} - J_{mpB} \quad , \tag{2}$$

where J_{mp}, J_{mpT}, J_{mpB} represent the current densities at the maximum power point of the cascade V-I curve, and of the independently operated V-I curves of top and bottom cells, respectively. The excess current parameters, exhibited in figure 2(b), are a measure of the power which is not delivered to the cascade cell terminals and which, as a result, is dissipated internally. In our studies, the values of ΔJ_{exT} and ΔJ_{exB} are typically less than 0.1 mAcm^{-2} for an optimized design.

Reduction of the excess current of the top and bottom cells results in increasing the current, J_{mp}, at the maximum power point on the cascade cell V-I curve. This is shown in figure 2(c) where J_{mp} increases for increasing E_{GT} values above 1.88 eV, attains a pronounced maximum at 1.94 eV, and is reduced for bandgap values above 1.94 eV. Thus, it is seen that the maximum value, 15.8 mAcm^{-2}, occurs at the same E_{GT} value as for maximum efficiency.

In figure 2(d) is shown the power utilization factor P_u vs E_{GT}, which is defined by the relationship

$$P_u = \frac{P_{mpc}}{P_{mpT} + P_{mpB}} , \qquad (3)$$

where P_{mpc}, P_{mpT}, and P_{mpB} are the power at the maximum power point of the cascade, top, and bottom cell V-I curves, respectively. The ratio in equation (3) is typically less than 0.98, and contains only losses due to current mismatch, and tunnel junction joule power loss. It is independent of optical, recombination, and dark current loss contributions. P_u also increases to a sharp peak at 1.94 eV and falls off quite rapidly on either side of its maximum.

Region 3 donor concentration is the second parameter selected in the sequence of parameter optimization in the determination of an optimized design. The range chosen for the concentration is 5 x 10^{16}cm^{-3} to 8 x 10^{18}cm^{-3}, all other parameters held constant using the values given in figure 1. Maximum efficiency is shown to occur in figure 3(a) at 8 x 10^{17}cm^{-3}. While the slope is small for concentration values less than 8 x 10^{17}cm^{-3}, it is strongly negative for higher values. Figure 3(b) describes the monotonic decrease of the hole normalized collection efficiency which results because of the monotonic decrease of the hole diffusion length with increasing concentration. Both parameters decrease gradually with increasing concentration up to 3 x 10^{18}cm^{-3} and for higher values they decrease sharply. Thus, the rapid decrease in conversion efficiency above 3 x 10^{18}cm^{-3} has its source in the rapid decrease in the hole diffusion length. This occurs because the model contains the effects of the rapid decrease in hole lifetime and mobility in Region 3 in the concentration range above 3 x 10^{18}cm^{-3}.

The hole dark current coefficient is also strongly influenced by the donor concentration as shown in figure 3(c). The hole dark current coefficient decreases inversely with donor concentration whereas the electron dark current coefficient is constant. The decrease is rapid up to 3 x 10^{18}cm^{-3}, becoming less rapid for higher concentration values. The latter results because of an opposing trend in which the rapid decrease in hole diffusion length tends to increase the hole contribution to dark current. Consequently the total dark current coefficient, the sum of the hole and electron components, decreases rapidly up to a concentration of 8 x 10^{17}cm^{-3} where the electron and hole contributions approach equality and then levels off as the invariant electron component comes to dominate the sum. This saturation effect is reflected in the behavior of the voltage at the maximum power point which is also shown. Thus it is seen that the balancing of the dark current coefficient components determines the optimum value of donor concentration. If the rapid decrease in collection efficiency

had occurred at a concentration lower than $8 \times 10^{18} cm^{-3}$ then the situation would have been reversed. The breakpoint in collection efficiency slope rather than the breakpoint in dark current coefficient slope would have determined the optimum value of donor concentration.

Maximum power available from the top cell, P_{mpT}, to the cascade unit, shown in figure 3(d), increases gradually up to $8 \times 10^{17} cm^{-3}$ and then shows a rapid decrease for higher concentrations, which is attributed to the behavior of the hole collection efficiency in this range. Also shown, the power utilization ratio is constant up to $2 \times 10^{18} cm^{-3}$ and then decreases for higher concentration values. This decrease arises because the decrease in hole collection efficiency produces an increasing current mismatch between top and bottom cells.

In determining the optimum thickness of Regions 2 and 3 a two-step procedure is employed. The first step is to obtain the optimum value of the ratio $(X_2-X_1)/(X_3-X_1)_{opt}$, denoted p-ratio, and the second to obtain the optimum value of the ratio $(X_3-X_1)/X_3-X_1)_{opt}$, where $(X_3-X_1)_{opt}$ is the optimum value of the sum of the p- and n- region thicknesses. Subsequently, it is shown that the value of $(X_3-X_1)_{opt} = 1.46$ μm.

Maximum efficiency is 27.6% in figure 4(a), occurring at the value 0.3 for the p-ratio. It is seen not to exhibit a strong dependency on the p-ratio in the range 0.2 to 0.7. The maximum normalized electron collection efficiency is 0.81 and also occurs at 0.3, whereas for holes it ranges from 0.88 to 0.99. The most striking feature of figure 4(b) is that the electron collection efficiency in the top cell is significantly lower than it is for holes over the range of p-ratios studied. This is a direct result of surface recombination loss in the window layer, for which the surface recombination velocity (SRV) is $10^6 cm\, sec^{-1}$. It will be shown that the electron collection efficiency increases significantly when SRV = 0. Moreover, the electron diffusion length in the window layer is 0.6 μm and in consideration of the window layer thickness being 0.1 μm, bulk recombination is negligible. Thus, we conclude that for SRV = $10^6 cm\, sec^{-1}$ the surface recombination loss may be the major loss factor in the cascade cells studied.

It is instructive to compare the normalized collection efficiencies of this study with that reported for the AlGaAs-GaInAs [ref. 4]. In the latter, the collection efficiency exceeds 0.91 over the p-ratio range 0.1 to 0.9. The bandgap at the window surface is 1.80 eV which is a direct transition alloy and where the electron mobility is high. In figure 1 the window surface bandgap is 2.09 eV, which is an indirect transition alloy for which the mobility is significantly lower than it is for 1.80 eV in the model used in these studies. In both studies the window layer thickness is the same and the difference in photon absorption cannot completely explain the lower electron collection efficiency in Figures 4(b) and 5(b). Therefore, we conclude that the lower mobility in the AlGaAs-GaAs cascade cell window layer is partially responsible for the low electron collection efficiency and lower conversion efficiency.

Figure 4(c) shows the dependency of the electron and hole dark current co-efficients on the p-ratio. The energy barriers located at X_1 and X_3 serve to form a "Potential Well" solar cell of the top cell [ref. 1-5]. Electrons are confined in Region 2 and holes in Region 3, producing electron and hole accumulation in their respective regions. This results in a further shift in the quasi-Fermi levels in each region in a direction which reduces dark current. Electron contribution to dark current increases as the p-region widens as shown in figure 4(c). Similarly, the hole contribution to dark current increases as the n-region widens (i.e., p-ratio decreases). The cascade photovoltage is a maximum in the p-ratio range 0.3 to 0.6, decreasing sharply outside this range.

Maximum power of the top junction, P_{mpT}, available to the cascade cell is 22.75 mW/cm^2, occurring at 0.4 as shown in figure 4(d). P_{mpT} follows the general behavior of the normalized electron collection efficiency. The electron collection efficiency is the stronger influence on P_{mpT} than the hole efficiency because a substantially higher photoexcited carrier concentration is produced on the p-side of the top junction than on the n-side.

The power utilization ratio is constant at 0.98 up to the p-ratio equal to 0.5 as is shown in figure 4(d). Decreasing at a slow rate for p-ratios greater than 0.5, it does not exhibit a strong function of this ratio. This results because the p-ratio, when normalized to the optimum value of X_3-X_1, cannot greatly affect the current mismatch between top and bottom cells.

Imposed on the curves calculated in figure 5 is the optimum p-ratio equal to 0.3, where the ratio $(X_3-X_1)/1.46$ is allowed to vary from 0.5 to 2.0. Maximum conversion efficiency is 27.6% in figure 5(a) and it occurs at 1.0 for the ratio. Therefore, the optimum thickness of the p-region is 0.44 μm while it is 1.02 μm for the n-region, where the sum is 1.46 μm. Ratios less than 1.0 show the conversion efficiency curve to have a large positive slope, resulting from decreases in the incomplete absorption loss in the top cell with increasing total thickness. The slope is more gradual and negative for ratios greater than 1.0, which is a result of less effective carrier confinement as Regions 2 and 3 widen with increasing $(X_3-X_1)/1.46$. This gives increased dark current and greater minority carrier recombination in the top cell.

The normalized collection efficiencies for electrons and holes are presented in figure 5(b). While the electron collection efficiency is relatively constant, the hole collection efficiency is decreasing sharply at a relatively constant rate over the ratio range 0.5 to 2.0. The behavior is obtained because of the relative values of the electron and hole diffusion lengths and the corresponding optimum p- and n-region thicknesses. The electron diffusion length is 1.5 times longer than the hole diffusion length, but at the same time the optimum p-region is less one-third the sum of the p- and n-region thicknesses. Thus, with increasing values of $(X_3-X_1)/1.46$, the ratio $(X_2-X_1)/L_n$ is less than unity, while the ratio $(X_3-X_2)/L_p$ exceeds unity in the range 1.5 to 2.0.

Excess current for top and bottom cells are shown in figure 5(c), where the affects of incomplete absorption loss decreases and recombination increases in the top cell with increasing values of $(X_3-X_1)/1.46$. In the range $(X_3-X_1)/1.46 < 1$ incomplete absorption loss is greater than the recombination loss, but in the range $(X_3-X_1)/1.46 > 1$ the opposite is true. Incomplete absorption serves to significantly increase ΔJ_{exB}, while producing only small changes in ΔJ_{exT}. Similarly, recombination loss produces a change in ΔJ_{exT}, while ΔJ_{exB} is nearly constant, in the range $(X_3-X_1)/1.46 > 1$.

For reasons similar to those discussed above, in figure 5(d) the maximum power of the top cell, P_{mpT}, and the power utilization ratio increase significantly with decreasing incomplete absorption loss, but they are nearly constant in the range where recombination loss dominates. Maximum power of the bottom cell, P_{mpB}, decreases with increasing $(X_3-X_1)/1.46$, because photon absorption in the top cell increases which results in a smaller photon flux available to the bottom cell. An asymptotic value is achieved when the top cell absorbs all of the photons with energy equal to or greater than 1.94 eV.

Figure 6 shows some of the effects produced by changes in the donor impurity concentration of Region 7 in the range $1 \times 10^{16} cm^{-3}$ to $3.2 \times 10^{18} cm^{-3}$. They correspond to the set of curves in figure 3, which show the effect on the top cell parameters arising from changes in the donor concentration in Region 3. There are striking similarities between the two sets of curves. The optimum donor concentration is $7 \times 10^{17} cm^{-3}$ for which the efficiency is 27.6% as shown in figure 6(a). The slope of the efficiency curve is not as steep for higher concentration values as is shown in figure 3(a). This results because the bottom cell makes a smaller contribution to the total cascade efficiency than does the top cell. Therefore, any change arising from the bottom cell affects the efficiency less than corresponding changes in the top cell. The top cell contributes 60% and the bottom cell 40% of the cascade cell efficiency.

The normalized collection efficiency and lifetime of holes in the bottom cell, shown in figure 6 (b), exhibit a behavior corresponding to those in figure 3(b) and produce similar results in the maximum power of the bottom cell as was produced in the top cell. Moreover, the power utilization ratio, maximum power point voltage of the bottom cell V-I curve, and the dark current components shown in figures 6(c) and 6(d) all exhibit a similar relationship as those shown in figure 3(c) and 3(d), respectively.

Corresponding ratios are defined for the bottom cell in the determination of optimum layer thicknesses as were used in the top cell optimization. The bottom cell p-ratio is defined by $(X_6-X_5)/3.25$ and the total thickness ratio is $(X_7-X_5)/3.25$, where it is shown subsequently that the optimum total thickness of the bottom cell is 3.25 μm.

Figures 7 and 8 exhibit the computer modeling results related to the bottom cell, and correspond to figures 4 and 5, respectively, of the top cell. While there are similarities between the corresponding curves in the figures, the

differences are more significant in comprehending the device physics of cascade cells.

Figure 7(a) shows maximum conversion efficiency to occur at a p-ratio of 0.4, whereas it occurs at 0.3 for the top cell. Comparing the curves in figures 7(b) and 4(b) shows that the bottom cell normalized electron collection efficiency appears to show greater sensitivity to the p-ratio of the bottom cell than the corresponding curves of the top cell. This is attributed to the absence of a loss in the bottom cell corresponding to the surface recombination loss, higher recombination loss in the bottom cell, and a less effective "Potential Well" in Region 7. These factors also give rise to the electron normalized collection efficiency being higher than for holes in the bottom cell which is exhibited in figure 7(b), whereas the opposite is true for the top cell as is evident in figure 4(b).

The curves in figures 7(c) and 4(c) behave similarly with the exception that the electron and hole dark current scale of the bottom cell is eight decades higher. This is due to the higher dark current in the bottom cell produced by its smaller bandgap value. The power utilization ratio and the respective maximum power in figures 7(d) and 4(d) also show similar behavior.

Conversion efficiency is relatively constant over the range 0.6 to 1.7 of the normalized total thickness as shown in figure 8(a), because the electron and hole normalized collection efficiencies, presented in figure 8(b), are not strong functions of the total thickness ratio in this range. In contrast, the top cell hole collection efficiency, figure 4(b), shows a strong dependency on the top cell total thickness ratio. This also results in a smaller change in ΔJ_{exT} and ΔJ_{exB} in figure 8(c) compared to the curves in figure 4(c). Similarly, the changes occurring in P_u and P_{mpB} in figure 8(d) are somewhat smaller than they are in figure 4(d). The value of P_{mpT} is constant because changes in the bottom cell cannot affect the top cell V-I curve.

Surface Recombination Loss

Studying the device performance characteristics presented in the above discussion, it is concluded that surface recombination in the window layer produces the biggest loss in the cascade cell model used above. Electron collection efficiency of the top cell, given in Figures 4(b) and 5(b), is significantly lower than either the hole collection efficiency of the top cell or the electron collection efficiency of the bottom cell. Although the hole collection efficiency of the bottom cell is less than 0.8, it makes a smaller contribution to the overall efficiency than do the photoelectrons generated in the top cell.

To illustrate the significance of the surface recombination loss, figure 9 shows the conversion efficiency vs the top cell bandgap, with surface recombination velocity a parameter. Each curve in figure 9 exhibits a pronounced maximum, at which the optimum bandgap value is obtained. The maximum efficiency value of each curve and its corresponding optimum bandgap increase with decreasing SRV. Decreasing SRV makes more photocurrent available to the top

145

cell and this results in an increase in $|\Delta J_{exT}|$. By increasing E_{GT}, $|\Delta J_{exT}|$ and the current mismatch between top and bottom cells are reduced which produces an increase in efficiency.

The structure used is that of the optimized design, including the window layer. While the serial optimization procedure was not used to obtain the results given in figure 9, at each of the maximum efficiency points the excess current and current mismatch between cells are characteristic of an optimized design.

Figure 9 shows that the efficiency may exceed 29% for SRV values less than 10^5cm sec^{-1}. The rate of decrease of efficiency in the SRV range 0 to 10^5cm sec^{-1} is considerably less than the rate above 10^5cm sec^{-1}. These results suggest that there may be merit in considering a substitute of the AlGaAs window used in our model.

Alternative structures are deserving of consideration to affect a reduction of the surface recombination loss. An obvious structure is to replace the window layer with a wide bandgap transparent layer which results in an interfacial recombination velocity less than 10^5cm sec.

The desirable window material characteristics are for lattice matching to p-AlGaAs, the direct and indirect bandgap energies are to be sufficiently high so that the photon absorption in the window layer is small compared to the absorption in the top cell, and for the interfacial recombination velocity to be less than 10^5cm sec^{-1}. In figure 1 this requires a material for which its bandgap energy exceeds 2.3 eV which cannot be achieved using the AlGaAs ternary. One candidate is ZnSe, which is under investigation for use in single junction n/p GaAs solar cells [ref. 14]. The lattice mismatch with GaAs is 0.3% for 2.6 eV bandgap ZnSe. In this work, it is reported that electron-hole recombination is reduced near the interface using an n-ZnSe window [ref. 14]. It is not clear from this work that interfacial recombination is also reduced using a p-ZnSe window on p-AlGaAs.

SUMMARY AND CONCLUSIONS

Computer modeling studies of the AlGaAs-GaAs, two-junction, cascade solar cell are reported suggesting that the upper limit on conversion efficiency is approximately 27%. A study of the device performance characteristics obtained shows that the surface recombination is responsible for the major loss in the theoretical device design which evolves. This results because the bandgap energy of the AlGaAs window layer is too small to serve as an effective window. Values of surface recombination velocity less than 10^5cm sec^{-1} result in an increase in the upper limit of efficiency to approximately 29%. For the AlGaAs-GaAs cascade cell to be an attractive alternative to other material combinations, it is recommended that effort be directed to reducing the surface recombination loss. There are a number of approaches for reducing the surface loss, however, it is not clear at this time which is the most promising or if the problem is solvable.

REFERENCES

1. Lamorte, M. F. and Abbott, D. H.: 12th IEEE Photovoltaic Specialists Conf., Baton Rouge, LA, Nov. 15-18, 1976.

2. Lamorte, M. F. and Abbott, D. H.: 13th IEEE Photovoltaic Specialists Conf., Washington, D.C., June 5-8, 1978.

3. Lamorte, M. F. and Abbott, D. H.: Solid-State Electronics 22, 467-73, 1979.

4. Lamorte, M. F. and Abbott, D. H.: IEEE Trans. Elect. Devices ED-27, 231-49, 1980.

5. Lamorte, M. F. and Abbott, D. H.: IEEE Trans. Elect. Devices ED-27, 831-40, 1980.

6. Bedair, S. M.; Lamorte, M. F. and Hauser, J. R.: Appl. Phys. Lett. 34, 38-39, 1979.

7. Bedair, S. M.; Lamorte, M. F.; Hauser, J. R.; and Mitchell, K. W.: IEEE International Elect. Devices Mtg., Washington, D. C., Dec. 5, 1978.

8. Casey, H. C., Jr.; and Panish, M. B.: Heterostructure Lasers Part A: Fundamental Principles, Academic Press, New York, 1978.

9. Hovel, H. J.: Solar Cells; Semiconductors and Semimetals, Vol. 11; Ed. R. K. Willardson and A. C. Beer, Academic Press, New York, 1975.

10. Bedair, S. M.: J. Appl. Phys. 50, 7267-68, 1979.

11. Bedair, S. M.: J. Appl. Phys. 51, 3935-37, 1980.

12. Bedair, S. M.: private communication.

13. Sze, S. M.: Physics of Semiconductor Devices, New York, Wiley, 1969.

14. Walsh, D. and Shing, Y. H., 14th IEEE Photovoltaic Specialists Conf.,
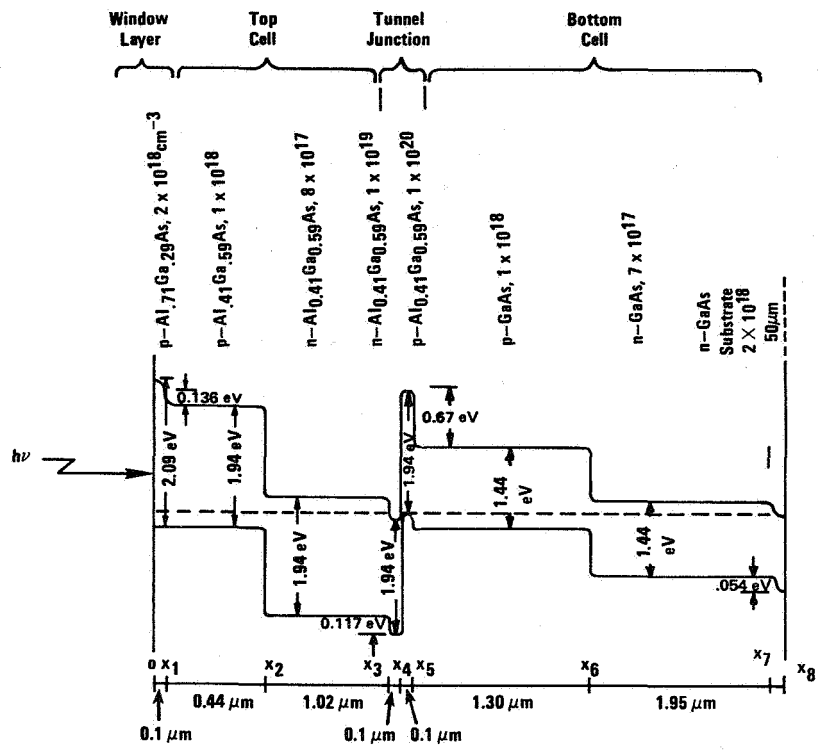
Figure 1. Bandstructure used in the study and parameters obtained for optimized design by maximizing conversion efficiency.
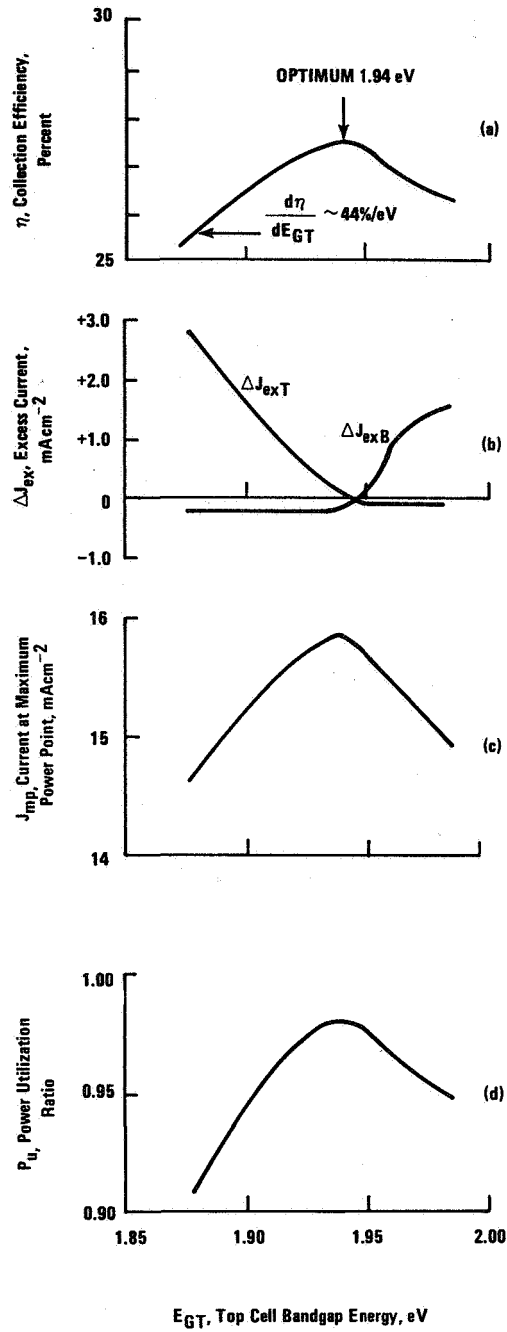
Figure 2. Determination of optimum top cell bandgap, E_{GT}: (a) conversion efficiency, (b) excess current, (c) current at maximum power point on cascade cell V-I curve, and (d) power utilization ratio; vs. E_{GT}.

Figure 3. Determination of optimum donor concentration in Region 3, N_{D3}: (a) conversion efficiency, (b) normalized collection efficiency and diffusion length of holes, (c) voltage at maximum power point of top cell V-I curve and diffusion limited dark current coefficients, and (d) power utilization ratio and the maximum power point of top cell V-I curve; vs. N_{D3}.

150

OPTIMUM 0.3

η, Conversion Efficiency, Percent

30

25

(a)

Q_{nT}°, Q_{pT}°, Normalized Collection Efficiency of Top Cell

1.00

Q_{pT}°

(b)

Q_{nT}°

0.75

V_{mpT}, Voltage of Top Cell at Maximum Power Point, Volts

1.44

V_{mpT}

(c)

10^{-27}

1.43

J_{DnoT}

J_{DpoT}

10^{-28}

1.42

10^{-29}

Diffusion Limited Dark Current Coefficient, A cm^{-2}

P_u, Power Utilization Ratio

1.00

P_u

(d)

24

0.95

P_{mpT}

22

0.90

20

0   0.5   1.0

P_{mpT}, Maximum Power of Top Cell, mW cm^{-2}

$$\frac{x_2 - x_1}{1.46}$$, Normalized p-Region Thickness of Top Cell

Figure 4. Determination of top cell optimum p-ratio, $(x_2 - x_1)/1.46$: (a) conversion efficiency, (b) normalized collection efficiencies (c) voltage at maximum power point of top cell V-I curve and diffusion limited dark current coefficients, and (d) power utilization ratio and maximum power point of top cell V-I curve; vs. $(x_2 - x_1)/1.46$.

151

Figure 5. Determination of top cell optimum total thickness ratio, $(x_3 - x_1)/1.46$:
(a) conversion efficiency, (b) normalized collection efficiencies, (c) excess
currents of top and bottom cells, and (d) power utilization ratio and
maximum power points of the top and bottom cell V-I curves; vs.
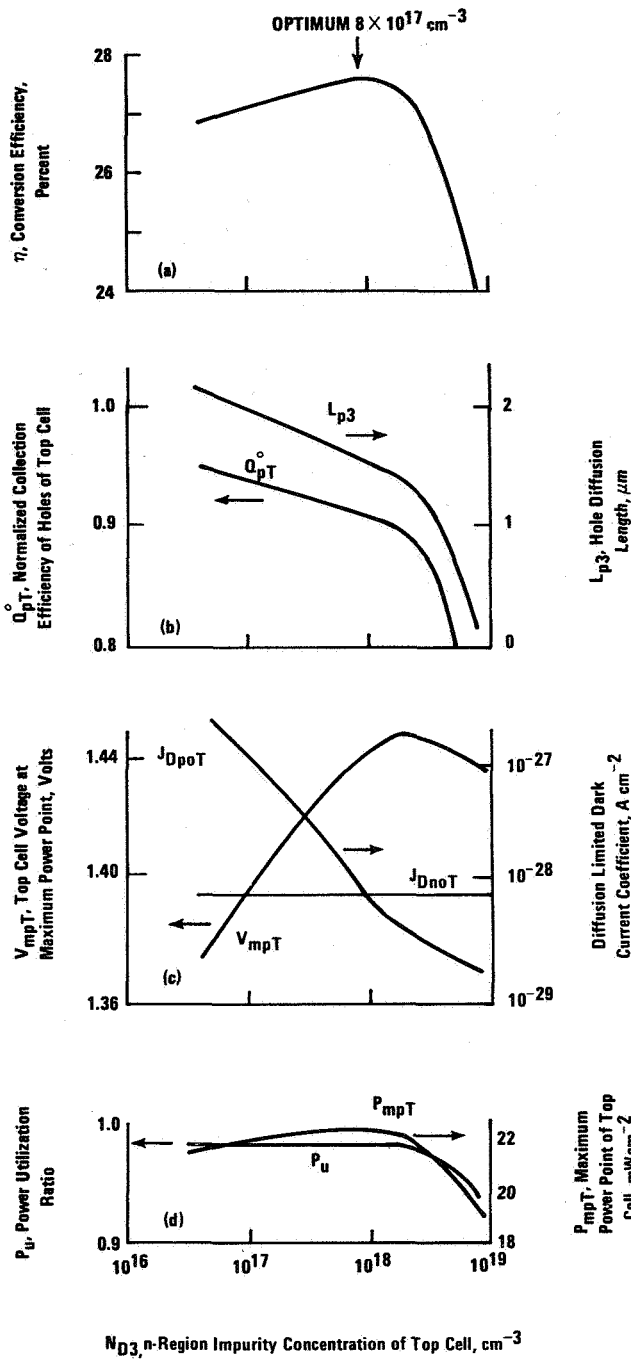$(x_3 - x_1)/1.46$.
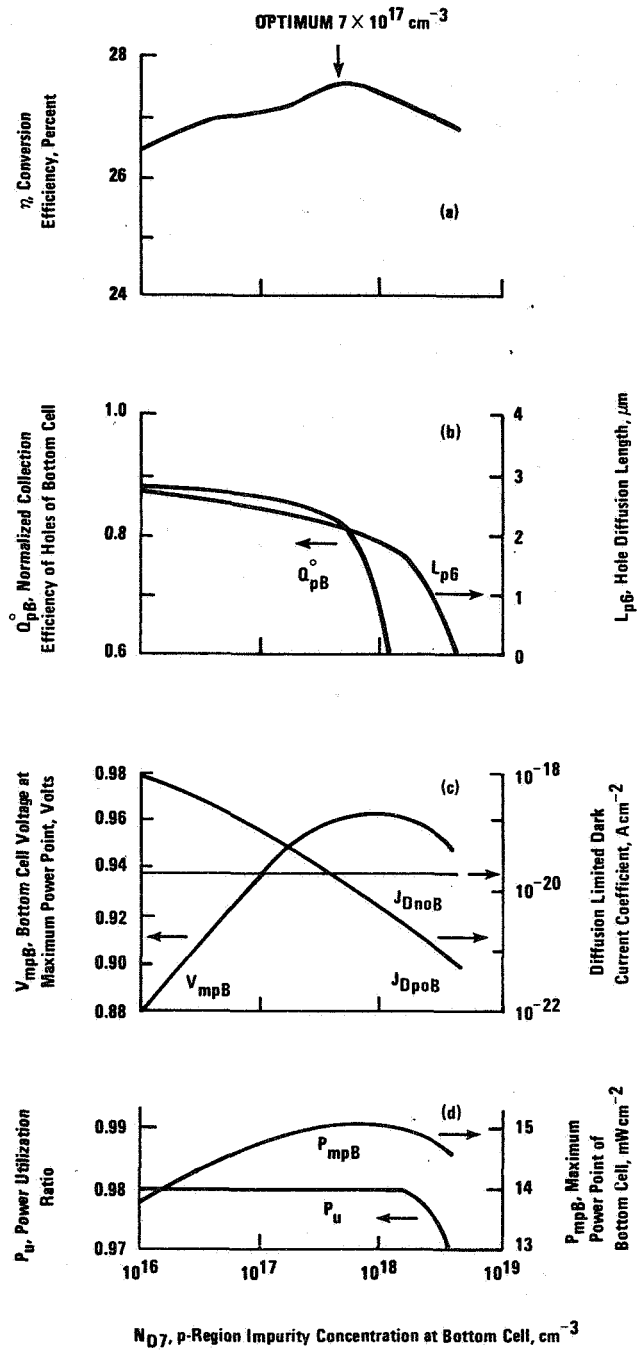
Figure 6. Determination of optimum donor concentration in Region 7, N_{D7}:
(a) conversion efficiency, (b) normalized collection efficiency and
diffusion length of holes, (c) voltage at maximum power point of
bottom cell V-I curve and diffusion limited dark current coefficients,
and (d) power utilization ratio and maximum power point of
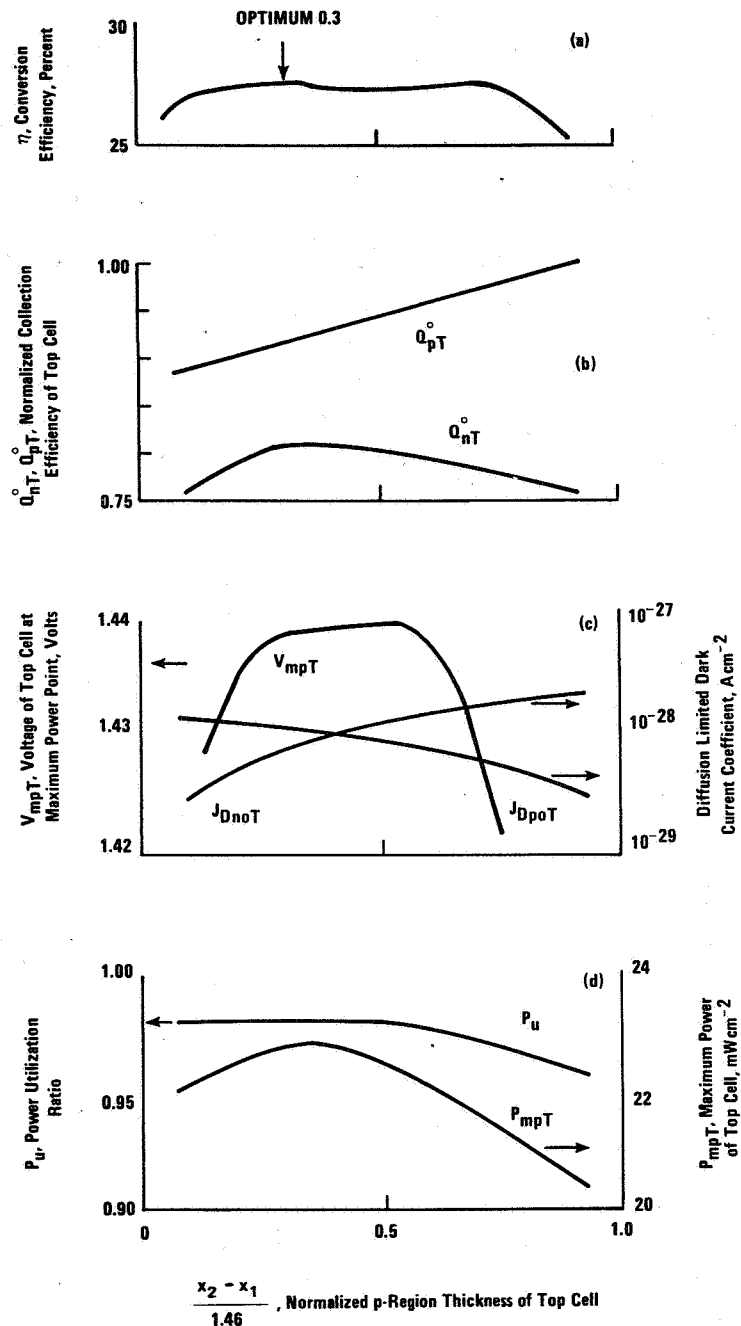bottom cell V-I curve; vs. N_{D7}.
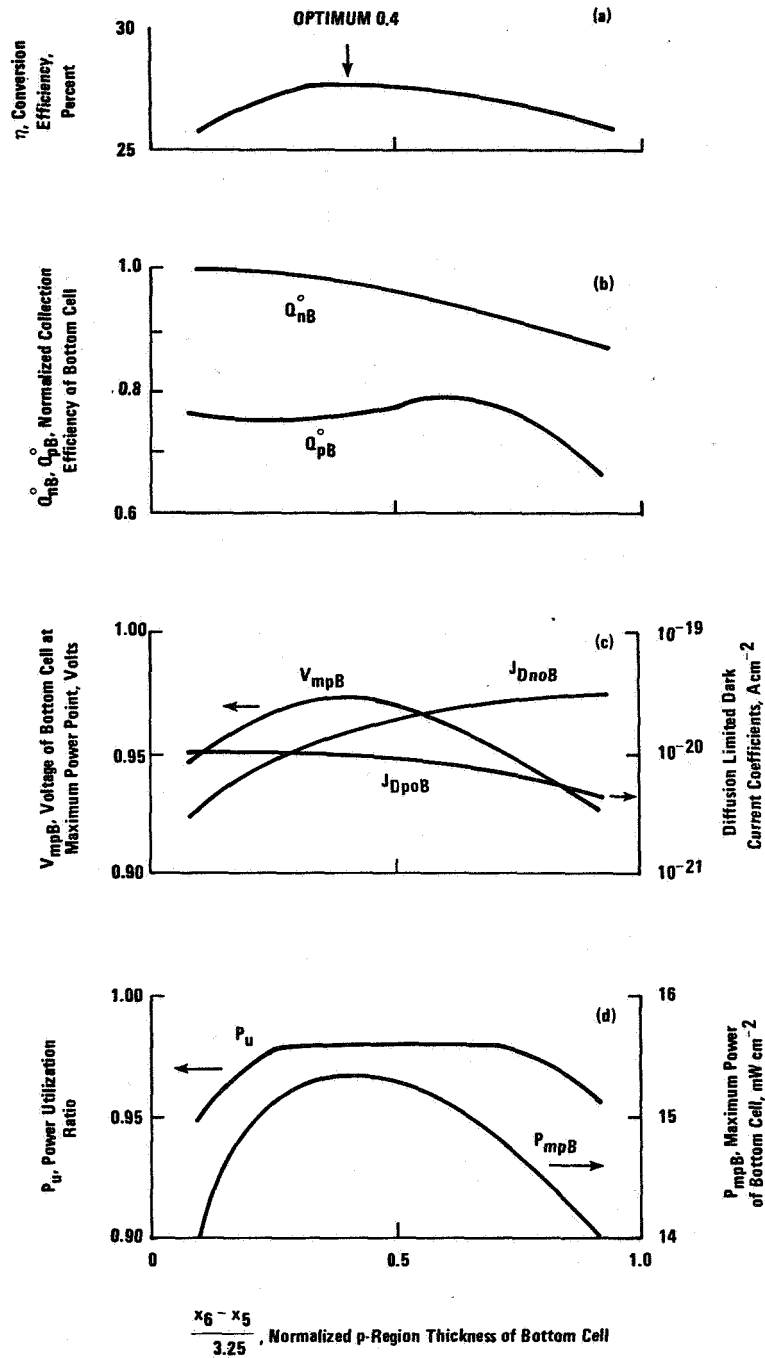
Figure 7.   Determination of optimum p-ratio, $(x_6-x_5)/3.25$: (a) conversion
efficiency, (b) normalized collection efficiencies, (c) voltage at
the maximum power point of bottom cell V-I curve and
diffusion limited dark current coefficients, and (d) power utilization
ratio and maximum power point of bottom cell V-I curve;
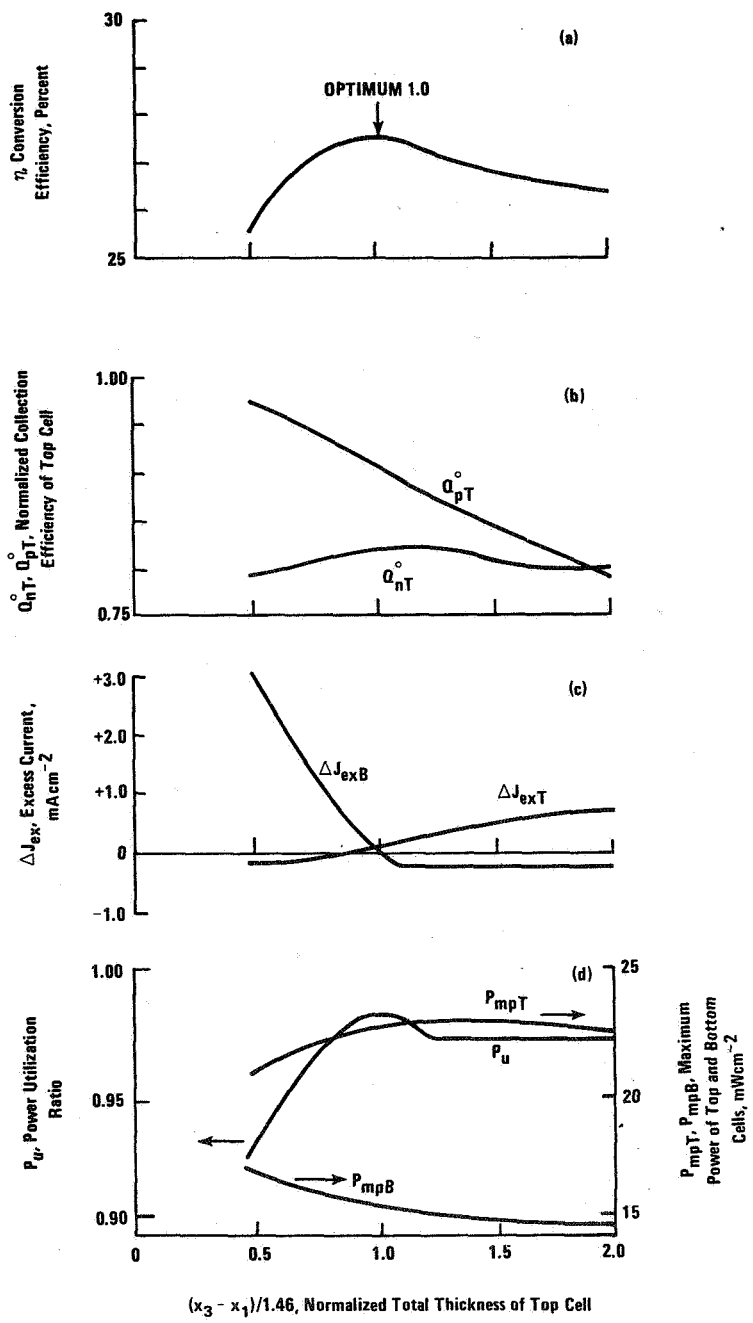$(x_6-x_5)/3.25$.

Figure 8. Determination of bottom cell optimum total thickness
ratio, $(x_7 - x_5)/3.25$: (a) conversion efficiency,
(b) normalized collection efficiencies, (c) excess currents,
and (d) power utilization ratio and maximum power
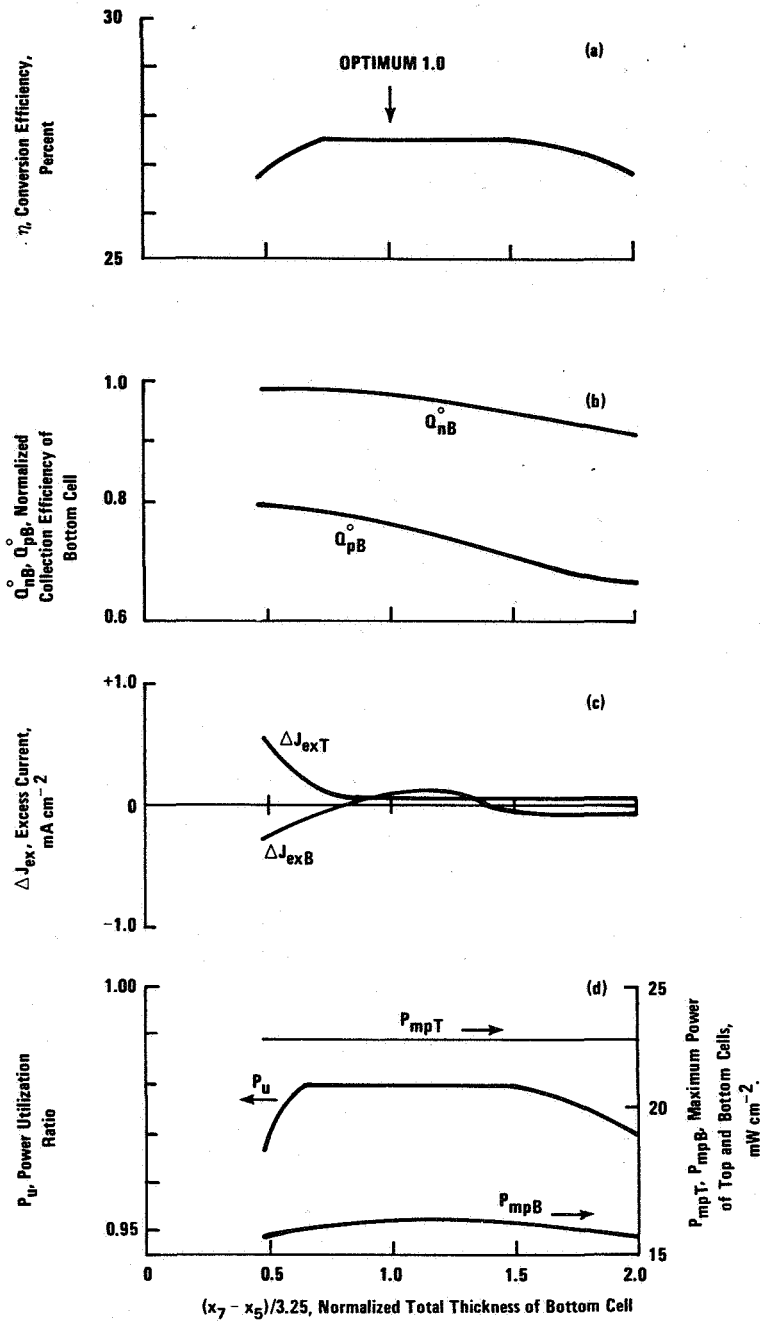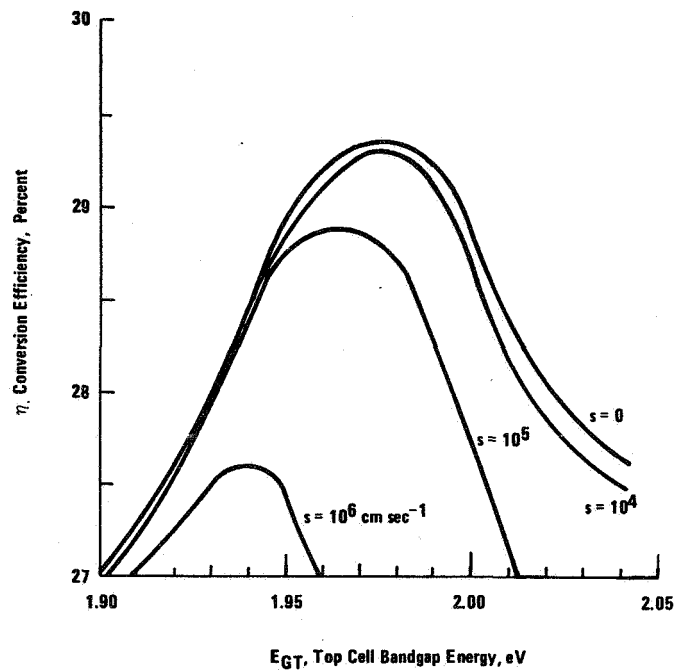points on top and bottom cell V-I curves; vs.
$(x_7 - x_5)/3.25$.

155

Figure 9. Conversion efficiency vs. top cell bandgap with surface
recombination velocity as a parameter.

FABRICATION OF AlGaAs/GaAs CASCADE SOLAR CELL BY LPE

S. M. Bedair
Research Triangle Institute
Research Triangle Park, North Carolina

SUMMARY

Multi-junction, variable bandgap cascade solar cells offer the potential of achieving significantly higher conversion efficiencies than single junction cells and are therefore attractive candidates for future terrestrial and space applications. This paper reports on the successful fabrication of high efficiency cascade solar cells in the Al-Ga-As system.

INTRODUCTION

Stacking two or more photovoltaic junctions in electrical and optical series results in higher conversion efficiency since each junction can be tailored to respond more efficiently to a smaller range of photon energies. An efficiency of about 30% has been predicted for a two junction cascade cell having the optimum bandgap values (1,2).

A number of III-V materials systems are currently being considered for use in fabricating cascade solar cells (3). The Al-Ga-As system (4) is attractive from a developmental standpoint since it employs a proven materials system that is closely lattice matched throughout its compositional range. This system (figure 1) employs a GaAs low bandgap cell and 1.9 eV AlGaAs high bandgap cell connected by an AlGaAs tunnel junction. Although this cell does not posses the optimum bandgap values, an efficiency of 25% is predicted at 300°K under AMO, 1 sun illumination.

Experimental and Results

The cascade cell shown in figure 1 is a seven-layer structure epitaxially grown on a GaAs substrate ($n \approx 10^{18} cm^{-3}$). It consists of two diffused GaAs and $Al_{0.35}Ga_{0.65}As$ junctions which are electrically connected by an $Al_{0.35}Ga_{0.65}As$ tunnel junction. Junction depths are in the 0.5 to 1 μm range as determined by SEM measurements. Table 1 shows the composition, doping concentration and thickness of each layer. Beryllium was chosen as the p^+-dopant for the window layers of both junctions because of its low vapor pressure, necessary for the multiwell LPE growth technique. Also higher doping concentrations can be more easily achieved in high bandgap AlGaAs with Be. Doping characteristics and electrical properties of Be-doped AlGaAs have been reported elsewhere (5).

Several problems are associated with using Be as an impurity. First, it is a toxic material and several precautions have to be considered in its handling. Second, because it is very reactive successful use of Be is limited to LPE systems that are completely oxygen free. The third problem is its very high distribution coefficient; thus very small amounts on the order of micrograms are used in the LPE melts.

For $Al_xGa_{1-x}As$ in the direct bandgap region ($0 < x < 0.37$) it is very hard to achieve doping concentrations lower than the mid 10^{18} range when using Be. However, for $x > 0.5$ doping concentrations in the high $10^{17}cm^{-3}$ and low $10^{18}cm^{-3}$ regions can be routinely achieved (5). Thus, as shown in Table I, the $Al_xGa_{1-x}As$ window layer, which is used as a source for Be diffusion into the GaAs junction, was chosen such that $x = 0.7$. This then allowed the carrier concentration in the p-side of the GaAs junction to be limited to the high $10^{17}cm^{-3}$ range, thereby maintaining a good electron diffusion length.

Junctions formed by Be diffusion in $Al_xGa_{1-x}As$ ($0 < x < 0.37$) grown on GaAs substrates have been characterized by excellent electrical properties as shown in figure 2 for $Al_{0.35}Ga_{0.65}As$. Open circuit voltages in the 1 to 1.3 V range have been obtained both at AM0 and AM2 at 1 sun. The best fill factors have varied from 0.8 to 0.84. Short circuit current densities at AM0 have varied from 8 to 13 mA/cm^2 (based on active device area) without an antireflection coating. This cell had an AM0, 1 sun efficiency of $\simeq 10\%$ without an antireflection coating. Figure 3 shows the quantum efficiency of an $Al_{0.3}Ga_{0.7}As$ cell without an antireflection coating. A quantum efficiency up to about 0.7 indicates excellent current collection for this high bandgap cell. These results have been obtained by minimizing the window layer thickness and optimizing the junction depth.

The AlGaAs tunnel junctions have been fabricated using Ge and Te as the p^+ and n^+ dopants, respectively (6). Both impurities have the low diffusion coefficients in GaAs and AlGaAs as required for abrupt tunnel junction formation. Several difficulties have resulted from the use of Te in the tunnel junction. Tellurium tends to form compounds (7) both with Ga and Al such as Al_2Te_3, GaTe, etc. These compounds form precipitates that create and propagate lattice defects in the top AlGaAs cell. Although the phase diagram of the Al–Ga–As–Te quaternary alloy has not been studied, growth at temperatures above 900°C has been found to eliminate the formation of these unwanted compounds. However, this temperature is too high to obtain the necessary abrupt doping profile for the tunnel junction. This difficulty was significantly reduced in the present study by performing the growths at 800°C according to the following procedure (8). Gallium and GaAs were first baked together at 900°C two hours and then cooled to room temperature before the addition of Te and Al to the melt. Upon reheating to the deposition temperature of 800°C and performing the growth, a smooth, specular AlGaAs epitaxial layer was obtained. A possible explanation is that when the prebaked (saturated) GaAs melt is quenched to room temperature, GaAs crystallites are formed. These solid crystallites in the melt may act as nucleation sites for the Te compounds during the process of melt saturation at 800°C. It appears that the GaAs crystallites are of sufficient concentration to trap most of the Te compound that will otherwise disturb the epitaxial layer. Defects propagated into the top AlGaAs junction from the tunnel junction have

158

been further reduced through the use of a rather thick n-AlGaAs layer separating the two structures.

The terminal I-V characteristic of a complete cascade cell consisting of an AlGaAs top cell and connecting junction and a GaAs bottom cell is shown in figure 4. Open circuit voltages in the range of 1.9 to 2.15 V have been obtained under 1 sun, AM0 illumination. Short circuit current densities up to 12 and 13 mA/cm^2 (based on active device area) have been obtained at AM1 and AM0, respectively, without antireflection coatings. This has been achieved by close matching of the currents generated by each cell (each cell absorbs one half of the solar spectrum). These current densities are equal to one half of the J_{sc} reported for the best GaAs single-junction solar cell. The best cascade cell fabricated to date had efficiency values of 15.2% at AM0 and 16.4% at AM1 without AR coating and 19.5% at AM0 and 21% when corrected for losses due to surface reflectance. The spectral response of the total cascade structure is shown in figure 5. The dip between 0.65 and 0.7 μm occurs at the wavelength where the GaAs junction starts to cut off due to photon absorption by the tunnel junction and the AlGaAs junction. A flat response is desired for maximum quantum and power conversion efficiencies.

At high concentrations (≃30 suns) the tunnel junction starts to show some undesirable effects depending on its abruptness and bandgap. High series resistance and in some cases non-ohmic behavior have been observed. This has resulted in a poor fill factor and a drop in efficiency of the total structure. In cases when a high-quality tunnel junction is present between the two cells, a negative resistance region is observed in the I-V characteristics shown in figure 6. Here the short-circuit current density resulting from high solar concentration has exceeded the peak current value (I_p) of the AlGaAs tunnel junction (8).

CONCLUSION

High efficiency AlGaAs/GaAs cascade solar cells have been fabricated. The conditions for current matching between the junctions have been met by optimizing the cell parameters in this structure. Efficiencies of 15.2% at AM0 and 16.4% at AM1 have been achieved without AR coating which corresponds to 19.5% at AM0 and 21% at AM1 when corrections for reflectance losses are included.

REFERENCES

1. Lamorte, M. F.; and Abbott, D. H.: Proc. 13th Photovoltaic Specialists Conference, 874 (1978).

2. Moon, R. L.; James, L. W.; Vander Plas, T. O.; Antypas, G. A.; and Chai, Y.: Proc. 13th Photovoltaic Specialists Conference, 859 (1978).

3. Bedair, S. M.; Phatak, S. B.; and Hauser, J. R.: IEEE Elect. Devices, ED-27, 822 (1980).

4. Bedair, S. M.; Lamorte, M. F.; and Hauser, J. R.: Appl. Phys. Lett. 34, 38 (1979).

5. Fujita, S.; Bedair, S. M.; Littlejohn, M. A.; and Hauser, J. R.: accepted for publication, J. Appl. Phys.

6. Bedair, S. M.: J. Appl. Phys. 50, 7267 (1979).

7. Wagner, W. R.: J. Appl. Phys. 49, 173 (1978).

8. Bedair, S. M.: J. Appl. Phys. 51, 3937 (1980).

Table I. Composition, Doping Level and Thickness of Each Layer

Layer	n	p	Thickness (μm)	AlAs%
n-GaAs	10^{17}		4	
p^+-AlGaAs (window)		1×10^{18} (Be)	0.5	70
p^+-AlGaAs		$\simeq 5 \times 10^{18}$ (Ge)	0.4	35
n^+-AlGaAs	$\simeq 5 \times 10^{18}$ (Te)		0.4	35
n-AlGaAs	10^{17}		5	35
p^+-AlGaAs (window)		2×10^{18} (Be)	0.2	90
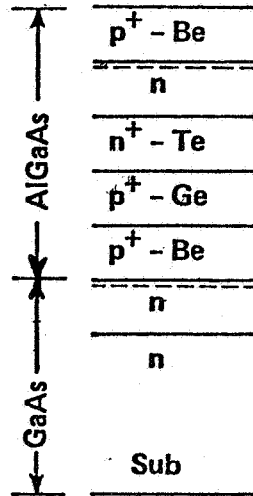
Figure 1.   Structure of AlGaAs/GaAs Cascade Solar Cell
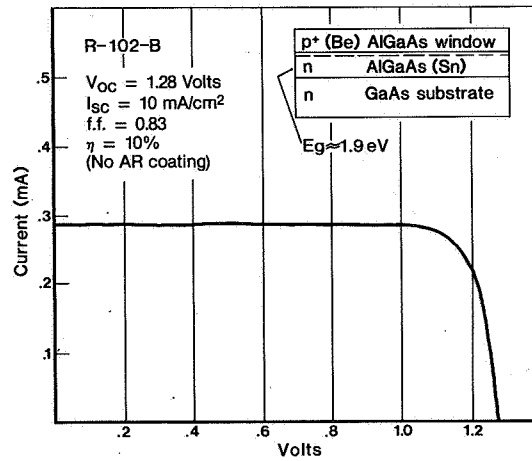
Figure 2.   V-I Characteristics for
AlGaAs Top Cell at AMO, 1 sun

162
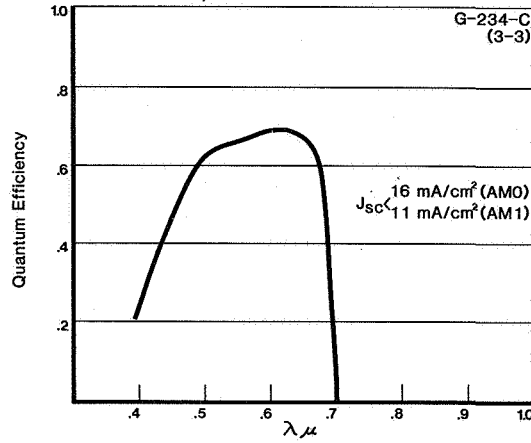
Figure 3. Quantum Efficiency of $Al_{0.3}Ga_{0.7}As$
p-n Junction Without AR Coating
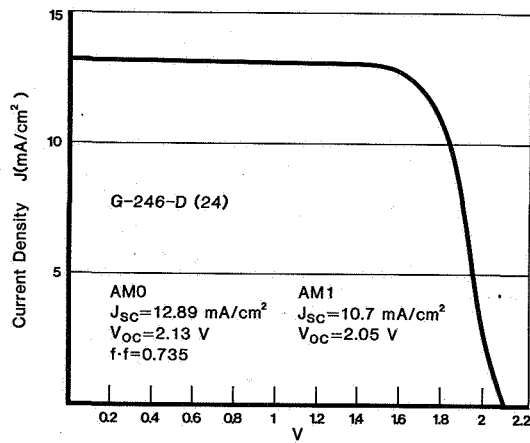
Figure 4. V-I Characteristics for AlGaAs/GaAs.
Cascade Cell Without AR Coating

163
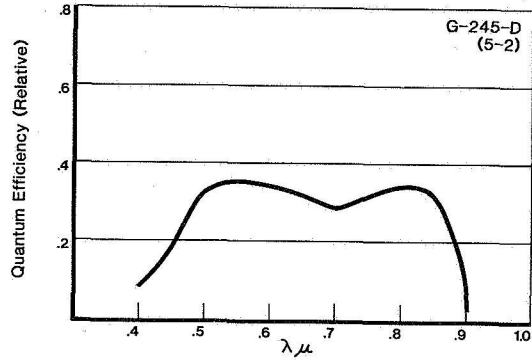
Figure 5.   Spectral Response of AlGaAs/GaAs
             Cascade Solar Cell
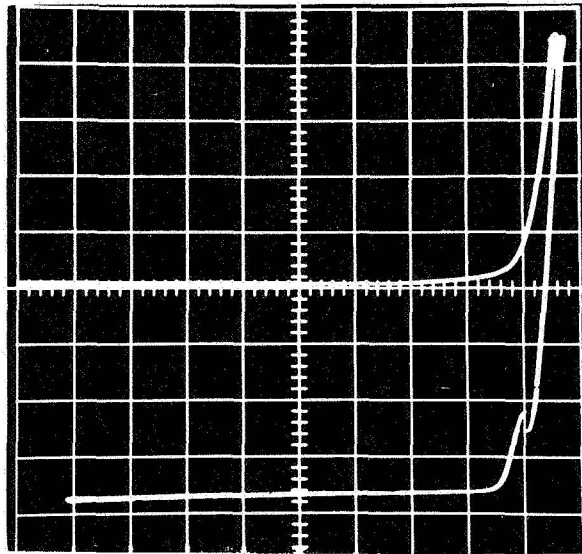
Figure 6.   Effect of AlGaAs Tunnel Junction on the Characteristics of
            AlGaAs/GaAs Cascade Solar Cell at 30 suns AMO
                   Scale: 0.5 V/div   Horizontal
                            0.1 mA/div   Vertical

OM-VPE GROWN MATERIALS FOR HIGH EFFICIENCY SOLAR CELLS

R. Saxena, B. Cooper, III, M. Ludowise, P. Borden, and P. Gregory
Varian Associates, Inc.
Palo Alto, California

SUMMARY

The versatility of organometallic vapor phase epitaxy (OM-VPE) for the production of photovoltaic materials is reviewed. Organometallic sources are available for all the III-V elements and a variety of dopants; thus it is possible to use the technique to grow a wide variety of semiconductor compounds, e.g., AlGaAsSb and AlGaInAs alloys for multijunction monolithic solar cells have been grown by OM-VPE. While the effort at Varian has concentrated on terrestrial applications, the success of OM-VPE grown GaAs/AlGaAs concentrator solar cells (23% at 400 suns) demonstrates that OM-VPE is suitable for growing high efficiency solar cells in large quantities for space applications. In addition, OM-VPE offers the potential for substantial cost reduction of photovoltaic devices with scale-up and automation and due to high process yield from reproducible, uniform epitaxial growths with excellent surface morphology.

INTRODUCTION

GaAs solar cells for space applications are attractive for a number of reasons. These include high conversion efficiencies as compared to Si solar cells, capability of high temperature operation without significant loss in efficiency, and less radiation damage in space compared to Si cells owing to a much shorter absorption length for sunlight with a direct bandgap material, which with smaller diffusion lengths can withstand greater radiation flux and defect densities before significant performance degradation takes place [1]. In addition, recent studies show promise of in-situ annealing of radiation damage when GaAs cells operate at temperatures circa 250°C [2]. It has been suggested that GaAs cells would find increased use in space applications if large-scale production of "space qualified" cells is demonstrated [3]. Thus the major problem area is considered to be a reliable high-throughput epitaxial growth technique.

Organometallic vapor phase epitaxy (OM-VPE) has proven to be a highly successful method of growing GaAs/AlGaAs solar cells for concentrator systems applications. Efficiencies of 23.2 ±0.2% at 400 AM2 suns have been achieved in packaged devices [4]. The pilot production facility has demonstrated yield of 65% for packaged OM-VPE-grown cells with efficiency in excess of 20%. The electrical contacts have been examined in detail and contact resistances about 1×10^{-6} ohm-cm^2 are achieved for both n- and p-type contacts. In addition, accelerated aging studies have been done and are currently in progress. The lifetime studies have shown that OM-VPE cells have superior environmental stability compared to LPE-grown solar cells [5].

This paper will discuss the advantages of the OM-VPE technique for growing high efficiency GaAs/AlGaAs solar cells. The growth of multijunction solar cells will also be discussed. Finally, the application of the technique for GaAs space solar cells will be described.

OM-VPE

Organometallic vapor phase epitaxy derives its name from the use of organometallic source compounds for the column III and V elements and the dopants for epitaxial growth of compound semiconductors. The epitaxial growth of GaAs and AlGaAs, for example, is done using trimethylgallium, trimethyl-aluminum and arsine. Arsine is used in place of the organometallic source trimethylarsenic, since it is much cheaper compared to TMAs and is available in electronic grade purity because of its long-standing usage in the semiconductor industry.

A schematic diagram of the OM-VPE reactor used for the experiments discussed here in shown in Fig. 1. An rf generator is used as the source of power to heat the graphite susceptor on which the wafers are placed. The organometallic compounds decompose at elevated temperatures and the III and V species combine for epitaxial growth. Although the use of vertical reactors has been reported, the horizontal geometry was chosen to simplify later scale up of the system and to avoid problems associated with thermal convection in a vertical cold-wall system.

OM-VPE-grown epitaxial layers have been shown to exhibit excellent thickness and doping uniformity over a large area (about 8 sq.in. in the present system). Also, abrupt GaAs/AlGaAs heterojunctions (<40 Å) have been demonstrated using Auger profiling technique [6,7]. OM-VPE has significant advantage over LPE in its capability of high throughput production and automation, superior surface morphology and control of growth rates down to 0.01 microns/min. Conventional chloride transport VPE is not suitable for growing Al-containing alloys due to thermodynamic constraints and MBE equipment is much more complex and difficult to be set up for high throughput production.

OM-VPE growths usually take place in the mass transport-limited regime so growth rates are easily controlled by changing the input fluxes. In addition, close to one to one correspondence is observed between input gas ratios and incorporation in solid for ternary and quaternary alloys [6].

GaAs/AlGaAs SOLAR CELL

OM-VPE and LPE-grown solar cell fabrication has been pursued in parallel at Varian for a number of years. Conversion efficiencies at 50°C of 23% for LPE cells [8] and 19% for early OM-VPE cells were demonstrated [9]. Both types of cells were unpackaged with 0.566 cm^2 active area. The OM-VPE solar cell was subsequently redesigned, taking full advantage of the capability of the technique and 23.2% efficiency for packaged cells with 1.25 cm^2 active area at 400 suns and 50°C has been obtained [4].

The epitaxial structure of the current design solar cell is shown in Fig. 2. The modified structure utilizes a thin (about 1500 Å) $Al_{0.9}Ga_{0.1}As$ window layer. Computer modeling calculations show that the collection efficiency increases as the window layer thickness is reduced. The results of the model are shown in Fig. 3. The short circuit current increases as the window layer thickness is reduced. Also, the junction depth is a critical parameter and a value of 0.5 micron is used in our design. The p-type doping level is increased halfway into the active layer to provide a drift field that helps in collecting the photo-generated carriers and for reduced series resistance. The cap GaAs layer is used to protect the AlGaAs window layer against oxidation in air and is etched away just prior to depositing Si_3N_4 antireflection coating. The metallization and packaging of these cells is discussed in the paper by Borden et al at this conference.

MULTIBANDGAP SOLAR CELLS

The conversion efficiency can be significantly increased over single p-n junction cells by utilizing multibandgap schemes. The feasibility of the concept was demonstrated at Varian using a spectral splitter approach [10]. A spectral splitter module of 10 Si and $Al_{0.2}Ga_{0.8}As$ cell pairs has recently been completed for Sandia, and greater than 20% system efficiency was measured [11]. The system operates at 37°C and the efficiency includes losses due to the fresnel lens, the dichroic filter, and wiring interconnects. The efficiency of the average cell pair unit is 27.5% at 840 W/m^2 insolation. With improved design for the fresnel lenses and the spectral splitting filter, higher system efficiency can be obtained, as discussed by Borden et al at this conference.

The monolithic structure calls for series-connected p-n junction solar cells grown epitaxially on a substrate. Conversion efficiency of 30% or better is expected from an optimized structure. Although many III-V material systems can be used, the work at Varian has concentrated on the AlGaInAs pseudo-quaternary system [12]. This system encompasses materials with bandgaps varying from 0.4 to 2.1 eV. The proposed structure is shown in Fig. 4.

AlGaInAs

Extensive experimentation has been done to develop techniques for growing alloys in AlGaInAs material systems. It was discovered early in the work that In organometallic compounds react with arsine at room temperature and the In incorporation in the epitaxial layer is not obtained. This problem can be bypassed by employing a concentric tube input design so that the gases do not mix until just before deposition. This scheme is not suitable for reproducible growths, particularly in a scaled-up version of the reactor. It has been reported that growths at low pressures avoid this problem by pyrolyzing PH_3 before it enters the reactor [13]. The solution at Varian has been chemical in nature. It has been demonstrated that trimethylarsenic (TMAs) and In organometallic compounds do not react with each other, and InGaAs layers can be grown on GaAs substrates [14]. This solution makes it possible to retain the advantages of a one atmosphere reactor system.

The first set of experiments for grading InGaAs layers on GaAs were done using TMAs, TMGa, and TEIn. The growths were found to be nonuniform in In content and growth rates across the wafer. This problem was solved by using trimethylindium in place of TEIn and uniform In incorporation and growth rates were obtained [15]. It is thought that since the mechanism of epitaxial growth involves diffusion of species across the boundary layer and breaking the organometallic molecules, the presence of common organic radicals for both In and Ga is helpful. Similar results have been observed in low pressure systems where TEIn and TEGa are used for uniform growth of epitaxial layers of InGaAs.

The doping levels in graded InGaAs have been investigated in detail both as a function of the growth temperature and the input flux of dopant. Zinc p-type dopant and selenium n-type dopant have been investigated in this work. The incorporation of the dopants increases at lower temperatures due to the reduced probability of the dopant atoms escaping from the surface. It is considered preferable to develop techniques for controlled growth at lower growth temperatures, since that reduces the extent of Zn diffusion in a multi-layer structure. It has so far not been possible to obtain mid-10^{17}cm^{-3} p-type doping levels at 600°C growth temperature.

Considerable progress has been made in determining conditions for the growth of AlGaInAs alloys. It is found that with a fixed TMIn and (TMGa + TMAl) flux the bandgap can be varied by changing the TMGa/TMAl input ratio while the lattice constant remains unchanged. The growth conditions have been established for the growth of 6% and 20% In compounds over a wide range of bandgaps.

Various grading schemes have been investigated for InGaAs layers grown on GaAs substrates. Dislocation etch pit studies show that with step grading the etch pit density reduces compared to ungraded and linearly-graded layers. A few low-bandgap solar cells have been fabricated using an AlGaInAs window layer. The best spectral response to date is observed in a sample grown with a large number of closely spaced steps. In this respect, the results are similar to previously-reported work with chloride transport VPE-grown InGaAs/InGaP low-bandgap solar cell [16]. Experiments are underway to investigate the effect of various grading schemes on the performance of the cell and optimize the structure.

The other two components for the multijunction cell are the high bandgap cell and a suitable connecting junction. The work on the high bandgap cell is expected to proceed smoothly now, since the basic materials experiments are successfully in progress. The connecting junction can be a tunnel junction in the high bandgap material. To demonstrate the feasibility of a tunnel junction by OM-VPE, we have attempted to fabricate a tunnel junction in GaAs. This work is still in progress and alternate approaches are also being considered.

AlGaAsSb

We have investigated the basic materials growth of alloys in AlGaAsSb quaternary system. This system covers a wide range of bandgaps and is suitable

for multibandgap solar cell structures. GaSb growth conditions have been optimized and ternary GaAsSb and AlGaSb and quaternary AlGaAsSb alloys have been grown.

The GaSb growth experiments were done on InAs substrates, since they are nearly lattice matched and InAs substrates are easily available. It is found that the growth morphology is quite sensitive to the III/V ratio and unlike GaAs which grows best in our system with a III/V ratio of 1/10, the growth of GaSb requires a III/V ratio of the order of or greater than 1 [18]. This might be due to the low melting of Sb compared to As.

Graded GaAsSb layers have been grown and it has been possible to grow GaAs-graded GaSb/InAs substrate and vice versa, GaSb-graded GaAs/GaAs substrate layers. It is found that as with AlGaAs alloys, Al can be substituted for Ga without changing the lattice constant. Thus, quaternary AlGaAsSb alloys have been grown on graded GaAsSb layers. Ternary AlGaSb layers have also been grown on InAs substrates.

CONCLUSION

The OM-VPE technique has matured in the past few years and a wide variety of III-V semiconductor alloys have been grown using this technique. It has proven to be a potentially high-throughput epitaxial technique which produces the highest efficiency packaged GaAs/AlGaAs solar cells to date. It is expected that monolithic multibandgap solar cells with 30% and greater efficiencies will be attainable with OM-VPE in the future. The application of this technique to growing solar cells for space use is currently under investigation and is expected to lead to greater use of GaAs-based solar cells in space.

REFERENCES

1. R. L. Moon, L. W. James, D. R. Locker, W. P. Rahilly and J. M. Mees, 12th IEEE Photovoltaic Spec. Conf. Proc., 1975, p. 255.

2. J. H. Heinbockel, E. J. Conway and G. H. Walker, 14th IEEE Photovoltaic Spec. Conf. Proc., 1979, p. 1085.

3. H. W. Brandhorst and D. T. Bernatowicz, 14th IEEE Photovoltaic Spec. Conf., 1979, p. 677.

4. R. R. Saxena, V. Aebi, C. B. Cooper III, M. J. Ludowise, H. S. Vander Plas, B. Cairns, T. J. Maloney, P. G. Borden and P. E. Gregory, J. Appl. Phys. 51, 4501 (1980).

5. Varian Associates, Final Report on Contract SAN 13-5674, to be published.

6. V. Aebi, C. B. Cooper III, R. L. Moon and R. R. Saxena, Varian Corporate Research Memorandum 367, to be published in J. Crys. Growth.

7. R. D. Dupuis, P. D. Dapkus, C. M. Garner, C. Y. Su and W. E. Spicer, Appl. Phys. Lett. 34, 335 (1979).

8. H. A. Vander Plas, L. W. James, R. L. Moon and N. J. Nelson, 13th IEEE Photovoltaic Spec. Conf., 1978, p. 934.

9. N. J. Nelson, K. K. Johnson, R. L. Moon, H. A. Vander Plas and L. W. James, Appl. Phys. Lett. $\underline{33}$, 26 (1978).

10. R. L. Moon, L. W. James, H. A. Vander Plas, T. O. Yep, G. A. Antypas and Y. G. Chai, 13th IEEE Photovoltaic Spec. Conf., 1978.

11. Varian Associates, Final Report Contract SAN 13-0308, to be published.

12. Varian Associates, Quarterly Report on SERI Contract XP-9-8081-1 (1979-80).

13. J. P. Hirtz and J. P. Duchemin, Electr. Matls. Conf. $\underline{H-1}$ (1980).

14. C. B. Cooper III, M. J. Ludowise, V. Aebi and R. L. Moon, J. Electron. Matls. $\underline{9}$, 299 (1980).

15. M. J. Ludowise, C. B. Cooper III and R. R. Saxena, Electron. Matls. Conf. $\underline{D-6}$ (1980), to be published in J. Electron. Matls.

16. R. R. Saxena and R. L. Moon, Electron. Lett. $\underline{15}$, 826 (1979).

17. Varian Associates, reports on Contract DE-AC03-79SF10610.

18. C. B. Cooper III, R. R. Saxena and M. J. Ludowise, Electron. Matls. Conf. $\underline{H-4}$ (1980).

OM-VPE SYSTEM SCHEMATIC DIAGRAM
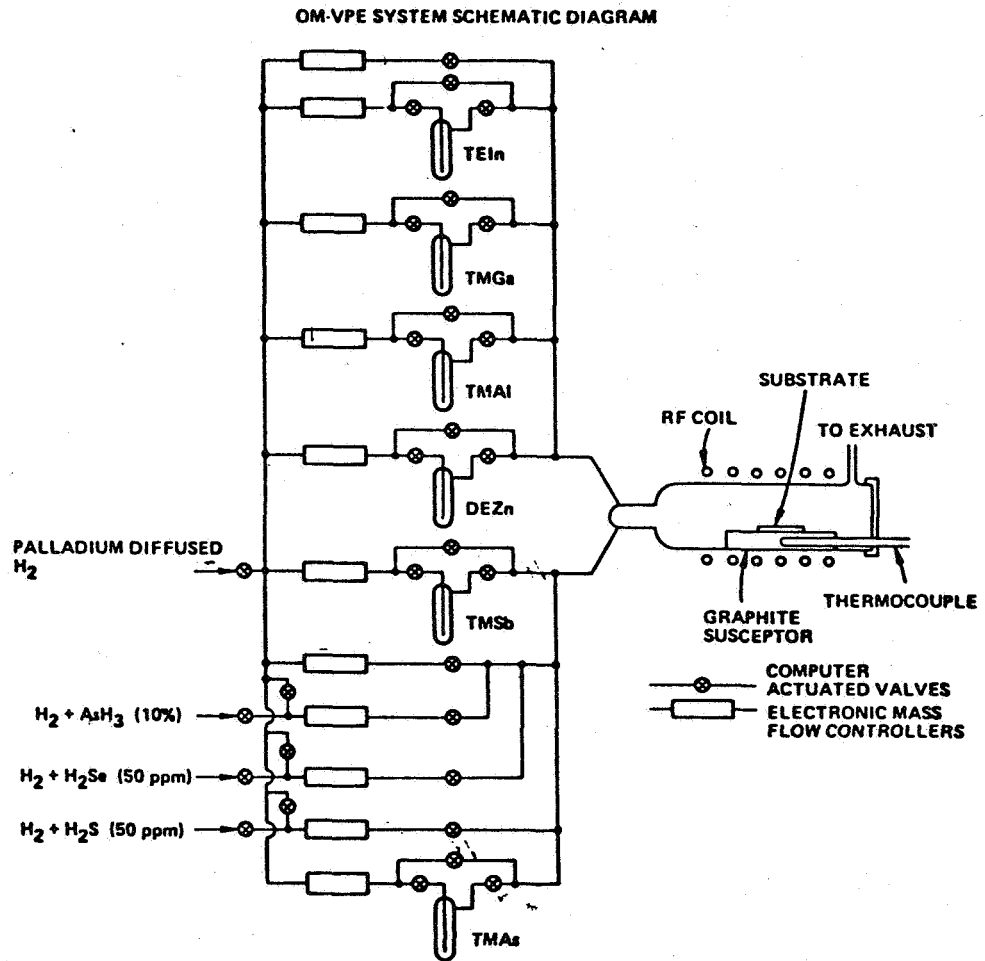
Fig. 1   Schematic diagram of the OM-VPE system.

p — GaAs:Zn	0.5 MICRON
p — AlGaAs:Zn	0.15 MICRON
p — GaAs:Zn	0.5 MICRON
n — GaAs:S	5.0 MICRON
n — GaAs:Sn	
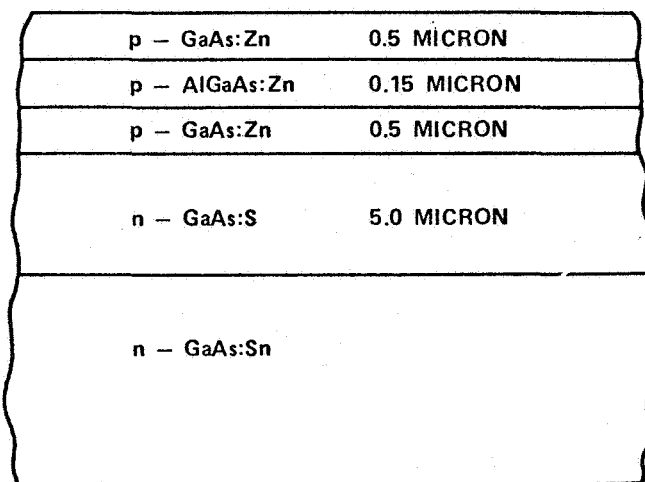
Fig. 2 Epitaxial structure of GaAs/AlGaAs concentrator solar cell.

Fig. 3 Predicted AM2 short circuit current as a function of window layer thickness for different junction depth values.

MULTI-BANDGAP CELL

AlGaInAs p	
AlGaInAs p	◄— HIGH GAP CELL
AlGaInAs n	
AlGaInAs n^{++}	
AlGaInAs p^{++}	◄— TUNNEL JUNCTION
GaInAs p	
GaInAs n	◄— LOW GAP CELL
GaInAs n	
GaAs	

Fig. 4   Multibandgap cell epitaxial structure.

CASCADE SOLAR CELL WORKSHOP REPORT

J. A. Hutchby
Research Triangle Institute
Research Triangle Park, North Carolina

The Cascade Solar Cell Workshop defined and considered several issues related to the feasibility, research and development, and demonstration of a 30% AMO cascade solar cell. These issues are:

1. Maximum Achievable Efficiency and Recommended Cell Operating Conditions
2. General Considerations to Obtain Maximum Efficiency
    A. Three active photovoltaic junctions vs two junctions
    B. Radiation resistance
3. Device Structures
    A. Monolithic cascade cell (two terminal)
        (1) Materials selection
        (2) Growth technique
        (3) Device development strategy
        (4) Important issues
            (a) Suitable acceptor technology for OM-CVD growth of tunnel junctions
            (b) Adequate transport, optical, and structural properties of various required compound semiconductor layers
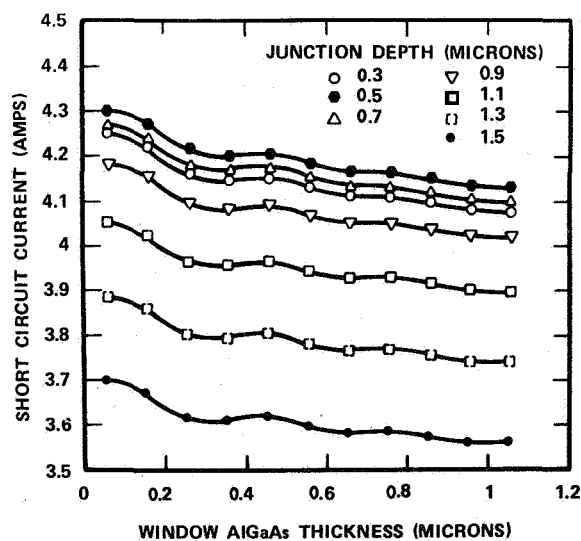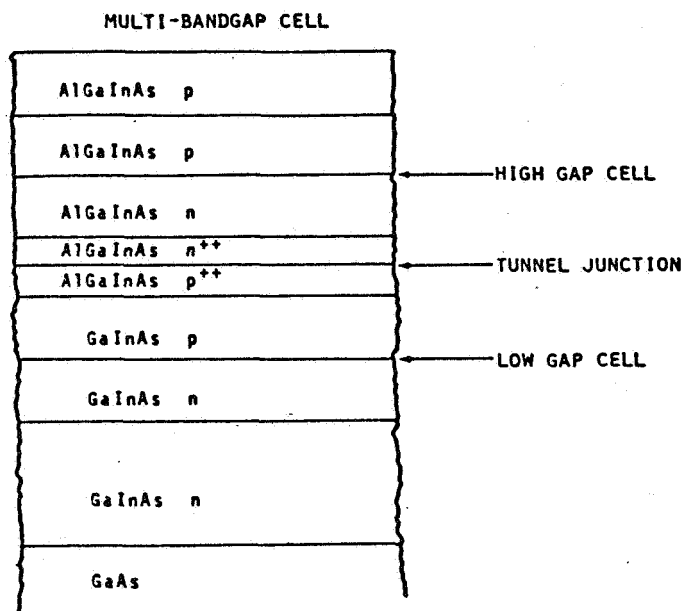   (c) Suitable growth of ten or more epitaxial layers over large area required for three-junction structure
            (d) Lattice defect generation and propagation through cascade structure
    B. Hybrid cascade cell (four terminal)
        (1) Materials selection
        (2) Fabrication techniques
        (3) Important issues
            (a) Interconnect technology
            (b) Proper connection to load
    C. Spectral splitting device (three cells)
        (1) Important issues
            (a) Parts count
            (b) Power/weight ratio

Based upon consideration of these issues, the workshop offers the following recommendations:

A. Achievement of 30% AMO efficiency for a cascade cell exposed to 100 sun concentration and a temperature of 80°C is a reasonable long-range goal

B. Initiate a long-range research program to develop a three-junction, monolithic, cascade cell
   (1) Choose either AlGaAsSb-GaAsSb or AlGaInAs-GaInAs material system
   (2) Emphasize OM-CVD epitaxial growth technique, perhaps combined with other technologies in the near term to obtain tunnel junctions
   (3) Develop a two-junction device first

C. Initiate a cascade solar cell modeling program to study and compare performance of two and four terminal cascade devices exposed to electron and proton irradiation

D. Encourage and be open to new ideas for developing four terminal, hybrid, cascade cells exploiting novel component-cell interconnect technologies

DISCUSSION

Maximum Achievable Efficiency

The workshop agreed that, given certain solar cell operating conditions, a power conversion efficiency goal of 30% AMO is a reasonable and practical long-range target. The required cell operating conditions are solar concentration of 100 suns and a cell temperature of approximately 80°C.

General Considerations

One question which arises immediately is whether the 30% AMO goal can be achieved in a monolithic cascade cell with only two photovoltaic junctions (separated by one optically transparent, low resistance, interconnect junction), or will three photovoltaic junctions be required. While various theoretical modeling studies have shown that limit efficiencies in excess of 30% are possible with an optimum two-junction cell, practical efficiencies of 30% AMO are more likely to be achieved in a three-junction cell in the long term. The workshop did feel, however, that the maximum possible practical efficiency for a two-junction structure operating on a relatively cool concentrator system might reach 30%. Also, a practical AMO cell efficiency of approximately 27% realized in an optimum two-junction structure was felt by the workshop to be a worthwhile interim goal, due to the requirement for fewer semiconductor layers and only one interconnect junction.

A second issue addressed, related to the general approach, was the effect of energetic particle radiation upon degradation of the two-terminal, three-junction, monolithic cascade cell versus that of a hybrid cascade cell in which each of the three component cells are

176

independently, electrically accessible to the load through a four-terminal connection. For the two-terminal cell, the total cascade cell degradation will follow that of the most sensitive component cell. However, the two-terminal cell can be designed for maximum EOL efficiency to minimize this problem. The four-terminal device allows each component cell to be connected independently to the load, therefore, in principle, minimizing the overall effect of the fastest degrading cell on the total system performance in a radiation environment. This approach, however, requires a complex, four-terminal, interconnect technology for the three component cells and requires a scheme for managing the cell output/load interface for the three component cells under changing output conditions. The workshop recommends that a theoretical cascade solar cell modeling program be initiated to study the relative merits and liabilities of the two-terminal monolithic structure compared to the hybrid four-terminal cascade solar cell. It was also felt that either the monolithic-grown or the hybrid structures would have definite weight advantage over approaches requiring use of separate and independent solar cells.

Device Structures - Monolithic Cell (Two-Terminal)
The workshop agreed upon the following criteria for selecting compound semiconductor materials for a three-junction, monolithic, cascade structure:

1. Material system must be lattice-matched through the entire active device structure. However, the active structure was not required to lattice-match the binary compound substrate.

2. The thermal coefficient of expansion must also be matched as closely as possible for the component semiconductor layers.

3. Given the assumed operating conditions (100 suns, 80°C), the minimum bandgap of the bottom cell should be 1.15 eV or a little less, and the minimum bandgap (direct) of the top cell should be 1.95 eV or larger.

It was agreed that only two compound systems come close to meeting these requirements: AlGaAsSb-GaAsSb (GaInAs) system and the AlGaInAs-GaInAs system. Various photovoltaic devices have been demonstrated in the AlGaAsSb-GaAsSb system grown by liquid-phase epitaxy (LPE), including a reasonable tunnel junction and a complete, two-junction, cascade structure (including two photovoltaic junctions separated by a tunnel junction). However, this material system grown by LPE usually (but not always) exhibits short electron diffusion lengths, and the photovoltaic junctions yield relatively low open-circuit voltages. Also, growth of this material system from GaAs to GaSb has been demonstrated using the preferred organometalic-chemical vapor deposition (OM-CVD) technique.

Layers of the relatively new material system AlGaInAs have recently been grown on GaInAs substrates using the OM-CVD technique and a p/n junction grown in GaInAs has been demonstrated. Theoretically, this system offers a somewhat larger energy top bandgap cell material, and is believed by some to be relatively easy to grow by OM-CVD. Yet, of various compound semiconductor systems considered for cascade solar cell research (or for other electron devices) AlGaInAs is by far the newest,

177

and any problems with this system are yet to be identified.

The workshop felt that both material systems considered offered substantial promise to realization of a monolithic, three-junction cascade cell, and both should be considered as viable candidates.

The workshop agreed that a sensible overall strategy to the long-range development of a three-junction, monolithic cascade cell is to first demonstrate a relatively high efficiency, two-junction structure in one of the recommended compound systems. This approach allows demonstration of several significant solutions to key problems in a simpler device structure. It also provides a means for continued visible progress in a long-range program.

The workshop identified several key issues which must be addressed and resolved (perhaps singularly) in the development of a three-junction, monolithic cascade solar cell. These are:

(a) Development of a suitable acceptor impurity technology for the OM-CVD growth of the cascade devices, and particularly the tunnel junction. This acceptor must be available in the vapor phase in a compound which can be pyrolyzed at a relatively low temperature (600-700°C). It also must provide high doping concentration ($~10^{19} cm^{-3}$) in preferable wide bandgap materials (not an absolute necessity) and have a low diffusion coefficient at 600-700°C.

(b) Demonstration of adequate transport, optical, and structural properties of the various required compound semiconductor layers. As mentioned above, the two material systems recommended by the workshop for development of the three-junction monolithic cascade cell are AlGaAsSb-GaAsSb (GaInAs) and AlGaInAs-GaInAs. The prime feature offered by both systems is their ability to nearly cover the assumed absorption wavelength region of interest (1.15 eV–2.05 eV) with direct bandgap material which is lattice-matched through the active structure. Yet the materials are not without their problems. The AlGaAsSb and GaAsSb systems grown by LPE have traditionally exhibited short electron diffusion lengths ($\ell_n ~ 0.5 \mu m$), and p/n junctions fabricated in these materials typically exhibit a relatively low open-circuit voltage (compared to their bandgap energy). However, somewhat larger values of ℓ_n have been observed for AlGaSb (Rockwell International, ERC, Thousand Oaks), for GaAsSb ($\ell_n > 1 \mu m$, Research Triangle Institute), and for GaSb ($\ell_n \cong 4 \mu m$, Physikalisches Institute, Universitat Stuttgart, F. R. G.).

Much speculation exists as to the origin of both the short electron diffusion lengths and the large p/n junction dark currents, but the workshop was not aware of any definitive evidence related to this problem. Therefore, the workshop agreed that in exploring an AlGaAsSb-GaAsSb (GaInAs) cascade cell, specific attention should eventually be addressed to understanding and solving these problems.

A second issue, that of a miscibility gap existing for both $GaAs_{1-x}Sb_x$ and $Ga_{1-y}Al_yAs_{1-x}Sb_x$ for x > 0.20, is not viewed as a problem for the monolithic cascade cells. This

is because bandgap values of interest can be achieved for
x < 0.20, for which single-phase growth occurs.
The AlGaInAs-GaInAs system offers (theoretically) a larger
spread of direct bandgap energies on a constant lattice-
parameter line than does the AlGaAsSb system (1.15 eV to
2.05 eV versus 1.15 eV to 1.90 eV, respectively), which
possibly offers an advantage to the AlGaInAs system for
achieving the optimum bandgap values. Also, it is suggested
that the AlGaInAs system is relatively easy to grow since
Al substitutes readily for Ga in the quaternary crystal.
However, this is a relatively new material system, for which
the growth parameters (OM-CVD) are now being established.
Experimental data for bandgap energies (direct and indirect),
minority carrier lifetimes and diffusion lengths, and p/n
junction properties as functions of material composition
are yet to be determined. Also, fabrication of a p/n junc-
tion is yet to be accomplished in AlGaInAs, although there
are no apparent reasons why this should not be successful.

(c) A third important issue is the suitable growth of ten or more
epitaxial layers over a large area for the three-junction
cascade cell. Growth of multiple layers of thin material has
been demonstrated repeatedly by the OM-CVD process. The
problem becomes one of growing all layers at relatively low
growth temperatures, to stabilize impurity diffusion problems
of the two required tunnel junctions, while maintaining
adequate transport properties to the optically absorbing/
carrier collection layers.

(d) Lattice defect generation and propagation through the cascade
structure is also seen to be an important issue. The problem
of large p/n junction dark currents causing a low V_{oc} in the
AlGaAsSb system may well be due to a 1.2% lattice mismatch
between the GaAs$_{.9}$Sb$_{.1}$ p/n junction (a = 5.72 Å) and the GaAs
substrate (a = 5.65 Å), even though substantial caution is
exercised to grow several lattice-matching layers between
the substrate and the p/n junction. Also, defect formation
in the highly-doped tunnel junctions is quite likely, which
may then propagate into the charge generation and collection
layers grown on top of these disordered layers.

Device Structures – Hybrid Cascade Cell (Four Terminal)

The hybrid cell is one which is still monolithic in the sense that
the component cells are connected in optical and electrical series, but
is hybrid in the sense that the cell uses a component-cell interconnect
technology which does not involve growth of semiconductor materials
(i.e., does not use a tunnel junction). The interconnect layer must be
optically transparent, have a very low electrical resistance, and be
accessible to the external world. In addition, the materials used in
bonding individual cells together must be thermally (thermal expansion
coefficient) and chemically compatible with the bonded cells. However,
since growth of semiconductor layers is not involved in fabrication of

179

the interconnect layer, the component cells do not need to be lattice matched.

The advantages of this approach are obvious. First, a wide selection of component-cells is now available, each of which can be optimized to meet its own requirements without having to be lattice matched to the other component cells. Also, the condition of current match between component cells may be relaxed somewhat (since each component cell is separately connected to the load). This means that degradation of one component of a hybrid cell in an electron or proton radiation environment may have less impact on the degradation of the photovoltaic system compared to the monolithic cascade cell system.

The key challenges of the hybrid cell are development of an adequate component-cell interconnect technology and proper connection of a four-terminal cell to the load. Each component-cell of a hybrid structure needs to be connected to the load in such a way that unequal variations in component-cell output yields a minimum variation in power delivered to the load.

One example of a hybrid, four terminal cell would use Si (1.1 eV) for the low bandgap cell, GaAs (1.44 eV) for the middle bandgap cell, and $Al_{.35}Ga_{.65}As$ (1.95-2.00 eV) for the high bandgap cell.

The workshop agreed that the hybrid approach is attractive, and recommends that new ideas related to the interconnect technology be encouraged and supported.

Device Structures - Spectral Splitting Device (Three-Cells)

The spectral splitting concept was only briefly considered as an alternative technology to obtaining high efficiency, cascade structures. It was suggested that a two-cell version of this approach is closer to realization of relatively high efficiency, but that a three-cell version would require additional development, particularly of the beam splitting optics. Other issues identified were a comparatively large parts count and the impact of three separate cells together with beam splitting optics on overall system power-to-weight ratio important to space application.

ANNEALING OF RADIATION DAMAGE IN LOW RESISTIVITY
SILICON SOLAR CELLS

I. Weinberg and C. K. Swartz
NASA Lewis Research Center
Cleveland, Ohio

Silicon solar cells with base resistivity of 0.1 ohm–centimeter are projected to achieve 18 percent air mass zero efficiencies (ref. 1). It has been found in the past that these low–resistivity cells require annealing temperatures of approximately 500° C to restore performance after radiation–induced degradation (ref. 2). However, if annealing in space is to become a reality, temperatures of 200° C or lower are required to prevent irreversible damage to other parts of the solar array. Hence, we have been conducting a program to reduce the temperatures required to restore cell performance after irradiation. Previous investigations into the annealing behavior of radiation–induced defects produced in p–type silicon indicate that oxygen and carbon are constituents of the major defects observed after irradiation with 1–MeV electrons (refs. 3 and 4). Hence, our current efforts are concerned with the annealing characteristics of two groups of cells containing different amounts of oxygen and carbon.

Junction formation in one group of cells was achieved by phosphorous ion implantation into 0.1–ohm–cm float–zone silicon with oxygen and carbon concentrations $<5\times10^{15}/cm^3$. The second group of cells was fabricated by phosphorous diffusion into 0.1 ohm–centimeter float–zone silicon whose oxygen and carbon concentrations were $10^{16}/cm^3$. After irradiation by 1–MeV electrons the cells were isochronally annealed, time at temperature being 20 minutes. Results for the diffused junction cells are shown in figure 1 where annealing temperatures around 500° C are indicated. The isochronal annealing data for the ion–implanted cells are shown in figure 2, where it is seen that the annealing temperatures are fluence dependent and where, at a fluence (ϕ) of $10^{14}/cm^2$, an annealing temperature of 300° C is observed. With increasing fluence, the temperature increases until, at $\phi = 3\times10^{14}/cm^2$, annealing occurs around 500° C. An additional feature of the data is the appearance of reverse annealing, which occurs at temperatures above 400° C as the fluence increases above $10^{14}/cm^2$.

The presently observed 200° reduction in annealing temperature is highly significant but not sufficient to achieve the goal of annealing at 200° C. Further reduction appears possible by identifying and removing the defects responsible for the occurrence of annealing at 300° C. The first step in this procedure is defect identification, which we attempt by considering some of the properties of known defects in p–type (boron–doped) silicon. However, because of sensitivity limitations, data from deep–level transient spectroscopy (DLTS) are not available for 0.1–ohm–centimeter boron–doped silicon. On the other hand, defect spectra from DLTS are available from previous work for 0.3–ohm–centimeter silicon (ref. 3). Figure 3 shows the DLTS data for this low resistivity boron–doped silicon,

and table I summarizes the information available on the defects shown in the figure.

Referring to table I and figure 3, the defects at $E_v + 0.48$ and $E_v + 0.26$ eV are unidentified. For the remaining defects, although identifications are available, many are ambiguous. The defect at $E_v + 0.38$ eV has been ambiguously identified as a vacancy-oxygen-carbon complex (V-O-C) (ref. 3) or a carbon-interstitial carbon-substitutional pair (C_I-C_S) (refs. 5 and 6). We note from figure 3 that the annealing temperature for this defect favors the V-O-C identification. However, the simultaneous presence of both defects below 300° C is not precluded. The defect at $E_v + 0.23$ eV with annealing temperature at 300° C has been unambiguously identified as the divacancy (refs. 3 and 5). As seen from the table, the defect at $E_c - 0.27$ eV is a boron related defect (refs. 3 and 5). It is observed that disappearance of this defect is followed by growth of the defect at $E_v + 0.30$ eV (ref. 3). This latter defect has been tentatively identified as either a boron-oxygen vacancy complex (ref. 3) or the silicon di-interstitial (ref. 5). However, from figure 3 it is seen that this defect anneals out at a temperature slightly above 400° K, while the silicon di-interstitial anneals out at 500° C (ref. 7). The preceding discussion indicates that the possible defects that anneal out at 300° C are the divacancy and the silicon di-interstitial. If these were the only significant defects present at the lower fluence, they could be responsible for the annealing observed at 300° C. This could be possible if a fluence dependence existed for the production rate of the remaining defects such that their concentration was very low at $\phi = 10^{14}/cm^2$ and increased significantly with increasing fluence. However, there is no experimental evidence to support the postulated fluence dependence. With respect to the fluence dependent reverse anneal observed between 400° and 500° C, it is difficult from the present data to assign this effect to a specific defect or defects.

The preceding consideration of defect behavior in irradiated boron-doped silicon leads to the tentative conclusion that further reduction in annealing temperature could be achieved by decreasing the carbon concentration and either neutralizing the divacancy and/or minimizing its formation as a result of irradiation. We emphasize the speculative nature of this conclusion. The fact remains, however, that the present work has demonstrated a significant reduction in the temperature required to remove radiation-induced degradation in 0.1-ohm-centimeter silicon solar cells.

REFERENCES

1. Godlewski, M. P.; Brandhorst, H. W., Jr.; and Baraona, C. R.: Effect of High Doping Levels on Silicon Solar Cell Performance. Eleventh Photovoltaic Specialists Conference - 1975, IEEE, 1975, pp. 32-35.
2. Weinberg, I.; and Swartz, C. K.: Annealing of Radiation Damage in 0.1 and 2 ohm-cm Silicon Solar Cells. NASA TP-1559, 1979.
3. Mooney, P. M.; et al.: Defect Energy Levels in Boron Doped Silicon Irradiated with 1-MeV Electrons. Phys. Rev. B, vol. 15, no. 8, Apr. 15, 1977, pp. 3836-3843.

4. Weinberg, I.; and Swartz, C, K.: Origin of Reverse Annealing in Radiation-Damaged Silicon Solar Cells. Appl. Phys. Lett., vol. 36, no. 8, Apr. 15, 1980, pp. 693-695.

5. Kimerling, L. C.: Defect States in Electron-Bombarded Silicon: Capacitance Transient Analysis. International Conference on Radiation Effects in Semiconductors, Dubrovnik, Yugoslavia, 1976, N. B. Urli and T. W. Corbett, eds. Institute of Physics (London) Conference Series no. 31, 1977, pp. 221-230.

6. Brower, K. L.: EPR of a John Teller Distorted <111> Carbon Interstitialcy in Irradiated Silicon. Phys. Rev. B, vol. 9, 1974, pp. 2607-2617.

7. Brower, K. L.: EPR of a <001> Si Interstitial Complex in Irradiated Silicon. Phys. Rev. B, vol. 14, pp. 872-883 (1976).

Energy level, eV	Defect	Anneal temperature, °C		Capture cross section, cm^2		Detection method
		In	Out	σ_n	σ_p	
$E_v + 0.38$	V–O–C or C$_I$–C$_S$	30 ———	400 300	0.3×10^{-13} ———————	2×10^{-16} ———————	EPR, DLTS EPR, DLTS
$E_v + 0.23$	Divacancy	———	300	4×10^{-13}	3×10^{-16}	EPR, DLTS
$E_c - 0.27$	B$_I$O$_I$ or B$_I$–B$_S$	——— ———	200 180	2×10^{-13} ———————	——————— ———————	DLTS DLTS
$E_v + 0.30$	B–O–V or S$_I$–S$_I$	170 200	400+ 500	3.6×10^{-13} ———————	2×10^{-16} ———————	DLTS EPR, DLTS
$E_v + 0.26$	———————	270	330	10^{-13}	———————	DLTS

FIGURE 1: - ANNEALING TEMPERATURES OBSERVED IN RADIATION DAMAGED SILICON SOLAR CELLS

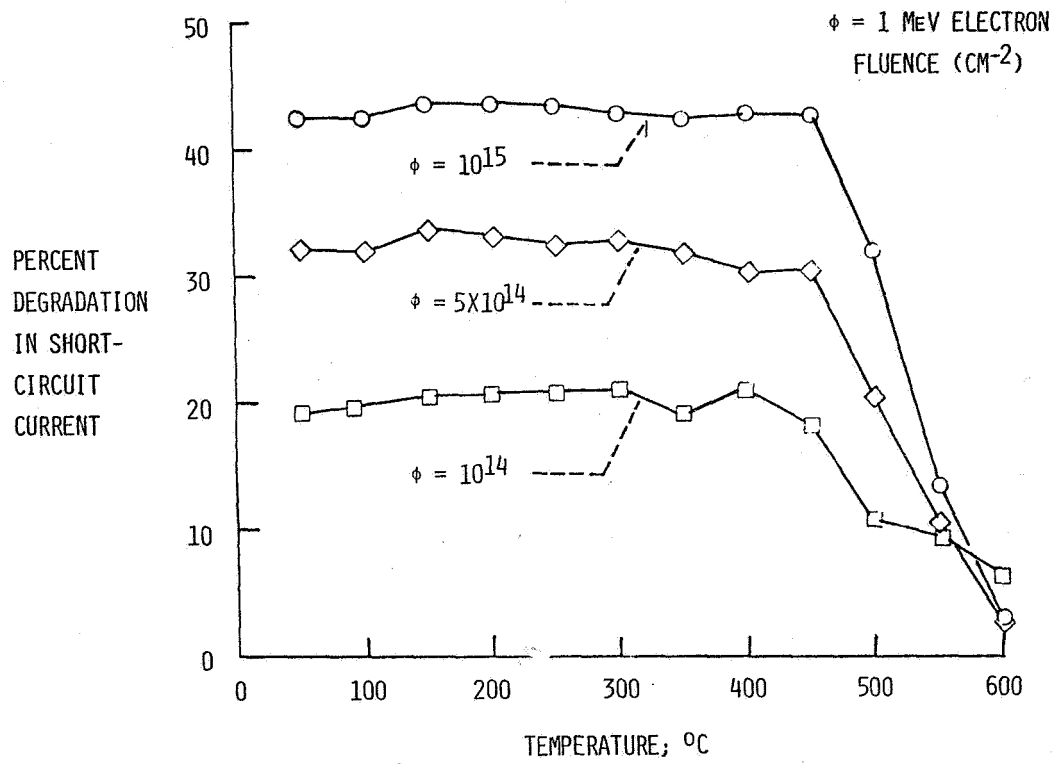(CELL P-N JUNCTION FORMED BY DIFFUSION; RESISTIVITY = 0.1 OHM-CM)

FIGURE 2: - REDUCED ANNEALING TEMPERATURES IN RADIATION DAMAGED SILICON SOLAR CELLS

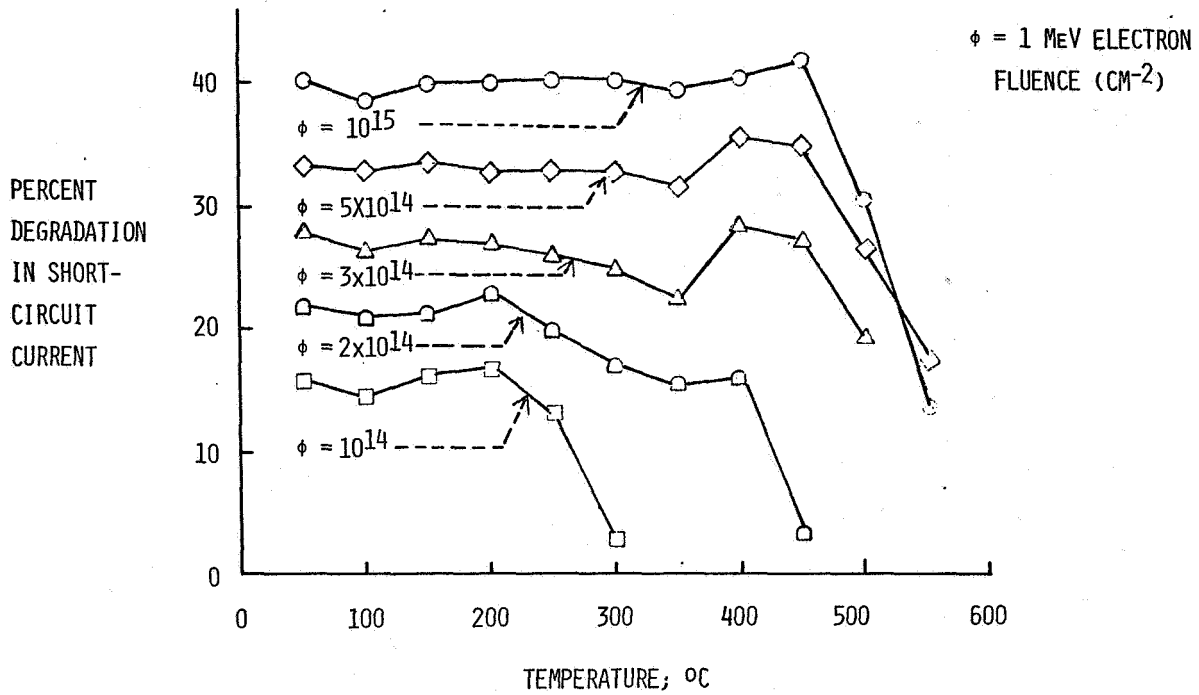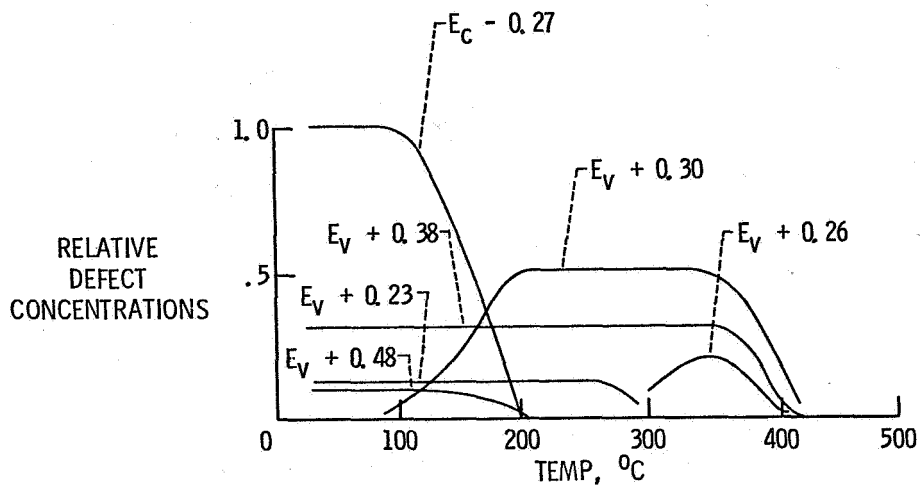(CELL P-N JUNCTION FORMED BY ION-IMPLANTATION; RESISTIVITY = 0.1 OHM-CM)

FIGURE 3: - DLTS DATA FOR 0.3 Ω-CM P-Si ISOCHRONALLY

ANNEALED AFTER 1 MeV ELECTRON IRRADIATION

186

MODELING OF RADIATION DAMAGE IN SILICON SOLAR CELLS

Gottlieb Oehrlein, James P. Karins, and James W. Corbett
State University of New York
Albany, New York

and

Patricia M. Mooney and Bernard Pajot
University of Paris VII
Paris, France

EXTENDED ABSTRACT

The goal of this program is the quantitative analysis of damage production and annealing in silicon solar cells. This necessitates treating all the defects present in the solar cells. But no measurements monitor all the defects. Silicon solar cell performance depends on the defects responsible for the minority carrier lifetime, but is insensitive (at room temperature) to major defects which have sufficiently shallow electrical levels, such as the [vacancy + oxygen] center in n-type material. Transient capacitance techniques (such as DLTS) monitor only carrier traps, infrared techniques only infrared active defects, EPR only defects with unpaired spins, etc. But the dynamics of defect production and annealing reflect all the defects and hence information from all the sources must be exploited to get as complete a picture as is possible.

The qualitative features of defect production in silicon at room temperature have now emerged (although some aspects need confirming work).

One MeV electron irradiation produces preponderantly isolated vacancy-interstitial pairs. If neither of these defects are mobile, the concentration of each grows linearly with fluence (until extremely high fluences where saturation occurs, a regime we will not consider further here).

Annealing of damage depends on the nature of the damage. Vacancy-interstitial pairs which are bound by an interaction such that they mutually annihilate rather than dissociate are termed close-pairs; close-pair recovery usually occurs at a lower temperature than the temperature at which long distance defect migration occurs. Annealing of the remaining frozen-in damage occurs when a temperature is reached where the vacancy or interstitial is mobile; usually the interstitial is more mobile than the vacancy. The recovery occurs in two regimes which may be resoluable. The first is termed correlated recovery in that the mobile interstitial, say, annihilates with "its own" vacancy, i.e., the one with whom it is spatially correlated because of the damage production process. The interstitials that escape correlated recovery can find other vacancies and undergo annihilation, which process is

called <u>uncorrelated</u> recovery.

If the interstitial is mobile during irradiation and if there is no interstitial agglomeration or trapping, then a steady-state concentration of interstitials and vacancies is established, which decays to zero when irradiation ceases, i.e., there is no permanent damage. If agglomeration can occur then permanent damage will be produced, as is also true if the vacancy is also mobile.

If there is an impurity capable of trapping a mobile defect in the material then the trapping process will compete with defect-annihilation and -agglomeration. The trapping efficiency in the uncorrelated recovery regime is proportional to the impurity concentration until all the uncorrelated recovery is suppressed by trapping. Several experiments suggest that this uncorrelated trapping occurs in n-type silicon. Additional impurity concentration will intrude on the correlated recovery, trapping one of the defects and suppressing some of the correlated recovery. The hall-mark of this process is that the impurity trapping efficiency in the correlated regime is that it is proportional to the square root of the impurity concentration. Several experiments suggest that defect trapping by boron in p-type silicon occurs by this process.

Experimentally we do not have firm identities for all the defects. Progress has been made, however, by the identification of some defects. For example, it has been found that carbon plays an important role in defect-production in p-type silicon, which has led to the thrust to obtain low-carbon, low-oxygen silicon. We have found (on the basis of experimentation with the small amounts of this material available to us) that indeed the damage (as monitored by DLTS measurements) is reduced in this material. (See Fig. 1.) Clearly further experimentation of this type is warranted.

The quantitative analysis of all the electrically active defects has thus far proven illusive, because of the complexity of the processes and many parameters involved. We have consequently gone to high fluence experiments where we have determined the capture parameters for the substitutional carbon, interstitial carbon, and interstitial oxygen. Of particular interest is the enhancement of vacancy-oxygen production by increased boron concentration, which we explain by the substitutional-boron (with the Coulomb interaction radius of 70 Å) attracting the interstitial from the correlated-recovery and freeing the vacancy to interact with oxygen.

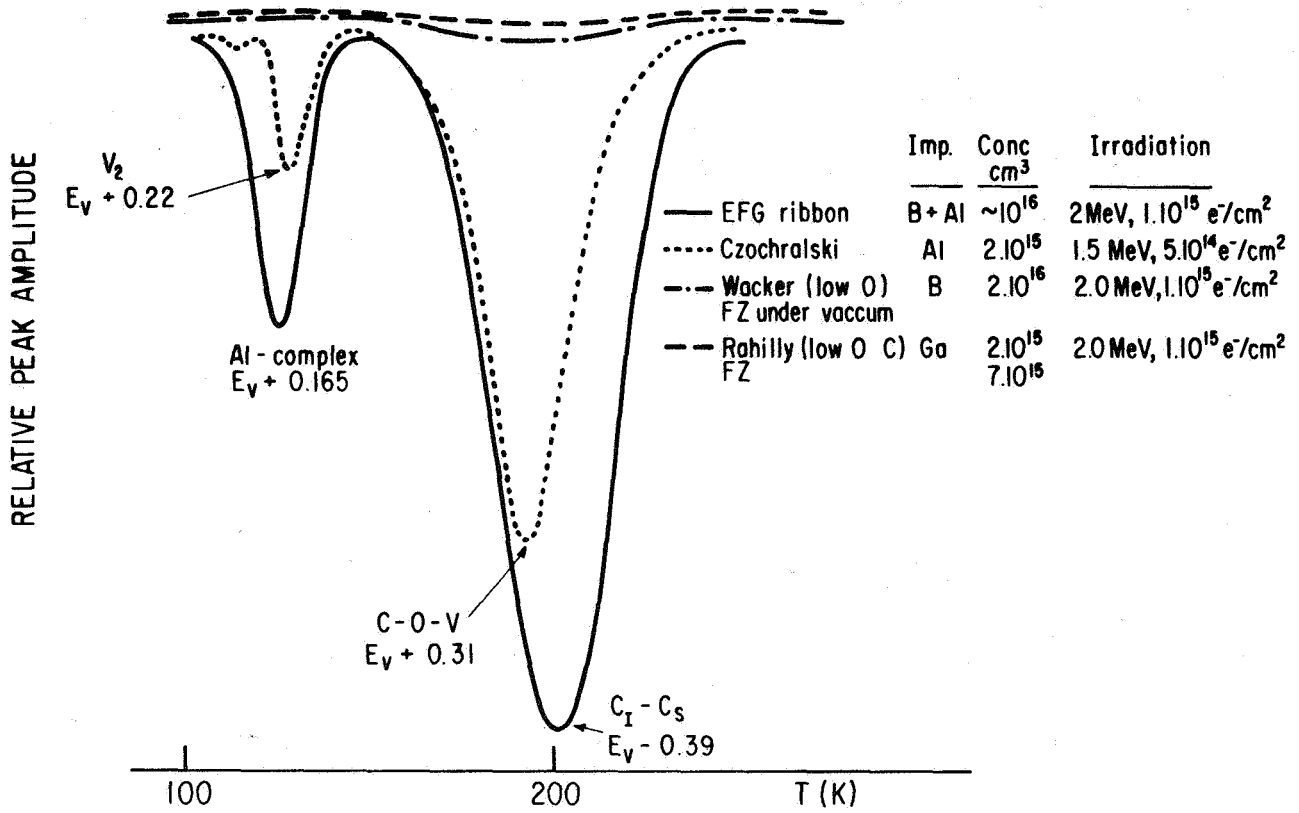The quantitative modeling of damage production and annealing is continuing.

Figure 1. Pulsed Capacitance (DLTS) measurements vs Temperature (T) for several types of silicon samples.

189

DISTRIBUTION OF OXYGEN IN SILICON AND ITS EFFECTS ON
ELECTRONIC CHARACTERISTICS ON A MICROSCALE

H. C. Gatos, P. Rava, and J. Lagowski
Massachusetts Institute of Technology
Cambridge, Massachusetts

ABSTRACT

The microdistribution of oxygen in silicon was obtained by scanning IR absorption in as-grown Czochralski crystals. The crystals were subsequently submitted to various heat treatments. The profiles of the generated thermal donors were determined by spreading resistance measurements. Contrary to the prevailing views, it was found that the concentration of the activated thermal donors is not strictly a function of the oxygen concentration, but depends strongly on an additional factor, which was shown to be associated with vacancy concentration. These conclusions could only be reached on the basis of microscale characterization. In fact, commonly employed macroscale analysis has led to erroneous conclusions.

INTRODUCTION

Oxygen is invariably present in Czochralski-grown Si crystals at concentration levels in the vicinity of $10^{18}/cm^3$. It originates from the interaction of molten Si with the SiO_2 crucible and, like all impurities in Si, oxygen is not uniformly distributed (ref. 1). It is a highly undesirable impurity in a number of device applications.

The interstitial oxygen, in as-grown crystals is electrically inert. It has been generally accepted for many years that the concentration of oxygen donors activated upon heat treatment at 450°C is directly related to the interstitial oxygen concentration. Although quantitative relationships have been proposed based on macroscale (average) determinations of oxygen concentration by IR absorption and the (mean) activated oxygen donor concentration (ref. 2) they have not been generally confirmed (ref. 3).

In the present study, by correlating the oxygen concentration and activated oxygen donors in Si on a microscale, the main uncertainties stemming from earlier macroscale measurements are, for the first time, clarified.

EXPERIMENTAL

Oxygen concentration microprofiles were obtained by scanning IR absorption employed earlier for the determination of carrier concentration microprofiles (refs. 4,5). As seen in Fig. 1, it consists of a tunable CO_2 laser, an optical system for monitoring the power and wavelength of the laser beam, a stage with x-y motion and an IR detector. The wafer was mounted on the stage and the intensity of the collimated beam (~30 μm in diameter) passing through the wafer was measured as a function of the position along the sample.

The laser beam was chopped in order to use lock-in detection of the signal. Since the smallest wavelength attainable with the CO_2 laser was 9.17 μ, whereas the peak of the oxygen absorption band is at 9.04 μm, a ratio of $\alpha_o(9.04 \ \mu m)/\alpha(9.17 \ \mu m) = 1.95$ was obtained using a Fourier transform spectrometer; this ratio was used for making the necessary correction in determining the oxygen concentration (ref. 6).

Both parallel faces of the Si samples were polished to a mirror finish and coated with a quarter wavelength zinc sulfide antireflection coating to reduce the reflection coefficient and avoid interference caused by multi-reflections of the light beam inside the sample. This coating was employed by Ohsawa et al (ref. 3) who have also recently obtained oxygen profiles in Si crystals by scanning IR absorption using a semiconductor laser.

Carrier concentration profiles were determined from spreading resistance measurements at 10 μm intervals.

An oxygen concentration microprofile taken parallel to the growth direction 6 mm from the periphery of the crystal is shown in Fig. 2a. It is seen that the oxygen concentration fluctuates from about 1×10^{18} to $1.5 \times 10^{18}/cm^3$. The fluctuations are more random than periodic, indicative of turbulence convection in the melt during growth (ref. 1). The crystal was (commercial) dislocation-free, Czochralski-grown p-type, B-doped with a mean carrier concentration of $1.5 \times 10^{15}/cm^3$. A carrier concentration profile along the IR transmission scan of Fig. 1a exhibited essentially no fluctuations, typical for B-doped crystals (ref. 1).

Subsequently, the Si slice was heat treated at 450°C for 4 hours, to activate oxygen donors, and a spreading resistance scan was taken along the line of the IR absorption scan. The results are shown in Fig. 2b. The hole concentration is decreased from its original value of 1.5×10^{15} by the amount of activated oxygen donors. It is seen that the oxygen and carrier concentration profiles exhibit in general similar features. As an average the donor concentration is about three orders of magnitude smaller than the oxygen concentration.

A close examination of profiles 2a and 2b shows that in some locations there is no direct correspondence between oxygen and activated donor concentrations. For example, in location B the concentration of oxygen is greater than that in location A, whereas the corresponding oxygen donor concentration in B is smaller than in A. Similarly, in location C the oxygen concentration exhibits a peak which does not appear in the carrier concentration profile.

Upon heat treatment of the slice at 650°C for 4 hours the oxygen donors, as expected, were annihilated; the slice was then heat treated again at 450°C for 8 hours. The resulting carrier concentration profile is shown in Fig. 3c. It is seen that in this case the overall activated donor concentration is significantly smaller than before the 650°C heat treatment. Here again (as in Fig. 2b) in locations A and B there is no direct correspondence between oxygen and oxygen donor concentration. Furthermore, the oxygen concentration peak in location C becomes visible in Fig. 2c, whereas it was not present in Fig. 2b.

It is important to point out that with each subsequent heat treatment of the same slice at 650°C and then at 450°C the concentration of the activated oxygen donors continuously decreased. In the present case after a cumulative heat treatment of about 15 hours at 650°C the oxygen donor concentration activated by heat treatment at 450°C for a few hours was greatly reduced.

The discrepancies between oxygen and oxygen donor concentrations were found to be very pronounced near the periphery of the crystal. An oxygen concentration profile taken parallel to the growth direction 4.5 mm from the periphery of the same crystal and the corresponding carrier concentration profile taken after heat treatment at 450°C for 4 hours are shown in Figs. 3a and 3b, respectively. As is well known, the mean concentration of the oxygen is smaller near the periphery than towards the center of the crystal.

The striking result presented in Fig. 3b is that in entire regions no oxygen donors were formed, and in fact the carrier concentration in some of these regions ($\sim 1.5 \times 10^{15}$/cm^3) is the same as prior to the heat treatment. There are, of course, regions in which activation of oxygen donors took place. After the oxygen donors were annihilated by a heat treatment of 650°C for 4 hours, the slice was heat treated again at 450°C for 8 hours. The resulting carrier concentration profile is shown in Fig. 3c. It is seen that activation of oxygen donors took place in regions in which activation was not pronounced or not observed after the first heat treatment (region B, for example). In regions where pronounced activation took place after the first heat treatment the concentration of oxygen donors decreased following the second 450°C heat treatment (for example, region A) consistent with results presented in Fig. 1.

With subsequent heat treatments of the same slice at 650°C and then at 450°C the concentration of the oxygen donors in the regions where activation had not taken place after the first heat treatment continued to increase to a maximum value and then decreased eventually reaching very small values Fig. 3d). Thus, the oxygen activation behavior near the periphery and towards the center of the crystal is shown in Fig. 4.

A series of oxygen profiles taken on the same silicon crystal at various distances from the periphery (abscissa) are shown in Fig. 5. It is seen that the variations in oxygen concentration are more pronounced near the periphery of the crystal than near the center. It is further seen that certain patterns of inhomogeneities persist from the periphery to the center of the crystal. The corresponding carrier concentration profiles are shown in Fig. 6. Here again it is apparent that near the periphery there are extended regions in which no donor activation took place during the initial heat treatment at 450°C.

DISCUSSION

It is apparent that the concentration of oxygen is not necessarily the controlling factor in the thermal activation of oxygen donors. Although their quantitative analysis is being pursued, the present results, at least qualitatively, are in good agreement with a proposed model (ref. 7) which postulates the interaction of interstitial oxygen with Si vacancies.

According to this model, during thermal activation of donors the interstitial oxygen, O_i, first occupies a Si vacancy, V_{Si}, and then it combines with a neighboring Si vacancy V_n.

$$O_i + V_{Si} \rightarrow O_{Si} \tag{1}$$

$$O_{Si} + V_n \rightarrow O_{Si}^+ V_n^- \tag{2}$$

The oxygen-vacancy complex is then readily ionized as a donor:

$$O_{Si}^+ V_n^- \rightarrow O_{Si}^{+2} V_n^- + e^- \tag{3}$$

This model implies that the activation of oxygen donors does not depend only on oxygen concentration but requires the presence of vacancies. However, since the oxygen concentration fluctuates significantly in Si crystals, this implication could not be tested without knowledge of the actual concentration of oxygen on a microscale.

The present results show that the concentration of activated donors may not be proportional to the oxygen concentration. In the light of the model this result is not surprising since the distribution (or availability) of vacancies does not necessarily coincide with the oxygen distribution. During heat treatment at 650°C diffusion makes more vacancies available to the oxygen sites; thus upon subsequent heat treatment at 450°C (consistent with the present experimental results) activation of donors can take place in regions where vacancies are not available and activation could not have taken place; on the other hand, in regions where activation had taken place, additional vacancies, V_f, render the activated donor electrically inert by forming inert stable complexes as follows:

$$O_{Si}^+ V_n^- + V_f \rightarrow O_{Si}^{+2} V_n^- V_f^- \tag{4}$$

Although the annihilation of thermal donors at 650°C is not entirely clear at present, it is possible that the bonding of the donor complex is altered to an electrically inert configuration. According to the authors of the above model (ref. 7) this process can be viewed as a low-energy phase transition probably due to elastic recovery processes and thus correlated to vacancy-supported stability of substitutional oxygen.

Regarding the donor activation behavior near the periphery of the crystal it is very likely that it is associated with the distribution of swirl microdefects in dislocation-free crystals. It has been reported (ref. 8) that high density of microdefects (vacancy clusters) is present near the periphery of the crystals (referred to as B-type). These defects are essentially vacancy getters and thus extensive activation of donors does not take place in this region of the crystal until prolonged heat treatment at 650°C releases vacancies from these clusters which then participate in donor activation. The density of this type of clusters becomes significantly smaller away from the crystal periphery. On the other hand, the type of microdefects present towards

the center of the crystals, referred to as A-type, are larger than the B-type and may not constitute active vacancy clusters.

It should be pointed out that not only vacancies, but also acceptor atoms, play a role in the activation of oxygen donors. Preliminary results in our laboratory with p-type crystals doped with acceptors other than B(e.g., Al, In and Ga) indicate that the donor activation rates are different for the different dopant elements. This work is currently being pursued further.

In summary, we have shown that thermal oxygen donor formation is not controlled solely by the oxygen concentration. The equally important role of vacancies in this process was clearly demonstrated by direct microscale analysis of oxygen and thermal donor concentrations.

REFERENCES

1. A.Murgai, H.C. Gatos, W.A. Westdorp, J. Electrochem. Soc. 126, 2240 (1979); A. Murgai, J.Y. Chi and H.C. Gatos, J. Electrochem. Soc. 127, 1182 (1980).

2. W. Kaiser, H.L. Frisch and H. Reiss, Phys. Rev. 112, 1546 (1958).

3. A. Ohsawa, K. Honda, S. Ohkawa and R. Ueda, Appl. Phys. Lett. 36, 147 (1980).

4. L. Jastrzebski, J. Lagowski and H.C. Gatos, J. Electrochem. Soc. 126, 260 (1979).

5. W. Walukiewicz, J. Lagowski, L. Jastrzebski, P. Rava, M. Lichtensteiger, C.H. Gatos and H.C. Gatos, J. Appl. Phys. 51, 2659 (1980).

6. Standard test method for interstitial atomic oxygen content of silicon by infrared absorption, ASTM Standard F 121-76.

7. D. Helmreich and E. Sirtl, Semiconductor Silicon, 1977, edited by H.R. Huff and E. Sirtl, Electrochem. Soc., p. 626.

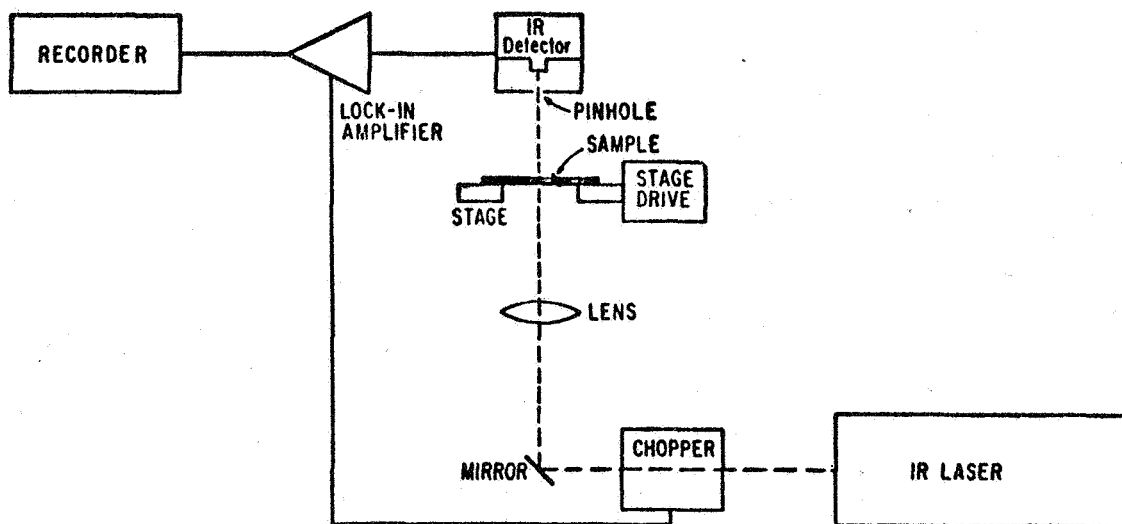8. A.J.R. De Kock, Philips Res. Repts. Suppl. 1973, No. 1.

Figure 1. Schematic representation of IR scanning apparatus for oxygen microprofiling.
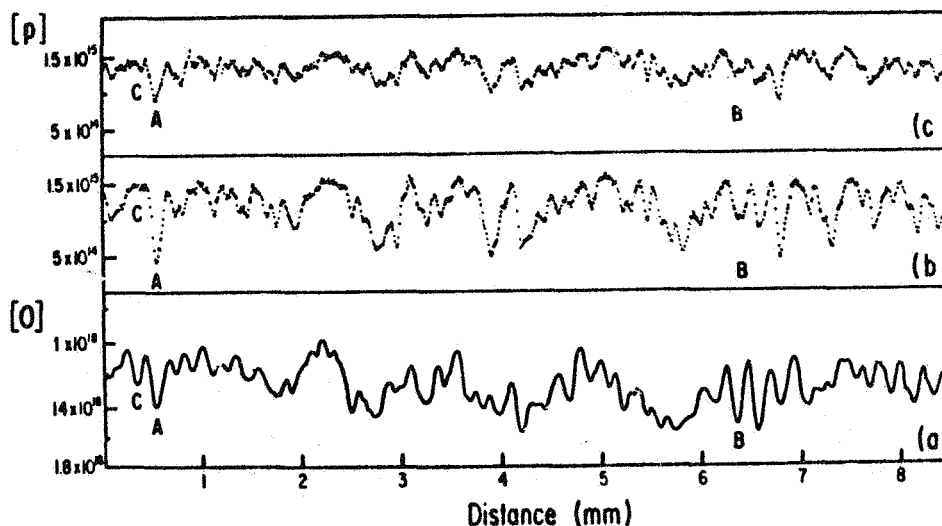

Figure 2. (a) Oxygen concentration, [0], (0/cm^3) as a function of distance parallel to the direction of growth at a distance of 6 mm from the periphery of the crystal obtained by scanning IR absorption. (b) Hole concentration, [p], (p/cm^3) obtained with spreading resistance measurements along the same location as in (a) after 4 hrs heat treatment at 450°C. (c) Hole concentration along the same location as in (a) after 4 hrs heat treatment at 450°C followed by heat treatments for 4 hrs at 650°C and 8 hrs at 450°C.
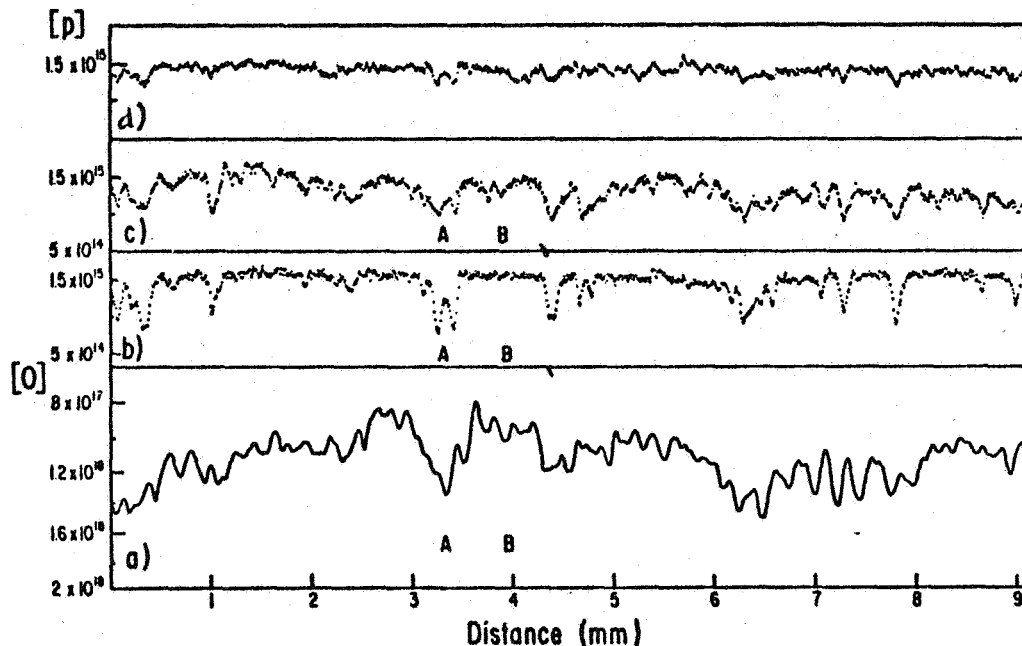
Figure 3. (a) Oxygen concentration, [0], (0/cm³) as a function of distance parallel to the direction of growth at a distance 4.5 mm from the periphery of the crystal obtained by scanning IR absorption. (b) Hole concentration, [p], (p/cm³) obtained with spreading resistance measurements along the same location as in (a) after 4 hrs heat treatment at 450°C. (c) Hole concentration along the same direction as in (a) after 4 hrs heat treatment at 450°C followed by heat treatment for 4 hrs at 650°C and 8 hrs at 450°C. (d) Hole concentration as in (c) after following heat treatments for 4 hrs at 650°C and 8 hrs at 450°C.
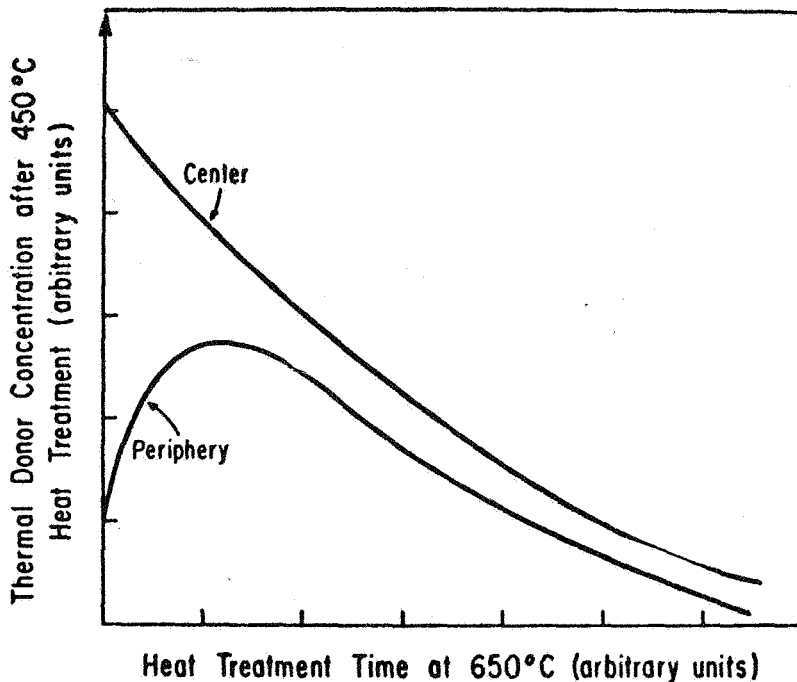

Figure 4. Thermal donor concentration after heat treatment cycles at 450°C, 650°C, 450°C as a function of cumulative 650°C heat treatment times.
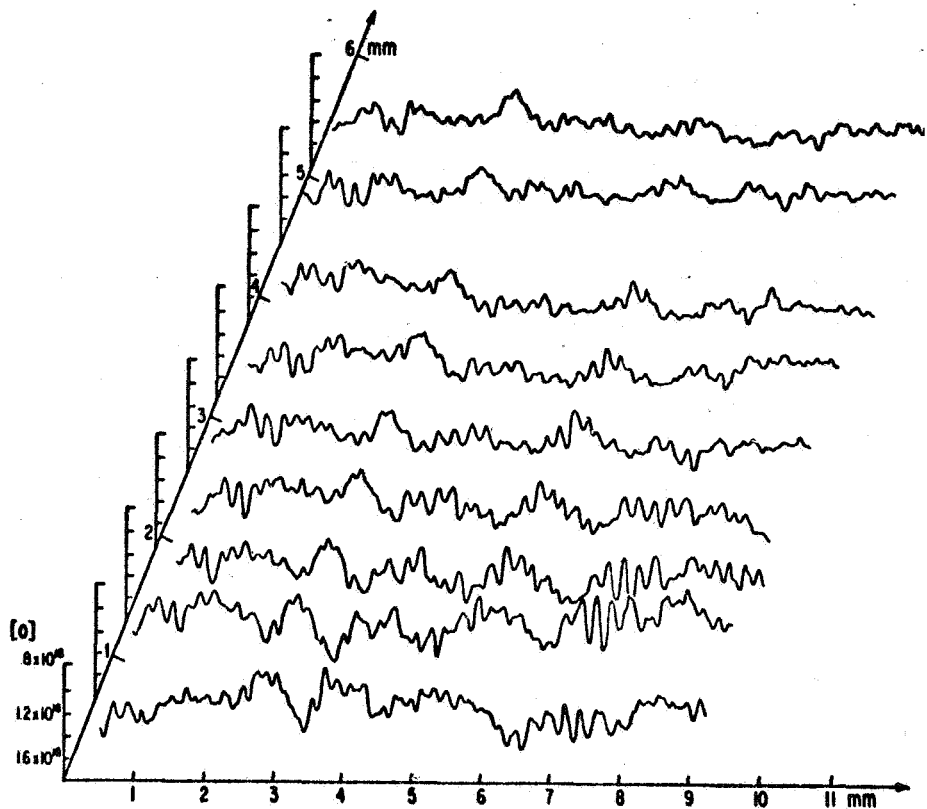
197

Figure 5. Oxygen profiles in a silicon crystal at various locations (abscissa) from the periphery towards the center of the crystal.
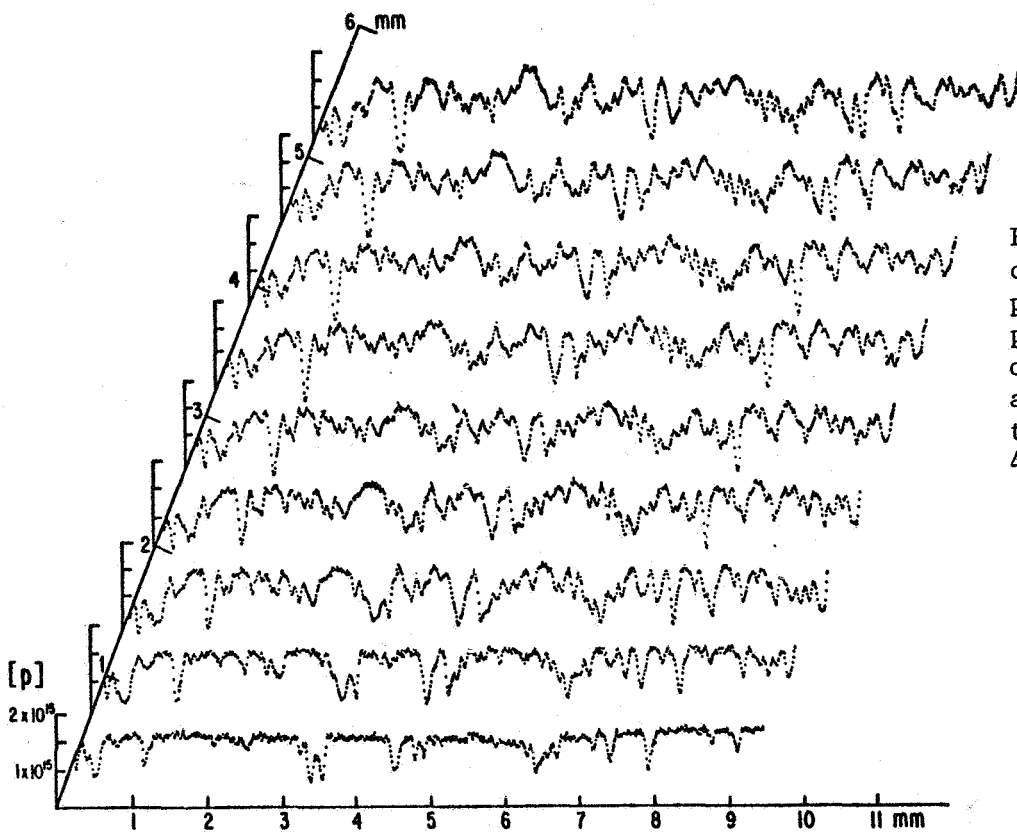

Figure 6. Carrier concentration profiles corresponding to the oxygen profiles after heat treatment at 450°C for 4 hrs.

RADIATION DAMAGE IN SILICON NIP SOLAR CELLS

I. Weinberg, C. Goradia*, C. K. Swartz,
and A. M. Hermann**
NASA Lewis Research Center
Cleveland, Ohio

INTRODUCTION

Solar cells with high base resisitivities have the potential, if prop-
erly designed, of providing high radiation tolerance. In the past however,
radiation damage studies have been largely limited to cells with base re-
sisitivities of 20 ohm-centimeters or less. Hence, because of the potential
for increased radiation resistance, we have determined the performance
parameters after 1-MeV electron irradiation of n^+ p p^+ silicon solar
cells of varying thicknesses with boron-doped p-base resisitivities of 1250
and 84 ohm-centimeters. Although more appropriately described as n^+ p p^+,
the higher resistivity cells approach the NIP condition. Because of the low
majority carrier concentration in the base, a significant portion of the
cell is in high injection under air mass zero (AMO) illumination. Thus high
injection theory was used in analyzing the experimental data.

EXPERIMENTAL

The pre-irradiation cell characteristics are shown in table I. The
cells were fabricated by Comsat under a program aimed, among other things,
at demonstrating that high-quality, thin-high-resisitivity cells could be
made using processing compatible with conventional practice (ref. 1). The
cells were irradiated, at room temperature, by 1-MeV electrons to a maximum
fluence of 10^{15} per square centimeter. Normalized short-circuit currents
as a function of fluence are shown in figures 1 and 2, while normalized open
circuit voltages are shown in figures 3 and 4.

ANALYSIS AND DISCUSSION

From figures 1 and 2, it is seen that the degradation in short-circuit
current is small for the thinner cells in both resistivities. On the other
hand, the highest degradation in I_{sc} occurs for the thickest 1250 ohm-
centimeter cell. This phenomenon is associated with bulk resistivity and
the absence of conductivity modulation occurring in high-injection
(ref. 2). We are presently formulating a comprehensive theory of NIP solar
cells which will be used in analyzing the complete cell characteristics. In

---

*NASA-ASEE Faculty Fellow. Permanent Address: Electrical Engineering
     Department, Cleveland State University, Cleveland, Ohio 44115.
**Temporary Employee. Present Address: Solar Energy Research Institute,
     Golden, Colorado 80401.

the absence of such a complete closed-form theory, we have limited ourselves, for the present to consideration of the open-circuit voltage. Our analysis is based on a theory which is valid for both low and high injection (ref. 3). A schematic diagram of the cell structure is shown in figure 2 where V_J and V_{JB} are the voltage developed across the front and back junctions, respectively, and V_B is the voltage drop across the cell base. For illumination from the n^+ side (ref. 3)

$$V_{oc} = V_J + V_{JB} - V_B \tag{1}$$

$$V_J = \frac{kT}{q} \ln \frac{I_{sc}}{I_o} \tag{2}$$

$$V_{JB} = \frac{kT}{q} \ln \left(1 + \frac{n_p(w)}{N_{ap}} \right) \tag{3}$$

$$V_B = \frac{kT}{q} \left(\frac{b-1}{b+1} \right) \ln \left(\frac{n_p(o) + \frac{bN_{ap}}{b+1}}{n_p(w) + \frac{bN_{ap}}{b+1}} \right) \tag{4}$$

In equation (4) $b = \mu_n/\mu_p$ where μ_n and μ_p are the mobilities of electrons and holes, respectively, in the base region, $n_p(o)$ and $n_p(w)$ are the base minority carrier concentrations at the front and back junctions, respectively, and N_{AP} is the acceptor concentration in the base.

Typical results for the voltage components are shown in figures 6 and 7. Considering the components of V_{oc}, we note that V_J, the front junction potential for the 84 ohm-centimeter cell, is significantly greater than that for the 1250 ohm-centimeter cell. Analysis based on equation (2) indicates that this differential is due predominantly to a lower value of I_o the device saturation current, for the 84 ohm-centimeter cell. Considering V_{JB}, it is noted that the rear junction potential is several times greater for the 1250 ohm-centimeter cell than for the lower resistivity cell. Analysis based on equation (3) shows that this is due primarily to the decreased acceptor concentration in the 1250 ohm-centimeter cell. With respect to V_B, it is noted from the figures that this component increases with fluence, contrary to what is observed for the other components. Computation of the base minority carrier concentrations at the junctions show that these concentrations change with fluence. Hence, from equation (4), a change in the minority carrier distribution with fluence is responsible for the observed rise in V_B.

In computing the preceding voltage components, the base minority carrier diffusion length was treated as an adjustable parameter, thus yielding computed values of diffusion length. The resultant pre-irradiation values are shown in table II where the high-injection values correspond to the present AMO data, while the low-injection values were obtained using a low level X-ray excitation technique (ref. 4). Also shown in the table are

diffusion length damage coefficients K_L obtained for both the high and low injection conditions. A thickness-dependent diffusion length is noted in high injection, while the diffusion lengths for low injection are significantly smaller than those obtained under high injection. In addition, the damage coefficients for high injection are lower than those for low injection. We are at present unable to give a consistent explanation for the thickness dependence of the diffusion length. On the other hand the relative diffusion length values are consistent with a saturation of recombination centers under high injection conditions.

CONCLUSION

The present results, obtained from an analysis of open-circuit voltages, show a much greater contribution to V_{oc} from the back junction than is the case for the lower resistivity ($\rho \leq 20$ ohm-centimeters) in common use. The base minority carrier distribution is seen to be significant in determining the contribution of V_B, the base contribution to V_{oc}. Although V_B is small, its value increases with increasing radiation fluence. In this connection, it is noted that, with illumination from the p^+ side, the sign of V_B becomes positive, and V_B itself becomes an additive term to V_{oc}.

Diffusion lengths determined under high injection conditions are significantly greater than those obtained under low injection, while damage coefficients under low injection are higher than these obtained under high injection conditions. Although additional analysis is required, this result appears to be consistent with a saturation of recombination centers under high injection.

REFERENCES

1. Allison, J. F.; Arndt, R. A.; and Muelenberg, A., Jr.: Thin n-i-p Radiation Resistant Solar Cell Feasability Study. NASA CR-159871, 1980.
2. Schwartz, R. J.; and Lundstrom, M. S.: Degradation of BSF Solar Cell Performance at High Intensity Due to a Loss of Base Conductivity Modulation. The Conference Record of the Fourteenth IEEE Photovoltaic Specialists Conference - 1980. IEEE, 1980, pp. 1392-1393.
3. Wu, C.-Y.; and Shen, W-Z: The Open Circuit Voltage of Back-Surface-Field (BSF) p-n Junction Solar Cells in Concentrated Sunlight. Solid State Electron., vol. 23, no. 3, Mar. 1980, pp. 209-216.
4. Rosenzweig, W.: Diffusion Length Measurements by Means of Ionizing Radiation," Bell Syst. Tech. J., vol. 41, no. 5, Sept. 1962, pp. 1573-1588.

TABLE I. – PRE-IRRADIATION CELL CHARACTERISTICS
[AR Coating; Ta_2O_5.]

Resistivity, ρ, ohm-cm	Thickness, t, μm	Open-circuit voltage, V_{oc}, mV	Short-circuit current, I_{sc}, mA	Fill factor, percent	Effi- ciency, percent	Number of cells
1250	61	577	128.9	74.8	10.3	2
1250	101	579	141.9	72.2	10.8	
1250	250	580	146.8	69.9	10.9	↓
85	56	589	130.5	75.4	10.6	
85	250	572	152.5	70.2	11.2	3

TABLE II. – DIFFUSION LENGTHS AND DAMAGE COEFFICIENTS

Resistivity, ρ ohm-cm	Thickness, t, μm	Diffusion length, L, μm		Damage coefficient, K_1	
		High injection[a]	Low injection[b]	High injection[a]	Low injection[b]
1250	61	859	224	4×10^{-12}	————
1250	101	1075	220	5.2×10^{-12}	9×10^{-12}
1250	250	1667	219	5.7×10^{-12}	20×10^{-12}
84	56	610	130	8.4×10^{-12}	18×10^{-12}
84	250	914	155	12×10^{-12}	40×10^{-12}

[a]From AMO data.
[b]From X-ray data.

202

NORMALIZED SHORT-CIRCUIT CURRENT VS 1 MeV
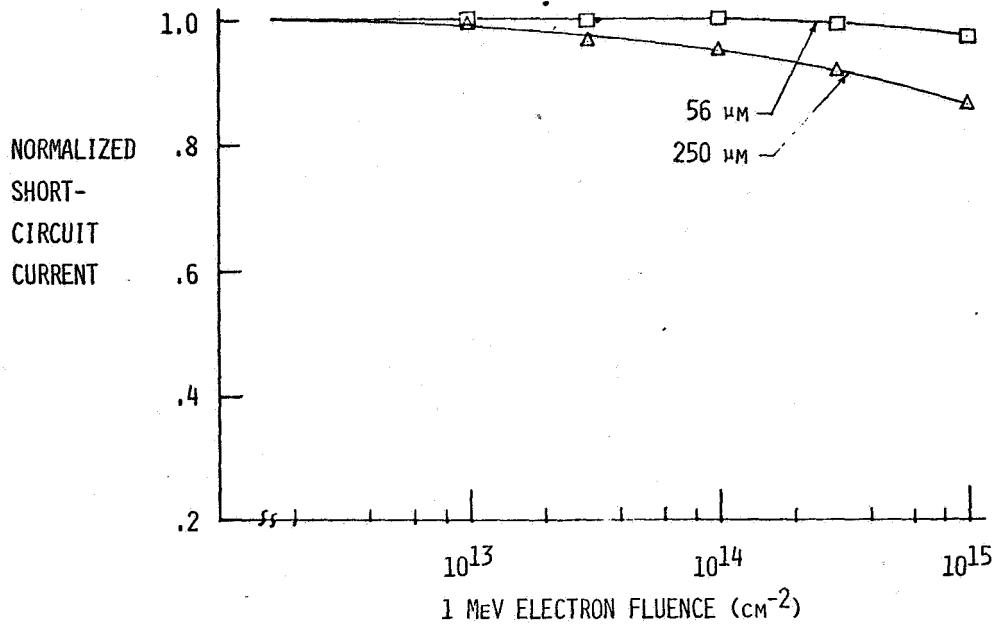ELECTRON FLUENCE FOR 84 OHM-CM N$^+$PP$^+$ CELLS

FIGURE 1

NORMALIZED SHORT-CIRCUIT CURRENT VS 1 MeV
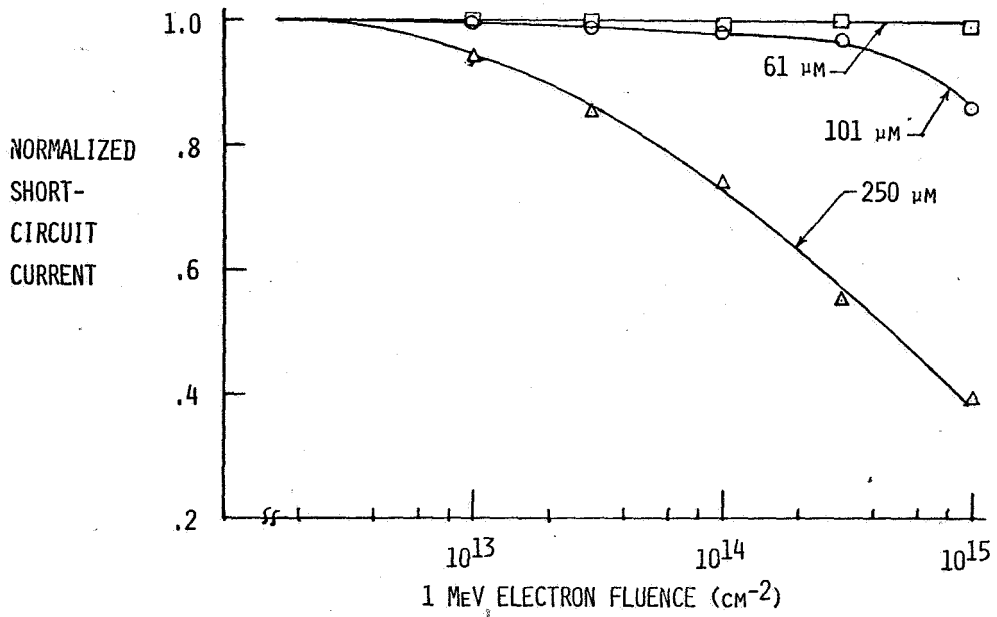ELECTRON FLUENCE FOR 1250 OHM-CM N$^+$PP$^+$ CELLS

FIGURE 2

NORMALIZED OPEN-CIRCUIT VOLTAGE VS 1 MeV ELECTRON FLUENCE
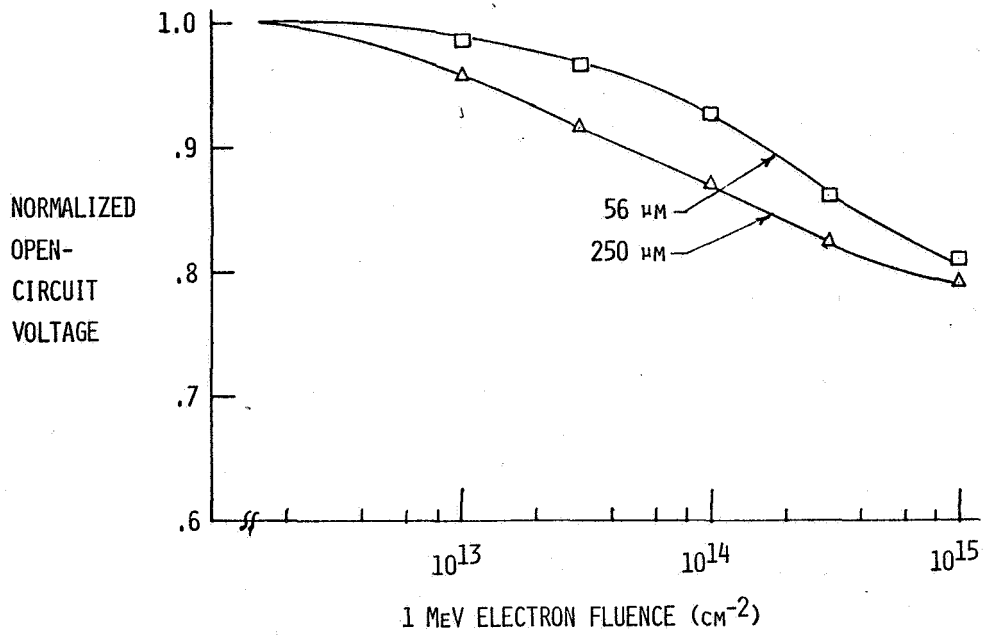FOR 84 OHM-CM N^+PP^+ CELLS

FIGURE 3

NORMALIZED OPEN-CIRCUIT VOLTAGE VS 1 MeV ELECTRON FLUENCE
FOR 1250 OHM-CM N^+PP^+ CELLS
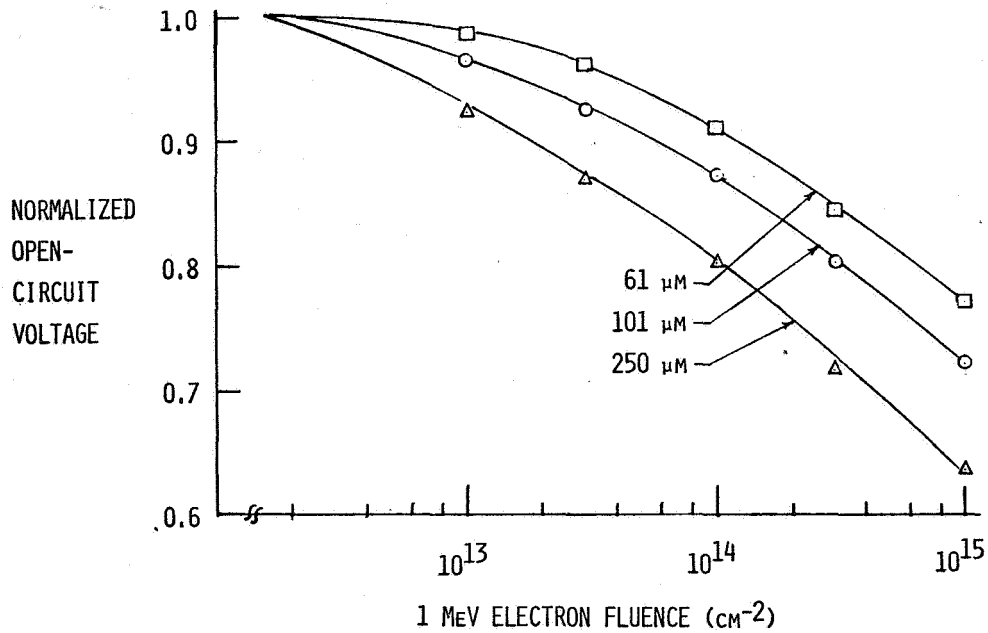

FIGURE 4

204
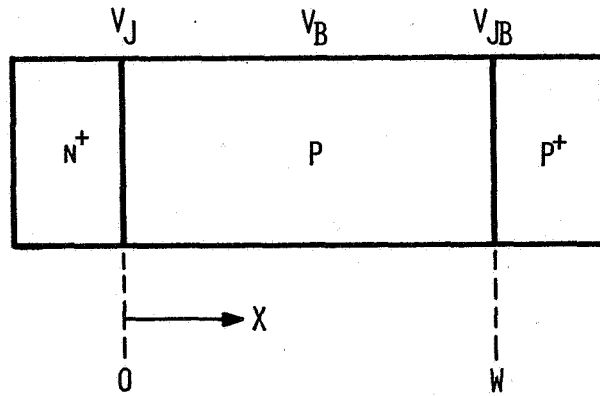
FIGURE 5

COMPONENTS OF OPEN-CIRCUIT VOLTAGE

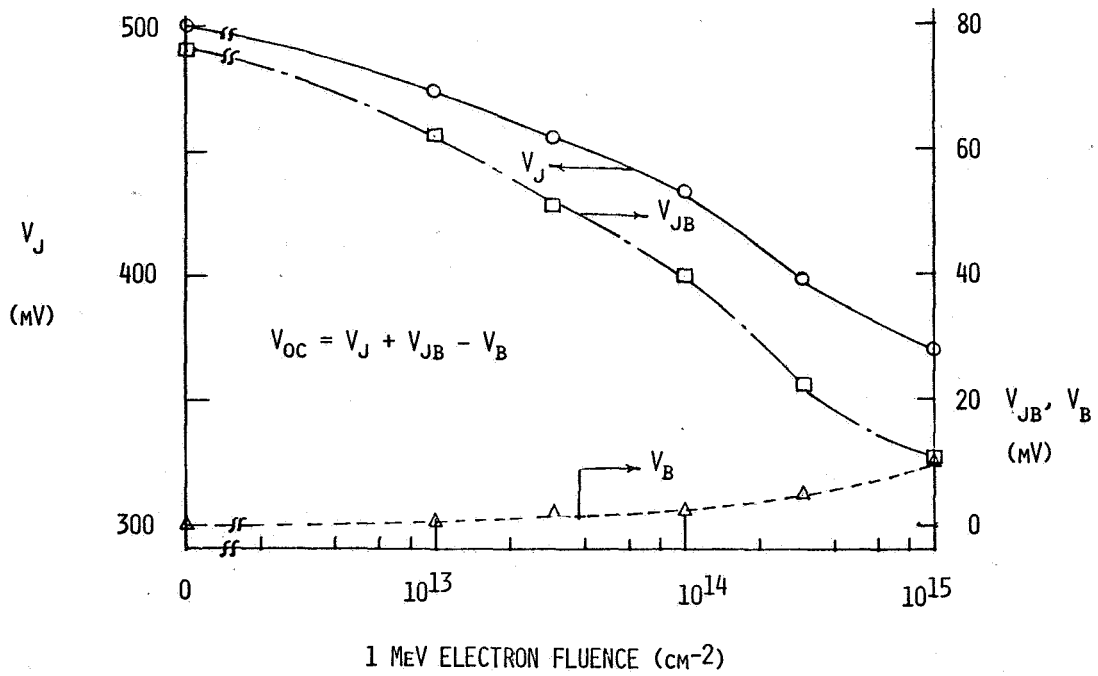FOR $\dot{N}^+PP^+$ CELLS 1250 Ω-CM, 250 μM THICK

$$V_{OC} = V_J + V_{JB} - V_B$$

1 MeV ELECTRON FLUENCE (CM^{-2})

FIGURE 6

205

COMPONENTS OF OPEN-CIRCUIT VOLTAGE

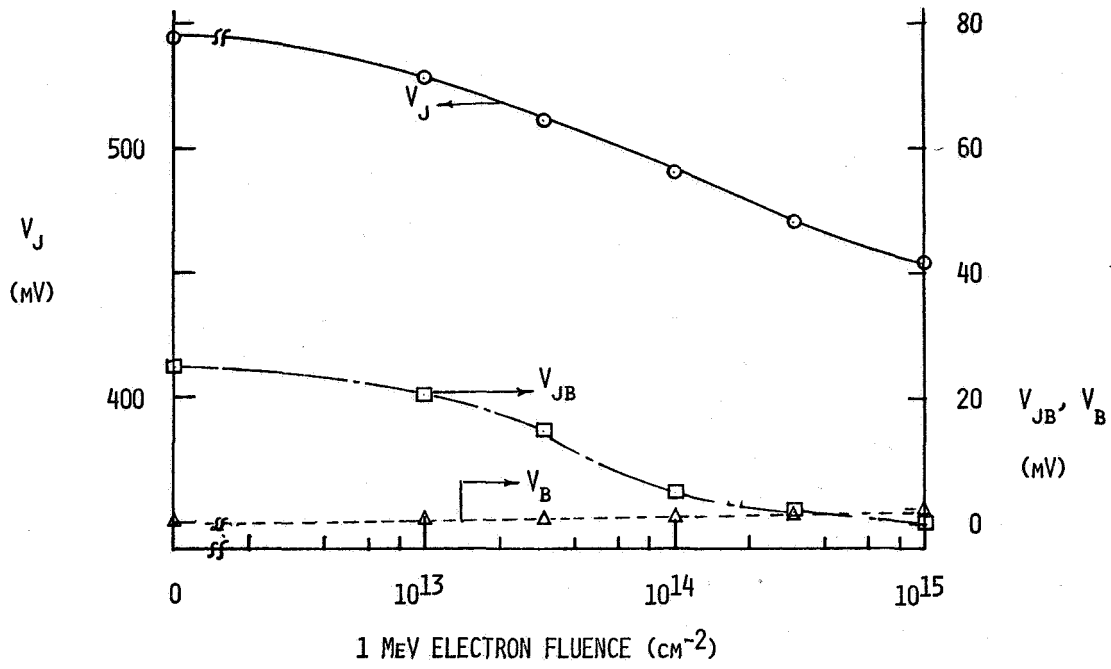FOR N^+PP^+ CELLS 84 Ω-CM, 250 μM THICK

FIGURE 7

RADIATION TOLERANCE OF VERTICAL
JUNCTION SOLAR CELLS*

Alan Scheinine and John Wohlgemuth
Solerex Corporation
Rockville, Maryland

SUMMARY

Extensive radiation testing of vertical junction (VJ) solar cells has demonstrated a radiation tolerance better than both planar silicon cells and at least one type of (AlGa)As-GaAs cell. Due to trade-offs between short circuit current and open circuit voltage the end of life (10^{16} 1 MeV electrons/cm^2) maximum power point is nearly independent of bulk resistivity between 2 and 10 ohm-cm, increases slightly with increasing wafer thickness between 3 and 11 mils, and increases slightly with increasing groove depth between 1 and 3 mils.

SILICON GEOMETRY

Vertical junction solar cells are made from wafers on which narrow grooves are formed using a preferential KOH etch. The echant is masked using a thermally grown oxide. The cells discussed in this report were made using a mask with 2.5 micron wide slots with 17.5 micron step and repeat. The geometry is shown in Figure 1. The bottom of a groove is as narrow as 2.5 microns while the top of a groove opens slightly so that a 75. micron deep groove has a groove width of about 5. microns and a wall width of about 12.5 microns at the top.

The grooved region is radiation tolerant because carriers generated in the narrow walls need diffuse only a short distance to the junction. While tapered walls would trap additional light, much of the additional light enters the silicon below the grooves thereby generating carriers relatively far from a junction. With straight walls, on the other hand, most of the light enters the flat tops of the walls. The cells described in this report use straight walls and a double layer antireflection coating to assure high absorption at the wall tops.

The wafers can be thinned prior to groove etching. We report herein vertical junction cells of 3, 5, 7 and 11 mils wafer thickness. The five mil thick cells have grooves as deep as three mils while the three mil thick cells have only one mil deep grooves.

DESCRIPTION OF VJ CELLS

The VJ cells reported herein were made with p-type CZ grown silicon of 2 ohm-cm and 10 ohm-cm bulk resistivity. The junction was formed by gaseous phosphorus diffusion. A p^+ back surface field was made using aluminum paste alloy. The contacts are titanium/palladium/silver. A double layer AR coating is used, which for uncoverslided cells consists of TiO_2 and MgF_2.

Using the above parameters cells have been made with peak power as high as 82 mW for a 2 cm x 2 cm cell (15.1% efficiency). It is this kind of cell whose radiation tolerance is described in this report.

A new type of VJ cell has been developed recently that uses both a back surface field and a back surface reflector (BSF/BSR). The reflector is made from vacuum evaporated aluminum. Prior to the aluminum evaporation the paste alloyed back is thoroughly cleaned in HCl acid. The BSF/BSR cells have had a peak power as high as 84 mW (15.5% efficiency) and lot averages as high as 82 mW. The BSF/BSR cells have not yet undergone radiation testing.

RADIATION TOLERANCE

A matrix of cells underwent radiation testing. The cells consisted of 2 and 10 ohm-cm bulk resistivity; 3, 5, 7 and 11 mils wafer thickness; and 1, 2 and 3 mils groove depth. The irradiation was done at the Naval Research Laboratory in Washington, D.C. The cumulative dosages were 3. x 10^{13}, 1.2 x 10^{14}, 3. x 10^{14}, 1. x 10^{15}, 3. x 10^{15} and 1. x 10^{16} 1 MeV electrons/cm^2. The electrical measurements shown on the graphs were made using a Xenon light source calibrated to AMO. The cells were annealled for 16 hours and 60°C.

The maximum power point at the end of life (EOL: 10^{16} 1 MeV e^-/cm^2) was similar for various resistivities, wafer thicknesses and groove depths. This is due to trade-offs between current and voltage. In regards to groove depth the deeper grooves have better current collection but lower voltage for a given dosage. Also, lower resistivity cells have higher voltage but lower current for a given dosage. The short circuit current for the various VJ cell parameters are shown in Figures 2, 3, 4 and 5 as a function of radiation dosage. Each cell type is represented by two 2 cm x 2 cm VJ cells.

Individual cell differences can be eliminated by dividing by initial electrical measurements. Figure 6 shows the relative short circuit current for 11 mil thick VJ cells and for planar cells co-processed with the VJ cells.

The open circuit voltage for various cell parameters are shown in Figure 7. The measurements for 2 mil groove depth are not shown since in all cases the results are intermediate between to 1 mil and 3 mil groove depths. Notice that the trend at the end of life -- 2 ohm-cm, 1 mil groove depth is highest and 10 ohm-cm, 3 mil groove depth is lowest -- is essentially the reverse of the trend in regard to current.

It is interesting to look at the voltage as a function of groove depth. As the junction area increases the voltage decreases. At first thought, one might expect the open circuit voltage to decrease as a logarithmic function of junction area such that a ten fold increase in junction area results in a 60 mV decrease in voltage. The actual decrease is about 20 mV. The relative insensitivity to junction area can be explained qualitatively by realizing that the diode saturation current is a function of the distribution and density of recombination sinks rather than the junction area. Viewed in another way, minority carriers injected from one wall junction may show up at the opposing wall indistinguishable from photogenerated carriers.

The open circuit voltage divided by the initial open circuit voltage is plotted versus radiation dosage in Figure 8.

The maximum power as a function of radiation dosage is shown in milliwatts in Figure 9 and relative to initial values in Figure 10. Only 7 mil thick wafers are shown since 11 and 5 mil wafers had very similar results. The differences in maximum power at the end of life can be seen more clearly on a magnified scale as used in Figure 11. The results for 2 ohm-cm and 10 ohm-cm silicon are averaged in Figure 11.

COMPUTER MODELLING

The damage coefficient of the silicon can be estimated by comparing the measured short circuit current with a computer program that models the VJ cells. The computer model solves the diffusion equation in two dimensions. The computer program takes into account the back surface recombination velocity, which in this case we assume to be 1000. cm/sec. The program also models the distribution of photogeneration inside the grooved silicon.

The computer model results depend on the diffusion length rather than the radiation dosage. The two are related by equation 1,

$$\left(\frac{1}{L}\right)^2 - \left(\frac{1}{L_{initial}}\right)^2 = K\Phi \qquad (1)$$

where Φ is the fluence, K is the damage coefficient, and L is the diffusion length. By fitting the computer model to the actual data we deduced a damage coefficient of roughly $1. \times 10^{-10}$ for 2 ohm-cm silicon and $4. \times 10^{-11}$ for 10 ohm-cm silicon.

The computer model was also used to study deeper groove depths. Four and five mil grooves were found to have power that is nearly identical to three mil grooves. This is consistent with the measured results which shows diminishing returns between two and three mil groove depth.

TILT ANGLE

An interesting phenomenon is that the VJ cell current increases for small tilt angles. This is particularly evident at the end of life, as shown in Figure 12. The explanation is that when the cell is tilted light that enters the groove must reflect from the groove walls several times before reaching the bottom, which enhances light absorption in the radiation tolerant walls. The percentage increase in power between 0° and 12.5° tilt is 2.3%, 4.5% and 9.1% for 1, 2 and 3 mil groove depths, respectively. The ratio of initial power under direct normal illumination to EOL power (10^{16} 1 MeV e^-/cm^2) at 12.5° tilt is 59.6%, 64.9% and 67.2% for 1, 2, and 3 mil deep grooves, respectively. Therefore the VJ cell has the capability of providing even more end of life power by proper orientation.

CONCLUSION

Figure 13 compares a VJ cell with a planar cell and with a (AlGa)As-GaAs cell. The VJ cell has 2 mil grooves, 11 mils wafer thickness and 10 ohm-cm resistivity. The planar cell is silicon with 2 ohm-cm resistivity. The (AlGa) As-GaAs cell was reported in "High Efficiency Solar Panel, Phase II, Gallium Arsenide", Interim Report, September 77 – January 79, Hughes Aircraft Company.

Since vertical junction solar cells have shown excellent radiation tolerance as well as good beginning of life power they should receive serious consideration for use in future missions.
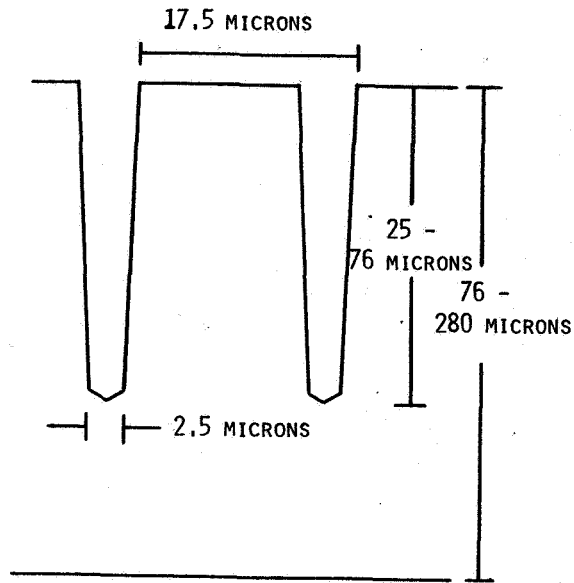
FIGURE 1. VERTICAL JUNCTION GEOMETRY

CUMULATIVE DOSAGE

(1 MEV ELECTRONS/CM^2

FIGURE 2. SHORT CIRCUIT CURRENT VS. FLUENCE, 2 CM X 2 CM
VJ CELL, 11 MILS WAFER THICKNESS.

CUMULATIVE DOSAGE

(1 MeV ELECTRONS/CM^2)

FIGURE 3. SHORT CIRCUIT CURRENT VS. FLUENCE, 2 CM X 2 CM
VJ CELL, 7 MILS WAFER THICKNESS

CUMULATIVE DOSAGE
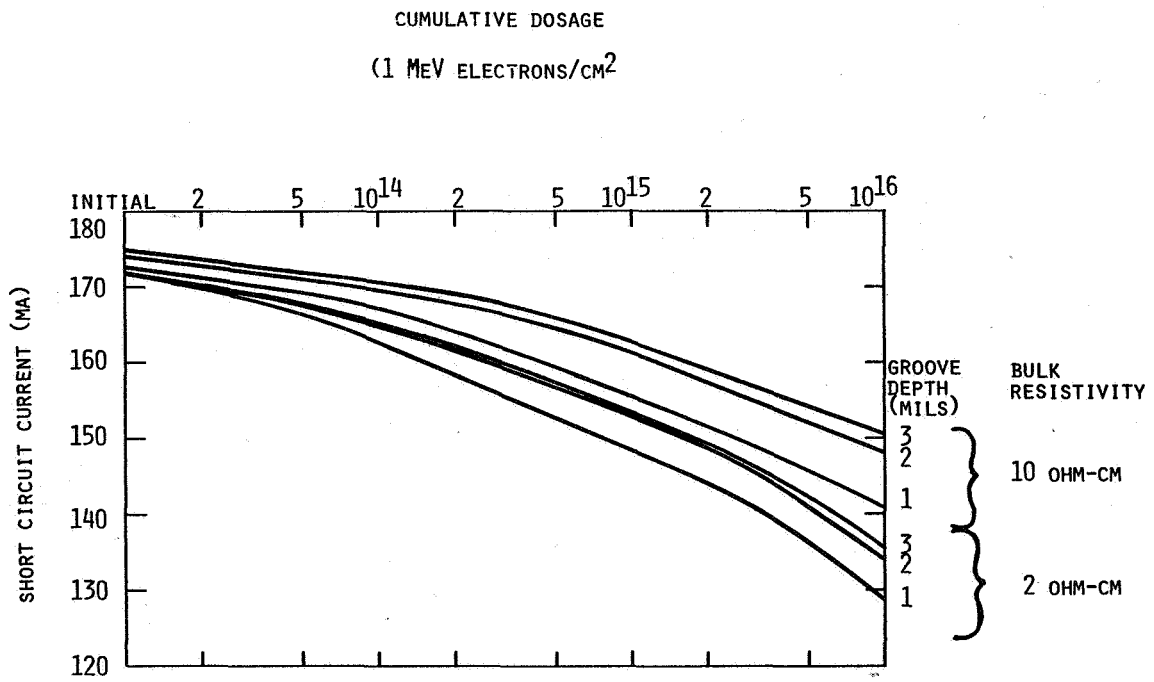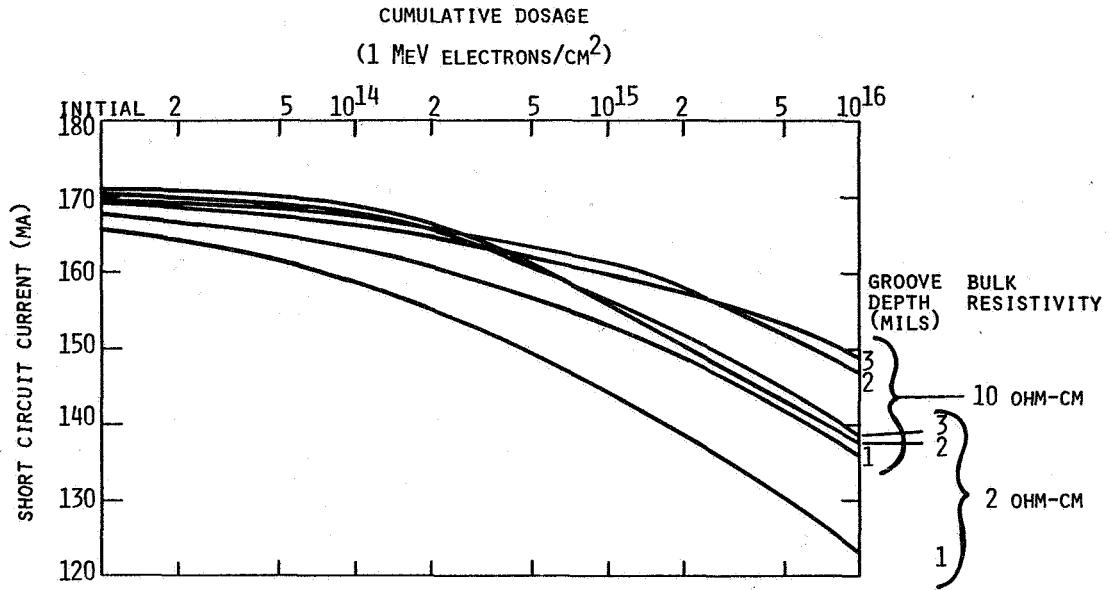
(1 MeV ELECTRONS/CM^2)
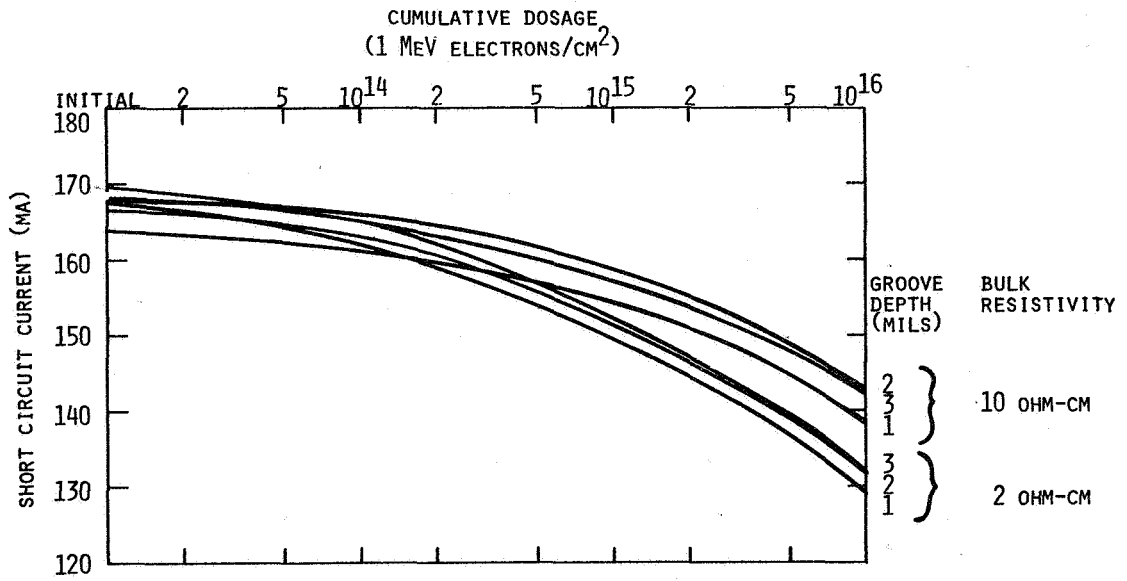
FIGURE 4. SHORT CIRCUIT CURRENT VS. FLUENCE, 2 CM X 2 CM
VJ CELL, 5 MILS WAFER THICKNESS

212
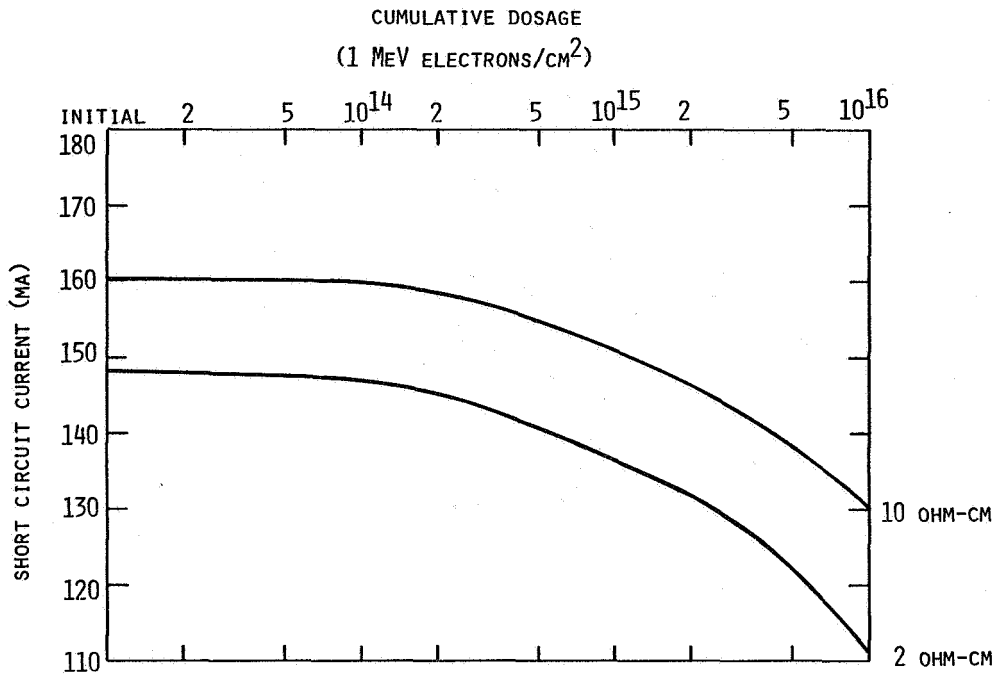
FIGURE 5. SHORT CIRCUIT CURRENT VS. FLUENCE, 2 CM x 2 CM VJ
CELL, 3 MILS WAFER THICKNESS, 1 MIL GROOVE DEPTH.
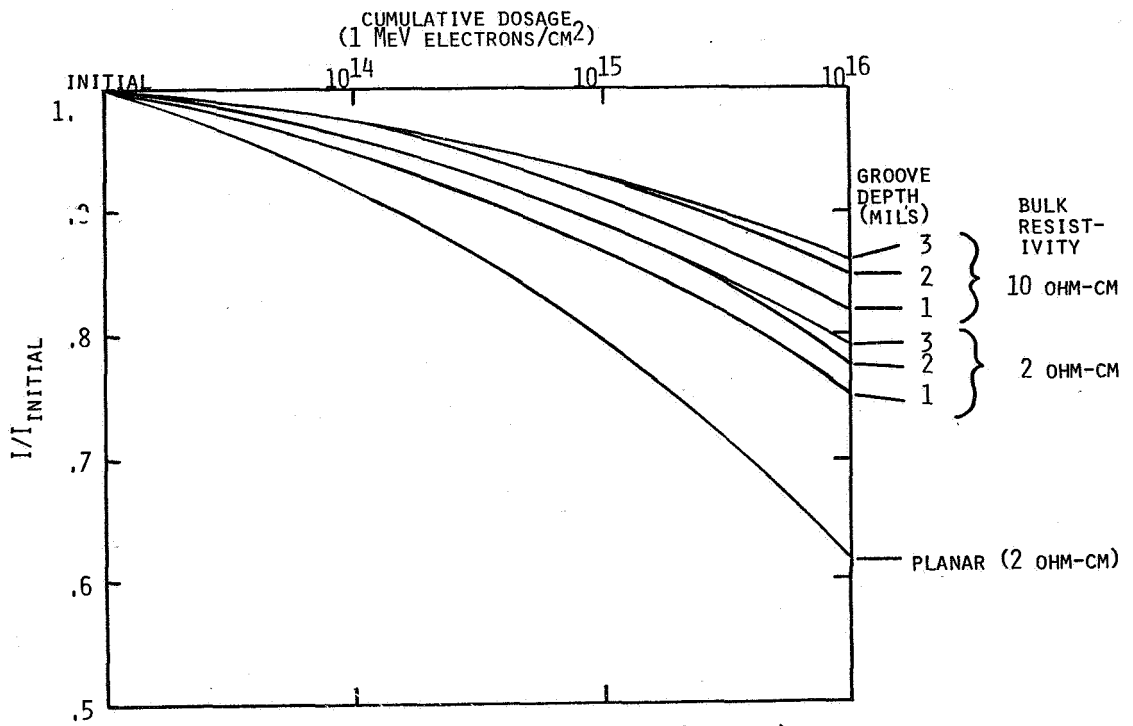
FIGURE 6. RELATIVE SHORT CIRCUIT CURRENT $(I/I_{INITIAL})$ FOR
VJ CELLS AND PLANAR CELL.
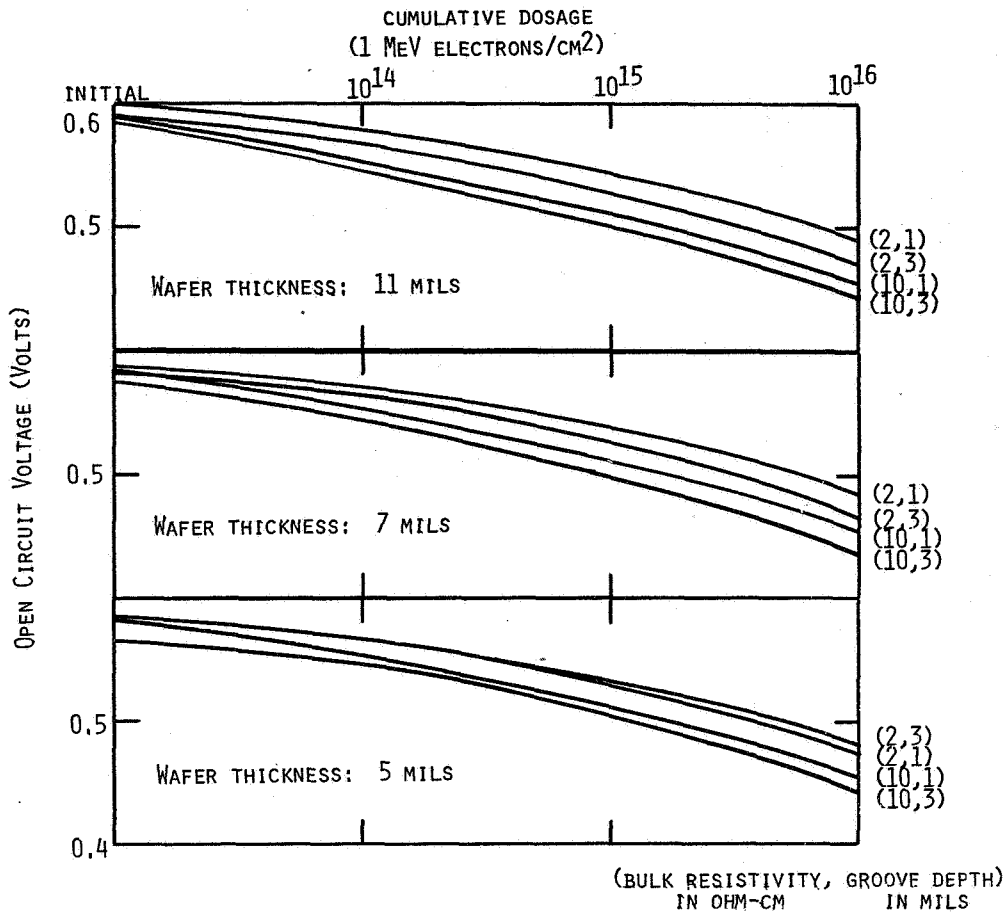
FIGURE 7. OPEN CIRCUIT VOLTAGE VERSUS RADIATION FLUENCE
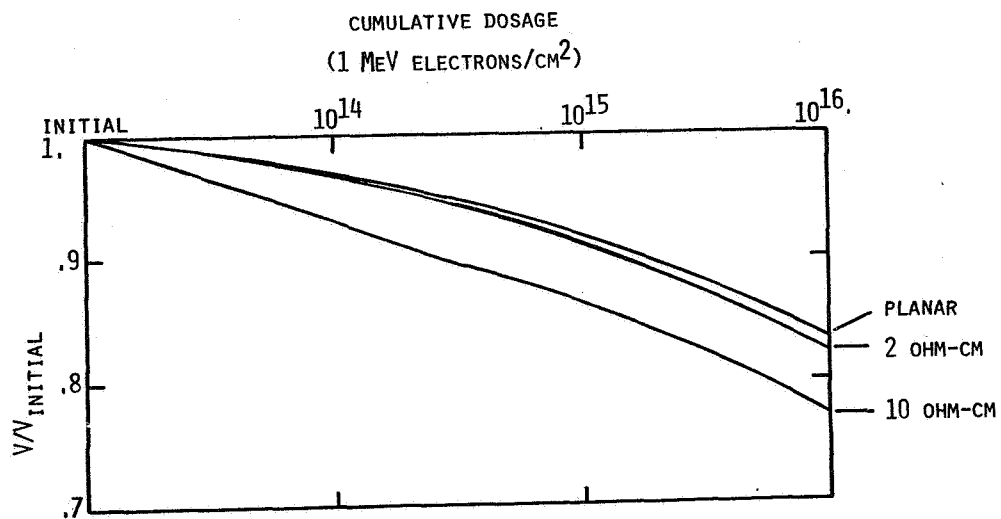
FIGURE 8. RELATIVE OPEN CIRCUIT VOLTAGE $(V/V_{INITIAL})$ FOR VJ CELLS AND PLANAR CELL.
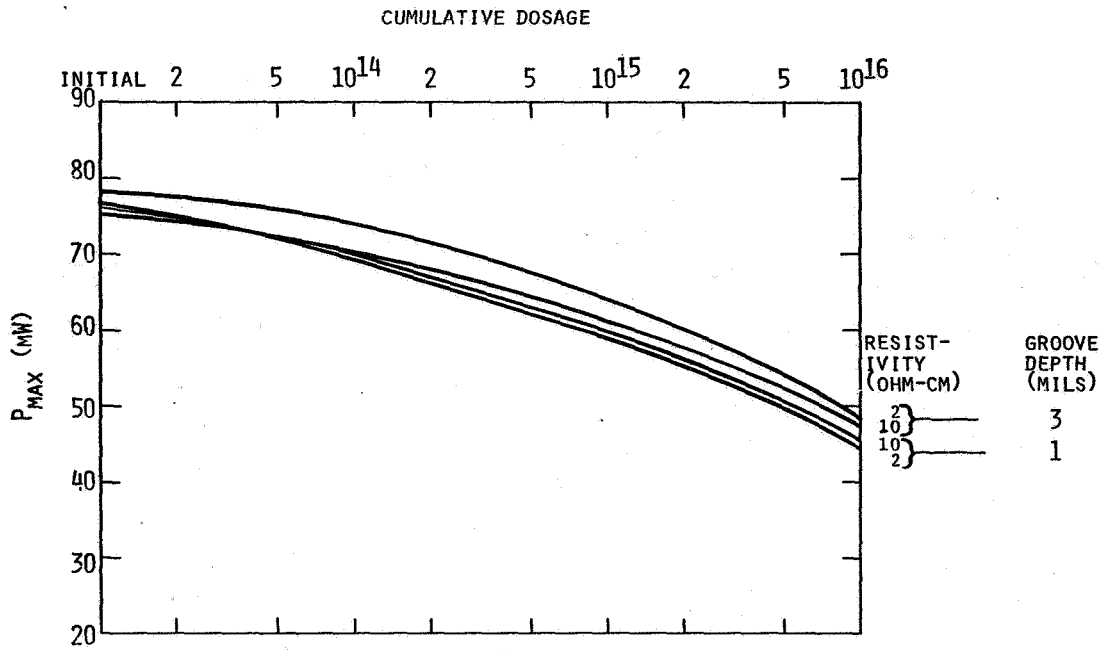
FIGURE 9. MAXIMUM POWER POINT VS. FLUENCE, 2 CM X 2 CM
VJ CELL, 7 MILS WAFER THICKNESS
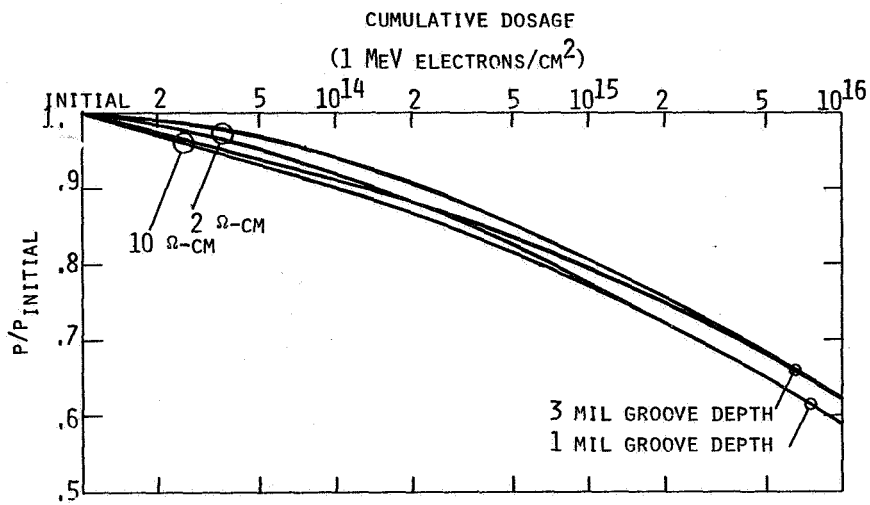
FIGURE 10. RELATIVE MAXIMUM POWER POINT $(P/P_{INITIAL})$ VS.
FLUENCE FOR 2 CM X 2 CM VJ CELLS, 7 MILS WAFER
THICKNESS.

215
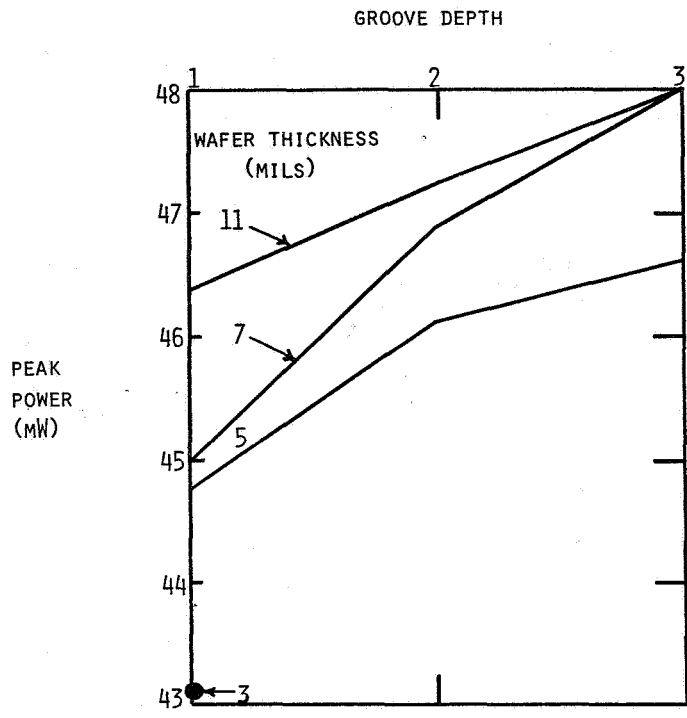
GROOVE DEPTH

FIGURE 11. END OF LIFE (10^{16} 1 MeV e^-/cm^2)
PEAK POWER AS A FUNCTION OF
WAFER THICKNESS AND GROOVE
DEPTH (AVERAGE OF 2 & 10 OHM-CM
BULK RESISTIVITIES)
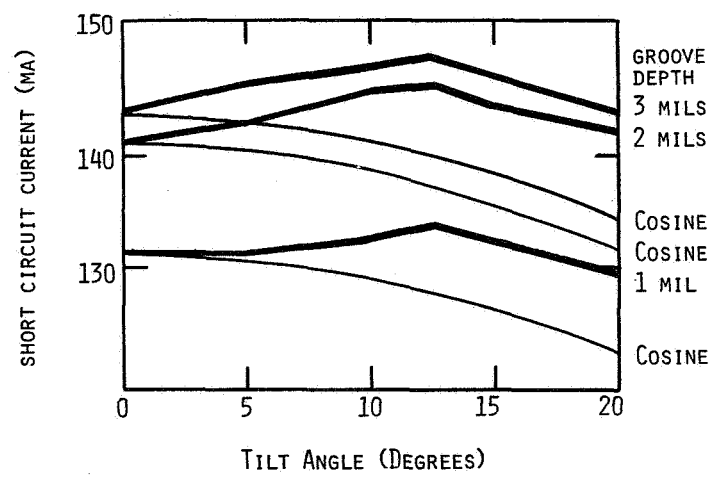
FIGURE 12. SHORT CIRCUIT CURRENT VS.
TILT ANGLE. CELL SPEC-
IFICATIONS: 10 OHM-CM,
11 MILS THICKNESS, 10^{16}
1 MeV ELECTRONS/CM^2
IRRADIATION.
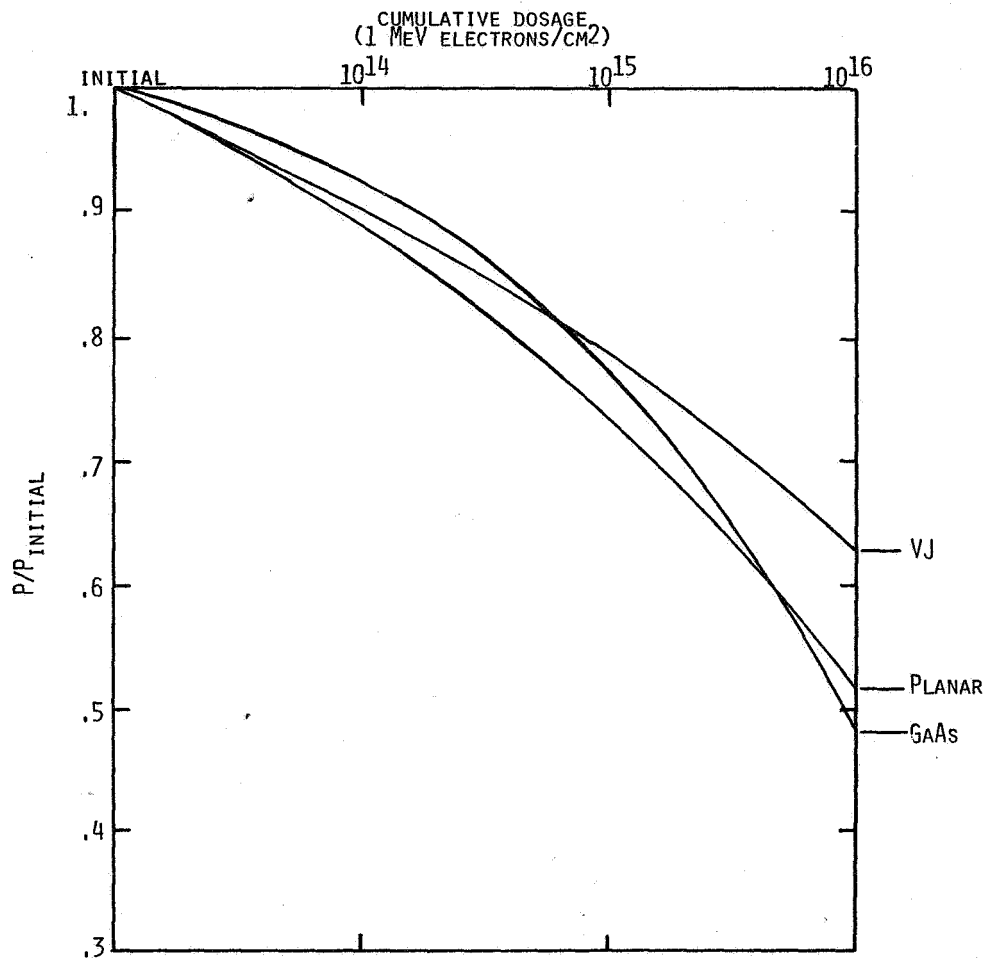
FIGURE 13. RELATIVE MAXIMUM POWER POINT $(P/P_{INITIAL})$ FOR
VJ CELL, SILICON PLANAR CELL, AND GAAS CELL

THREE-YEAR PERFORMANCE OF THE NTS-2 SOLAR CELL EXPERIMENT*

R. L. Statler and D. H. Walker
Naval Research Laboratory

SUMMARY

Twelve different solar cell modules from the NTS-2 experiment are functioning after more than three years in a severe trapped radiation orbit of 20,367 km (10,990 nm) circular, 63° inclination. The rate of maximum power (P_M) degradation may be fit to a predicted rate which is based on twice the value of 1-MeV electron equivalent damage fluence calculated from the space electron model AEI-7. The photovoltaic parameters of the cells are compared to their original values to demonstrate rank order of performance.

INTRODUCTION

Solar cell experiments on satellites can, in principle, provide the most reliable information for evaluating actual operating efficiency, degradation effects from the space environment, and synergystic effects of combined space environmental factors. It is obviously infeasible to duplicate in the laboratory the long term exposures to radiation spectrums, ultra-violet photons, high vacuum, and temperature cycling which are continuously present during a satellite experiment. There are, however, certain experimental difficulties which have impaired many space solar cell experiments, for example, a non-stabilized spacecraft, electronics failure, unknown error voltages sometimes attributed to ground loops, etc. The NTS-2 solar cell experiments have been fortunate to avoid these problems, having a stabilized spacecraft with the test panels favorably located to send data when the sun is within 3° of the zenith to the panel surface. The data acquisition system has functioned without any problems.

SYMBOLS

I-V curve	photovoltaic current-voltage curve
I_{sc}	short-circuit current, mA
P_M	maximum power point, mW
V_{oc}	open circuit voltage, mV
BOL	beginning of life

DENI   damage equivalent normally incident

P/Po   relative maximum power

X_j p/n junction depth

OBJECTIVES OF THE EXPERIMENT

The objectives of the experiment may be listed as follows:

- Compare radiation damage among advanced silicon cells utilizing textured surfaces, shallow junctions, and back surface fields.

- Study space environment degradation damage in an aluminum-gallium-arsenide cell (AlGaAs/GaAs) having a junction depth of 1 μm.

- Compare space degradation in a conventional deep-junction cell (0.3-0.5 μm) using an adhesively bonded coverslip vs. the cell using an electrostatically bonded coverslip.

- Compare degradation in the Comsat nonreflecting cell using a conventional fused silica coverslip with an ultraviolet cutoff filter vs. a coverslip without a filter.

- Study the performance of the vertical junction cell developed by Solarex for the Air Force Aero Propulsion Laboratory.

- Compare space degradation in a textured shallow junction cell having an adhesively bonded fused silica coverslip vs. the cell having an FEP Teflon bonded fused silica coverslip.

- Compare performance of lithium-doped p/n cells on NTS-2 with similar cells on NTS-1.

- Study the performance of a 1 x 2 cm planar blocking diode developed by Spectrolab for the Air Force Aero Propulsion Laboratory.

- Compare the values of solar cell parameters measured with a solar simulator to those obtained in space.

- Evaluate the accuracy of space degradation predictions based on trapped radiation models.

DESCRIPTION OF EXPERIMENTAL PANELS

The experimental hardware consists of two solar panels and an

220

electronics subsystem. The panels each have 7 modules of five cells connected in series. The cells individually measure 2 cm x 2 cm. The modules are mounted on two 0.64-cm-thick aluminum honeycomb panels. There is also an experimental blocking diode which is a 1 x 2 cm planar device with a polished aluminized surface. This diode, in series with the lithium-doped cells of module #11, comprise the experiment designated Experiment 12 in Table 1. The panels are thermally isolated from the spacecraft structure; therefore, in order to allow for heat dissipation which can only be accomplished by thermal radiation from the front panel surface, the modules were evenly spaced on the panel and the intervening regions were coated with a white thermal control coating, Dow Corning 92007, which covers 52 percent of the panel surface. Temperatures are monitored at the rear surface of four cells by means of three thermistors and one wire resistance thermometer. The thermistors are accurate to within $\pm$ 3 degrees C up to 100 degrees C, and the wire thermometer is accurate to within $\pm$ 2 degrees C to above 120 degrees C.

The experimental panels are continuously illuminated by the sun (except during the biannual eclipse season of 25 days). The experiment is mounted on the satellite surface which faces the direction of travel about the earth, and twice during each orbit the satellite is rotated 180 degrees in yaw so that the paddles (and experiment) face the sun. Table 1 gives a brief description of the experiments showing the type and thickness of the solar cell, the type and thickness of the coverslip, the type of coverslip bonding, the interconnect material, and the beginning-of-life (BOL) cell efficiency.

EXPERIMENTAL RESULTS

Data were recorded at weekly intervals during the first 6 months, then at monthly intervals thereafter. The data shown here extend from the first day to day 1116. It should be pointed out that day one is designated as the day the main solar paddles were deployed. Although the spacecraft was launched on 23 June 1977, the main paddles remained folded over the experiment panels until NTS-2 was on station and despun on 7 July 1977. At that time the main solar paddles were unfolded, and the experimental panels were exposed to the total space environment.

The current-voltage characteristics of the solar cell arrays are telemetered in real time as the satellite passes over the tracking station at Blossom Point, Maryland. The electronic circuit measures the I-V curve for each module in sequence reading out current-voltage values for evenly-spaced points from I_{sc} to V_{oc}. Each cell module is short-circuited except when it is being stepped through the I-V curve. The average value of I_{sc} measured in space on the first day of exposure agreed with the solar simulator values to 1.41 $\pm$ 0.99 percent. The agreement between V_{oc} on initial space exposure and the solar simulator values was 1.24 $\pm$ 2.02 percent. The values of I_{sc}, V_{oc} and P_M measured on the first day in orbit are listed in Table 2.

221

Module Failures

Three experiments have ceased to function: on day 69, the Solarex space cell (Exp. 8) failed; on day 729 the Solarex vertical junction cell (Exp. 7) failed; on day 783 the Spectrolab Textured Helios Reflector cell (Exp. 9) failed. After analyzing the data acquisition electronics it was decided that these failures were not caused by faults in the data processor but were the result of open circuits occurring in the cell modules. These failure modes are discussed in references 1 and 2.

Radiation Environment

The observed degradation rates of the NTS-2 solar cell experiments were utilized to estimate equivalent 1 MeV electron fluence in the 11,000 nm circular orbit. Prior to launch, an estimation of the equivalent fluence based on the AEI-7 LO electron model (ref. 3) from the National Space Science Data Center gave a value of 2×10^{14} DENI 1-MeV e/cm^2-yr for a solar cell with a 0.030 cm fused silica coverglass. An earlier estimate based on the values published in reference 4 gave a lesser value of 3.3×10^{13} 1-MeV electron annual fluence. This result is obtained using the electron environment models designated as AE 3, AE 4, and AE 5. These models have been superseded by the more accurate AEI 7 model. We have attempted to fit the observed degradation rates in several of the silicon cell experiments to degradation curves in reference 4 which were obtained by irradiating similar types of solar cells with electron accelerators. For this purpose we have used the space data from experiments 1, 2, 3, 4, 10, and 13. It is to be noted that the proton fluence at this orbit is defined by the proton models AP5, AP6, and AP7 to be negligible with respect to the electron damage environment (at least three orders of magnitude less). Solar flare proton events since launch have been weak enough to be ignored. The results of fitting power degradation rates from space data to the reference 4 curves indicate that the equivalent 1-MeV electron annual fluence is approximately 3.5×10^{14} e/cm^2-year. Although this is nearly twice the value obtained from the AEI 7 model, it is not large compared to the stated intrinsic uncertainties in the space flux data from which the models are generated. These uncertainties range from x2 to x10 (ref. 4).

Gallium Arsenide Solar Cell

An (AlGa)As-GaAs solar cell covered with 12 mil 7490 fused silica and DC93-500 comprises Exp. 15. This module, which was made by the Hughes Research Laboratory, had an efficiency of 13.6 percent. These cells have a junction depth of 1 micon, and are interconnected by a metal-filled epoxy. This experiment behaved in a very unusual manner during the first 3 months. The GaAs cells sustained a sharp drop in power output as measured on the first orbit and throughout the next 28 days as shown in figure 1. The P_M gradually increased to its peak value on the 100th day, then the normal rate of radiation degradation became evident. The behavior during the early days has not been positively explained; it may be related to the epoxy interconnect material for lack of other identifiable mechanisms in the cell.

222

The maximum power degradation of the gallium arsenide cell is shown in figure 1 along with that of the highest output cell, which was the Comsat nonreflective cell, and with the Spectrolab Helios cell, referred to also as "K-6." The Helios cell is a shallow junction, polished surface, back surface field cell. The fourth cell on the figure is a p/n lithium-doped cell from the 1972 period when there was a concerted effort to develop a radiation hardened solar cell. Lithium was observed to enhance room temperature annealing of radiation induced defects in p/n silicon cells. . The annealing was observed to be more prominent in the case for proton damage than for electron damage. Hence the NTS-2 results shown here are somewhat surprising, in that the power output of this cell is nearly as high as the power of the Helios cell after 1116 days (equivalent to 1.1×10^{15} 1-MeV e/cm^2). This behavior leads to the speculation that the reason for the increased radiation environment, which is about twice that predicted from the trapped radiation models, may be ascribed to an enhanced proton environment at this altitude.

Another example of simultaneous annealing occurring during the radiation damage process is illustrated in the case of the gallium arsenide cell in fig. 2. This figure shows the relative power (power remaining after radiation divided by the initial power) reported by Loo, Kamath, and Knetchli (ref. 5) for aluminum-gallium/gallium arsenide solar cells with junction depths of 1.0 μm and 0.5 μm, obtained after electron accelerator measurements at near room temperature. The NTS-2 gallium arsenide cells are known to have junction depths of 1.0 μm. The relative power of these cells is plotted at 1, 2, and 3 years, assuming an annual fluence of 3.5×10^{14} 1-MeV e/cm^2-year. After 3 years, the cells which have been at temperatures near 100°C almost continuously while being irradiated have 50 percent greater power than those in accelerator tests. This behavior suggests the possibility of annealing of primary radiation defects during the time at which radiation lattice displacements are being made.

Effect of Junction Depth

One source of improvement in cell efficiency has been to reduce the depth of the diffused p/n junction in silicon cells. Shallow junction cells are more efficient converters of ultraviolet energy. One cell type, module #1, the OCLI conventional, was included as a baseline to show the improvements in the advanced cells. The OCLI conventional is a typical "deep-junction" 10 ohm-cm cell, in which the diffused junction is about 0.5 μm deep. More advanced cells have junctions in the range of 0.15 to 0.30 μm. Figure 3 clearly shows the gain in power afforded by the newer cells, such as the OCLI Violet, the HESP, and the Spectrolab Textured Hybrid. At 1116 days the power output of the advanced cells was higher by 22 to 31 percent. Figure 3 also shows the interesting fact that the slope of the power degradation curve of the Textured Hybrid cell is much less than that for the other cells. This Hybrid cell module is the one utilizing FEP Teflon as the coverslip bonding medium, while the other modules shown here use an adhesive system. These results suggest that the adhesive bonded cells undergo additional power loss attributed to radiation and/or

ultraviolet darkening of the adhesive. These conclusions are presented in more detail in reference 1.

CONCLUSIONS

The power output at beginning of life and after 1116 days are compared in the bar graph in fig. 4. All data have been corrected to cell temperatures of 50°C. The temperature coefficients used are discussed in ref. 6. Table 3 is a listing of the percentage changes in I_{sc}, V_{oc}, and P_M for all experiments after three years.

The following conclusions may be stated after observing three years of orbital performance:

(1) The effect of the trapped electron environment at 11,000 nm, 63° inclination orbit on silicon solar cells can be fairly well predicted by multiplying the equivalent 1-MeV fluence obtained from the NASA AEI-7 model by a factor of two. The harder environment may be due to higher fluxes of trapped protons.

(2) The total loss in P_M for production type silicon cells varies from a high of 35.0 percent in a 10.7 percent conventional two ohm-cm cell with adhesive bonded 12 mil silica cover to 21.1 percent loss in a 11.1 percent textured shallow junction cell with an FEP bonded 6 mil silica cover.

(3) The (AlGa)As-GaAs cell with a 1 micron junction depth retains good power output at 44.0 mW. being surpassed only by the Comsat Nonreflecting cell (Exp. 6) at 49.4 mW and the OCLI violet cell at 46.6 mW.

REFERENCES

1. Statler, R.L.; Walker, D.H.; and Faraday, B.J.: Performance of the
Solar Cell Experiment on the NTS-2 Satellite. Photovoltaic Generators
in Space Symposium. ESA SP-147. June 1980, pp. 167-176.

2. Statler, R.L.; and Walker, D.H.: NTS-2 Solar Cell Experiment After Two
Years in Orbit. Fourteenth Photovoltatic Specialists Conference,
Institute of Electrical and Electronics Engineers, Inc., 1980, pp.
1234-1239.

3. Stassinopoulos, E.G.: Charged Particle Radiation Environment for NTS-2
and NTS-3 Satellites. NASA Goddard Space Flight Center. X-601-80-1,
December 1979.

4. Tada, H.Y; and Carter, J.R.: Solar Cell Radiation Handbook. Jet
Propulsion Laboratory, JPL Publication 77-56.1 November 1977.

5. Loo, R.; Kamath, G.S.; and Knechtli, R.C.: Radiation Damage in GaAs
Solar Cells. Fourteenth Photovoltaic Specialists Conference, Institute
of Electrical and Electronics Engineers, Inc., 1980, pp. 1090-1097.

6. Statler, R.L.; and Walker, D.H.: The NTS-2 Satellite Solar Cell
Experiment. Proceedings of the Thirteenth Intersociety Energy
Conversion Engineering Conference. 1978, pp. 97-104.

Table 1

Exp. No.	Cell Type	Thickness (cm)	Coverslip (cm)	Coverslip Bond (cm)	Interconnect	Efficiency 28°C (%)
1	OCLI Conventional, 2 ohm-cm	0.025	Corning 7940, AR and UV, (0.030)	R63-489	Cu/Ag	10.7
2	Spectrolab "Helios" p^+ 15-45 ohm-cm	0.0228	Ceria microsheet w/o AR, (0.025)	DC 93-500	Moly/Ag (.0025)	11.5
3	Spectrolab Hybrid Sculptured 7-14 ohm-cm	0.020	Corning 7940, AR and UV, (0.0152)	DC 93-500	Moly/Ag (.0025)	10.5
4	Spectrolab Hybrid Sculptured 7-14 ohm-cm	0.020	Corning 7940, w/o AR or UV, (0.0152)	FEP Teflon (0.0051)	Moly/Ag (.0025)	11.1
5	Comsat Non-Reflecting, p^+ Textured, 1.8 ohm-cm	0.025	Corning 7940, AR, w/o UV (.030)	R63-489	Ag, thermo-compression bonding	14.5
6	Comsat Non-Reflecting, p^+ Textured, 1.8 ohm-cm	0.025	Corning 7940, AR and UV (.030)	R63-489	Ag; thermo-compression bonding	14.6
7	Solarex Vertical Junction, p^+, 1.5 ohm-cm	0.030	Ceria microsheet w/o AR (.0152)	Sylgard 182	Ag mesh	13.0
8	Solarex Space Cell, p^+ 2 ohm-cm	0.025	Ceria microsheet w/o AR (0.0152)	Sylgard 182	Ag mesh	12.8
9	Spectrolab "Helios" p^+ Sculptured, BSR, 10 ohm-cm	0.030	Corning 7940 (.030) w/o AR or UV	FEP teflon (.003)	Ag mesh (.003)	14.2
10	OCLI Violet, 2 ohm-cm	0.025	Corning 7940 (.030) AR and UV	R63-489	Cu/Ag	13.5
11	Spectrolab P/N Li-doped 15-30 ohm-cm, Al contacts	0.020	Corning 7940, AR and UV, (0.015)	Silicone	Aluminum (.0025) Ultrasonic welding	10.8
12	Spectrolab Planar Diode in series with Exp. 11	NA	NA	NA	NA	NA
13	OCLI Conventional, 2 ohm-cm	0.025	Corning 7070 (.028)	Electrostatic bonding	Cu/Ag	10.2
14	Spectrolab HESP, no p^+, Sculptured, 2 ohm-cm	0.030	Corning 7940, AR and UV (0.0305)	R63-489	Moly/Ag (.0025)	13.6
15	Hughes Gallium-Aluminum Arsenide	0.0305	Corning 7940, AR and UV, (0.0305)	DC 93-500	Aluminum GPD (.0025), epoxy	13.6

Table 2
NTS-2 SOLAR CELL EXPERIMENTS

EXPERIMENT NO.	CELL TYPE	FIRST DAY IN ORBIT		
		V_{OC}(MV)	I_{SC}(MA)	P_M (MW)
1	OCLI CONV. 2 OHM-CM	549	136.5	56.3
2	SPECTROLAB HELIOS (NTS-2)	546	155.5	60.6
3	SPECTROLAB TEXT. HYBR., F.S.	508	154.0	53.5
4	SPECTROLAB TEXT. HYBR., FEP, F.S. W/O FILTER	505	149.6	55.4
5	COMSTAT TEXT. F.S., W/O FILTER	555	180.4	74.7
6	COMSAT TEXT., F.S.	549	178.7	72.0
7	SOLAREX VERT. JUNC.	521	160.5	62.2
8	SOLAREX SPACE CELL	541	158.8	63.1
9	SPECTROLAB TEXT. HELIOS REFLECTOR	545	175.8	70.0
10	OCLI VIOLET, F.S.	552	164.3	66.6
11	SPECTROLAB HASP W/O DIODE	559	132.6	55.8
12	SPECTROLAB HASP W/DIODE	523	132.4	42.1
13	OCLI CONV., ESB	490	146.1	46.8
14	SPECTROLAB HESP	528	165.8	63.8
15	HRL AlGaAs	895	100.6	61.4

*THESE DATA HAVE BEEN CORRECTED TO 50°C AT ONE-SUN AND AIR MASS ZERO (AM0)

Table 3
NTS-2 SOLAR CELL EXPERIMENTS

SUMMARY OF CHANGES IN PHOTOVOLTAIC PARAMETERS*

EXPERIMENT NO.	CELL TYPE	PERCENT LOSS DAY 1 TO DAY 1116		
		MAXIMUM POWER	SHORT-CIRCUIT CURRENT	OPEN-CIRCUIT VOLTAGE
1	OCLI CONV. 2 OHM-CM	35.0	30.0	7.3
2	SPECTROLAB HELIOS (NTS-2)	33.2	25.3	11.5
3	SPECTROLAB TEXT. HYBR., F.S.	28.0	23.2	5.3
4	SPECTROLAB TEXT. HYBR., FEP, F.S. W/O FILTER	21.1	15.1	4.8
5	COMSAT TEXT. F.S., W/O FILTER	55.3	49.2	9.7
6	COMSAT TEXT., F.S.	31.3	28.4	7.1
7	SOLAREX VERT. JUNC.	(MODULE FAILED ON DAY 759)		
8	SOLAREX SPACE CELL	(MODULE FAILED ON DAY 69)		
9	SPECTROLAB TEXT. HELIOS REFLECTOR	(MODULE FAILED ON DAY 783)		
10	OCLI VIOLET, F.S.	30.0	24.7	6.0
11	SPECTROLAB HASP W/O DIODE	29.7	19.0	7.2
12	SPECTROLAB HASP W/DIODE	35.7	19.3	8.6
13	OCLI CONV., ESB	23.9	15.7	7.1
14	SPECTROLAB HESP	32.1	25.3	10.2
15	HRL AlGaAs	28.3	28.9	4.6

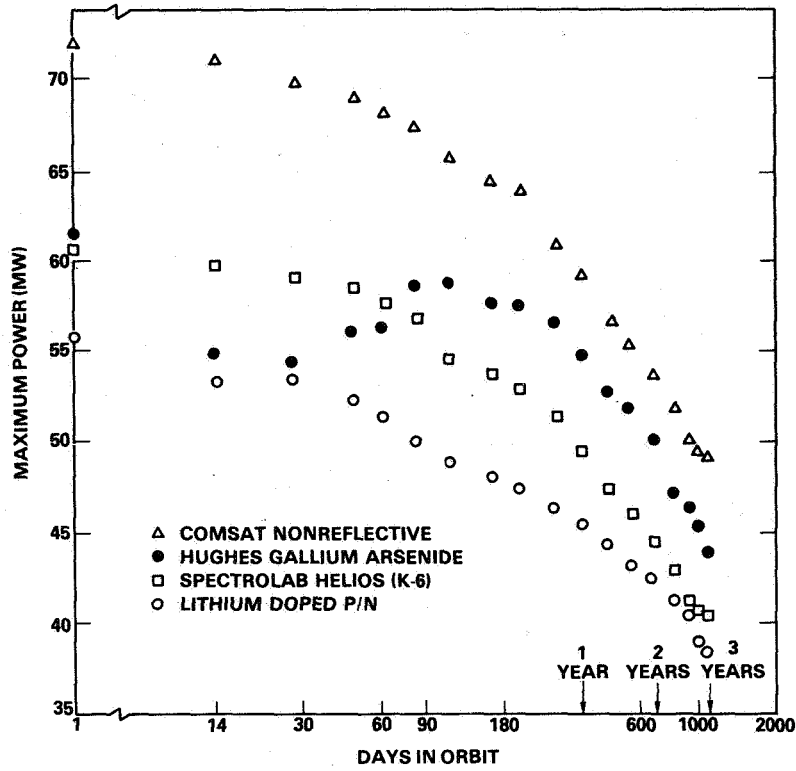* THESE DATA HAVE BEEN CORRECTED TO 50°C AT ONE-SUN AND AIR MASS ZERO (AM0)

Fig. 1. Maximum power degradation of four cell types: Exps. 2, 6, 11, and 15.
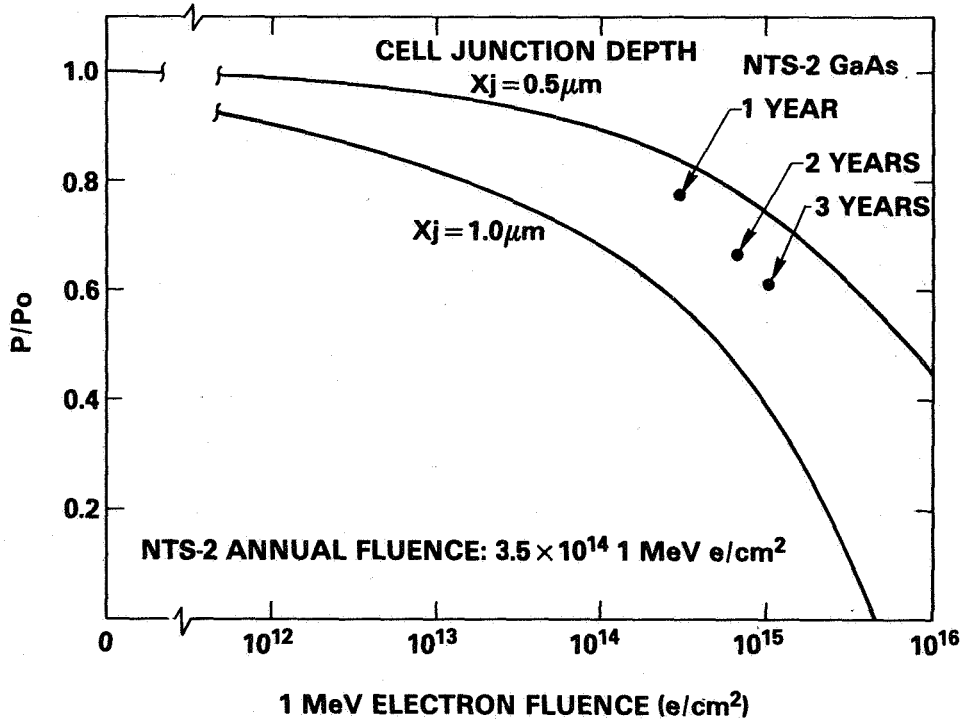

Fig. 2. Comparison of NTS-2 gallium arsenide with electron accelerator degradation (ref. 5)
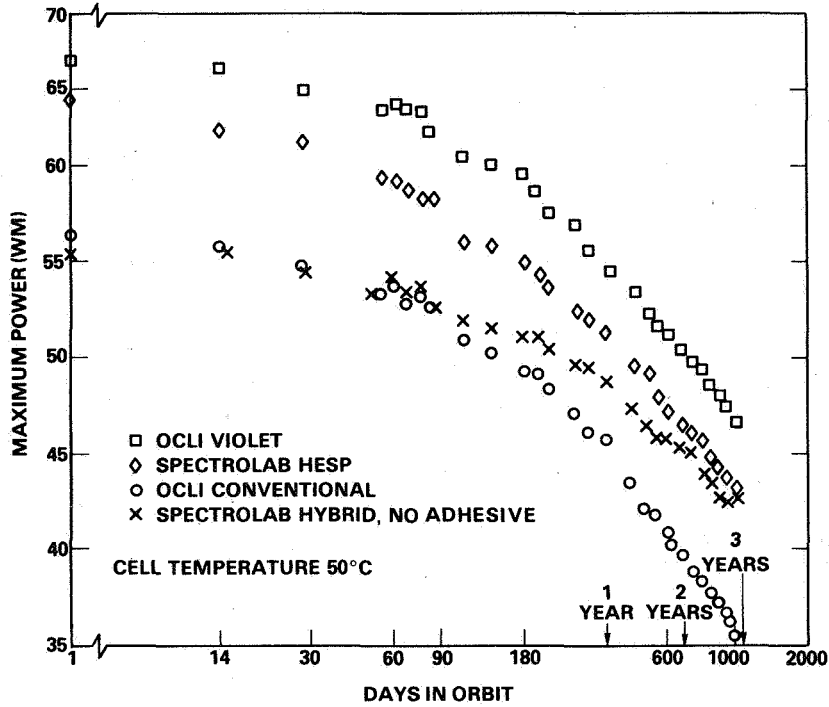
Fig. 3. Maximum power degradation of four cell types: Exps. 1, 4, 10, and 14.

CELL MAXIMUM POWER BEFORE LAUNCH AND AFTER 1116 DAYS IN ORBIT
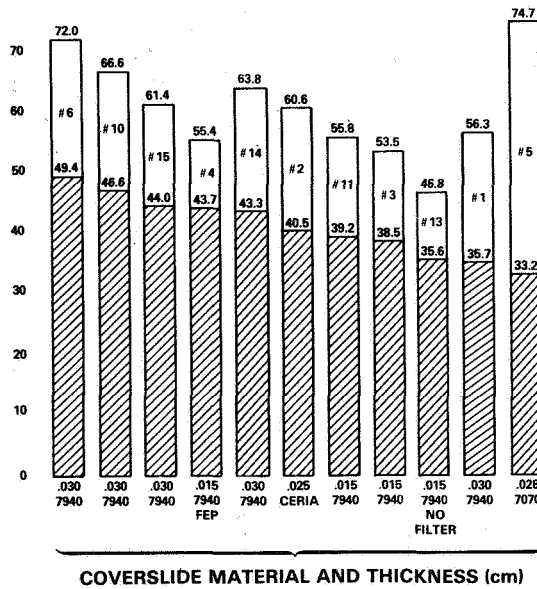
(2 ×2 CELL TEMPERATURE IS 50°C)

Fig. 4. Maximum output before launch and after 1116 days .

EFFECTS OF LOW ENERGY PROTON, ELECTRON, AND SIMULTANEOUSLY COMBINED PROTON AND ELECTRON ENVIRONMENTS IN SILICON AND GaAs SOLAR CELLS

W. E. Horne, A. C. Day, and D. A. Russell
Boeing Aerospace Company
Seattle, Washington

ABSTRACT

Degradation of silicon and GaAs solar cells due to exposures to low-energy proton and electron environments and annealing data for these cells are discussed. Degradation of silicon cells in simultaneously combined electron and low-energy proton environments and previous experimental work is summarized and evaluated. The deficiencies in current solar array damage prediction techniques indicated by these data and the relevance of these deficiencies to specific missions such as intermediate altitude orbits and orbital transfer vehicles using solar electric propulsion systems are discussed.

INTRODUCTION

The concept of large solar power stations has recently increased interest in the annealing of radiation damage in space. The cost and weight of such systems make it desirable to launch them into a low earth orbit (LEO) and then transfer them to geosynchronous earth orbit (GEO). However, such a transfer, if powered by ion thruster engines, takes times on the order of a few months. This time, which is spent in the trapped proton and electron belts, results in severe electrical power output degradation. Further, other missions flying intermediate altitude orbits ($\leq$ 10,000 nmi) or elliptical orbits must pass through severe environments of electrons and protons. Thus, it is desirable to be able to anneal the cells and restore their power generating capabilities. It is the purpose of this paper to 1) look at the feasibility of such annealing, 2) consider the effects on damage level of combined environments of electrons and protons such as those encountered in such intermediate altitude orbits, 3) discuss the adequacy of current prediction techniques for predicting degradation during such missions, and 4) to assess the impact of any synergisms between simultaneous electron and proton exposures on annealing behavior and mission lifetime.

ENVIRONMENTAL

A typical transfer orbit from an initial 28° inclination to a geosynchronous orbit of 0° inclination would require approximately three months with a

variable thrust ion engine. During that time the vehicle would pass through
a combined environment of vacuum, UV photons, electrons, and protons. While
the UV radiation would remain constant in time (except during periods in the
earth's shadow) and spectral content, the electron and proton environments vary
continuously with time, position, and altitude both in intensity and energy
spectrum. The actual environment varies with each orbit and during each orbit
and must be determined by integration using detailed flux maps and the actual
orbital history of the vehicle. However, for purposes of illustration figure 1
shows a simplified average of the integrated flux of electrons and protons as
a function of altitude for a single inclination.

As a general rule the proton damage dominates for altitudes below 8,000 to
10,000 nautical miles and the electron damage dominates above that altitude
(subject to variation during solar events).

For LEO to GEO orbital transfer missions most of the heavy damage to solar
cells is incurred early in the mission where protons and UV, and combinations
of protons, electrons, and UV are present. The proton damage, particularly
the softer spectra typical of about 6,000 nmi produces a complex damage scenario
inside the solar cell. Figure 2 shows a typical proton spectrum inside the
solar cell as the incident spectrum is modified by shielding. As can be seen
for cover glasses on the order of 2 to 3 mils thick (.012 to .018 gm/cm^2
shielding) the proton spectrum incident on the solar cell (at the interface)
is quite rich in protons of energy less than 2 MeV. Particles of these energies
are very damaging to solar cells. Figure 3 shows the type of gradient in damage
produced across a cell due to the proton energy spectra. For example, the lower
energy protons stop shortly after entering the cell and produce heavy localized
damage near the ends of their tracks. The subsequent drop in intensity and
effectiveness of the proton flux causes the relative amount of damage to de-
crease as the depth into the cell increases. It should also be pointed out
that the types of defects produced and the relative concentration of each type
of defect produced will also vary across the cell since these factors are
energy dependent.

These observations are important not only for predicting damage level but
for their impact on the annealing behavior of the cells since the annealing
kinetics are different for the different defect species.

In order to better assess the impact of these environments an experimental
study of low energy (E $\leq$ 1.5 MeV) proton damage and annealing in both silicon
and gallium arsenide solar cells has been performed at Boeing. This program
has been reported in detail elsewhere (ref. 1) and, therefore is only sum-
marized here as it pertains to evaluating missions in low and intermediate
altitude orbits.

Low Energy Proton Damage and Annealing

Experiments have been performed in which 2 ohm-cm N/P MAR coated silicon
solar cells were irradiated with protons of energy .25 and 1.5 MeV. The cells
were irradiated at the Boeing Dynamitron accelerator. Two groups of 12 silicon
cells each were exposed to 3 x 10^{11} and 3 x 10^{12} p/cm^2 respectively with 1.5

MeV protons and one group of 12 cells to 7 x 10^{11} p/cm^2 0.25 MeV protons. Isochronal and isothermal anneals were then performed to observe the annealing behavior of the cells. A similar program was conducted with GaAs cells with one group of two each exposed to 2 x 10^{13} p/cm^2 at 1.5 MeV energy and one group exposed to 1 x 10^{12} p/cm^2 at 0.25 MeV energy. The results of the isochronal annealing experiments for both types of cells are shown in figure 4. These curves show evidence of the break up of several defect species in the silicon cells. Some of these species appear to be products of new combinations of defects and impurities pairing as the original defects break up and their constituents migrate away from their original sites (refs. 1, 2). The new species usually have different electrical degradation properties from their predecessors and are considerably different in their annealing properties. The relative amounts of the different defect species also appear to be rather strong functions of the incident proton energy.

The isochronal anneals of the GaAs cells also show structure indicating the annealing of multiple defect species. However, they do not show the reverse annealing as in the case of silicon cells. This is probably indicative of less interaction between the defects and impurities in GaAs cells.

Figure 5 shows typical isothermal annealing behavior for both silicon and GaAs cells. In both cases, the curves show evidence of the recovery of multiple species having different annealing time constants corroborating the observations of the isochronal anneals.

Other significant observations of this study were that 1) in the silicon cells both the rate and extent of recovery are functions of proton energy and of damage level or fluence, 2) recovery appears to be more rapid and more complete when the cells are heated rapidly above 400°C, with recovery levels of 96 percent of maximum power in times on the order of five minutes being typical, 3) the rate and extent of recovery under a given set of conditions varies widely between cells with very similar initial electrical characteristics and radiation degradation responses as a function of fluence. For the GaAs cells the rate and extent of recovery was also a function of incident proton energy.

Combined Environments of Electrons, Protons, and UV Radiation

Another complexity that needs to be considered for orbits $\leq$ 10,000 nmi is that of synergistic effects between simultaneous environments of UV, electrons, and protons. In the past, at least three experiments have been performed on solar cells with combined environments of these three constituents. These experiments are summarized in table 1.

The first two experiments summarized in table 1 are in general agreement in that they both experienced combinations of electrons, protons, and UV radiation and both showed less damage than would be expected for the linear sum of the defects produced by the particulate beams taken separately. A typical difference is illustrated in figure 6. However, the third experiment summarized in table 1 showed significantly different results in that a rather strong synergism was reported between the electron and proton environments as illus-

231

trated in figure 7. If one examines the conditions of the three experiments some significant differences are noted that could account for the seemingly conflicting results. In the third experiment the synergism between the electron and proton environments was a rather strong function of the ratio of electron and proton fluxes. In the first two experiments the proton beams were spread over the sample fields by rastering, or scanning, the beams in the vertical and horizontal planes. This resulted in an instantaneous proton flux much higher than the average number reported, or a much lower ratio of electron flux to proton flux than was reported. Looking at the results of the third experiment, a low ratio of electrons to protons shows little or no synergism so that the results may in fact not be in conflict at all. It should be further pointed out that in both the first and third experiments linear accelerators were used to supply the electrons. These machines operate in a single or repetitive pulsed mode but do not supply a continuous beam of electrons. In the second experiment a continuous field of scattered Compton electrons was present but the proton beam was rastered. Thus it can be concluded that none of the experiments have really been a satisfactory simulation.

Summary of Impact on Mission Performance

If one considers the synergism of figure 7 a possible mechanism could be that a high level of electrons during the proton exposure tends to break up the initial defect complexes produced by the protons allowing the formation of more electrically degrading complexes in much the same way observed for the reverse annealing of low energy proton damage at moderate temperature. If this is the true mechanism, or if different defect species are being formed, then the annealing kinetics of the damage would be altered considerably. For example, it was observed in the low energy proton damage annealing experiments that when cells were rapidly heated above 400°C then less of the secondary or daughter defects were produced during the annealing process and the annealing progressed more rapidly and completely than at lower temperatures or during isochronal anneals which slowly stepped the cells to > 400°C through a series of incremental temperature steps. Thus, if the combined environments produce the equivalent of the reverse anneal observed in the isochronal anneal experiments then both the rate and the extent of final annealing would be affected.

Thus, it can be seen that the complexity of the damage produced across the thickness of a solar cell by a spectrum of low energy protons and the possibility of synergisms can radically alter the behavior of arrays during long term missions in intermediate and low altitude orbits both in terms of initial degradation and in the feasibility of annealing of the damage.

CONCLUSIONS

From the above observations it is concluded that low-energy proton damage and annealing is not sufficiently understood or characterized to permit accurate engineering evaluations of large-scale power supply performance in orbits $\leq$ 10,000 nmi. More work is required in the area of understanding basic mechanisms of annealing and the results of repetitive irradiate-anneal cycles.

232

It is also concluded that the area of synergisms between electron, low-energy proton, and UV environments has not been adequately explored to permit certainty in engineering design of power systems and annealing cycles to optimize mission performance.

REFERENCES

1. Day, A. C., Horne, W. E., and Arimura, I., "Proton Damage Annealing for Use in Extended Life Solar Arrays," to be published in IEEE Transactions on Nuclear Science, Volume 27, No. 6, December 1980.

2. Weinberg, I. and Swartz, C. K., "Origin of Reverse Annealing in Radiation Damaged Silicon Solar Cells," Appl. Phys. Lett. 32(8), 1980.

3. Arndt, R. A., Bernard, J, and Reulet, R., "Effects of Simultaneous Ultraviolet, Electron, and Proton Irradiation of Silicon Solar Cells," IEEE Photovoltaic Specialist's Conf. Proceedings, 1975.

4. Horne, W. E., Madaras, B. V., and Greegor, R., "Real Time Space and Nuclear Effects on Solar Cells (Accelerated Evaluation Methods)," AFAPL-TR-72-69, 1974.

TABLE 1. SUMMARY OF COMBINED ENVIRONMENT EXPERIMENTS ON SOLAR CELLS

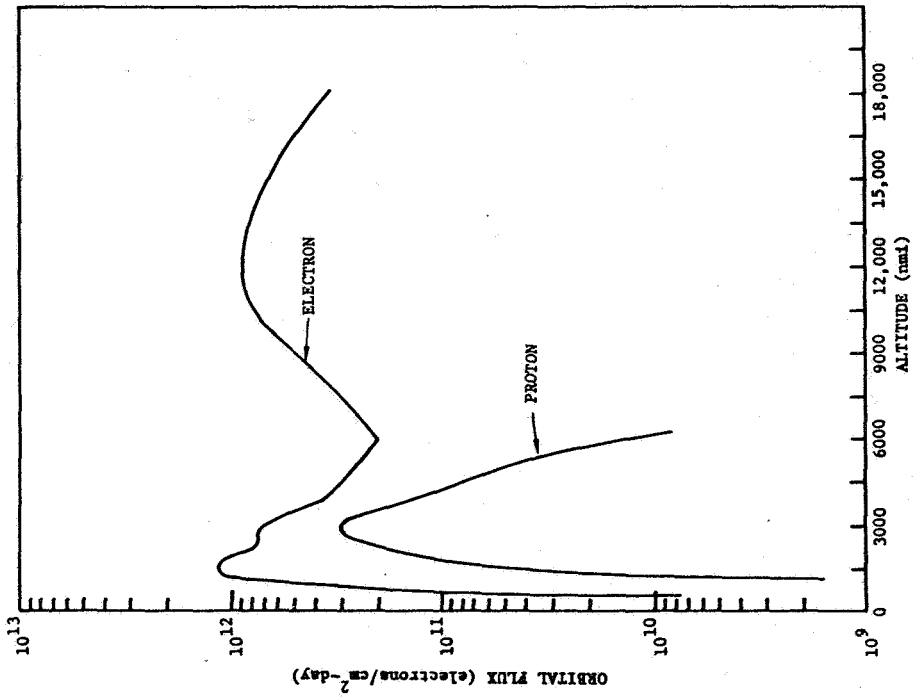| SOURCE OF DATA	DESCRIPTION OF ENVIRONMENTS									TYPES OF CELLS EXPOSED	RESULTS OBSERVED
	PROTONS			ELECTRONS			UV				
	ENERGY	FLUX (p/cm²-s)	EXPOSURE TECHNIQUE	ENERGY	FLUX (e/cm²-s)	EXPOSURE TECHNIQUE	ENERGY	FLUX	EXPOSURE TECHNIQUE		
Arndt, et al. (ref. 3)	2.5 MeV	2×10^7 2×10^8 (average)	Rastered Beam	2.0 MeV	2×10^{10} 2×10^{11}	Scattered Pulsed Field (rep. rate unk.)	Unfiltered Xenon Lamp	1 UV Sun (average)	Variable Intensity	1 Ω-cm Float Zone 10 Ω-cm Float Zone 10 Ω-cm Crucible N/P	• No Synergism Between Electron and Proton Environments • Less Damage in Cells Exposed to UV Plus Particulate Radiation Than in Those Exposed to Particles Only
Horne, et al. (ref. 4)	0.1 MeV	1.2×10^5 (average)	Rastered Beam	1.33 MeV (average)	9.1×10^6	Scattered Compton Electron Continuous Field	Quartz Iodide Lamps	~ 1 UV Sun (average)	Continuous	10 Ω-cm Crucible N/P Crucible P/N (lithium) Float Zone P/N (lithium)	• Less Damage Than Expected Based on Linear Sum of Particulate Environments Similar to Above Experiment Where UV Radiation Was Present
Horne, et al. (ref. 4)	0.26 MeV	$\sim 10^7$ $\sim 10^8$	Scattered Continuous Field	10 MeV	$\sim 10^{10}$	Scattered Pulsed Field (rep. rate 15 p/s)	None	——	——	10 Ω-cm Crucible N/P Crucible P/N (lithium) Float Zone P/N (lithium)	• Synergism Observed Between Electron and Proton Environment • More Damage Than Would Be Expected From Linear Sum of Separate Environments • Synergism a Function of Ratio of Electron Flux to Proton Flux

234

FIGURE 2. TYPICAL MODIFIED SPECTRUM INSIDE SOLAR CELL STRUCTURE (6000 nmi, 30° INCLINATION)

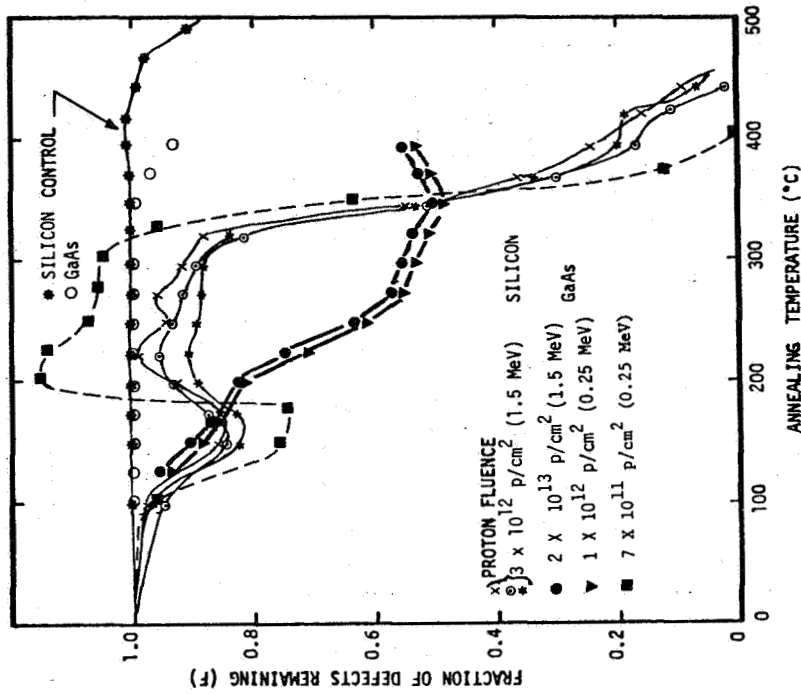FIGURE 1. VARIATION OF ORBITAL FLUX WITH ALTITUDE

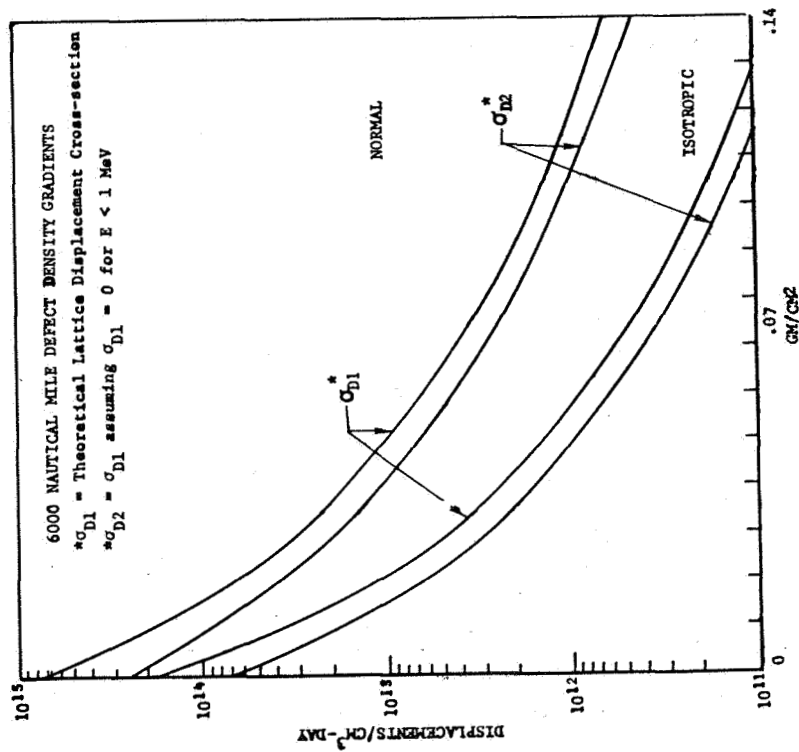FIGURE 4. ISOTHERMAL ANNEALING DATA FOR SILICON AND GaAs SOLAR CELLS

FIGURE 3. TYPICAL DISPLACEMENT DENSITY GRADIENT INSIDE SOLAR CELL DUE TO SPACE SPECTRUM

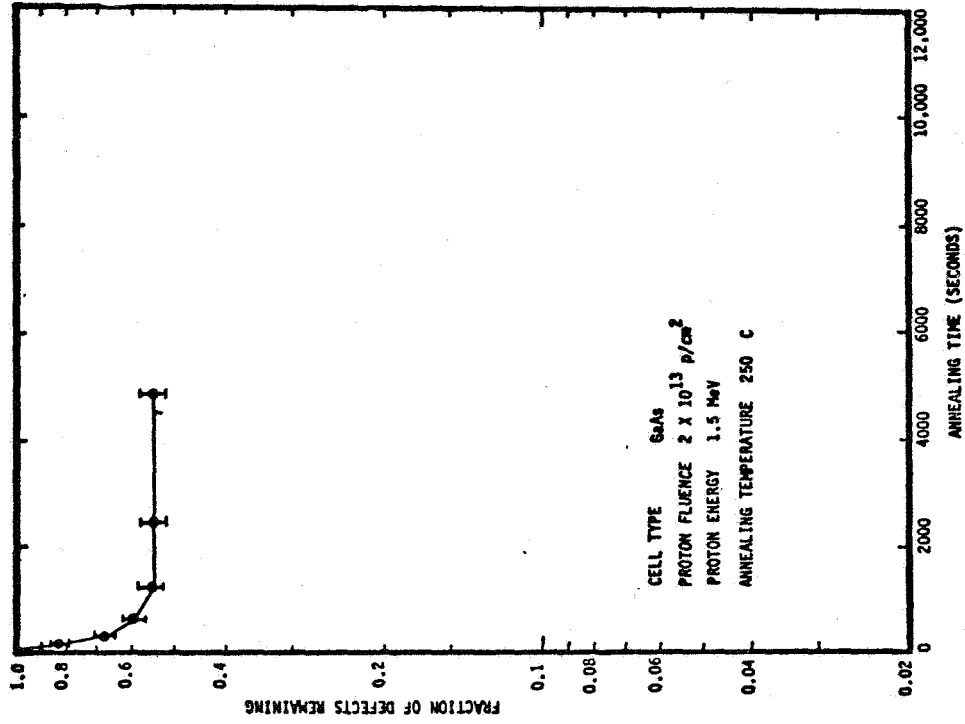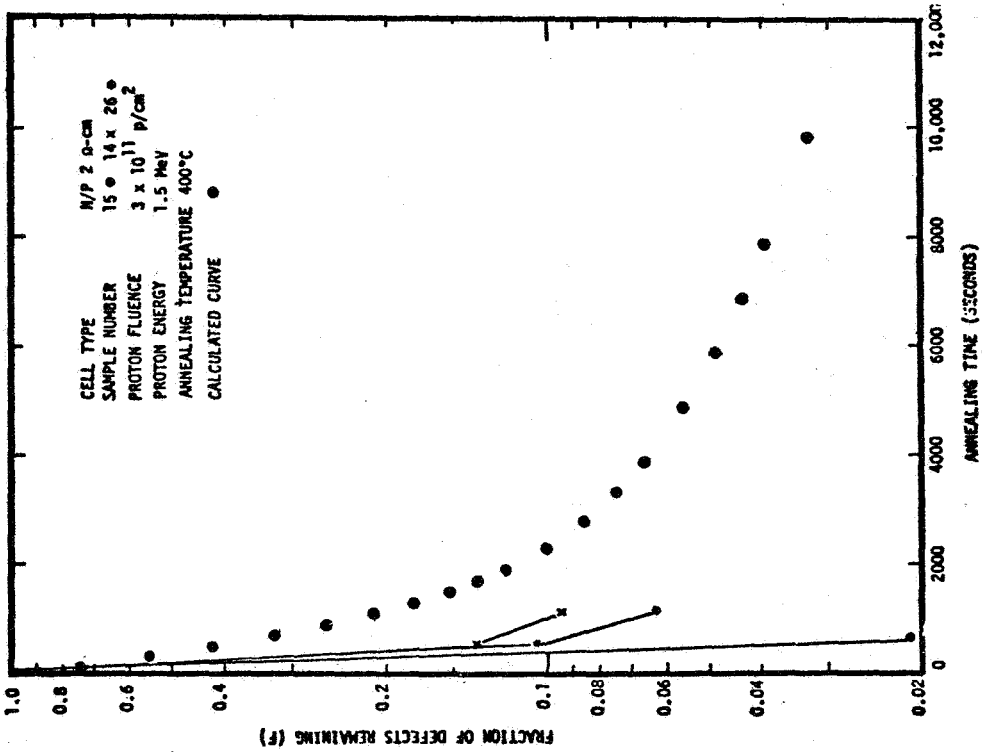FIGURE 5b. ISOTHERMAL ANNEAL OF GaAs CELLS

FIGURE 5a. ISOTHERMAL ANNEAL OF SILICON CELLS FOLLOWING 3×10^{11} p/cm^2
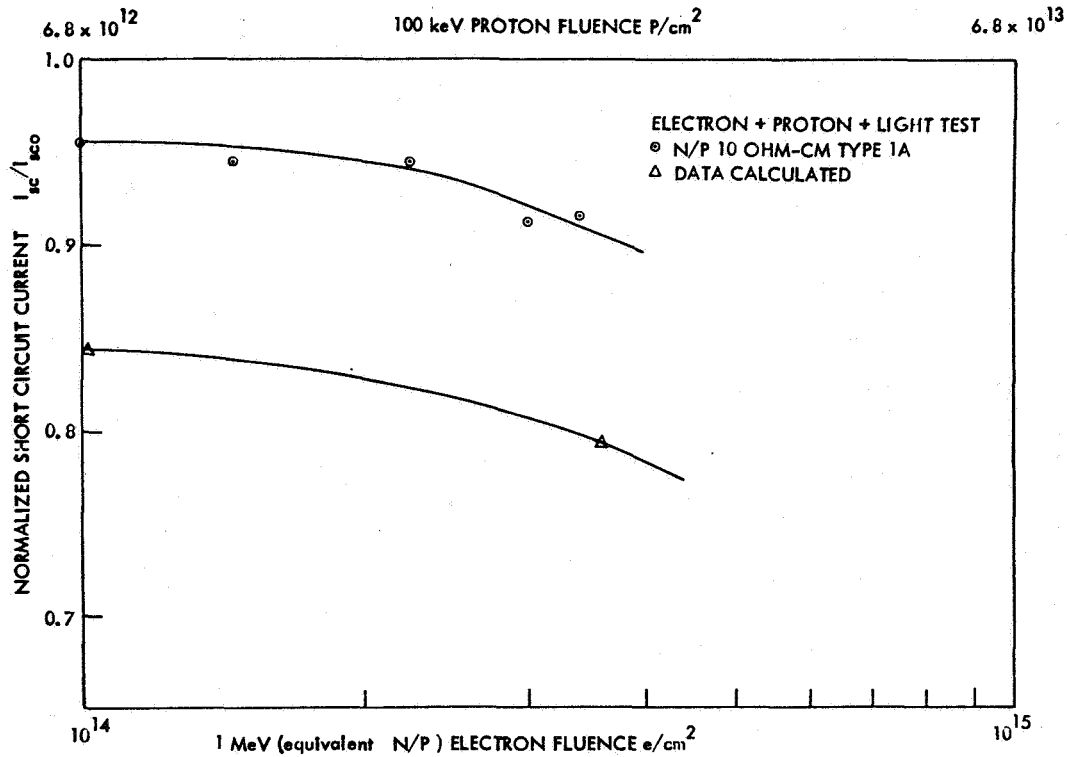
237

FIGURE 6. COMPARISON OF CALCULATED VERSUS MEASURED DATA FOR COMBINED
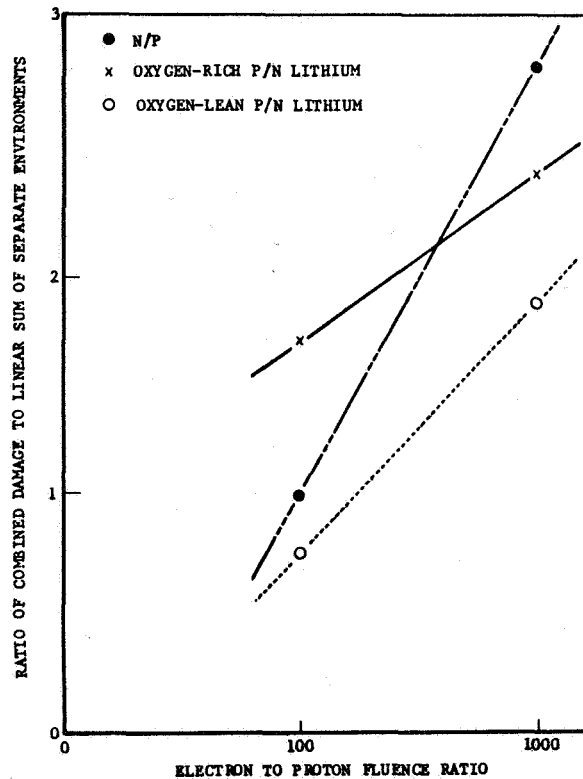ENVIRONMENT REAL-TIME TEST

FIGURE 7. RATIO OF ENHANCED COMBINED EFFECTS DAMAGE TO LINEAR SUM OF SEPARATE
DAMAGE COMPONENTS VERSUS THE ELECTRON TO PROTON FLUENCE RATIO DURING
THE COMBINED TESTS

GaAs HOMOJUNCTION SOLAR CELL DEVELOPMENT

Dennis J. Flood, Clifford K. Swartz,
and Russell E. Hart, Jr.
NASA Lewis Research Center
Cleveland, Ohio

SUMMARY

The Lincoln Laboratory $n^+/p/p^+$ GaAs shallow homojunction cell structure (ref. 1) has been successfully demonstrated on 2- by 2-cm GaAs substrates (ref. 2). Air mass zero efficiencies of the seven cells produced to date have ranged from 13.6 to 15.6 percent. Current-voltage (I-V) characteristics, spectral response, and $I_{sc}-V_{oc}$ measurements have been made on all seven cells. Preliminary analysis of 1-MeV electron radiation damage data indicate excellent radiation resistance for these cells.

INTRODUCTION

The compound semiconductor GaAs has several physical properties that make it a potentially useful material for space solar-cell applications. Because GaAs has a direct band gap, the absorption length for near band gap sunlight in a single-crystal of the material is only about 2 μm (ref. 3), or approximately a factor of 100 shorter than that in silicon. As a result, the solar-cell active layer thickness can be reduced to a few micrometers. In addition, GaAs solar cells should exhibit excellent radiation resistance in space since, in principle, it is possible to have minority carrier diffusion lengths that are several times greater than the absorption length. As a result, photocurrent collection should not be significantly affected until relatively large space radiation fluences have been accumulated. Radiation damage data for GaAs solar cells in general are sparse, although results for the LPE (liquid-phase epitaxy) -grown p/n heteroface cell are becoming more available (e.g., refs. 4 to 8). By comparison, data on the VPE (vapor-phase epitaxy) -grown $n^+/p/p^+$ shallow homojunction cells exist only for relatively small area (0.5 cm^2) cells (ref. 9). In the present work six 2- by 2-cm cells, fabricated at the Lincoln Laboratory under NASA Lewis Contract C-30969-D, have been irradiated with 1-MeV electrons at five fluences from 10^{13} to 10^{15} e-/cm^2. Current-voltage, spectral response, and $I_{sc}-V_{oc}$ measurements were made on each cell after each irradiation. The irradiations were performed using the Lewis Research Center's Dynamitron Accelerator.

RESULTS AND DISCUSSION

Table I contains the pre-irradiation values of short-circuit current I_{sc}, open-circuit voltage V_{oc}, maximum power P_m, fill factor FF, and AMO efficiency η of each of the cells used in this study. All cells have $0.05-\mu m$-thick n^+ layers doped with sulfur to $\sim 5\times10^{18}$ cm^{-3}, $0.085-\mu m$-thick anodic oxide antireflection (AR) coatings, electroplated tin contacts on the front surface, and an electroplated gold contact on the back surface. Thicknesses of the p and p^+ regions varied from cell to cell, as did the zinc concentration in the p region. The p^+ region, also zinc doped, is approximately the same for all cells at 5×10^{18} cm^{-3}. Figure 1 shows the basic cell structure without AR coating and contacts.

Figure 2 is a plot of normalized short-circuit current as a function of fluence for the best and worst cases among the six cells. Degradation after 10^{15} e^-/cm^2 1-MeV electrons ranged from 10 to 20 percent of beginning-of-life (BOL) currents. Spectral response measurements show clearly that, as expected, degradation occurs only at the longer wavelengths (see fig. 3). Figure 4 is a plot of normalized open-circuit voltage as a function of fluence again for the same two cells of figure 1. As shown, the cell with the least current degradation exhibits the greatest voltage degradation, a result not yet fully understood. Relative degradation after $\phi = 10^{15}$ ranged from 9 to 16 percent for the six cells. The degradation of normalized maximum power is shown in figure 5. Relative degradation ranged from 24 percent in the best case to 30 percent in the worst case at the maximum fluence. Figure 6(a) contains the I-V characteristics at $\phi = 0$ and $\phi = 10^{15}$ e^-/cm^2 for the cell with the greatest degradation in I_{sc}. As shown in the figure, there was a slight decrease in fill factor at the highest fluence. Figure 6(b) contains the I-V characteristics for the cell with the least degradation in I_{sc} (and P_m) for comparison. Figure 7 is a typical plot of I_{sc} versus V_{oc} for the cells used in this study at $\phi = 0$ and 10^{15} e^-/cm^2. Shunt resistances were typically on the order of 10^6 ohms for these cells. Figure 8 is a plot of $I_{sc}-V_{oc}$ for cell 5426. The $I_{sc}-V_{oc}$ data are obtained by varying the intensity of the light source to obtain a range of short-circuit currents comparable to dark forward bias currents. The data are thus automatically corrected for the series resistance of the cell. The data of figure 8 indicate a large current in the generation-recombination regime of the $I_{sc}-V_{oc}$ characteristic. The shunt resistance of this cell was estimated to be on the order of 500 ohms.

Figure 9 is a plot of the electron damage coefficient for p-type GaAs as a function of p-layer doping density, calculated from electron radiation damage data to small-area, shallow-homojunction cells (ref. 2). Similar calculations are in progress with data obtained from the 2- by 2-cm cells of this work, and indicate agreement with the data of figure 9.

CONCLUSION

The shallow homojunction $n^+/p/p^+$ GaAs solar cells tested in this study show good resistance to 1-MeV electron irradiation. Although the $n^+/p/p^+$ structure has not yet been optimized for maximum BOL performance and maximum radiation resistance, cells produced to date are comparable to the best GaAs p/n cells of similar BOL efficiencies. Careful attention to optimization of the cell structure should yield cells with improved radiation resistance over the cells reported here.

REFERENCES

1. Bozler, C. O.; and Fan, J. C. C.: High Efficiency GaAs Shallow-Homojunction Solar Cells. Appl. Phys. Lett., vol. 31, Nov. 1, 1977, pp. 629-631.

2. Fan, J. C. C.: GaAs Shallow Homojunction Solar Cells. NASA CR-165167, October 1980.

3. Kamath, S.; and Wolff, G.: High Efficiency GaAs Solar Cell Development. AFAPL-TR-78-96, Hughes Aircraft, 1979. (Available from NTIS as AD-A066616.)

4. Loo, R.; Kamath, G. S.; and Knechtli, R.: Electron Radiation Damage of (AlGa)As-GaAs Solar Cells. NASA CR-162425, 1979.

5. Conway, E. J.; and Walker, G. H.: Radiation Damage in GaAs Solar Cells. Solar Cell High Efficiency and Radiation Damage - 1979. NASA CP-2097, 1979, pp. 201-207.

6. Moon, R. L.; et al.: Performance of AlGaAs/GaAs Solar Cells in the Space Environment. 12th Photovoltaic Specialists Conference Record. IEEE, 1976, pp. 255-261.

7. Pearce, L. S.; et al.: Proton and Electron Irradiation of Liquid Phase Epitaxial GaAlAs Solar Cells. Photovoltaic Specialists Conference, 13th, Washington, D.C., June 1978, Conference Record. IEEE, 1978, pp. 557-561.

8. Li, Sheng S.; et al.: Effects of Thermal Annealing on the Deep-Level Defects and I-V Characteristics of 200 KeV Proton Irradiated AlGaAs-GaAs Solar Cells. Energy to the 21st. Century; Proceedings of the Fifteenth Intersociety Energy Conversion Engineering Conference. Vol. I. AIAA, 1980, pp. 354-357.

9. Fan, J. C. C.; Chapman, R. L.; and Bozler, C. O.: Shallow-Homojunction GaAs Cells with High Resistance to 1-MeV Electron Radiation. Appl. Phys. Lett., vol. 36, Jan. 1, 1980, pp. 53-56.

TABLE I. - CELL PARAMETERS

Cell	Short-circuit current, I_{sc}, A	Open-circuit voltage, V_{oc}	Maximum power, P_m, mW	Fill factor, FF	Air mass zero efficiency, η, percent
5239	0.1088	0.961	81.82	78.2	14.9
5245	.1034	.983	82.56	81.2	15.1
5340	.0976	.970	73.56	77.7	13.4
5344	.1074	.984	85.46	80.8	15.6
5348	.1020	.992	82.40	81.4	15.0
5426	.1045	.987	80.90	78.4	14.8
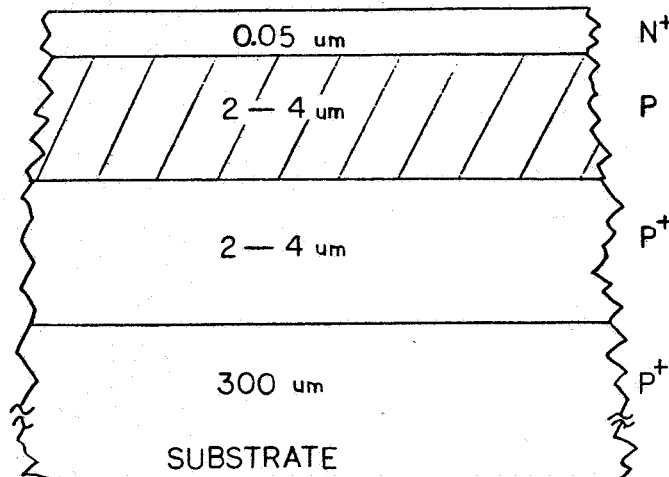
FIGURE I. SHALLOW HOMOJUNCTION CELL STRUCTURE.
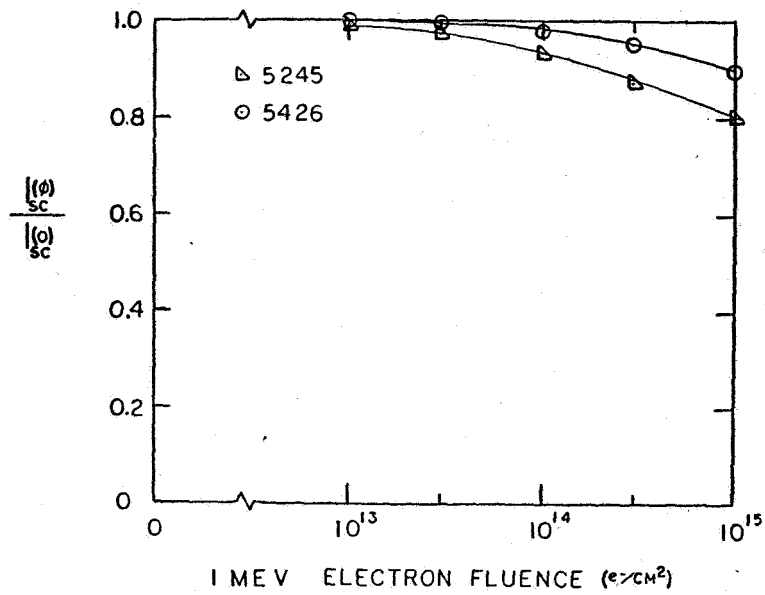
FIGURE 2. SHORT-CIRCUIT CURRENT DEGRADATION (NORMALIZED).
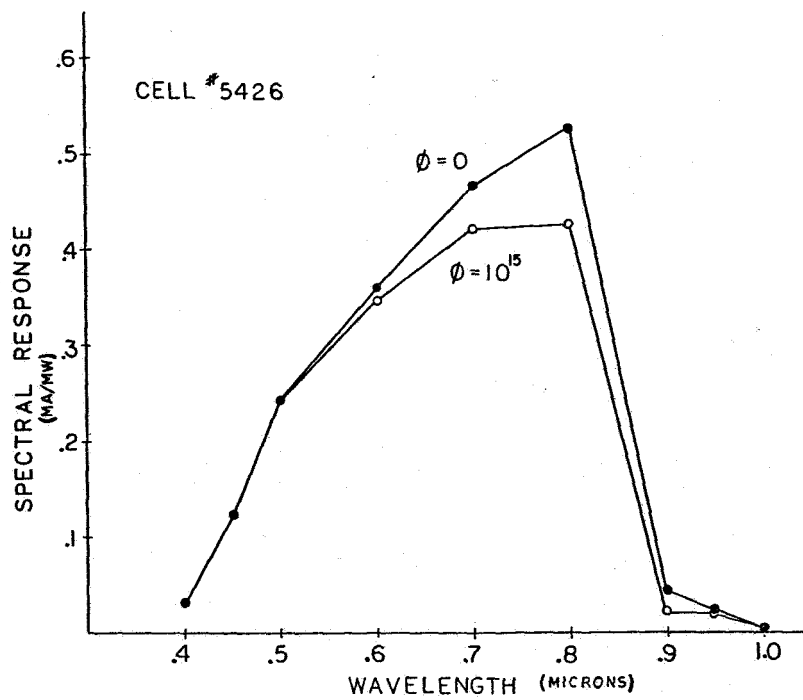
FIGURE 3. SPECTRAL RESPONSE, $N^+/P/P^+$ GAAS CELL.
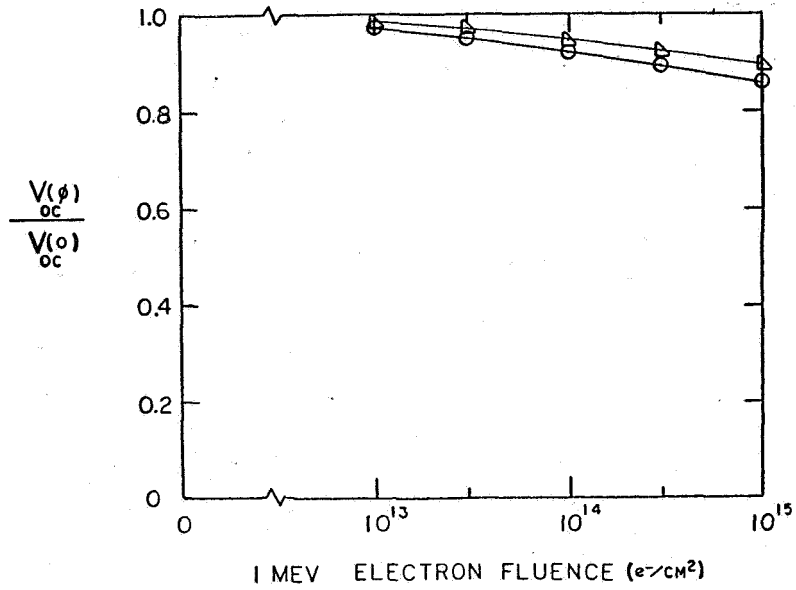
FIGURE 4. OPEN CIRCUIT VOLTAGE DEGRADATION (NORMALIZED).
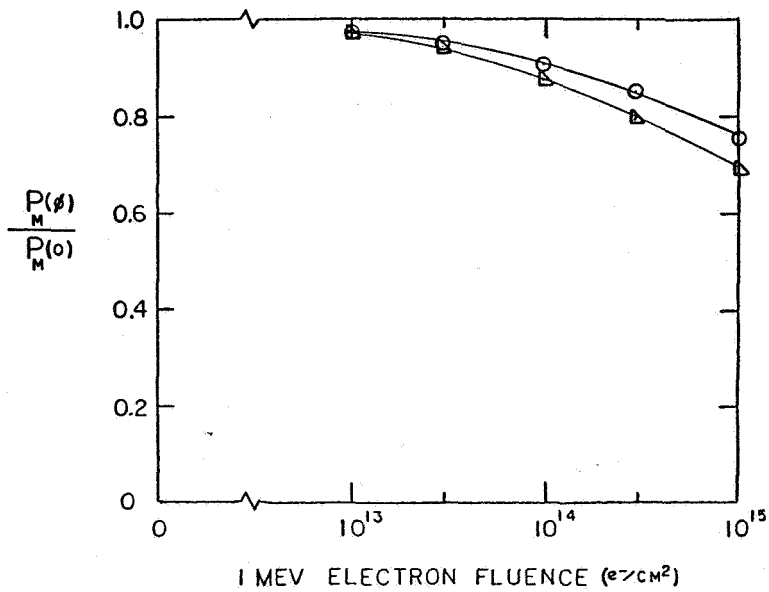
FIGURE 5. MAXIMUM POWER DEGRADATION (NORMALIZED).
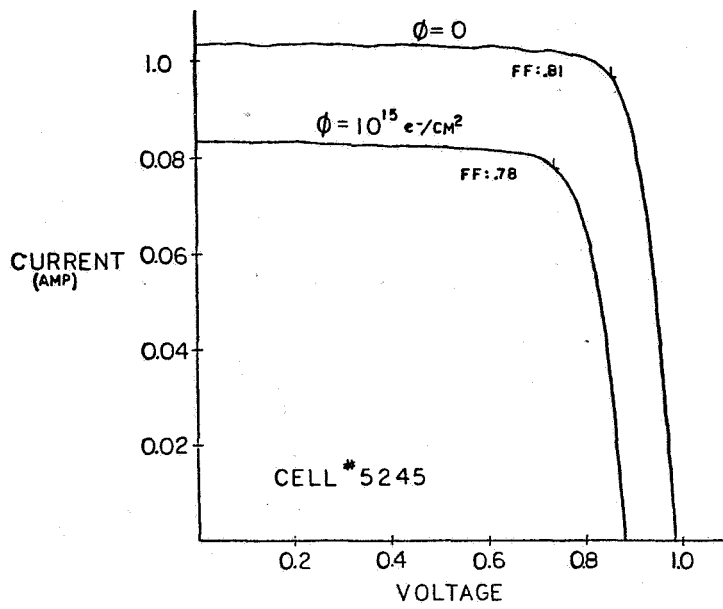
FIGURE 6a. CURRENT-VOLTAGE CHACTERISTICS, "WORST CELL".
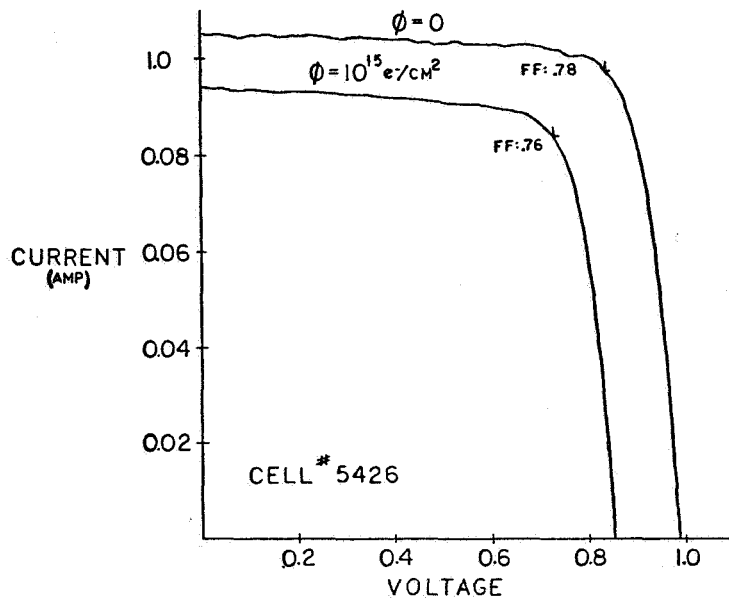
FIGURE 6b. CURRENT-VOLTAGE CHARACTERISTICS, "BEST CELL"
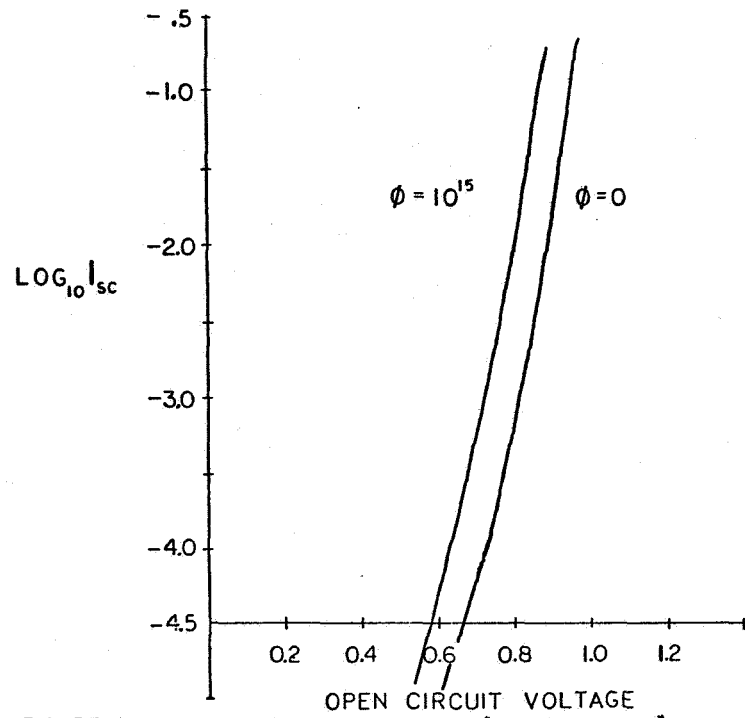
FIGURE 7. I_{sc}-V_{oc} CHARACTERISTICS, "TYPICAL CELL".
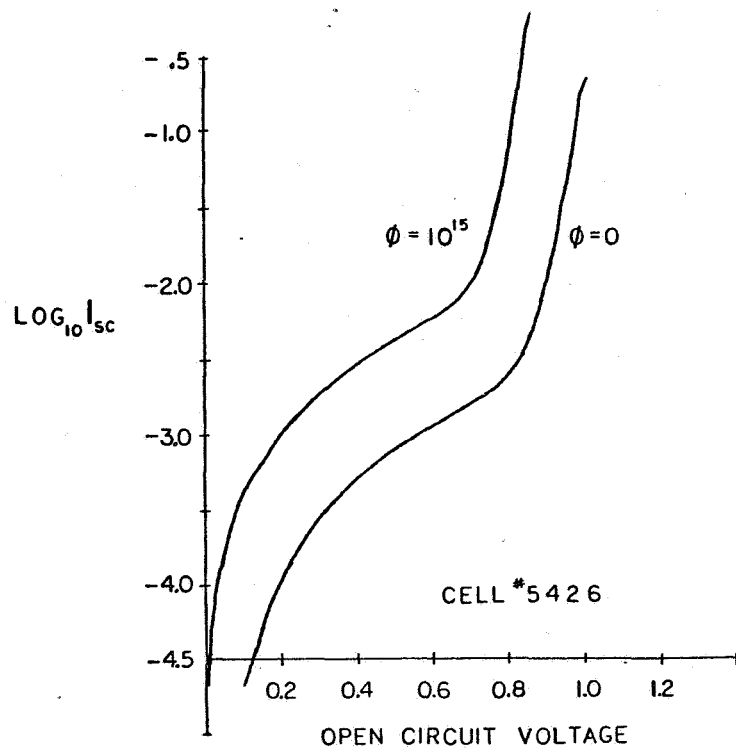
FIGURE 8. I_{sc}-V_{oc} CHARACTERISTICS, "BEST CELL".
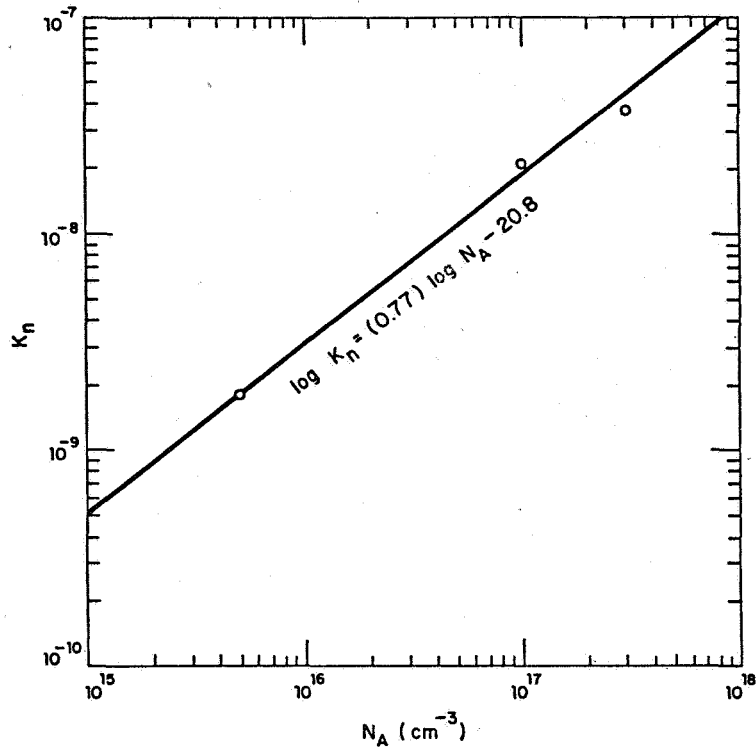
Figure 9. A plot of damage coefficient $K_n \phi$ as a function of doping levels in p-type GaAs.

The plot shows a straight line with the equation:

$$\log K_n = (0.77) \log N_A - 20.8$$

Y-axis: K_n

X-axis: N_A (cm^{-3})

PERIODIC ANNEALING OF RADIATION DAMAGE IN GaAs SOLAR CELLS

R. Y. Loo, R. C. Knechtli, and G. S. Kamath
Hughes Research Laboratories
Malibu, California

INTRODUCTION

A leading motiviation for our study of radiation damage in GaAs solar cells is their capability to offer better resistance to radiation damage in space than Si cells. Key parameters known to affect the nature and the severity of such radiation damage are:

1. Type and energy of damaging particles (electrons, protons or neutrons).

2. Particle fluence.

3. Cell temperature during irradiation.

It is also known that GaAs solar cells can recover substantially from electron damage at temperatures as low as 200°C, with some evidence that even lower temperatures may be effective (ref. 1). We have, however, found that in some cases, conventional annealing of proton radiation damage is much less effective than the annealing of electron radiation damage. We have therefore studied in more detail the annealing of proton radiation damage in our GaAs solar cells. We wished to determine if and how proton radiation damage can effectively be annealed at relatively low temperatures ($\leq 200^{\circ}$C). The first results of this study are reported in this paper.

ANNEALING PROCESS

Radiation damage can be annealed by a number of different ways. The specific ones which we consider here are:

1. Post-annealing.

2. Periodic annealing.

3. Continuous annealing.

Post-annealing means annealing the solar cells by keeping them at a given temperature, after irradiation at room temperature. By continuous annealing we refer to the process of continuous recovery from radiation damage while irradiation proceeds; this is achieved by maintaining the solar cells at the

249

desired annealing temperature (above room temperature) while irradiation takes place. The concept of continuous annealing has been proposed some time ago (ref. 2) and attractive extrapolations have already been made on the basis of existing electron radiation damage data. These extrapolations indicate that continuous annealing could in fact prevent electron radiation damage (ref. 2) at surprisingly low annealing temperatures (<150°C). The data which we have recently obtained shows that continuous annealing can also be remarkably effective in preventing proton radiation damage. This data is given and discussed in the next section.

In periodic annealing, we irradiate the solar cells at room temperature up to a given fluence, anneal them thereafter for a limited time at the selected annealing temperature, and repeat this sequence a number of times. In space applications, this process could be attractive if the annealing time can be kept a small fraction of the irradiation time. Furthermore, this is a compromise between continuous annealing and a single post-annealing sequence. Periodic annealing is attractive because it leads to recovery from radiation damage before radiation damage has accumulated to a point where excessive loss of solar cell power output does occur. It will be interesting to determine if an adequate frequency of periodic annealing can provide results as favorable as these obtained with continuous annealing. Since the radiation flux rates in space are relatively low, this seems possible.

EXPERIMENTAL RESULTS

The measurements reported below were performed on 2 cm x 2 cm (AlGa)As-GaAs solar cells made at the Hughes Research Laboratories (HRL) with the parameters shown in Fig. 1. Both the (AlGa)As window thickness D and the junction depth x_j were equal to 0.5 μm. Irradiation was provided by 200 keV protons, in an ion implantation machine at HRL. The proton energy of 200 keV was selected because damage caused by this radiation had been found to be especially severe (ref. 3) in the GaAs solar cells with the structure given in Fig. 1. We performed two sets of experiments. In the first set, we compared periodic annealing to post-annealing. In the second set of experiments, we performed continuous annealing.

The flow chart of the measurements performed in the first set of experiments is shown in Fig. 2. Our original plan had been to perform all annealing steps at the same temperature of 200°C, for the periodic as well as for the post-annealing. We found, however, that the amount of radiation damage recovery observable after 200 keV proton irradiation and annealing at 200°C is quite small, in contrast to the recovery observed at the same temperature after 1 MeV electron irradiation. We proceeded, therefore, with higher annealing temperatures, even though this led to a less systematic set of data. The results of these measurements are given on Tables 1 and 2. The key observations which result from inspection of these two tables are that:

1. The proton radiation damage caused by 200 keV protons is not effectively annealed at 200°C, neither by post-annealing nor by periodic annealing.

250

2. After annealing at an elevated temperature of 500°C, the amount of recovery attained in periodic annealing after these irradiation and annealing periods is approximately the same (P/P_O = 77.4%) as that observed after a single post-annealing sequence (P/P_O - 79%).* Similarly, periodic annealing can be compared to post-annealing at 300°C, where the solar cell power is seen to recover in both cases** to the same value of approximately 65%. In all comparisons considered above, the cumulative fluence was 3×10^{11} pcm^{-2}.

3. While the final power was the same in both the periodic and in the post-annealing sequences, periodic annealing did provide the anticipated advantage that the maximum power loss experienced in the course of periodic annealing (P/P_O = 58%) was less severe than that experienced with a single post-annealing sequence (P/P_O = 50.6%).

In the first set of periodic annealing experiments reported above, we note that the first annealing sequence was applied after the radiation fluence had already reached a relative high value of 1×10^{11} pcm^{-2}, leading to correspondingly severe radiation damage (P/P_O = 61%). In our second set of experiments reported below, we shall show that more favorable results are obtained with continuous annealing. This leads to the prospect that more favorable results may also be attained if periodic annealing is initiated at lower fluences than those used in our first experiments.

The results of our continuous annealing experiment at 150°, 200° and 250° C are shown in Fig. 3. For reference, we show in the same figure the effect of post-annealing one of our GaAs solar cells for 50 h at 200°C, after exposure to a 200 keV proton fluence of 10^{10} pcm^{-2}. Consistent with our previous observations, post-annealing at 200°C is seen to provide very little recovery, in contrast to the substantial improvement obtained with simultaneous annealing at the same fluence. The key observations to be made as a result of inspecting Fig. 3 are that:

1. Continuous annealing is much more effective than post-annealing in limiting proton irradiation damage or in providing recovery from it.

2. A continuous annealing temperature as low as 150°C is effective in limiting proton radiation damage.

3. In the continuous annealing experiment of Fig. 3., because of the high flux rate, the total time was very short (1 h) compared to the time in space to reach the same proton fluence. It is therefore plausible that at the lower flux rates prevalent in space, temperatures even lower than 150°C may be effective in providing continuous annealing.

_____

*We have to qualify this observation by noting that, in the periodic annealing sequence, the first annealing sequence went only up to a temperature of 300°C, while the other annealing steps and post-annealing went up to 500°C.
**Note that a temperature of 500°C was reached in the course of the second periodic annealing step.

Since continuous annealing at 150°C or lower seems a distinct possibility to minimize proton radiation damage, methods of achieving such a goal have to be seriously considered. A simple method of realizing such an objective is to use solar concentrations of the order of 5 to 10 suns and design the solar panel to achieve an equilibrium temperature of approximately 150°C. The loss in solar cell efficiency due to the higher operating temperature should be compared to the benefits obtainable from improvement in end-of-life efficiency for the specific mission. While our observations relate to proton radiation damage, electron radiation damage has been found to anneal even more readily. This approach appears, therefore, even more attractive for missions where electron radiation damage is present or is predominant.

SUMMARY AND CONCLUSION

In our two sets of experiments, we have compared continuous annealing of GaAs solar cells with periodic annealing to determine their relative effectiveness in minimizing proton radiation damage. The main conclusions are:

1. Continuous annealing of the cells in space at 150°C can effectively reduce the proton radiation damage to the GaAs solar cells.

2. Periodic annealing is most effective if it can be initiated at relatively low fluences (approximating continuous annealing), especially if low temperatures of less than 200°C are to be used.

3. If annealing is started only after the fluence of the damaging protons has accumulated to a high value ($\geq 10^{11}$ pcm^{-2} in our experiments), effective annealing is still possible at relatively high temperatures. However, the practicality of such annealing in most space panels remains to be determined.

Finally, since electron radiation damage anneals even more easily than proton radiation damage, we can expect that substantial improvements in GaAs solar cell life can be achieved by incorporating the proper annealing capabilities in solar panels for practical space missions where both electron and proton radiation damage have to be minimized.

REFERENCES

1. Walker, G. H. and Consay, E. J.: "Annealing Kinetics of Electron-Irradiated GaAs Heteroface Solar Cells in the Range 175 to 200°C," Appl. Phys. Lett. 35, p 459 (15 Sept. 1979).

2. Heinbockel, J. H.; Conway, E. J.; and Walker, G. H.: "Simutaneous Radiation Damage and Annealing of GaAs Solar Cells," Conference Records of the Fourteenth IEEE Photovoltaic Specialists Conference (IEEE, New York, 1980, p 1085).

3. Knechtli, R. C.; Kamath, G. S.: Ewan, J.; and Loo, R. Y.: "Development of Space-Qualified GaAs Solar Cells," Proceedings of Second European Symposium on Photovoltaic Generators in Space, ESA publication SP-147, p 124, Fig. 8 (Heidelberg, Germany, 1980).

Proton Temp °C	Irradiation Fluences p cm^{-2}	Thermal Temp °C	Annealing Time hr	Total Annealing Time hr	I_{sc} ma	V_{oc} v	FF	P_m mW	η %	Power Ratio* P/P$_o$ %
					114	0.99	0.76	86.1	15.9	
25	1x10^{11}				84	0:84	0.74	52.5	9.7	61
		200	21		85	0.86	0.75	54.8	10.1	63.5
		300	4.5		89	0.89	0.75	59.3	11.0	69.2
25	1x10^{11}				82	0.84	0.73	50.4	9.3	58.5
		300	4.0		88	0.88	0.74	57.3	10.6	67
		500	2		108	0.93	0.75	75.1	13.9	87.4
25	1x10^{11}				80	0.84	0.74	49.7	9.2	58
		200	1		82	0.85	0.73	51.1	9.4	59.3
		"	3	4	82	0.85	0.73	51.1	9.4	59
		"	18	22	83	0.85	0.74	52.5	9.7	61
		"	72.5	94.5	84	0.86	0.74	53.3	9.8	61.6
		"	51	145.5	84	0.86	0.74	53.3	9.8	61.6
		300	4		87	0.85	0.74	56.2	10.4	65.4
		"	74	78	88	0.87	0.73	55.7	10.3	64.8
		350	2.5		89	0.87	0.73	56.9	10.5	66
		400	1	1	93	0.89	0.72	59.8	11	69.2
		"	3.5	4.5	94	0.89	0.73	61.2	11.3	71.0
		500	1		101	0.90	0.73	66.4	12.3	77.4
		550	1		105	0.90	0.69	64.8	12	75.5

* P = power after annealing

P$_o$ = power before irradiation

Table 2. Thermal Annealing Result on Cell #4440
Bombarded by 200 keV Proton

| Proton Temp °C	Irradiation Fluences p cm^{-2}	Thermal Temp °C	Annealing Time hr	Total Annealing Time hr	I_{sc} ma	V_{oc} v	FF	P_m mW	η %	Power Ratio P/P$_o$ %
					113	0.99	0.76	85.5	15.8	
25	1x10^{11}				85	0.84	0.74	52.5	9.7	61.4
25	1x10^{11}				81	0.82	0.73	48.3	8.9	56.3
25	1x10^{11}				76	0.80	0.71	43.2	8.0	50.6
		200	1		79	0.81	0.72	46.2	8.54	54
		"	3	4	79	0.81	0.72	46.2	8.54	54
		"	18	22	81	0.82	0.73	48.4	8.95	56.6
		"	72.5	94.5	83	0.82	0.72	49.6	9.2	58.2
		"	51	145	83	0.82	0.72	49.6	9.2	58.2
		300	4		87	0.85	0.73	53.9	10.0	63.2
		"	74	78	89	0.87	0.73	56.1	10.4	65.8
		350	2.5		88	0.86	0.73	55.4	10.2	64.5
		400	1		91	0.87	0.72	56.8	10.5	66.4
		"	3.5	4.5	92	0.87	0.70	56.1	10.4	66
		500	1		106	0.90	0.71	67.7	12.5	79
		550	1		106	0.91	0.72	69.4	12.8	81
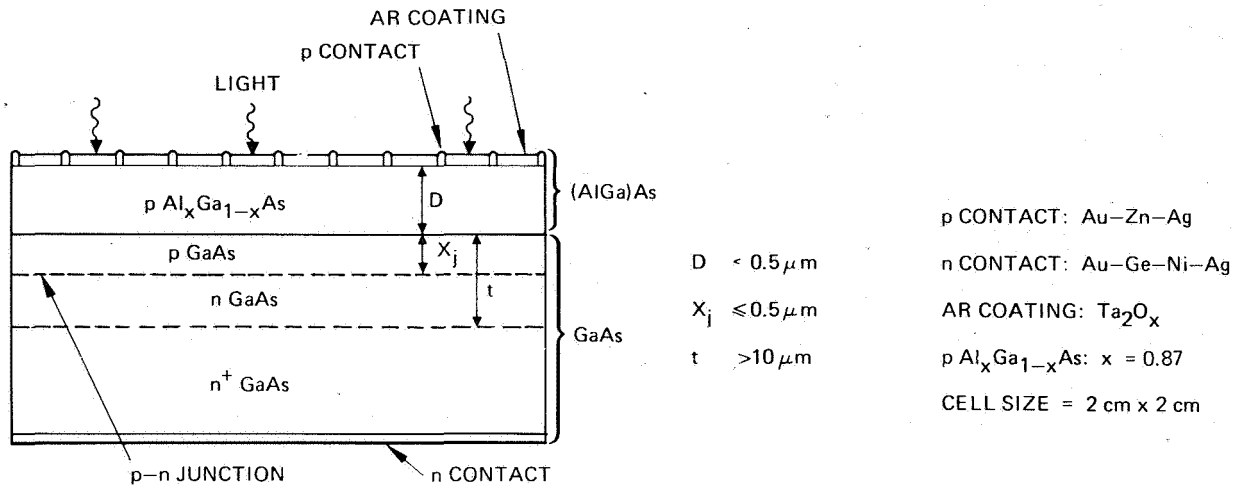
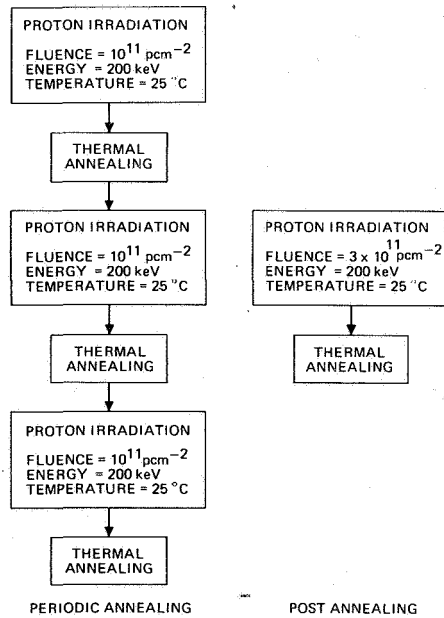Figure 1. (AlGa)As-GaAs solar cell structure

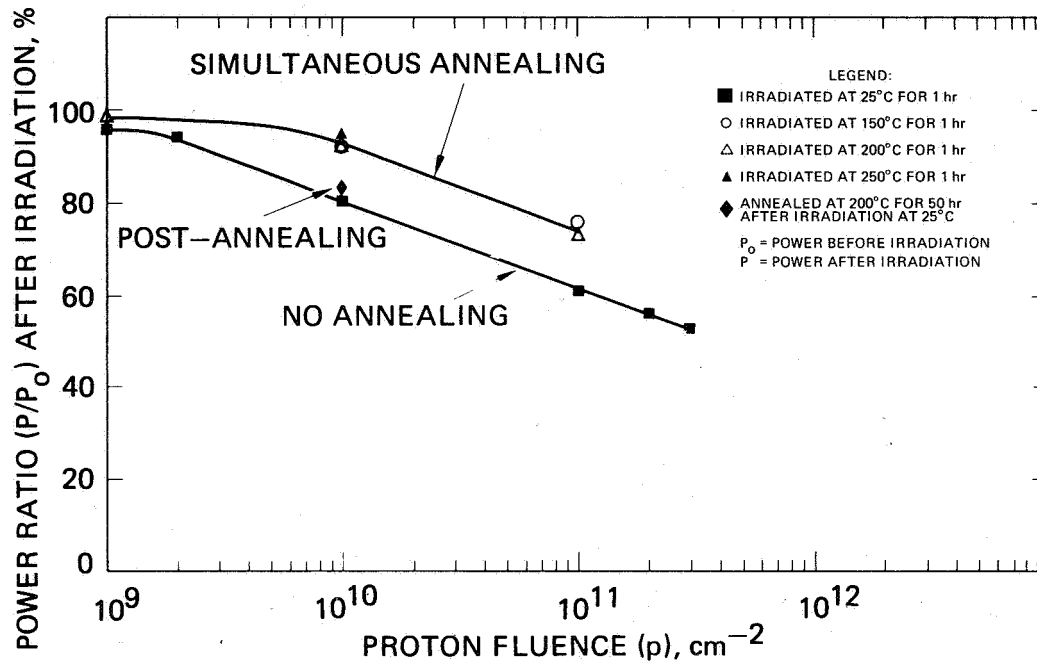Figure 2. Flow chart for periodic annealing experiment

Figure 3. Continuous annealing during irradiation with 200 keV protons

STUDY OF RADIATION INDUCED DEEP-LEVEL DEFECTS IN
PROTON IRRADIATED AlGaAs-GaAs SOLAR CELLS*

Sheng S. Li
University of Florida
Gainesville, Florida

EXTENDED ABSTRACT

The purpose of this paper is to report our findings on the study of the radiation induced deep-level defects (both electron and hole traps) in the proton irradiated AlGaAs-GaAs p-n junction solar cells and to show the correlation between the measured defect parameters and the solar cell performance parameters. This work was carried out in collaboration with Dr. Loo of Hughes Research Labs in conjunction with their high efficiency GaAs solar cell program for space applications. The range of proton energies was from 50 KeV to 10 MeV and the proton fluence was varied from 10^{10} to 10^{13} P/cm^2. Experimental tools employed include deep-level transient spectroscopy (DLTS), capacitance-voltage (C-V), current voltage (I-V), and SEM-EBIC methods. Defect and recombination parameters such as defect density and energy level, capture cross section, carrier lifetimes and effective hole diffusion lengths in n-GaAs LPE layers have been determined from these measurements. Detailed discussions of the measurement techniques and experimental results on the proton induced defects in GaAs solar cells can be obtained from our recent NASA technical reports and publications listed in ref. 1 through ref. 6. Highlights of our technical findings are summarized as follows:

(1) From the DLTS and C-V measurements, it is found that (a) the defect density (both electron and hole traps) increases with increasing proton fluence, (b) 50 KeV protons only produced damages in the p-AlGaAs window layer and the p-GaAs LPE layer and showed the least degradation to the solar cell performance, (c) the most severe damages were created by protons with energies between 200 and 300 KeV in which defect densities were high and defect spectrum was complicated; on the other hand, the defect density in the 0.8 and 10 MeV proton irradiated samples was lower and the defect spectrum was simpler than those samples with lower proton energies, (d) the dominant electron trap levels observed are the E_c-0.52 eV and E_c-0.71 eV, which are the main recombination centers in these proton-irradiated samples; increasing the proton fluence will result in the increase in the amplitude of E_c-0.52 eV level and the reduction of E_c-0.71 eV level. Fig. 1 and Fig. 2 show the DLTS spectra as a function of proton energy for the electron and hole traps, respectively, for proton fluences of 10^{12} P/cm^2. It is clearly illustrated in both figures that defect spectra in the 200 KeV and 290 KeV proton irradiated samples are more complex than those in the 100 KeV and 10 MeV samples. Fig. 3 and Fig. 4 show the DLTS spectra for the electron and hole traps respectively as a function of proton energy, for proton fluence of 10^{13} P/cm^2. The dominant electron trap in this case is due to the E_c-.52 eV level while the main hole trap is due to the E_v + 0.52 eV level. The effect of thermal annealing on the deep-level defects in

the 200 KeV proton irradiated samples has also been studied by using a 300°C thermal annealing in vacuum for one hour. The results show that defects produced by the 200 KeV protons can be effectively reduced or annealed out for proton fluences less than 10^{12} P/cm^2; this is illustrated in Fig. 5. From the dark forward I-V measurements, it is found that the recombination current in the junction space charge region of the cell dominates the dark current and its magnitude increases with increasing proton fluence. The increase in the dark current with proton fluence has been attributed to the increase in the density of recombination centers in the depletion region of the cell with increasing proton fluence, as was confirmed by the DLTS data shown above. 300°C thermal annealing process reduces the dark current significantly, as is shown in Fig. 6. Fig. 7 shows the effective carrier lifetimes in the junction space charge region vs. proton fluence for two proton energies (i.e. 100 and 200 Kev), as calculated from the dark forward I-V data shown in Fig. 6. The results show that carrier lifetimes vary from around 4 ns for the unirradiated cell to less than 0.1 ns as proton fluence increases to 10^{13} P/cm^2. A 300°C thermal annealing recovers the effective lifetime from 0.2 ns to about 1 ns. From the results of the SEM-EBIC measurements, it was found that the effective hole diffusion lengths in the n-GaAs LPE layers were reduced from around 3 μm for the unirradiated cell to less than 0.5 μm for the 10^{13} P/cm^2 and 290 KeV proton irradiated cell. A quantitative comparison between the measured defect parameters and the solar cell performance parameters shows good correlation existed between these two sets of parameters.

In short, the research finding from this work would indeed provide a useful information to guide the design of a radiation hardened GaAs solar cell for space applications, and gain a better understanding of the deep-level traps and the role of these deep-level defects on the proton irradiated solar cell performance.

REFERENCES

1. S. S. Li: "Studies of Electronic Properties in proton Irradiated AlGaAs-GaAs Solar Cells." NASA Semi-Annual Technical Report, Sept. 1, (1978), (1979), and (1980).

2. S. S. Li, W. L. Wang, P. W. Lai, T. R. Owen, R. Y. Loo and S. Kamath: J. Elec. Matr.. 9, 335 (1980).

3. S. S. Li, W. L. Wang, P. W. Lai, R. Y. Loo, G. S. Kamath, and R. C. Knechtli: Proc. IEEE Photovoltaic Specialist, Conf. Pp. 1080-84 (1980).

4. S. S. Li, W. L. Wang, P. W. Lai, R. Y. Loo, G. S. Kamath: IEEE Trans. Elec. Devices. ED-27, 857 (1980).

5. S. S. Li, D. W. Schoenfeld, T. T. Chiu and R. Y. Loo: Proc. of the 15th Intersociety Energy Conversion Engineering Conf.. Vol. 1, pp 354-357 (1980).

6. S. S. Li, T. T. Chiu, D. W. Schoenfeld, and R. Y. Loo: Proc. of the 11th International Conf. on Defects and Radiation Effects in Semiconductors. Sept. 8-11 (1980).

Fig. 1 DLTS scans of electron traps in proton irradiated AlGaAs-GaAs solar
cells as a function of proton energy, for proton fluence of 10^{12} P/cm^2.
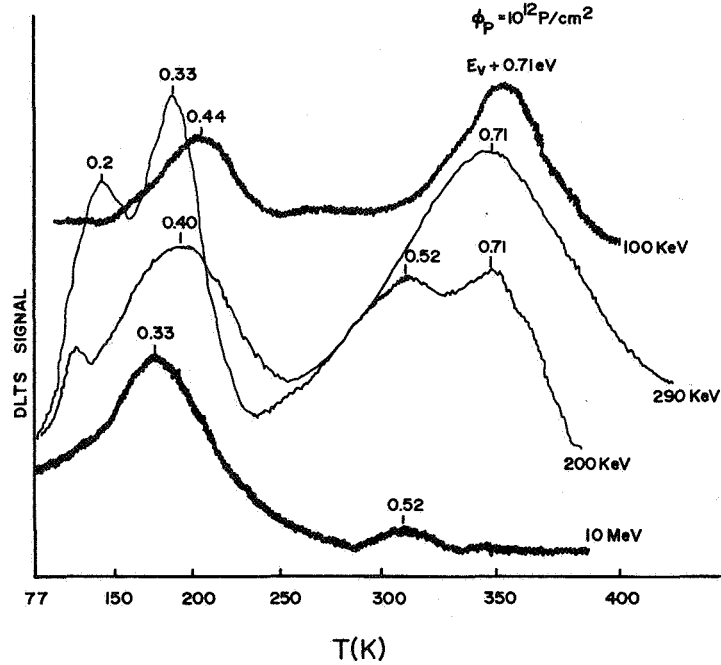
Fig. 2 DLTS scans of hole traps in proton irradiated AlGaAs-GaAs solar cells
as a function of proton energy, for proton fluence of 10^{12} P/cm^2.
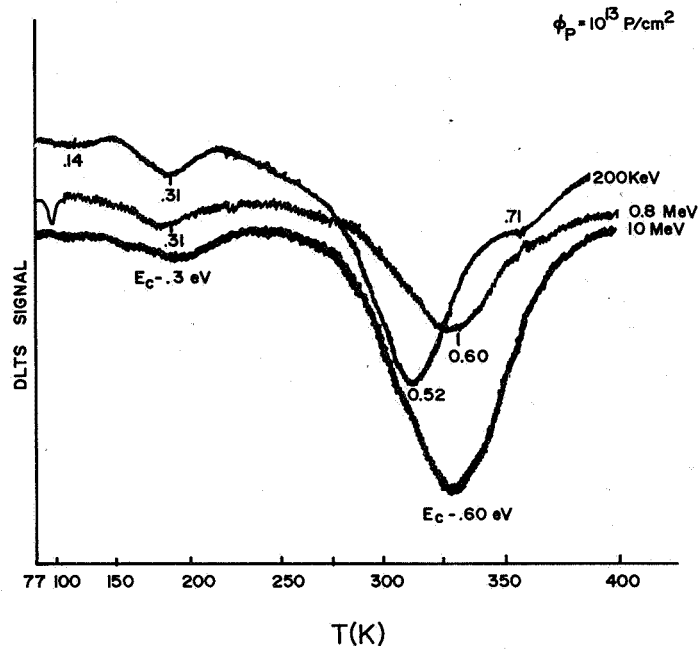
Fig. 3 DLTS scans of electron traps in proton irradiated AlGaAs-GaAs solar cells as a function of proton energy, for proton fluence of 10^{13} P/cm^2.
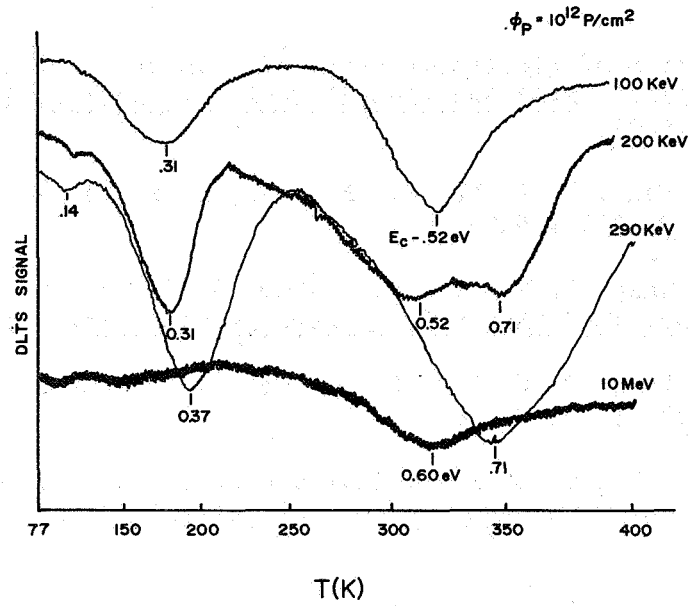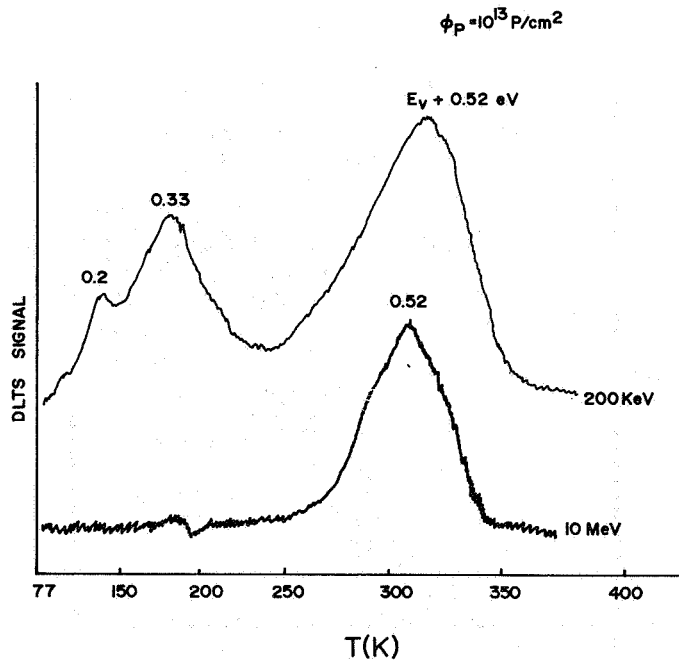

Fig. 4 DLTS scans of hole traps in proton irradiated AlGaAs-GaAs solar cells as a function of proton energy, for proton fluence of 10^{13} P/cm^2.
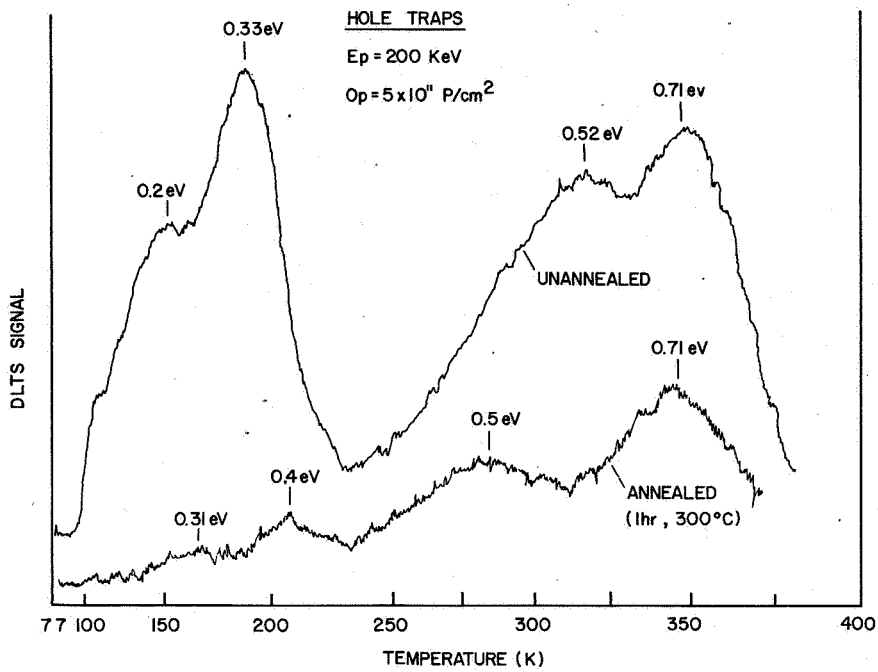
Fig. 5 DLTS scans of hole traps in 200 KeV proton irradiated AlGaAs-GaAs solar cells before and after 300°C thermal annealing, for proton fluence of 5×10^{11} P/cm^2.
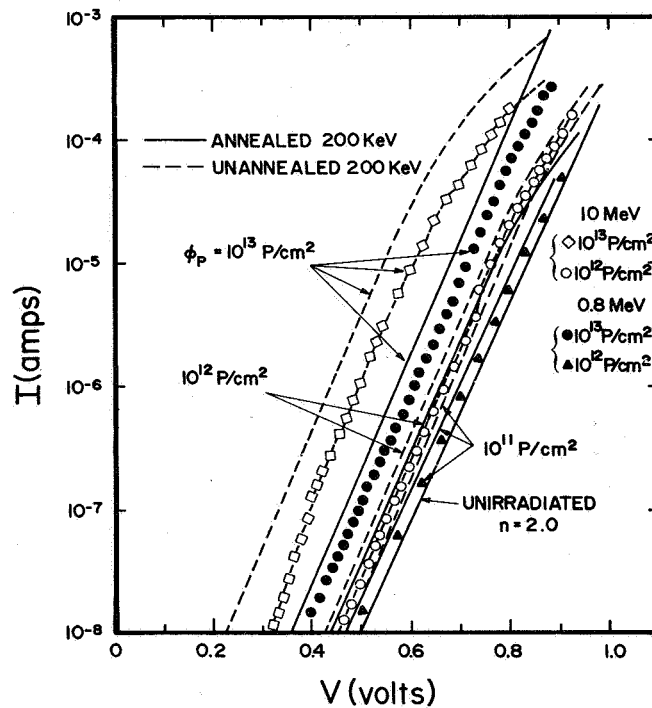
Fig. 6 Comparison of dark forward I-V characteristics for proton irradiated AlGaAs-GaAs solar cells, for different proton fluence and proton energy.
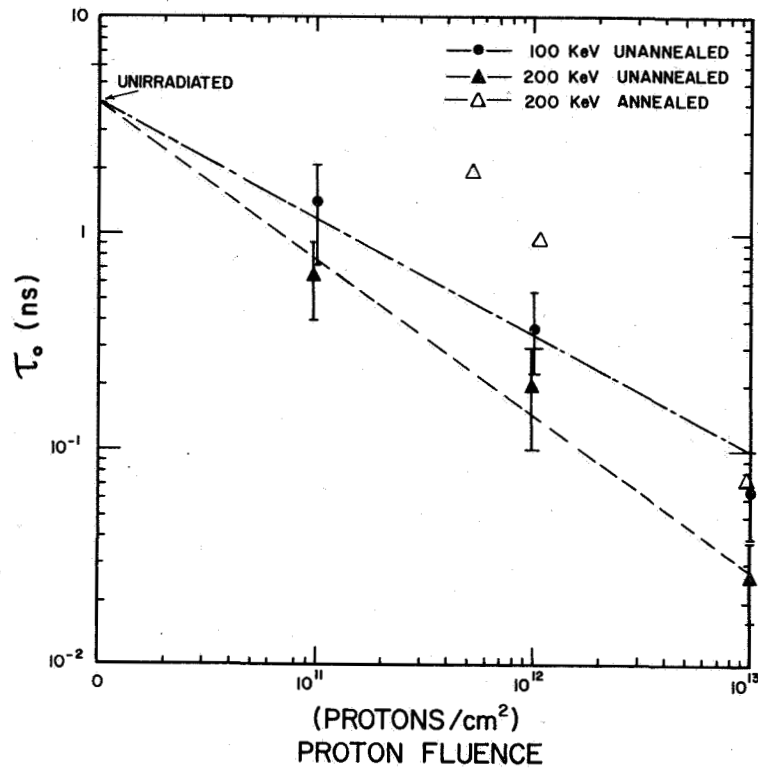
Fig. 7 Effective carrier lifetime vs proton fluence for the 100 and 200 KeV proton irradiated samples with and without thermal annealing. As calculated from the I-V data shown in Fig. 6.

PROTON RADIATION DAMAGE IN BULK n-GaAs

W. E. Stanchina*
University of Notre Dame
Notre Dame, Indiana

and

D. C. Liu, J. W. Blue, and D. J. Flood
NASA Lewis Research Center
Cleveland, Ohio

SUMMARY

Bulk samples of Te-doped n-type GaAs were irradiated using 10 MeV to 24 MeV protons to fluences between 2×10^{11} protons/cm^2 and 2×10^{14} protons/cm^2. Majority carrier electrical effects were measured using the van der Pauw techniques and it was observed that radiation damage was minimal at the 10^{11} proton/cm^2 fluence. For the higher fluences, carrier removal was proportional to $\Delta E/\Delta x$ for the protons indicating ionization interactions between the protons and atoms. Thermal annealing was observed at 155°C.

INTRODUCTION

Gallium arsenide is of interest for space photovoltaic solar-cells because of its expected increased resistance to space radiation damage and higher solar cell efficiencies than possible for silicon. Proton induced damage to GaAs solar cells, however, has been examined only in a limited number of studies (ref. 1-3). These investigations have been focused primarily on protons with energies $\leq$ 1 MeV with only a few data points at higher energies. Also, the various specialized solar cell structures have been irradiated independent of each other. In contrast to these above mentioned studies, the investigation described in this report has been directed toward evaluating changes in fundamental material properties (as opposed to specific device performance) for higher energy protons. The intent is to begin to identify regimes in which proton radiation effects are significant in determining electrical characteristics of GaAs. This information will hopefully aid in the development of designs for more radiation-resistant solar cells.

Many GaAs solar cell designs are being aimed at high efficiency cell performance in geosynchronous earth orbit ($\sim$ 35,800 km altitude) for 10 or more years. It appears that solar flare protons are the dominant source of radiation in this environment (ref. 4). Solar cells in geosynchronous orbit will also be exposed, to a lesser extent, to trapped electrons in that orbit and to trapped electrons and protons during transfer orbits. The indication is that the solar flare protons with energies > 10 MeV may impinge on cells in synchronous orbits

---

*NASA/ASEE Summer Faculty Fellow at Lewis Research Center.

with total fluences of nearly 10^{11} protons/cm^2 or more (ref. 5-7). This fluence, however, will depend on the life of the spacecraft beyond 10 years and the particular flare cycle.

The intent of this study was to begin to identify those middle-range energy protons and fluences which are detrimental to GaAs electrical properties. Based on this consideration, and the numbers and energies of solar flare protons found in synchronous orbit, it was decided to investigate proton energies between 10 MeV and 25 MeV and fluences in excess of 1 x 10^{11} protons/cm^2. These protons were readily available at the NASA Lewis Research Center variable energy cyclotron.

One measure of semiconductor defect production resulting from irradiation is the majority carrier removal (i.e. percent decrease in majority carrier concentration) as a function of radiation fluence (ref. 8). Data of this nature and other majority carrier effects such as mobility and resistivity changes were easily obtained by making pre-irradiation and post-irradiation Hall effect measurements.

In addition to describing more fully the experimental procedures for the above mentioned proton irradiations and Hall measurements for n-type GaAs, this paper will also describe a technique for accurate determination of total proton fluences in irradiated GaAs. Results will be presented linking decreases in mobility and majority carrier concentration to proton energies and fluences as well as data linking 1 MeV electron damage to 10 MeV through 24 MeV proton damage for possible equivalences.

EXPERIMENTAL

Samples used in this study were Czochralski grown n-type bulk gallium arsenide obtained from Metals Research Ltd. (England). The (100) oriented, Te-doped wafers had initial carrier concentrations of about 1 x 10^{17} electrons/cm^3, resistivities of 2 x 10^{-2} Ω - cm, and majority carrier mobilities of about 3900 cm^2/V-s. The 0.38 mm (15 mil) thick wafers, polished on both sides, were diced into 8mm x 8mm samples.

Room temperature Hall effect measurements were used to characterize the GaAs before and after irradiation. The Hall measurements were made using the contacts in each of the four corners (ref. 10). The ohmic contacts were made using pure indium. The sample was first etched for 30 seconds in a warm solution of $3H_2SO_4$:$1H_2O_2$:$1H_2O$ to remove oxides from the surface. Dots of pure In were placed in each of the four corners of the sample using a low-power ultrasonic soldering iron in contact with the gallium arsenide (heat-sinked to an aluminum plate) for approximately 1 second. I-V characteristics of all contacts were checked using a transistor curve tracer and were accepted when these characteristics were linear for currents ranging from 0.01 mA to 100 mA. Non-linear Schottky barrier contacts were successfully alloyed further to obtain linear characteristics by applying voltages in excess of the breakdown voltage.

Good ohmic contacts provided for symmetric van der Pauw technique Hall

266

measurements when the applied currents and magnetic fields were reversed. Applied currents ranged from 10 mA to 50 mA and the applied magnetic induction was 10,000 Gauss. Hall data was collected on each sample before and after irradiations.

All irradiations with protons were conducted at the NASA Lewis Research Center variable energy cyclotron facility. Proton energies of 12.5 MeV and 38.8 MeV were obtained from the cyclotron, and scattering foils were used to more evenly disperse the beam over a wider area ($\approx 3in^2$). Also, in one arrangement, samples were stacked vertically with varying thicknesses of aluminum between them to allow for simultaneous irradiation of different samples with different energy protons all to the same fluence. The result was that irradiations of gallium arsenide were conducted with protons having incident energies of 9.9 MeV, 12.0 MeV, 16.4 MeV, and 24.0 MeV to total fluences ranging between approximately 2×10^{11} protons/cm^2 to 2×10^{14} protons/cm^2. All irradiations reported here were done with the samples in air. To prevent annealing during irradiation, the samples were mounted on a heavy stainless steel plate and the entire apparatus was cooled by a fan. Also, a low proton beam current of 0.2 μA was used.

A direct technique was utilized in this study to measure total proton fluence for each sample. This technique was based on assaying the 39.2 hour half-life Ge-69 isotope, in each irradiated sample, produced by the $Ga^{69}(p,n)$ Ge^{69} reaction. Cross sections, $\sigma(E)$, as a function of proton energy were experimentally determined for the above reaction and several others in GaAs. The curve for this cross section is shown in figure 1. This data was obtained using a 15% Ge-Li solid-state detector. The total proton fluence in the GaAs sample could then be determined by

$$\phi_{proton} = \frac{N_{Ge-69}}{[N_{Ga-69}]\sigma(E)} \qquad (1)$$

where N_{Ga-69} = 60% of the Ga atoms in the original sample

N_{Ge-69} = the number of radioactive isotopes produced by the proton radiation; measured by counting the γ-radiation from the Ge-69 isotope.

This method for determining total fluence was believed to be quite accurate since it did not rely on the accuracy of any secondary standards or detectors.

RESULTS AND DISCUSSION

Results presented in this section are for proton irradiations of four samples of Te-doped GaAs labeled A-D. Original Hall data (i.e. before irradiation) and energies of the incident protons for the four samples are shown in table 1. The proton energies listed are the incident proton energies, transmitted proton energies, and average energies. Note that in these irradiations, the protons traveled completely through the 15 mil GaAs samples although their energies did decrease. A 15 mil thick sample of GaAs will stop any protons

with energies $\leq$ 9.4 MeV.

Figure 2 shows the fractional decrease in room temperature Hall mobility as a function of total fluence. It appears that for incident protons having energies $\geq$ 10 MeV, fluences must be in excess of 10^{13} protons/cm^2 before majority carrier mobility degradation becomes significant.

This same phenomena can be observed for majority carrier removal as shown in figure 3. In fact, if these curves are extrapolated down to the horizontal axis, it appears that noticeable degradation of a GaAs device will not occur below $\sim 10^{11}$ protons/cm^2 for incident proton energies in excess of 10 MeV. This result also demonstrates that as the average energy of the protons increases, their incremental effect in damaging the material decreases. In other words, this supports the tenet that lower energy particles do more damage. This same principle is shown more clearly in figure 4. Here the carrier removal is shown to be a linear function of the proton energy loss per unit distance traveled in the gallium arsenide. The linear nature of this plot suggests that the proton interaction with the gallium and arsenic atoms involves an ionization process.

In an effort to verify that the Hall measurements made in this study were good, it was decided to attempt duplication of 1 MeV electron irradiation results of Look and Farmer (ref. 11). Samples from the same crystal as samples A-D were irradiated with 1 MeV electrons at the NASA Lewis Research Center dynamitron. Total fluences were 4 x 10^{15} e$^-$/cm^2, 1 x 10^{16} e$^-$/cm^2, and 3 x 10^{16} e$^-$/cm^2. As can be seen from figure 5, this data agrees quite well with that of Look and Farmer (ref. 11). Not only does this add validity to our Hall measurements, but it provides some indication of possible equivalence of 9.9 MeV proton damage in GaAs with 1 MeV electron damage in that material. The equivalences in terms of majority carrier removal in n-type GaAs are shown in figure 5. Although the ratios of electrons to protons are not constant (varying between 250 and 326), it appears that a 9.9 MeV proton is approximately equivalent to 300--1 MeV electrons.

Figure 6, a plot of mobility degradation factor as a function of fluence, may provide a clearer picture of equivalence. The mobility degradation factor, b, is defined as follows (ref. 8):

$$b = \frac{\mu_i}{\phi} \left(\frac{1}{\mu_f} - \frac{1}{\mu_i} \right) \tag{2}$$

where $b \, (\text{cm}^2)$ = Mobility degradation factor

$\mu_i \, (\text{cm}^2/\text{V-s})$ = Initial Hall mobility

$\mu_f \, (\text{cm}^2/\text{V-s})$ = Final Hall mobility

$\left. \begin{array}{l} \phi \, (\text{p}^+/\text{cm}^2) \\ \phi \, (\text{e}^-/\text{cm}^2) \end{array} \right\}$ = Total fluence

In this figure the incremental mobility degradation appears to be about the

same for 16.4 MeV protons and 1 MeV electrons. In this case, it appears that 1--16.4 MeV proton does about as much damage as 190--1 MeV electrons.

Low temperature (155°C) annealing of proton and electron damage was briefly examined. Two samples were examined which had been irradiated (1 MeV electrons to 1 x 10^{16} e$^-$/cm^2 and 16.4 MeV protons to 6.5 x 10^{13} p$^+$/cm^2) to obtain approximately 30% carrier removal. Results of this isothermal annealing in forming gas are shown in figure 7. Percent recovery is defined for this figure as:

$$R = \left(\frac{n_{annealed} - n_{damaged}}{n_{undamaged} - n_{damaged}} \right) \times 100\% \qquad (3)$$

In this definition "n" means majority carrier concentration. Although recovery was not complete after 50 hours of annealing, this data does indicate that annealing was occurring. Thus there is some indication that self-annealing at low temperatures may be feasible especially when particle flux is low such that the permanent damage will occur only in small amounts over the life of the gallium arsenide solar cell.

CONCLUSION

Results of this study indicate that protons with energies between 10 MeV and 25 MeV will probably not adversely affect n-type gallium arsenide for solar cell performance unless the total fluence exceeds 10^{11} protons/cm^2. For proton fluences between 10^{11} protons/cm^2 and 10^{14} protons/cm^2, it appears that the lower energy protons do more damage even for complete penetration through the material. The proton-atom interaction appears to be an ionization process for these radiation conditions. Defects introduced under these conditions appear to be at least partially removed by annealing at 155°C. One might speculate that continuous cell operation at this relatively low annealing temperature would reduce the damaging effects of proton radiation and extend solar cell life.

REFERENCES

1. Rahilly, W.P.; and Anspaugh, B.: Electron, Proton and Fission Spectrum Neutron Radiation Damage in Advanced Silicon and Gallium Arsenide Solar Cells. Solar Cell High Efficiency and Radiation Damage - 1977. NASA CP-2020, 1977.

2. Anspaugh, B.; Kamath, S.; Knechtli, R.C.; and Loo, R.: Fabrication of High Efficiency and Radiation Resistant GaAs Solar Cells. Solar Cell High Efficiency and Radiation Damage - 1979. NASA CP-2097, 1979.

3. Conway, E.J.; and Walker, G.H.: Radiation Damage in GaAs Solar Cells. Solar Cell High Efficiency and Radiation Damage - 1979. NASA CP-2097, 1979.

4. Rauschenbach, H.S.: Solar Cell Array Design Handbook; Van Nostrand Reinhold Co., New York, 1980. pp. 443-459.

5. Tada, H.Y.; and Carter, J.R., Jr.: Solar Cell Radiation Handbook. JPL Publication 77-56, November 1977.

6. Imhof, W.L.; Bostrom, C.O.; Beall, D.S.; Armstrong, J.C.; Heckman, H.H.; Lindstrom, P.J.; Nakano, G.H.; Paulikas, G.A.; and Blake, J.B.: Models of the Trapped Radiation Environment, Vol. VII: Long Term Time Variations. NASA SP-3024, 1971.

7. Intelsat V, Request for Proposals and Alternatives. Comsat BG-8-23E, W/3/74, 28 March 1974.

8. Chaffin, R.J.: Microwave Semiconductor Devices: Fundamentals and Radiation Effects; Wiley-Interscience, New York, 1973, pp. 88-146.

9. van der Pauw, L.J.: A Method of Measuring Specific Resistivity and Hall Effect of Discs of Arbitrary Shape. Philips Res. Repts., Vol. 13, 1958, pp. 1-9

10. Chwang, R.; Smith, B.J.; and Crowell, C.R.: Contact Size Effects on the van der Pauw Method for Resistivity and Hall Coefficient Measurement. Solid-St. Electron., Vol. 17, 1974, pp. 1217-1227.

11. Farmer, J.W.; and Look, D.C.: Electron Irradiation Defects in n-Type GaAs. Phys. Rev. B, Vol. 21, April 1980, p. 3389.

TABLE 1 – SAMPLE CHARACTERISTICS

SAMPLE	Original Hall Data			Proton Energies (MeV)		
	ρ_o (Ω-cm)	n_o (e^-/cm^3)	μ_o (cm^2/V-s)	E_{in}	E_{out}	E_{aver}
A		1.08×10^{17}	4248	9.9	1.6	5.8
B	1.74×10^{-2}	9.30×10^{16}	3864	12.0	6.0	9.0
C	1.42×10^{-2}	1.11×10^{17}	3960	16.4	12.0	14.2
D	1.90×10^{-2}	8.35×10^{16}	3938	24.0	20.9	22.5

σ (m barn)

E_{in} (MeV)
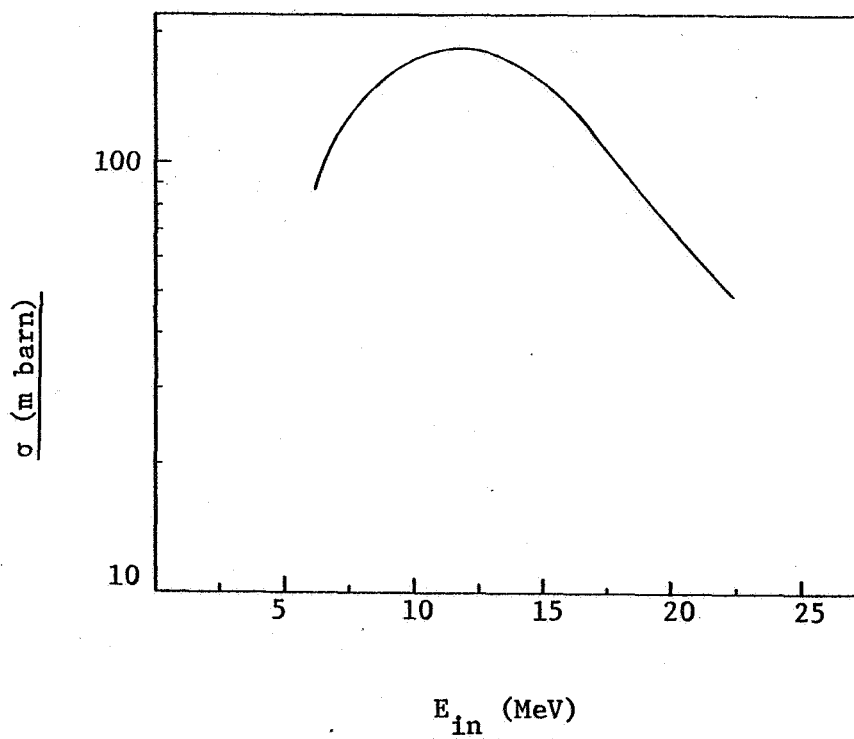
Figure 1. Cross section as a function of incident proton energy for the $Ga^{69}(p,n)Ge^{69}$ reaction
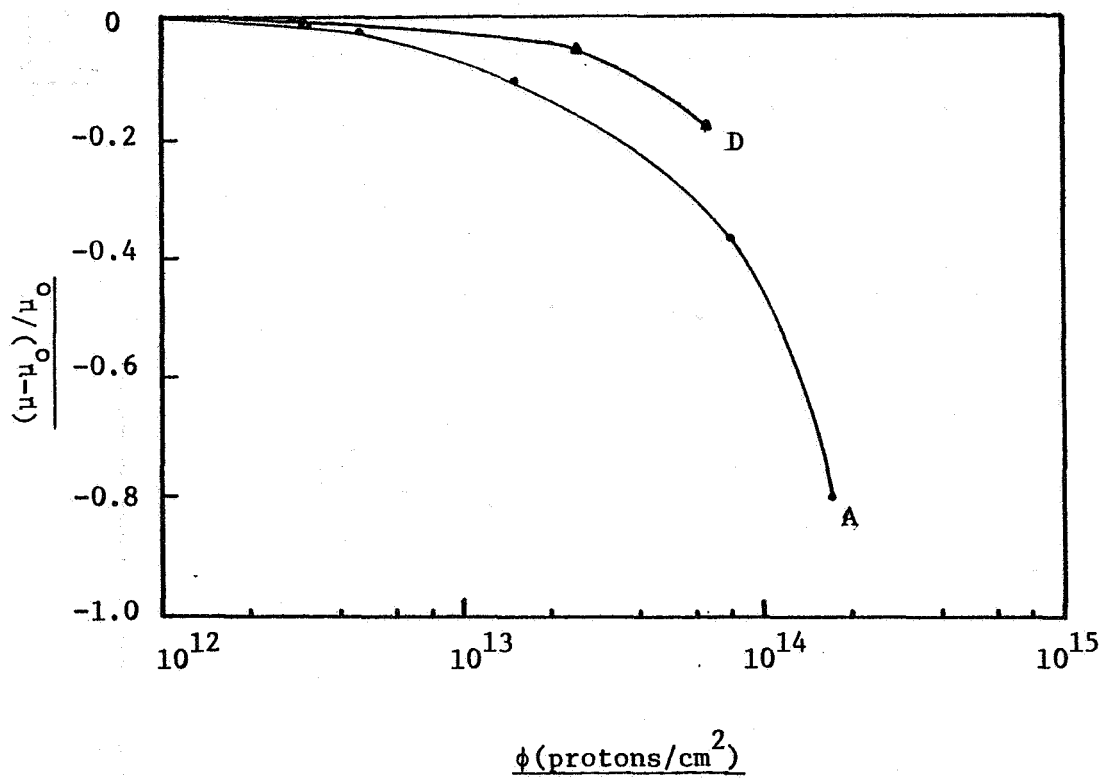
Figure 2. Fractional decrease in room temperature
Hall mobility as a function of proton fluence
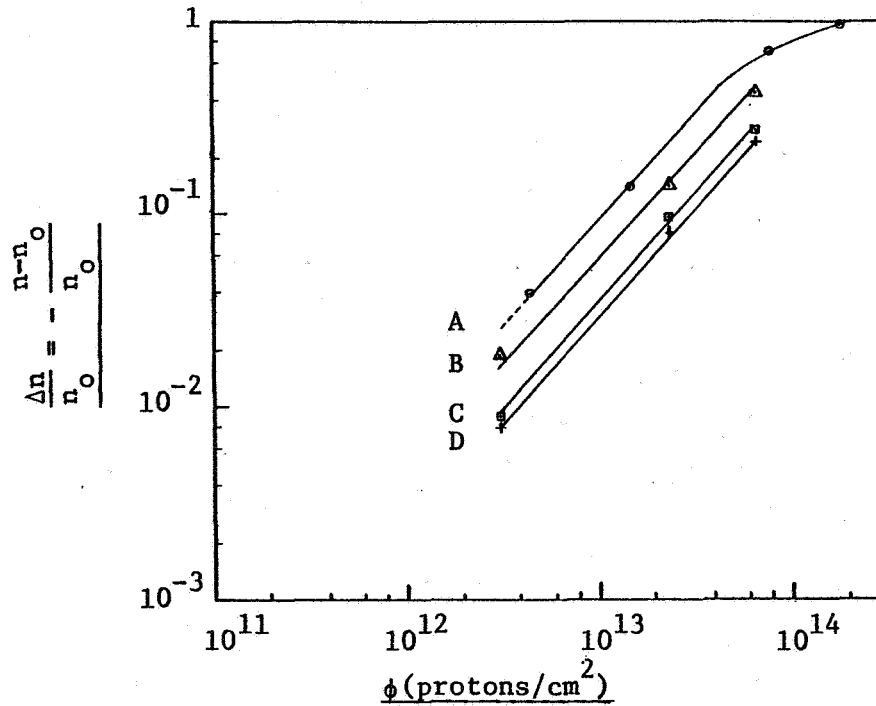
Figure 3. Carrier removal in Te-doped GaAs($n \cong 1\mathrm{x}10^{17}$ cm^{-3}) as a function of proton fluence
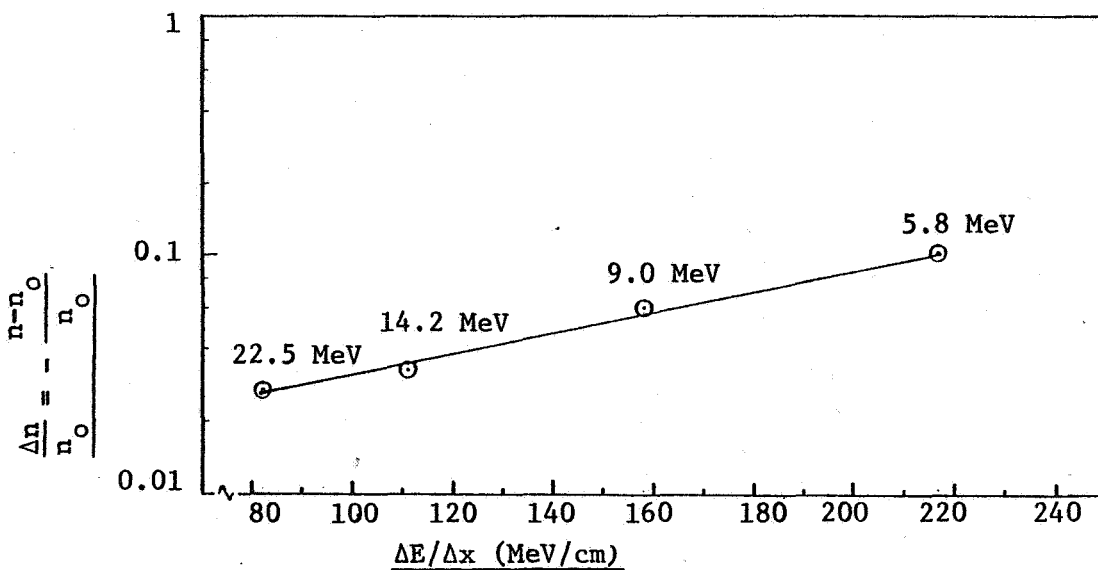
Figure 4. Carrier removal vs. the ratio of the total proton energy loss to the sample thickness. For all samples, $\Delta x = 0.038$ cm and $\phi = 1\mathrm{x}10^{13}$ protons/cm^2. Energies listed are average energies.

273
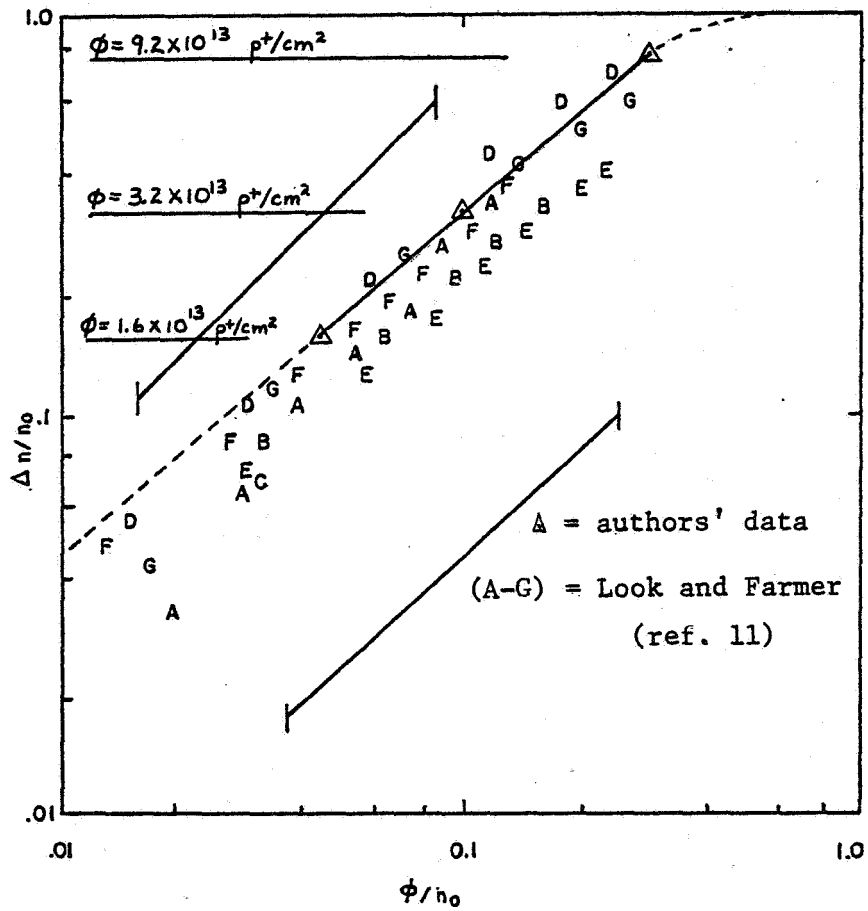
Figure 5. Free carrier removal as a function
of fluence for 1 MeV electrons. Horizontal lines
indicate equivalent damage produced by 9.9 MeV protons.
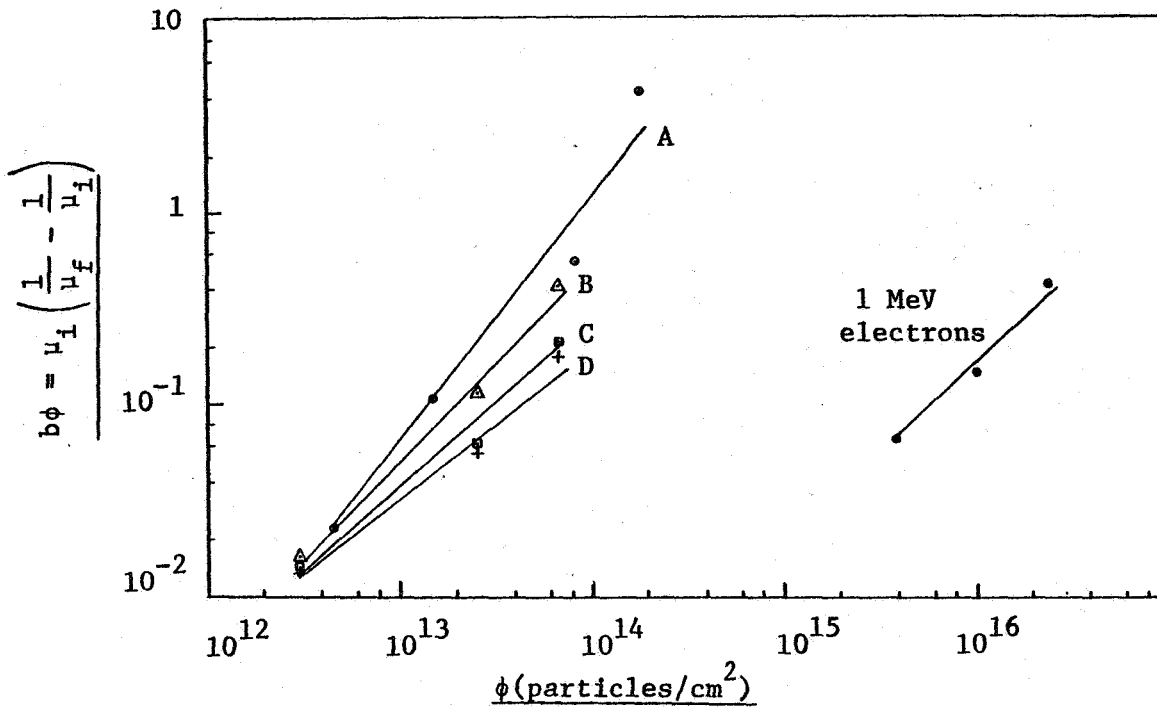
Figure 6. Mobility degradation vs. total fluence. Shown is a comparison of damage for 9.9 MeV, 12.0 MeV, 16.4 MeV and 24.0 MeV protons and 1 MeV electrons.

Figure 7. 155°C annealing results for proton and electron irradiated samples. $\Delta n/n_o \approx 0.3$ for both cases.

ANNEALING RADIATION DAMAGED SILICON SOLAR CELLS
WITH A COPPER HALIDE LASER

Thomas J. Pivirotto
Jet Propulsion Laboratory
Pasadena, California

ABSTRACT

A multiply pulsed copper halide laser has been used to significantly anneal out the damage to silicon solar cells caused by a simulated space radiation environment. Preliminary experiments have demonstrated that the amount of damage can be decreased by 41% as measured by the maximum power generated.
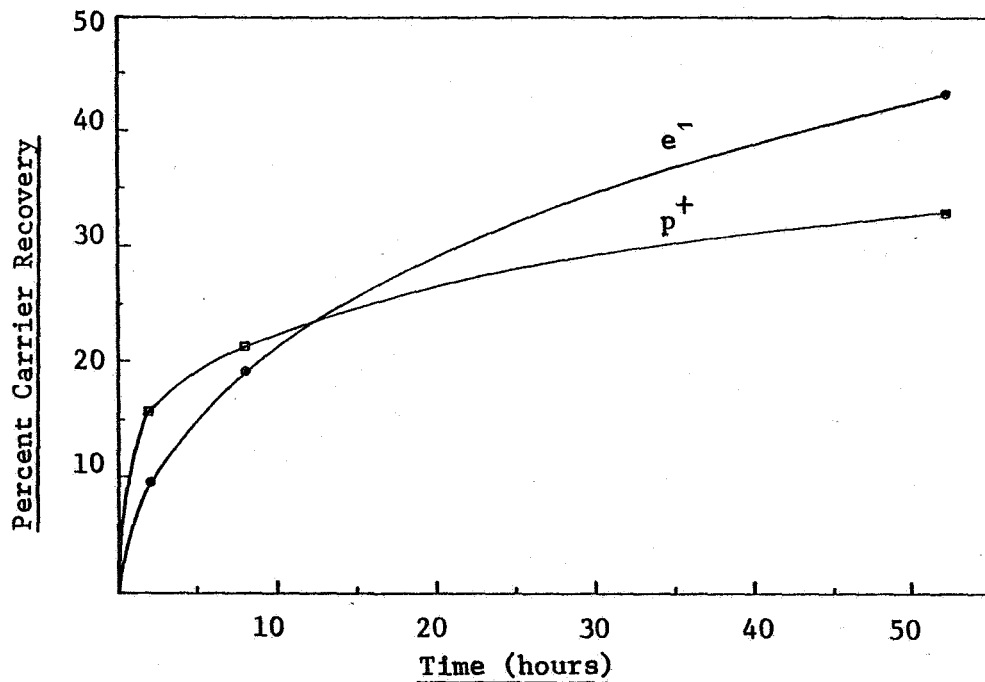
INTRODUCTION

The performance of silicon solar cells is degraded in the radiation environment of space by energetic particles such as electrons, protons, neutrons and ions. This degradation increases with time and results in a reduced power generation capability of the irradiated solar array. To overcome this degradation effect on mission performance the solar panels are generally built large enough to supply the spacecraft power required at the end of the mission. This solution results in overly large and heavy solar panels at launch and an excess initial output power.

An alternative approach to this problem would be a provision for periodically annealing the damaged cells in situ. This could be conveniently accomplished with a high efficiency laser which has an output wave length that is readily absorbed by silicon. This approach could result in a lower launch weight, simplified power conditioning, and extended mission life times.

Some previous experimental studies of the ability of various lasers to anneal radiation damaged silicon solar cells have been reported[1,2]. The lasers used were: 1) CO_2 with a wave length (λ) of about 10 μm and an absorption length (a^{-1}) in silicon of about 10^4 μm; 2) YAG with a λ of 1.06 μm and a a^{-1} of 80 μm; and 3) Ruby with a λ of 0.694 μm and an a^{-1} of 10 μm. Performance recovery, as measured by the maximum generated power, of from 20 to 80% was observed.

Because of the encouraging results of the previous work it was felt that a copper halide laser (CHL) should be investigated for this application because of: 1) the small absorption length for the CHL radiation in silicon;

2) the potential scalability to very high average powers; and 3) its demonstrated high efficiency. The absorption length, in silicon, of the two CHL output wave lengths (511 and 578 nm) is about 1 μ. This short absorption length will become more important as the thickness of the silicon cells decreases in the future. The potentially high average power will decrease the time required to fully anneal large solar panels in space and the high efficiency will reduce the size and weight of the laser power supply and heat rejection system.

EXPERIMENTAL APPROACH

A preliminary experiment, utilizing existing equipment, was developed to test the feasibility of the CHL for solar cell annealing. The CHL used in these experiments had a maximum pulse energy of 1.5 mj, a pulse width of about 20 ns, peak pulse intensity of 75 kW/cm^2 (with 60% of this intensity at 511 nm and the remainder at 578 nm), a beam diameter of about 1 cm, a pulse repetition rate variable between about 10 and 30 kHz, an average power of 15 watts and an efficiency of about 1%.

As shown in Figure 1, the laser beam was reflected into the vertical plane, for convenience, then focused with an achromatic lens to the desired spot diameter at the solar cell surface. The solar cell was housed in a small vacuum chamber to prevent oxidation of the hot silicon and to partially simulate the heat transfer conditions in space. The vacuum chamber was mounted on a motor driven, traversing platform. This platform could sweep the cell through the focused beam in the X direction at a pre-determined speed and move in the Y direction with pre-determined step sizes. In this way the entire cell surface could be treated with an approximately uniform energy density.

RESULTS

Preliminary tests of this system were performed on cells manufactured by Spectrolab Inc. (K6 3/4, BSF, BSR, MLAR). The I-V characteristics of the cells were measured three times: firstly, as received from Spectrolab; secondly, after irradiation with 1 Mev electrons to a fluence of 10^{15} e/cm^2 and a room temperature cure; and then a third time after annealing with the CHL. Typical results are shown in Figs. 2 and 3. In both of these experiments the spot size was 0.17 cm with a spot overlap, in the Y direction, of 2/3. The average energy density in the spot was 0.013 j/cm^2. The average power was 4.3 watts and the pulse repetition rate was 14.3 kHz. For the results of Fig. 2, the traversing speed was 0.16 cm/sec, resulting in a total applied energy density of about 500 j/cm^2 on the cell surface. The corresponding data for the results of Fig. 3 are 0.13 cm/sec and 690 j/cm^2.

The results shown in Fig. 1 and 2 clearly indicate that the damaged cells were partially annealed in these preliminary experiments. The shape of the characteristic was altered by the annealing process in the experiment of Fig. 2, but the performance recovery was substantial. In Fig. 3 it is seen that, although the performance recovery is not as great as that shown in Fig. 2, the shape of the characteristic was retained. These results are in general agreement with those obtained with a YAG and Ruby laser and reported on in Ref. 1 and 2.

DISCUSSION

Once the feasibility of using a CHL for annealing radiation damaged silicon solar cells was established by these preliminary experiments, an improved experimental set-up was developed. This new set-up includes: 1) an oscillator-amplifier system with a 25 watt average power and 2.5 mj/pulse capability; 2) near-optimum optical elements including an unstable resonator which produces a near-diffraction-limited beam for better focusing at the solar cell surface; and 3) an automatic traversing and indexing system with a much wider range of speed and step size and a larger capacity. With the new set-up the deficiencies of the preliminary set-up have been overcome and the parametric range, such as spot diameter, traversing speed and amount of spot overlap, has been greatly increased.

Additional experiments with this set-up should indicate the amount of solar cell performance recovery which could be expected in an operational environment. With these improvements in experimental equipment and procedure, it is expected that the CHL annealing process can be made more efficient and that the solar cell performance can be increased to near its pre-radiation level.

CONCLUSIONS

It has been demonstrated that a Copper Halide Laser can be used to anneal radiation damaged silicon solar cells. To date 41% of the loss of maximum power, due to radiation damage, was recovered by annealing with a CHL. Future experiments with the improved experimental set-up should establish the potential of the CHL for this application.

REFERENCES

1. Kirkpatrick, A. R.; Neal, W. R.; Minnucci, J. A.; "Annealing of Radiation Damage in Silicon Solar Cells", Phase I Report, March 15, 1977, Simulation Physics, Inc., Bedford, Mass.

2. Minnucci, J. A.; Matthei, K. W.; Kirkpatrick, A. R.; "In-Situ Annealing of Space Radiation Damage", Record of the 13th Photovoltaic Specialists Conference, IEEE, Pg. 586 to 589, (June 1978).
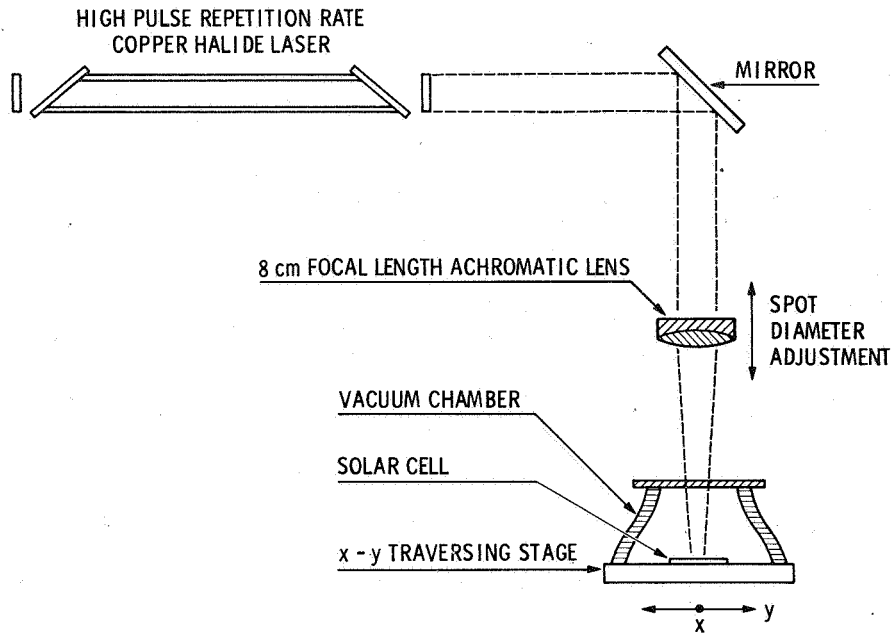
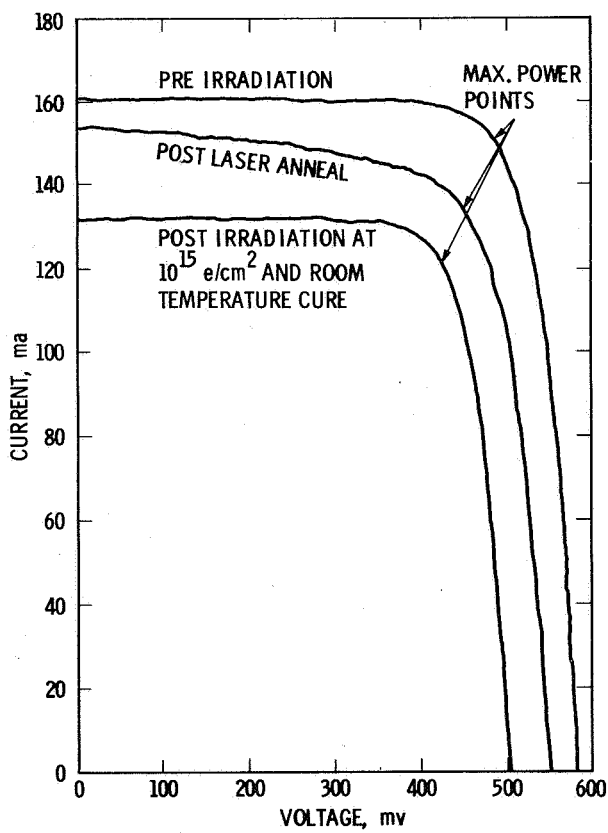Figure 1.   Schematic of Solar Cell Annealing Experiment

Figure 2.   Effect of Annealing
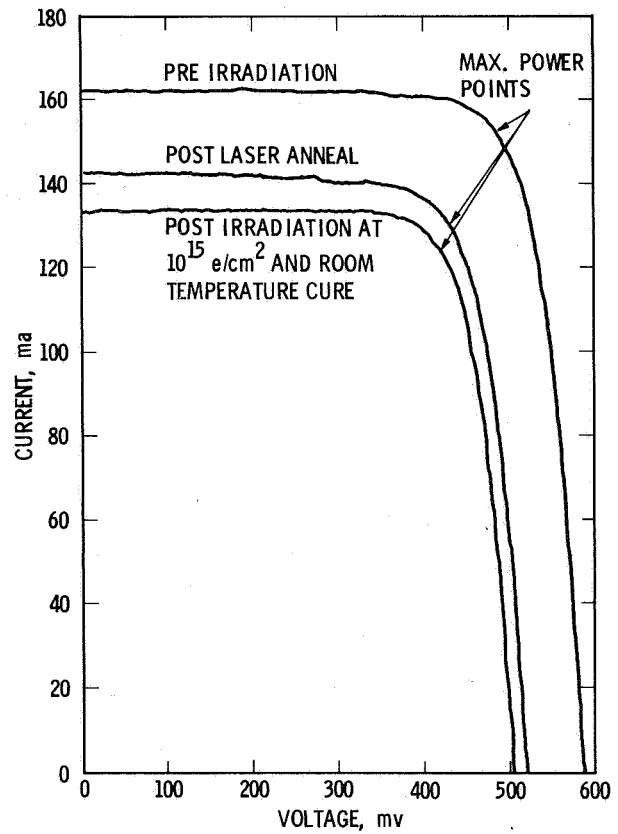Radiation Damaged Silicon Solar Cells
with a Copper Halide Laser

Figure 3.   Effect of Annealing
Radiation Damaged Silicon Solar Cells
with a Copper Halide Laser

RADIATION TOLERANCE OF BORON DOPED DENDRITIC WEB

SILICON SOLAR CELLS

A. Rohatgi
Westinghouse R&D Center
Pittsburgh, Pennsylvania

SUMMARY

The potential of dendritic web silicon for giving radiation hard solar cells is compared with the float zone silicon material. Solar cells with n^+-p-p^+ structure and ~15% (AMl) efficiency were subjected to 1 MeV electron irradiation. Radiation tolerance of web cell efficiency was found to be at least as good as that of the float zone silicon cell. The study of the annealing behavior of radiation-induced defects via deep level transient spectroscopy revealed that $E_v + 0.31$ eV defect, attributed to boron-oxygen-vacancy complex, is responsible for the reverse annealing of the irradiated cells in the temperature range of 150-350°C.

INTRODUCTION

Important considerations for improving efficiency and radiation hardness of silicon solar cells include high purity silicon, proper cell design, and careful cell processing. High efficiency (ref. 1,2) is very important for both terrestrial and space solar cells, however, solar cell life is drastically reduced in space by the exposure to the radiation environment unless some means is provided to restore the radiation damage (ref. 3,4). For high efficiency silicon crystal growth should keep the level of metal impurities at its minimum because they can reduce the carrier lifetime (ref. 5,6) and degrade the cell performance. The level of other impurities, such as carbon and oxygen, should also be minimized for the radiation hardness because they are known to form complexes with dopants and radiation-induced point defects and give rise to recombination centers (ref. 7,8). Dendritic web silicon is a single crystal ribbon which offers several advantages for producing low cost and radiation hard solar cells. This paper will compare these web features with float zone silicon. For better understanding of the radiation effects, we have used deep level transient spectroscopy (ref. 9) to delineate the radiation-induced traps and study their annealing behavior.

EXPERIMENTAL

Silicon Dendritic Web Growth

Web is a ribbon form of single crystal silicon which is shaped by crystallographic and surface tension forces rather than by potentially contaminating dies. Web crystal for solar cells is generally grown 2-8 mils thick, 2-5 cm wide, and several meters in length. The web results from freezing of a liquid silicon film supported between two bounding dendrites (ref. 10) with the general geometry shown in figure 1. The web can be grown very thin (~2 mils), which makes it cost effective and very attractive for radiation hard solar cells. The surfaces of the ribbon are nearly perfect crystallographic (111) facets which require only minimal cleaning procedures and no mechanical treatments prior to device fabrication. The growth apparatus is relatively simple: a furnace chamber and a molybdenum susceptor which holds the fused quartz crucible; a molybdenum lid assembly with a slot through which the ribbon is withdrawn; and a reel which serves both as a pull mechanism and material storage. Heat is introduced into the system by induction coupling to the molybdenum susceptor. Melt replenishment permits essentially continuous growth.

Cell Fabrication

A large number of n^+-p-p^+ solar cells were fabricated by a diffusion process on several different p-type, boron-doped, web crystals in the resistivity range of 1-10 Ω-cm. The precleaned web crystals along with a few boron doped (111) float zone wafers (10-15 Ω-cm) were phosphorous diffused at 850°C for 35 minutes for the front junction and the p^+ back surface field was formed by boron diffusion at 950°C for 20 minutes. No special attempts were made to obtain high efficiency cells. The n^+ junction depth was approximately 0.35 μm and the sheet resistance was 60 $\Omega/\square$. A mixed oxide, TiO_2-SiO_2, antireflective coating was applied on the front by a spin-on process. The cells with an area of 1.03 cm^2 were metallized with Ti-Pd-Ag using an electron-beam system and then mesa etched. The front pattern was a five-finger grid with 5.4% area coverage. Solar cells were tested under illumination from a quartz-iodide simulator which was set at 91.6 mW/cm^2 using a NASA-Lewis calibrated standard cell.

Electron Radiation and Deep Level Transient Spectroscopy

Radiation tolerance of the cells was investigated by subjecting them to 1 MeV electron radiation in the fluence range of 10^{13} - 5 x 10^{15} electrons/cm^2. Deep level transient spectroscopy was used to determine the trap levels generated by electron irradiation. In order to conduct the DLTS measurements, the solar cells were subdivided into 30 mil diameter mesa diodes with Ti-Au contacts. For the annealing studies, DLTS samples and solar cells were simultaneously subjected to heat treatment in air, in 50°C steps, in the temperature range of 100-450°C, the annealing time was 30 minutes at each temperature.

RESULTS AND DISCUSSION

Figure 2 shows the effect of 1 MeV electron radiation on the parameters of a web and a float zone silicon cell. The dopant (boron) concentration in the float zone silicon was four times smaller than in the web and both cells were about 8 mils thick. The data show that 1 MeV electron radiation, beyond a dose of 10^{13} electrons/cm^2, begins to impair the cell performance. It is noteworthy that web cells, in spite of higher boron concentration, are at least as radiation tolerant as the float zone silicon cells. Table 1 shows that after a dose of 10^{15} electrons/cm^2 three deep levels, at E_V + 0.21 eV, E_V + 0.37 eV and E_C - 0.24 eV, were observed in the float zone silicon cell as well as in the web cell. E_V + 0.21 eV level is associated with divacancy and E_V + 0.37 eV and E_C - 0.24 eV levels are attributed to vacancy-carbon-oxygen and interstitial oxygen-boron complexes, respectively (ref. 7). These data show that the rate of introduction and the concentration of the divacancy and the carbon related center is nearly the same in both the cells. Schott et al. (ref. 8) reported that the rate of introduction of carbon related center was higher in the crucible-grown material compared to a float zone material. This suggests that carbon content of the web may be less than other crucible-grown materials, like Czochralski silicon, because there are no graphite components in the web growth system. Most notable difference, however, is about an order of magnitude smaller concentration of the interstitial boron-oxygen defect (E_C - 0.24 eV) in the float zone silicon after the 1 MeV electron irradiation. Since the boron content of the float zone material is low only by a factor of four, the order of magnitude lower concentration of the E_C - 0.24 eV trap suggests higher oxygen content in the web compared to the float zone silicon. This is expected because web is grown from a silicon melt which is in contact with a fused quartz crucible.

Table 1 shows that after 5 x 10^{15} electrons/cm^2 radiation three more deep levels, at E_V + 0.31 eV, E_V + 0.54 eV and E_C - 0.17 eV, were detected in float zone silicon, and one more level, at E_C - .17 eV, was observed in the web cell, in addition to the E_V + 0.21 eV, E_V + 0.37 eV and E_C - 0.24 eV traps. Figure 3 shows that the response of these radiated cells to isochronal annealing is very similar. The data show a reverse annealing of the cells in the temperature range of 150-350°C. The cell efficiency drops by about 1% in the temperature range of 150°C-250°C and stays constant until about 350°C, before the rapid recovery begins. The recovery is not complete even after 450°C anneal if the damage is extensive (5 x 10^{15} electrons/cm^2). Figures 4 and 5 show the annealing behavior of the traps present in the web and float zone silicon cells after 5 x 10^{15} electrons/cm^2 radiation. Most noteworthy is the behavior of E_V + 0.31 eV trap which grows in the temperature range of 150-250°C, stays constant until 350°C and anneals out at approximately 400°C. Figure 6 shows more clearly that these data strongly indicate that E_V + 0.31 eV level, attributed to boron-oxygen-vacancy complex, is responsible for the reverse annealing.

CONCLUSIONS

Dendritic web silicon is capable of producing solar cells with radiation tolerance comparable to the float zone silicon cells. From the densities of

carbon and oxygen-related cneters, $E_v + 0.37$ eV and $E_c - 0.24$ eV, respectively, we conclude that carbon content of the web is as low as float zone silicon but the oxygen content is higher. Annealing of the electron-irradiated solar cells show an appreciable drop in the cell efficiency in the temperature range of 200-350°C, prior to the cell recovery. $E_v + 0.31$ eV trap, generally attributed to boron-oxygen-vacancy complex, is found to be responsible for this reverse annealing.

REFERENCES

1. J. G. Fossum and E. L. Burgess, Appl. Phys. Lett. 33(3), p. 238 (1978).

2. M. Wolf, Proc. 14th IEEE Photovoltaic Conf., San Diego, Ca, p. 674 (1980).

3. H. Y. Tada and J. R. Carter, Jr., Solar Cell Radiation Handbook, JPL Publication 77-56, Contract No. NAS7-100 (1977).

4. I. Weinberg and C. K. Swartz, Appl. Phys. Lett. 36(8), p. 693 (1980).

5. J. R. Davis, A. Rohatgi, R. H. Hopkins, P. D. Blais, P. Rai-Choudhury, J. R. McCormick and H. C. Mollenkopf, IEEE Trans. on Electron Devices, ED-27(4) (1980).

6. A. Rohatgi, J. R. Davis, R. H. Hopkins, P. Rai-Choudhury, P. G. McMullin and J. R. McCormick, J. Sol. St. Elec. 23(5), p. 415 (1980).

7. P. M. Mooney, L. J. Cheng, M. Suli, J. D. Gerson and J. W. Corbett, Phys. Rev., B15, p. 3836 (1977).

8. J. T. Schott, H. M. DeAngelis and P. J. Drevinski, J. Elec. Mat. 9(2), p. 419 (1980).

9. G. L. Miller, D. V. Lang and L. C. Kimerling, Ann. Rev. Mat. Sci. p. 377 (1977).

10. R. G. Seidensticker, L. Scudder and H. W. Brandhorst, Jr., Proc. IEEE 11th Photovoltaic Specialists Conference, New York, p. 299 (1975).

TABLE 1

Energy levels and concentrations of defects observed in 10 Ω-cm, boron-doped, float zone silicon solar cell and 3 Ω-cm, boron doped, web solar cell after 1 MeV electron irradiation

Energy level (eV)	Defect Concentration (cm^{-3}) 10^{15} e/cm^2 irradiation		Defect Concentration (cm^{-3}) 5×10^{15} e/cm^2 irradiation	
	FZ silicon cell	Web cell	FZ silicon cell	Web cell
E_V+0.21	1.40×10^{12}	1.20×10^{12}	2.1×10^{13}	2.8×10^{13}
E_V+0.31	–	–	2.0×10^{12}	–
E_V+0.37	3.7×10^{12}	4.0×10^{12}	4.2×10^{13}	5.2×10^{13}
E_V+0.54	–	–	1.2×10^{12}	–
E_C-0.17	–	–	2.5×10^{12}	1.7×10^{12}
E_C-0.24	1.7×10^{12}	1.9×10^{13}	3.1×10^{13}	2.9×10^{14}
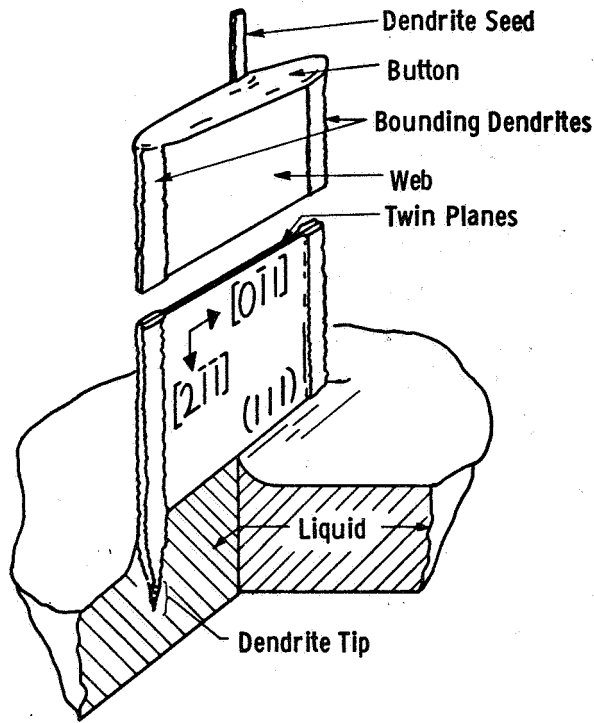
Figure 1:   Schematic section of web growth.
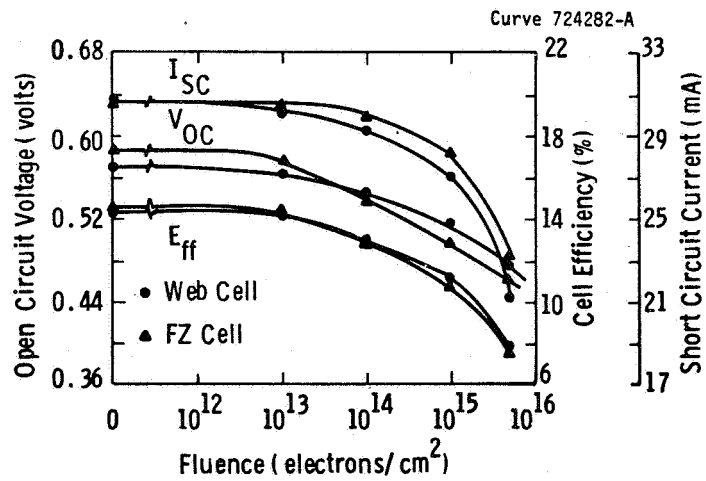
Figure 2:   Effect of 1 MeV electron irradiation on float
zone silicon and web solar cell.
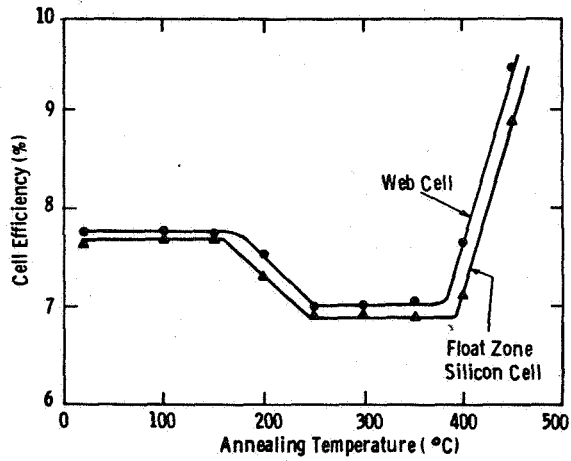
Figure 3: Change in efficiency of electron irradiated (5x10^15 e/cm^2) cells as a function of isochronal anneal. Efficiencies prior to irradiation were ~14.5%.
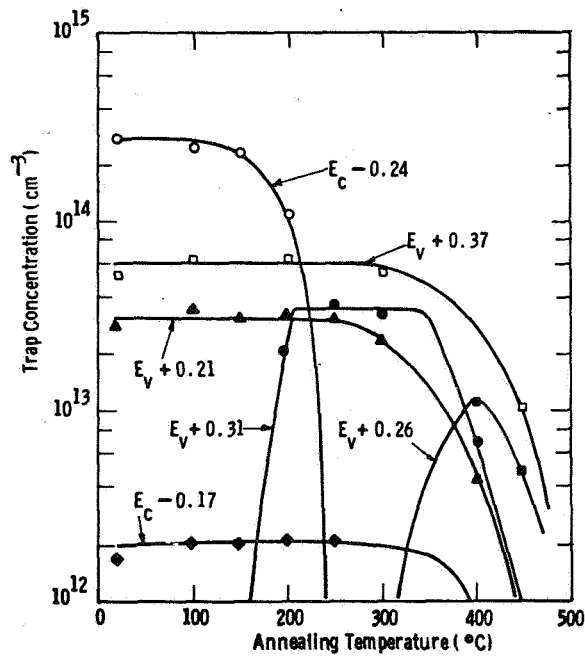
Figure 4: Change in defect concentrations during isochronal anneal of electron irradiated (5x10^15 e/cm^2) web solar cell.
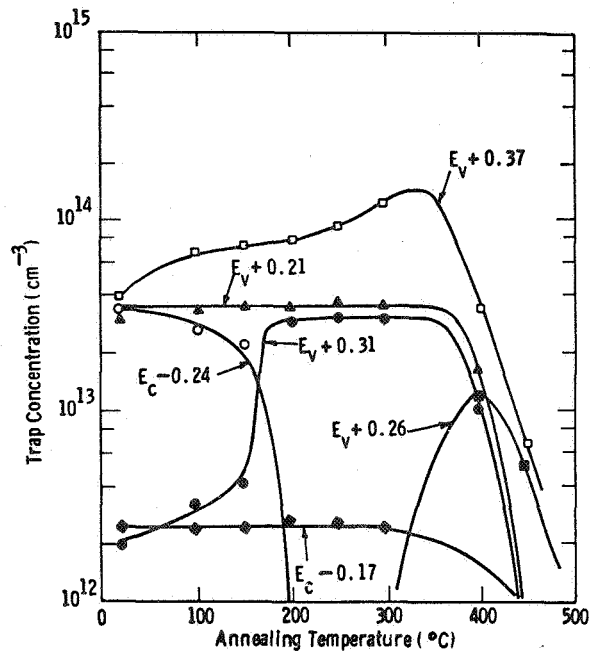
Figure 5: Change in defect concentrations during isochronal anneal of electron irradiated $(5\times10^{15}$ e/cm^2) float zone silicon cell.
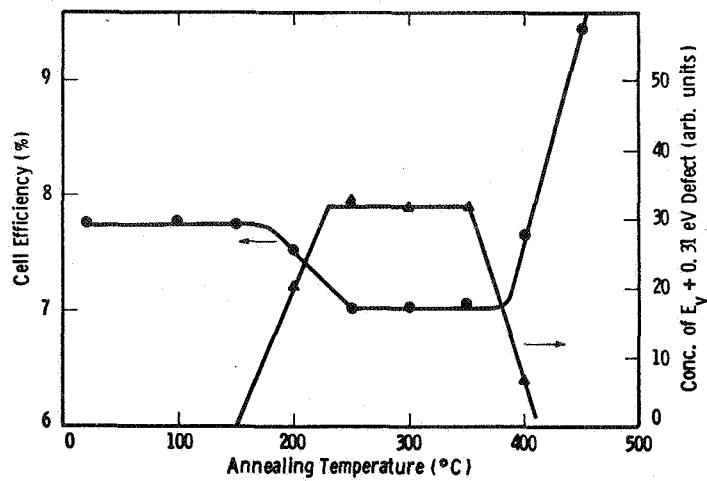
Figure 6: Relationship between the annealing behavior of E_v + 0.31 eV defect and reverse annealing of electron irradiated web solar cell.

RADIATION DAMAGE WORKSHOP REPORT

W. Patrick Rahilly
AF Wright Aeronautical Laboratories
Wright-Patterson AFB, Ohio

INTRODUCTION

The discussions were held to aspects concerned with Si and GaAs solar cell technologies. It was agreed that the multi-bandgap cell research is premature for radiation damage discussions since the materials used in such devices are not well characterized in terms of solar cell parameters (diffusion lengths, defects, growth methods, etc.). Some radiation damage work in the AlGaAs cell in GaAs cell is proceeding and will be included in the next HERD Conference.

WORKSHOP CONCLUSIONS/RECOMMENDATIONS

Three general categories were considered for the Si and GaAs cells - namely, Starting Material, Cell Design/Geometry and Cell Processing/Fabrication. The results and recommendations of the discussion are summarized below:·

Silicon

Starting Material - Purity of the starting material was concluded to be a fruitful area of research. It was emphasized that carbon and oxygen be held to as low as possible. In fact, a suggestion was made to purposely reduce all impurities by many zone processes of already high purity poly-silicon and then to make a final single crystal pass during which boron in one case and gallium in another would be introduced to achieve the desirable conductivities. The ingots would then be processed into solar cells for evaluation. However, it was understood that the true purity of these materials would not be known because of severe limitations on present diagnostic sensitivity - again for carbon and oxygen inparticular. Thus, increased sensitivity of diagnostic methods was considered a very crucial matter in the discussions with the recommendation that emphasis be placed on improving such techniques at least by an order of magnitude. Basic research on defect formation interactions and annealing mechanisms was considered important in light of achieving low temperature anneal of radiation induced defects (below 200°C). The SUNY (Corbett) work is addressing this issue but more work is needed to determine the effect of high purity material on defect formations interactions and anneal. Tied to the subject of defect dynamics is synergistic effects and it was concluded that combined proton and electron effects testing should be conducted with samples provided to SUNY. It was recommended that B and Ga be investigated on a comparison basis to determine advantages/disadvantages of these dopants in high purity materials. In summary, the following recommendations resulted:

289

(a) Reduce impurities - specifically O and C

(b) Increase sensitivity of O and C detection

(c) Conduct basic research on defect formation, interactions and anneal mechanisms

(d) Include in (c) synergistic electron and proton effects

(e) Continue research comparing B and Ga dopants in high purity material

(f) Emphasize in all research achievement of annealing of defects at temperatures <200°C.

Cell Design/Geometry - For very high power-to-weight ratios at end-of-life, the thin cell and a thinned version of the vertical junction cell have promise. It was concluded that emphasis continue on both these structures with the addition of a thin cell with a drift field placed thereon very similar to the Westinghouse drift field cells of the mid to late sixties. Also, P-I-N structures offer the potential for very high radiation resistance in a thin geometry. Not enough work has been accomplished in the P-I-N structure and more is needed. The vertical junction structure may be very beneficial if the "tilt" is used. More research into this aspect of the VJ cell is needed. All of these cell concepts require input from the high purity material efforts to make a final judgement of which geometry is best suited for high end-of-life efficiency and low mass/cell design. In summary, the following recommendations were made:

(a) Continue thin cell development with and without drift fields

(b) Continue vertical junction cell work with further investigation of the "tilt" advantage

(c) Continue the P-I-N effort - definitely need more radiation damage characterization on this device.

Cell Fabrication/Processing - Discussions were somewhat inconclusive in this area since not enough data has been generated. The discussions led to the conclusion that experiments should be conducted to decide on the advantages/disadvantages of P/N junction formation using N^+ diffusions and N^+ ion implantations. Radiation effects on rear contacts for low intensity, low temperature applications need further study. In summary:

(a) Determine relative merits of diffusion and implantation for P/N junction formation with respect to radiation damage.

(b) Place some effort on radiation effects to back contacts for low temperature, low intensity cell applications.

Gallium Arsenide

Starting/Grown Materials - Purity and crystallinity were considered important for GaAs cells from the point of view of high end-of-life. The substrates now available are very suspect of containing fastdiffusers that move into the LPE or MO-CVD grow photovoltaic layers. These impurities can tie to Ga and/or As vacancies as well as intersitial Ga and As atoms. It is not known at this point how serious the problem is. Crystalline quality also may play a major role (dislocations, etc.) since these defects will propogate into upper layers during growth and can become active during radiation exposure. It was concluded that emphasis should be placed on comparisons of very pure defect-free substrate material and conventional substrate material. The grown layers also require purity and crystalline quality. It was not clear that a real problem exists for the grown layers since those persons engaged in GaAs cell technology routinely check their source melt or gas materials for electronic grade purity. Although very good and more consistent quality GaAs cells are being made, it was concluded that variations on dopant species and concentration levels could potentially yield considerable gains over present cells in end-of-life efficiency; these aspects deserve high emphasis. As for annealing of damage, the basic mechanisms need considerable attention. The parameters such as damage coefficients, carrier removal rates, etc., have yet to be determined in GaAs cell materials, especially as functions of dopant species and levels. In summary, the following recommendations were made:

(a) Role of substrate quality in relation to radiation damage must be determined

(b) Increase emphasis on effects of purity, crystallinity and dopants in grown layers on performance with respect to radiation damage

(c) Radiation induced defects and their kinetics must be determined

(d) As for silicon, increased diagnostic sensitivity is a must for GaAs material purity evaluations

(e) Along with (b) and (c), basic studies must commence to define damage introduction and recovery processes as related to temperature effects

(f) A systematic study of annealing with a goal of 100% recovery at temperatures below 200°C, for fluences up to 1×10^{16} of 1MeV electrons

(g) Determine electron and proton damage equivalences in conjunction with variations of dopant species and concentration levels.

Cell Design/Geometry - This area of discussion concerned P/N versus N/P structures. It was concluded that research as discussed above, was needed to determine the relative merits of the various dopant types and levels. Such data will influence GaAs cell design (thin P layer?, thin N layer?, etc.). Thus, the recommendation concerning cell design and geometry was:

Perform modelling of GaAs cell structures as data becomes available to determine alternates to present designs.

Cell Fabrication/Processing - This discussion was limited to aspects of LPE and MO-CVD cell processing (processed induced defects) in relation to radiation damage. There is little data available to support any interrelation of process/fabrication and radiation damage. The recommendation was to:

(a) Examine LPE and MO-CVD growth processes in relation to radiation damage, but perform pre and post irradiation characterizations (DLTS for example) to make comparisons

(b) Perform (a) above in light of dopant species and levels.

OVERALL SUMMARY

In general, it was concluded that diagnostic sensitivities and material purities were basic to making significant gains in end-of-life performance and thermal annealability. Further, GaAs material characterization is so sketchy that a well defined program to evaluate such material for solar cell application is needed to maximize GaAs cell technology benefits.

PARTICIPANTS

The participants in this session were:

Cliff Swartz - NASA Lewis RC

Irv Weinberg - NASA Lewis RC

Al Scheimine - Solarex

Bill Stachina - Notre Dame

Ed Horne - Boeing

Bill Taylor - Spectrolab

Ron Knechtli - Hughes Research Laboratories

Russ Hart - NASA Lewis RC

Jim Cusih - NASA Lewis RC

Pat Rahilly - Chairman, AFWAL/POOC-2, Wright-Patterson AFB OH

EVALUATION OF SOLAR CELL COVERS AND ENCAPSULANT
MATERIALS FOR SPACE APPLICATION*

Dennis A. Russell
Boeing Aerospace Company
Seattle, Washington

SUMMARY

Testing of covered or encapsulated solar cells employing new materials and methods is described. Cover materials evaluated include glass resins, 2-mil glass applied with adhesives or electrostatically bonded and thin plastic films of FEP or PFA applied with adhesive. Solar cells were exposed to environmental conditions simulating those encountered in outer space. These test conditions include 1 MeV electrons, 0.5 MeV protons and thermal cycling in vacuum. During testing the solar cells were monitored for variations in electrical characteristics and structural changes.

INTRODUCTION

The ever increasing emphasis on high power/weight ratio of solar cell arrays and improved economy of manufacture of these structures requires new efforts to investigate methods in the application of light materials suitable for use as solar cell covers. The general objective of this program is to evaluate the effects of space radiation (electrons, protons, and ultraviolet), vacuum and thermal cycling on a variety of solar cell covers applied to solar cells. The approach is to expose groups of individual cells and cell modules encapsulated or covered with various materials to environmental conditions simulating those encountered during 10 years in geosynchronous orbit.

In this paper the test systems and methods used to simulate the space environments are presented. Test results from the electron irradiations interspersed with thermal cycling and proton irradiations interspersed with thermal cycling are presented including photographs of test cells.

SYSTEMS AND METHODS

Electron and Proton Irradiation

The Boeing Radiation Effects Laboratory's Dynamitron particle accelerator was the source of both the 1.0 MeV electrons and the 0.5 MeV protons used in

---

this study. Basically the particle beam after being analyzed by a 90 degree bending magnet, is directed into an evacuated chamber where it impinges on a high-purity aluminum foil. The thickness of the scattering foil is selected to give the desired profile for the scattered particle field at the sample plane. The incident particle beam is adjusted in energy so that, after losing energy in traversing the scattering foil, the particles emerge with the desired energy on the sample plane. The scattered particle field is mapped using a remotely controlled rotating Faraday cup. The incident flux profile on the sample plane is then determined from this relative beam profile and absolute intensities measured by a Faraday cup located in the sample plane. Fluences are then obtained by integrating the current collected at the sample plane or by timing the exposure.

UV Exposure

At the time of the writing of this paper the UV vacuum test chamber is being setup. The UV exposure will be done at a four equivalent UV sun rate. The UV source will be a Spectrolab X25L Solar Simulator. The vacuum chamber and simulator will be setup to operate continuously except when I-V measurements or thermal cycling is required.

Thermal Cycling

The test cells were mounted on a 1/8-inch thick copper plate with small beryllium-copper clips. Figure 1 is a view of the test cells mounted on the copper plate in the test chamber. A thin layer of thermal heatsink compound was placed between each cell and the copper plate to ensure good thermal conductivity. The sample plate was attached to a copper thermal control plate equipped with integral resistance heaters and cooling tubes. The back of this plate is shown in figure 2.

During thermal cycling the sample plate assembly was rotated 90° and the thermal cycling cover plate also containing integral resistance heaters and cooling tubes was moved into close proximity of the sample plate assembly (fig. 3). This method insures that the test cells were thermal cycled regardless of the thermal conductivity of the encapsulated cells. The cells were cycled from -175°C to +55°C. Liquid nitrogen was run through both plates to obtain the lower limit of 175°C. To warm the cells to 55°C a combination of the resistance heaters and hot gas was used. The cycling was conducted with a five-minute soak at both -175°C and +55°C. The heating rate was controlled within 10°C/min to 13°C/min and the cooling rate controlled within 10°C/min to 20°C/min.

I-V Measurements

I-V measurements were made both ex situ and in situ. The ex situ measurements were made before the start of irradiation and after the

completion of all irradiation and thermal cycling. The in situ measurements differ from the ex situ measurements only in that the solar simulator is beamed through a GE124 optical-grade fused silica window and the intensity is monitored by two monitor cells located in the vacuum test chamber but protected from the irradiation. The same Spectrolab X25L solar simulator with an AMO close-match filter was used for both the ex situ and in situ measurements. The I-V measurements were made at a nominal 25°C.

The data acquisition and reduction system consisted of a Tektronix 4051 minicomputer and graphics system. The 4051 was used to drive a load bank, store the raw data and analyze the data. A Tektronix 4662 plotter was used to plot computer fitted I-V and power curves and list I_{sc}, V_{oc}, P_{Max} and the fill factor for each level. Figures 4 and 5 are examples of a computer-plotted family of I-V and power curves.

Temperature Monitoring and Control

Test cell temperature was monitored by attaching a copper-constantan, Type T, thermocouple with epoxy to the surface of representative cells in each run. The temperature of the sample plate was also monitored.

During the I-V measurements the sample plate temperature and cell surface temperatures differed by 2°C to 8°C with the majority of cells differing by 3°C to 5°C. In order to bring the majority of cells to 25°C +1°. The sample plate temperature was reduced to 22°C. A temperature controlled water bath was used to control the sample plate temperature during both the I-V measurements and the irradiations. All particle irradiations were done at 55°C ± 5°.

TEST CONDITIONS

Table 1 lists both the electron and proton test conditions by stress level. Each level is either an irradiation or a set of 15 thermal cycles. I-V measurements were taken at each stress level. Visual inspection of the physical integrity of the cell was also made at each stress level. In situ photographs were taken of one representative cell of each type before testing and of each cell after testing.

TEST RESULTS

There were eight types of covers or encapsulants on cells in the testing. The cover materials included Glass Resins, 2-mil glass applied with adhesives or electrostatically bonded and thin plastic films such as FEP or PFA applied with adhesive. Table 2 lists the cell type designation and the components of the cell system including the cover, back, cell and adhesive used.

A-Series

(8-10 mils thick cell, 4-mil 0211 Ceria-doped cover, no backing, 0.5-mil 93-500 adhesive)

Electron Irradiation. The cells showed only normal behavior during irradiation or thermal cycling. Figure 6 is a plot of the average normalized maximum power versus fluence. (Where there are two data points at the same fluence value there has been a set of 15 thermal cycles run on the cells. Table 1 indicates at which fluences the thermal cycles have been performed.)

Proton Irradiation. There was no visible damage to the cells throughout the test. Figure 7 shows that the thermal cycling at 3×10^{14} P/cm^2 and 3.3×10^{15} P/cm^2 did not change the maximum power and that the 4-mil 0211 Ceria-doped cover protected the cell from proton damage.

C-Series

(2-mil cell, 2-mil FEP-A cover, 1-mil Kapton back, 2-mil 93-500 adhesive front and back)

Electron Irradiation. The first visible damage was observed after a fluence of 5×10^{15} e/cm^2 and 30 thermal cycles. At this point the FEP-A covers started cracking loose from the cell. Before this point there was no visual damage observed; therefore, the second set of 15 thermal cycles induced the cracking of the FEP-A. The cracking became worse after the third set of thermal cycles were completed. Figure 8 is a photograph of a cell after the complete irradiation schedule. The FEP-A has many small cracks and is raised up from the cell in many places. Figure 9 shows that after the second and third sets of thermal cycles there was a 2% reduction in maximum power due to light scattering from the cracks.

Proton Irradiation. The only visible and electrical damage observed was after a total fluence of 3.3×10^{15} p/cm^2. This caused the cell to have a hazy or foggy appearance and a loss of 3% in maximum power as shown in figure 10. This loss was due to a 3% decrease in I_{sc}. There was no observable damage directly caused by thermal cycling.

D-Series

(8-mil cell, ∿1.5-mil 93-500 cover, no backing no adhesive)

Electron Irradiation. There was only normal behavior observed electrically or visually. Figure 11 shows that thermal cycling did not affect the maximum power even after a fluence of 1×10^{16} e/cm^2.

Proton Irradiation. Cracks started to show in the 93-500 after 3×10^{14} p/cm^2 without any thermal cycling. The rest of the proton fluence and thermal cycling caused further cracking until the 93-500 looked like "alligator skin." It appears that the 93-500 hardened in the proton beam. Figure 12 is a photograph after the completed proton irradiation. Figure 12 indicates that the cracks allowed large electrical damage to occur.

E-Series

(10-mil cell, 2-mil GE 615/UV-24 cover, no backing, no adhesive)

Electron Irradiation. There was no unusual behavior observed electrically or visually. Figure 14 indicates that the first set of thermal cycles caused some improvement in the maximum power and further cycling did not affect the power.

Proton Irradiation. Cracks started to show in the GE cover material after the first set of thermal cycles. The rest of the proton fluence and thermal cycling caused further cracking until the GE 615/UV-24 looked like "alligator skin" similar to the D-Series cells. Figure 15 is a photograph after the completed proton irradiation. Figure 16 shows that thermal cycling improved cell performance slightly and that the cracks in the covering caused protons to reach the cell and degrade it.

P-Series (Pantek Cell)

(2-mil cell, 0.5-mil GR650 cover, no backing, no adhesive)

Electron Irradiation. The cells showed no visible damage until they received 5×10^{15} e/cm^2 and 30 thermal cycles. At this point four cells were cracked with parts of the cell broken out on two of them. At the completion of the electron irradiation there were two cells with additional parts broken out (fig. 17), one cell with no more damage than a crack and two cells with no visible damage at all. Figure 18 shows that initially thermal cycling improved the cells output. However, by a fluence of 1×10^{16} e/cm^2 the thermal cycles had no effect.

Proton Irradiation. Three of the five cells exhibited cracks after the first set of thermal cycles and by the completion of the test schedule a fourth cell cracked. The power output of the cell degraded tremendously during the first irradiation (fig. 19) There was no visible damage to explain the loss of output at that point. It is clear that the GR 650 cover is not thick enough to stop the protons. Figure 20 is a photograph showing the cracks in the cells at the completion of testing.

(2-mil cell, 2-mil PFA "hard-coated" cover, 1-mil Kapton backing, 93-500 front and back adhesive)

Electron Irradiation.   The GE cells all had bubbles trapped in the encapsulant before mounting in the test chamber. The edges of the cells would not lay flat on the sample plate. The cells exhibited no visible damage until they had received a total fluence of 1 x 10^{15} e/cm^2 and 15 thermal cycles. At this point three cells had cracks in the PFA cover material. After a total fluence of 5 x 10^{15} e/cm^2 and 30 thermal cycles, the PFA covers on four cells had many cracks and three of the four cells were cracked by curling during thermal cycling.   After a total fluence of 1 x 10^{16} e/cm^2 and 45 thermal cycles all the cells and PFA covers were badly cracked (fig. 21). The PFA and Kapton had become very brittle.

There is no electrical data after the 5 x 10^{15} e/cm^2 fluence because the cells were broken and shorted-out (fig. 22).

Proton Irradiation.   The GE cells showed visible damage after the first proton fluence of 3 x 10^{14} p/cm^2 and no thermal cycling. Four of the five cells had started to curl up from the contact bar end. One cell's cover had started to blister. After the first 15 thermal cycles the only additional damage was more curling. After a total fluence of 3.3 x 10^{15} p/cm^2 and 15 thermal cycles the PFA covers were blistered and peeling off on all five cells. The last 15 thermal cycles only made the blistering and peeling worse. Figure 23 is a photograph showing the blistering and peeling after the completed proton test.

The maximum power plot (fig. 24) shows that after the first set of thermal cycles the PFA cover had peeled enough to allow protons to damage the cell. The data point for the last set of thermal cycles is an average of one point because only one cell had an output, therefore it is of little significance.

Double-Number Cells

(2-mil cell; 2-mil 0211 cover; 2-mil FEP-20C, 1 1/2-mil fiberglass, 2-mil FEP-20C and 1-mil Kapton backing; 2-mil FEP-A adhesive)

Electron Irradiation.   There was a slight haze when viewed at an angle between the covers and the cells and one cover was cracked after the first set of thermal cycles. The next visible damage occurred after a total fluence of 1 x 10^{16} e/cm^2 in which two more cells had cracked covers. After the final set of thermal cycles the cell-cover interface looked hazy when viewed at an angle and it appeared the covers were coming loose. When the cells were removed from the chamber it was found that the ends of the cells had curled up

from the sample plate. The maximum power plot (fig. 25) shows that the last set of thermal cycles caused a 15% decrease due to the reduced light through the hazy adhesive and poor thermal contact to sample plate.

Proton Irradiation. The cells exhibited no visible damage during the entire proton test. There was essentially no electrical damage either (fig. 26).

Electrostatically Bonded Cells

(2-mil cell, 2-mil 7070 cover electrostatically bonded)
(Reference 1)

Electron Irradiation. The ESB cells showed no visible damage until they had received a total fluence of 1×10^{15} e/cm^2 and 15 thermal cycles. At this point four of the five cells had cracks in the cover or portions of the cover were missing or coming loose. After a total fluence of 1×10^{16} e/cm^2 and 45 thermal cycles the damage became worse with the cover coming loose on two cells. One cell displayed no visible damage throughout the test. Figure 27 is the maximum power versus fluence plot showing the effects of the thermal cycling. It should be mentioned that the cells used in this test were some of the first cells made during the parameter optimization phase of the electro-static bonding program (ref. 1) did not have the quality bond that was later achieved.

Proton Irradiation. No visible damage was observed until after the first set of thermal cycles. At this point two of the five cells had cracked and had a reduced output or no output at all. There were no further changes in the cell appearance until the testing was completed. At this point, two cells showed no change from the beginning of the test except some curling on the ends, two cells were cracked and curled and had no output and one cell was curled and had several lengthwise cracks in the glass. Figure 28 indicates no electrical damage caused by the protons.

2-mil 7070 Glass

Samples of 2-mil 7070 glass 2 cm x 2 cm in size were also included in the electron and proton irradiations. The glass will be returned to NASA-Lewis for transmission measures.

Electron Irradiations. There was no visible damage to the glass throughout the electron irradiation.

Proton Irradiation. The glass started to curl on the ends which were not held down after the first set of thermal cycles and 3×10^{14} p/cm^2 fluence. The curling continued throughout the test. The glass curled up as much as 5-mm off the surface of the plate at the ends. It is thought that the protons may be compacting the glass at the surface, changing its density and causing the curling.

CONCLUSIONS

There are a few general conclusions that can be reached now without more extensive reduction of the electrical data and the completion of the UV testing.

1. The A-Series cell which is the more standard type of cell withstood the electron and proton environments very well, as would be expected.

2. The cells coated with only 93-500 (D-Series) or GE 615/UV-24 (E-Series) have no chance of surviving the proton environment.

3. The Pantek cell (P-Series) with a thin coating of GR 650 will not survive the proton environment because of either pin holes in the coating or just not enough of it. The cell also tended to break apart during thermal cycling.

4. The C-Series cell's 2-mil FEP-A cover came loose in the electron environment.

5. The PFA "hard-coated" GE cells did not withstand the combination of proton irradiation and thermal cycling.

6. The ESB cells showed promise in the electron environment due to the fact that one of the better quality bonded cells showed no physical damage and normal electrical degradation. The ESB cells withstood the proton environment well.

7. For the Double-Number cells, it appears that the FEP-A adhesive became hazy and would not hold the cover in the electron environment.

REFERENCE

1. Egelkrout, D. W.; Horne, W. E.: Electrostatic Bonding of the Thin ($\sim$3 mil) 7070 Cover Glass to Ta_2O_5 AR-Coated Thin ($\sim$2 mil) Silicon Wafers and Solar Cells. 4th HERD Solar Cell proceedings, 1980.

TABLE 1. ELECTRON AND PROTON TEST CONDITIONS

STRESS LEVEL	ELECTRON TEST		PROTON TEST	
	TOTAL ELECTRON FLUENCE (e/cm^2)	TOTAL NUMBER THERMAL CYCLES	TOTAL PROTON FLUENCE P/cm^2	TOTAL NUMBER THERMAL CYCLES
0	0	0	0	0
1	5×10^{14}	0	3×10^{14}	0
2	1×10^{15}	0	3×10^{14}	15
3	1×10^{15}	15	3.3×10^{15}	15
4	5×10^{15}	15	3.3×10^{15}	30
5	5×10^{15}	30		
6	1×10^{16}	30		
7	1×10^{16}	45		

TABLE 2. CELL TYPE DESIGNATION

DESIGNATION	CELL THICKNESS (mils)	COVER	BACK	ADHESIVE
A-Series	8-10	4 mil 0211 ceria doped	None	93-500 ∿0.5 mil
C-Series	∿2	2 mil FEP-A	1 mil Kapton	93-500 ∿2 mil ea. front and back
D-Series	∿8	∿1.5 mil 93-500	None	None
P-Series	∿2	∿0.5 mils GR650	None	None
GE Cells	∿2	2 mil PFA "Hard-coated"	1 mil Kapton	93-500 front and back
Double Number Cells	2	2 mil 0211	2 mil FEP-20C 1 1/2 mil Fiberglass 2 mil FEP-20C 1 mil Kapton	2 mil FEP-A
E-Series	∿10	2 mil GE 615/UV-24	None	None
ESB Cells	∿2	2 mil 7070 glass	None	None
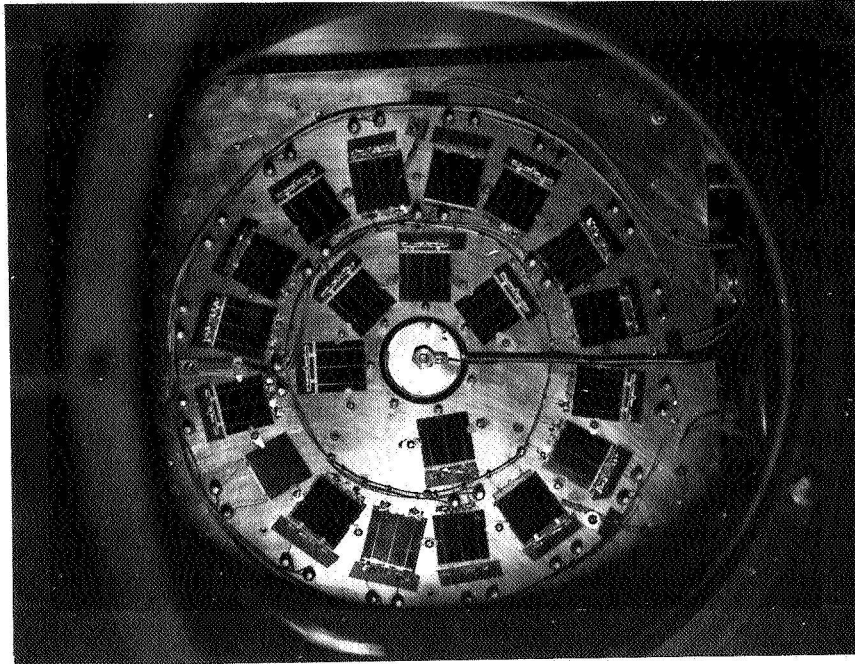
Figure 1. Test Cells Mounted in Test Chamber as Viewed Through Chamber Window.
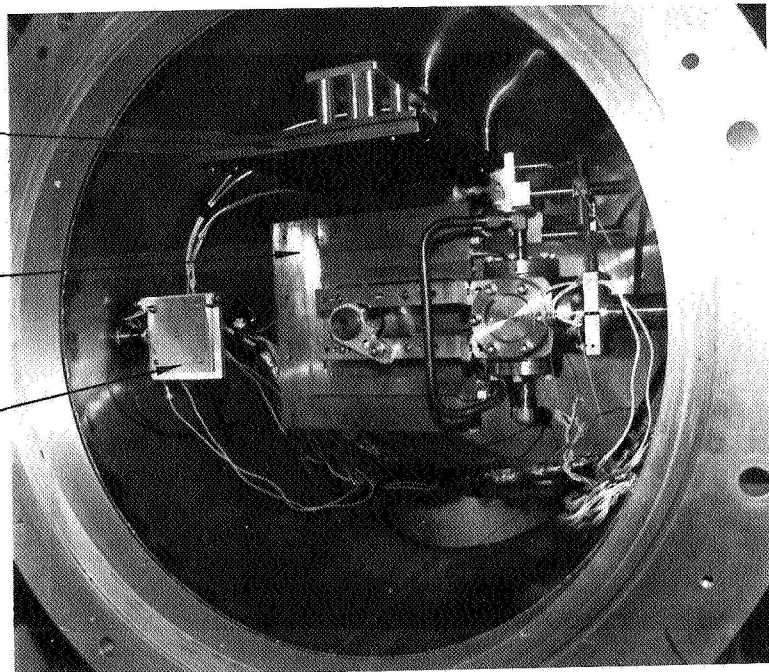

Figure 2. Inside of Test Chamber Viewed From Back of Chamber (Beam coming out of page)

302
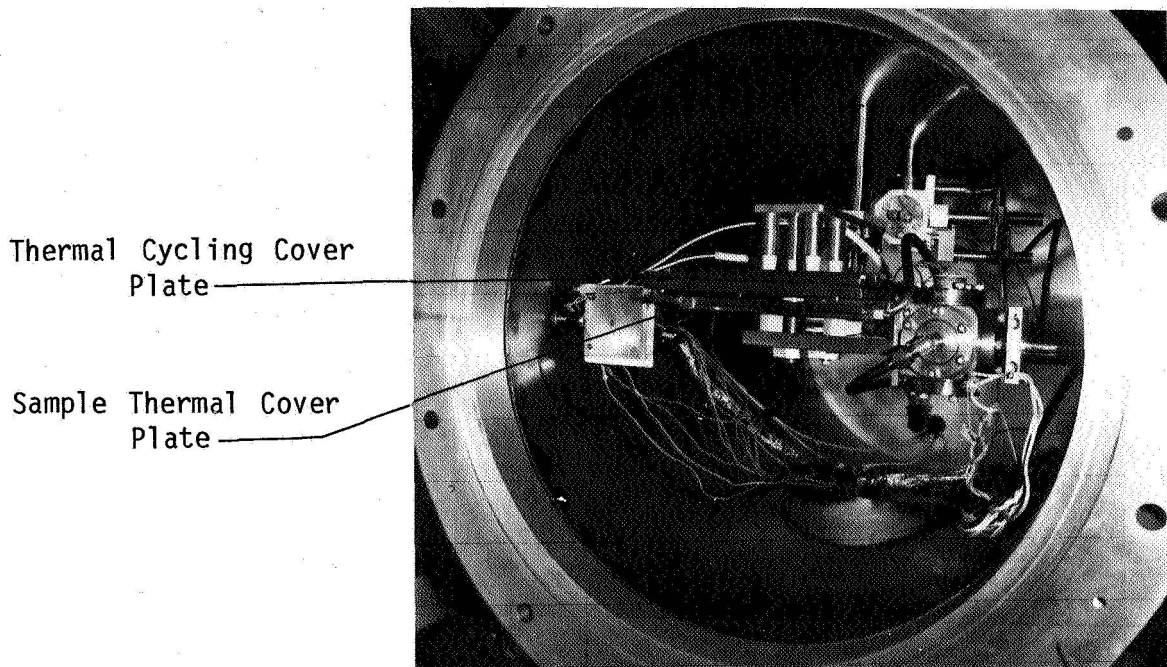
Figure 3.   Inside of Test Chamber With Sample Plate in Thermal Cylcing Position.
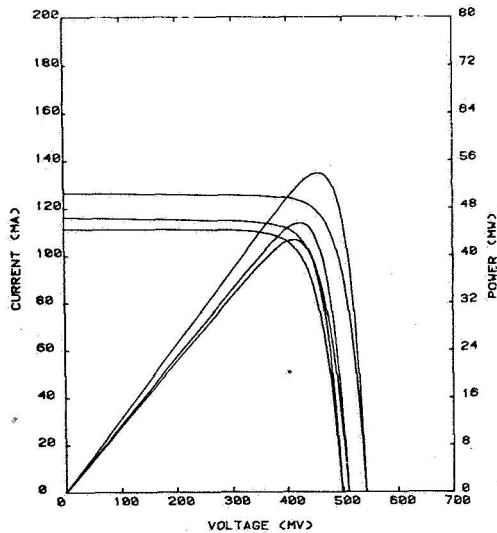
E SERIES ELECTRON IRRADIATION IN-SITU

Figure 4.   Computer Plotted I-V
and Power Curves.
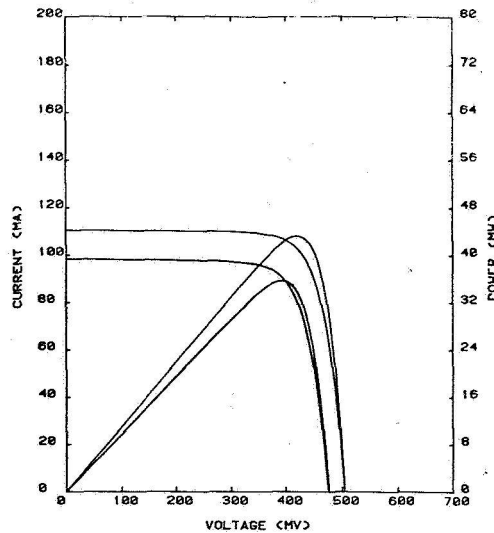
E SERIES ELECTRON IRRADIATION IN-SITU

Figure 5.   Computer Plotted I-V
and Power Curves.

Figure 6. Normalized P_{max} vs. Fluence for A-Series Cells - Electron Test.

Figure 7. Normalized P_{max} vs. Fluence for A-Series Cells - Proton Test.

Figure 8.   C-Series Cell at Completion of Electron Test.

Figure 9.   Normalized P_{max} vs. Fluence for C-Series Cells - Electron Test.

Figure 10. Normalized P_{max} vs. Fluence for C-Series Cells - Proton Test.
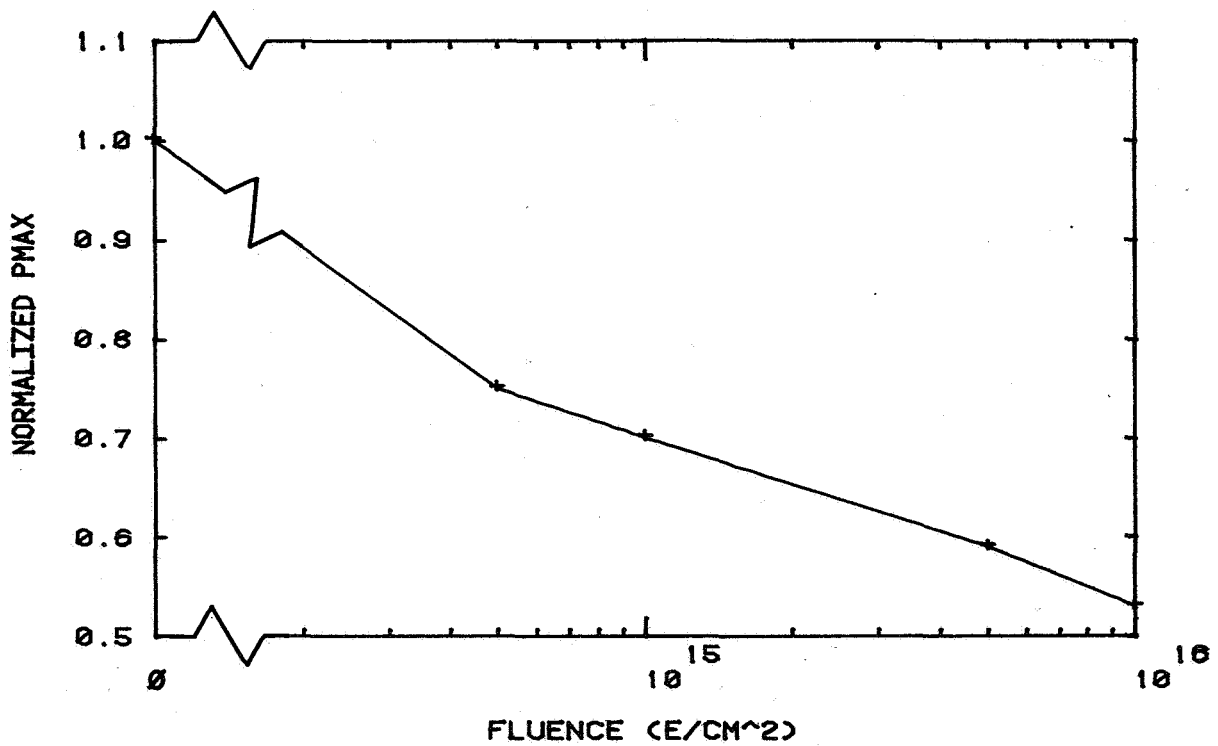
Figure 11. Normalized P_{max} vs. Fluence for D-Series Cells - Electron Test.

306
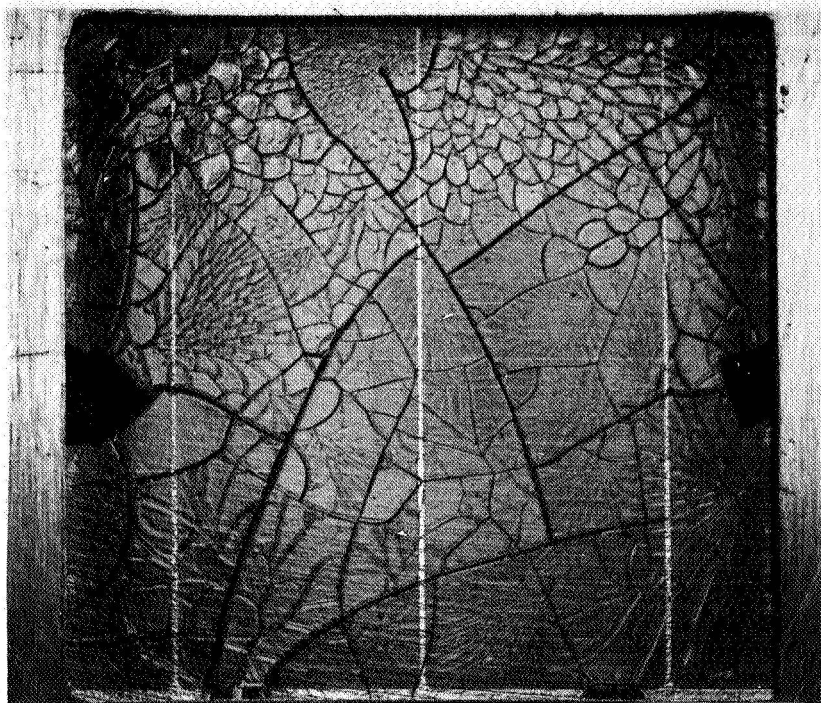
Figure 12. D-Series Cell at Completion of Proton Test.
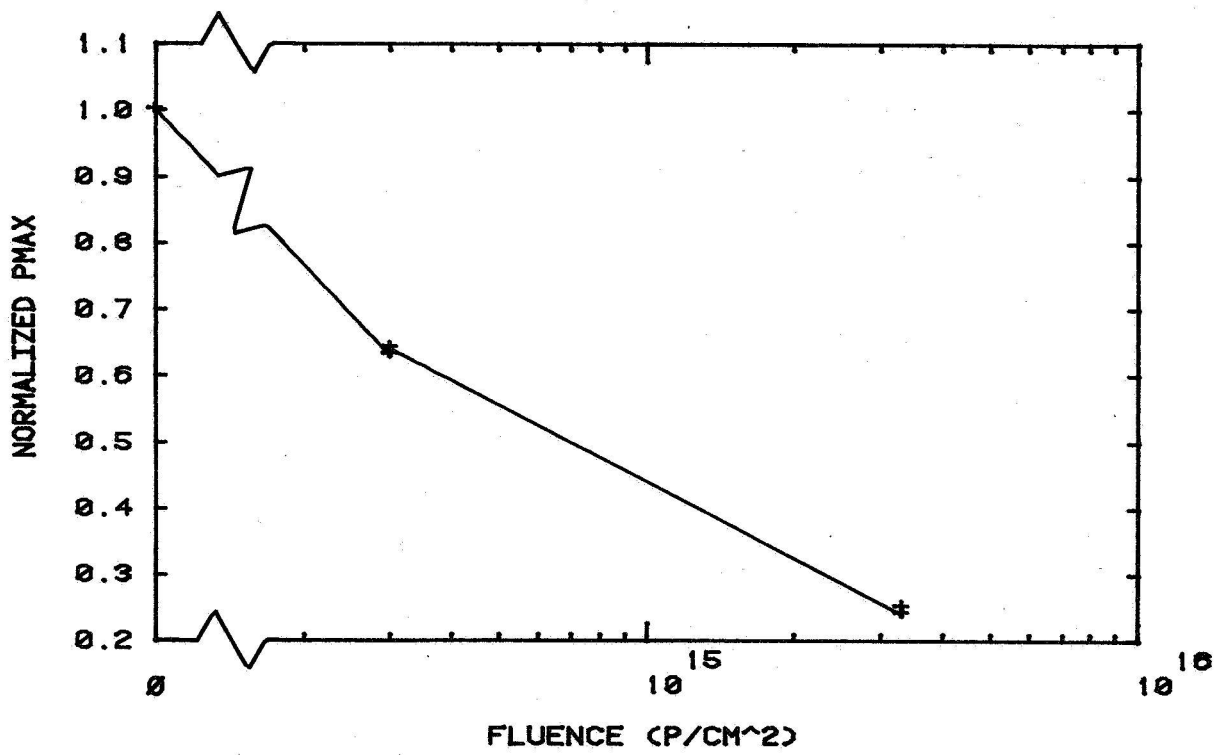
Figure 13. Normalized P_{max} vs. Fluence for D-Series Cells - Proton Test.
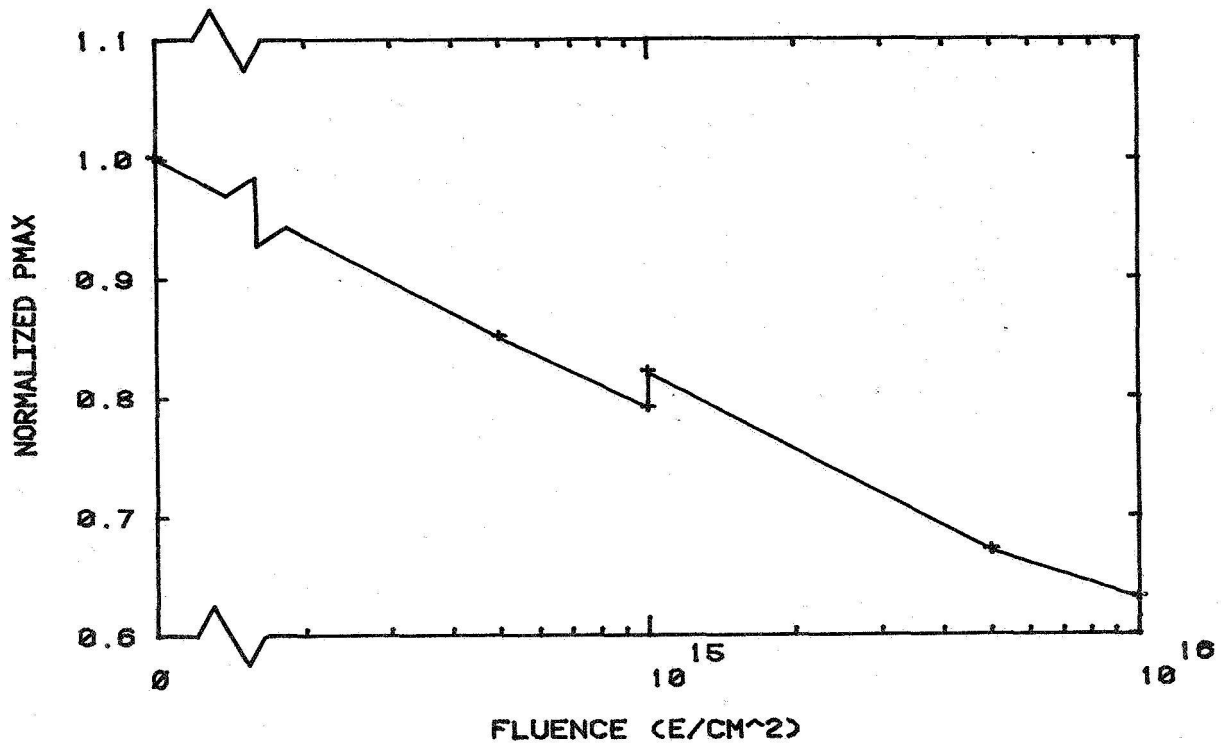
Figure 14. Normalized P_{max} vs. Fluence for E-Series Cells - Electron Test.
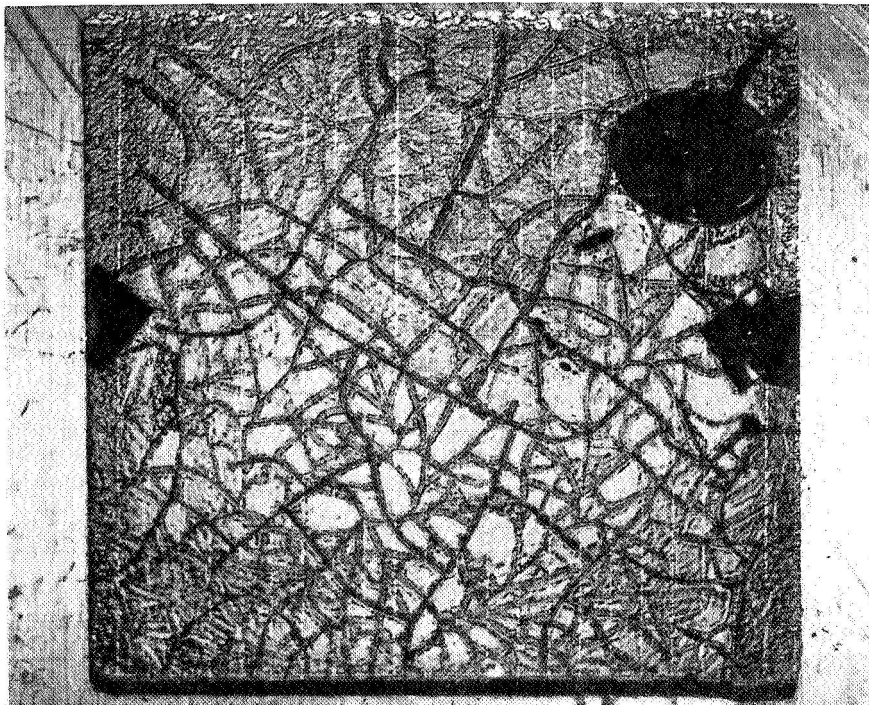
Figure 15. E-Series Cell at Completion of Proton Test.
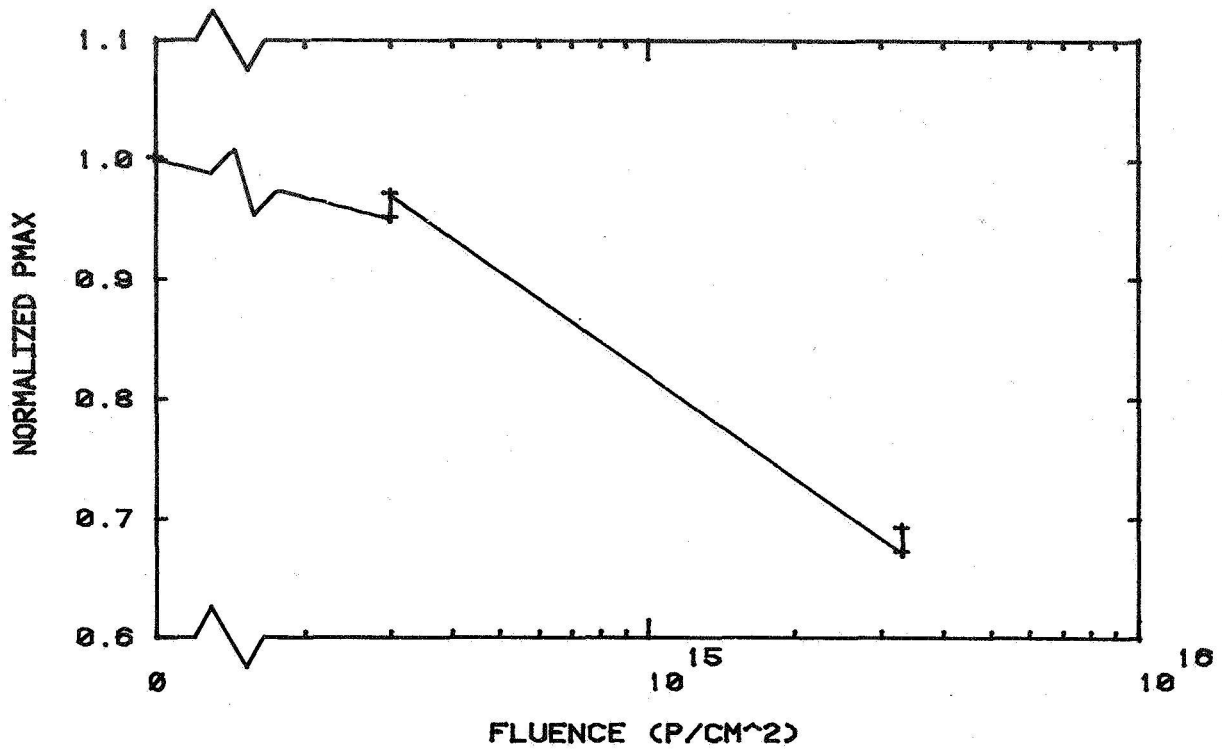
Figure 16. Normalized P_{max} vs. Fluence for E-Series Cells - Proton Test.
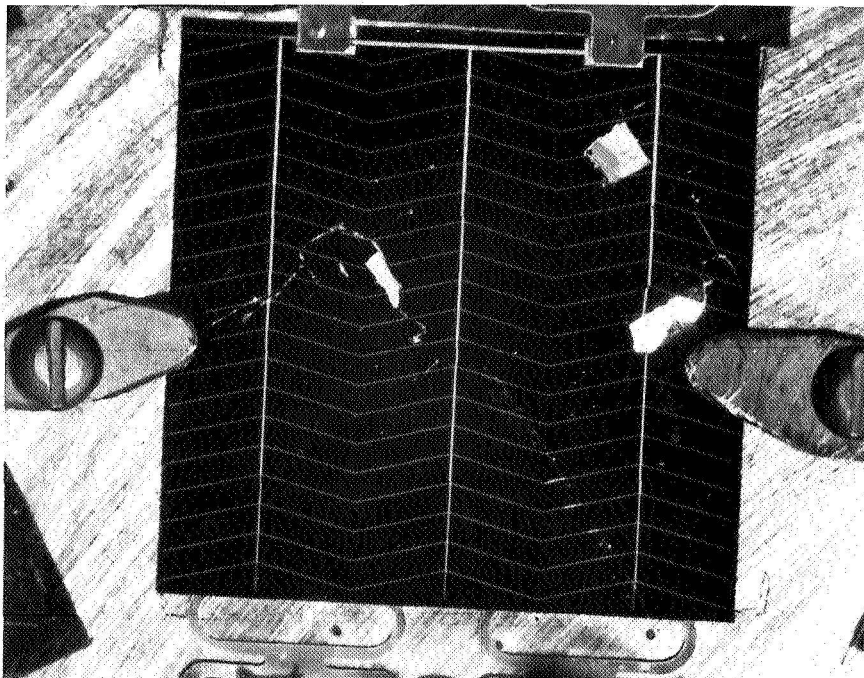
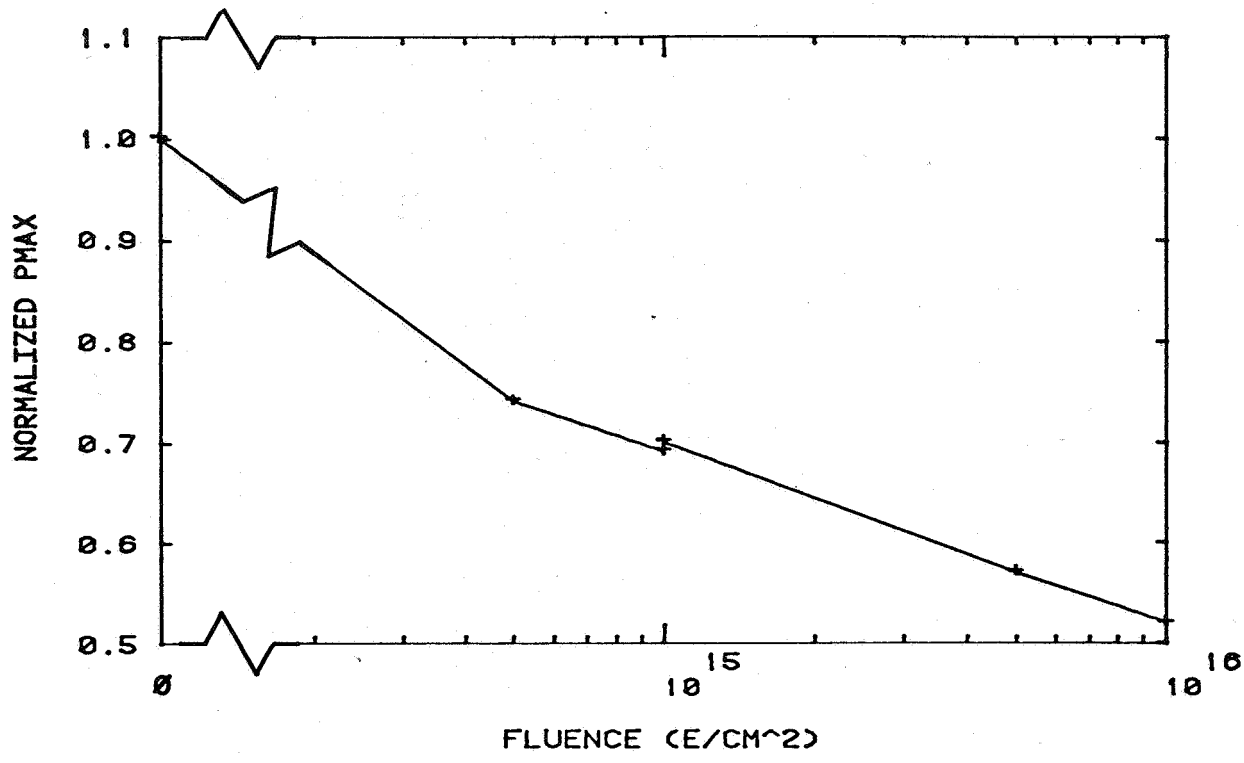Figure 17. P-Series Cell at Completion of Electron Test.
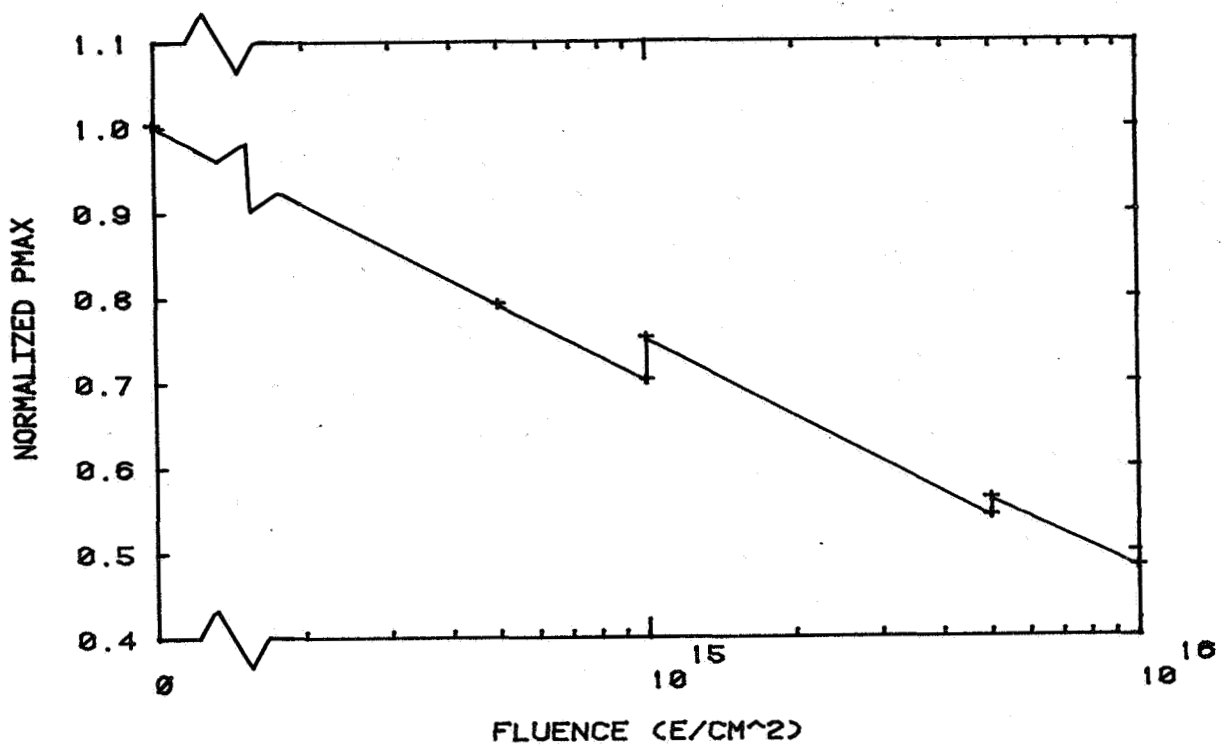
Figure 18. Normalized P_{max} vs. Fluence for P-Series Cells - Electron Test.
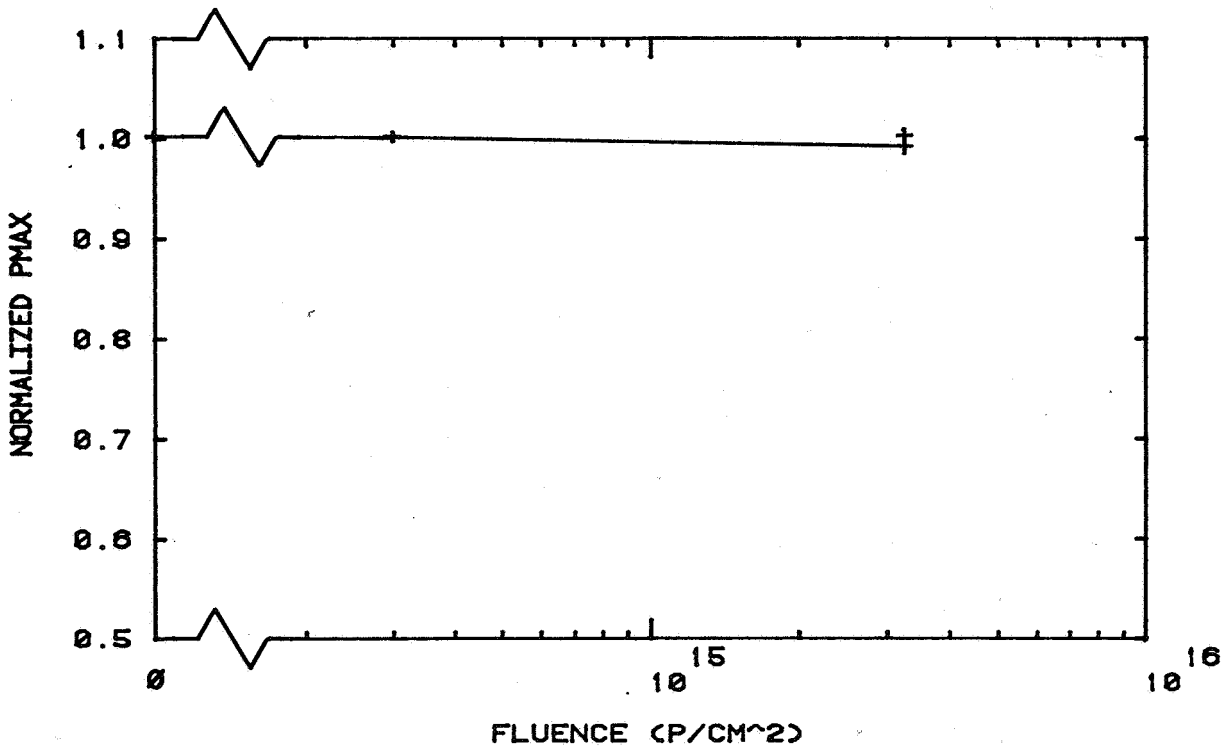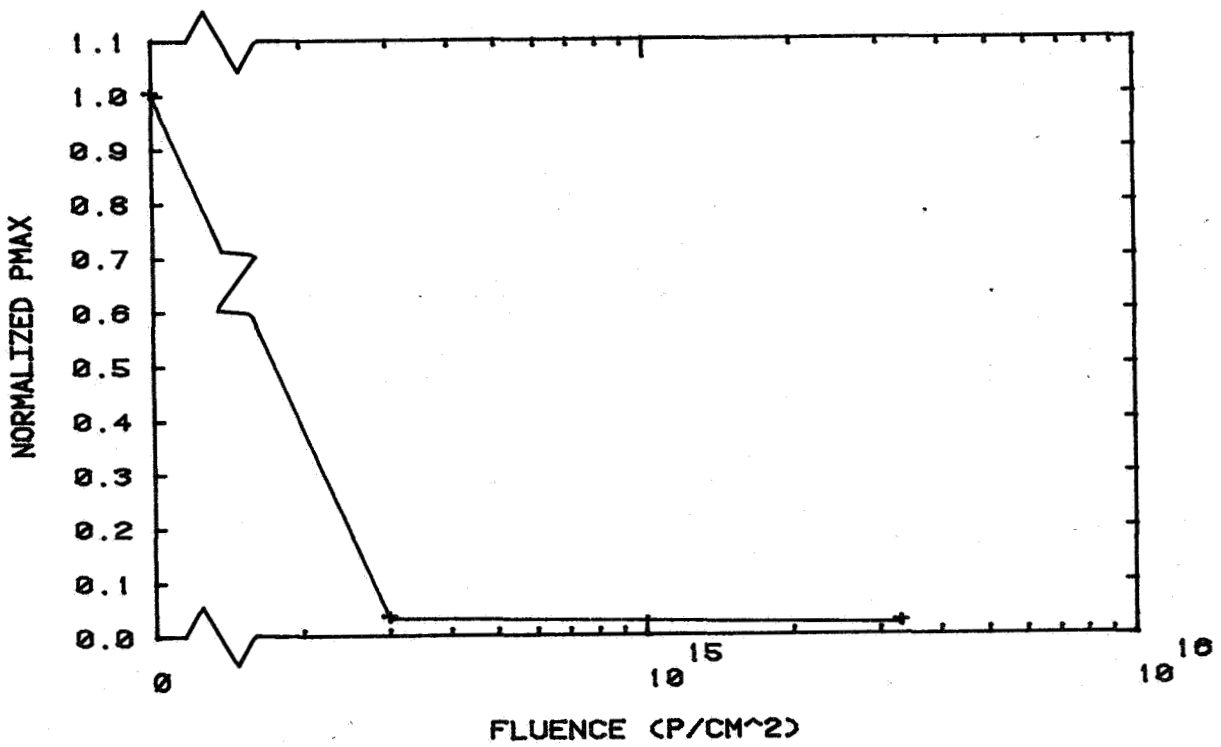

Figure 19. Normalized P_{max} vs. Fluence for P-Series Cells - Proton Test.
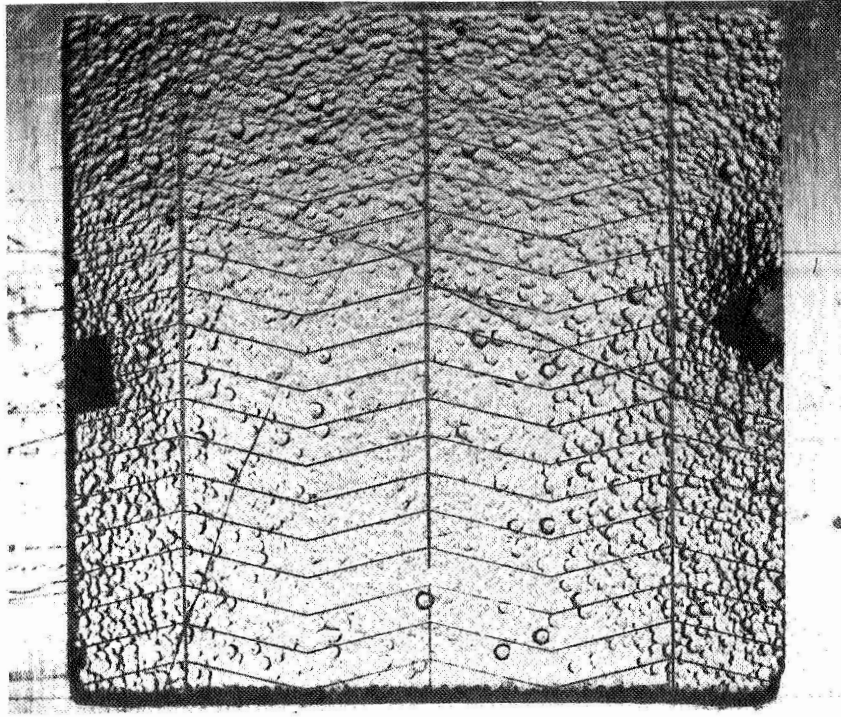
Figure 20. P-Series Cell at Completion of Proton Test.
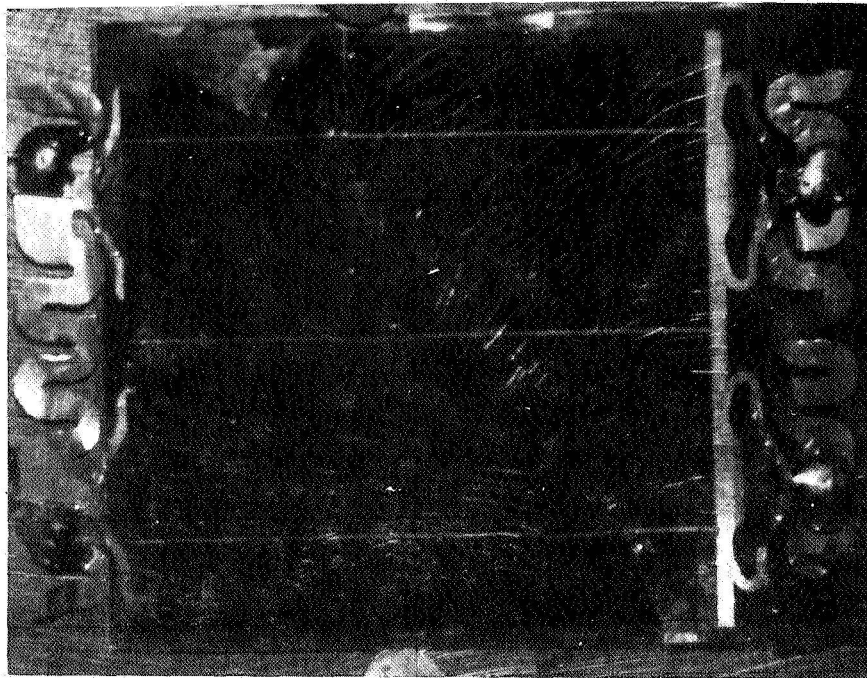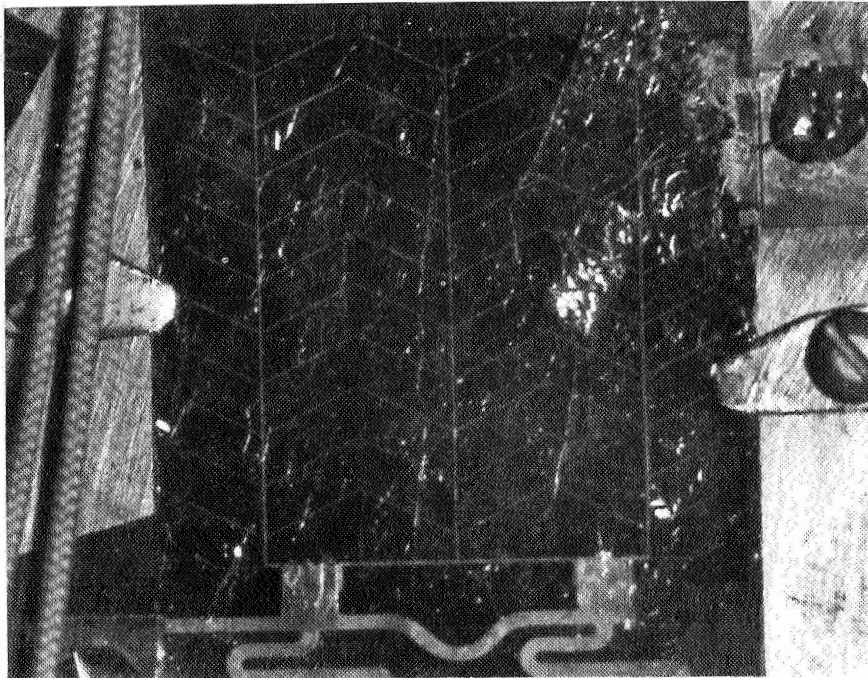

Figure 21. GE Cell at Completion of Electron Test.
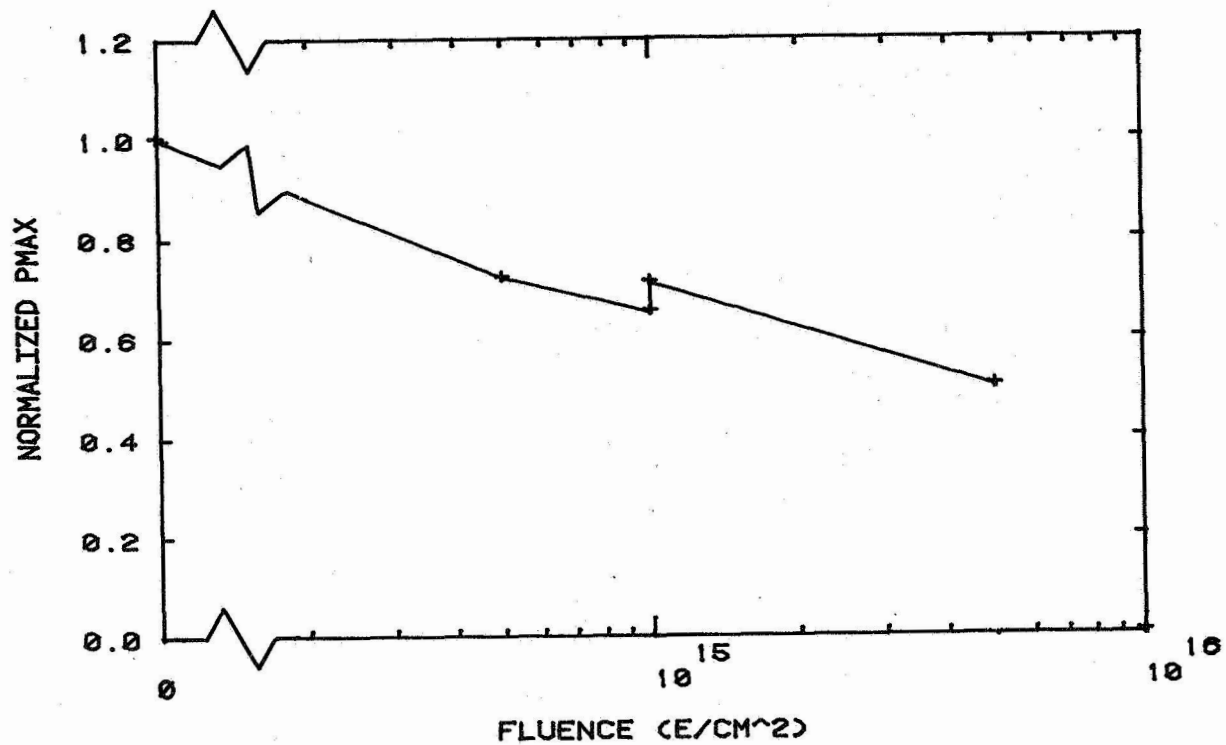
Figure 22. Normalized P_{max} vs. Fluence for GE Cells - Electron Test.
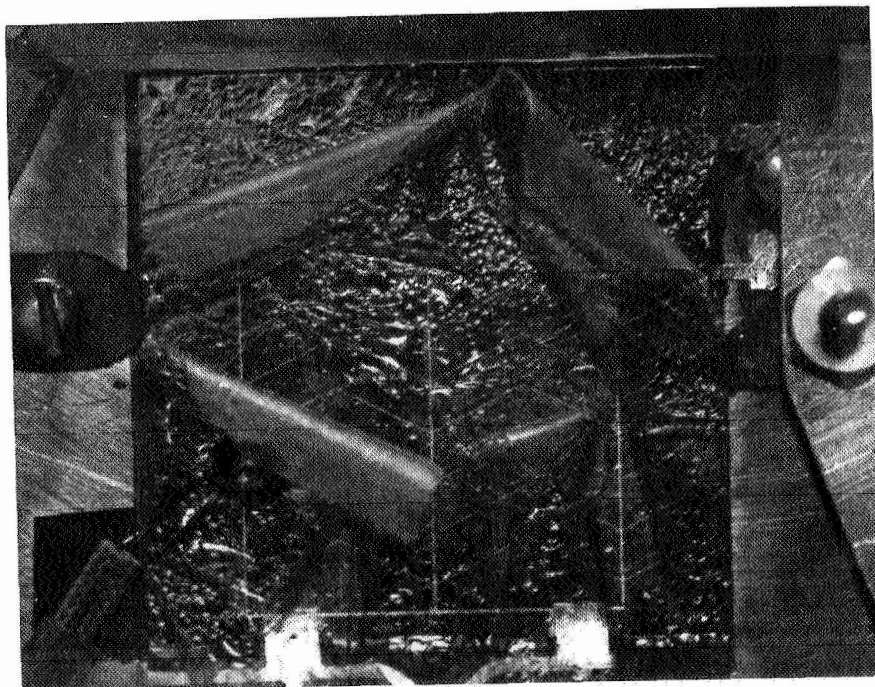
Figure 23. GE Cell at Completion of Proton Test.

312
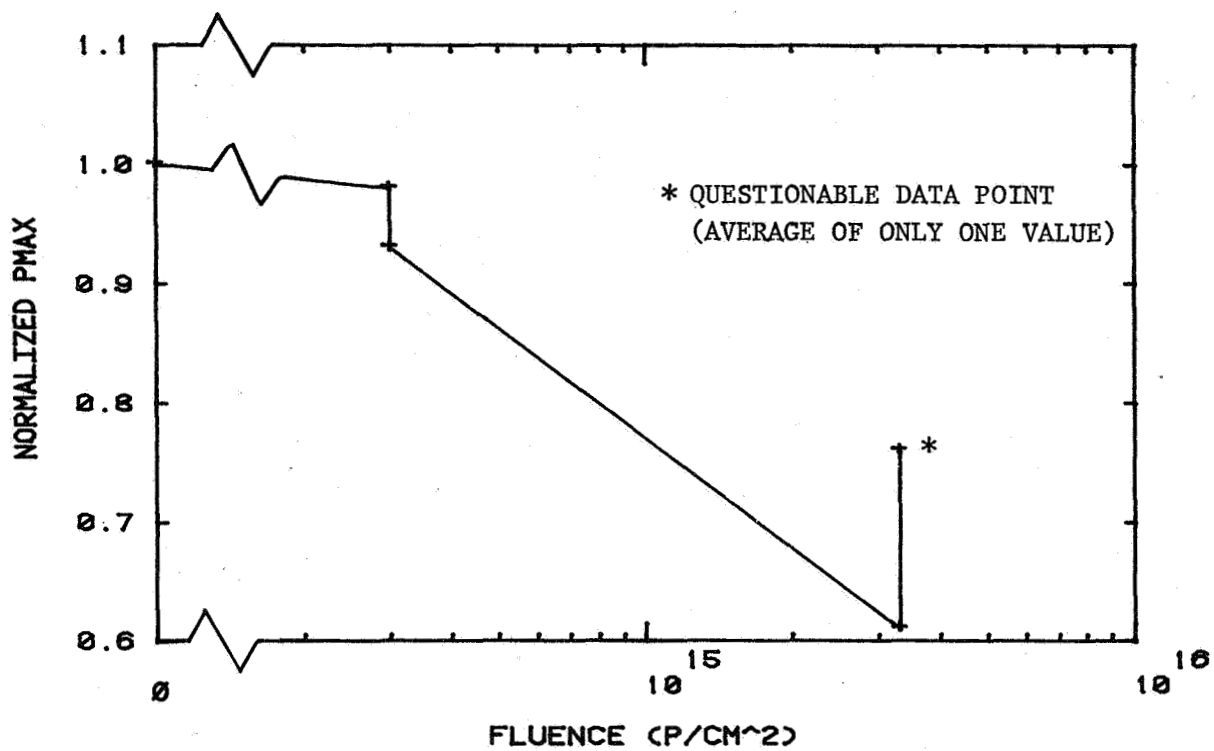
Figure 24. Normalized P_{max} vs. Fluence for GE Cells - Proton Test.
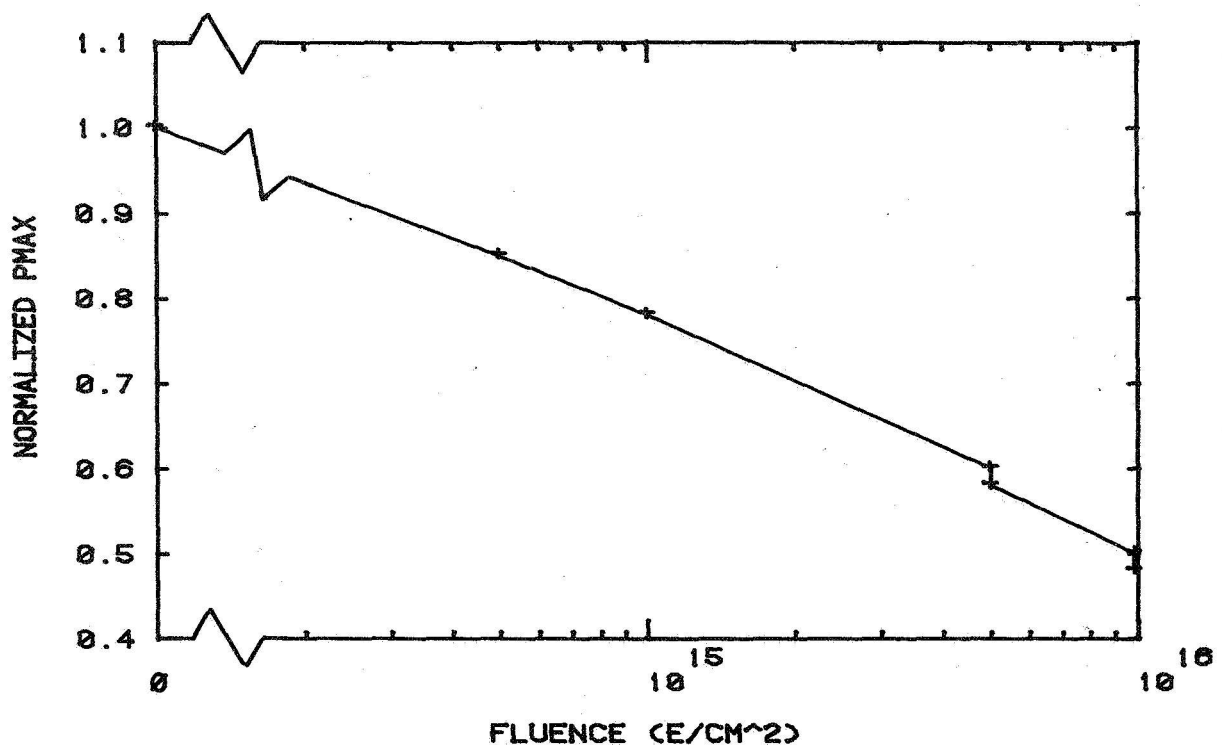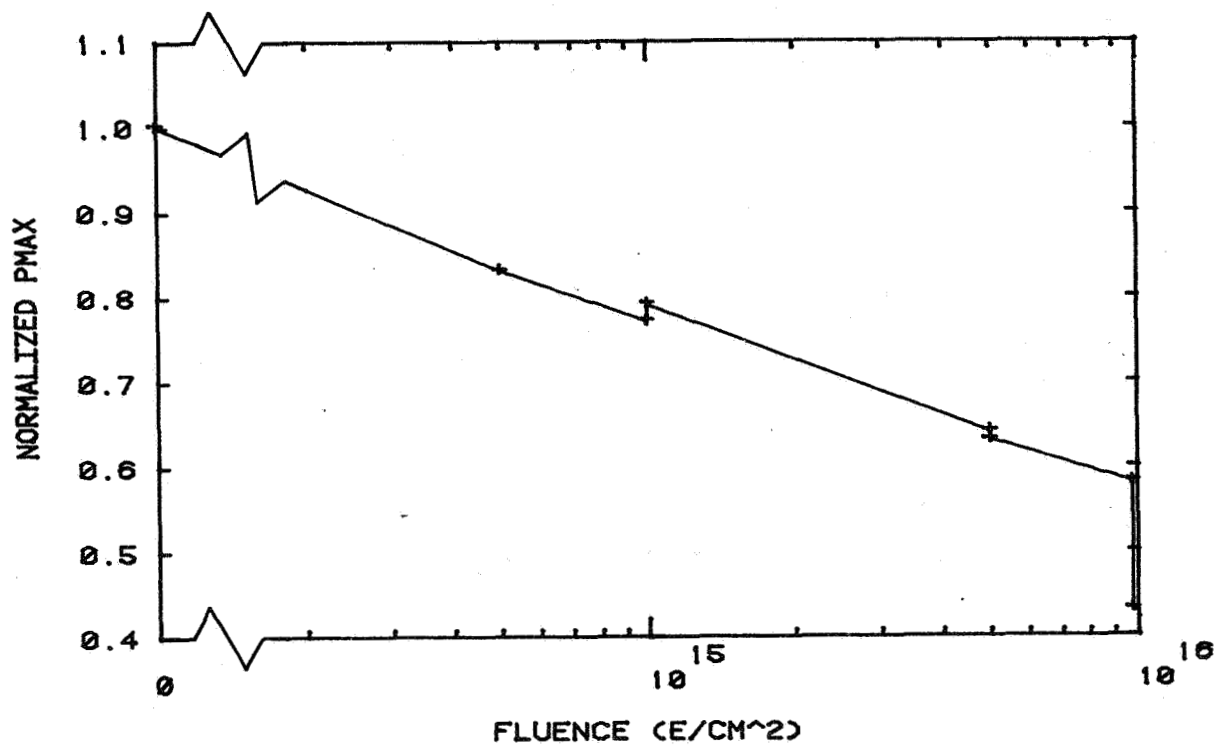

Figure 25. Normalized P_{max} vs. Fluence for Double-Number Cells - Electron Test.

313
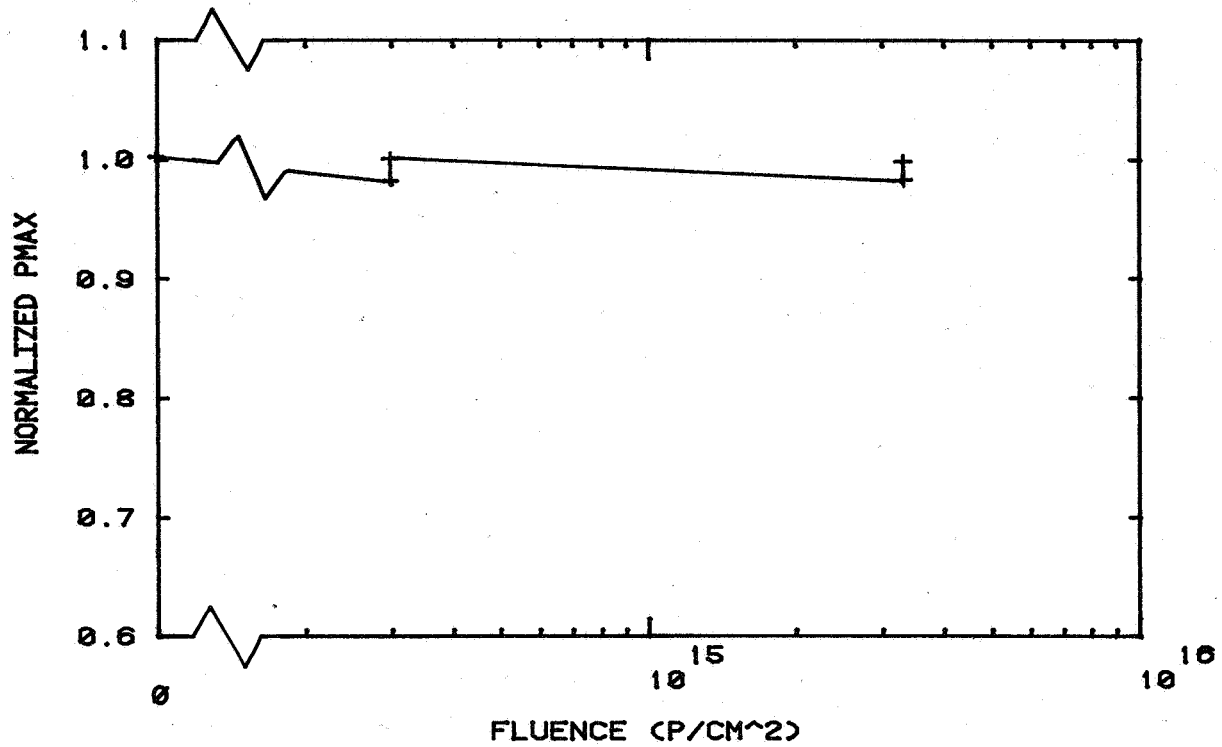
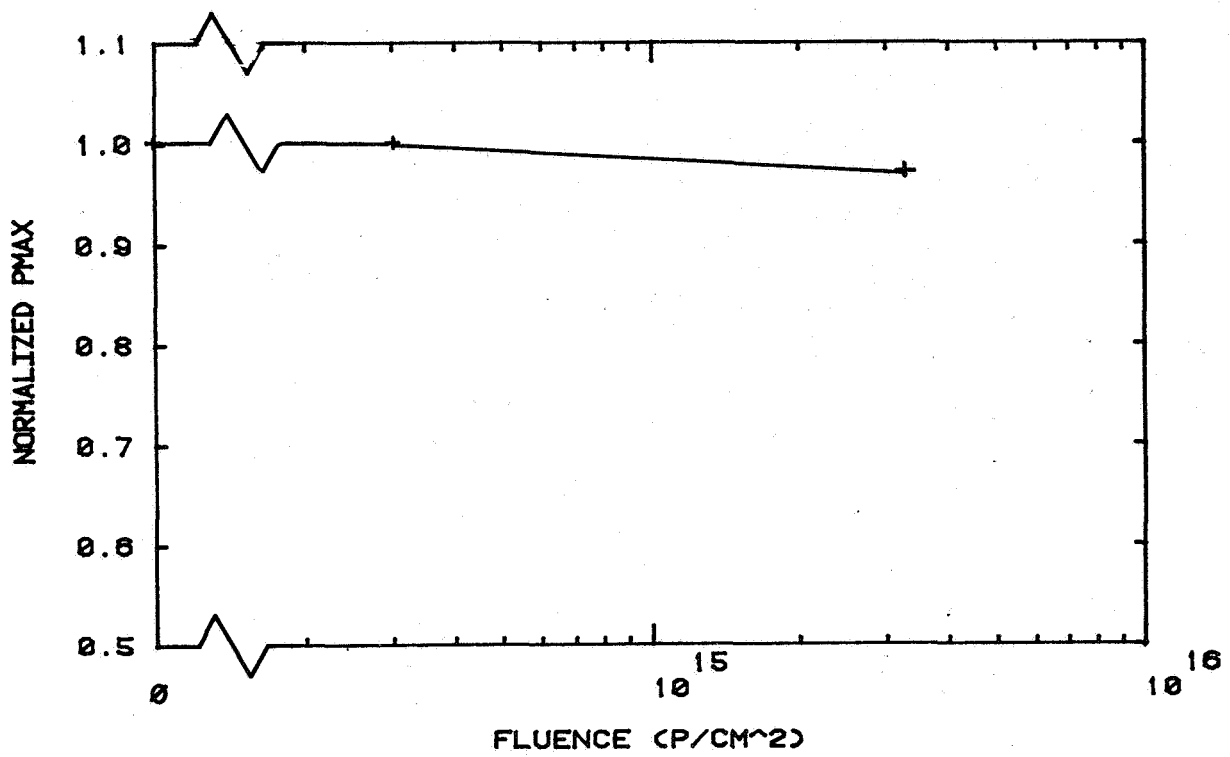Figure 28. Normalized P_{max} vs. Fluence for ESB Cells - Proton Test.
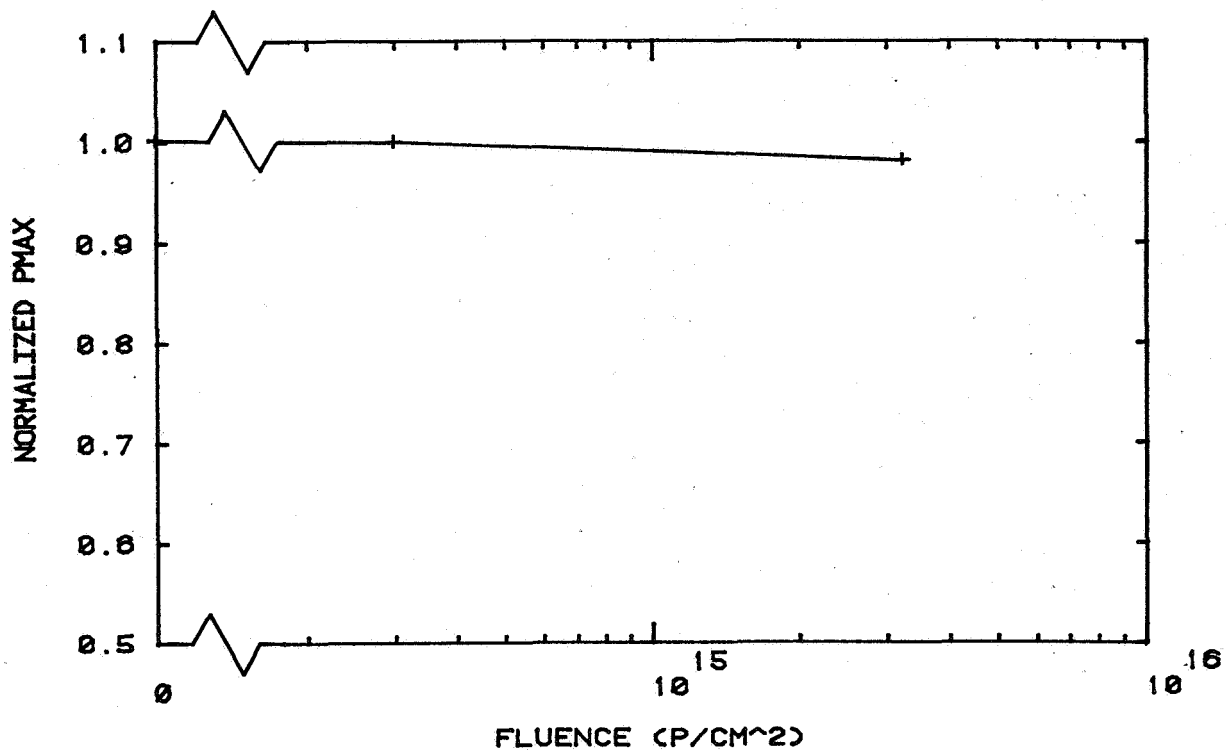
Figure 26. Normalized P_{max} vs. Fluence for Double-Number Cells - Proton Test.
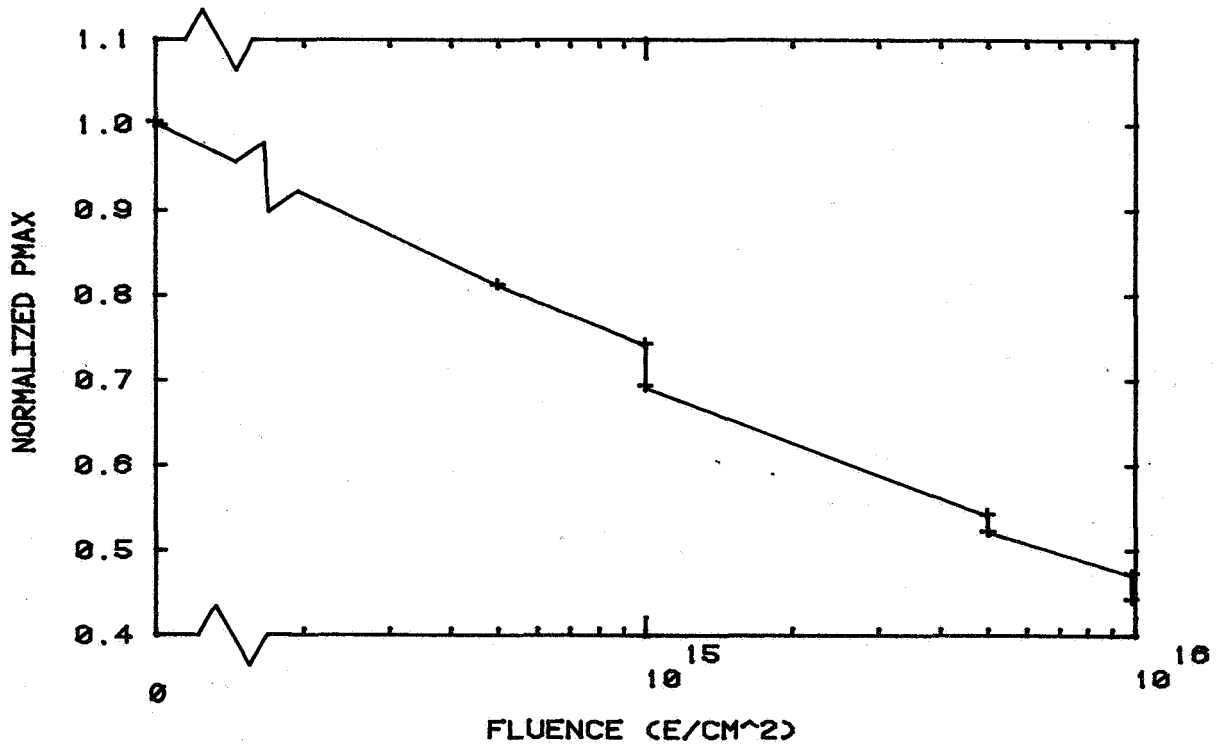
Figure 27. Normalized P_{max} vs. Fluence for ESB Cells - Electron Test.

315

ELECTROSTATIC BONDING OF THIN (~3 mil) 7070 COVER GLASS TO Ta$_2$O$_5$
# AR-COATED THIN (~2 mil) SILICON WAFERS AND SOLAR CELLS

D. W. Egelkrout and W. E. Horne*
Boeing Aerospace Company

SUMMARY

Electrostatic bonding (ESB) of thin (~ 3 mil) Corning 7070 cover glasses
to Ta$_2$O$_5$ AR-coated thin (~ 2 mil) silicon wafers and solar cells was investi-
gated. An experimental program was conducted to establish the effects of
variations in pressure, voltage, temperature, time, Ta$_2$O$_5$ thickness, and
various prebond glass treatments. Flat wafers without contact grids were used
to study the basic effects for bonding to semiconductor surfaces typical of
solar cells. Solar cells with three different grid patterns were used to
determine additional requirements caused by the raised metallic contacts.

INTRODUCTION

Thin covers are needed to exploit the advantages of thin solar cells
planned for use in future space missions. Glass has proven to be the best
cover material over many years of use. Historically, thick glass covers have
been attached to thick cells using adhesives. In order to eliminate the ad-
hesive layer, electrostatic bonding (ESB) of Corning 7070 glass using heated
covers and cells has been accomplished under Air Force contract (ref. 1).
Corning 7070 appears to have the best match of physical, optical, and elec-
trical properties for use with silicon. In previous work, ~ 10 mil thick cells
and glass were typical. Prior to the current effort the ESB process had not
been successfully applied to thin (~ 2 to 3 mil) glass and cells. The present
effort was undertaken to extend the use of the ESB process to thin cells and
thin covers.

The electrostatic bonding process (also referred to as field assisted,
glass-metal sealing) was first described in the literature in 1969 (ref. 2).
In the ESB process glass and metal (or semiconductor) surfaces are placed in
contact and heated to a temperature on the order of 300°C to 600°C. A voltage
ranging from a few hundred to 2000 volts is then applied so that the glass is
negative with respect to the metal. Under these conditions the glass forms a
strong, permanent bond to the metal surface. The unique feature of this
process is the relatively low temperature at which the bond is made. It is
generally 200°C to 400°C below the softening point of the glass.

The application of this process to the formation of integral cover glass solar cell assemblies was first reported in 1975 (ref. 1). The application of the process to integral cover glasses has been of considerable interest for both terrestrial and space purposes (ref. 3). Development of the back surface, field enhanced solar cell which permits high efficiencies in thin (2 mil) cells has increased interest in the ESB process since the full exploitation of the potential of a lightweight array of thin cells requires a thin cover glass (2 mils is desirable) and since for such thin cells and cover glasses, the ESB technique offers significant advantages from the standpoint of reduced weight and ease of fabrication by eliminating the adhesive layer.

The physics of the processes responsible for electrostatic bond formation are not well understood. It is, however, generally assumed that the final bond is a chemical bond. This is based on the fact that the bond strength (typically 2000 to 3000 psi) (refs. 1,4) is usually as good as the strength of the glass itself. For chemical bonding of two materials to take place, it is necessary to bring the surfaces within molecular distances of each other. When one material is in a liquid form, this is called wetting. Solid surfaces normally considered to be flat are in fact usually quite irregular on a microscopic scale and particularly on a molecular scale so that when two solid surfaces are brought together, they are actually only in contact at a few points.

It has been postulated (refs. 1,4) that one role of the electrostatic field in the ESB process is to pull two irregular surfaces into the intimate contact required to form a chemical bond. Most glasses contain mobile positive ions compensated by almost immobile negative ions. Considering such a material sandwiched between two electrodes which are not sources for mobile positive ions, the positive ions in the glass would be pulled away from their respective anions toward the cathode. This is depicted in figure 1 which illustrates some aspects of the ESB process. Since electrons are available from the electrodes, they will move into the glass to combine with the displaced positive ions causing a net negative charge in the glass. Thus, the glass will be attracted to the positive anode with an electrostatic force. It was hypothesized that a negative space charge occurs initially over a thin glass region near the anode and widens as time progresses. For a given degree of polarization and space charge, the attraction between the glass and anode will be largest at the smallest gap points. As the space charge grows with time, the glass is pulled together from the gap edges and the field strength in the gaps will become larger so that initially wider gap areas are pulled together. Thus, intimate contact and bonding would progress outward with time from the initial points of contact consistent with observations of the ESB process. An electrostatic attraction of 350 psi between Pyrex and a metal anode has been measured with "zero" gap at 300°C, and 800 volts, under conditions which did not produce bonding (refs. 1,4).

The work reported in this paper was primarily empirical. Basic parameters of bonding glass to the semiconductor surfaces of solar cells were investigated using wafers having texturized surfaces similar to solar cells but without contact grids. The effects of varying bonding pressure, voltage, temperature, and time in the region of $\leq$ 55 psi, $\leq$ 800 volts, $\leq$ 550°C, and $\leq$ 10 s were determined. Effects of glass and wafer variables were also evaluated.

These variables included the thickness of Ta_2O_5 AR-coatings, silicon surface texture, and various glass treatments. The glass treatments involved 1) immersion in molten $LiNO_3$ in an attempt to exchange Na ions in the glass for more mobile Li ions, and 2) immersion in aqueous solutions of various metallic salts to produce adsorption of the metallic elements into the glass surfaces.

Bonding to solar cells having various grid patterns was also investigated. The most significant problem encountered in bonding to solar cells with contact grids was deforming the glass over the grid so that the glass and AR-coated silicon surfaces were close enough to allow the ESB process to progress. (The ESB process was restricted to solar cell temperatures below the softening point of the glass to avoid undue thermal degradation of the cells.)

Two methods of attacking the problem of deforming cover glasses over contact grids were investigated. One method involved heating the glass with a short burst of laser energy using a wavelength such that most of the energy was absorbed in the glass and not the cell. This method showed promise, however, optimization of bonding parameters, hardware configuration, etc., must still be worked out. The other method utilized a bonder cathode material with appropriate compressibility ("cathode pillow") such that the glass over the raised contacts presses into the pillow while the surrounding pillow material bends the glass into the valleys between the contact fingers. This method has been used to produce many well bonded samples without undue degradation in cell electrical performance.

BONDING APPARATUS AND BASIC PROCEDURE

The important aspects of the apparatus used to make electrostatic bonds in this investigation are depicted in figure 2.

In the bonding runs, the glass was laid on the cathode heater, C/H block, and the cell was laid front side down on the glass. The bell jar was evacuated at which time power was applied to heating coils in the C/H block to heat the cathode and glass. The cathode temperature was monitored using a thermocouple at the point indicated in figure 2. When the cathode temperature reached the desired value, the desired pressure was applied uniformily over the sample surfaces by raising the gas pressure in the anode bellows to an appropriate level. The cathode and anode surfaces were machined flat to close tolerances to apply pressure over the entire sample area. The anode temperature was also monitored with a thermocouple at the point indicated in figure 2. Whenever a temperature is given without qualification, it is understood to be the anode temperature averaged over the time of bonding. When the anode temperature reached a value which indicated that the sample had heated to the desired temperature, the bonding voltage was applied from anode to cathode and bonding proceeded. When the bonding interval was over, gas pressure was applied to the cooling bellows so that the cooling block contacted the C/H block and cooled the sample. When the temperature of the cathode dropped to a level so that it would not oxidize ($\lesssim 100°C$), the bell jar was brought to atmosphere and the sample was removed.

319

The bonder was constructed to facilitate bonding of one sample at a time
with the possibility of varying and monitoring important bonding para-
meters. The C/H block temperature, anode temperature, applied voltage, sample
current, and integral of sample current were recorded on each bonding cycle
as a function of time using strip chart recorders.

SAMPLE DESCRIPTIONS

The silicon wafers, glass samples, and solar cells were all 2 cm x 2 cm
square. Glass samples were received in three lots. Based on random samplings
of five each, the measured thicknesses were:

$$\text{Lot I,} \quad \bar{x} = 3.5 \text{ mil and } s = 0.13 \ \bar{x};$$
$$\text{Lot II,} \quad \bar{x} = 2.7 \text{ mil and } s = 0.09 \ \bar{x};$$
$$\text{Lot III,} \quad \bar{x} = 2.8 \text{ mil and } s = 0.08 \ \bar{x}.$$

The surface of the samples had considerable structure. A photograph of a
wafer surface is shown in figure 3a. Figure 3b shows a wafer surface with a
cover glass bonded to it. Figure 4 shows glass and wafer surface profiles
determined with a Tally Surf (an instrument which mechanically tracks the sur-
face profile by dragging a micro sharp needle over the surface). The wafer
surfaces contain rounded pits of varying size separated by relatively sharp
ridges. The wafers received could visually be separated into two classes based
on dominant pit size and density. A random sample from each of these categories
is represented as "large" and "small" grain in figure 4. Many glass samples
had visible surface striations. An example surface prifile of a typical
striation is also shown in figure 4.

The surface structure of the wafers led to considerable bond structure on
a microscopic scale. This is visible in figure 3b which shows the unbonded
spots as light regions and the bonded areas as dark regions. A closer look at
the degree of bonding on a microscopic scale is shown in figure 5. Unbonded
regions are visible as regions with interference fringes. It was established
that on a microscopic scale, bonding begins at the peaks between the pits and
progresses with increasing time and other bonding parameters deeper into the
pits filling the shallower pits first.

Three types of solar cells were used in this investigation. They are
identified by the three grid patterns as shown in figure 6. The cells are
referred to as herring bone, rectangular and bar grid. The thicknesses were
respectively $\sim$ 3 mil, $\sim$ 2 mil, and $\sim$ 3 mil. The surface finish of the herring
bone and rectangular grid samples were similar to the wafers described above.
The bar grid samples, however, had a surface which was much finer in structure.
The surface appeared velvetized at magnifications similar to figure 5 and had a
sharp, random, crystalline appearance at magnifications of 450x.

BASIC PARAMETERS FOR BONDING TO WAFER SURFACES

The initial intent of this portion of the effort was to establish the surface in the four dimensional pressure, voltage, temperature, and time, (P, V, T, t) space which separates the regions leading to adequate and inadequate bonding. However, due to the inherent physical variations between samples and the limited sample quantity available, the degree to which this could be accomplished was limited. Considering the large electrostatic forces that exist at small sample separations, it was expected that beyond initial flattening of the samples, variations in pressure below 55 psi would not have a great effect for the wafers without contact grids. It was thus decided that an adequate pressure should be selected and used so that more variations in the T, V, t space could be made. The rate of heat transfer from the C/H to anode through the vacuum, glass, and wafer layers, is a function of sample surface mating. Based on observations of the rate of anode temperature rise versus pressure it was concluded that $\sim$ 15 psi was probably adequate to maximize initial sample contact in most cases.

Using 15 psi, glass samples primarily from lot II, and primarily small grain wafers, the (T, V, t) surface depicted in figure 7 was defined to the degree indicated by the vertical bars. The complete shape of the surface is a matter of speculation at this time. An example of the strip chart records of bonding voltage, bonding current, C/H temperature, and anode temperature is shown in figure 8. The temperature values used for plotting the data are the average anode values during the time of bonding voltage application. Experiments where a 1 mil ribbon thermocouple was bonded between a glass cover and flat silicon wafer showed that the interface temperature most closely tracked the anode temperature at a level of about 10 to 20 percent higher than the anode temperature. The individual data are plotted in figure 9. In the figure, the symbol, $\vee$, means that a sample bonded at the corresponding axis values had an acceptable bond and the symbol $\wedge$ means that it did not. The definition of an acceptable bond was $\gtrsim$ 50 percent bonding of the interface area on a microscopic scale and $\gtrsim$ 95 percent bonding on a macroscopic scale. Typical examples of $\sim$ 50 percent microscopic bonds were shown in figures 3b and 5.

The scatter in the data, or spread in the T, V, t surface determined, is due to the sample-to-sample variations. It appears that these variations are primarily in the cover glasses used. The evidence of striations in the glass indicate that factors affecting the glass composition varied during the glass microsheet fabrication. Experimental observations such as discussed below indicate that the degree of bonding is related to the magnitude of current that flows during bonding. Measurements of current variations from sample to sample using identical polished wafers supported the conclusions that the variation was primarily due to the glass.

A circuit was constructed to provide $\int_0^t I(t)dt$ during each bond run. Figure 10 is a scatter plot of the degree of bonding versus this integral at the end of the bond runs. The significant factor is that regardless of temperature, time, or voltage, an acceptable bond was essentially always observed above a value of $\int I(t)dt \gtrsim 0.25$ mA-min. It was concluded that the optimum bonding time for each sample is best set by monitoring this integral. To test

this conclusion, nine samples were bonded using a C/H temperature of 550°C, a pressure of 15 psi, a voltage of 600 volts, and $\int I(t)dt \sim 0.5$ mA-min. The anode temperature at the start of bonding for each sample was 320°C. Differences in $\int I(t)dt$ resulted in bond times ranging from ~ 0.75 minutes to ~ 7.6 minutes. Variations in bond times and to a lesser extent variations from sample to sample in heat transfer rate resulted in end point temperatures ranging from a low of 335°C to a high of 408°C. The resultant bonds were essentially identical in quality with about 50 percent of the interface area bonded in a randomly uniform manner on a microscopic scale and about 95 to 100 percent on a macroscopic scale.

All wafer data were obtained using a hard tantalum cathode surface. The bulk of the C/H structure was copper but initial experiments indicated that damaging effects possibly resulting from reactions between the glass and C/H surface were minimized with a highly polished Ta overlay between the glass and Cu. As discussed below, the hardness of the cathode surface was found to be a critical factor in bonding to solar cells with raised contact grids. Cathode surfaces having more compressible properties such as discussed in the next section might have been beneficial for bonding to wafers but were not tried.

BONDING TO SOLAR CELLS

Attempts were made to bond glass to solar cells using the procedures established for good bonding to wafers as discussed above. When applied to solar cells, these procedures resulted in no bonding at all. The application of higher pressures, voltages, temperatures and times resulted in some bonding but the results were unsatisfactory. The primary problem in bonding to solar cells of this type was the initial deformation of the glass over the raised contact grid. One solution to this problem would be to develop solar cells with recessed contact grids; however this increases manufacturing steps and cost. The objective of this effort was to establish conditions for bonding to existing solar cells and therefore means were sought to enhance the deformation of the glass over the grids at minimum solar cell temperatures.

Considering the ESB process with a hard, flat cathode, it is apparent that the glass over the contact grid bars must be compressed by the amount of the grid thickness before the glass and semiconductor surfaces can be put into intimate contact as illustrated in figure 11a. It was speculated that due to the thinness of the glass relative to the spacing between grid bars, it might be easier to bend the glass between the bars than to compress it over the bars. It was conceived that if a C/H surface were provided with appropriate viscosity or compressibility, such glass bending might be achieved as illustrated in figure 11b. The term cathode pillow was applied to this soft cathode concept.

A cathode pillow might be constructed by captivating a viscous solid, a liquid, or a gas inside a thin conducting membrane. However, it was felt that if a material could be found with the proper compressive, conductive, and heat resistance properties the desired result would be more easily attained using the bare material.

After considering the properties of a number of materials, a preliminary acceptable material was found which yielded results which were dramatically superior to a hard cathode. A typical bond formed using a cathode pillow is shown in figure 12a for comparison to the typical result using a hard cathode (fig. 12b). The conditions used to achieve the bonds shown in figure 12a and 12b respectively were: (44 psi, 600 volts, 426°C, 2.0 min, and 2.6 mA-min) and (44 psi, 600 volts, 470°C, 2.5 min, and 1.0 mA-min).

It has been determined by further bonding of about 40 rectangular grid cells using a soft cathode that acceptable bonds are fairly reliably achieved using the conditions: $P \sim 55$ psi, $V \sim 600$ volts, $\int I(t)dt \sim 3$ mA-min, and starting the bonds at anode temperatures of 415°C with cathode temperatures of about 55°C. Anode temperatures usually level out at about 495°C before the bonding voltage is removed. Bonding times under these conditions are typically < 3.0 minutes. The degree of microscopic bonding was found to increase considerably with further increases in $\int I(t)dt$ up to ~ 5 mA-min, however, the cell degradation also increases significantly. It has not yet been determined if the benefits of this increased degree of microscopic bonding are worth the extra penalty in electrical degradation of the cells. The changes in cell electrical parameters caused by ESB are summarized in figure 13 which shows the short circuit current, ISC, open circuit voltage, VOC, maximum power, P_{MAX}, and fill factor F.F. Level 0 and 1 refer to before and after bonding respectively. It was typical that considerably more degradation in ISC occurred than in VOL and in many cases the fill factor actually went up.

The above results pertain to the rectangular grid samples only. Herring bone samples were more difficult to bond and the bar grid samples did not bond at all under conditions which led to good bonds on the rectangular grid samples. The reasons for these differences have not yet been fully investigated, but seem to be due to thicker, closer spaced grid bars for the herring bone and a radically more complex semiconductor surface structure for the bar cells.

As shown by the above data, some cell degradation due to the thermal soak during the ESB process occurs even under the shortest bonding times. While this degradation can be slight for some cells, it could be catastrophic for other cell designs. In an attempt to develop means of further reducing the thermal stress to the cells, a technique using a pulsed laser beam to heat the glass to the softening point in a very short burst was conceived. The technique would involve a background temperature sufficient to allow ion migration in the glass to establish an electric field between the glass and cell in a manner similar to the standard ESB technique. The background temperature would be maintained below the level at which the solar cell would degrade. The laser pulse would then soften the glass allowing the electric field to form the glass into the solar cell surface and around the contact grid. During subsequent cool down the interface would be bonded by the standard ESB process. It was calculated that this would be accomplished with the cell temperature above the threshold temperature for degradation for times on the order of seconds rather than minutes.

Exploratory tests were performed to establish the feasibility of this technique. The cell-glass combination was mounted in a "picture frame" which clamped it together around the edges and permitted the application of bias voltage across the cell and glass as required for the ESB technique; however, electrical contact was only made around the extreme perimeter of the assembly by the "picture frame" clamp. The clamp was then mounted in a thermally insulating holder inside a vacuum chamber and bias voltage was applied. Background heating to 350°C was provided using an incandescent light beam concentrated onto the back of the solar cell. This shuttered light beam required about five seconds to heat the cell-glass assembly from room temperature to 350°C as indicated by a ribbon thermocouple between the cell and the glass. A CW CO_2 (10.6 μm) laser beam was then directed onto the glass surface through a shuttering mechanism which allowed continuous variations of the exposure time from ∿ 3 ms to 30 seconds. Several exposures were made and it was found that with the laser intensity available (∿ 20 watts/cm^2) a pulse of about one second duration would soften the glass. As observed through a window in the vacuum chamber, in the configuration described, the glass would first buckle upward away from the cell surface during heating. When the softening point was reached the glass could be observed to instantaneously collapse into the cell surface as would be expected if an electric field were present. At this point the current across the assembly, monitored by a chart recorder increased dramatically (on the order of mA) and after a short interval the assembly would short apparently signaling breakdown of the glass. Examination of the cell and cover glass indicated that the glass had deformed around the contact grid bars and that bonding had occurred around the periphery of the cell to a distance of about 1/8 inch inside the periphery of the "picture frame" clamp where the voltage was applied. Evidence of electrical breakdown was observed near the edge of the glass under the electrode clamp assembly.

A photomicrograph of the resulting bond is shown in figure 14a compared to that of an ESB bond produced using the "cathode" pillow technique shown in figure 14b. It appears that the bonding produced by the pulsed laser technique is more complete on a microscopic scale and the deformation around the contact is more complete. This bonding was accomplished in a very short time interval (< 1 s following laser pulse).

So far, such laser bonding has not been achieved over a large cell area. This is no doubt due to lack of uniformity in the laser beam. The desired uniformity however should be obtainable with further effort. Thus, although further work is needed to fully develop the parameters and optimize the configuration, it appears that laser pulse softening of the glass can enhance the ESB technique. The advantages offered include better conformation between the glass and the silicon surface and greatly reduced bonding times which should minimize or eliminate thermal degradation of electrical parameters.

AR-COATING THICKNESS AND GLASS TREATMENT EFFECTS

A cursory empirical investigation was made of the effects of Ta_2O_5 thickness and also various prebond glass treatments to see if such parameters could be adjusted to provide better or more easily achieved bonds. The variations tried and the results obtained are discussed below under pertinent subheadings.

Ta_2O_5 AR-Coating Thickness

Since the AR-coating is a dielectric material it is reasonable to assume that it might behave electrically in a manner similar to the glass. If the AR-coating had significant ionic conduction with neutralization of the displaced ions similar to the glass, the residual negative space charge might screen out some of the attractive electrostatic force between the glass and silicon. Depending on the ionic content of the AR-coating and its thickness, it was thought that it could be a significant factor in the ESB process. Therefore, samples were prepared with varying thicknesses of Ta_2O_5 coatings. The samples were prepared by NASA Lewis Research Center. The thicknesses are listed in table I. The wafer surfaces were not texturized for this experiment.

Bonding conditions were determined which gave partial bonding on a macroscopic scale on the thickest of these samples and then two samples of each available thickness were bonded using these conditions. The conditions were: $P \sim 15$ psi, $V \sim 600$ volts, $\int I dt \sim 0.5$ mA-min, and an anode starting temperature of $\sim 245°C$. Assuming that the degree of bonding is proportional to $\int I(t)dt$ if other conditions are constant, glass variations should have been cancelled by using $\int I(t)dt$ instead of time. Thus any changes in bond completeness would have been due to the Ta_2O_5 variations.

The results showed remarkably identical degrees of macroscopic bonding for all available sample thicknesses for the Ta_2O_5 coated wafers but polished silicon wafers without any AR-coating bonded under identical conditions showed essentially complete bonding. Since the bare wafers were from a different source and of different thickness than the Ta_2O_5 coated wafers it is not certain if the effect is entirely due to the lack of AR-coating but it seems most likely. Typical examples of the resultant bonds are shown in figure 15.

Ion Exchange

It was hypothesized that the current during the bonding process might be the result of the movement of relatively mobile Li ions in the 7070 glass. This was in part based on the observation that bonding could not be achieved with an old batch of 7070 glass thought not to contain Li as opposed to newer 7070 which did bond and did contain Li. If the hypothesis were true, it might be that exchanging mobile Li ions for less mobile Na ions in the glass would result in enhanced bonding. The technique tried for increasing the Li ion content is commonly known as ion exchange. If an insoluble solid is brought in contact with a molten solution, its surface can exchange ions. The ion

325

exchange process is used routinely in the glass industry in chemical tempering of glasses (ref. 5). The tempering is accomplished by exchanging potassium ions from a molten potassium nitrate solution for the sodium ions in the surface layers of the glass. This exchange of larger potassium ions for smaller sodium ions creates compressive forces in the glass surface and effects the tempering.

On this program, glass samples were treated by immersion in solutions of molten, $\sim$ 300°C, $LiNO_3$ for varying periods of time. It was found that if immersion was maintained too long (usually $\gtrsim$ 2 hours) the glass would become etched and milky in appearance. Since this was considered intolerable, the immersion time was reduced to a level just short of causing this effect (usually $\sim$ 1 hour). To avoid confusion due to the sample to sample variation in the glass, samples were immersed only halfway into the molten $LiNO_3$. Samples were pretreated by cleaning with detergent and rinsing in distilled H_2O and also by immersion in H_2O_2. It was assumed based on visible change in the glass color (reflection) in the treated areas that the glass composition had been changed by the treatments.

Samples treated as described above were bonded to Ta_2O_5 coated texturized wafers using conditions which normally lead to marginal bonding. No significant difference was detectable in the degree of bonding between the treated and untreated parts of the samples. If the treatment was of any value the treated parts should have been bonded to a greater microscopic degree.

Cation Adsorption

The configuration of tantalum in Ta_2O_5 might strongly affect the adhesion of SiO_2 with Ta_2O_5 antireflection layers. For example, the $SiO_2-Al_2O_3$ system is very compatible and bonds readily since both Si and Al are in tetrahedral configurations. On the other hand, it is known that SiO_2 and Cr_2O_5 do not adhere probably due to the octahedral configuration of Cr which results in poor "mixing" of these systems. Based on such considerations, treatment of the glass surface with metallic ions to form better matching properties was thought to be one possible means of improving the bondability of cover glasses.

It has been observed that glass surfaces exposed to aqueous solutions of heavy metal ions will adsorb varying amounts of the metal ions (ref. 6). In an attempt to introduce metallic ions which might have better matching properties with the Ta_2O_5 layer, samples were half immersed in saturated aqueous solutions of the metallic salts listed in table I. That some change in the glass took place for most of these treatments was evidenced by visible changes in the reflective properties of the glass. These samples were bonded to Ta_2O_5 coated texturized wafers using conditions leading to partial bonding. In no case was there any significant difference in the degree of bonding in the treated versus untreated sides.

326

Cleaning With H_2O_2

Cleaning processes are known to be very important in glass to metal bonding and wetting. Because of this and also due to the possible significance of interstitial oxygen atoms in the bonding process, some samples were cleaned in an ultrasonic bath of 30 percent H_2O_2 (a strong oxidizing agent) for times ranging from 1 to $\sim$ 240 hours. As with many other treatments, a visible change in glass color and or reflectivity occurred indicating that the treatment had changed the glass. However, no effect was noted in the degree of bonding between treated and untreated parts of the glass in any case.

CONCLUSIONS

It was determined that bonds with $\gtrsim$ 95 percent interface area coverage on a macroscopic scale and $\gtrsim$ 50 percent coverage on a microscopic scale were adequate to withstand Scoth type 810 tape peel tests and $-175°C$ to $+60°C$ temperature cycling. With this definition of a good bond, the conditions of pressure, voltage, temperature and time required to make good electrostatic bonds to Ta_2O_5 coated texturized silicon surfaces typical of solar cells were established. To minimize thermally induced degradation of solar cells, a minimum time and temperature are required. The optimum conditions for this are to use a maximum voltage. For anode pressures of 15 psi, glass of $\sim$ 2.8 mil mean thickness, and hard smooth cathode and anode surfaces, it was usually possible to apply 800 volts at chamber vacuums in the range of 1 μm to 10 μm of Hg without arcing. However to reliably avoid arcing, a 600 volt bias was found to be more appropriate. At this voltage, an anode starting temperature of 320°C was adequate with a cathode temperature of 550°C. Since a correlation between the total integral of bonding current and the degree of bonding was established, it appears that the current integral is a good parameter to use in determining when bonding voltage should be removed to minimize the bonding time. A value of 0.5 mA-min was found to be best for the Ta_2O_5 coated Si surfaces.

In bonding glass to solar cells, deformation of the glass over the contact grid was found to be the dominant problem. This problem was greatly alleviated by employing a "cathode pillow" with the appropriate compressibility so that the thin glass is bent around the grid as opposed to compressing the glass over the grid as required with a hard cathode. Maximizing the pressure with this method yields significant benefits, but, enhanced arcing around the edges of the glass as the glass is pushed into the pillow was a sporadic problem. Careful control of cathode pillow size and alignment of all elements were usually successful in allowing arc free bonding. Thus far, many good bonds of $\sim$ 2.8 mil glass to 2 mil cells have been made with acceptably small thermal degradation of cells. The best conditions appear to be $\sim$ 55 psi, 600 volts, a C/H temperature of 550°C, an anode starting temperature of 415°C and a total bonding current integral of $\sim$ 3 mA-min. Bond times for these conditions typically ranged from 1 to 5 minutes. Additional softening of the blass during the bonding process using a short burst of laser heating was achieved over a small region of solar cell. This procedure shows promise for improving the bond quality while reducing the cell thermal stress. Further development is required however to determine if the laser method is practical and to optimize the process.

Investigations of the effects of Ta_2O_5 AR-coating thickness and various glass treatments indicated no significant effects on bonding. Inherent variations in the glass however were quite significant. These were manifest as variations in the rate of heat transfer, and the bonding current under fixed bonding conditions. As a result, to obtain the same degree of bonding from sample to sample, different bond times were required resulting in different degrees of cell degradation. To minimize degradation further investigation of the factors causing these observed variations from sample to sample is needed.

REFERENCES

1. Kirkpatrick, A. R., Kreisman, W. S., and Minnvcci, J. A., Stress Free Application of Glass Covers for Radiation Hardened Solar Cells and Arrays, AFAPL-TR-77-28, May 1977.

2. Wallis, G, and Pomerantz, D. I., "Field Assisted Glass-Metal Seating," Journal of Applied Physics, Vol. 40, No. 10, pp. 3946-3949, Sept. 1969.

3. Younger, P. R., et al., Integral Glass Encapsulation for Solar Arrays, Interim Report No. 1, JPL Contract No. 954521, Nov. 1977.

4. Wallis, G., "Field Assisted Glass Sealing," Electrocomponent Science and Technology, Vol. 2, No. 1, pp. 45-53, 1975.

5. Hutchins, J. R. III., and Harrington, R. V., Encyclopedia of Chemical Technology, Vol. 10, 2nd Edition, Kirk-Othmer, Ed. (Wiley and Sons, New York, 1966).

6. Weyl, W. A. and Marboe, E. C., The Constitution of Glass, (John Wiley and Sons, N.Y. 1960).

TABLE I. AR-COATING THICKNESS AND GLASS TREATMENTS

Ta_2O_5 THICKNESS	GLASS TREATMENTS
NONE	$LiNO_3$
385 Å	H_2O_2
431 Å	$H_2O_2 + LiNO_3$
570 Å	$MgCl_2 \cdot 6H_2O$
610 Å	KCL
660 Å	$CdCl_2$
760 Å	

CRITICAL PARAMETERS

PRESSURE   P
VOLTAGE   V
TEMPERATURE   T
TIME   t

PRESSURE

ANODE

CHEMICAL BONDING

SOLAR CELL

ELECTROSTATIC
ATTRACTION

~200 V
TO
~2000 V

GLASS

CATHODE

HEATER
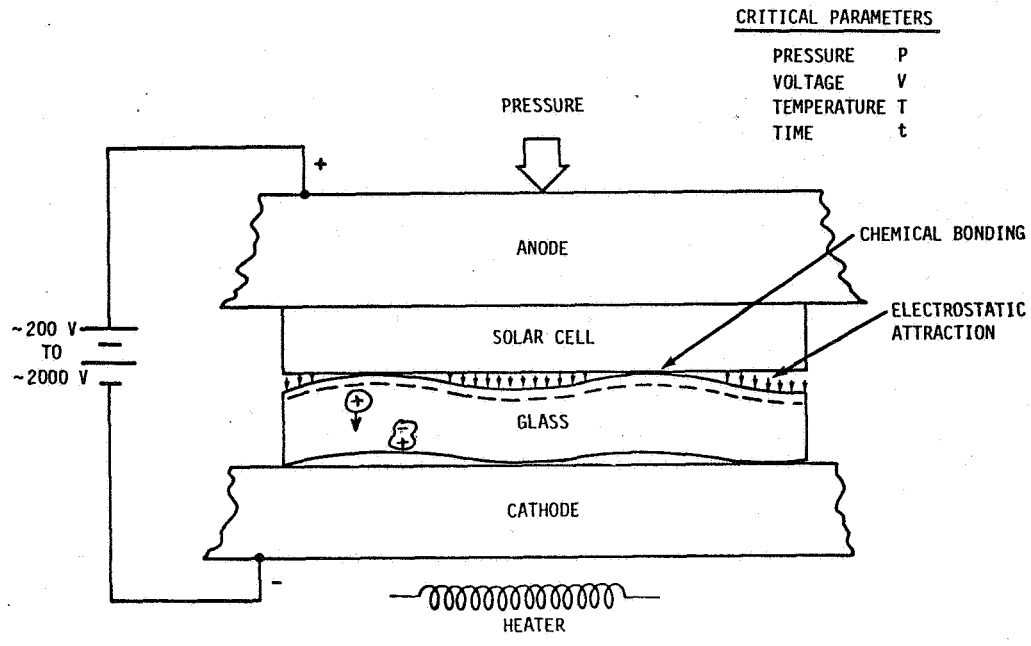
FIGURE 1. SCHEMATIC SHOWING ASPECTS OF ELECTROSTATIC BONDING

BELL JAR

BELLOWS
PRESSURE
LINE

ANODE
SUPPORT

ANODE BELLOWS

A/P BLOCK TEMP

STAINLESS
ANODE

C/H BLOCK TEMP

GUIDE

Cu C/H BLOCK

Cu COOLING BLOCK

COOLANT OUT
FLEX LINE

COOLANT IN
FLEX LINE

COOLING BLOCK
BELLOWS

BELLOWS
PRESSURE
LINE

STANDOFFS

TO VACUUM SYSTEM
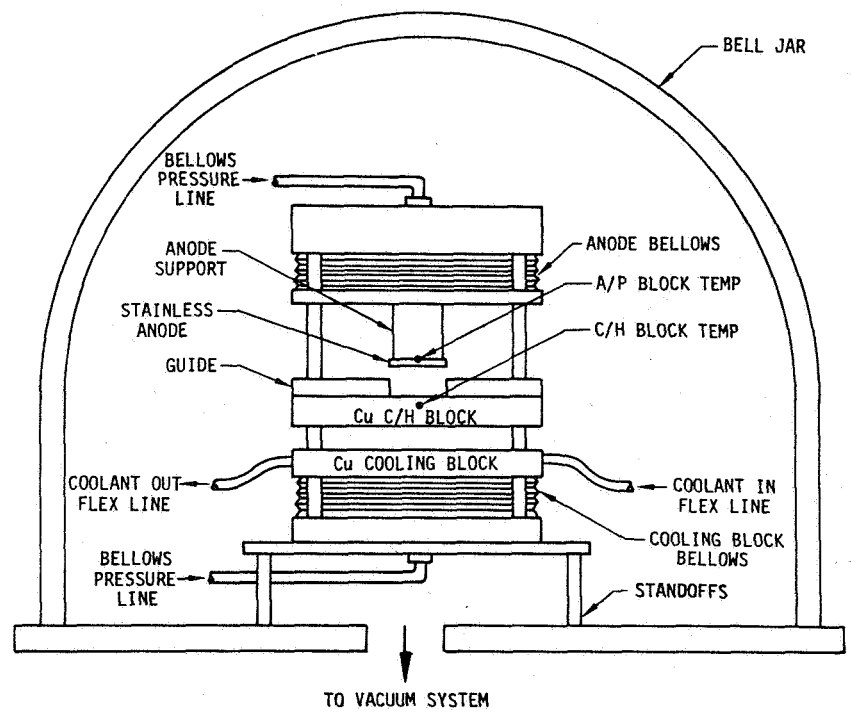
FIGURE 2. CONCEPTUAL DRAWING OF BONDER HEAD

329
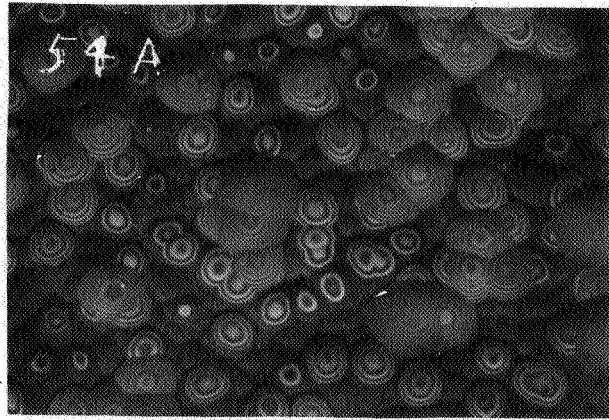
FIGURE 5. EXAMPLE PHOTOMICROGRAPH OF WAFER WITH GLASS BONDED

HERRINGBONE   RECTANGULAR   BAR
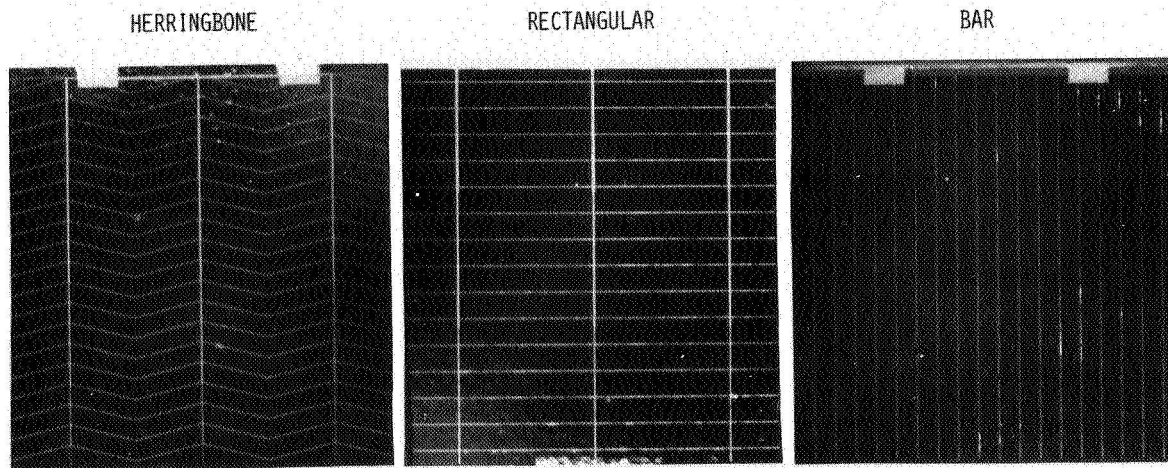
FIGURE 6. SOLAR CELL GRID PATTERNS

(A) BARE WAFER   (B) WAFER WITH GLASS BONDED
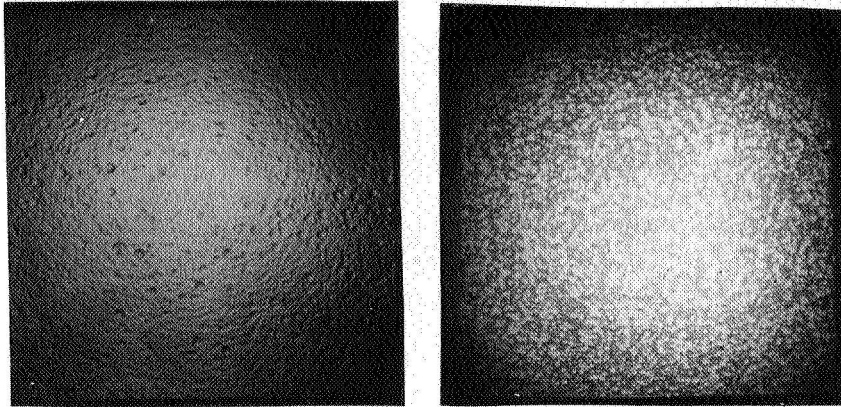
FIGURE 3. EXAMPLE PHOTOS OF WAFER SURFACES
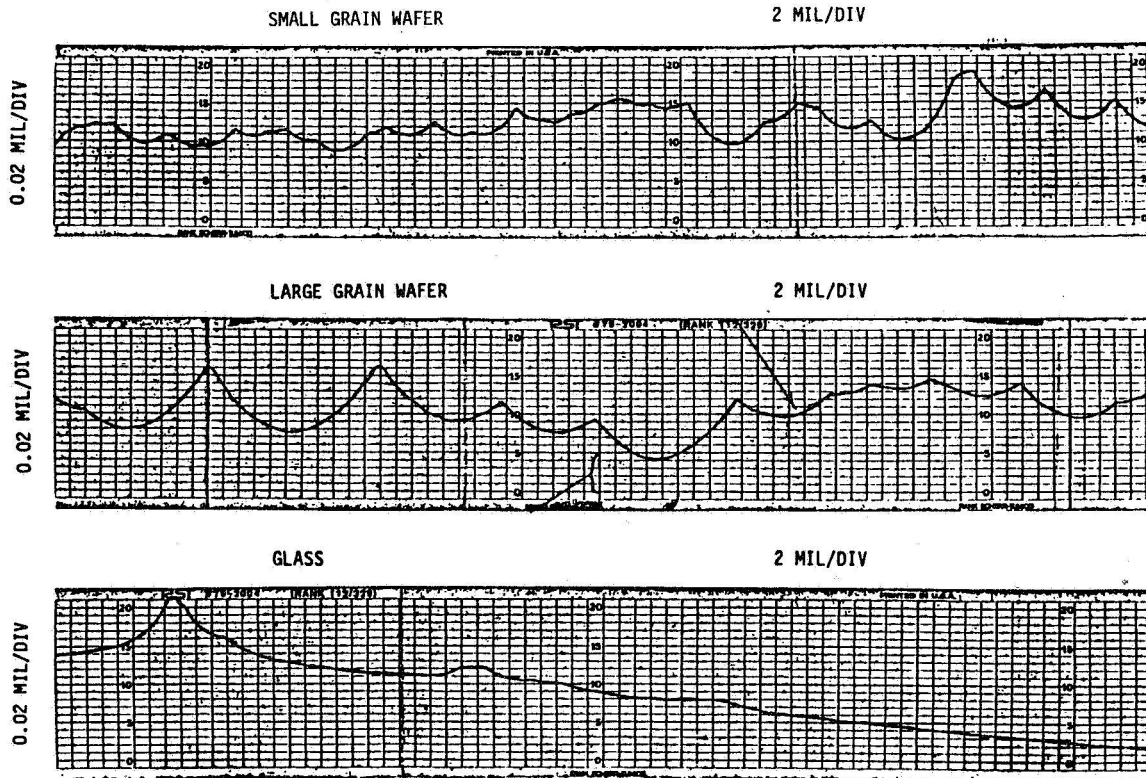
FIGURE 4. WAFER AND GLASS SURFACE PROFILES

331
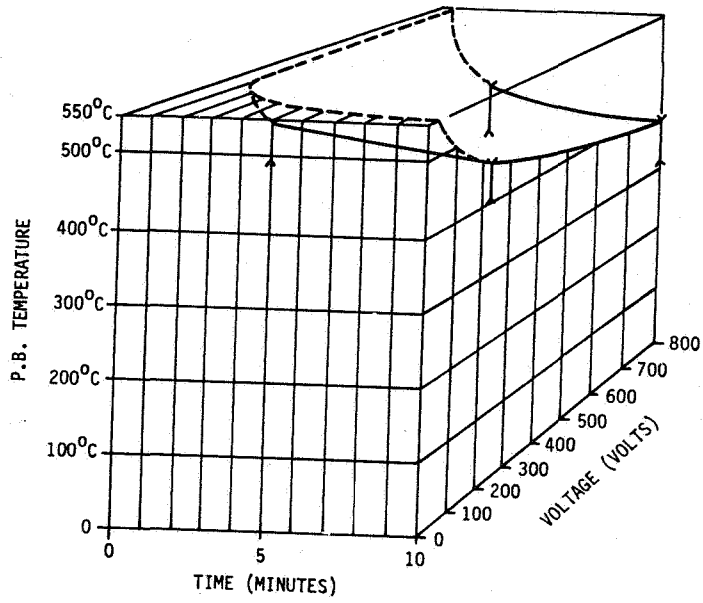
FIGURE 7. ELECTROSTATIC BONDING T, V, τ SURFACE

(TIME SCALE, τ, 1 MINUTE/DIV)
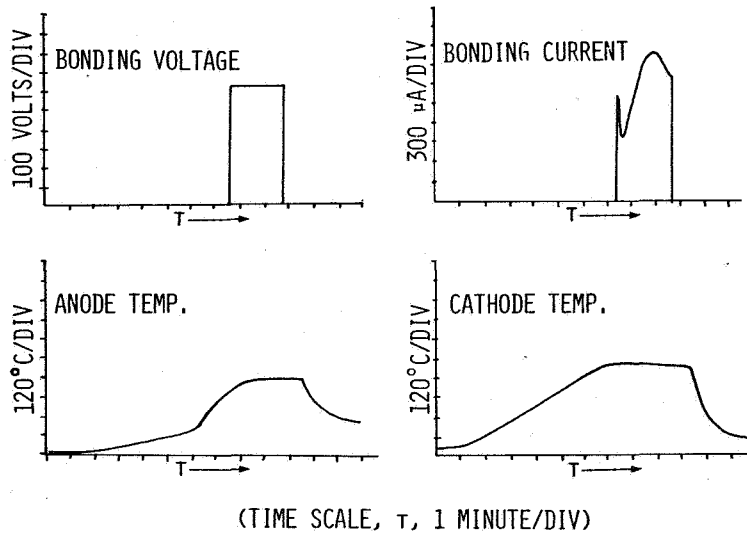
FIGURE 8. EXAMPLE STRIP CHART RECORDS OF BONDING PARAMETERS
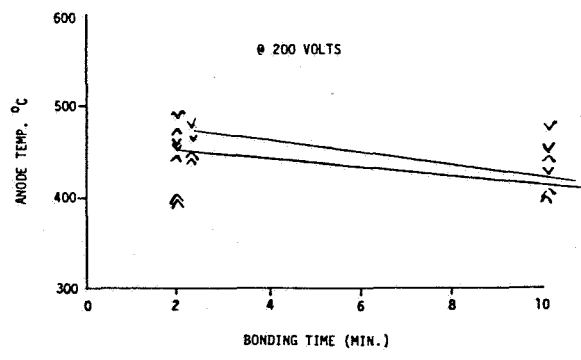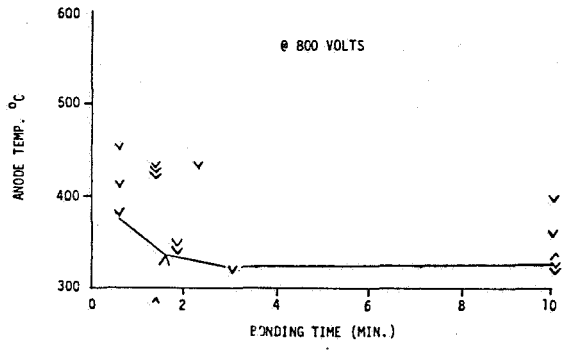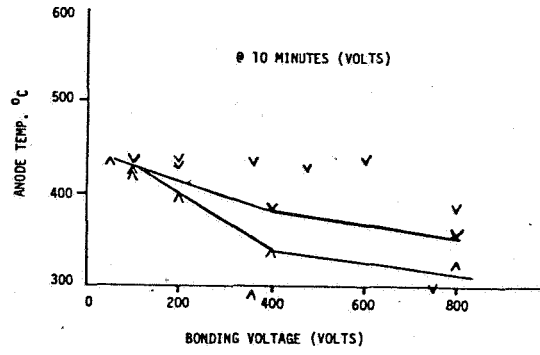
FIGURE 9. TWO-DIMENSIONAL PLOTS OF BONDING PARAMETER
DEPENDENCES FOR WAFERS (∧ BAD BOND, ∨ GOOD BOND).

333
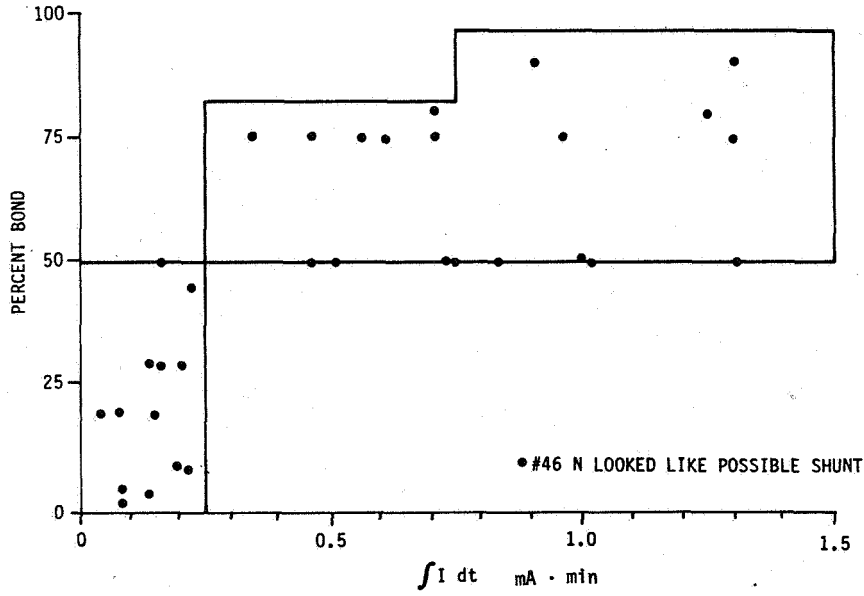
FIGURE 10. MICROSCOPIC PERCENTAGE BOND VERSUS $\int_I(T)_{DT}$
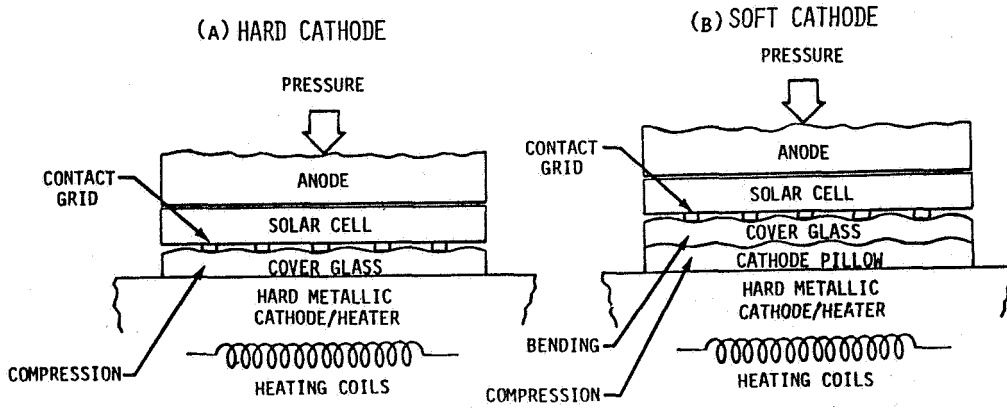
FIGURE 11. PHYSICAL FEATURES OF ESB PROCESS USING HARD AND SOFT CATHODES

334

(A) CATHODE PILLOW   (B) HARD CATHODE
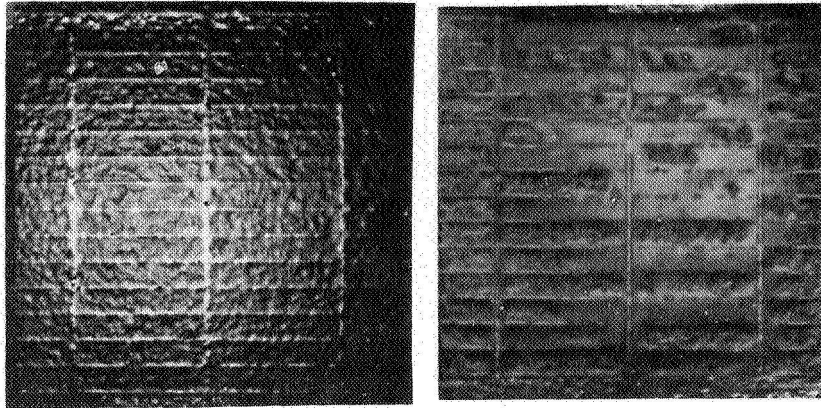
FIGURE 12. EXAMPLE SOLAR CELLS WITH GLASS BONDED USING HARD AND SOFT CATHODE

EXAMPLE IV PLOTS

S/N : 30	LEVEL :	0	1
TEMP: 25 C	ISC(MA) :	147.8	135.8
AREA: 4 CM^2	VOC(MV) :	601.9	598.2
INT. : AM0	PMAX(MW):	69.8	63.5
	F.F. :	0.784	0.787

SUMMARY
PMAX DEGRADATION

(EACH POINT = 8 SAMPLES)
(BARS = 1 STANDARD DEVIATION)
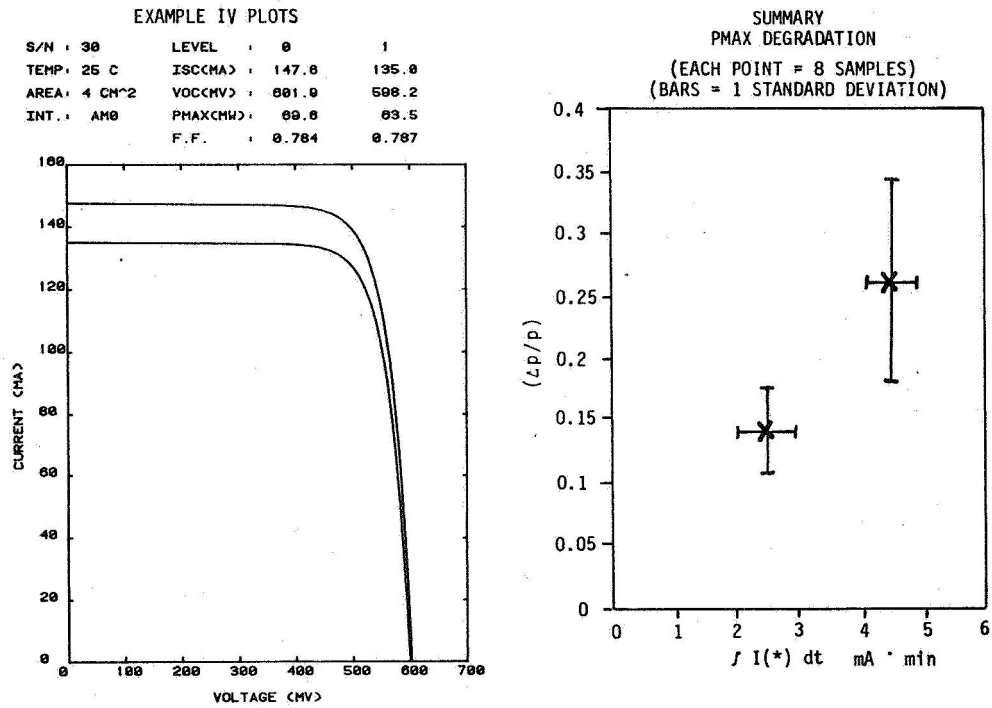
FIGURE 13. EFFECT OF ESB ON CELL ELECTRICAL PARAMETERS

335

(A) LASER HEATING (B) CATHODE PILLOW
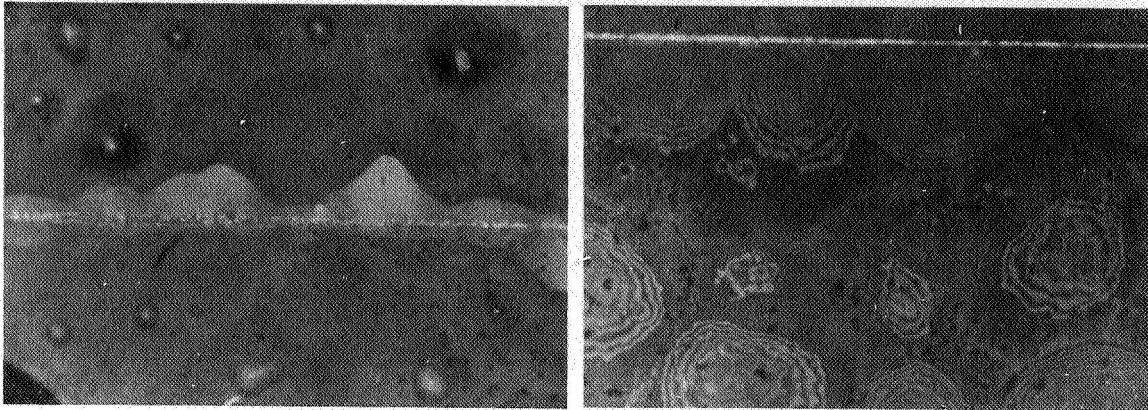
FIGURE 14. COMPARISON OF MICROSCOPIC BONDING USING
CATHODE PILLOW AND LASER HEATING

BARE WAFER 385 $\overset{\circ}{A}$ Ta_2O_5 760 $\overset{\circ}{A}$ Ta_2O_5
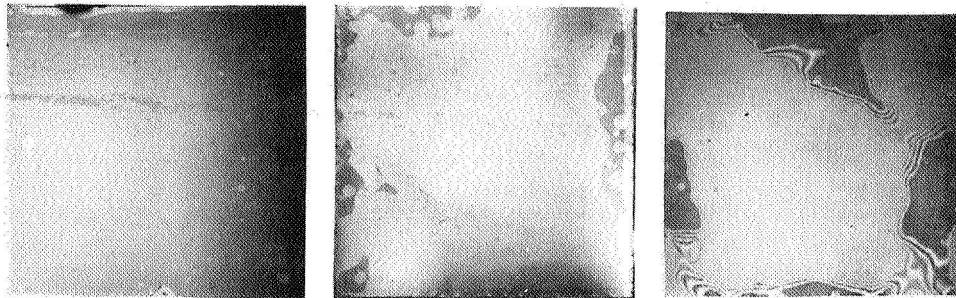
FIGURE 15. EXAMPLE OF BOND DEGREE VERSUS WAFER SURFACE COATING THICKNESS
(USING IDENTICAL BONDING CONDITIONS)

HERMETIC ENCAPSULATION TECHNIQUE FOR SOLAR ARRAYS

Czeslaw Deminet and William E. Horne
The Boeing Company
Seattle, Washington

ABSTRACT

A concept is presented for encapsulating solar cells between two layers of glass either individually, in panels, or in a continuous process. The concept yields an integral unit that is hermetically sealed and that is tolerant to high temperature thermal cycling and to particulate radiation.

Data are presented on both high temperature solar cells and special glasses that soften at low temperatures for use with the concept. The results of encapsulating experiments are presented which show the successful application of the concept to the special high temperature cells. The mechanical feasibility of encapsulating 2 mil cells between two layers of 2 mil glass is also demonstrated.

INTRODUCTION

The desirability of an integral bond between solar cells and cover glasses has long been recognized. Such a bond would eliminate the need for UV rejection filters and would increase the resistance of the stack to thermal transients and thermal shock. Early efforts were motivated by requirements for deep space probes and array hardening against nuclear weapons environments. More recent motivation comes from three basic areas, 1) the need for arrays that are hardened against thermal transients induced by laser weapons, 2) the need for arrays that can be thermally annealed in space in order to increase mission life in radiation environments, and 3) the need for low-cost, high reliability encapsulating techniques for terrestrial arrays.

The earlier attempts at making integrally bonded cell-cover glass stacks utilized such techniques as sputtering (ref. 1) of glass layers onto the cells. To date, these processes have been too time consuming to be economical. They also resulted in excessive shear stresses at the interface between the cell and the glass. A more recent process has been the use of electrostatic field-assisted bonding techniques (ESB) (refs. 2, 3, 4) for sealing the glass to the solar cell. This process is still under development and shows promise. Indeed some of the glasses being developed for the present concept may also prove useful for the ESB process.

The present concept offers an alternative for an adhesiveless structure that is applicable to individual cell processing and also to low-cost automated continuous process fabrication.

337

Concept Description (ref. 5)

The process starts with rolling a sheet of glass out of a glass melting tank as is commonly done in the glass industry. A top roller forms indentations having the dimensions of the solar cells to be encapsulated. The cells are then deposited into the indentations when the glass is just below the softening temperature. The solar cells are interconnected at this point by a metal foil or by spraying interconnectors in a liquid metal form similar to computer printer techniques. The second sheet of glass which is at a higher temperature and, hence, has a lower viscosity is then rolled on to the array. This completes the encapsulation. The process is illustrated in figure 1. Where metal foils are used for the interconnects the pressure of the glass laminations is sufficient to press the contacts into electrical contact. The nature of the heremetic seal prevents corrosion and degradation of these contacts.

The first attempts at demonstrating this encapsulation technique were performed in an inert atmosphere using 7740 borosilicate glass between graphite dies at a temperature of 750°C for 15 minutes and 1 psi contact pressure. These parameters yield a close fitting interface as shown in figure 2.

The mechanical feasibility of the process has been demonstrated for both thick and thin solar cells. Figure 3 shows a 2-mil thick cell encapsulated between two sheets of 2-mil thick 7740 borosilicate glass.

However, it is well known that conventional solar cells degrade rapidly at temperatures in excess of 450 to 500°C. Thus, for the present concept it is desirable to have a radiation resistant glass that closely matches the thermal expansion coefficient of silicon which softens at a temperature lower than that of commercial borosilicate glasses. These borosilicate glasses can be formulated to closely match the thermal expansion coefficient of silicon. However, these low expansion coefficient glasses have a relatively high softening point temperature (∿ 800°C). While it appears that the process would be most efficient at a rolling speed of about 2 meters per second resulting in each cell being at the encapsulating temperature less than one minute, this time-temperature combination still severely degrades conventional cells. Thus, it was concluded that work should be done to develop improved glasses and solar cells for the process.

High Temperature Cell Development (ref. 6)

Boeing electronics has developed a proprietary process (ref. 6) for fabricating concentrator solar cells using a mesa type contact structure that reduces the series resistance and increases the thermal resistance of the cells. These cells have been encapsulated by the above process and survived a 15 minute soak at a temperature of 750°C with only minimal degradation of the final electrical parameters. Figure 4 shows the electrical characteristics of these cells before and after encapsulation. A number of these cells have been successfully encapsulated in Corning Code 7740 (Pyrex) glass.

This cell fabrication concept is currently being extended to space type 1 sun (AMO) cells; however, the results are not available at this time.

Glass Development

In order to avoid excessive shear stress at the glass-solar cell interface the thermal expansion coefficient of the glass must closely match that of the solar cell. For silicon cells the expansion coefficient is about 4×10^{-6} cm/cm°C. The glasses of borosilicate composition can be formulated to match silicon very closely. During this effort five different borosilicate glasses have been examined (Corning Code 7050, 7070, 7720, 7740, and 3320). These glasses were fabricated into 2-mil thick microsheet on a glass blower's lathe by blowing a large diameter cylinder from 30 mm glass tubing. This yielded very uniform microsheet with a slight curvature which could be flattened due to its flexibility as illustrated in figure 5. The encapsulating experiments were performed using the microsheet between two high density graphite dies. The graphite dies were separated by blocks of soda lime glass which softened at a lower temperature than the borosilicate glasses. This prevented the microsheet from being crushed initially and allowed the dies to be slowly forced together as the temperature increased and the borosilicate glass softened to the point that it would not crack under the $\sim$ 1 psi pressure of the dies.

Another constraint on the glass is that it must be radiation resistant. For the borosilicate glasses this leads toward the selection of a low alkali content glass such as Corning Code 7070; however, this glass is approximately 26 percent boron oxide and tends to undergo phase separation when heated to the softening temperature for a significant length of time.

Two additional types of borosilicate glass formulated by Schott Glass Company, Schott 8250 and Schott 8330 where doped with ceria in hopes of increasing their radiation tolerance; however, it was found that they darkened severely after the ceria doping so that no further experiments were performed on them.

The soda-lime microsheet doped with Cerium Oxide is in use successfully for discrete solar cell covers in space, but cannot be used for integral encapsulation because the thermal expansion coefficient is too high. However, there is a family of glasses based on phosphorous pentoxide as a glass former rather than silicon dioxide. These phosphate glasses are not being used extensively for terrestrial applications because they are to some extent soluble in water. For space applications this is not a problem. Phosphate glasses are a good host for many oxides and are used for laser glasses. A glass of phosphate composition matching the coefficient of silicon and doped with $\sim$ 3 percent ceria has been melted and did not show any appreciable loss of light transmission after being irradiated to a fluence of $\sim 4.0 \times 10^{15}$ proton per cm^2 at 1.5 MeV as shown in figure 6.

Since this ceria doped phosphate glass meets the thermal expansion requirements, is radiation tolerant, does not undergo phase separation at high temperature and promises a lower softening temperature than borosilicate glass, it appears to be an excellent candidate for the encapsulating process discussed herein. It is also being investigated as a candidate for electrostatic field-assisted bonding.

CONCLUSIONS

In conclusion, a process for heremetically encapsulating solar cells either individually, in panels, or in a continuous process has been demonstrated. The mechanical feasibility of the process for extremely thin array-cell fabrication has been demonstrated and signicant progress has been made in the development of solar cell fabrication techniques and glasses uniquely suited for the process has been shown. The encapsulation process promises arrays of good reliability, light-weight, and low cost since automation is readily applicable.

REFERENCES

1. Anon, "Survey and Study for an Improved Solar Cell Module, STOD TASK NO. 43," JPL Document No. 900-270, August 1969.

2. Kirkpatrick, et al., "Stress Free Application of Glass Covers for Radiation Hardened Solar Cells and Arrays," AFAPL-TR-77-28, May 1977.

3. Younger, P. R., Kreisman, W. S., and Kirkpatrick, A. R. "Integral Glass Encapsulation for Solar Arrays," Spire Corporation Interim Report for DoE/JPL-954521-77/3, November 1977.

4. Egelkrout, D. W. and Horne, W. E., to be presented at the Fourth High Efficiency and Radiation Damage Solar Cell Meeting, NASA Lewis Research Center, Cleveland, Ohio, October 1980.

5. Deminet, Czeslaw and Oettle, Richard, "Process for Fabricating Glass Encapsulated Solar Cell Arrays," Patent Granted May 1980.

6. Corwin, Rudolph E and Stanbery, Billy J., "Improved Electrodes for Light Transducers Such as Solar Cells and Concetrator Solar Cells, and Methods for Manufacture Thereof," Boeing Patent Application, July 1978.
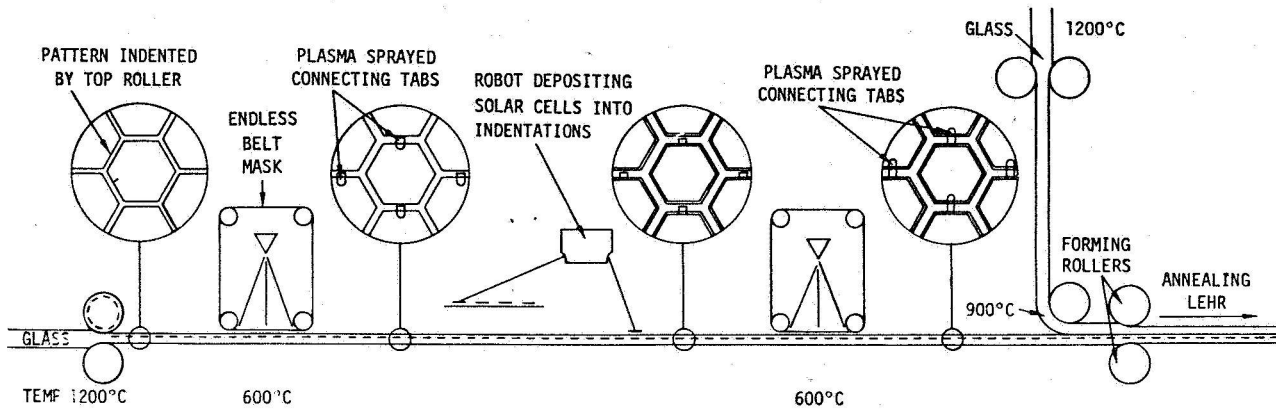
FIGURE 1. METHOD OF FABRICATING GLASS ENCAPSULATED SILICON SOLAR CELL ARRAYS
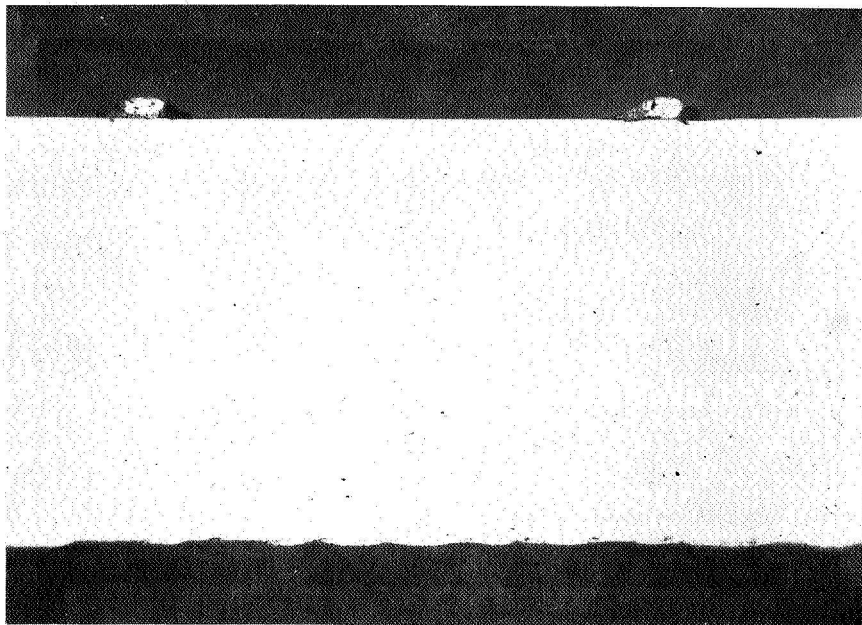
FIGURE 2. ILLUSTRATION OF GLASS CONFORMATION TO SILICON AND CONTACT SURFACES
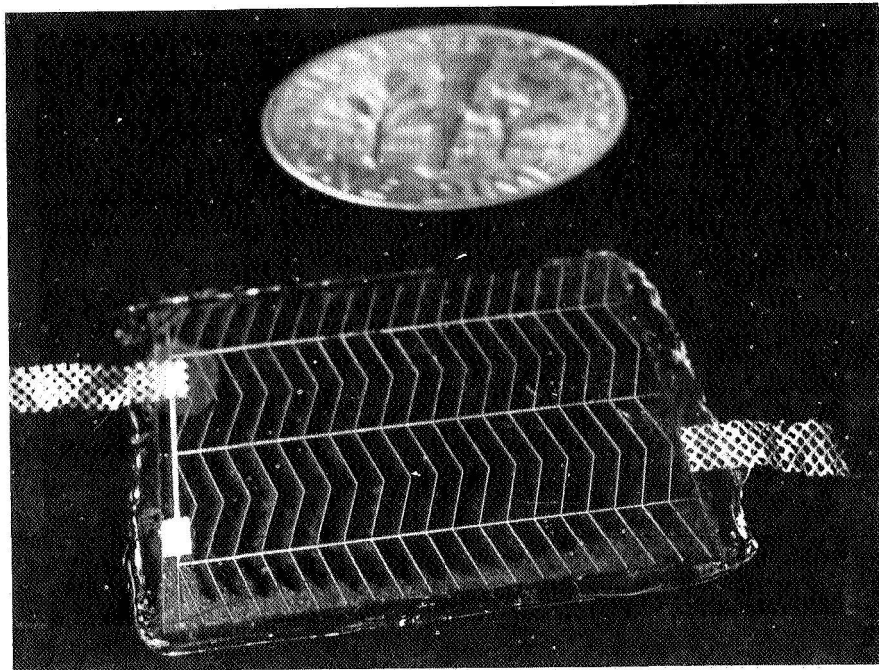
FIGURE 3. 2-MIL CELL ENCAPSULATED IN 2-MIL GLASS FRONT AND BACK
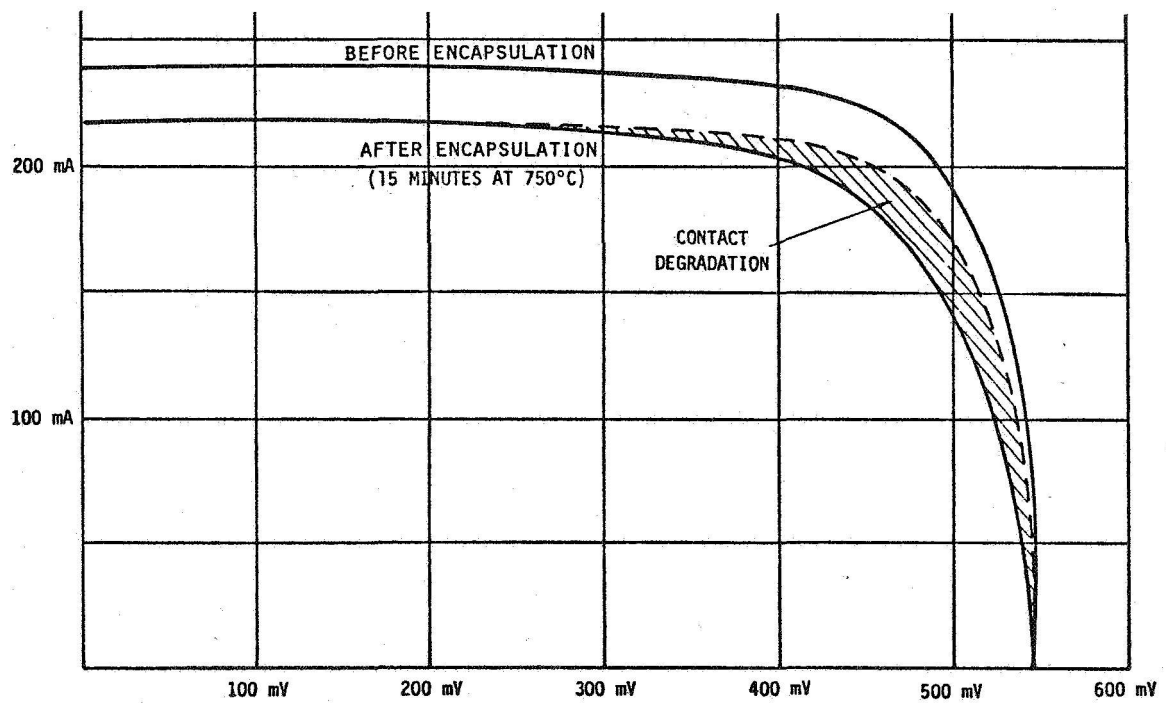
FIGURE 4. PERFORMANCE OF HIGH TEMPERATURE SOLAR CELLS

342
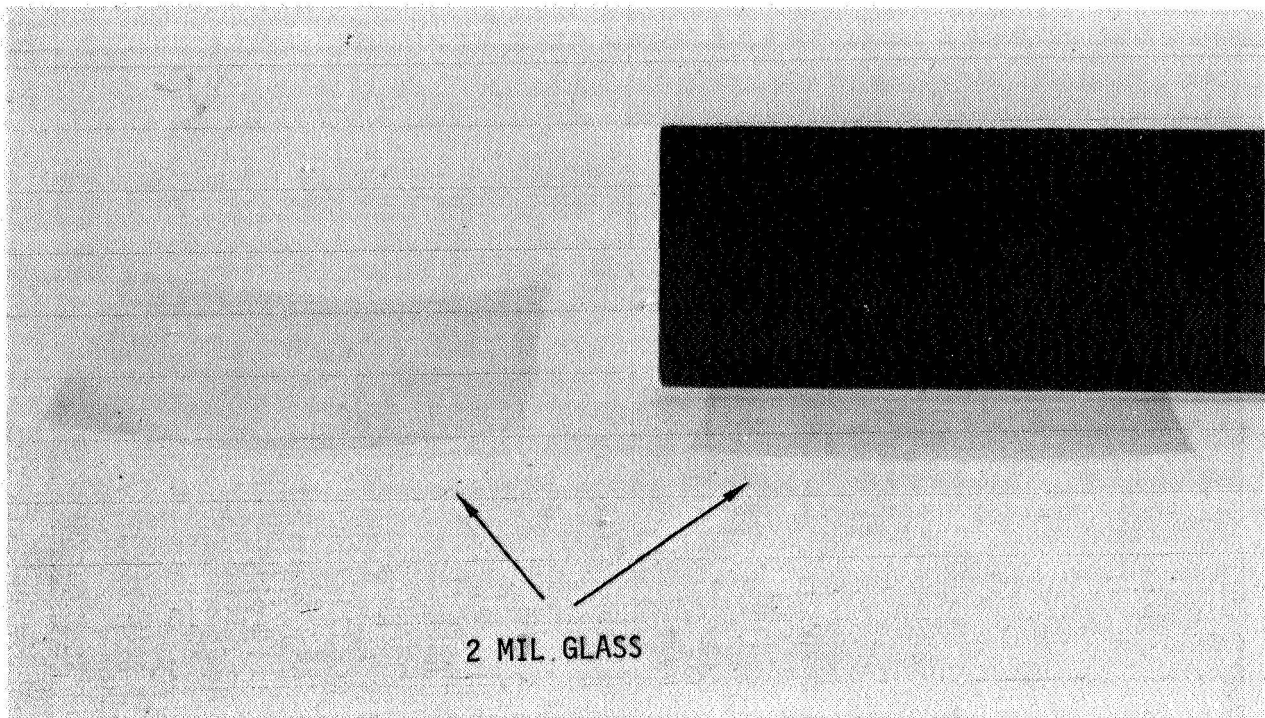
FIGURE 5. DEMONSTRATION OF 2 MIL 7070 BOROSILICATE MICROSHEET FLEXIBILITY
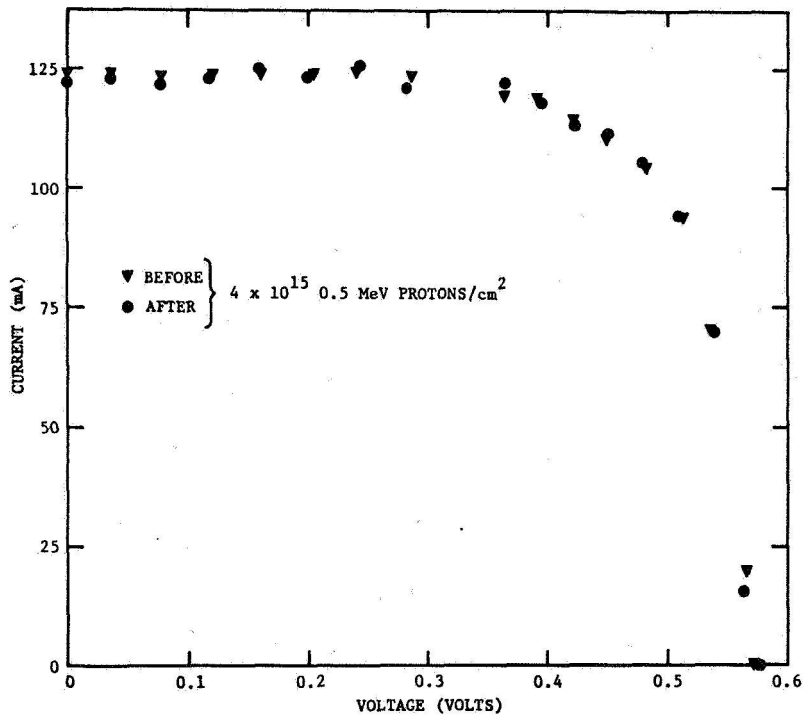
FIGURE 6. RESPONSE OF SOLAR CELL COVERED WITH CERIA-DOPED PHOSPHATE GLASS BEFORE AND AFTER IRRADIATION

343

RECENT DEVELOPMENTS IN LIGHTWEIGHT SOLAR CELL MODULES

J. D. Broder and A. F. Forestieri
NASA Lewis Research Center
Cleveland, Ohio

SUMMARY

Two types of lightweight solar cell modules have been prepared. The goal is to achieve a module with a power to weight ratio of 350 watts per kilogram. Both structures use thin cells approximately 50 micrometers thick and glass covers approximately 75 micrometers thick. In one structure the glass is bonded to the module using 93-500 silicone adhesive; while the other relies on heat and pressure bonding using FEP as the adhesive. Specific powers of about 335 watts per kilogram have been achieved.

INTRODUCTION

Some future space missions will require solar cell modules with high power to weight ratios. The use of lightweight materials is necessary to achieve this goal. The 50-micrometer-thick cell forms the basis of the modules prepared in this program. These cells still require a protective cover to reduce the harmful effects of trapped electrons and protons. To minimize the weight and still protect the cells, only the thinnest available cover glasses were considered. In this program the recently available 50- to 75-micrometer-thick 7070 glass was used. Substrate and support materials were also chosen from among the thinnest available and included 7.5-micrometer-thick Kapton, 25-micrometer-thick fiberglass, and 12.5- and 25-micrometer-thick FEP. Also of importance towards achieving the high specific power goal is the use of thin interconnect material, in this case, 12.5-micrometer silver (ref. 1). The two structures will be discussed in this paper.

The 93-500 Bonded Module

The first attempt to prepare a lightweight module made use of 93-500 as the glass-to-cell adhesive. The module was prepared using parallel-gap welding to interconnect thin cells into a three-by-three configuration and available 50-micrometer silver plated Invar interconnects. Gently abraded 25-micrometer Kapton was used as the substrate. A one piece 65- by 65-millimeter 7070 glass cover was attached to the nine cells using 93-500 adhesive. Standard aerospace technology was used in fabricating the module.

Since mechanical sample cells were used for the module, no electrical measurements were made. However, the module weighed 2 grams, and the thickness in the central portion was about 215 micrometers. The thickness at the interconnect was 265 micrometers. It is expected that a module using 12.5-micrometer silver interconnects instead of the 50-micrometer Invar

would be more uniform in thickness across the whole module. A schematic of a structure using thin interconnects is shown in figure 1.

FEP Bonded Module

This module was assembled by parallel-gap welding 12.5-micrometer silver interconnects to 50-micrometer cells in a three-by-three configuraration. 25-micrometer-thick fiberglass cloth and 7.5-micrometer-thick Kapton together with 12.5 micrometer thick FEP-C formed the substrate of this module. The remaining components included a 25-micrometer layer of FEP-A, another layer of 12.5-micrometer-thick FEP-C, and a one-piece 75-micrometer-thick, 65- by 65-millimeter 7070 cover glass. A schematic of this structure is shown in figure 2. The technique for preparing this module is substantially the same as described in reference 2. After fabrication, the module was trimmed, weighed, and its electrical performance measured. Figure 3 shows the module and its current-voltage (I-V) characteristic. The module weighs approximately 2.07 grams and has a power to weight ratio of 335 watts per kilogram. It is noteworthy that the interconnected module efficiency was over 14 percent based on solar cell active area. The average thickness of the module between contacted areas is about 222.5 micrometers and at the contacts about 232.5 micrometers.

In addition to the advantage in weight saving gained by using the 12.5-micrometer silver interconnect, another advantage is in reduced glass breakage at the top contact areas. Before the use of 12.5-micrometer silver interconnects, the glass cover would break at the top contact. Since the 12.5-micrometer silver interconnect was introducted, several modules have been prepared with no cracking whatsoever.

CONCLUDING REMARKS

Two methods of preparing lightweight solar cell modules capable of achieving a specific power of 350 watts per kilogram have been demonstrated. Both methods use the new approach of covering several cells (nine) with a single large piece of thin glass. This approach also demonstrates that there should be no difficultly in covering the new large area solar cells, currently under development, with a single piece of thin glass.

Another key technique for achieving the high power to weight ratios is the use of 12.5-micrometer silver interconnect material. Considerable testing has yet to be done to prove that the methods, materials, and techniques described here are space qualified. However, the materials and technologies used in this program were chosen because of their past good performance in space arrays.

The advent of high specific power modules should now lead to high specific power solar cell blankets and thence to arrays. Several of the techniques described (single large piece of glass and FEP adhesive) should also be instrumental in reducing the cost of future solar cell arrays.

REFERENCES

1. LaRoche, Guenther J.: Ultrathin Cell Module Technology. Photovoltaic
   Generators in Space. ESA SP-147, European Space Agency, 1980, pp.
   21-27.
2. Forestieri, A. F.; and Broder, J. D.: Improvements in Silicon Solar Cell
   Cover Glass Assembly and Packaging Using FEP Teflon. NASA TM X-52875,
   1970.

75 μm 7070 glass cover

31 μm 93-500   12.5 μm Ag

50 μm silicon solar cell

12.5 μm Ag   31 μm 93-500

25 μm abraded kapton
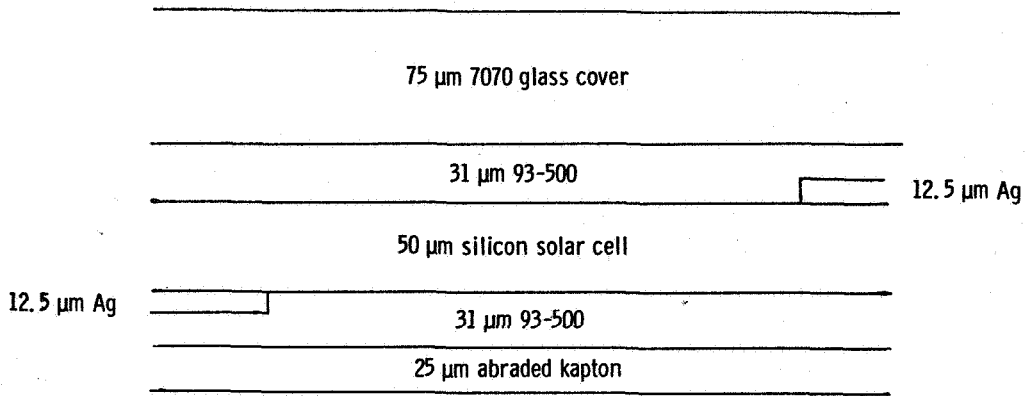
Figure 1. - Thin module build-up with 93-500.

75 μm 7070 glass cover

25 μm FEP-A   12.5 μm Ag

50 μm silicon solar cell

12.5 μm Ag   12.5 μm FEP-C

25 μm fiberglass

12.5 μm FEP-C   7.5 μm kapton
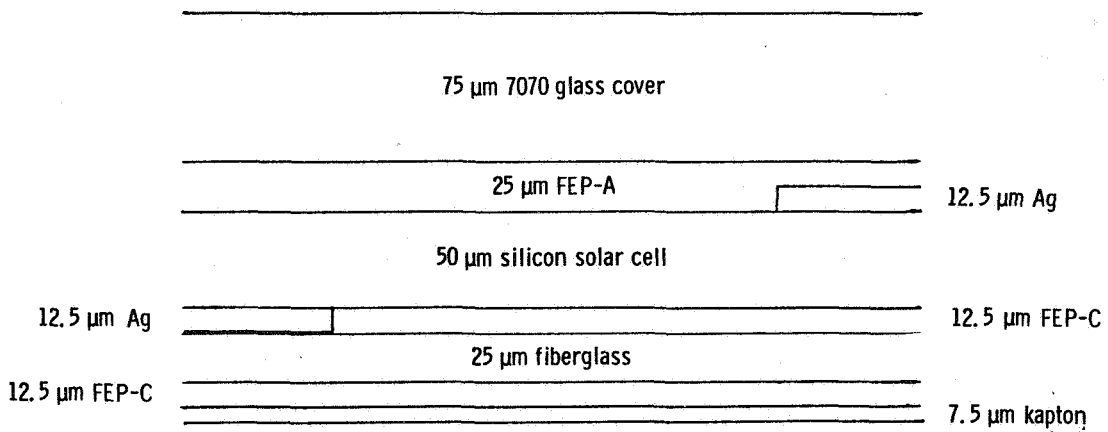
Figure 2. - Thin module build-up with FEP.

CELL   ARRAY # 9-29   ISC =-0.5011
DATE   9/30/80   VOC = 1.807
REFCELL A-52 151.9   IMAX=-0.4584
AREA   36   CM+2   VMAX= 1.514
AM   0   PMAX= 693.78
TEMP   25   (C)   F.F.=   76.6
  WEIGHT 2.07 GM   EFF.=   14.07
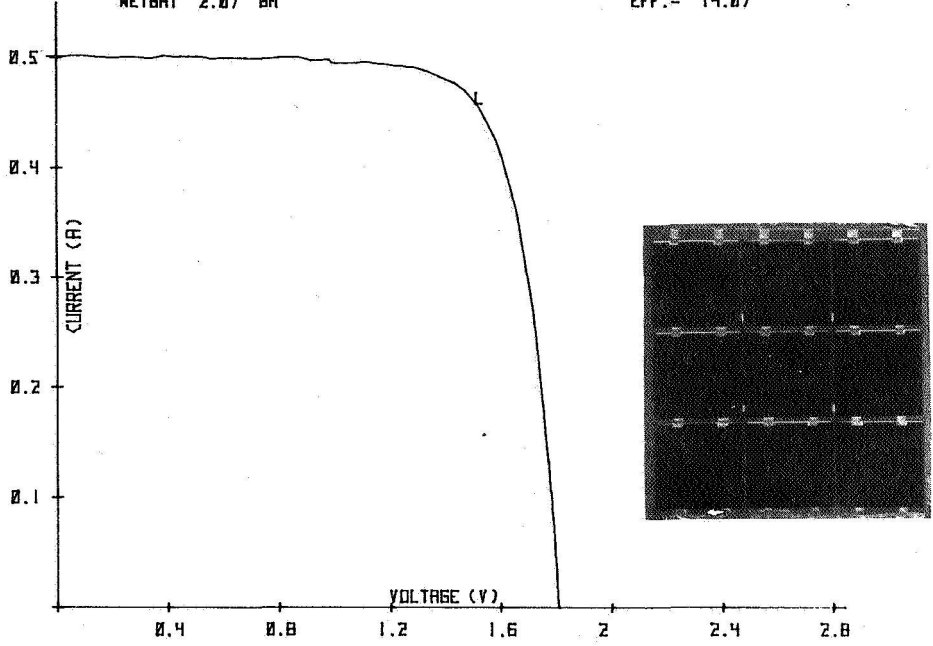
Figure 3. - 335-watt-per-kilogram module.

PROSPECTS FOR ENHANCING SEP ARRAY PERFORMANCE*

John A. Scott-Monck
Jet Propulsion Laboratory
Pasadena, California

SUMMARY

Three advanced blanket design models, all employing the OAST thin cell, have been developed for potential incorporation into the SEP array. The beginning-of-life (BOL) specific power of these blankets ranges from 180 to 660 W/kg. Coupling these blanket designs to the baseline SEP array structure yields array specific powers of from 90 to 200 W/kg. It is shown that certain modifications to the SEP array structure, coupled with the advanced blanket designs, could allow the BOL specific power to reach approximately 250 W/kg.

INTRODUCTION

The Solar Electric Propulsion (SEP) array developed by LMSC for NASA-MSFC represents the most advanced technology now in existence for producing photovoltaic power in space. The current design is rated at 66 W/kg beginning-of-life (BOL), and is capable of delivering at least 12.5 kw per wing (Ref. 1) The purpose of this paper is to describe approaches which can improve the performance of the SEP array with respect to specific power.

This analysis scrupulously avoids any consideration of end-of-life (EOL) specific power. There are a variety of reasons for this tack. The purpose of this work is to determine reasonable limits for planar solar array technology. Therefore, trends are more important than precise determinations. There are many mission classes, each with its own set of unique requirements and particular EOL definition. Admittedly, this will certainly have a strong influence on both blanket and structure design, but in the interests of clarity, this study will be confined to BOL conditions to avoid changing the blanket design to accomodate a particular mission.

351

As presently configured, the SEP array has a mass of 379 kg, with the blanket accounting for 235 kg, while the support structure, deployment mechanism and container make up the remaining 144 kg of mass. As originally designed, the SEP blanket employed a very advanced, for its time, silicon solar cell. During the period in which the SEP array was brought to technical readiness, there has been dramatic progress made in improving silicon solar cell power output and mass. As a result, it is now possible to project that the SEP blanket can be modified to achieve a specific power approaching 650 W/kg. Coupling this blanket with a more refined array structure could yield a system rated at greater than 250 W/kg BOL.

The key to blanket improvement is the NASA-OAST thin silicon solar cell developed for NASA-JPL by the Solarex Corp (Ref. 2). Pilot production of this 50µm thick cell has demonstrated that the device can be manufactured in volume (>10,000 2 x 2 cm cells per month) with an AMO efficiency of 12 percent (Ref.3). Other versions of the cell, developed by space qualified suppliers, have shown conversion efficiencies approaching 15 percent (Ref. 4). Three blanket designs employing pilot production and more sophisticated variations of 50µ m cell technology are described in the following section of this paper. Based on the specific power of these blanket models, allowable reductions in the mass of the SEP array structure are projected. From this it is possible to estimate the upper limit for the SEP array BOL specific power.

BLANKET 1

This design employs the presently available OAST pilot production thin cell. A mass breakdown of the blanket is given in Table 1. An additional 5 kg increment per wing is assumed for each blanket model to account for the mass of the hinges, padding, stiffeners and other miscellaneous mechanical apparatus required for the proper functioning of the SEP baseline blanket design. A prototype module, very similar in design to blanket 1, has been produced for JPL by TRW (Ref.5), and is currently undergoing preliminary testing at MSFC prior to being incorporated into the SEP deployment and wing retraction space experiment. Blanket 1 uses planar rather than wraparound contact cells. Other major differences are the use of 50µ m ceria-doped microsheet covers and silver plated Invar in-plane interconnectors. The printed circuit substrate laminate used in the SEP blanket has been replaced in this design by a 50µ m Kapton sheet.

The approach taken in calculating the specific power of the three blanket models is to assume that the blankets are merely substituted in place of the current SEP design. Therefore, in each case the amount of power per wing will be different since the number of cells is held constant. A blanket packing factor of 80 percent is used to obtain the number of cells per wing. A power loss of 4 percent due to assembly and cell mismatching is used for this calculation. The circuit is assumed to be operating off the maximum power point which introduces an additional 6 percent penalty in the output power of the cell. These conditions are held constant for each blanket

352

model. For blanket 1, which employs cells with no back surface reflectors, the blanket operating temperature is assumed to be 55°C, resulting in a further reduction in cell output.

Based on this set of assumptions, the BOL specific power of blanket 1 is calculated to be 182 W/kg for the 12 percent OAST thin cell case. Using the SEP array structure mass as a baseline, the array would now have a BOL specific power of 91 W/kg at operating temperature and deliver 13 kw per wing. Reductions in the mass of the array structure, now possible because of the lower blanket mass, would lead to further improvements in the array's specific power. Some of the estimates of the mass reduction that could be achieved in the SEP array structure elements are provided in a subsequent section of this paper.

BLANKET 2

This model, the details of which are provided in Table 2, represents a logical extension of existing blanket technology. An examination of the first model shows that the mass of the interconnect, cell contacts and plating contribute over 30 percent to the total blanket mass. In this model, therefore, the specific power is increased, by not only using a more efficient cell, but also seeking to significantly reduce the mass of the cell contacts and interconnect.

The cell employed in blanket 2 is a higher efficiency version of the pilot production OAST thin cell. Since conversion efficiencies greater than 14 percent AMO have already been demonstrated (Ref. 4), the choice of a 14 percent cell is justified. Two new technologies are incorporated into this cell, a gridded back contact to reduce mass and a back surface reflector (BSR) to decrease the cell absorbtivity. It has been reported that absorptances as low as 0.60 are possible when BSR technology is utilized (Ref. 6). Calculations show that an optimized BSR could reduce the cell operating temperature by 25°C.

Further mass reductions are achieved by substituting aluminum interconnects and significantly reducing the amount of silver plating on them. It should be mentioned that the present SEP blanket has copper interconnects and that aluminum had been seriously considered as a low mass alternate. If this blanket were to be operated in geosynchronous orbit where much wider thermal excursions are encountered, it might be necessary to retain the blanket 1 interconnect material.

The cell contact thickness has been reduced from $10\,\mu m$, employed in the first model, to $5\,\mu m$, since it is felt that welding silver plated aluminum to silver will present fewer challenges, due to the types of metals involved. The gridded back contact would be no problem, since OAST thin cells are made with back surface fields which result in a highly conducting silicon surface. Other elements where mass reduction can be achieved are in the amount of adhesive used to mount the cell to the substrate and the area of the interconnector design. Since these are minor influences, in this model they are held constant.

Using the same factors for assembly loss and off-maximum power point operation, the BOL specific power of blanket 2 is calculated to be 331 W/kg. Each wing now is capable of delivering 17 kw under operating conditions, due to the combination of a higher efficiency cell operating at a much lower temperature. Once again, the mass of the baseline SEP array structure is used to obtain the BOL specific power of the array, which for this model is 138 W/kg.

BLANKET 3

The previous models were based entirely on technology which has been demonstrated in one form or another. In this model, an attempt is made to estimate the ultimate BOL specific power that might be obtained from a planar silicon solar cell blanket. Table 3 shows the mass breakdown for such a blanket. From Table 2, it can be seen that the cell cover and adhesives comprise approximately 35 percent of the blanket's mass. As in the case of blanket 2, this model attempts to increase specific power by increasing the power output and simultaneously decreasing the blanket mass.

Blanket 3 incorporates two new elements of technology, very high efficiency cells and encapsulants, both of which are now being actively investigated. The solar cell is projected to have a conversion efficiency approaching 18 percent. The rationale for choosing this value will be discussed. It has become apparent in recent years that the last remaining barrier to achieving the practical upper limit for silicon solar cell efficiency is open circuit voltage (V_{OC}). It has been predicted that a V_{OC} of 700 mV is feasible (Ref.7). Combining this value with what has already been accomplished with respect to short circuit current and curve fill factor, yields an efficiency of approximately 18 percent AMO. At this point, it appears that success in obtaining a very high V_{OC} will not be partial. Therefore, it is assumed for this model that the mechanism controlling the V_{OC} in silicon solar cells will be understood and successfully exploited. In the event that this does not occur, it would seem unlikely that practical conversion efficiencies for silicon solar cells much greater than that used in blanket 2 will be achieved.

There is another approach which can be taken to obtain an upper limit for silicon blanket technology. Silicon solar cells of 25μm thickness have been fabricated with conversion efficiencies greater than 12 percent AMO (Ref. 8). Employing a cell of this type in place of the extremely high output cell upon which this model is based would result in a blanket specific power only about 15 percent lower than in the case of using an 18 percent 50μm thick OAST thin cell.

In this model, the cell thickness has been reduced to 50μm. Some allowance for handling problems caused by the use of very thin cells had been made in the previous models. However, since traditional methods of covering cells are not assumed for blanket 3, the cell thickness is taken to be 50μm. There may be some objection to projecting extremely high efficiencies for very thin cells, but at present, there is no significant difference in output between ultrathin and conventional thickness cells. It is not expected, that the mechanism controlling V_{oc} will be related to cell thickness; in fact, according to some theorists (Ref. 9), an ultrathin cell may be a better configuration for obtaining high V_{oc} in silicon solar cells.

The second major element of new technology is the use of an encapsulating material which will replace both the present Kapton substrate and the ceria-doped microsheet covers of the previous designs. A great deal of work has already been done in the area of encapsulants (Ref. 10,11) and the development of ultrathin solar cells has provided further stimulus. The encapsulant used in blanket 3 is not a glass, but rather a transparent, ultraviolet resistant, organic material which can be provided in sheet form and is capable of being joined without the use of primers or adhesives which would add mass to the blanket. The advantages of such a material are obvious with respect to blanket fabrication.

The choice of encapsulant thickness is somewhat arbitrary. The encapsulant should have a thickness equivalent to that of 25μm of fused silica in order to provide sufficient shielding to protect the cells from low energy proton degradation. Obviously, the radiation environment encountered during the mission and the inherent radiation resistance of the cell used will be the determining factors in selecting the amount of shielding required for both the front and rear sides of the blanket.

Further reductions in blanket mass may be achieved by replacing the silver contact system with aluminum. It has been demonstrated that the aluminum contact system is viable for silicon cells (Ref. 12,13), although at that time the cell junction was much deeper than currently used. The thickness of the interconnect could be reduced to 12μm. In fact, there is evidence available to indicate that 12μm interconnects are more compatible with ultrathin cells (Ref. 14). There is some risk that with very high efficiency cells, there might be an undesirable voltage drop in the circuits due to the

narrow cross sectional area of this interconnect. However, for this exercise, both modifications have been incorporated into the blanket 3 model.

Blanket 3 has a calculated BOL specific power of 660 W/kg. As in the previous cases, the assumptions concerning packing factor, assembly loss and off-maximum power operating point have been held constant. Using the present SEP array structure mass of 72 kg per wing, the BOL specific power at the array level is increased to 205 W/kg with each wing delivering 21.5 kW. This blanket results in a greater than threefold improvement in BOL specific power from the SEP array as it is presently designed.

STRUCTURAL CONSIDERATIONS

Additional improvements in BOL specific power at the array level can only be realistically achieved by reducing the mass of the structure which is used to store, deploy, tension and support the blanket. In the case of the SEP array, great caution must be exercised in choosing areas which may show potential for mass reduction. This particular array has many unique features, such as the ability to partially or fully retract. In addition, the system is designed to be capable of operating over a wide thermal environment, since it must function from 0.3 to 6.0 AU. The natural frequency requirement acts as a further constraint. Thus, it should be obvious that reducing structure mass is not a straightforward task.

An examination of the principal components making up the array structure shows that the mast and its cannister are responsible for half of the total array structure mass. This would therefore appear to be a logical place for mass savings. Due to the lower mass of the blanket, it might be possible to resize the diameter of the mast. In doing so, it may create a situation which allows the cannister volume to be reduced, saving additional mass. There is also the distinct possibility that portions of these elements could be constructed with alternate materials which have a lower density. However, it is not possible to make quantitative projections of mass reduction without a great deal of additional information concerning the effects of these potential adjustments on the dynamic and thermal characteristics of the array.

Another major contribution to the structure mass ($\sim$25 percent) comes from the container and cover which are used to store and maintain the blanket properly during launch and re-entry. These items are basically static and therefore probably have a smaller impact on the operating characteristics of the array. Since in this exercise, the blanket volume has not been changed, it is unlikely that the container or cover can be resized. There is the possibility that lower mass materials of construction can be employed. However, the critical properties of these components, such as rigidity and strength, cannot be compromised.

In order to provide some estimate of the impact of structure mass reduction on the BOL performance of this array, a plot of array specific power as a function of structure mass is provided in Figure 1. Four blanket cases are presented, the baseline SEP design and the three models described in the preceding sections of this paper. The choice of the mass reduction range is somewhat arbitrary, and does not imply that these are reasonable limits to which the structure mass can be reduced.

CONCLUSIONS

It would appear from this analysis that the SEP array has the potential to achieve a BOL specific power of between 200 and 250 W/kg. It is likely that this would be reached by a combination of a higher performance blanket in conjunction with some modifications in array structure. The most important conclusion is that, in this case, progress in blanket development seems to offer a greater return as far as array performance improvement is concerned. Reduction to practice of the elements comprising blanket 2 would double the performance capabilities of the SEP array. There would be no realistic way to match this improvement by modifying structure. It is also apparent that if arrays capable of achieving greater than 250 W/kg at BOL are required, new concepts in array design must be developed.

REFERENCES

1. Elms, R. V. Jr.; and Young, L. E.: SEP Solar Array Technology Development. Eleventh Intersociety Energy Conversion Engineering Conference, Sept.1976.

2. Lindmayer, J.; and Wrigley, C. Y.: Ultrathin Silicon Solar Cells. Thirteenth IEEE Photovoltaic Specialists Conference, June 1978.

3. Storti, G.; Culik, J.; and Wrigley, C.: Development of a High Efficiency Thin Silicon Solar Cell. Pilot Line Report, JPL Contract No. 954883, July 1980.

4. Gay, C. F.: Thin Silicon Solar Cell Performance Characteristics. Thirteenth IEEE Photovoltaic Specialist Conference, June 1978.

5. Mesch, H. G.; and Rockey, D. E.: High Temperature, Low Mass Solar Blanket Development. Fourteenth Intersociety Energy Conversion Engineering Conference, Aug. 1979.

6. Chai, A-T.: Back Surface Reflectors For Solar Cells. Fourteenth IEEE Photovoltaic Specialists Conference, Jan. 1980.

7. Brandhorst, H.W., Jr.: Silicon Solar Cell Efficiency - Practice and Promise. Ninth IEEE Photovoltaic Specialists Conference, May 1972.

8. Iles, P.A.: Private Communication. 1979.

9. Neugroschel, A. and Lindholm, F.A.: Design of High Efficiency HLE Solar Cells for Space and Terrestrial Applications. Solar Cell High Efficiency and Radiation Damage. NASA Conference Publication 2097, June 1979.

10. Broder, J.D.; and Mazaris, G.A.: The Use of FEP Teflon in Solar Cell Cover Technology. Tenth IEEE Photovoltaic Specialists Conference, Nov. 1973.

11. Lockheed Missiles & Space Company: Sprayl'on Fluorocarbon Encapsulation for Silicon Solar Cell Arrays. Final Report, JPL Contract No. 954410, June 1977.

12. Sudbury, R.; Stirrip, K.; and Smith, D.: Aluminum Contact Deposition and Testing for Silicon Solar Cells. Seventh Photovoltaic Specialists Conference, Nov. 1968.

13. Rahilly, W.P.: Hardened Solar Cells. Seventh Photovoltaic Specialists Conference, Nov. 1968.

14. La Roche, G. J.: Ultrathin Cell Module Technology. Proceedings Second European Symposium. "Photovoltaic Generators in Space," April, 1980.

TABLE I
SILICON BLANKET 1 MASS BREAKDOWN (125 M^2 WING AREA)

ELEMENT	DESCRIPTION t(μm)	MASS (KG/M^2)	NOTES
Substrate	50 Kapton	.072	
Adhesives	25 DC 93-500	.049	Substrate & Cover
Solar Cell	62 Silicon	.115	80% Packing Factor
Cell Contacts	10 Silver	.088	
Cell Cover	50 CMS	.101	
Interconnect	25 Invar	.052	
IC Plating	20 Silver	.054	
Misc.	-------	.040	Padding, Stiffeners, etc.
TOTAL		.571	

TABLE II
SILICON BLANKET 2 MASS BREAKDOWN (125 M^2 WING AREA)

ELEMENT	DESCRIPTION t(μm)	MASS (KG/M^2)	NOTES
Substrate	50 Kapton	.072	
Adhesives	25 DC 93-500	.049	Substrate & Cover
Solar Cell	62 Silicon	.115	80% Packing Factor
Cell Contacts	5 Silver	.013	20% Back Coverage
Cell Cover	50 CMS	.101	80% Packing Factor
Interconnect	25 Aluminum	.018	
IC Plating	1 Silver	.003	
Misc.	-----	.040	Padding, Stiffeners, etc.
TOTAL		.411	

TABLE III
SILICON BLANKET 3 MASS BREAKDOWN (125 M^2 WING AREA)

ELEMENT	DESCRIPTION t(μ m)	MASS (KG/M^2)	NOTES
Substrate	25 Encapsulant	.056	Fused Silica Equivalent
Adhesives	-----	-0-	None Required
Solar Cell	50 Silicon	.093	80% Packing Factor
Cell Contacts	5 Aluminum	.003	20% Back Coverage
Cell Cover	25 Encapsulant	.056	Fused Silica Equivalent
Interconnect	12 Aluminum	.009	80% Packing Factor
I. C. Plating	1 Silver	.003	80% Packing Factor
Misc.	----	.040	Padding, Stiffeners, etc.
TOTAL		.260	
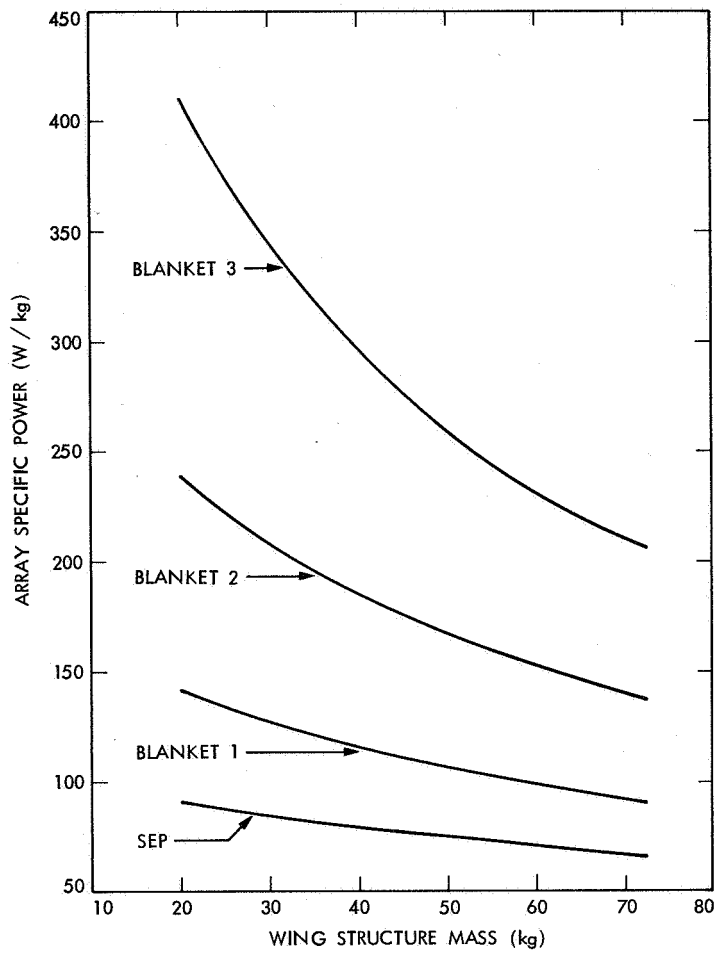
Figure 1. EFFECT OF STRUCTURAL MASS REDUCTION ON THE SPECIFIC POWER
OF THE SEP ARRAY

EFFICIENT STRUCTURES FOR GEOSYNCHRONOUS-SPACECRAFT SOLAR ARRAYS*

John M. Hedgepeth
Astro Research Corporation
Carpinteria, California

INTRODUCTION

A program is outlined to create and evaluate structural concepts for deploying and supporting lightweight solar-array blankets for geosynchronous electrical power. First, the requirements for new, more mass-efficient solar arrays is established by describing future needs. Then analytical results are set forth which show that not only must lighter weight blankets be developed but also the supporting structure must be improved proportionately.

The SEPS configuration is taken to be the state-of-the-art point of departure for improved structural concepts. Several directions for improvement are indicated.

BACKGROUND

Recent studies (ref. 1) have indicated a need for power systems of up to 20 kW for geosynchronous communication satellites and platforms. They have also established that the projected capability of the Space Transportation Systems is insufficient for launch to geosynchronous altitudes unless significant advances are made in the mass efficiency of the several spacecraft subsystems. One of these subsystems, of course, is the solar-cell array which, in current communication satellites, occupies about 6 percent of the total spacecraft mass. In order to maintain this percentage as the power load is increased, the solar array must become much more mass efficient than those at present; need exists for efficiencies of 60 W/kg (all power levels quoted herein are beginning-of-life values) by 1985 and 200 W/kg by 1990.

In contrast to many other missions, the commercial satellite communication business is already well established. Revenues for private-line traffic reached two billion dollars in 1978 (ref. 2). Continued steady growth is expected, the growth being filled by a proliferation of small ground stations and by a continued reduction in the cost of service. Thus by the end of the century, the predictions are that the annual volume of purchases of spacecraft power systems will be several billions of dollars according to reference 1. If this potential market is going to be serviced from the United States, it is necessary to be

able to build solar arrays in the 5- to 50-kW range at a reasonable cost and to deliver 200 W/kg or better.

An array effectiveness of 200 W/kg is three times better than that of the Solar Electric Propulsion System (SEPS) array. Development of this array has proceeded far enough to enable it to represent the present hardware state-of-the-art. The factor of three, therefore, is the gain that needs to be achieved during the next decade.

The SEPS array delivers about 100 W/m^2 of blanket area (including spaces) (see ref. 3). The blanket weighs about 1 kg/m^2 and the supporting structure about one-half this much. Research programs for better arrays over the past few years have quite properly concentrated on the blanket. Not only is it the heaviest part of the system, but it is also the most costly. In addition, array performance is expected to be significantly enhanced by an increase in power density delivered by higher efficiency solar cells.

The push toward better blankets is being led by JPL in the United States and by AEG Telefunken in Europe. Progress to date is typified by the 50-μm-thick silicon solar cell with 14-percent efficiency. This cell was used by General Electric (GE) in their study aimed at 200 W/kg solar arrays. Their blanket delivers about 140 W/m^2 and weighs about 0.4 kg/m^2 (ref. 3). They mount the blanket on a structure that weighs about 0.25 kg/m^2. This design, of course, meets the 1990 requirements. Unfortunately, it is a "paper" design only. Furthermore, the radiation shielding of the solar cells has been deemed to be inadequate for long-time geosynchronous operation.

Work continues on the improvement of solar-cell blankets. For example, TRW has demonstrated a flight-production-capable blanket utilizing the 50-μm cells and including cover glasses with a weight of 0.55 kg/m^2 (ref. 4). Other studies indicate that silicon-cell blankets weighing as little as 0.25 kg/m^2 may exhibit good power efficiency and sufficient resistance to radiation degradation. Gallium arsenide is touted by many as being the material of the future, especially for arrays with concentrating reflectors. And basic research is being directed to more exotic approaches such as multibandgap cells for increased efficiency (see presentation by J. Mullin in ref. 2).

The time has come to improve the structural configurations that will support these blankets. If very lightweight blankets are a realistic expectation, then we should also have very lightweight supporting structures. Otherwise the performance gain from a better blanket will be vitiated by an overly heavy structure.

The influence of structural mass on the array performance is shown in figure 1. Here the ordinate is the ratio of array specific power to the blanket specific power and the abcissa is the ratio of the structural mass to the blanket mass. For mass ratios around one-half (values appropriate to the SEPS and GE rollout array designs) the specific power is around 65 percent of its blanket-only value. On the other hand, if the mass ratio were around one (FRUSA) or two (Hermes array), the resulting specific power would be only 50 percent or 35 percent, respectively, of the blanket-only value.

The consequence of simply substituting lighter blankets on unimproved structures is seen in figure 2. Here the structure-blanket mass ratio is plotted versus the array natural frequency. The curves are based on the parametric results reported in reference 3 for the SEPS fold-out and GE rollout arrays. Those curves labeled $m_{B\ell}$ = 0.940 kg/m^2 and 0.386 kg/m^2 for SEPS and GE respectively, come directly from Pages E-19 and E-144 of reference 3. The masses for the 200 W/kg array have been reduced by excluding the slip ring mass of 3.5 kg which is considered not to be part of the array. Note that the two examples have almost the same blanket area and wing length (~100 m^2 and ~25 m) so that the results are comparable from a structural point of view.

If a lighter blanket is mounted on the same structure, the effect will be to increase the structure-blanket mass ratio and to increase the natural vibration frequency. In figure 2, the frequency values are estimated by assuming that the frequency is proportional to the inverse square root of the blanket mass density. This relationship is particularly valid for situations in which the blanket comprises most of the sprung mass, as is the case for the present examples.

The curves show that decreasing the blanket weight causes a large increase in structure-blanket mass ratio without increasing the natural frequency nearly enough to compensate. The SEPS structure can be termed to be a good one for a blanket density of 0.940 kg/m^2. On the other hand, it is poor if the blanket density is reduced to 0.386 kg/m^2, for which the GE array is designed. It is unacceptable, even for low frequencies, for blankets with the smaller density of 0.250 kg/m^2. The GE array exhibits low structural mass with its design blanket but becomes marginal with a 0.250 kg/m^2 blanket, especially at the higher frequencies. Note that the terms "good," "poor," and "unacceptable" correspond to array-to-blanket efficiency ratios of about 65, 50, and 40 percent, respectively.

Comparison between the two designs should be made with care. The SEPS array, for example, is retractable with some attendant weight penalty. More importantly, the SEPS design has been proven through the engineering model stage and is currently being qualified for Shuttle flight, whereas the GE design is unproven. Nevertheless, the latter design should be more efficient inasmuch as it makes use of the blanket itself as part of its bending stiffness. If this approach can indeed be made to work, the factor of two advantage over the SEPS structure shown on figure 2 would be real.

JUSTIFICATION OF RESEARCH

Further work on advanced very lightweight structural configurations is needed because of the following reasons:

- The SEPS design is unsuitable for light blankets.

- The GE design is marginal for 0.250 kg/m^2 blankets for the higher frequencies.

- Alternative structural arrangements should be investigated.

The last of these reasons is probably the most important. Both present designs support the blanket only at its ends and depend on tension stiffening to control the blanket position. During the last few years, work on space structures has been directed to other arrangements. For example, the use of a truss type of structure proved highly successful as a deployer and support for the synthetic-aperture-radar antenna on Seasat. This structure, shown in figure 3, was designed and built by Astro to meet demanding accuracy requirements. The Europeans have taken a different route in their ULW array design, choosing to simplify packaging and deployment by foregoing a deep structure. These and other configurations should be evaluated for application to the efficient support of very lightweight blankets. The point must be made that the aforementioned multibillion dollar market for solar power systems will involve a large variety of vehicles and missions including dedicated spacecraft and multiuse platforms. The successful array design is the one which will be able to meet the variety of requirements posed by that diverse marketplace.

DESIGN REQUIREMENTS

Since 1977, we have been examining the requirements that govern the design of large space structures. This work is now in the process of being reported to the technical community (see refs. 5 through 10). The work takes full cognizance of the practical problems that must be solved in order to fabricate good flight hardware at a reasonable cost, as described generally in reference 6. For the critical requirements for the present application, the following comments are made.

Design and Fabrication Phase

The solar blanket is an expensive and fragile component. The design and fabrication processes must recognize this by maximizing the modularity and replaceability of the blanket components. The blanket components must be assembled to the structure as late in the fabrication process as possible so as to minimize the amount of handling of these items. In particular, no critical adjustment or bonding procedures should be allowed during or after blanket assembly to the structure.

Full cognizance must be paid to the provisions for the necessary harnesses and instrumentation.

Ground-Test Phase

The array is destined for deployment in geosynchronous orbit. The cost of assuring that this deployment can be done reliably will be reduced greatly if full ground deployment and test is possible without overelaborate gravity compensation fixtures. Reasonable toughness and detail strength is therefore required.

Launch Phase

During launch the main concern is to protect the blanket from damage. Experience has shown that ordinary care in packaging will avoid damage to the structure itself or its actuating mechanisms. The amount of care required for the blanket will depend greatly on its design. The difficulties with cover cracking reported in reference 4 should be noted.

During interorbit transportation the spacecraft will require power. The structural arrangement that allows this power to be supplied without auxiliary units is at an advantage.

Deployment Phase

All steps in the deployment should be fully controlled and capable of being stopped and restarted on command. The deployment rate should be slow enough so that dynamic loadings are inconsequential. Remote repackaging is specifically not a requirement for this application. On the other hand, any degree of automated packaging can be a great convenience in ground testing.

Operational Phase

Loads - During operation, the externally applied loads are small. In fact, figure 4 shows that at GEO the largest environmental load is solar pressure.

Loads induced by altitude controls should also be small. The loads due to station keeping and relocation may be important and should be evaluated.

Larger than any of the above will probably be the internal loads that are required for tension stiffening and pretensioning. These loads are, of course, dependent on the particular configuration chosen. They should be treated as the primary loads to which the structure is designed.

Stiffness - The stiffness required of the structure is a primary condition for the design. It can be characterized by the natural vibration frequencies allowable.

Present large arrays are designed for fairly low frequencies. The relatively small FRUSA array has a flight-measured lowest frequency of 0.25 Hz, and the Hermes array of 0.13 Hz. The larger SEPS and GE arrays are designed for about 0.5 Hz.

The allowable natural vibration frequency is usually chosen as a result of a complex and not completely rational process involving the interaction with the control system design and the desire to minimize residual vibrations due to transient events, such as solar eclipse. For ordinary geosynchronous applications with a usual amount of damping, values around 0.05 Hz are adequate. However, in cases in which very tight pointing accuracy is required or in which vibrational disturbance must be minimized, frequencies of 1 Hz or more are

367

required. This topic is discussed in reference 11, which implies that antennas with very tight beams must be very stiff. If the arrays are not similarly stiff then they must be isolated from each antenna in some, possible expensive, manner. The conclusion is that the application of an array design to a large variety of spacecraft and platform missions would be considerably enhanced if it can deliver a high natural frequency with an attractive weight. Even if high-frequency requirements are irrational, meeting them may be necessary to capture the market. "The customer is always right."

Dimensional Accuracy – The unconcentrated solar-cell array places very modest demands on surface accuracy. Those demands should therefore present only secondary design requirements. Much more important are the internally generated problems. One of these is the spacecraft disturbance that would arise if large distortions occur in the array in passage from sunlight to shadow back to sunlight. These must be minimized. If the structure is designed to provide high stiffness, then these disturbances will be acceptable.

A more basic requirement is that the stiffness of the structure itself must be maintained. If axial-load-carrying members are permitted to curve, then their axial stiffness is reduced. This effect is of particular concern for the slender members composing very lightweight trusses. Also, those elements that are pretensioned must retain their pretension if full stiffness is to be maintained. The same is true of tension-stiffened portions. Inaccuracies in the internal preloading of the structure arises from the errors in fabricating the detail parts from which the structure is assembled. They are worsened by thermal strain, particularly if the structure is composed of materials with widely varying expansion coefficients. Keeping these errors within acceptable limits is a primary requirement for some configurations.

STRUCTURAL CONFIGURATIONS

State of the Art

The structural configurations for deployable arrays fall into two main groups: hinged panels which fold out like an accordion, and flexible blankets which are unrolled or unfolded by one or two separate extendible booms. The first group has so far been the configuration of choice for flight hardware. The FRUSA and Hermes arrays are the only flying representatives of the second group, and both of these flight programs were intended primarily for technology development. The upcoming Shuttle flight of the SEPS array is again technologically, rather than operationally oriented. The first operational use of a flexible-blanket array will be on the Space Telescope vehicle. This, incidentally, is the only such example currently under flight-hardware development. The accordion-folded panel arrays dominate the flight field.

Nevertheless, the flexible blanket approach must eventually prevail if lightweight arrays are to be flown. Of the accordion-folded arrays, only the ULW approach is lightweight; and it is actually a hybrid, utilizing flexible-blanket panels.

Supporting a flexible blanket is a straightforward task. Tension is applied to the edges of the panel which behaves structurally as a membrane. External structure is required to apply the tension and to position the edges properly.

Of course, there are a myriad of detailed problems encountered in an actual design. The SEPS array is an outstanding example of a successful solution to the problems. The structure is light enough for the purpose and is considered to work reliably. All expectations are that the Shuttle flight experiment will uncover only the normal small deficiencies that plague first-article flight programs.

The SEPS structure can be considered to be a sound point of departure for the creation of lighter weight structures. Various directions of improvement are outlined below.

Design Improvements

Partition the Blanket – The amount of tension necessary to stiffen the blanket to the desired amount is inversely proportional to the square of the blanket length. If the blanket were divided into small sections, the tension can be reduced to a very small value. This would essentially eliminate the reduction in bending stiffness caused by the tension. Note, however, that the contribution of the tension to the torsional stiffness would be lost. The boom must supply all that is needed.

Deepen the Structure – In order to increase the stiffness and to reduce the weight, the structure must be deepened. The GE array design goes in this direction. It is limited by the amount that the blankets can be tilted from perpendicularity with the sun's rays.

The structural depth of current designs is limited basically by the deployment devices chosen. Larger boom diameters require much longer and heavier canisters or deployers. One way to increase the depth economically would therefore be to eliminate the deployer and allow the boom to deploy itself. This would have the additional benefit of eliminating the canister weight, only part of which would be used to furnish the mechanisms needed to haul the blanket out on the fully deployed boom. Note that all Astromasts currently flying are of the self-deploying type.

The other approach to deepening the structure is to shift to a different type of structure entirely. For example, the Extendible Support Structure that served so admirably on Seasat can be modified to be suitable for supporting blanket panels. This structure can be made up of any number of bays, each one of which could support a panel of blanket which would be accordion pleated for packaging. Thus the advantages of blanket partitioning could also be realized.

A more advanced concept could be based on the modular column research that Astro has been conducting for the Large Space Structures program. The externally stiffened column described in references 5 and 12 and shown in

figure 5 can be converted to a boom in which the only compression-carrying (and thus heavy) elements are the central boom (an Astromast) and the spokes. The boom could be a slender Astromast which would have the sole purpose of supplying the pretension to the external truss structure. Here again, interfacing with the blanket at a number of locations along the length would be possible.

Change the Planform – Flexible-blanket arrays are arranged as high-aspect-ratio wings. Many fold-out panel arrays, on the other hand, utilize the advantages of lower aspect ratio. The FRUSA geometry goes part way in this direction by attaching to each wing at its center, cutting its structural length in half, and multiplying the bending frequency by four. More efficiency is possible by further decrease in the aspect ratio at the expense of increased complexity. One interesting possibility would be to use the tetrahedral-truss type of structure. A modular version, which would require extensive modification to adapt to the present application, is described in reference 3.

PROGRAM DESCRIPTION

Various structural concepts should be created and examined with the aim being to provide stiffness with low weight while observing the necessary practical requirements of integrating with operational spacecraft. The study should consist of three parts.

I.   Concept Generation

Array concepts should be generated that meet the following requirements:

1.   Package, protect, deploy, and support fragile solar-cell blankets

2.   Integrate with a variety of spacecraft and missions

3.   Operation at geosynchronous orbit

4.   Shuttle launch

5.   Make extensive use of modularity

6.   Capable of being built with a range of sizes with minimum redesign

7.   Be ground testable

II.   Concept Evaluation

Parametric analyses should be conducted on the above concepts. The outputs would be the structural geometry and weight required to support arrays with the following characteristics:

1.   Array areas from 50 to 200 m^2/wing

2.   Blanket densities of 0.4 kg/m^2 and 0.25 kg/m^2

3.   Cantilever natural vibration frequencies of 0.05 to 1 Hz

370

III. Point Design

One concept shall be selected for point design. For a single size, blanket density, and vibration frequency, the array geometry will be determined with enough detail to exhibit the concept's workability. Those parts of the structure that are critical would be defined and their operation demonstrated by analysis or models as appropriate.

REFERENCES

1. Power Technology for Future Synchronous Satellites and Platforms. Space Systems and Technology Advisory Committee. NASA Advisory Council. Minutes of Meeting, 2 and 3 May 1979.

2. Power Technology for Future Synchronous Satellites and Platforms. Space Systems and Technology Advisory Committee. NASA Advisory Council. Minutes of Meeting, 13 and 14 December 1978.

3. Garba, J.A., et al: Parametric Study of Two Planar High Power Flexible Solar Array Concepts. JPL Publication 78-95, 15 December 1978.

4. Mesch, H.G.: Final Report on High-Temperature Low-Mass Solar Blanket. TRW Publication under JPL Contract No. 955139, August 1979.

5. Hedgepeth, J.M.: Required Strength and Stiffness of Large Space Structures. ARC-TN-1050, Astro Research Corporation, 28 October 1977.

6. Hedgepeth, J.M.; Mikulas, M.M.; and MacNeal, R.H.: Practical Design of Low-Cost Large Space Structures. Astronautics & Aeronautics. vol. 16, no. 10, October 1978, pp. 30-34.

7. Hedgepeth, J.M.: Requirements for the Structural Design of Large Antenna Reflectors. Oral Presentation to NASA Langley Research Center, 2 November 1979.

8. Hedgepeth, J.M.; and Miller, R.R.: Effects of Member-Length Imperfections on the Deformations and Loads in an Isogrid-Truss Structure. ARC-R-1012, Astro Research Corporation, 1 April 1980.

9. Hedgepeth, J.M.: Influence of Fabrication Tolerances on the Surface Accuracy of Large Antenna Structures. ARC-R-1013, Astro Research Corporation, 22 April 1980.

10. Hedgepeth, J.M.; Knapp, K.; and Finley, L.A.: Structural Design of Free-Flying Solar-Reflecting Satellites. SAWE Paper No. 1303; Presented to the 38th Annual Conference of the Society of Allied Weight Engineers, Inc., New York, 7-9 May 1979.

11. Fager, J.A.: Large Space Erectable Antenna Stiffness Requirements. J. Spacecraft, vol. 17, no. 2, Article No. 78-590R, March-April 1980.

12. Knapp, K.: Study and Fabrication of a Tension-Wire-Stiffened Column "Expandable Truss Column." ARC-TN-1060, Astro Research Corporation, 25 April 1978.
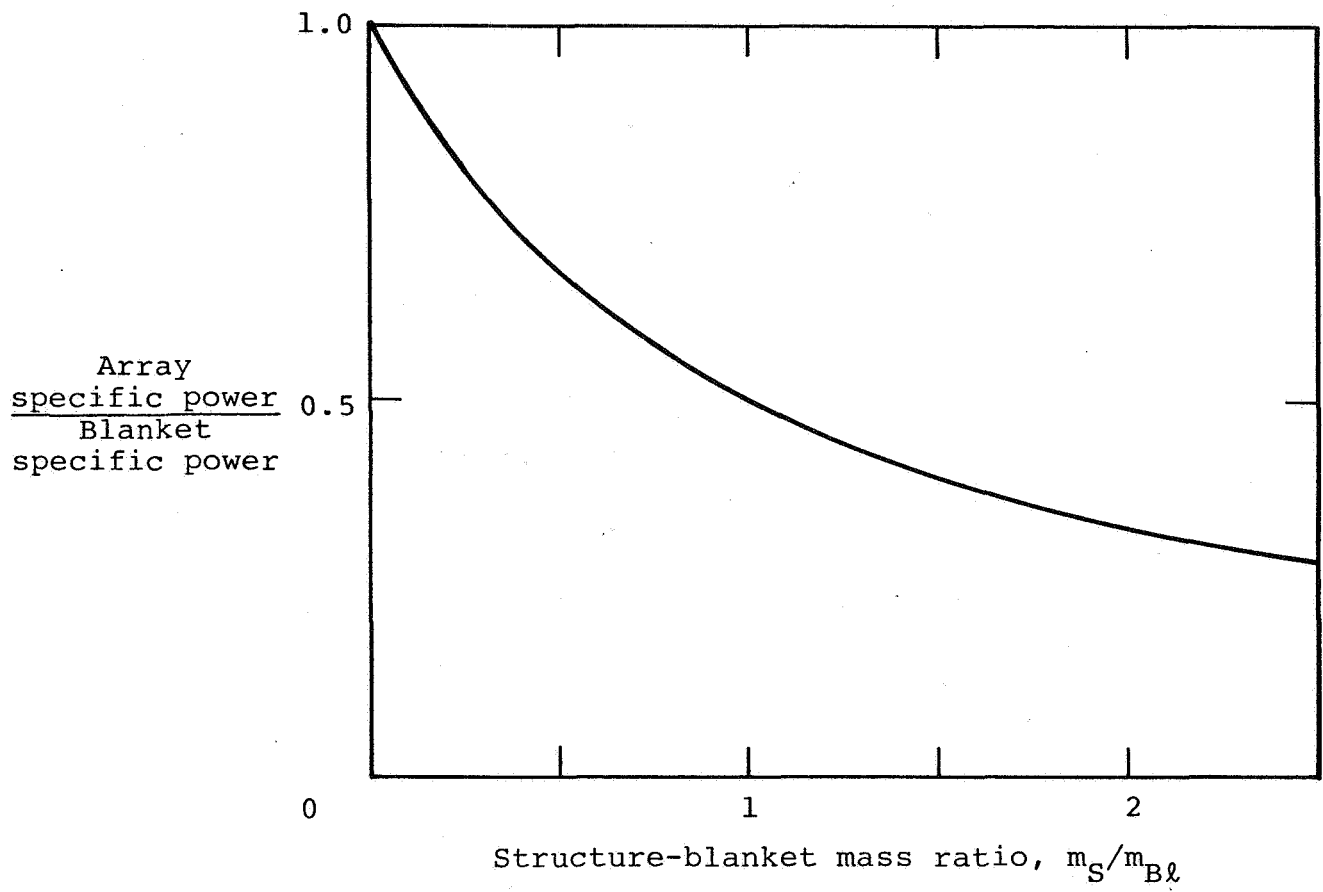
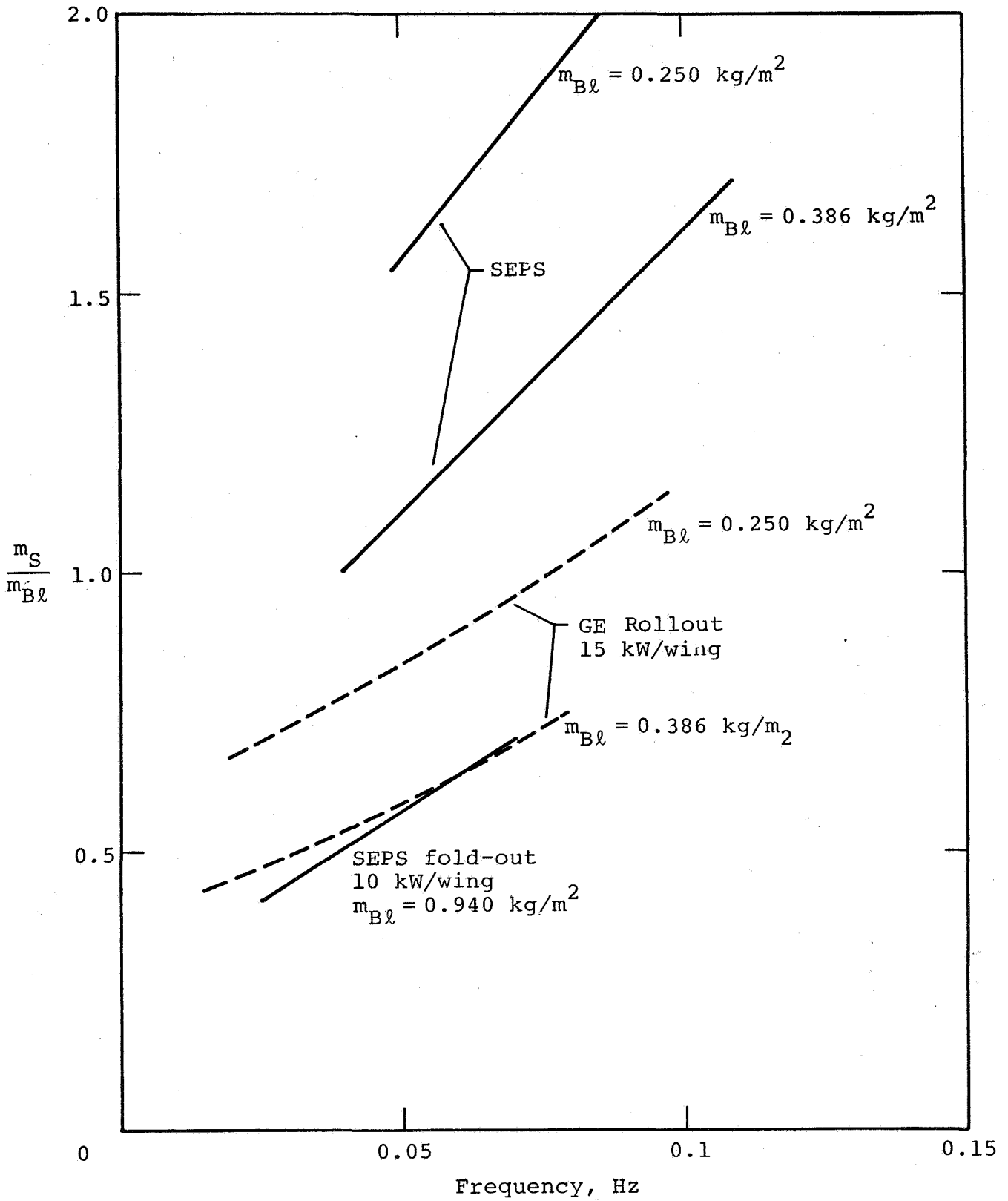Figure 1. Effect of structural mass on array specific power.

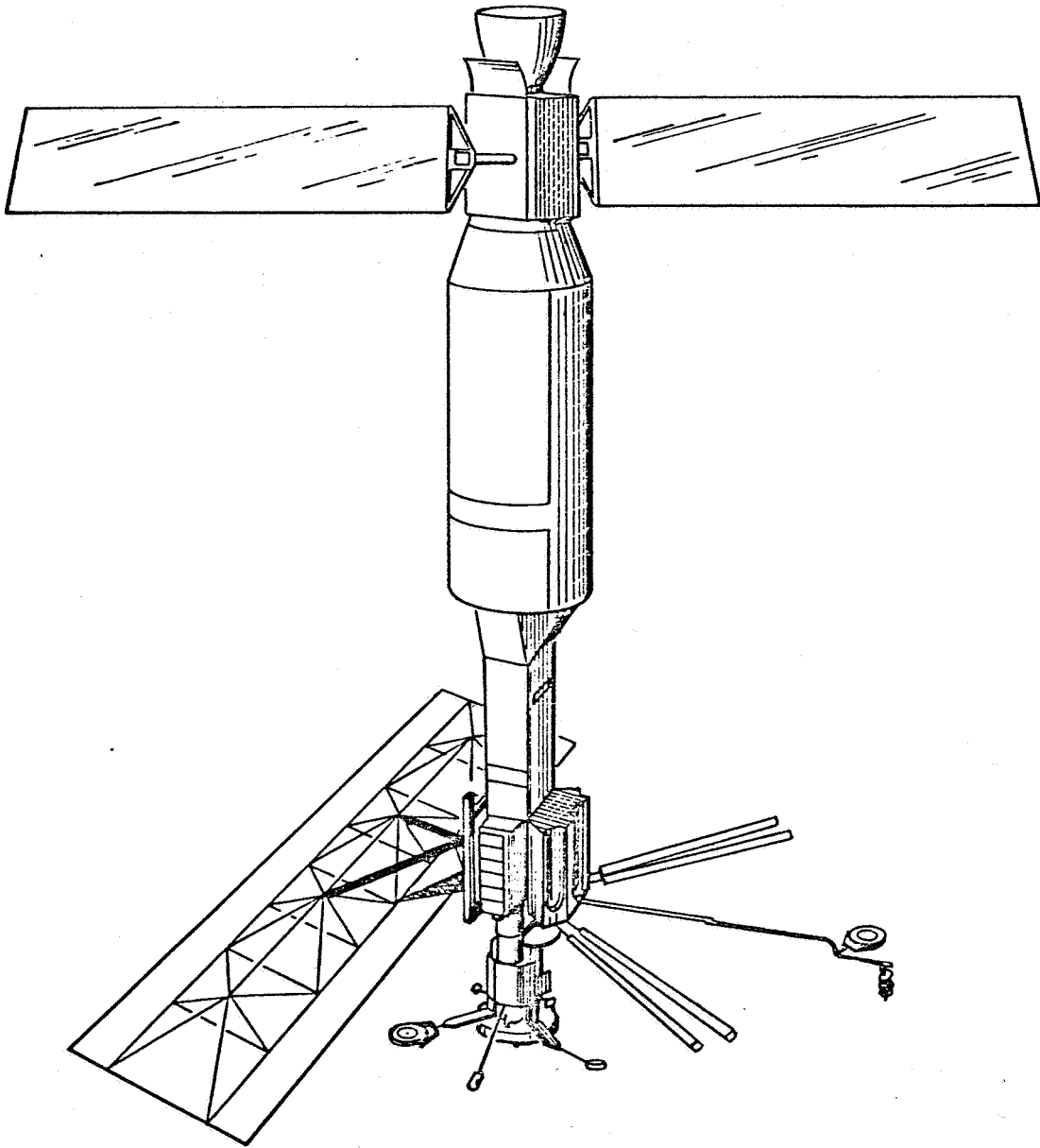Figure 2. Structural-blanket mass ratio.

Figure 3.   Extendible Support Structure for Seasat
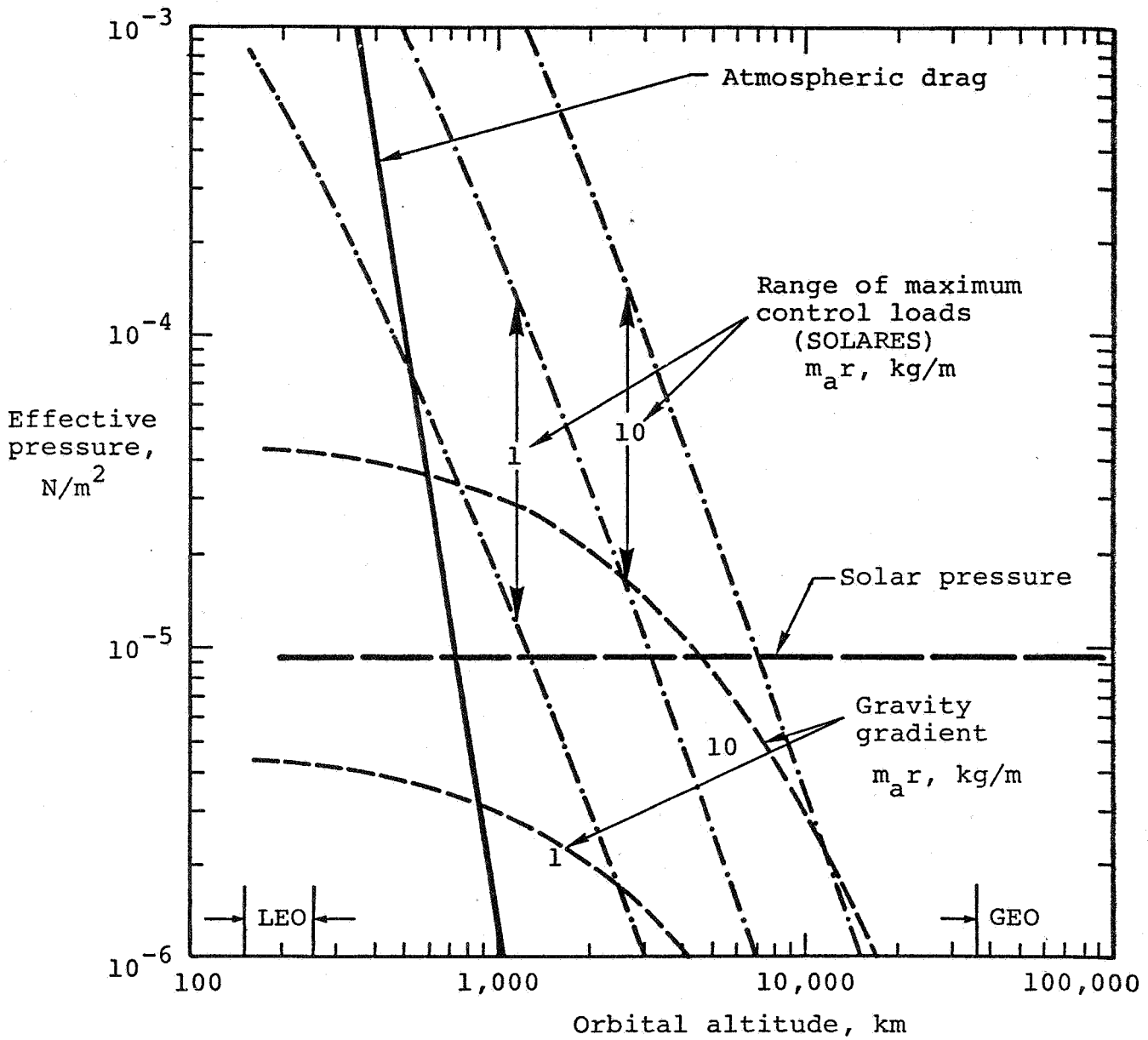synthetic aperture radar antenna.

375

Figure 4. Maximum lateral loads on reflecting
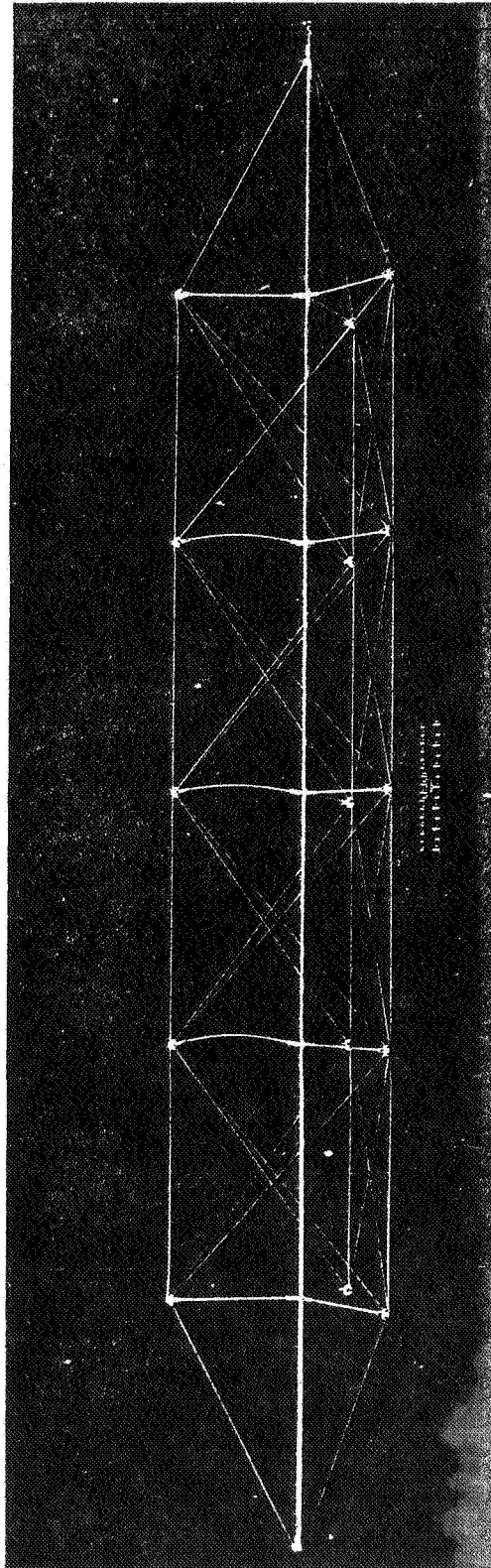films at different orbital altitudes.

376

Figure 5. Expandable truss column.

THE HEWAC PILOT LINE EXPERIENCE

M. Gillanders and R. Opjorden
Spectrolab, Inc.
Sylmar, California

INTRODUCTION

High Efficiency Wraparound Contact Solar Cells (HEWACS) are advanced silicon solar cells with both electrical contacts on the back side of the cell. Figure 1 shows a sketch of this device, which utilizes a screen-printed dielectric insulation layer to isolate the "N" and "P" contacts from each other. The NASA-Lewis Research Center is supporting the development work of this cell under Contract NAS3-21270 (and previously on NAS3-20065). The specific goals of this program are to develop a device exhibiting high AMO conversion efficiencies, and to mature and formalize the processing of such cells to a point where cell fabrication can be carried out by production personnel under operating production line conditions. Pilot production will then manufacture and deliver 1000 acceptable cells (minimum cell performance 13½%, minimum lot average 14%, AMO @ 25°C).

BACKGROUND

The flow chart in Figure 2 shows the baseline process sequence developed under NAS3-20065, and the process modifications made under the current program, NAS3-21270. The cells produced under NAS3-21270 measure 2 x 4 x 0.02 cm, feature a polished or planar front surface with dual AR coating, chromium-palladium-silver contact system and an aluminum back surface field in addition to the wraparound contacts and silica-seal dielectric insulator. A back surface reflector is not utilized. Material used is "P" type, boron doped, 7-14 ohm-cm, CZ silicon with (100) crystal orientation.

Laboratory experiments designed to optimize cell performance and cell processing have resulted in a device with high electrical performance. Some average performance data for these cells are as follows: Open-circuit voltage 620 mV, short-circuit current 340 mA, maximum power 159.8 mW, curve fill factor 0.752, efficiency (η) 14.8% and lot yielded approximately 65% (test data @ AMO, 25°C).

In addition to electrical tests, many screening tests have been performed on these devices. These include temperature cycling (100 cycles, -170°C to +75°C), tape peel tests, soldered tab pull tests and humidity testing. Although limited in nature, these tests do provide some idea as to the reliability of the cells. The devices tested were within contract requirements for all of the tests performed.

For more information about laboratory experiments, electrical performance, and screening tests, see "High Efficiency Wraparound Contact Solar Cells (HEWACS)", 14th IEEE Photovoltaic Specialists Conference - 1980 Proceedings.

Prior to the initiation of pilot production, a number of items had to be completed. First was the preparation of production-suitable software and quality control elements. The pilot line for this program is to be carried out by production personnel under operating production line conditions, therefore it is necessary to implement a complete software file. This means that an MCD (Manufacturing Control Document) had to be prepared, listing all of the process steps and Q.C. Inspection stages. Procedures had to be written and approved for each of the process steps and Engineering Line Instructions (ELI's) developed.

In addition, the need for a reconfigured back contact system was identified. An alternate back contact configuration is required for the HEWACS cell to make the device more suitable for some panel manufacturers' designs. Although the baseline wraparound design does simplify cell interconnecting compared to standard space cells, a back contact configuration utilizing the centerline of the cell for both N and P contacts would simplify cell interconnecting even further for some panel manufacturers. A sketch of the reconfigured contact that has been designed is shown in Figure 3.

RECONFIGURED BACK CONTACT

Approach

The approach used in the development of the reconfigured back contact HEWACS cell was as follows:

First the design and procurement of new tooling was necessary. This tooling included screens to be used in the dielectric print-on step, masks for the contact evaporation step, and a new electrical test fixture. Secondly, test lots were made and evaluated until a satisfactroy process was achieved. And finally, the pilot production software was revised to reflect the alternate back contact cell. It was decided to amend the program requirements for the contract and make the 1000 deliverable devices include 500 baseline type cells, and 500 alternate back contact cells. All electrical performance requirements and acceptance test requirements would be the same for both cell types.

Problems/Solutions

Problems, not common to those of the baseline cell design, were encountered and resolved with the reconfigured back contact. In the initial experiments, the same size (mesh) screens were used to print the dielectric insulation onto the ABC (alternate back contact) cells as were used on the

baseline cells. This caused what proved to be the major stumbling block in the development of this cell type. By comparing the sketches of the two cell designs in Figures 1 and 3, it is obvious that the ABC cell (Figure 3) has much more of its back surface area covered with insulation material than does the baseline device. The additional insulation caused unacceptable bowing of the cells when the insulation layer was fired.

Several experiments were conducted employing different combinations of screen types and mesh sizes. Some cells were processed using a single layer of insulation, instead of the standard double-layer method used on the baseline cell. (Double-layer insulation minimizes the chances of pinholes which could lead to shunting of the cells.) Others were processed using double-layer insulation, but with finer mesh screens. The combination which was found to be acceptable from all aspects was the use of a fine mesh screen for the initial print-on step, followed by a standard mesh screen for the second print-on step. The single layer experiment failed because of shunting due to pinholes. The double-layer, fine mesh screen experiment failed because an inadequate amount of insulation was being applied to the wraparound edge of the cell, and the edges of the silicon were protruding from beneath the insulation layer, therefore causing shunting and poor cell performance.

Results

The flow chart in Figure 4 shows the process sequence used in the manufacturing of the baseline cell type. To the right, opposite its respective process step, are listed the changes required to make a HEWACS cell utilizing the alternate back contact. It is apparent that the ABC cell types can be made using the same process as the baseline cell, with a minimum of changes.

Electrical Performance

Since only a few process changes had to be made to produce the alternate back contact cell, it would seem logical that the electrical characteristics of the device would also remain very similar to the baseline cell type. This was found to be the case. Figure 5 shows a cell performance comparison of the baseline cell and the reconfigured contact cell. Note that both cell types in this comparison have only a single-layer antireflection coating, which explains the low short-circuit current (I_{sc}) and I_{mp} values. Also note that the reconfigured contact cells were tested at 28°C instead of 25°C. Therefore, they have lower open-circuit voltage (V_{oc}) and V_{mp} values than the baseline cell type. Otherwise, the two cell types are very similar to each other.

ADDITIONAL EXPERIMENTS

One of the contract requirements on the HEWACS device is that the cell utilizes a back surface reflector (BSR). However, during the development

stages it was determined that a BSR would be impractical for this cell. First, the high temperature used to fire the dielectric insulation was too close to the aluminum-silicon eutectic temperature (577°C) and it was thought that the BSR on these cells would be rendered useless by the dielectric firing step. Secondly, through experimentation it was shown that in order to maximize adherence of the dielectric insulation to the back of the cell, the residual aluminum (post back surface field (BSF) formation) should remain on the device. It is standard procedure to use boiling HCl to remove the residual aluminum after BSF formation, and evaporate an aluminum BSR directly onto the aluminum-silicon regrowth layers. An advantage of leaving the residual aluminum on the back of the cell is that it acts as a back contact.

In order to further investigate the effects of residual aluminum on the device, additional experimentation was carried out under Spectrolab R&D. Conventional contact 2 x 2 cm cells with screen-printed back surface fields were fabricated with and without the residual aluminum left on the cell. Absorptance data are indicated below:

Cell Type	α
Residual Aluminum + Heat Treatment	.720
Residual Aluminum	.761
Evaporated BSR	.785

As can be seen, the cell group with the residual aluminum and the heat treatment had a significantly lower absorptance than the other cell types. Also of great interest was that this group had the highest value of open circuit voltage.

PILOT PRODUCTION

Start

With the completion of development of the reconfigured back contact cell, proofing of the evaporation tooling and finalization of the production software, the Pilot Line is at present under way. The material to be used has been grown, slabbed, and sliced into approximately 1150 wafers, 1.70" x 1.70" x 0.14" thick. (During processing, each wafer will be diced into two 2 x 4 cm cells, thereby providing for a maximum of 2300 cells.) These wafers were divided into 12 lots of 96 wafers each (one lot has only 94 wafers). Six of these lots will be used to make the baseline cells, and the other six lots for the alternate back contact type cell. All twelve lots went through the 30% NaOH etch, 3-1-2 polishing etch and phosphine diffusion. At this point a trial run was initiated before the actual pilot line. Two lots (one for each cell type) were run through the manufacturing process by production line personnel. This was done in an effort to determine what problems, if any, would be encountered by switching the process from the laboratory to the production line.

These two lots did run into some difficulty. Besides a few small problems which only required some minor adjustments to remedy, one large problem was ultimately responsible for the loss of both lots. Shortly before the start of the pilot production, OSHA banned the use of one of the solvents widely used at Spectrolab to clean cells. A substitute solvent was incorporated into the production process after it was found suitable for cleaning conventional cells. This new solvent simply replaced the old one in the already established cleaning sequence. Although this cleaning procedure with the new solvent worked satisfactorily on standard space cells, it failed on the HEWACS devices. The cleaning procedure and solvent used was not designed for cells that had a dielectric insulation layer screen printed onto the cell. The surfaces onto which the insulation layer was printed were not adequately prepared to allow for good adhesion between substrate and insulation. Therefore, when tape peel tests were run on these cells they exhibited excessive peeling of the dielectric insulation from the substrate.

New Cleaning Procedure

Experiments were then conducted in an attempt to develop a new solvent and/or cleaning procedure. Many combinations of solvents and procedures were tried. It was found that the most successful combination tried involved the use of the same solvent Production was using, but the cleaning procedure had to be changed. The software was then changed and the formal pilot line started.

Current Status

The pilot production is currently in progress. The ten lots of cells have been processed through the screen-printed aluminum back surface field (BSF) step and are now in the cell dice step. All ten lots should be completed by the end of October.
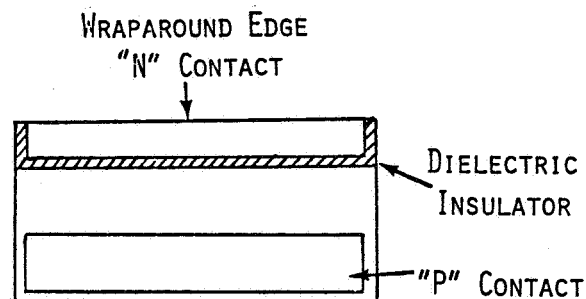
FIGURE 1

SKETCH SHOWING BACK CONTACT CONFIGURATION
OF BASELINE HEWACS CELL

```
BASELINE PROCESS SEQUENCE          PROCESS CHANGES
Developed under NAS3-20065         under NAS3-21270

┌─────────────────────────┐
│   SURFACE PREPARATION    │    <    Planar Front Surface
│      30% NaOH ETCH       │
│  2% NaOH TEXTURING ETCH  │
└─────────────────────────┘
            │
            ▼
┌─────────────────────────┐
│    JUNCTION FORMATION    │
│    PHOSPHINE DIFFUSE     │
└─────────────────────────┘
            │
            ▼
┌─────────────────────────┐
│    BACK SURFACE FIELD    │    <    Lower Firing
│    PRINT & FIRE Al PASTE │         Temperature
└─────────────────────────┘
            │
            ▼
┌─────────────────────────┐
│      SHAPE WAFER         │
│     SECTION WAFER        │
└─────────────────────────┘
            │
            ▼
┌─────────────────────────┐
│  WRAPAROUND DIELECTRIC   │    <    Change Mesh Orientation
│ PRINT, FIRE, PRINT AND FIRE │
│     DIELECTRIC PASTE     │    <    Lower Firing Temperature
└─────────────────────────┘
            │
            ▼
┌─────────────────────────┐
│      METALLIZATION       │    <    Change Cell-to-Source
│   EVAPORATE FRONT GRID   │         Angle
│  PATTERN, WRAPAROUND AND │
│    BACK CONTACT PADS     │
└─────────────────────────┘
            │
            ▼
┌─────────────────────────┐
│       AR COATING         │    <    Dual AR Coating
│   EVAPORATE $Ta_2O_5$    │
└─────────────────────────┘
            │
            ▼
┌─────────────────────────┐
│          TEST           │
└─────────────────────────┘
```

Figure 2. FLOW CHART SHOWING BACK CONTACT CONFIGURATION
OF BASELINE HEWACS CELL

WRAPAROUND EDGE
"N" CONTACT
↓

DIELECTRIC
INSULATOR

"P" CONTACT

FIGURE 3

SKETCH SHOWING BACK CONTACT CONFIGURATION
OF ALTERNATE BACK CONTACT HEWACS CELL

HEWACS
BASELINE PROCESS
SEQUENCE

BASELINE PROCESS
CHANGES REQUIRED
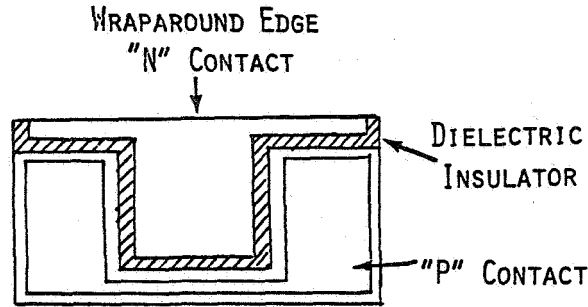FOR ALTERNATE BACK
CONTACT HEWACS CELLS

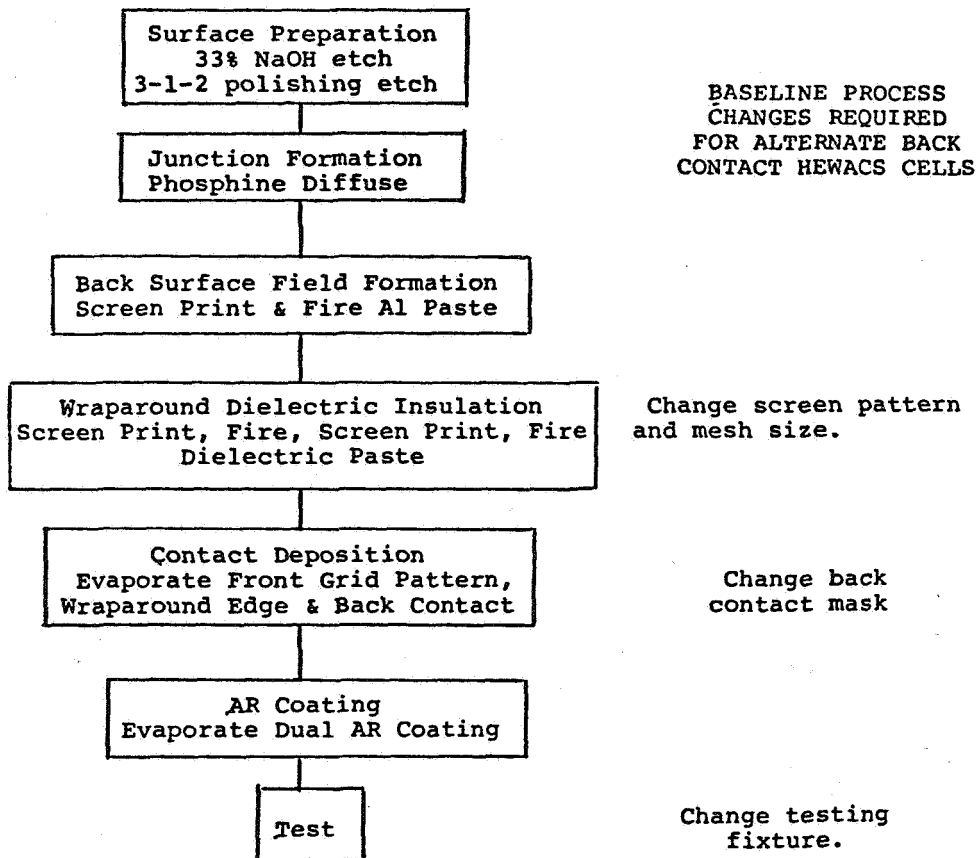|	
Surface Preparation 33% NaOH etch 3-1-2 polishing etch	
Junction Formation Phosphine Diffuse	
Back Surface Field Formation Screen Print & Fire Al Paste	
Wraparound Dielectric Insulation Screen Print, Fire, Screen Print, Fire Dielectric Paste	Change screen pattern and mesh size.
Contact Deposition Evaporate Front Grid Pattern, Wraparound Edge & Back Contact	Change back contact mask
AR Coating Evaporate Dual AR Coating	
Test	Change testing fixture.

FIGURE 4

FLOW CHART AT LEFT SHOWS BASELINE PROCESS SEQUENCE
USED TO MAKE THE HEWACS BASELINE CELL. PROCESS
CHANGES REQUIRED TO MAKE THESE CELLS WITH THE
RECONFIGURED BACK CONTACT ARE LISTED TO THE RIGHT,
OPPOSITE EACH RESPECTIVE PROCESS STEP.

385

	V_{oc} mV	I_{sc} mA	V_{mp} mV	I_{mp} mA	P_{max} mW	EFF %	CFF –	Yield %
BASELINE HEWACS CELL @ 25°C (Average based on 4 cell lots)	623	326	514	302	155.2	14.3	0.764	71
RECONFIGURED CONTACT HEWACS CELL @ 28°C (Average based on 2 cell lots)	612	324	504	302	152.3	14.0	0.767	70

*Both cell types have single-layer AR Coating

Figure 5

CELL PERFORMANCE COMPARISON BETWEEN BASELINE CELL AND ALTERNATE BACK CONTACT CELL

DESIGN REQUIREMENTS FOR HIGH-EFFICIENCY HIGH CONCENTRATION
RATIO SPACE SOLAR CELLS

H. Rauschenbach and R. Patterson
TRW DSSG
Redondo Beach, California

SUMMARY

A miniaturized Cassegrainian concentrator system concept has been developed for low cost, multi-kilowatt space solar arrays. The system imposes some requirements on solar cells which are new and different from those imposed for conventional applications. The solar cells require a circular active area of approximately 4 mm in diameter. High reliability contacts are required on both front and back surfaces. The back area must be metallurgically bonded to a heat sink. The cell should be designed to achieve the highest practical efficiency at 100 AMO suns and at 80°C. The cell design must minimize losses due to non-uniform illumination intensity and non-normal light incidence. The primary radiation concern is the omnidirectional proton environment.

INTRODUCTION

Recently, a practical, low cost sunlight concentrator system concept for space applications has been developed (reference 1). Multi-kilowatt solar arrays can be assembled using miniaturized Cassegrainian type optical concentrator elements that are assembled into matrices of parallel and series connected solar cells, modules, panels, and array blankets. Predicted solar cell operating temperature in earth orbit in the order of 80°C for solar illumination levels of 100 air mass-zero suns makes silicon an acceptable solar cell material; however, significant system efficiency improvements and cost reductions are projected for use of higher efficiency cells such as gallium arsenide and multiple-bandgap cells. This concentrator system imposes some requirements on the cells whether silicon or gallium arsenide, that are new and different from those that are typically imposed on non-concentrator solar cells for space arrays.

This paper defines those solar cell parameters that play important roles in the over-all array system efficiency and reliability which cannot be optimized by the array manufacturer, but rather must be addressed by solar cell designers and manufacturers.

CONCENTRATOR SYSTEM DESCRIPTION

The miniaturized Cassegrainian concentrator concept is illustrated in figure 1. The primary parabolic reflector concentrates the incident sunlight onto a secondary hyperbolic reflector which in turn directs the sunlight to the solar cell. Under off-pointing conditions, the concentrated sunlight also reflects from the surfaces of a tertiary, conical reflector.

387

The solar cell back side is metallurgically bonded to a heat sink similar to the bonding of a power transistor to its heat sink. Analysis indicates that for this type of bonding the cell to heat sink temperature gradient is negligibly small for concentration ratios up to and beyond 1000. The heat sink which serves as part of the electrical circuit, is mechanically stiffer and stronger than the solar cell and will transmit during orbital thermal cycling thermomechanical stresses into the cell.

The interconnector/solar cell joints are made by parallel-gap welding or ultrasonic joining, depending upon the cell's sensitivity to welding. The cell front contact interconnector attachment pad will be larger in area than the solar cell, resulting in an overall size of about 6 by 6 mm. The concentrated sunlight will reach the solar cell through a 4 mm diameter hole in the pad.

A multiplicity of the elements depicted in figure 1 are assembled into modules, several modules into panels, and several panels into array "blankets". A panel would typically be 2 x 4 m in size and approximately 12 mm (0.5 inch) thick. On each panel, a number of solar cells are electrically connected in parallel and series in conventional fashion. The selected theoretical geometric concentration ratio of 150 is reduced by reflection losses, light spillage, and light blockage to a net ratio of approximately 100. The concentrator element packing factor at the panel level is 0.90.

SOLAR CELL ARRAY SYSTEM LEVEL REQUIREMENTS

From a system point of view, the key solar array design driver for solar cell arrays of multi-hundred kilowatt ratings in near-earth orbits is cost. The total cost of electrical power (kW) at any given time in orbit, as well as the cost of energy (kWh) throughout the useful mission life span, is composed of several cost elements that relate to various aspects of the array design as shown in table 1. The overall life cycle cost scenario for a space solar array system parallels that of a typical terrestrial system (not restricted to a photovoltaic power system): over a long period of service life, the accumulated maintenance and repair costs become substantial relative to the initial acquisition cost, and as the wear-out life is approached, periodic maintenance and repair costs increase to a level where it becomes more cost effective to replace the system.

For the space solar array discussed in this paper, a recurring cost goal of $30/W in 1979 dollars has been established. This cost includes all materials and labor up to the array blanket level, but excludes bench quality assurance, integration and test, and main structural support, orientation, power transfer, and other components. The $30/W goal is expected to be achievable by the mid 1980s with a Cassegrainian type concentrator concept and, if achieved, would reduce the equivalent cost for present planar space arrays by approximately one order of magnitude. The projected cost breakdown for the Cassegrainian concentrator array is shown in table 2. The solar cell unit cost will be approximately proportional to the amount of semiconductor material used as shown in figure 2 and, hence, will decrease by approximately the same factor as the sunlight concentration ratio increases. The amount of

material used for concentrator optical elements is, to a first order approximation, nearly independent of the concentration ratio. However, increasing manufacturing complexity and precision required at higher concentration ratios is expected to drive the cost for the optical elements upward. Summing the theoretical solar cell and optical element cost curves results in a cost minimum near concentration ratios between 50 and 200. For this reason, a concentration ratio of 100 to 150 was chosen for more detailed study.

CONCENTRATOR SOLAR CELL DESIGN REQUIREMENTS

The key requirements according to which a concentrator solar cell for the miniaturized Cassegrainian concentrator concept for space applications should be designed and optimized are summarized in figure 3. These requirements are discussed below in detail.

Solar Cell Size

The required solar cells are relatively small in size, approximately 5 x 5 mm over-all with a 4 mm diameter active area. The exact over-all size must be determined based on a trade-off between heat transfer from the cell to the heat sink, cell cost variation with size, thermomechanical stress considerations, required contact area and ease of assembly. The cells could be round; however, square or rectangular cells of this small size may be easier to manufacture.

Solar Cell Contacts

The contact metallization system must be chosen to assure high mechanical strength, long thermal cycling fatigue capability, metallurgical stability throughout the terrestrial as well as the space operational periods of the total life span.

The current densities in the contacts of concentrator cells will be high. As an example, at 20% in-orbit conversion efficiency and 100-sun input, a typical solar cell output would be about 0.7A at 0.5V. If all of this current were to be extracted from the 4 mm circular opening in the front contact through a 2.5 μm (0.1 mil) thick metal layer, the current density would be about 2000A/cm^2. While such current density is not expected to cause ion migration, it certainly could cause excessive series resistance losses.

The most convenient cell contact configuration is the conventional front/back contact. This configuration permits the entire back contact area to be metallurgically bonded to the heat sink, assuring the lowest possible electrical and thermal impendances between the solar cell and the heat sink. As an alternate to a back surface reflector, the back contact may have a circular opening of about 4.5 mm diameter to permit photovoltically unusuable infrared radiation to exit from the cells and reach space through a corresponding opening in the heat sink.

The front contact preferably covers the entire semiconductor front area, except for a central, circular, 4 mm diameter opening that permits the concentrated sunlight to reach the cell's active area. Even though the front contact covers the entire cell area to obtain high mechanical load carrying capability and low electrical resistance, it is desirable to minimize the shadowing of active cell area by the front contact.

The light catcher cone should preferably be metallurgically joined to the solar cell front side to maximize heat transfer from the cone to the heat sink and to eliminate light losses that would occur in the gap between the cell surface and the lower truncated cone edge of a light catcher cone not mounted to the cell front surface. If the cone could not be joined directly to the front cell contact, it would have to be joined to a flat interconnector which in turn would be joined to the front cell contact.

Electrical Requirements

The concentrator solar cell should be designed for the highest practically achievable cell efficiency at 100 AMO suns and at 80°C cell temperature. A minimum cell efficiency of 20% for silicon cells and 30% for GaAs and tandem-junction cells is required at 28°C and 100 AMO suns. The AMO (airmass zero) solar spectrum is somewhat modified by degraded mirror spectral reflectance and coverglass spectral transmittance. Optical degradation due to the space environment is expected primarily in the short-wavelength range of the spectrum below 0.4 μm.

An important aspect of efficiency optimization has to address (i) shadowing of the active cell area by contacts and grid lines, (ii) non-uniformity of the incident, concentrated solar illumination, and (iii) the angle of incidence of the concentrated sunlight on the solar cell active area.

The non-uniformity of illumination arises primarily from imperfections in the optical elements, alignment errors between the various optical elements, and from system sun pointing errors. Figure 4 illustrates the case of a perfectly aligned optical system oriented at 0° off-point angle and at a 1° off-point angle. (The actual intensity contours are smooth; the depicted contours were computer-generated by a ray-tracing program using a relatively small number of rays.)

The angle of incidence of the concentrated sunlight varies over a relatively large range of angles due to the wide entrance aperture geometry of the Cassegrainian system. Figure 5 shows the relative energy that is incident at various angles. Most energy reaches the cell at angles in the range between about 10 and 23 degrees. To maximize the solar energy input to the cell at such angles, surface texturing may be required.

Radiation Resistance

The concentrator solar cells are shielded from radiation by approximately 0.15 mm (0.006 inch) thick fused silica equivalent from the front and by a much greater thickness from the back side. Radiation damage in the cell is caused primarily by protons in the lower and intermediate earth orbits. At geosynchronous altitude, the damage is roughly one-half due to electrons and one-half due to protons. The proton energy spectrum of interest to the solar cells ranges from near-zero energy to over 10 MeV after emerging from the shields. The low energy protons (in the order of 10 to 100 keV) are especially worrisome in that they tend to come to rest on surfaces and near the junction where they do much more damage than the higher energy protons (MeV-level) that penetrate the cell. It may become necessary to increase the solar cell shield thickness to protect the ultrahigh efficiency solar cell structures from excessive damage; however, all one can do is to reduce the number of protons of a given energy that enter into a cell throughout the total mission duration.

Thermophysical Properties

Analyses have shown that the solar cell orbital operating temperature of concentrator arrays, and hence the orbital operating efficiency capability, is as strongly dependent on solar cell absorptance values as it is for planar arrays. Achievement of a low value of solar absorptance is therefore mandatory. With polished front surface, back surface reflector cells, values of 0.75 are in production today. However, front surface texturing, which may be required to reduce reflectance, raises the absorptance. Another approach is to let the incident excess infrared radiation pass through the cell and through an opening in the cell back side contact and heat sink. Another, more costly approach would utilize spectrally selective filters on the coverglass and/or the solar cell. Solar absorptance values near 0.6 would certainly be desirable.

The value of the cell's emittance is not critical because the small cell area contributes only negligibly to cooling of the system by radiation heat exchange.

Coverglass Interface

Four options for installing a coverglass in front of the concentrator solar cells are illustrated in table 3 together with the corresponding trade-off criteria. Each configuration has technical and economic considerations that need be examined.

Reliability Issues

High contact reliability and electrical stability of concentrator solar cells are of paramount importance. Table 4 illustrates some of the more important reliability issues.

CONCLUSIONS

The possibility of solar cell efficiency improvement by sunlight concentration opens a new avenue of potentially reducing space array system size, weight, and cost, especially in conjunction with the use of more advanced very high efficiency solar cell structures.

An order of magnitude reduction in space array recurring costs and an array area reduction by 5% relative to equal-output planar arrays (14% efficient cells at 28°C) has been projected in reference 1 for a 100-sun concentrator concept using 20% efficient silicon solar cells at 28°C. An area reduction of 30% could be achieved with 30% efficient (at 28°C) gallium arsenide or multiple bandgap solar cells at a negligible recurring cost penalty, allowing for as much as a $2 per cell ($8/cm^2) part cost.

REFERENCE

1. Study of Multi-kilowatt Solar Arrays for Earth Orbit Applications. TRW Final Technical Report No. 33295-6001-UT-00 on Contract NAS8-32986 with NASA MSFC dated 19 Sept. 1980.

Table 1. Cost Elements Related to Array Design

Array Design Parameter	Life Cycle Cost Relationship
Smaller Area	• Lower assembly cost • Lower cost for lesser amount of orbit maintenance fuel required • Higher solar cell unit cost
Lower Mass	• Lower recurring materials cost • Potentially lower launch cost (Volume-related)
Smaller Stowed Volume	• Potentially lower launch cost (Mass-related)
Longer In-orbit Life	• Potentially higher recurring cost • Lower cost for fewer replacement units (recurring and transportation) • Lower cost for less in-orbit repair/maintenance work

Table 2. Projected Concentrator Array System Recurring Specific Costs (in 1979 Dollars)

Element	Specific Recurring Costs ($/W) (1987 Technology)
	Concentrator Array
Solar Cells	5.7
Covers	-
Optical Elements	2.5
Substrates	-
Heat Sinks	0.7
Harnesses	4.3
Materials	1.9
Blanket Labor	5.5
Structures	4.6
Structure Labor	4.7
Total	30.0

Table 3. Coverglass Mounting Options

OPTION	TYPE	MASS	INTENSITY (SUNS)	DARKENING		COMMENTS
				COVER	ADHESIVE	
CONE → COVER, CELL	ELECTROSTATIC BOND OR INTEGRAL	LOW	100	POSSIBLY SEVERE	NONE	● REQUIRES DEVELOPMENT AND TEST EVALUATION
CONE → COVER, CELL	ADHESIVE MOUNTED	LOW	100	POSSIBLY SEVERE	SEVERE	● NOT PRACTICAL
CONE → COVER, CELL	SEPARATELY MOUNTED	MEDIUM	20	MEDIUM	NONE	● BASELINE DESIGN
COVER, CONE, CELL	SEPARATELY MOUNTED	HIGH	1	LOW	NONE	● IMPEDES CELL COOLING ● POOR MECHANICAL STRENGTH (VIBRATION FAILURES)
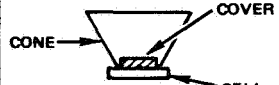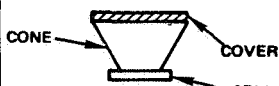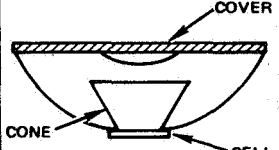
Table 4. Solar Cell Related Reliability Issues

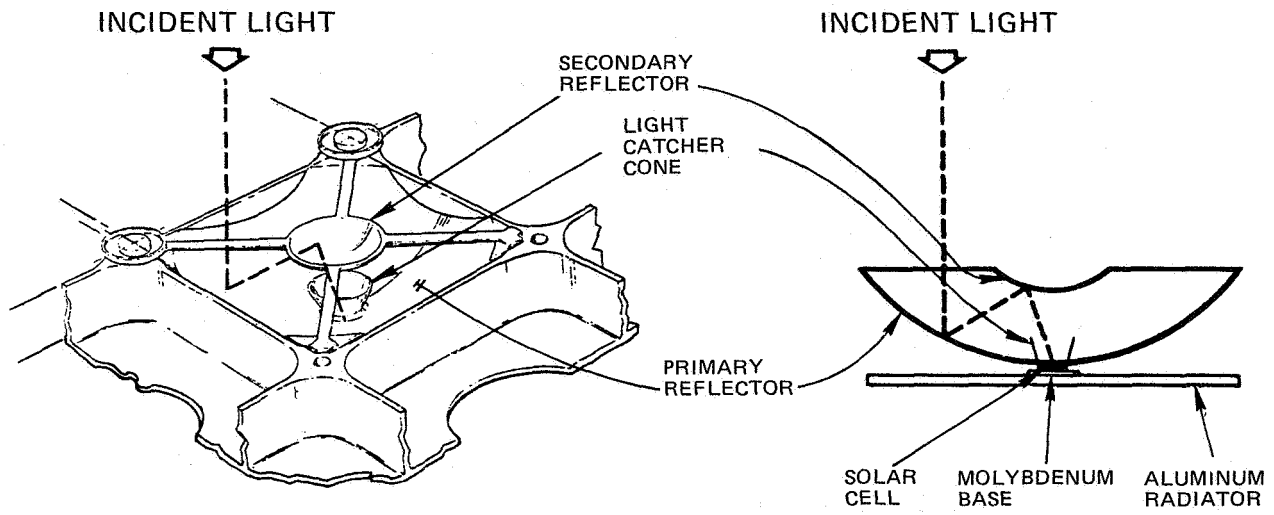| Potential Failure Modes	Failure Cause	Design Action
Cell contact separation from semiconductor material	● Failure rate increase with increasing temperature ● Hot spot phenomena	● Lowest possible solar absorptance ● Connection of many cells in parallel
Interconnector-to-cell contact and cell contact-to-heat sink joint fatigue cracking	● Thermal cycling in orbit	● Matching of coefficients of linear thermal expansion ● Selection of best joining process (ultrasonic, welding, brazing, etc.) ● Selection of long-fatigue life metals (durability, etc.) ● Reduction of temperature range
Anomalous electrical degradation (fill factor, efficiency, etc.)	● Thermal cycling in orbit ● Radiation	● Solar cells must be able to tolerate various environmental stresses

INCIDENT LIGHT

SECONDARY
REFLECTOR

LIGHT
CATCHER
CONE

PRIMARY
REFLECTOR

INCIDENT LIGHT

SOLAR
CELL

MOLYBDENUM
BASE

ALUMINUM
RADIATOR

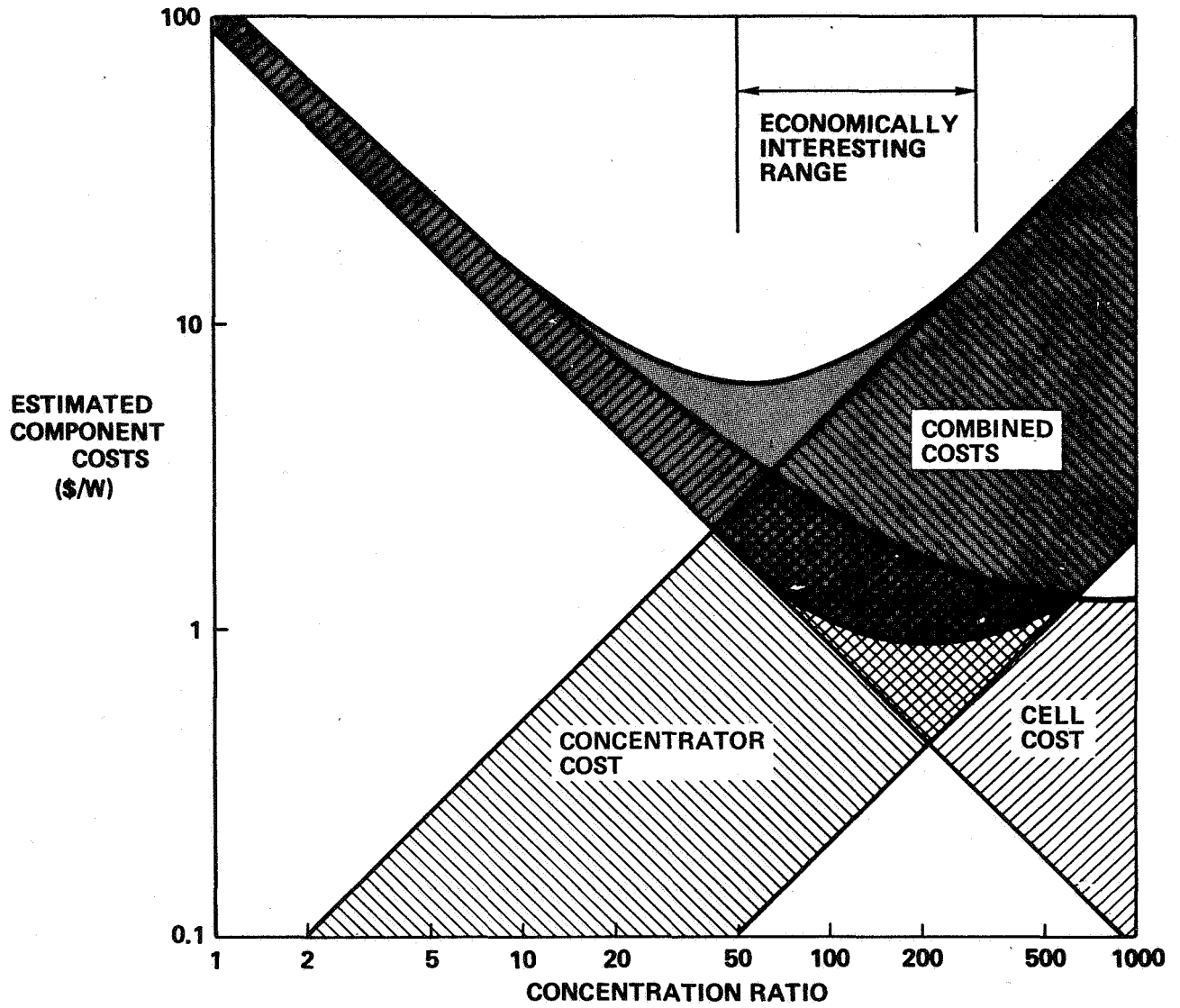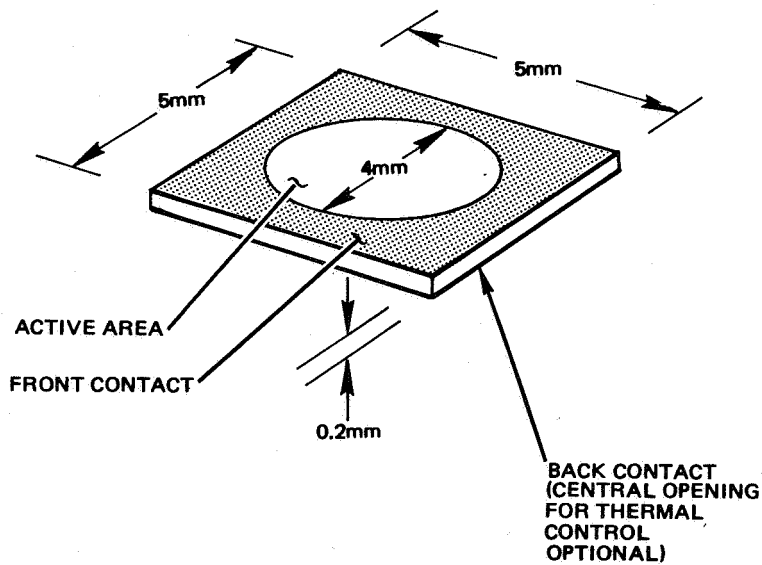Figure 1. Cassegrainian Concentrator Element Concept

Figure 2. Selection of Minimum-Cost Concentration Ratios

PARAMETER	REQUIREMENT
EFFICIENCY AT 28°C, 100 SUNS	20%, Si 30%, Ga As
NORMAL OPERATING TEMPERATURE	80°C
TEMPERATURE CYCLING RANGE	-100°C TO +100°C
TEMPERATURE CYCLES	60,000 CYCLES
SOLAR ABSORPTANCE	≤ 0.75
ANGLE OF INCIDENCE	0 TO 30°, 20° NOMINAL
RADIATION TOLERANCE	PROTONS 1 TO 10 MeV

Figure 3. Concentrator Solar Cell Reference Design and Requirements
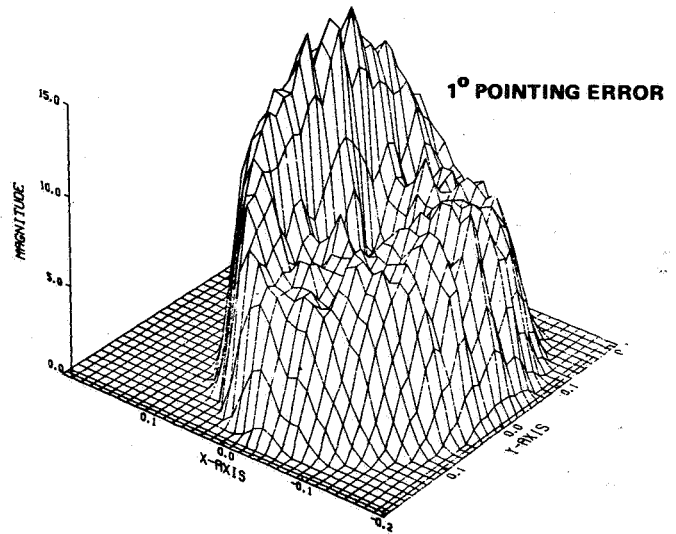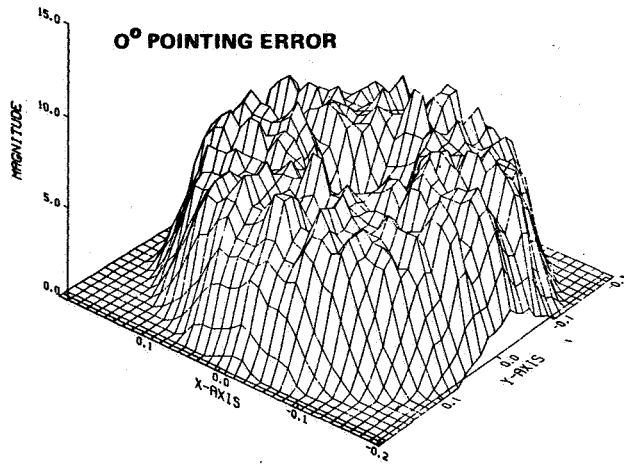
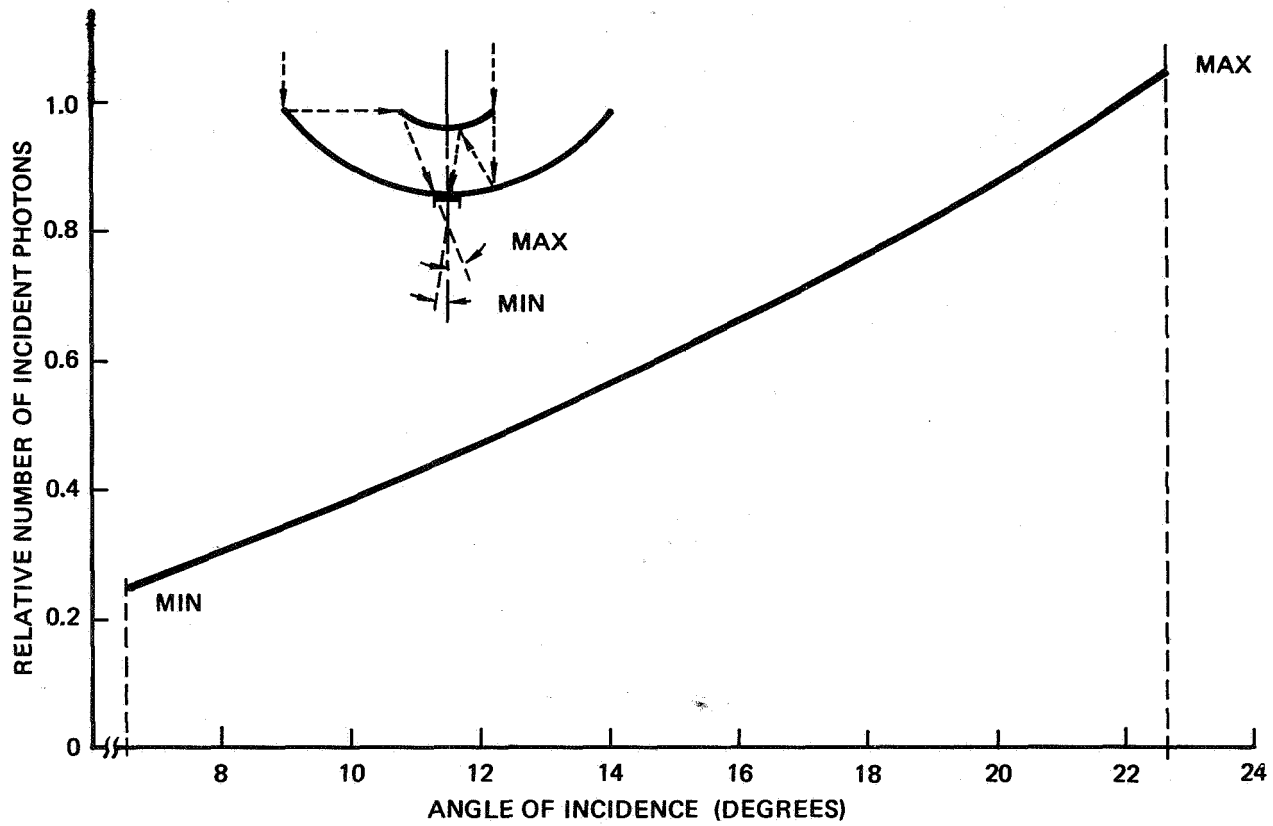Figure 4. Cassegrainian Concentrator Intensity Uniformity

Figure 5. Relative Angular Distribution of Solar Energy
Incident On a Concentrator Solar Cell

BLANKET TECHNOLOGY WORKSHOP REPORT

John A. Scott-Monck
Jet Propulsion Laboratory
Pasadena, California

The solar array blanket, defined as a substrate covered with inter-connected and glassed solar cells, but excluding the necessary support structure, deployment, and orientation devices, cannot be considered as a completely independent element of technology. Particularly in larger array designs, the interactions between the blanket and the structure that is used to package, deploy, support and, if necessary restow it, can be significant design drivers. Systems constraints such as spacecraft configuration, size and payload requirements also may influence blanket design. Thus it is extremely difficult to assign a blanket specific power goal without some knowledge of the mission class that will utilize it.

The three main mission classes considered were low Earth orbital (LEO), intermediate, or LEO to GEO transfer, and geosynchronous (GEO). Although interplanetary missions could be considered to be a separate class, their requirements, primarily power per unit mass, are generally close enough to geosynchronous missions to allow this mission class to be included within the third type. Examination of the critical elements of each class coupled with considerations of the shuttle capabilities was used to define the type of blanket technology most likely required to support missions that will be flown starting in 1990.

There are three user groups currently operating in the space environment; NASA, the military, and the communications satellite industry. NASA has interests in all three mission classes, as does the military to some degree, while the third group is primarily interested in geosynchronous orbits. All three user groups indicate the need for increasing array power levels, rising from the present 1-3 kW to upwards of 25 kW.

LOW EARTH ORBITAL REQUIREMENTS

Technology capable of satisfying the immediate forecasted needs for the Earth orbital applications does exist in the form of the SEP type array. Thus the question of standardizing this technology was considered. It was the general consensus that the requirements placed on the array by mission planners and spacecraft system designers will mandate continual modifications, minor and major, which will tend to prevent any high degree of array standardization.

The larger power systems, planned for the future, must of necessity be less expensive than smaller arrays which can cost in excess of 1000 dollars per watt EOL. Concern over the growing cost of photovoltaic arrays was expressed. Although the array typically makes up a very small fraction ($<$5 percent) of the total mission cost, the steady increase in cost may make photovoltaics less attractive for future missions and thus make it easier for alternative power sources to compete. The SEP array cost does not appear to be a major concern at this time, but cost of power will become very important as array requirements exceed 100 kW. Since LEO power costs

are determined by life cycle considerations, it is very important that the operating lifetime of LEO arrays be maximized. Technology to guarantee a minimum lifetime of 5 years is critical, while 10 year operation is highly desirable.

A key conern in this area is the question of orbital "drag," which becomes more important as the size of the array increases. To reduce this problem, higher efficiency cells which will reduce array size for a given power level, will be necessary, as will be in-orbit partial or full restowage capability.

The shuttle launch capability for LEO applications does not place significant mass constraints on arrays. However, the shuttle launch cost is determined by the amount of shuttle bay volume taken up by the mission. Thus more attention must be paid to properly packaging arrays and blankets rather than to reducing their mass.

INTERMEDIATE OR TRANSFER ORBIT REQUIREMENTS

Intermediate orbits (>500 km) which are used predominantly by military satellites place a critical requirement on radiation resistance. Equivalent 1 MeV fluences exceeding $1x10^{16}$ e/cm^2 would be experienced by the blanket. Radiation resistance is also required in order to consider using low thrust propulsion systems to boost payloads from LEO to GEO. Efforts to significantly reduced the amount of degradation presently observed in silicon solar cells is encouraged. The superior radiation resistance predicted for gallium arsenide argues for its consideration for these orbits. The alternative approach is to develop blankets capable of surviving the temperatures necessary to anneal the electrical degradation caused by the radiation environment.

GEOSYNCHRONOUS ORBIT REQUIREMENTS

There was a unanimous agreement that geosynchronous orbit requirements are the main driver for blanket technology. Shuttle costs and the IUS launch capability place a premium on lowering the array mass. There will always be pressure to reduce array mass in order to increase the satellite's "traffic" (communication channels, etc.) potential. The IUS is designed to launch ~2300 kg into GEO. Except for a few unique situations, the mass allowance for the solar array will be constrained to ~150 kg.

Power levels of 25 kW and up will be required for space platforms and space based radar. This leads to the conclusion that arrays possessing a beginning-of-life specific power of ~200 W/kg could be required. Translating the array specific power to a blanket specific power cannot be easily done since structural and systems requirements must be considered. Generally, the fraction of the array mass resulting from the structure becomes smaller as the array size increases. Thus, the overall specific power of the array would likely be greater for a large array (>10 kW) than a smaller array (~1 kW) even though the same specific power blanket was used for both.

A set of technology requirements necessary to support a 1990 launch was established. From previous experience, it was determined that these goals would have to be accomplished by 1985. It was determined that a 300 W/kg blanket (BOL) including bus mass, could be achieved by 1985 without the need for a major "breakthrough" in blanket technology. This will require that by

402

1985 silicon solar cells 50-60 μm thick with an AMO efficiency of 14 percent are in production. New and innovative processes for assembling and laying down very thin cells must have been reduced to practice. The present method of covering solar cells will have to be replaced. Possible alternatives suggested were thin (25-50 μm) integral covers or organic encapsulants. The approach to interconnecting must be modified to accomodate welding of extremely thin interconnects. To reduce the mass of the bus system it will be necessary to operate blankets near 200 volts. This led to a discussion concerning array space charging effects and plasma interactions. It was agreed that this was a potential major problem, and further, that very little is actually understood in this area. It was strongly recommended that space experiments aimed at providing information on the effects of plasma leakage on blanket performance be instituted once the shuttle is operational. In addition, as advanced blankets are developed, they should be flight tested as quickly as possible, preferably on an annual basis.

1990 REQUIREMENTS

It was conceded that blanket specific power must probably reach 400 W/kg EOL (1×10^{16} e/cm^2) to assure that arrays can satisfy the requirements for advanced geosynchronous missions. The members felt that revolutionary rather than evolutionary developments would be necessary. For example, the solar cells employed in this advanced blanket would have to be 15 to 16 percent efficient (EOL) at operating temperature. The cell's mass would have to be equivalent to no more than 50 μm of silicon. Obviously, advanced encapsulants or covers would be required. Although low mass blankets imply minimum back surface radiation shielding, the trade-offs seem to indicate that reduced shielding does result in improved EOL specific power in the cases studied to date. Further reductions in harness mass will be required, thus making even higher array operating voltages, in the order of 1000 V, necessary. Although not discussed in any great detail, concepts such as concentration and more efficient optical coupling, which would reduce the blanket operating temperature, were deemed appropriate areas for development. It was not possible to accurately forecast when advanced blankets ($\geq$400 W/kg EOL) would be available, but it was agreed that work aimed at developing this technology should begin immediately.

1. Report No. NASA CP-2169	2. Government Accession No.	3. Recipient's Catalog No.
4. Title and Subtitle SPACE PHOTOVOLATIC RESEARCH AND TECHNOLOGY - 1980 High Efficiency, Radiation Damage and Blanket Technology		5. Report Date
		6. Performing Organization Code 506-55-42
7. Author(s)		8. Performing Organization Report No. E-469
		10. Work Unit No.
9. Performing Organization Name and Address National Aeronautics and Space Administration Lewis Research Center Cleveland, Ohio 44135		11. Contract or Grant No.
		13. Type of Report and Period Covered Conference Publication
12. Sponsoring Agency Name and Address National Aeronautics and Space Administration Washington, D.C. 20545		14. Sponsoring Agency Code

15. Supplementary Notes

16. Abstract

This three-day conference, fourth in a series that began in 1974, was held at the NASA Lewis Research Center on October 15 to 17, 1980. The conference provided a forum for the discussion of space photovoltaic systems, their research status, and program goals. Papers were presented and workshops were held in a variety of technology areas, including high-efficiency silicon solar cells, gallium arenside solar cells, cascade solar cells, blanket (or array) technology, and radiation damage.

17. Key Words (Suggested by Author(s)) Photovoltaic cells Solar cells Solar arrays	18. Distribution Statement Unclassified - unlimited STAR Category 44		
19. Security Classif. (of this report) Unclassified	20. Security Classif. (of this page) Unclassified	21. No. of Pages 412	22. Price* A08

* For sale by the National Technical Information Service, Springfield, Virginia 22161